SEISMIC ASSESSMENT AND RETROFIT OF REINFORCED CONCRETE COLUMNS

Konstantinos G. Megalooikonomou

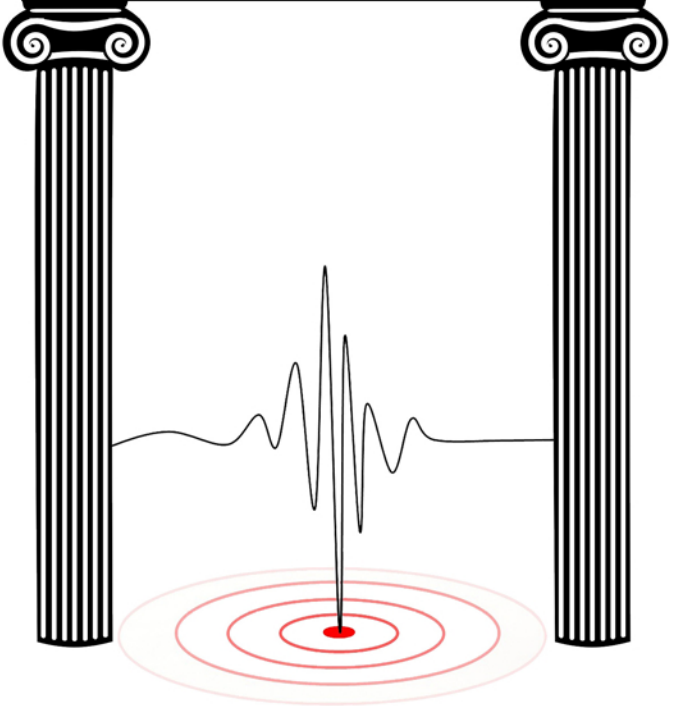

Seismic Assessment and Retrofit of Reinforced Concrete Columns

Seismic Assessment and Retrofit of Reinforced Concrete Columns

By

Konstantinos G. Megalooikonomou

Cambridge
Scholars
Publishing

Seismic Assessment and Retrofit of Reinforced Concrete Columns

By Konstantinos G. Megalooikonomou

This book first published 2019

Cambridge Scholars Publishing

Lady Stephenson Library, Newcastle upon Tyne, NE6 2PA, UK

British Library Cataloguing in Publication Data
A catalogue record for this book is available from the British Library

ISBN (10): 1-5275-2785-9
ISBN (13): 978-1-5275-2785-0

To My Dedicated Parents and Brother

TABLE OF CONTENTS

ACKNOWLEDGEMENTS

I would like to thank all the Professors and colleagues who I met throughout my research experience. Above all, I am grateful to the Alexander S. Onassis Public Benefit Foundation for providing me with a triennial scholarship (Scholarship Code: F ZI 086-1 2012-2013/ 01/09/2012 – 29/02/2016) to pursue a Ph.D. degree in Civil Engineering at the University of Cyprus. Without their financial support during this worldwide economical crisis, this book would not have been realized.

CHAPTER ONE

INTRODUCTION

Existing reinforced concrete buildings constructed before the development of modern seismic design provisions represent one of the largest seismic safety concerns worldwide. Such buildings are vulnerable to significant damage and even collapse when subjected to strong ground shaking. The collapse of reinforced concrete buildings has been the cause of many of the fatalities in past earthquakes. Since 1980, after the capacity design concept was introduced into the seismic design code provisions, the seismic safety gap between the newly designed seismic resistant buildings and those constructed before 1980 has widened, causing worldwide concern. The crucial issue that was evident after the earthquakes in 1999 in Athens (Partnitha) and in Turkey (Kocaeli) and was underlined by the destructive earthquake of L'Aquila (2009) in Italy (an event which the author experienced personally as a resident of L'Aquila at the time) is the need to improve assessment and retrofit procedures for existing reinforced concrete buildings.

Reinforced concrete (RC) columns play a very important role in structural performance. Behaviour of RC columns in shear and flexure has been studied for decades. In the case of flexural behavior, sectional analysis, or a fiber model in one-dimensional stress field gives acceptable predictions in terms of ultimate strength and yielding deformation. Performance of reinforced concrete columns dominated by shear or shear-flexure cannot be estimated by applying only a sectional analysis because shear behavior is not taken into account in the approach. For evaluating the shear response of structural elements, such as beams and columns, many analytical models and theories have been presented in the past. Some of the most commonly used approaches are strut and tie models (Mörsh 1902, Ritter 1899) and the Modified Compression Field Theory (MCFT) (Vecchio & Collins 1986). MCFT is a powerful tool to model the response of RC elements subjected to in-plane shear and normal stresses. The method is based upon a large number of membrane elements tests and treats reinforced concrete in an average way. Specifically, the method is formulated in terms of average stresses and strains across the element and

is supplemented by local crack checks. The method is formulated with consideration to equilibrium, compatibility, and approximate stress-strain relationships of the materials.

Recently, another aspect that has roused the interest of researchers is the axial failure of columns that can lead to collapse of a building (Elwood and Moehle 2005). Before the introduction of special requirements in the 1970s, reinforced concrete building frames constructed in zones of high seismicity had details and proportions similar to frames designed primarily for gravity loads. Columns generally were not designed to have strengths exceeding beam strengths, so column failure mechanisms often prevail in buildings dating from that era. Relatively wide spacing of transverse reinforcement was common, such that column failures may involve some form of shear or combined flexure – shear failure. As shear failure proceeds, degradation of the concrete core may lead to loss of axial load carrying capacity of the column. As the axial capacity diminishes, the gravity loads carried by the column must be transferred into neighboring elements. A rapid loss of axial capacity will result in the dynamic redistribution of internal actions within the building frame and may progressively lead to collapse.

During earthquake excitation columns can experience a wide variety of loading histories, which may consist of a single large pulse or several smaller-amplitude cycles, occasionally leading to either shear failure or even collapse – i.e. a loss of gravity-load bearing capacity of the column. Previous research has demonstrated that the onset of this type of collapse cannot be quantified unilaterally by a single combination of shear force and axial load values, but rather, it is characterized by an interaction envelope that depends on the history of loading and the peak magnitude of deformation exertion attained by the column (max. drift demand). Recent studies (Chapter 2) attribute particular influence to the final mode and characteristics of failure by the occurrence of fluctuating axial load about a mean value, on some occasions the load becoming actually tensile due to the overturning effects imparted by the earthquake. Furthermore it has been demonstrated that an increase in the number of cycles past the yield displacement can result in a decrease in the drift capacity at shear failure. Understanding these effects and developing mechanistic tools by which to identify the characteristics of failure at the loss of axial load bearing capacity and the implications of drift history is one of the objectives of this book.

In the present book a fiber beam-column element accounting for shear effects and the effect of tension stiffening through reinforcement-to-concrete bond was developed, in order to provide an analytical test-bed for

simulation and improved understanding of experimental cases where the testing of RC columns actually led to collapse. Emphasis is particularly laid on lightly reinforced columns. The combined experimental/numerical results provided useful information for the definition of plastic hinge length in columns through consideration of yield penetration effects. The required confined zone in critical regions of columns and piers undergoing lateral sway during earthquakes is related to the plastic hinge length where inelastic deformation and damage develops. The exact definition of the plastic hinge length stumbles upon several uncertainties, the most critical being that the extent of the inelastic region evolves and spreads with the intensity of lateral displacements. Design codes quantify a reference value for the plastic hinge length, through calibrated empirical relationships that account primarily for the length of the shear span and the diameter of primary reinforcing bars. The latter term reflects the effects of bar yielding penetration in the support of columns. Here a consistent definition of plastic hinge length is pursued analytically with reference to the actual strain state of the reinforcement.

Over the past three decades, fibre-reinforced polymer (FRP) composites have emerged as an attractive construction material for civil infrastructure, rehabilitation, and renewal. These advanced materials have been successfully used for reinforcing new structures as well as the strengthening/rehabilitation of existing buildings and bridges. The use of FRP composites, analysis and design, and techniques for installation are continually being researched and it is anticipated that the use of these advanced materials will continue to grow to meet the demands of the construction industry. Recent seismic events around the world continue to underline the importance of seismic retrofit and strengthening of existing concrete structures leading to the need for new, practical, occupant-friendly and cost-effective remedial solutions.

In this context, the Fiber Reinforced Polymer (FRP)-confined concrete model contained in a well-known Bulletin by the International Federation for Structural Concrete (*fib*) has been enhanced to take into account the superposition of the confining effects of the already existing steel reinforcement with that of the FRP jacketing applied when retrofitting RC columns. Columns are here modeled with a fiber-based nonlinear beam-column element (with displacement formulation) in which the constitutive law for concrete presented in this book is implemented. This allows for the immediate incorporation of shear strains (uncoupled from the normal ones) at the material level. The averaged response of the two different regions—concrete core and concrete cover—in the cross-section allows the assignment of a unique stress-strain law for all the fibers/layers of the

section. Correlation with experimental studies from the literature is performed to validate the proposed iterative procedure.

Specifically, the organization of the present book is the following: After the introduction in Chapter 1, Chapter 2 contains a literature review of the part of seismic assessment of old-type RC columns. Chapter 3 presents the correlation of - the state of the art – analytical models for seismic assessment of reinforced concrete columns with the experimental results of a well-known experimental database. Chapter 4 defines the plastic hinge length in columns though consideration of yield penetration effects. A mechanically consistent approach in determining inelastic rotation capacity of reinforced concrete columns is introduced. Chapter 5 presents the development of a force-based fiber beam-column element accounting for shear and tension stiffening effects. Chapter 6 presents new developments on FRP seismic retrofit of RC columns with confining wraps or jackets that has proven to be an efficient technique for the seismic retrofit of structures. A new constitutive model for FRP -and steel-confined concrete, including shear effects, is included in this Chapter. Finally, in Chapter 7 important conclusions based on the described research in this book are drawn.

To sum up, this book is introducing recent advances in research that intends to attract academic staff, researchers, under- or post- graduate students and professional engineers dealing with seismic assessment, repair and retrofit of RC structures such as buildings and bridges.

CHAPTER TWO

STATE OF THE ART ON SEISMIC ASSESSMENT OF REINFORCED CONCRETE COLUMNS

The procedure of estimating the strength, the deformation capacity and the expected mode of failure in primary members of a RC frame structure, that is, the complete process of seismic assessment, has been recently supported by background documents in both Europe and the U.S. (KAN.EPE. 2014, EN 1998-3 2005, ASCE/SEI-41 2007, and most recently by the draft of the New Model Code 2010 by the *fib*). The acceptance criteria proposed provide a complex system of evaluation, but the various steps of this process are not vested with a uniform level of confidence as compared with the experimental results. Strength values can be estimated with sufficient accuracy only if the modes of failure involved are ductile. The level of accuracy is degraded when considering brittle mechanisms of resistance, and the associated deformation capacities, which are used as a basis for comparison with deformation demands to assess the level of performance (i.e. the damage), generally do not correlate well with proposed Code estimations. However, in the process of assessment it is a critical matter seriously affecting public safety, to determine whether flexural yielding will precede shear failure (so as to ensure ductility) or whether a brittle failure ought to be anticipated prior to reinforcement yielding. Even when flexural yielding may be supported it is also important to dependably estimate the ductility level beyond which shear strength may be assumed to have degraded below the flexural strength, leading to a secondary post-yielding failure that limits the available deformation capacity (Fig. 2-1).

Stiffness properties and inelastic the earthquake response of frame members are usually studied based on a statically determinant structure comprising a cantilever reinforced concrete column under lateral loading. Given the material properties (be they nominal, assumed or experimentally measured), geometry, the loading conditions and loading history, it is theoretically possible to analyze the cantilever so as to study the interactions between various aspects of its response such as flexure, shear

and reinforcement development capacity. In recent years the fixed ended column specimen in lab experiments is preferred to be compared to the cantilever arrangement, since the interaction of two end moments and more realistic curvatures can be obtained, whereas they are more versatile in dynamic tests (as it is possible to mount masses on top of the restraining beam at the upper end of the column, thus simulating more realistically the actual circumstances in the field). Moreover, in the case of lightly reinforced concrete columns which are representative of older construction, major inclined shear cracks have been seem to occur in the midheight column region (near the point of column inflection), a crack pattern that cannot be reproduced with the cantilever specimen since its tip is free to rotate (only restrained in translation) and sustains no damage in that region. In addition the elongation due to damage of the double curvature member is more representative of a typical building column under earthquake loading. The assessment performance objectives in such experiments can be categorized and documented by obtaining the full inelastic response until the collapse of the RC column.

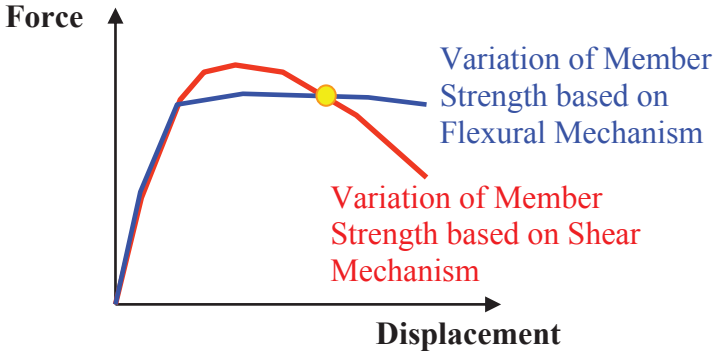

Fig. 2-1: Capacity curve due to flexural or shear mechanism.
Failure denoted with yellow point.

According to Eurocode 8, Part 3 (EN 1998-3, 2005), the fundamental performance criteria related to the state of the structural damage are defined through three Limit states that span the range of the member resistance curve (Fig. 2-2.a), and are defined according to the severity of damage that they represent as follows: “Damage Limitation (DL)”, “Significant Damage (SD)”, and “Near Collapse (NC)”. The target displacement of the column based on the earthquake load defines which of these Limit States are reached. In the following figure (Fig 2-2.b) the

performance objectives for these Limit States are documented in practical terms.

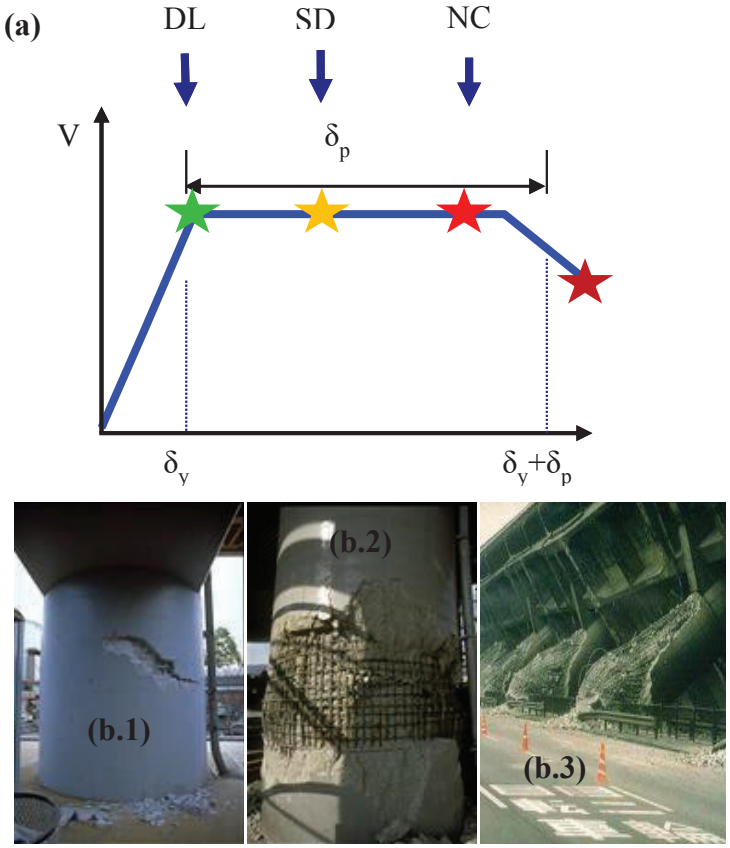

Fig.2-2: Damage of bridge columns: a) Member resistance curve and definition of limit states according with EN 1998-3 (2005). (b.1) Damage Limitation Limit State (b.2) Significant Damage Limit State (b.3) Near Collapse Limit State.

The objective of this chapter is to critically review and identify, through a thorough review of the published experimental evidence, the critical issues affecting the resistance curve of columns during earthquake action (strength and deformation capacity) and the limiting brittle modes

of failure. This is important since the column resistance curve eventually controls the buildings' resistance in a relatively straightforward manner (Fotopoulou et al., 2011) whereas a sudden loss of column strength to overbearing loads may lead to collapse and human losses. In the context of a displacement based evaluation framework, not only the relevant shear strength is important, but also the corresponding column displacement capacity. In this regard, recent experimental evidence of shear critical reinforced concrete columns will be reviewed along with recently developed analytical models and the relevant state of the art of code assessment procedures.

Existing Experimental Studies on Shear Dominated RC Columns

The behaviour of shear-critical reinforced concrete columns has been the subject of extensive study and research in recent years as this seems to remain a challenging concrete mechanics problem. Shear dominant behaviour is reported in columns with a low aspect ratio, but also in lightly reinforced columns containing low ratios of transverse reinforcement. Section geometry (rectangular or circular sections) is one of the parameters that differentiate the available test results; cyclic pseudo-static, hybrid pseudo-dynamic and dynamic tests are included in the review. Some experimental studies are dedicated to the influence of axial load fluctuation on the response of the column (fluctuation of axial load about the value that is affected by the overbearing loads occurring during the seismic event as a result of the overturning action of lateral loads, and is most significant in columns located at a distance from the centre of mass of the building, i.e., on the perimeter of the structure).

The same effect is seen in bridge piers belonging to multiple-column bents where it may be easily demonstrated that the axial load fluctuation is proportional to the horizontal (seismic) forces. Columns are also subjected to the vertical components of ground motion, which is not correlated concurrently with the horizontal loading. Past earthquake records have shown that in some cases, vertical ground motions cannot be ignored, particularly for near-fault situations. For example, the lateral displacement ductility of a column, designed based on constant axial load with a relatively low axial load ratio, can become unsatisfactory when the actual axial load due to the overturning effects or where the vertical ground motion exceeds the "balanced" axial load limit (i.e., about 40% of the column crushing load). The problem becomes even more significant when shear design is considered. The increase of axial load from the design level

(which typically is in the order of 5% to 10% of the crushing load) to the level of the balanced value generally increases the column flexural capacity causing a commensurate increase in the design shear demand (based on capacity design principles). On the other hand, a change in the axial load value from compression to tension may compromise significantly the column shear strength.

A review of Influential Cyclic Column Tests

From among the multitude of published tests on cyclically loaded columns under lateral displacement reversals (see also Chapter 3), a number of tests have received greater attention as their response was used as points of reference in calibrating the design expressions for shear published in the literature. On account of the weighty contribution of these experimental studies to the formation of the current assessment framework, these studies are reviewed separately in the present work.

Ang, Priestley and Paulay (1989) performed experimental tests to study the seismic shear strength of circular columns. A series of twenty-five 400 mm-diameter columns, considered to be approximately one-third scale models of typical bridge columns, were constructed and tested under cyclic reversals of lateral loading, as part of a major investigation into the strength and ductility of bridge pier columns. Variables in the test program included axial load level, longitudinal reinforcement ratio, transverse reinforcement ratio and aspect ratio. The column units were tested as simple vertical cantilevers. Results indicated that the shear strength was dependent on the axial load level, the column aspect ratio, the amount of transverse spiral reinforcement and the flexural ductility displacement factor. At low flexural ductilities, the additive principle for shear strength, based on a concrete contribution plus a 45-deg truss mechanism involving the spiral reinforcement and diagonal concrete compression struts, described the behavior quite well. But at flexural displacement ductilities greater than two, the tests demonstrated a gradual reduction of lateral load strength with increasing ductility, whereas the inclination of the diagonal compression struts of the truss mechanism relative to the longitudinal axis decreased. Here it is worth noting that significant rotations occurred at the base of these specimens artificially distorting the data in the direction of more excessive strength loss due to P-Δ effects (Ioannou and Pantazopoulou, 2016).

Wong, Paulay and Priestley (1993) conducted a series of biaxial tests that included 16 circular (400 mm-diameter) reinforced concrete cantilever columns with an aspect ratio of two and different spiral reinforcement

contents in order to investigate the sensitivity of the strength and stiffness of shear-resisting mechanisms to various displacement pattern and axial compression load intensities. Elastic shear deformations in squat circular columns with small or no axial compression load were found to be significant. It was concluded that shear deformation ought to be included explicitly in the estimation of initial stiffness of a column, so that a reliable relation between the ductility demand and the corresponding drift could be established. A general observation was that in comparison with uniaxial displacement paths, biaxial displacements led to more severe degradation of stiffness and strength, and thereby, increased energy dissipation. However, the reduction of initial shear strength and ductility capacity of squat columns (recall that the aspect ratio of the tested columns was equal to 2), subjected to biaxial displacement history was not very significant. The value of the dependable displacement ductility level attained during biaxial displacements was, on average, less (i.e. a value difference of 1) than that obtained in identical units subjected to uniaxial loading history. Initial shear strength of units with brittle shear failure was reduced by about 5 to 10 percent, depending on the axial load level when biaxial rather than uniaxial loading was considered. Finally, one more important finding was that the shear carried by spirals was underestimated when using a 45-deg potential failure plane; the observed major diagonal cracks developed in squat columns at much lower angles with respect to the longitudinal axis of the member.

Lynn et al. (1996) constructed and tested 8 full-scale square section (457 mm) columns that had widely-spaced perimeter hoops with 90-degree bends with or without intermediate S-hooks and with longitudinal reinforcement with or without short lap-splices. The columns had an aspect ratio of 3 and were loaded with constant axial load at low and intermediate levels, and were subjected to lateral deformation cycles until the column was incapable of supporting a lateral or vertical load. Failure modes included localized crushing of concrete, reinforcement buckling, lap-splice and flexural bond splitting, shear and axial load collapse. Loss of gravity load capacity occurred at or after significant loss of lateral force resistance. Where response was governed by a shear, gravity load failure occurred soon after loss of lateral force resistance. Where response was initially governed by lap-splice deterioration and gravity loads were relatively low, gravity load resistance was maintained until eventual shear failure occurred. Where response was predominantly flexural, gravity load capacity was maintained to relatively large displacements.

As earthquakes and laboratory experience show that columns with inadequate transverse reinforcement are vulnerable to damage including

shear and axial load failure, another study in this direction is by Sezen and Moehle (2006). The latter included four full-scale square section (457 mm) columns (aspect ratio equal to 3) with light transverse reinforcement that were tested quasi statically under unidirectional lateral loads with either constant or varying axial loads. Test results showed that responses of columns with nominally identical properties varied considerably depending on the magnitude and history of axial and lateral loads applied. For the column with a light axial load and reversed cyclic lateral loads (applied through a displacement history), apparent strength degradation triggered shear failure after the flexural strength was reached. Axial load failure did not occur until displacements had increased substantially beyond this point. The column with high axial load sustained brittle shear compression failure and lost axial load capacity immediately after shear failure, pointing out the necessity of seismic evaluations to distinguish between columns on the basis of axial load level. The column tested under varying axial load showed different behavior in tension and compression, with failure occurring under compressive loading.

A review of relevant Pseudodynamic Tests

It was stated earlier that columns in RC structures carry axial forces owing to dead and live loads and a combined varying axial force, moment and shear when excited by earthquake ground shaking. The varying axial loads lead to simultaneous changes in the balance between their supply and demand in axial, moment and shear to an extent that eludes adequate estimation by the code models. To consider the time varying effects of the ground motion on these combined actions, simulated dynamic loads were applied using a hybrid simulation of the earthquake effects on the structural model wherein the column specimen is assumed to belong. Kim et al. (2011) used hybrid simulation, where an experimental pier specimen was tested simultaneously and interactively with an analytical bridge model which was modelled on the computer; at each step of the dynamic test the forces applied on the specimen were calculated by solving the dynamic equation of motion for the structure where the stiffness contribution of the modelled column in the global structural stiffness was estimated from the measured resistance in the previous step. Additionally, two cyclic static tests with constant axial tension and compression were performed to study the effect of the axial load level on the bridge piers. It was found that by including vertical ground motion the axial force fluctuation on the test specimen increased by 100%, resulting at times in a net axial tension that was not observed under horizontal motion alone.

This high axial force variation led to a fluctuation of lateral stiffness and a more severe outcome of cracking and damage. Moreover, inclusion of vertical ground motion significantly affected the confining spiral strains. Thus, whereas the maximum spiral strain of the specimen subjected to horizontal ground motion occurred at 20% of the pier height, in the case of an identical specimen subjected to combined horizontal and vertical excitations it occurred at 55% of the pier height. Thus, it was estimated that the spiral strain increased by 200% when vertical ground motion was included. Therefore, in this example, the deterioration of shear capacity due to vertical ground motion was experimentally demonstrated. Also, whereas the test specimen that was subjected to constant axial compression experienced brittle shear failure including rupture of the spiral reinforcement, the companion specimen that was subjected to moderate tension showed ductile behavior. Comparing the strength at the first peak of displacement, it was found that the lateral load strength of a specimen with constant axial tension increased marginally with increasing displacement; the response of the specimen with axial compression showed significant strength degradation. Hence, considering observations from the two tests described above, it was clearly shown that different axial load levels influence the pier behavior significantly and can ultimately dictate the failure mode.

Shake Table Tests conducted on Columns

Shake table tests were designed by Elwood (2002) to observe the process of dynamic shear and axial load failures in reinforced concrete columns when an alternative load path is provided for load redistribution. The test specimens were composed of three columns fixed at their bases and interconnected by a beam at the upper level. The central square section column had a wide spacing of transverse reinforcement rendering it vulnerable to shear failure and subsequent axial load failure during testing. As the central column failed, the shear and axial loads were redistributed to the adjacent ductile circular columns. Two test specimens were constructed and tested. The first specimen supported a mass that produced column axial load stresses roughly equivalent to those expected for a seven-story building. In the second specimen hydraulic jacks were added to increase the axial load carried by the central column, thereby amplifying the demands for redistribution of the axial load when the central column began to fail. Both specimens were subjected to one horizontal component of a scaled ground motion recorded during the 1985 earthquake in Chile. A comparison of the results from the two specimens

indicates that the behavior of the frame is dependent on the initial axial stress on the center column. The specimen with a lower axial load failed in shear- but maintained most of its initial axial load. For the specimen with a higher axial load, shear failure of the center column occurred at lower drifts and earlier in the ground motion record, and was followed by axial failure of the center column. Displacement data from immediately after the onset of axial failure suggest that there are two mechanisms by which the center column shortens during axial failure: first, by large pulses that cause a sudden increase in vertical displacement after a critical drift is attained; and second, by smaller oscillations that appear to 'grind down' the shear-failure plane. Dynamic amplification of axial loads transferred from the center column to the outside columns was observed during axial failure of the center column.

An additional study by Ghannoum and Moehle (2012) includes earthquake simulation tests of a one-third-scale, three-storey, three-bay, planar reinforced concrete frame which was conducted to gain insight into the dynamic collapse of older-type construction. Collapse of the frame was the result of shear and axial failures of columns with widely spaced transverse reinforcement. The frame geometry enabled the observation of the complex interactions among the failing columns and the surrounding frame. The tests showed that the failure type and rate depended on the axial load level, stiffness of the surrounding framing, and intensity and duration of shaking. Column shear and axial behavior, including strength degradation, was affected by both large lateral deformation excursions and cycling at lower deformations. Low-cycle fatigue caused column collapse at significantly lower drifts than anticipated. It was concluded that current models and standards for estimating the shear and axial failure of columns do not account for low-cycle fatigue and can be unconservative, particularly for columns subjected to long-duration seismic motions. Moreover, models for shear strength degradation of reinforced concrete columns should account for both deformation and cyclically-driven damage. Finally, it was seen that structural framing surrounding the failing columns enabled vertical and lateral force redistribution that delayed or slowed down progressive structural collapse.

Code Criteria for Shear Strength Assessment of RC Columns

Behavior of reinforced concrete columns in combined shear and flexure has been studied extensively (see also Chapter 3). In the case of flexural behavior, sectional analysis, or a fiber model considering normal stresses

provides acceptable estimations in terms of ultimate strength and yielding deformation. Performance of reinforced concrete columns dominated by shear or shear-flexure cannot be estimated by applying only sectional analysis because shear behavior concerns the member and not a single cross section. In these cases it is necessary to couple a shear strength model with the flexural model – and by considering independently the degradation of each with increasing deformation, to determine the prevailing mechanism that controls the mode of failure of the member at the reference performance limit. Several code assessment procedures define the shear strength and its rate of degradation with increasing displacement ductility by evaluating the concrete contribution and the transverse steel reinforcement contribution to shear strength. Actually the existing code methodologies are differentiated regarding the concrete contribution term whereas the truss analogy for steel contribution is adopted almost universally in all proposals with a minor point of discussion being the angle inclination of the primary shear crack of the column that activates the steel stirrups contribution (Fig. 2-3). The various aspects of the code assessment of shear strength will be covered in the following sections.

It is generally acknowledged that shear failure of RC structures signifies rapid strength degradation and significant loss of energy dissipation capacity. Reconnaissance reports from past strong earthquakes highlight the susceptibility of RC column webs to diagonal tension cracking that frequently leads to a brittle shear failure. Shear strength degradation ensues after the opening of the diagonal cracks which eliminate the mechanism of force transfer via aggregate interlock. To avoid shear failure, shear strength should exceed the demand corresponding to attainment of flexural strength by a safety margin.

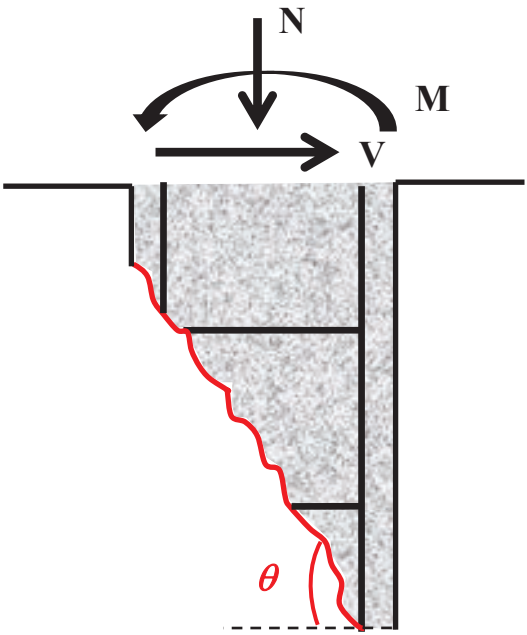

Figure 2-3: Angle inclination of the primary shear crack.

For the mechanics of shears in reinforced concrete, most issues relating to physical interpretation are still fraught with considerable debate. For example, consensus is lacking as to the physical significance of the concrete contribution term and to mathematical description of tension-based sources of shear-strength and their relationship to strain intensity and cyclic displacement history. According to EN 1998-3 (2005), the cyclic shear resistance, V_R, decreases with the plastic part of ductility demand, expressed in terms of ductility ratio of the transverse deflection of the shear span (Fig 2.4) or of the chord rotation (Fig. 2.4) at member end: $\mu_\Delta{}^{pl} = \mu_\Delta - 1$. For this purpose $\mu_\Delta{}^{pl}$ may be calculated as the ratio of the plastic part of the chord rotation, θ_p, normalized to the chord rotation at yielding, θ_y.

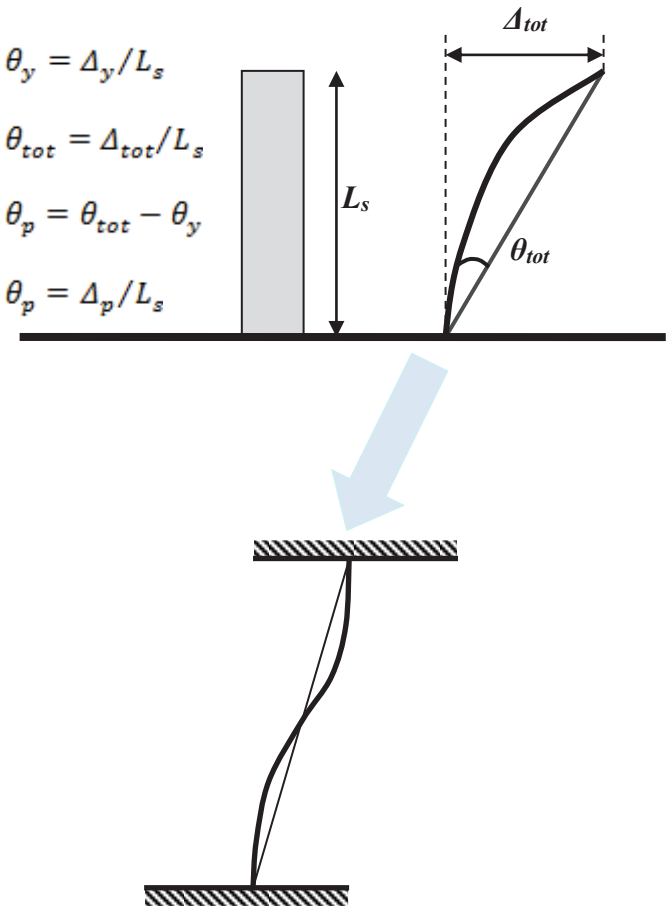

Figure 2-4: Definition of chord rotation of a cantilever reinforced concrete column (top) modeling the shear span of an actual column (bottom).

Thus, EN 1998-3 (2005) defines shear strength accounting for the above reduction as follows:

$$V_R = [(h-x)/2L_s]\min(N; 0.55A_c f_c) + [1 - 0.05min(5; \mu_\Delta{}^{pl})] \cdot \{0.16max(0.5; 100\rho_{tot})[1 - 0.16min(5; L_s/h)]\sqrt{f_c}A_c + V_w\} \quad (2\text{-}1)$$

where h: is the depth of the cross-section (equal to the diameter D for circular sections); x: is the compressive zone depth; N: is the compressive axial force (positive, taken as being zero for tension); L_s: M/V ratio moment/shear at the end section; A_c: is the cross-section area, taken as being equal to $b_w d$ for a cross-section with a rectangular web of width (thickness) b_w and structural depth d or to $\pi {D_c}^2/4$ (where D_c is the diameter of the concrete core to the inside of the hoops) for circular sections; f_c: is the concrete compressive strength, and ρ_{tot}: is the total longitudinal reinforcement ratio.

For a typical reinforced concrete column (mean concrete strength of 30 MPa) with a 1.5 meter shear span (i.e., a clear height of 3.0m) and a 350 mm circular section (clear concrete cover 20mm) with 14Φ12 longitudinal reinforcement (yielding a strength of 500MPa) and Φ10/10 spiral reinforcement (yielding a strength of 500MPa) and axial load ratio of 20%, the axial load and concrete contribution to shear strength calculated based on the above equation (Eq. 2-1) lead to the following results: 49 kN axial load contribution which is the first term of the above equation (Eq. 2-1) and the concrete contribution is 34 kN. The reduction factor for a displacement ductility of 3 is 0.9. Therefore, the reduced concrete contribution is 31 KN.

For the same column under the same axial load and with the same material properties as above but comprised of a square section (457 mm) with 8Φ20 longitudinal reinforcement and Φ10/20 transverse reinforcement, the axial load contribution and the concrete contribution to shear strength are 137 kN and 98 kN respectively. The concrete contribution for displacement ductility equal to 3 will be reduced to the value of 88 kN.

In Eq. 2-1 term V_w is the contribution of transverse reinforcement to shear resistance, taken as equal to:

a) for cross-sections with a rectangular web of width b_w:

$$V_w = \rho_w b_w z f_{yw} \tag{2-2a}$$

where ρ_w is the transverse reinforcement ratio (Fig. 2-5); z is height of the equivalent truss, set equal to the internal lever arm, i.e., *d-d'* in beams and columns (Fig 2-5); and f_{yw} is the yield stress of the transverse reinforcement; and S the stirrup spacing.

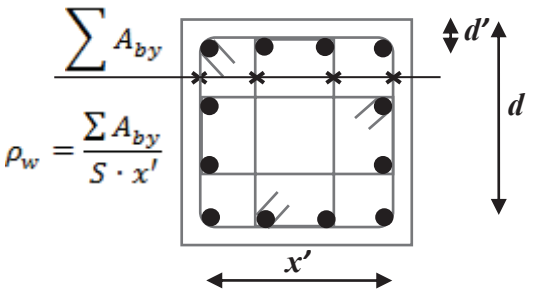

Figure 2-5: Transverse Reinforcement Ratio (*S*: spacing of the stirrups)

With regard to the example of the typical, square-sectioned column as described above based on Eq. 2-2a, the steel contribution in shear strength is 175 kN and the total shear strength of Eq. 2-1 is 410 kN. If the reduction factor is applied, the shear strength becomes equal to 383 kN. The variation of shear strength with spacing for this example under consideration leads to the following graph (Fig. 2-6).

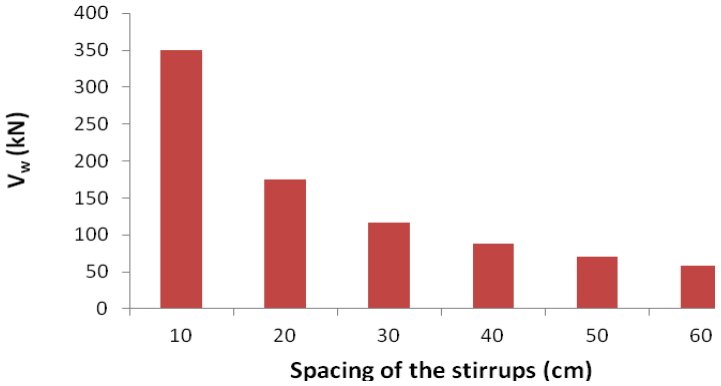

Figure 2-6: Effect of stirrup spacing to transverse steel contribution of a rectangular section in shear strength.

It is evident that for spacing greater than the effective depth of the section—which for the 45° degree truss analogy means that the shear crack doesn't intersect any stirrup—Eq. 2-2a simply leads to a lower value of steel contribution to shear strength. This is actually inconsistent – the

value ought to be zero in this case; Pantazopoulou and Syntzirma (2010) have suggested that the term be substituted by,

$$V_w = \sum_{n_i} A_{swi} \cdot f_{si} \; ; n_i = [d/s] \; (greatest\; integer\; function) \tag{2-2b}$$

For circular cross-sections (c: is the concrete cover):

$$V_w = \frac{\pi}{2} \frac{A_{sw}}{s} f_{yw} (D - 2c) \tag{2-3}$$

Regarding the example of the typical column with the circular section as described above based on Eq. 2-3, the steel contribution in shear strength is 382 kN and the total shear strength of Eq. 2-1 is 465 kN. If the reduction factor is applied the shear strength becomes equal to 424 kN. The variation of shear strength with spacing for the example under consideration leads to the following graph (Fig. 2-7).

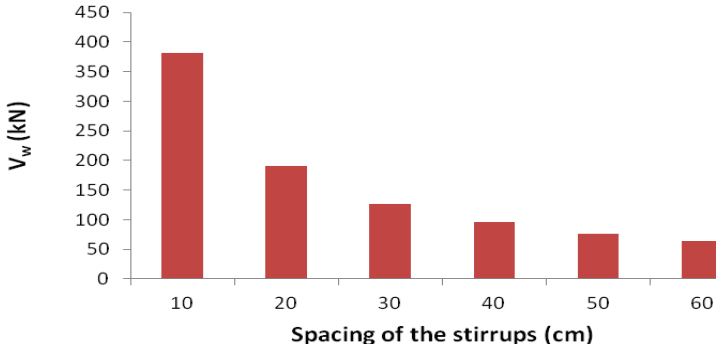

Figure 2-7: Effect of stirrup spacing on transverse steel contribution of a circular section in shear strength.

Based on Fig. 2-7, the steel contribution component should be based on the requirement that at least one stirrup layer must be intersected by the diagonal cracking plane; otherwise the steel contribution term ought to be taken as equal to zero.

In concrete columns with shear span ratio of L_s/h, less or equal to 2, the shear strength, V_R may not be taken as greater than the value corresponding to failure by web crushing along the diagonal of the column after flexural yielding, $V_{R,max}$, which under cyclic loading may be calculated from the expression:

$$V_{R,max} = (4/7)[1 - 0.02min(5; \mu_\Delta{}^{pl})][1 + 1.35(N/A_c f_c)][1 + 0.45(100\,\rho_{tot})]\sqrt{min(40; f_c)}\,b_w z \cdot sin2\delta \quad (2\text{-}4)$$

where δ is the angle between the cracking plane and the axis of the column ($\tan\delta = h/2L_s$). By implementing this equation to the example of the cases described above but with a change on the shear span so that the column be compliant to the shear span ratio limit of Eq. 2-4, the following results are obtained (L_s=700mm). It can be seen that for the circular column case shear strength is limited by web crushing along the diagonal.

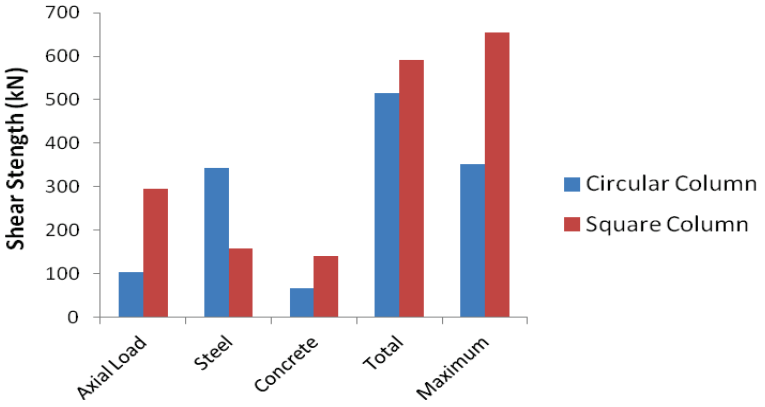

Figure 2-8: Shear Strength and its contributions for a typical reinforced concrete column.

ASCE/SEI 41 is the latest in a series of documents developed after the FEMA initiatives in the 1990s and 2000s towards the development of a consistent assessment framework for existing structures. The FEMA/ATC documents form the first integrated reference for performance-based engineering, whereby deformation and force demands for different seismic hazards are compared against the capacities at various performance limits

(i.e. states of damage). At the outset of this momentous project by FEMA, available data on the performance of existing components were rather limited and therefore reliability concepts were not applied evenly towards the establishment of performance criteria.

The issue of dependably estimating the shear strength of a RC element appears to be rather complicated as it presumes the full understanding of the several interacting behavior mechanisms under reversed cyclic loading, whereas it is strongly affected by the imposed loading history, the dimensions of the element (e.g. the aspect ratio), the concrete strength, the longitudinal reinforcement ratio but mostly the ratio and the detailing of the transverse reinforcement. So far it has not been possible to theoretically describe the strength of the shear mechanism from first principles of mechanics without the use of calibrated empirical constants. Therefore the shear strength estimates obtained from calibrated design expressions necessarily rely on the pool of experimental data used for correlation of the empirical expressions, as well as on the preconceived notions of the individual researchers as to the role each variable has in the mechanics of shear.

The following expression for estimation of the shear strength of reinforced concrete columns is proposed by the Code for seismic rehabilitation of existing buildings of the American Society of Civil Engineers ASCE/SEI 41 (2007):

$$V_R = V_c + V_w = k(\mu_\Delta)\left[\left(0.5\sqrt{f_c}/(L_s/d)\right)\sqrt{1 + N/\left(0.5A_g\sqrt{f_c}\right)}\right]0.8A_g + k(\mu_\Delta)\left[A_{sw}f_{yw}d/S\right] \quad (2\text{-}5)$$

where $\boldsymbol{V_c}$ is the concrete contribution in shear resistance; $\boldsymbol{V_w}$ is the contribution of transverse reinforcement; $\boldsymbol{d}$ is the effective depth; $\boldsymbol{L_s}$ is shear span of the column; N is the axial force (compression positive, taken zero for tension); $\boldsymbol{A_g}$ is the gross cross-sectional area of the column; $\boldsymbol{A_{sw}}$ is the cross-sectional area of one layer of stirrup reinforcement parallel to the shear action; and $\boldsymbol{S}$ is the centerline spacing of stirrups. If S is equal to or greater than half of the effective depth of the column then the contribution of steel reinforcement V_w in shear strength is reduced to 50% of its estimated value from the above equation. If S is equal to or greater than the effective depth of the column then zero shear strength contribution from steel reinforcement V_w is considered; $\boldsymbol{f_c}$ is the concrete compressive strength; $\boldsymbol{k(\mu_\Delta)}$ is the shear strength reduction factor that depends on

ductility. If ductility is less than or equal to 2 then the factor is set to equal to 1 (i.e. no strength reduction). If the ductility is greater than 6, then the reduction factor is equal to 0.6. For ductility between 2 and 6 the reduction factor is linearly interpolated between the proposed values.

The V_c estimate given by Eq. 2-5 for the example of the rectangular column presented in this Section is: $V_{c,ASCE}$ = 233 kN, while EN 1998-3 (2005) resulted in $V_{c,EC8\text{-}3}$= 88 kN which, when combined with the axial load component (137 kN) leads to a total of 225 kN, which is comparable to the result of Eq.2-5. For the case of the circular column results to $V_{c,\mathrm{ASCE}}$ = 81 kN whereas $V_{c,EC8\text{-}3}$=80 kN (49 kN axial load contribution+31 kN concrete contribution) – values calibrated well with each other.

The effect of the stirrups' spacing to the steel contribution to shear strength is depicted in the following figures for ASCE/SEI-41 (2007) and it is compared with the EN 1998-3 (2005) (here abbreviation EC8-III is used) results.

Despite the convergence of the calibrated expressions, the preceding comparisons highlight some of the uncertainties underlying the shear problem. For one, the concrete contribution term is taken—in both code documents—to be independent of the amount of transverse reinforcement, an omission that goes to the root of the truss-analogy model as originally introduced by Ritter and Moersch: there the concrete contribution component was thought to be a minor correction to the main component that was owing to transverse reinforcement (the truss posts) so as to improve correlation with the tests – it was never meant to be a component of commensurate importance and magnitude to that of transverse reinforcement. Another source of uncertainty lies in the treatment of the axial load: in the EN 1998-3 (2005) approach, the axial load contribution is dealt with as a separate term, whereas in the ASCE/SEI 41 (2007) approach it is treated as an offset to the tensile strength of concrete in the member web. This difference causes a departure in the V_c values near the upper limit in the axial load ratio ($v=N/A_g f_c$) as depicted in Fig. 2-11.

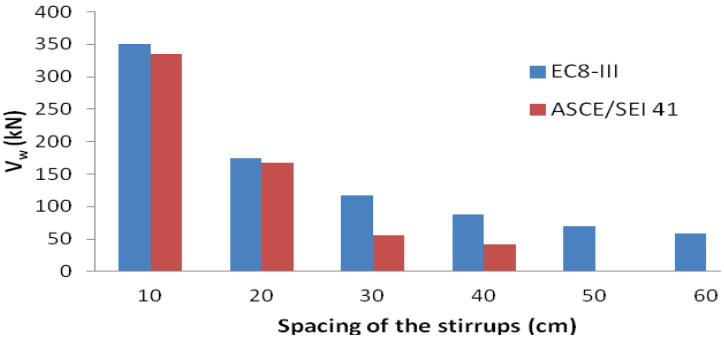

Figure 2-9: Effect of stirrup spacing to transverse steel contribution of a rectangular section in shear strength.

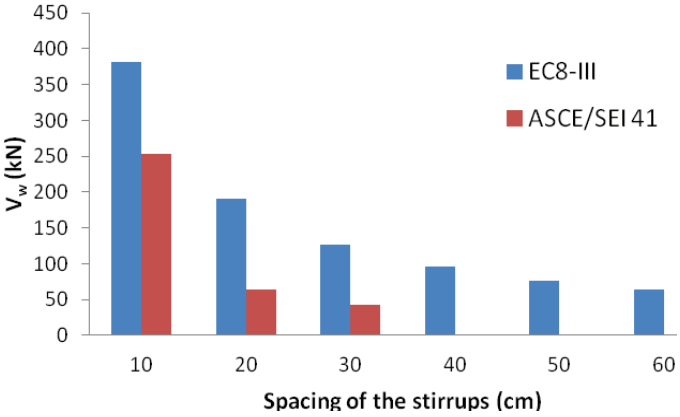

Figure 2-10: Effect of stirrup spacing to transverse steel contribution of a circular section in shear strength.

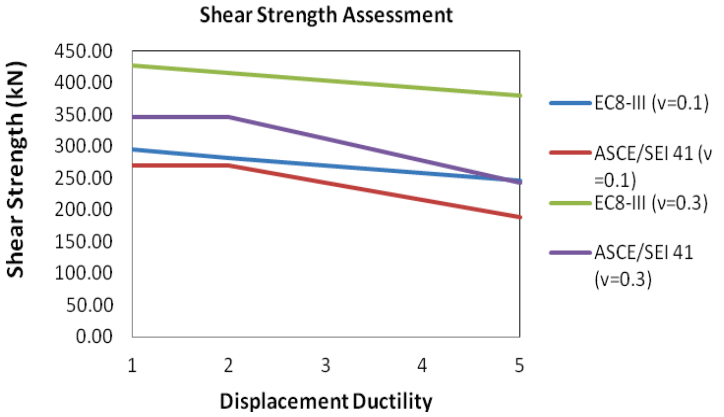

Figure 2-11: Shear strength vs. displacement ductility for the column with rectangular section.

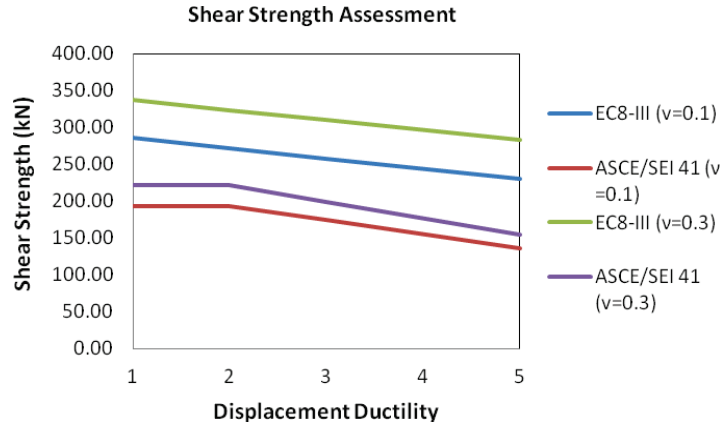

Figure 2-12: Shear strength vs. displacement ductility for the column with circular section.

Contrary to the shear strength assessment models of EN 1998-3 (2005) and ASCE/SEI 41 (2007), the shear model of *fib* Model Code (2010) is a design model which was not calibrated to specifically address members under seismic loads. The *fib*-MC2010 design section on shears provides the option of four different levels of model complexity depending on the level of detail needed at the time of calculation (intended to address the needs for preliminary design, detailed design and assessment). The four models are referred to here on as levels of approximation (LA) and are identified by Latin numbers. Thus, for members with shear reinforcement the LA-III model provides the point of reference since the higher the level of approximation is, the greater the design effort required. This is also the case for shear strength assessment of members with low volume of shear reinforcement (Sigrist et al. 2013).

For members with shear reinforcement the *fib* Model Code 2010 shear provisions are based on a general stress field approach (Muttoni A. et al. 1997, Sigrist V. 2011), combined with Simplified Modified Compression Field Theory (SMCFT, Vecchio and Collins 1986, Bentz et al. 2006). As in all preceding code formulations the shear resistance V_R is determined by the sum of a concrete contribution and web steel contribution term:

$$V_R = V_c + V_w \tag{2-6}$$

For structural assessment, the strain dependence of the shear resistance may be taken into account by estimating the strain value ε_x at the mid-depth of the effective shear section as depicted in (Fig. 2-13, *fib* Model Code 2010). Other deformation parameters could be selected but this value has a clear physical meaning as it represents the average longitudinal strain in the web and can be found from the sectional forces. For a reinforced member, the effective shear depth z is assumed to be $0.9d$. The tension chord force can be found from moment equilibrium in the section (Fig. 2-13) and the tension chord strain is determined accordingly from the tension chord force:

$$T = 2 \cdot E_s \cdot \varepsilon_x \cdot A_s = \frac{M}{z} + \frac{V}{2}\cot\alpha + N\left(\frac{1}{2} \pm \frac{\Delta e}{z}\right) \tag{2-7}$$

where M is the resisted moment, V is the applied shear force, N is the axial force, Δe is the eccentricity of the beam axis with respect to its mid-depth, E_s is the modulus of elasticity of longitudinal steel reinforcement and A_s is the area of tensile longitudinal reinforcement.

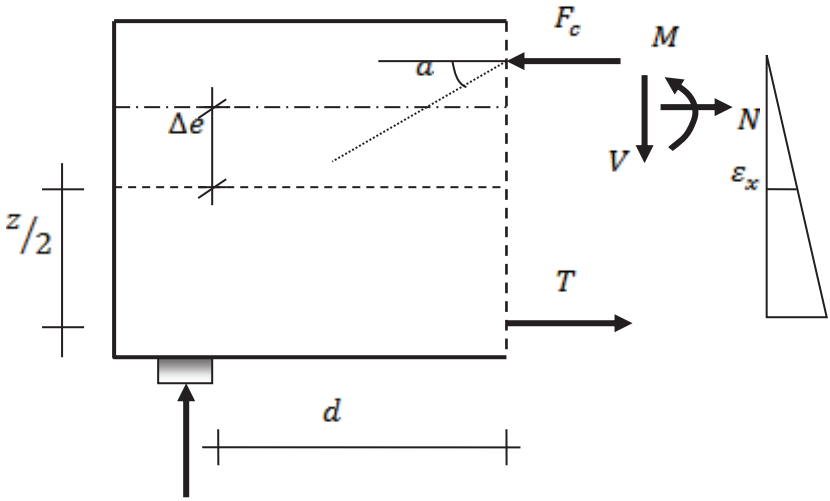

Figure 2-13: Equilibrium at cross-section and corresponding approximation of strain profiles for end support region.

For the sake of simplicity, and to avoid iteration (since the definition of the compressive stress field inclination angle a requires ε_x) for calculating the strain ε_x, the second item in Eq. 2-7 is approximated as $(V/2)\cot a \approx V$ (a compressive stress field inclination angle a close to 27° is assumed) (Fig. 2-13). With the conservative assumption that the compression chord strain is zero, it may be shown that the mid-depth strain may be taken as half the tension chord strain (Fig.2-13). The resistance attributed to concrete is:

$$V_c = k_v \sqrt{f_c} b_w z \quad (f_c \text{ in } MPa) \tag{2-8}$$

where k_v is a factor accounting for strain gradient effect and member size (Eq. 2-9), f_c is the concrete strength and b_w is the web width.

The k_v value, accounting for the demand in the concrete contribution term, is defined by:

$$k_v = \frac{0.4}{1+1500\,\varepsilon_x}\left(1 - \frac{V_{Ed}}{V_{Rd,max}(a_{min})}\right) \tag{2-9}$$

where V_{Ed} is the shear force demand at the control section.

The concrete contribution equation (Eq. 2-8) is limited to normal or moderately high concrete strengths up to f_c= 65MPa (the value $\sqrt{f_c}$ is limited to a maximum of 8 MPa); for higher strengths the equation may be deemed unconservative on account of the smoother crack faces where cracks pass through, rather than around, aggregate particles, resulting in larger variability in the shear resistance of members. For members with shear reinforcement, the shear resistance is the sum of the resistances provided by concrete (as per Eq. 2-8) and the contribution of stirrups:

$$V_w = \frac{A_{sw}}{s} z f_{yw} \cot a \tag{2-10}$$

where $\boldsymbol{A_{sw}}$ is the cross-sectional area of one layer of shear reinforcement, $\boldsymbol{f_{yw}}$ is the yield strength of shear reinforcement and $\boldsymbol{a}$ is the inclination of the compressive stress field relative to the longitudinal axis of the member (i.e., the angle of shear sliding cracks).

Shear strength is limited by the crushing of concrete according with:

$$V_{R,max} = k_c f_c b_w z \sin a \cos a \tag{2-11}$$

The strength reduction factor $k_c = k_\varepsilon \eta_{fc}$ accounts for the effect of compression softening due to transverse tensile strain through factor k_ε:

$$k_\varepsilon = \frac{1}{1.2+55\varepsilon_1} \leq 0.65 \tag{2-12}$$

and for the increasing brittleness of high strength concrete through factor η_{fc} which reduces the effective shear strength for $f_c > 30$ MPa:

$$\eta_{fc} = \left(\frac{30}{f_c}\right)^{1/3} \leq 1.0 \quad (f_c \text{ in } MPa) \tag{2-13}$$

The principal tensile strain that causes the compression softening effect in k_ε above, $\varepsilon_1 = \varepsilon_x + (\varepsilon_x - \varepsilon_2)\cot^2 a$, is defined by a Mohr's circle of strain (Fig. 2-14); as an adequate approximation, the (negative) principal strain $-\varepsilon_2$ may be taken as the concrete peak strain $\varepsilon_{c0} = 0.002$ and ε_x

from Eq. 2-7. Finally, the stress field or strut inclination (Fig. 2-14), relative to the longitudinal axis of the member, is limited to:

$$a_{min} \leq a \leq 45^o \tag{2-14}$$

$$a_{min} = 20^o + 10000\varepsilon_x \tag{2-15}$$

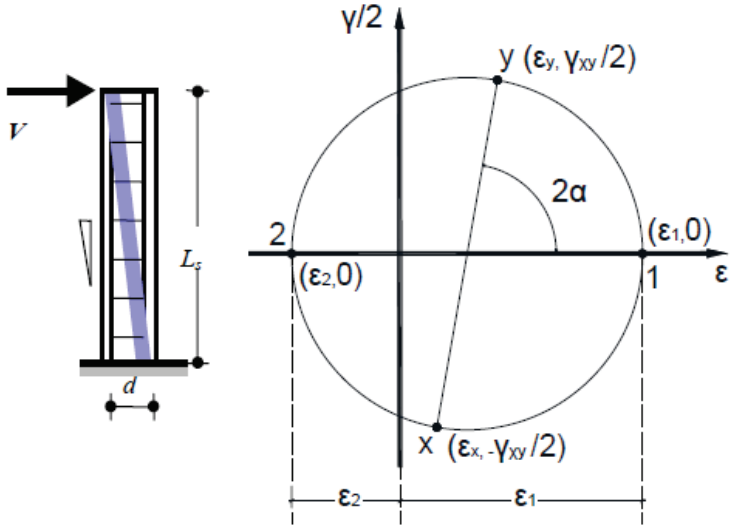

Figure 2-14: Strut inclination in a column and Mohr circle of strains.

A comparison of the assessment procedure described above based on the design model of *fib* Model Code 2010 with the assessment models of the previously presented Code requirements stated in this Section is illustrated in Figs. 2-16, 2-17. The columns under study have similar properties with the already described example columns. It may be observed that the general method of the *fib* Model Code 2010 gives a more conservative estimation of the concrete contribution to shear strength.

Similar to *fib* Model Code (2010), the design model of ACI-318-14 (2014) considers a concrete and a steel contribution to the shear strength of beam-columns:

$$V_R = V_c + V_w \tag{2-16}$$

The concrete term, V_c is taken as the shear force causing inclined cracking in the member, obtained by setting the maximum sectional shear stress to the principal tensile stress of concrete; after cracking, V_c is kept the same, but it is justified as a contribution supported by aggregate interlock, dowel action and the shear term transmitted across the concrete compression zone. As in all other codes, the shear strength is based on an average shear stress acting over the effective cross section $b_w d$ (b_w = web width or diameter of circular section, d = effective depth of cross section).

For non-prestressed members with axial compression, V_c is calculated from:

$$V_c = 0.17\left(1 + \frac{N_u}{14A_g}\right)\lambda\sqrt{f_c}\,b_w d \qquad (2\text{-}17)$$

where N_u is the axial force normal to cross section- to be taken as positive for compression, (Newton), A_g is the gross area of concrete section, mm^2, f_c is the specified compressive strength of concrete (MPa), λ is a modification factor to account for the reduced mechanical properties of lightweight concrete relative to normal weight concrete of the same compressive strength.

For non-prestressed members with significant axial tension, V_c is calculated from:

$$V_c = 0.17\left(1 + \frac{0.29 \cdot N_u}{A_g}\right)\lambda\sqrt{f_c}\,b_w d \geq 0 \qquad (2\text{-}18)$$

Required shear reinforement is obtained from a modified truss analogy, wherein the force in the posts (vertical ties, Fig. 2-15) is resisted by the shear reinforcement. However, considerable research on both nonprestressed and prestressed members has indicated that shear reinforcement needs to be designed to resist only the shear demand exceeding the force that causes inclined cracking, assuming the diagonal struts in the truss panels to be inclined at 45 degrees (Fig. 2-15).

From equilibrium it may be easily shown that V_w supported by web reinforcement is:

$$V_w = \frac{A_v f_{yt} d}{s} \qquad (2.19)$$

where S is the longitudinal spacing of transverse reinforcement (or the spiral pitch of tied columns with spiral transverse steel), mm; A_v is the cross sectional area of shear reinforcement parallel to the shear force within a single stirrup pattern, mm^2, and f_{yt} is the specified yield strength of transverse reinforcement, MPa. Observe the similarity with the

EN 1998-3 (2005) equation for the V_w term. For circular ties or spirals, A_v is two times the area of the spiral bar or wire. For calculation of V_c and V_w in solid circular sections, d is approximated by 0.8 times the diameter and b_w is taken as the diameter.

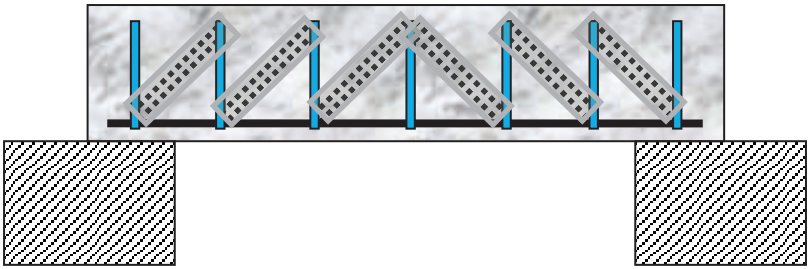

Figure 2-15: 45° Truss Model.

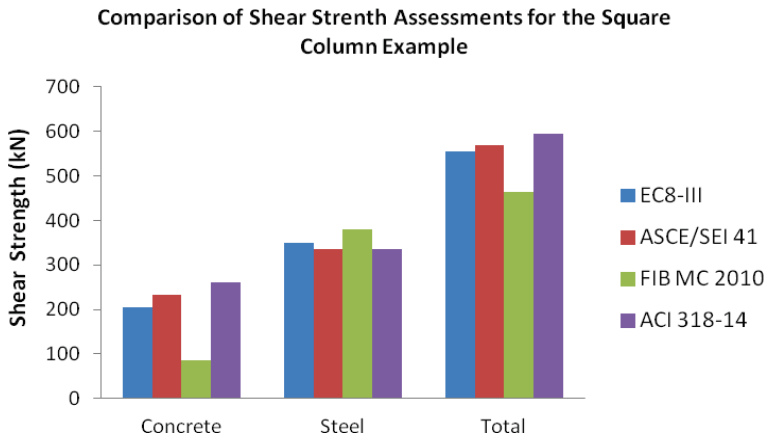

Figure 2-16: Comparison of shear strength assessment models for the square column example under study.

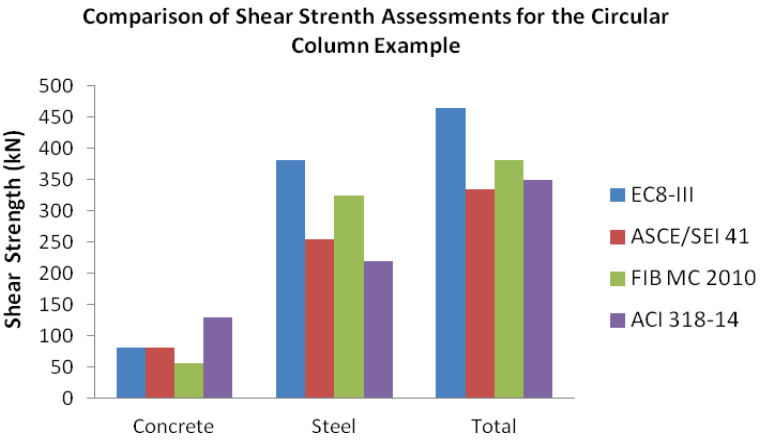

Figure 2-17: Comparison of shear strength assessment models for the circular column example under study.

Figures 2.16 and 2.17 compare the values obtained from the shear stregth models of the various code provisions including ACI 318-14 (2014) for the example columns considered. Note that ACI 318-14 (2014) gives a higher shear strength estimation for concrete contribution with respect to the other code models but it is closely calibrated to both EN 1998-3 (2005) and ASCE/SEI-41 (2007).

Finally, it should be mentioned that the Greek Code (KAN.EPE. 2014) containing the necessary provisions for structural assessment and interventions for reinforced concrete buildings adopts the Eurocode 8 – part 3 (EC8-III) procedures (EN 1998-3, 2005), already introduced in this Section.

Milestones in the Development of Models for Shear Strength Assessment of RC Columns

Reviewed Code provisions were developed and based on past research which was motivated by the extensive damages observed in modern construction in the earthquakes worldwide after 1990. In particular, defining the degradation of shear strength due to increasing inelastic deformations has been the objective of several older models (Aschheim and Moehle 1992, Priestley et al. 1994, Sezen and Moehle 2004).

The study by Aschheim and Moehle (1992) was the first to develop a degrading model for the shear strength envelope of columns and beams, after calibrating an empirical relationship with a database of laboratory data from cantilever bridge column tests. The data indicated that the column shear strength is a function of displacement ductility demand, μ_Δ, the quantity of transverse reinforcement and axial load. As is the general practice, the shear strength is calculated as the summation of strength contributions from transverse reinforcement and concrete. The transverse reinforcement contribution is computed from Eq. 2-19. The concrete contribution is defined as:

$$V_c = 0.3\left(k + \frac{N}{14A_g}\right)\sqrt{f_c}\,0.8A_g \tag{2-20}$$

$$\text{where } 0 \le k = \frac{4-\mu_\Delta}{3} \le 1 \tag{2-21}$$

So this model attributes the entire amount of strength degradation to deterioration of the concrete contribution term (through factor *k*). This model was intended to evaluate the shear strength in plastic hinge zones and was later adopted in FEMA 273 (1997). ASCE/SEI 41 is the most recent report for the subject of the "seismic rehabilitation of existing buildings," which succeeded the previous editions on the same subject, FEMA 273 (1997) and FEMA 356 (2000).

The approach by Priestley et al. (1994) further de-aggregates the shear strength of columns under cyclic lateral loads as comprising three distinct contributions – that of the concrete web, V_c, a truss mechanism (or transverse reinforcement), V_w, and an arch mechanism associated with an axial load, V_N, as follows:

$$V_R = V_c + V_w + V_N \tag{2-22}$$

The concrete component V_c is given by:

$$V_c = k\sqrt{f_c'}\,A_e \tag{2-23}$$

where $A_e = 0.80A_g$ and the parameter k depends on the member displacement ductility level as defined in the following equations:

$$\begin{aligned} For\ \mu_\Delta \le 2, k &= 0.29 \\ For\ 2 < \mu_\Delta < 4, k &= -0.095\mu_\Delta + 0.48 \\ For\ \mu_\Delta \ge 4, k &= 0.1 \end{aligned} \tag{2-24}$$

The contribution of transverse reinforcement to shear strength is based on a truss mechanism using a 30-degree angle between the diagonal compression struts and the column longitudinal axis. For rectangular cross-section columns, the truss mechanism component, V_w, is estimated from:

$$V_w = \frac{A_{sw} f_{yw} (d - d')}{s} cot 30^o \quad (2\text{-}25)$$

where $d - d'$ is the distance measured parallel to the applied shear between centers of the perimeter stirrup. For circular cross-section columns, the truss mechanism component, V_w, is defined from:

$$V_w = \frac{\pi}{2} \frac{A_{sw} f_{yw} D'}{s} cot 30^o \quad (2\text{-}26)$$

where D' is the distance measured parallel to the applied shear between centers of the perimeter hoop or spiral.

The arch component refers to the horizontal component of the inclined axial strut carrying the axial load to the support. In this model this term is given by

$$V_N = N \, tan\alpha = \frac{d - x}{2L_s} N \quad (2\text{-}27)$$

where α is the inclination of the diagonal compression strut with respect to the longitudinal axis of the column and x is the depth of the compression zone, whereas d is the effective depth of the section.

It should be noted that the depth, x, depends on both the axial load and aspect ratio (i.e. the amount of curvature required to develop a certain displacement ductility). Thus, with an increasing aspect ratio the axial load contribution to shear strength decreases. Similarly, a higher depth of compression zone (for higher axial load) affects the value of V_N, showing a subtle increase for higher compressive *N*. The effect of the axial tensile load on the shear strength is not defined in the model.

Sezen and Moehle (2004) updated the earlier model of Aschheim and Moehle (1992) also relating column shear strength to the displacement ductility demand; the novelty here is that the strength degradation factor k was taken to operate on both concrete and steel contributions (Fig. 2-18):

$$V_n = k(V_c + V_s) = k\left(\frac{0.5\sqrt{f_c'}}{L_s/d}\sqrt{1+\frac{N}{0.5\sqrt{f_c'}A_g}}\right)0.8A_g + k\frac{A_{sw}f_{yw}d}{s} \quad (2\text{-}28)$$

This model was later adopted in the ASCE/SEI 41 assessment provisions. The reasoning in applying a reduction to both terms is that the concrete component is expected to diminish owing to increased cracking and degradation of the aggregate interlocking mechanism, whereas the steel component is assumed to degrade due to a reduction in the bond stress capacity required for an effective truss mechanism.

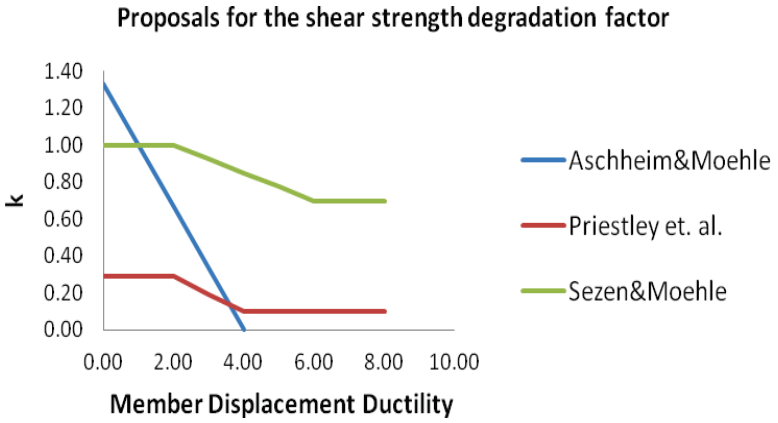

Figure 2-18: Variation of degradation coefficient *k* with displacement ductility.

The comparison of the models included in this Section for the example columns under study of this Chapter is illustrated in Figs. 2-19 and 2-20. Differences in the estimation of the transverse reinforcement contribution in shear strength between the 30-degree truss model (Priestley et al 1994) and the 45-degree truss model adopted by Aschheim and Moehle 1992, Sezen and Moehle 2004 are clearly evident. For the same stirrup arrangement, the 30-degree truss model gives a higher steel contribution to shear strength.

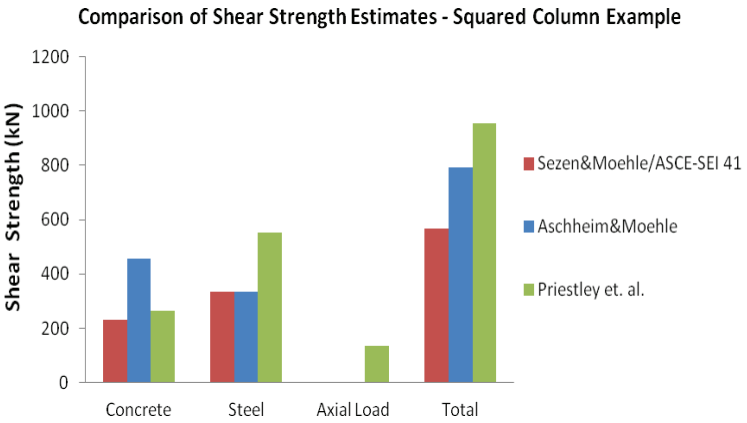

Figure 2-19: Comparison of shear strength assessment models for the square column example under study.

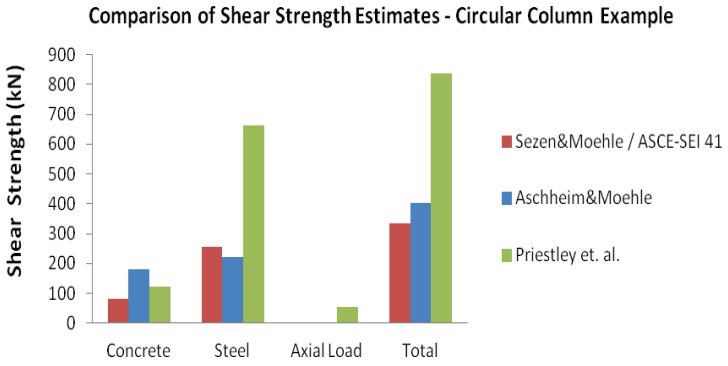

Figure 2-20: Comparison of shear strength assessment models for the circular column example under study.

The Modified Compression Field Theory (MCFT) (Vecchio and Collins, 1986) employs equilibrium, compatibility and experimentally verified stress-strain relationships to model the shear behavior of cracked

concrete. A fundamental relationship in the MCFT relates the shear stress on a cracked surface due to aggregate interlock to the crack's width, the maximum aggregate size and the concrete strength. The aggregate effect was first codified when a general method for shear design was derived based on the MCFT and implemented in the AASHTO-LRFD bridge design guidelines. In 1994 the general method of shear design was implemented in the CSA concrete design code for buildings in Canada. An updated and simplified version of the general method has been developed (Bentz et al., 2006) and implemented in the 2004 CSA design code. The new general method, referred to as the Simplified Modified Compression Field Theory (SMCFT) has been found by some to be simpler than the original general method with, in many cases, improved predictive capabilities (Sherwood et al., 2006).

According to SMCFT simple expressions have been developed for β (a parameter that models the ability of cracked concrete to transfer shear), the crack angle a, and the normal average strain in the web's longitudinal centroidal axis ε_x, thereby eliminating the need to iterate in order to solve for these values. The following general relationship is used to determine the shear resistance of a concrete section:

$$V_R = V_c + V_w = \beta\sqrt{f_c}\, b_w d_v + \frac{A_v f_y}{s} d_v \cot a \qquad (2\text{-}29)$$

Term β in Eq. 2-29 is a function of 1) the longitudinal strain at the mid-depth of the web ε_x, 2) the crack spacing at the mid-depth of the web and 3) the maximum coarse aggregate size, a_g. It is calculated using an expression that consists of a strain effect term and a size effect term:

$$\beta = (strain\ softening\ term) \cdot (size\ effect\ term) = \frac{0.40}{(1+1500\varepsilon_x)} \cdot \frac{1300}{(1000+s_{ze})} \qquad (2\text{-}30)$$

The longitudinal strain at the mid-depth of a beam web is conservatively assumed to be equal to one-half of the strain in the longitudinal tensile reinforcing steel as is adopted in the *fib* Model Code 2010 previously presented. For sections that are not prestressed, ε_x is calculated according to Eq. 2-31 which is practically the same as Eq. 2-7 (here, M is the resisted moment, V is the applied shear force, N is the normal force [positive if it is tensile], E_s the modulus of steel, and A_s is the area of tension reinforcement):

$$\varepsilon_x = \frac{M/d_v + V + 0.5N}{2E_s A_s} \quad (2\text{-}31)$$

The effect of the crack spacing at the beam mid-depth is accounted for by the use of a crack spacing parameter s_z. This crack spacing parameter is equal to the smaller of either the flexural lever arm ($d_v = 0.9d$ or $0.72h$, whichever is smaller) or the maximum distance between layers of longitudinal crack control steel distributed along the height of the web.

The term s_{ze} is referred to as an "equivalent crack spacing factor" and has been developed to model the effects of different maximum aggregate sizes on the shear strength of concrete sections by modifying the crack spacing parameter. For concrete sections with less than the minimum quantity of transverse reinforcement and constructed with a maximum aggregate size of 20mm, s_{ze} is taken as equal to s_z. For concrete with a maximum aggregate size other than 20mm, s_{ze} is calculated as follows:

$$s_{ze} = \frac{35 s_z}{15 + a_g} \geq 0.85 s_z \quad (2\text{-}32)$$

To account for aggregate fracture at high concrete strengths, an effective maximum aggregate size is calculated by linearly reducing a_g to zero as the compressive concrete strength f_c increases from 60 to 70 MPa. Term a_g is set equal to zero for higher concrete strengths (i.e., for f_c>70 MPa). The square root of the concrete strength is limited to a maximum of 8 MPa as in the *fib* Model Code 2010 previously introduced.

The angle of inclination of the cracks at the beam mid-depth, α, is calculated by the following equation:

$$\alpha = (29^o + 7000\varepsilon_x)(0.88 + s_{ze}/2500) \leq 75^o \quad (2\text{-}33)$$

For the example columns of this Chapter, Eq. 2-33 results in $\alpha = 43^o$ for the square column and $\alpha = 41^o$ for the circular column.

A campaign to re-evaluate the shear strength models for the V_c term was conducted by Tureyen and Frosch in 2003. As part of this effort, a new model was developed, taking the compressive zone part of the cross section (i.e. the part above the neutral axis) as the primary contributor to shear strength. As shown in Fig. 2-21, the model considers that while the shear can be transferred over the entire effective depth d between cracks, at the location of a crack, shear stress can only be transferred through the uncracked concrete above the neutral axis. The shear stress distributions

shown in Figure 2-21 (a) are theoretical; however, these can be simplified in considering average stress distributions as shown in Figure 2-21 (b).

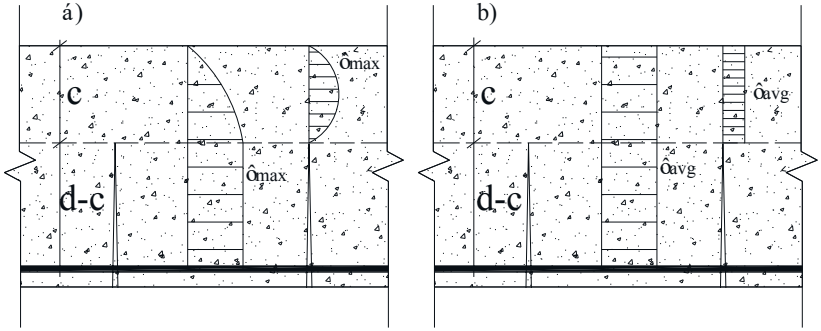

Figure 2-21: Theoretical (a) and Average (b) Shear Stress Distribution.

Using this model and considering the average shear stress distribution at a crack, a simplified expression for concrete contribution to shear strength was developed:

$$V_c = \frac{2}{5}\sqrt{f_c}\,b_w x \approx 0.4\sqrt{f_c}\,b_w x \qquad (2.34)$$

where x is the neutral axis depth (mm) measured from the compression face of the cracked, transformed cross section of the member. An advantage of this approach is that the effect of axial load is implicitly accounted for in the value of x.

Using shear-strength models such as those presented in the preceding figure is useful in estimating the available strength of members in conventional strength-based design and assessment. However, the strength-based approaches overlook a significant aspect that is essential in the performance context (i.e. when the focus is on damage sustained when the strength term materializes) – namely, the deformation capacity of the member and the mode of failure associated with the exhaustion of the shear strength terms, and the margin of safety required between this, brittle occurrence and the more ductile mechanisms of behavior before safety may be compromised. The above-mentioned limitation motivated the effort to develop displacement-based models for a dependable estimation of the drift capacity of flexure-shear critical columns, i.e., columns that

become critical in shear immediately after flexural yielding for a known axial load magnitude and member aspect ratio.

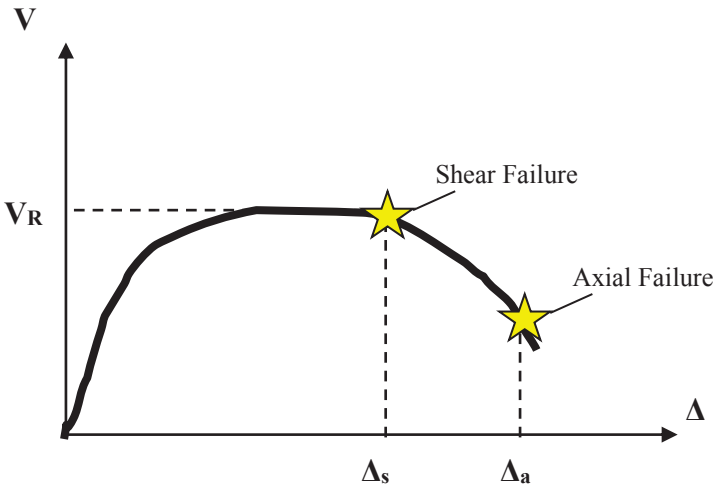

Figure 2-22: Shear and Axial Failure of a Reinforced Concrete Column.

The occurrence of a steep shear crack in a reinforced concrete column signifies the process of strength degradation that eventually leads to shear failure. If the reinforcement anchorages are sufficient, then, beyond this point the steep shear crack developed on the column leads to progressive sliding between the crack surfaces, permanent distortion of the web with simultaneous buckling of longitudinal reinforcement and fracturing of transverse reinforcing bars crossing the sliding plane; this type of failure eliminates the ability of the column to carry the overbearing loads and is therefore considered an axial failure. These two stages are distinct and not interchangeable; for the sake of clarity the two points of failure are marked on the notional element resistance curve in Fig 2-22.

The model developed by Pujol et al. (1999) related the magnitude of drift at shear failure with the aspect ratio of the column (L_s/d, where L_s is the column shear-span and d is the section depth from the centre of tension reinforcement to the extreme compression fibre of the column), the shear reinforcement ratio ρ_w (yield stress of f_{yw}), and with the column shear stress τ at shear failure (defined as the shear force at shear failure divided by the web area, $b_w d$). Based only on a statistical evaluation of the results of an experimental database that comprised 15 series of tests containing 94

specimens, and in an effort to establish a conservative estimate of the drift ratio at shear failure, Pujol et al. (1999) recommended the following relationship (L = clear height of column):

$$100\frac{\Delta_s}{L} = \frac{\rho_w f_{yw}}{\tau}\cdot\frac{L_s}{d} \leq \begin{cases} L_s/d \\ 4 \end{cases} \quad (2\text{-}35)$$

All the column specimens considered in the study were subjected to nominal shear stresses that may be assumed to be high enough so as to produce inclined shear cracking (shear stresses that exceed the tensile strength of the concrete). Failure was due to disintegration of the concrete core caused by sliding along inclined cracks and crushing of the concrete under compression. The ranges of the parameters for the employed experimental data leading to Eq. 2-35 were:

- f_c: 21-86 MPa, ρ_s (Longitudinal reinforcement ratio): 0.5-5.1%, $\rho_w f_{yw}$: 0-8 MPa, $\nu = N/(f_c A_g)$: 0-0.2, L_s/d: 1.3-5, $\tau/\sqrt{f_c}$: > 0.17.

Figure 2-23 depicts the results from Pujol's model and the database employed by Elwood (2003) (the database consists of 50 flexure-shear-critical columns representative of columns from older reinforced concrete buildings). It has been observed that the proposed expression for drift at shear failure is not conservative for six of the columns in the employed database. Three of those columns were subjected to axial loads in excess of the axial loads considered when developing the model. Although conservative with respect to the other specimens, there is nevertheless still significant discrepancy between calculated and measured drift values.

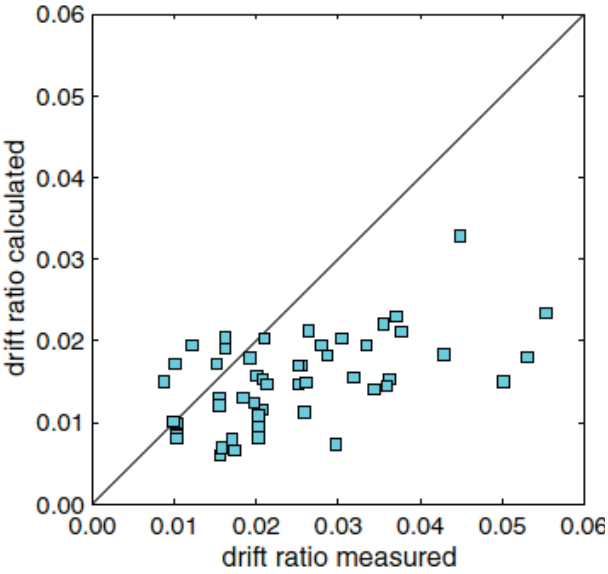

Figure 2-23: Comparison of calculated and measured drifts for Pujol et al. 1999 (Elwood 2003).

Elwood and Moehle (2005) proposed an empirical model that relates the shear demand to the drift at shear failure (Δ_s/L) based on the transverse reinforcement ratio ρ_w, shear stress ratio $(\tau/\sqrt{f_c})$, and axial load ratio $(\nu = N/A_g f_c)$. A database created by Sezen (2002) comprising 50 flexure-shear-critical specimens representative of older construction practices was employed for validation of the model. The test columns were selected based on a search of the literature for specimens tested under unidirectional cyclic lateral load with low transverse reinforcement ratios $(\rho_w \leq 0.007)$, yielding of longitudinal reinforcement prior to loss of lateral load capacity, and shear distress observed at failure suggesting that loss in lateral load capacity was due to degradation of the shear-transfer mechanism. The point of shear failure in the developed model was determined by the intersection of shear-drift curve for the column and the limit surface defined by a postulated drift capacity model (the limit surface is the outcome of Equation 2-36 for different pairs of shear force (and the corresponding shear stress) and the resulting displacement Δ_s plotted along with the element resistance curve- Figure 2-24). The proposed equation is:

$$\frac{\Delta_s}{L} = 3\% + 4\rho_w - 0.002 \cdot \frac{\tau}{\sqrt{f'_c}} - 0.025 \cdot \nu \geq 1\% \qquad (2\text{-}36)$$

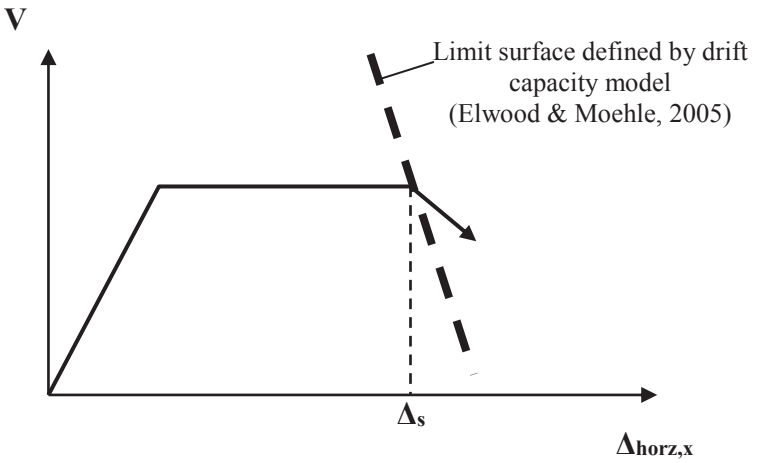

Figure 2-24: Shear failure by Elwood and Moehle (2005) drift capacity model.

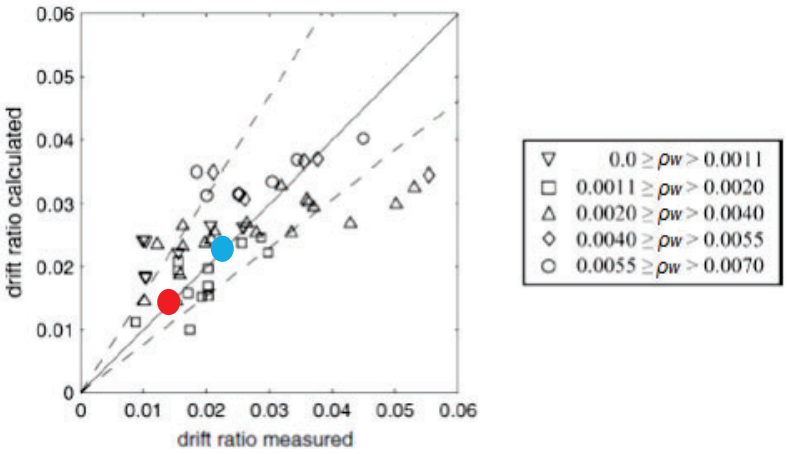

Figure 2-25: Comparison of calculated drift ratio at shear failure using Eq. 2-36 with database by Elwood. (Elwood 2003 – Dashed lined are +/- one standard deviation from the mean.)

For the example of the square column under study in this Chapter with 200 mm stirrup's spacing Pujol's model results in a 1.7% drift at shear failure and Elwood's model in 2.4 % drift at shear failure (in Fig. 2-25 depicted by the red and the blue dots, respectively). Therefore, the drift model by Pujol is more conservative.

To date, a limited number of models (Elwood and Moehle 2005, C. T. Ngoc Tran and B. Li 2013) have been developed to estimate the axial-drift failure of non-ductile columns. The model by Elwood and Moehle (2005) was developed considering the free body diagram of a column failed in the shear; here the only possible resistance is provided through shear friction along the sliding interface – collapse is imminent. Figure 2-26 depicts the free-body diagram of the upper portion of a column under shear and axial load. The external moment vector at the top of the column is not shown as it will not enter the equilibrium equations. The inclined free surface at the bottom of the free-body diagram is assumed to follow a critical inclined crack associated with shear damage. The "critical" crack is one that, according to the idealized model, results in axial load failure as shear friction demand exceeds the shear-friction resistance along the crack.

Several assumptions were made to simplify the problem. Dowel forces from the transverse reinforcement crossing the inclined crack are not shown in the free body diagram; instead, the dowel forces are assumed to be included implicitly in the shear-friction force along the inclined plane. Shear resistance due to dowel action of the longitudinal bars depends on the spacing of the transverse reinforcement, and it was ignored for the columns considered in this study. Given the tendency for buckling at axial load failure, the axial force capacity of the longitudinal reinforcement was assumed equal to zero. Finally, the horizontal shear force was assumed to have dropped to zero in the limit following shear failure and at the point of incipient axial failure.

The equilibrium of the forces shown in the free body diagram (Figure 2-26) results in the following equations:

$$\sum F_x = 0 \rightarrow P \sin\alpha' + V = V_{sf} \cos\alpha' + \frac{A_{sw} f_{yw} a_c}{s} \tan\alpha' + n_{bars} V_d \quad (2\text{-}37)$$

$$\sum F_y = 0 \rightarrow N = P \cos\alpha' + V_{sf} \sin\alpha' + n_{bars} P_s \quad (2\text{-}38)$$

In light of the foregoing assumptions, Equation 2-37 can be rewritten as follows:

$$P \sin\alpha' = V_{sf} \cos\alpha' + \frac{A_{sw} f_{yw} a_c}{s} \tan\alpha' \quad (2\text{-}39)$$

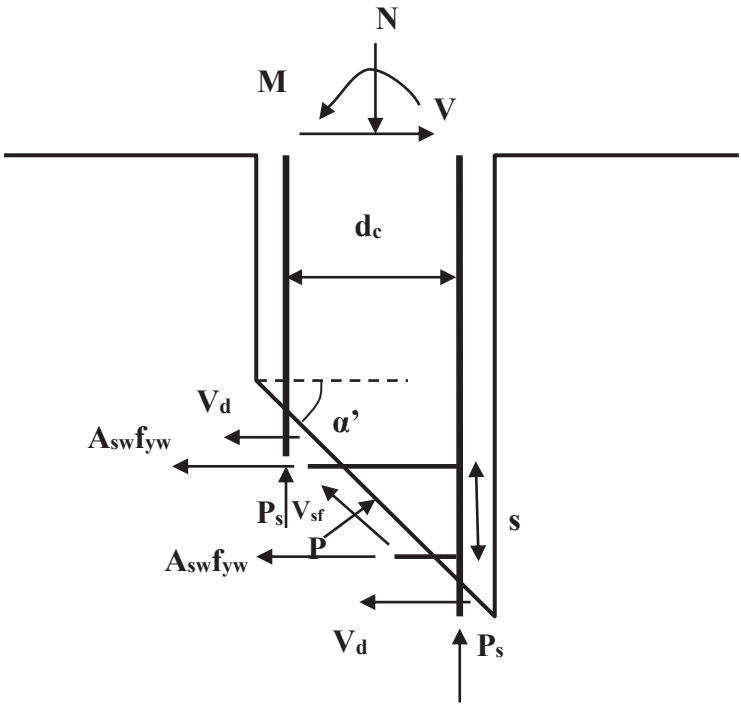

Figure 2-26: Free-body diagram of upper end of column (Elwood and Moehle 2005).

Based on Equations 2-38 and 2-39, on the axial capacity of the longitudinal reinforcement P_s and on the relationship between P and V_{sf} through the shear-friction model, the expression that relates axial load, transverse reinforcement, and drift ratio at axial load collapse is:

$$\left(\frac{\Delta_a}{L}\right)_{axial} = 4\% \cdot \frac{1+(\tan 65^o)^2}{\left[\tan 65^o + N\cdot\left(\frac{s}{A_{sw}\cdot f_{yw}\cdot d_c\cdot \tan 65^o}\right)\right]} \qquad (2.40)$$

where $d_c = d - d'$ is the depth of the column core between the centerlines of the ties. After experimental observation, the angle of the shear failure surface from horizontal was taken as equal to 65°. Similar to the shear-failure model described in the previous section, the axial drift model defines a limit surface at which axial failure is expected to occur (Fig. 2-27). For the square column under study in this Chapter and for a 200 mm

stirrup spacing, the drift ratio at axial load failure or collapse was estimated at 3.9%.

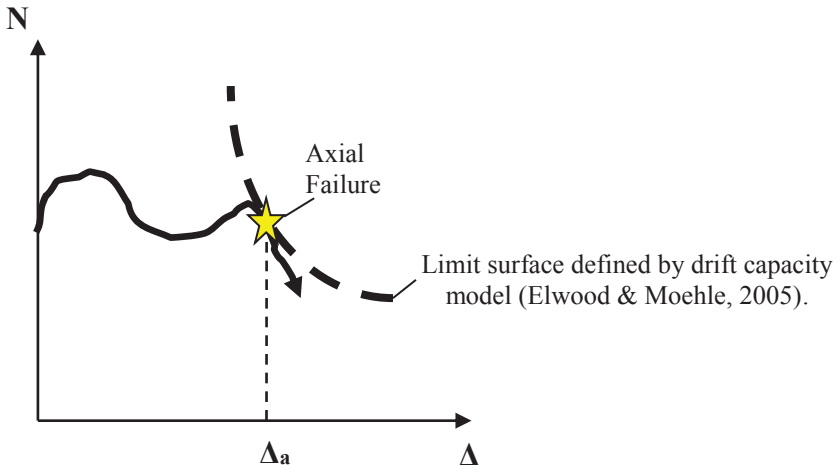

Figure 2-27: Axial Failure defined by Elwood and Moehle drift-capacity model (Elwood and Moehle 2005).

C. T. Ngoc Tran and B. Li (2013) presented analytical and experimental investigations carried out on RC columns with light transverse reinforcement. A semi-empirical model was developed to estimate the ultimate displacement (displacement at axial failure) of RC columns with light transverse reinforcement subjected to simulated seismic loading. The following basic assumptions were employed in deriving the model:

- The applied axial load at the point of axial failure is transferred through the shear failure plane.
- The angle of the shear failure plane of 60^o as defined by Priestley et al. 1994 was adopted. (30-degree angle between the diagonal compression struts and the column longitudinal axis as stated already in the description of Priestley et al. shear strength model).
- The shear demand on the columns was considered to be negligible and therefore ignored at the point of axial failure.
- Once the shear strength had degraded - corresponding to a displacement ductility of 2 for unidirectional lateral loading – then it was assumed that any additional deformation of the

columns was owing to sliding between cracking surfaces as shown in Fig. 2-28.

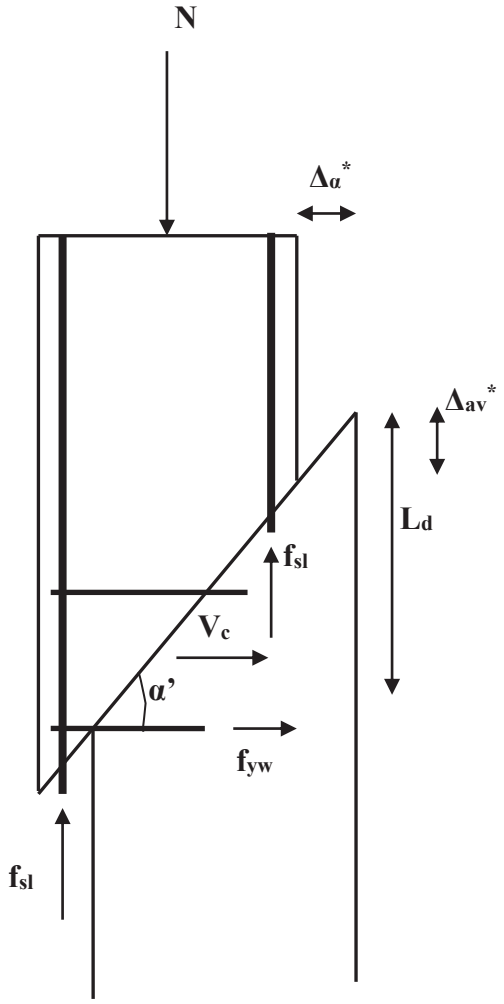

Figure 2-28: Assumed failure plane at the point of axial failure.

At the point of axial failure as shown in Fig. 2-28, the external and internal works W_{ext}, W_{int}, developed by the column were calculated according to the following:

$$W_{ext} = N \times \Delta^*_{av} \quad (2\text{-}41)$$

$$W_{int} = W_c + W_{sv} + W_{sl} \quad (2\text{-}42)$$

W_c, W_{sv}, and W_{sl} are the internal works done by deformation of concrete, transverse reinforcement and longitudinal reinforcement, respectively. As illustrated in Fig. 2-28, Δ^*_{av} is the vertical displacement due to sliding between cracking surfaces at the point of axial failure. Equating the external and the internal work leads to the following equation:

$$N = P_{sl} + P_{st} + P_c \quad (2.43)$$

where P_{sl}, P_{st}, P_c are the axial strengths contributed by longitudunal reinforcement, transverse reinfrocement, and concrete at imminent axial failure, respectively. Axial strength of longitudinal reinforcing bars at axial failure normalized by their nominal yield strength defines the yield strength ratio, η_{sl}, as follows:

$$\eta_{sl} = (N - P_{st} - P_c)/(\rho_l b_w h f_{yl}) \quad (2\text{-}44)$$

$$P_{st} = (d_c f_{yw} A_{sw})/S \quad (2\text{-}45)$$

$$P_c = V_c \cot\alpha' \quad (2\text{-}46)$$

where d_c is the depth of the core (centerline to centerline of ties) ρ_l is the total longitudinal reinforcement ratio; b_w and h are the width and the height of the column's cross section respectively; f_{yl} the yield strength of the longitudinal reinforcement. V_c is defined by Eq. 2-23. With reference to Fig. 2-28 the damaged length L_d is given by:

$$L_d = h \tan\alpha' \quad (2\text{-}47)$$

The ratio of horizontal displacement due to sliding between cracking surfaces at axial failure divided by the damaged length has the physical significance of a drift ratio, associated here with axial collapse. This term, δ^*_a, is given as:

$$\delta^*_a = \left[\underbrace{(\Delta_\alpha - 2\Delta_y)}_{\Delta^*_\alpha}/(h \tan\alpha')\right] \times 100\% \quad (2\text{-}48)$$

In the above, the yield displacement Δ_y is defined as the displacement associated with the secant to yield line in the force-displacement resistance curve of the member.

The developed model is calibrated using the collected data of 47 RC columns tested to the point of axial failure. These columns encompass a wide range of cross-sectional sizes, material properties, and column axial loads. They were subjected to a combination of an axial load and unidirectional cyclic loadings to simulate earthquake actions. Based on the employed database, an empirical equation was developed so as to relate the ratio of- the axial strength of longitudinal reinforcing bars to the yield strength of the longitudinal reinforcing bars- to the ratio of - the horizontal displacement due to the sliding between cracking surfaces to the damaged length - as follows:

$$\eta_{sl} = 1/(0.2046 \times \delta_a^* + 1) \tag{2-49}$$

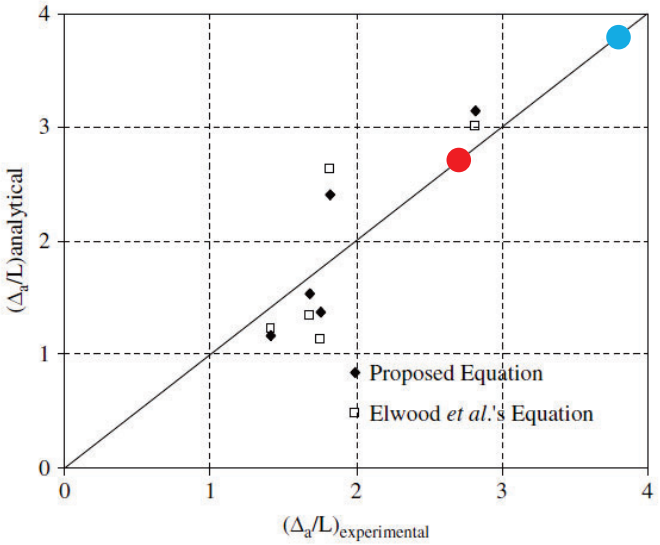

Figure 2-29: Comparisons between experimental and analytical ultimate displacements at axial failure of various equations (C. T. Ngoc Tran and B. Li 2013).

A series of experiments was conducted on five RC columns with light transverse reinforcement to validate the applicability and accuracy of the developed model. These tests were not included in the experimental database from which the developed semi-empirical model was derived. It is concluded from the study that the mean ratios of the experimental to estimated ultimate displacements and the corresponding coefficients of variation were 1.077 and 0.194, respectively. A comparison of the proposed equation by C. T. Ngoc Tran and B. Li (2013) with the model by Elwood and Moehle (2005) is depicted in Fig. 2-29. When applying the derived model by C. T. Ngoc Tran and B. Li (2013) described here to the example square column under study in this Chapter for 200 mm stirrups spacing, the drift at axial failure is 2.8 % which is much more conservative with respect to the result by Elwood and Moehle (2005) (3.9%; red and blue dots in the Figure, respectively).

CHAPTER THREE

PERFORMANCE OF EXISTING MODELS APPLIED TO THE EXPERIMENTAL COLUMNS DATABASE

The mode of failure of structural members such as reinforced concrete columns depends on several factors, such as their geometric characteristics, the longitudinal reinforcement, the efficiency of confinement through the transverse reinforcement and the loading history. Their behavior throughout the loading range is controlled by competing mechanisms of resistance such as flexure, shear, buckling of longitudinal bars when they are subjected to compressive loads, and in the case of lap splices, the lap-splice mechanism of bar reinforcement development. Very often a combination of such mechanisms characterizes the macroscopic behavior of the column, especially in cases of cyclic load reversals. Various predictive models have been developed in the past to determine both the strength as well as the deformation capacity of the columns, the uncertainty being at least one order of magnitude greater in terms of deformation capacity rather than strength, as evidenced by comparisons with test results.

In this Chapter, some of the models described analytically in Chapter 2 are tested for their performance against a widely used experimental database (2003, https://nisee.berkeley.edu/spd/) by Berry and Eberhard (2004). Known as the PEER Structural Performance Database, it assembles the results of over 400 cyclic, lateral-load tests of reinforced concrete columns. The database describes tests of spiral or circular hoop-confined columns, rectangular tied columns, and columns with or without lap splices of longitudinal reinforcement at the critical sections. For each test, where the information is available, the database provides the column geometry, column material properties, column reinforcing details, test configuration (including P-Delta configuration), axial load, digital lateral force displacement history at the top of the column, and top displacement that preceded various damage observations.

First, a parametric sensitivity for the employed database is conducted in order to highlight the statistical content and parameter trends with regard to basic indices that define the column behavior. Subsequently, flexure-dominant columns having either a circular or a rectangular cross section are studied so as to attempt to reproduce (and therefore fully comprehend) their hysteretic lateral experimental response. Shear critical columns are studied as a separate group - in terms of strength and deformation capacity. Some of the models presented in Chapter 2 for shear strength are tested against this group of experimental data. Lastly an experimental database for cyclic tests of reinforced concrete columns under variable axial load is assembled for the needs of the present study, and are used to corroborate the models outlined in Chapter 2 with regard primarily to deformation capacity as the axial load varies from compressive to tensile (modeling the overturning effects of the earthquake on perimeter frame columns in structures).

Parametric Sensitivity of PEER Structural Performance Database

The statistical profile of the data available in the PEER structural performance database (https://nisee.berkeley.edu/spd/) is outlined here. Distributions of key column properties (depth, aspect ratio, axial load ratio, longitudinal reinforcement ratio and transverse reinforcement ratio) provide the overall scope and limitations of the experimental investigations, and the degree of overlap and knowledge gaps between the available studies. The value of such collected databases is in crossing the boundaries of the individual experimental studies that have been conducted before, which, owing to the difficulty due to the size and expense of specimens, never include more than a handful of tests, always much smaller in number than the number of independent parameters and rarely if ever presented in replicas of two or three. In the context of understanding the scope of the database, principal indices of deformability (i.e. displacement ductility) are presented in correlation with key design parameters (concrete strength, axial load ratio, aspect ratio, maximum shear force and transverse reinforcement ratio).

Characteristics of Available Data

Table 3-1 provides the mean values (Mean), Standard deviation (std) and Coefficients of variation (CoV) of key column properties for 306 rectangular-reinforced columns and 177 spiral-reinforced columns. Statistics

are provided for the column depth, aspect ratio, axial-load ratio, longitudinal reinforcement ratio (ρ_l) and transverse reinforcement ratio (ρ_s).

Table 3-1: Column Property Statistics

	Rectangular-Reinforced (306 tests)			Spiral-Reinforced (177 tests)		
Column Property	**Mean**	**Std**	**CoV**	**Mean**	**Std**	**CoV**
Depth (mm)	323.43	116.5	0.36	420.97	202.11	0.48
Aspect Ratio	3.44	1.44	0.42	3.31	1.96	0.59
Axial-Load Ratio	0.27	0.19	0.73	0.14	0.14	1.04
ρ_l (%)	2.45	1.00	0.41	2.62	1.02	0.39
ρ_s (%)	1.34	1.07	0.80	0..93	0.74	0.80

The distributions of column depth used by researchers are illustrated in Figs. 3-1 and 3-2. Evidently, the rectangular-reinforced data is approximately normally distributed about a mean value of 300 mm. On the other hand the spiral column reinforcement data does not follow a normal distribution. Fig. 3-2 depicts a box plot for each of the two groups of specimens. (A Box Plot describes the five-number summary of a distribution that consists of the smallest (Minimum) observation, the first quartile (Q1), the median (Q2), the third quartile (Q3), and the largest (Maximum) observation written in order of smallest to largest. The central box spans the quartiles. A line within the box marks the median. Lines extending above and below the box mark the smallest and the largest observations (i.e. the range). Outlying samples may be additionally plotted outside the range.

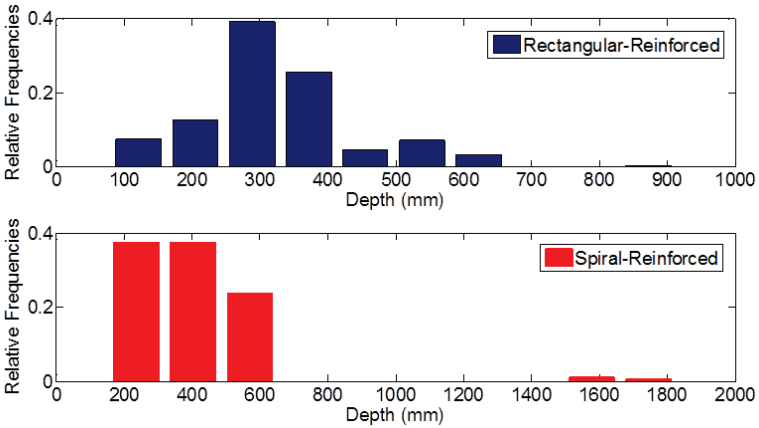

Figure 3-1: Distribution of Column Depth.

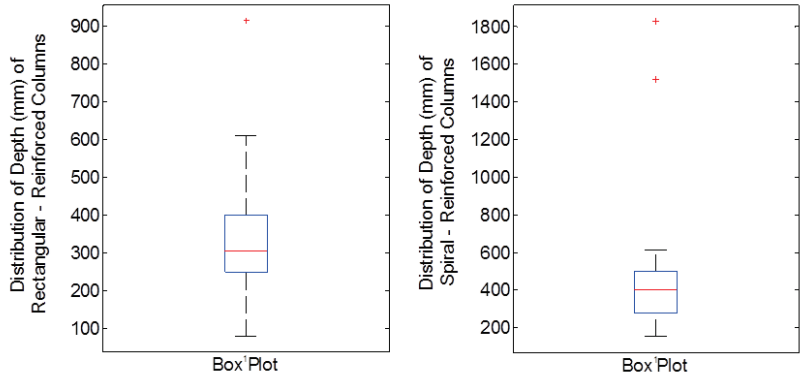

Figure 3-2: Box Plot of Column Depth.

The distributions of the column aspect ratio are illustrated in Fig. 3-3 & 3-4. The rectangular-reinforced data is approximately normally distributed about its mean value with a skew towards the lower aspect ratios. The spiral reinforced data is also weighted towards the lower aspect ratios. Fig. 3-4 depicts the box plot for the two groups of specimens. It should be noted that the length for the determination of the aspect ratio of each column is the equivalent cantilever column length.

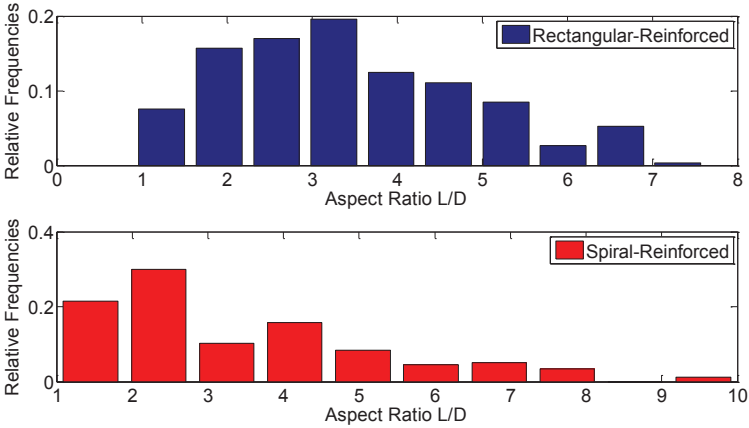

Figure 3-3: Distribution of Column Aspect Ratio.

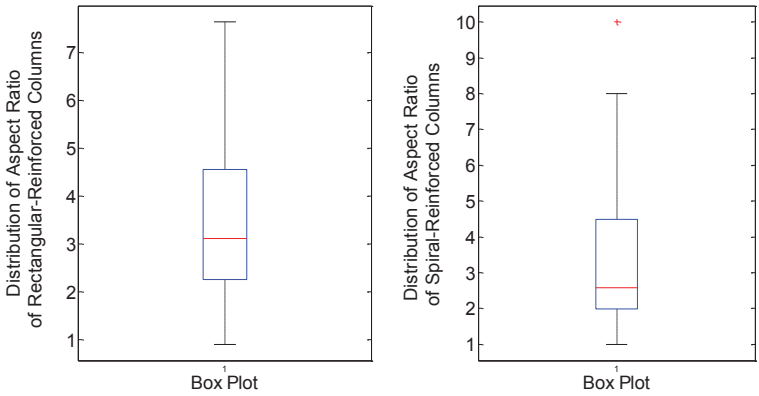

Figure 3-4: Box Plot of Column Aspect Ratio.

The distributions of the axial-load ratio are illustrated in Figs. 3-5 and 3-6. The spiral-reinforced data is approximately normally distributed about its mean value with a skew towards the lower axial load ratios. The rectangular reinforced data has a distribution weighted towards the lower axial-loads ratios. Fig. 3-6 depicts the box plot for the two groups of specimens.

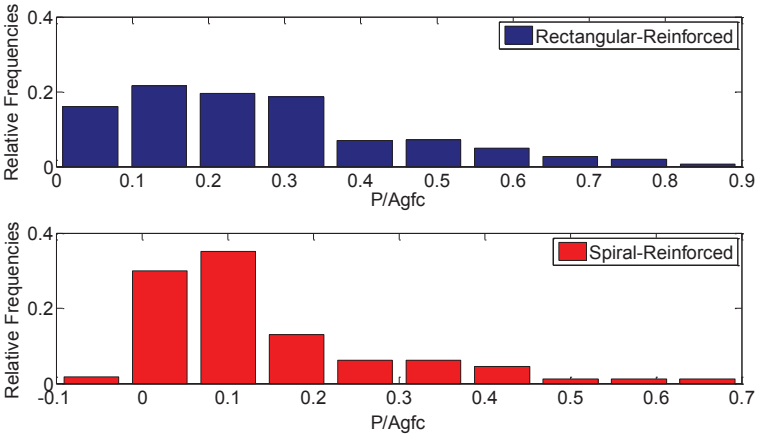

Figure 3-5: Distribution of Axial-Load Ratio.

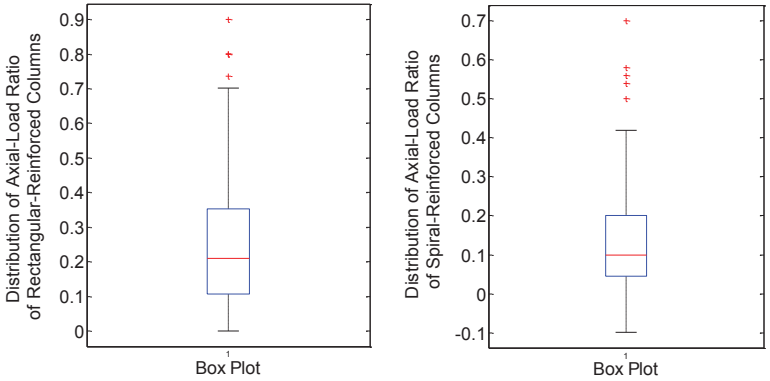

Figure 3-6: Box Plot of Axial-Load Ratio.

Figs. 3-7 and 3-8 plot the distributions of the longitudinal-reinforcement ratio, ρ_l. The rectangular-reinforced data is approximately normally distributed about its mean value with a skew towards the lower reinforcement ratios. Again, the spiral-reinforced data is not distributed normally. Fig. 3-8 depicts the box plot for the two groups of specimens.

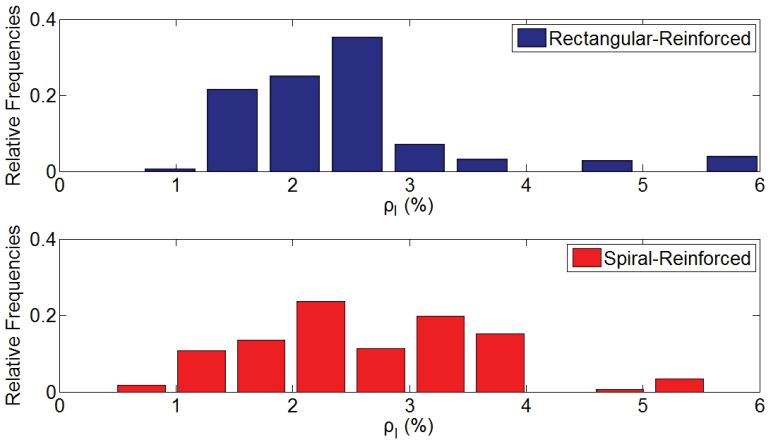

Figure 3-7: Distribution of Longitudinal-Reinforcement Ratio.

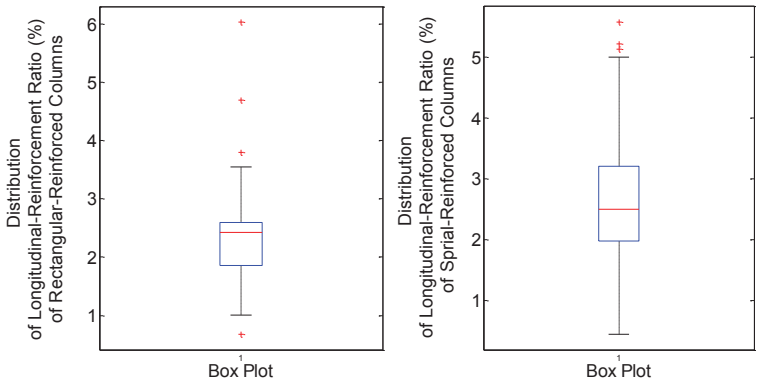

Figure 3-8: Box Plot of Longitudinal-Reinforcement Ratio.

Finally, the distributions of transverse reinforcement ratio are presented in Figs. 3-9 and 3-10. Both the rectangular-reinforced and spiral-reinforced columns have distributions weighted towards the lower transverse reinforcement rations and cannot be characterized easily by a specific distribution. Fig. 3-10 depicts the box plot for the two groups of specimens.

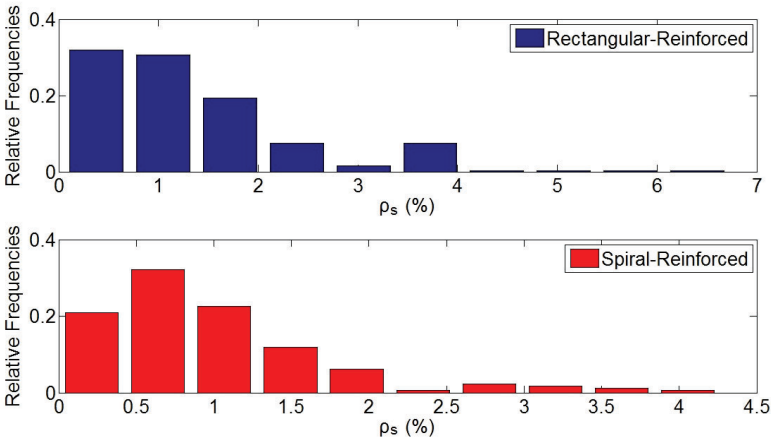

Figure 3-9: Distribution of Transverse-Reinforcement Ratio.

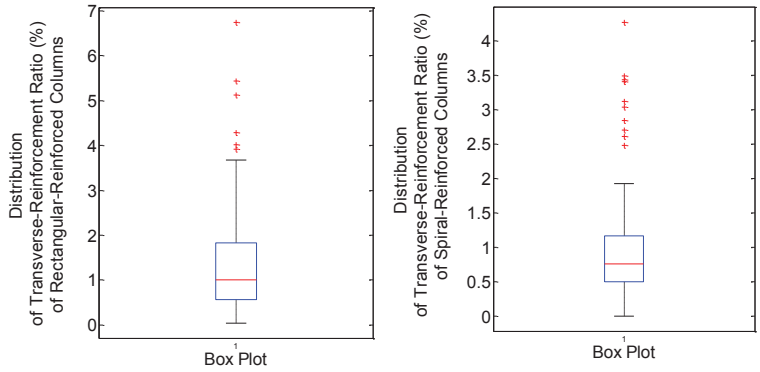

Figure 3-10: Box Plot of Transverse-Reinforcement Ratio.

Principal Indices of Deformability

One important goal in the seismic structural assessment procedures is the reliable estimation of the available capacity of structural members for inelastic deformation, as well as their available ductility. Ductility drives assessment since its magnitude underlies the general design philosophy (i.e., through the q-μ-T relationships it controls the magnitude of strength

reduction from the elastic demands that may be tolerated before failure) and, in current code practice, its magnitude is reflected on the specific reinforcing requirements of members and structures.

In this section the displacement ductility value clouds—as defined from the reported experimental responses—are correlated against important design parameters and plotted in graphs to illustrate the parametric dependencies of this variable.

For example, considering the concrete strength, the following points are made: (a) Higher strength materials are marked by lower ultimate strain, (b) strain can be enhanced through confinement, (c) a higher concrete strength results in a lower compression zone both at yielding and at failure. In general it can be said that higher concrete strength causes a reduction in ductility. This finding is confirmed by both groups of rectangular-tied columns and by the spiral-reinforced columns as can be seen in Figs. 3-11, 3-12. For the spiral-reinforced columns it is more clearly evident that the ductility is increased for specimens with lower concrete strengths.

During the flexural analysis of a section both at yielding and at failure the presence of a compressive axial load increases the depth of the compressive zone as compared to an identical section without axial force. Based on the above remark the presence of the compressive axial load reduces the curvature ductility of a section. In general it can be noted that the increase of the compressive axial force in a section reduces drastically the available ductility; it is also important to note that if the axial load increases beyond the point of balanced failure, the column section becomes brittle. This is confirmed by Figs. 3-13 and 3-14.

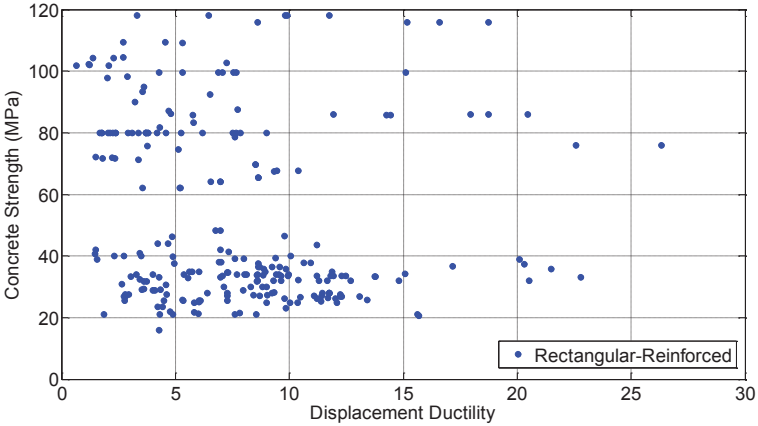

Figure 3-11: Effect of concrete strength on displacement ductility for the rectangular-reinforced columns of the Berry and Eberhard (2004) experimental database.

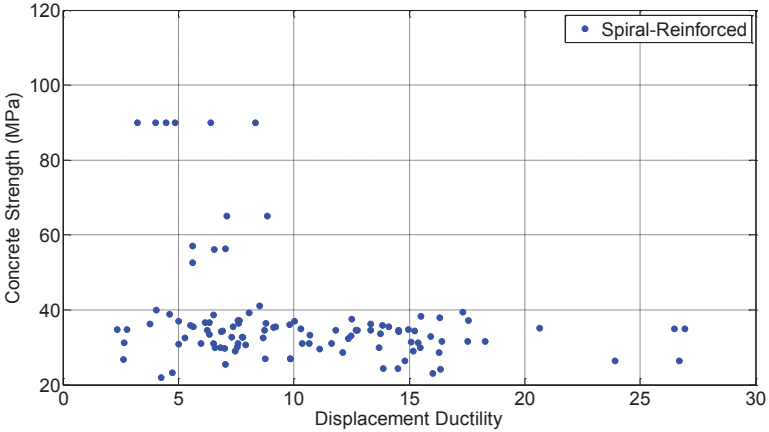

Figure 3-12: Effect of concrete strength on displacement ductility for the spiral- reinforced columns of the Berry and Eberhard (2004) experimental database.

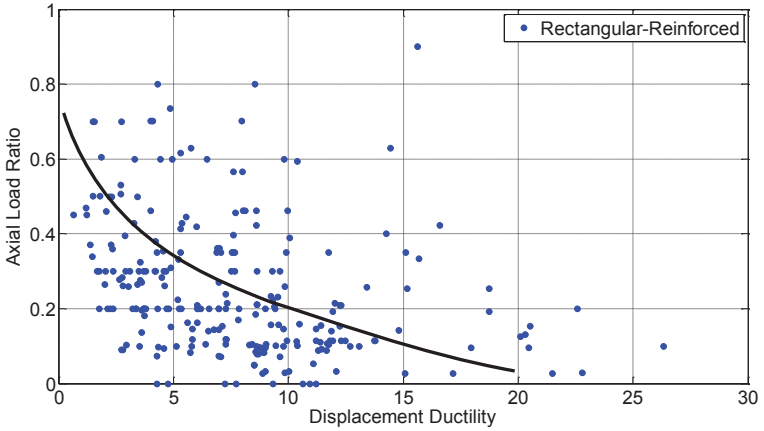

Figure 3-13: Effect of axial load ratio on displacement ductility for the rectangular-reinforced columns.

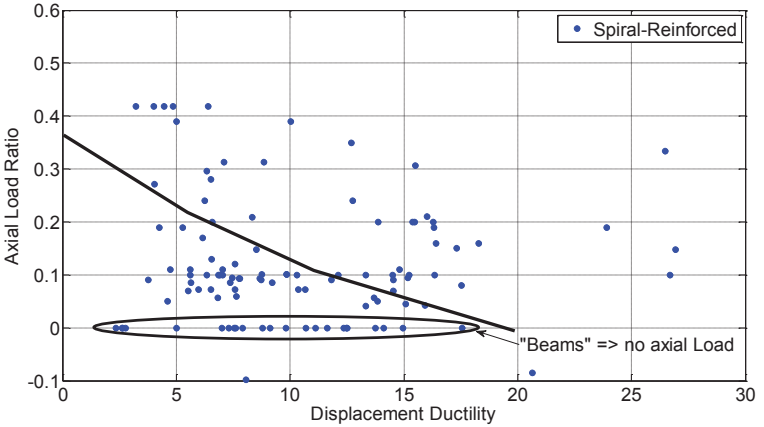

Figure 3-14: Effect of axial load ratio on displacement ductility for the spiral-reinforced columns.

Shear-span to depth ratio, known as aspect ratio, [a] is the most significant parameter that influences the shear behavior characteristics. In a column of small shear-span-to-depth ratio, shear deformation may become appreciable compared with the flexural deformation. A dominant

shear response causes a more pronounced pinching in the force-deformation (hysteresis) curve, and a faster degradation of the hysteresis energy dissipating capacity. Interestingly, the experimental data show that the ductility ratio increases with a decreasing aspect ratio (Figs. 3-15, 3-16); this perplexing result is attributed to the fact that the yield displacement increases at a quadratic rate with shear span length L_s, whereas the ultimate displacement is linear with L_s – and thus the ductility estimate is inversely proportional to L_s or [a]. The following expressions relate the flexural component of column response with aspect ratio, illustrating the source of the experimental trend:

-Yield Curvature: $$\phi_y = 2.1 \cdot \frac{\varepsilon_{sy}}{h} \tag{3-1}$$

-Yield Displacement: $$\Delta_y = \frac{1}{3} \cdot \phi_y \cdot L_s^2 \approx \frac{2}{3} \cdot \varepsilon_{sy} \cdot \frac{L_s}{h} \cdot L_s = \frac{2}{3} \cdot \varepsilon_{sy} \cdot \mathrm{a} \cdot L_s \tag{3-2}$$

-Ultimate Displacement:

$$\Delta_u \approx \Delta_y + \phi_{pl} \cdot \ell_{pl} \cdot L_s = \Delta_y + \frac{\varepsilon_{pl}}{2h/3} \cdot \ell_{pl} \cdot L_s = \Delta_y + 1.5\varepsilon_{pl} \cdot \ell_{pl} \cdot \mathrm{a} \tag{3-3}$$

-Displacement Ductility: $$\mu_\Delta \approx 1 + 2.3(\mu_\varepsilon - 1) \cdot \frac{\ell_{pl}}{L_s} \tag{3-4}$$

where ℓ_{pl} is the plastic hinge length, a the shear span (or aspect ratio), and ε_{pl} the nonlinear (past yielding) part of the tension reinforcement total strain, and μ_ε the required bar strain ductility.

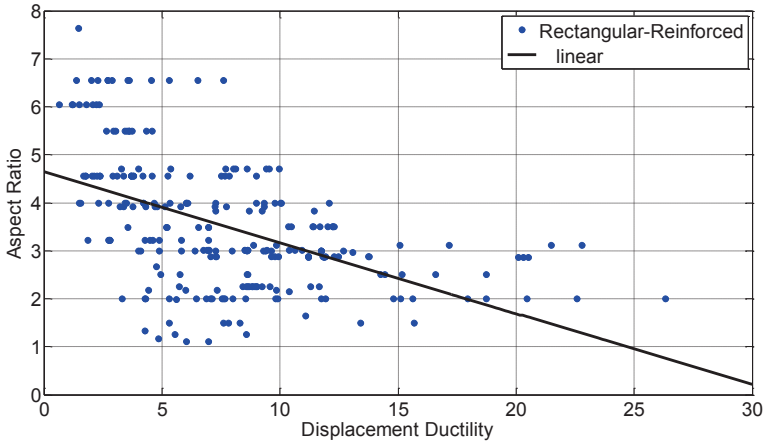

Figure 3-15: Effect of aspect ratio on displacement ductility for the rectangular- reinforced columns.

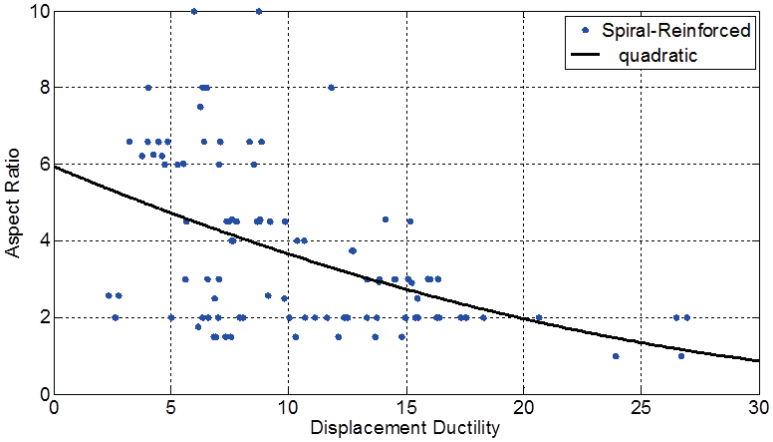

Figure 3-16: Effect of aspect ratio on displacement ductility for the spiral-reinforced columns.

Figs. 3-17 and 3-18 depict the relationship between the maximum shear stress (maximum experimental shear force divided by the gross area of the column) normalized by the square root of concrete strength of each column and the associated displacement ductility. It can be seen that columns with higher ductility also supported higher shear force, consistently with the result of Figs. 3-15, 3-16, which illustrated that displacement ductility is inversely proportional to aspect ratio, which in turn, for a given member flexural resistance, is inversely proportional to shear demand (since $V_{Ed}=M_{Ed}/(h\cdot a)$).

The database trends are also examined with reference to lateral confinement – which is generally acknowledged to enhance the deformation capacity of the column. The arrangement of confining reinforcement is important in this regard; a column with closely spaced stirrups and well-distributed longitudinal reinforcement shows very little strength decay even when being subjected to very high axial forces with magnitudes exceeding the limit of balanced failure. The plotted trends confirm this general expectation: the displacement ductility increases with the transverse reinforcement ratio as shown in Figs. 3-19 and 3-20.

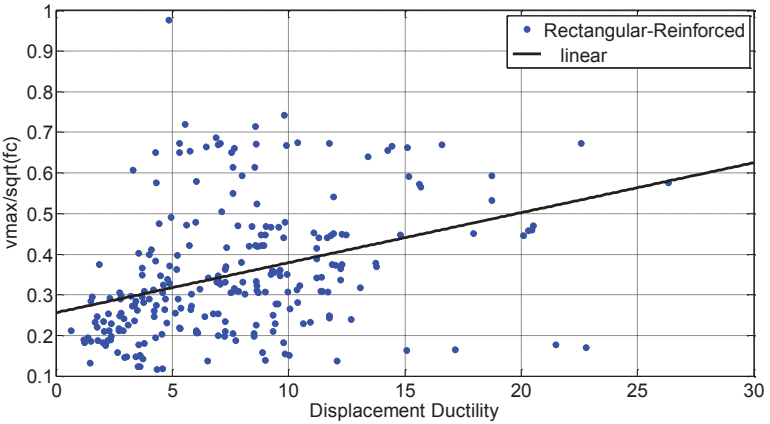

Figure 3-17: Maximum shear stress vs. displacement ductility for the rectangular- reinforced columns.

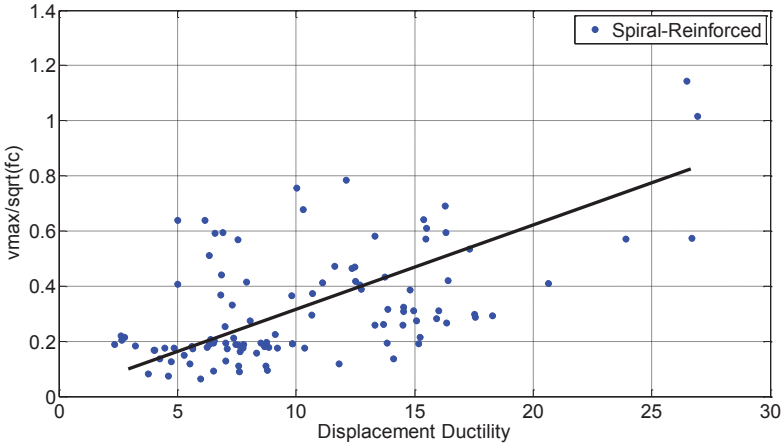

Figure 3-18: Maximum shear stress vs. displacement ductility for the spiral-reinforced columns.

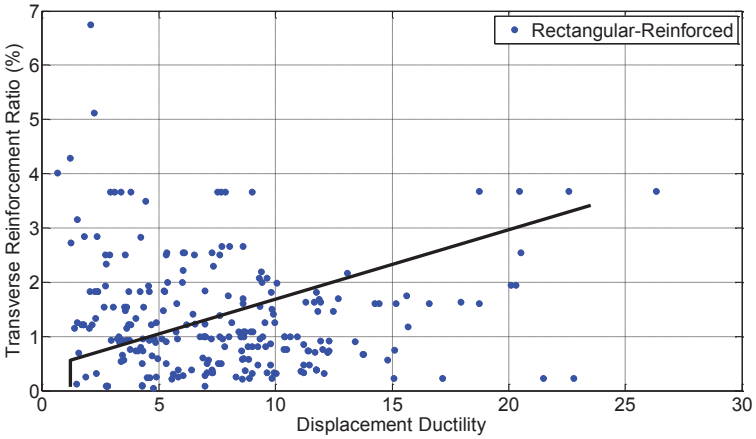

Figure 3-19: Effect of transverse reinforcement ratio on displacement ductility for the rectangular- reinforced columns.

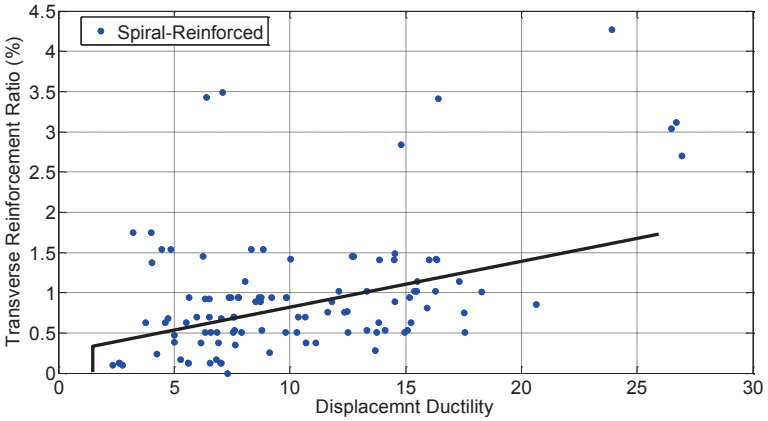

Figure 3-20: Effect of transverse reinforcement ratio on displacement ductility for the spiral- reinforced columns.

Analytical (F.E.) Simulation of RC Columns failed in Flexure

In the experimental database by Berry and Eberhard (2004) the nominal column failure mode was classified as (a) flexure-critical, (b) flexure-shear-critical, or (c) shear-critical, according to the following criteria:

- If no shear damage was reported by the experimentalist the column was classified as flexure-critical.
- If shear damage was reported, the absolute maximum effective force (F_{eff}: absolute maximum measured force in the experimental column response) was compared with the calculated "ideal" force corresponding to a maximum axial compressive strain in the concrete cover, equal to 0.004, which corresponds to spalling of unconfined concrete ($F_{0.004}$). The failure displacement ductility at an

  effective force equal to 80% of maximum, μ_{fail}, was determined from the experimental envelope. If the maximum effective force $F_{eff} < 0.95 \cdot F_{0.004}$ or if the failure displacement ductility was less than or equal to 2 ($\mu_{fail} \leq 2$), the column was classified as shear-critical. Otherwise, the column was classified as flexure-shear-critical. In the present section, only columns failed in flexure (i.e. classified as

flexure-critical) will be examined through simulation. These are divided into two groups according to cross-sectional shape (rectangular and circular section columns.

Circular-Reinforced Columns Failed in Flexure

Columns with a circular cross section that, upon lateral displacement reversals exhibited flexural failure are listed in Table A-1 in the Appendix of this Chapter. The hysteretic responses of several specimens from this group are analyzed in the present section using finite element cyclic static analysis.

The objective in conducting this analysis is to evaluate the available theory regarding their success and limitations in reproducing the experimental responses of those column specimens that did not experience failures beyond the scope of the models (e.g. shear failure). Numerical simulations were conducted using a nonlinear fiber beam-column element that considers the spread of plasticity. In this type of analysis the longitudinal beam element uses a force type formulation with linear moment distribution to derive a flexibility matrix for the element with progressing nonlinearity (step by step); the strain-displacement relationships are therefore defined implicitly after inversion of the flexibility matrix to obtain the stiffness. Assuming strain compatibility between materials comprising the member, the formulation samples sectional response at selected integration points along the length. At the sectional level the Bernoulli hypothesis (plane sections remaining plane and normal to the axis of the member) is used to relate strains in the different fibers to the sectional curvature and longitudinal axis normal strain. Nonlinear uniaxial material laws are used to relate normal stress with normal strain in the fibers, thereby neglecting the effect of shear in modifying the principal orientations through the height of the cross section. Typical discretization of a column section is shown in Fig. 3-21. Sectional stress resultants (Moment and Axial load) are obtained from the equilibrium of the contributions of fiber stress resultants [FEDEAS Lab (2004)].

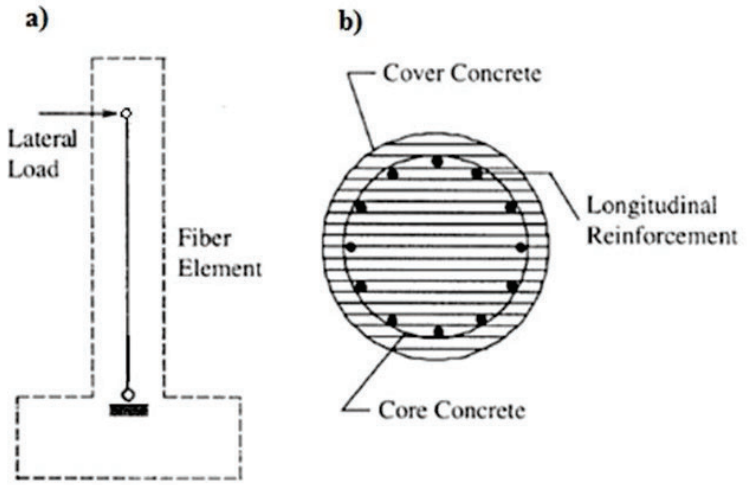

Figure 3-21: a) Numerical model for Spiral-Reinforced Columns failed in flexure b) Section discretization in fibers/layers.

For example, for the column with ID#43 in Table A-1 (axial load ratio ν=0.19), as it is depicted also in Fig. 3-21, a single beam-column element is assigned to the entire length of the cantilever column and five Gauss-Lobatto integration points [FEDEAS Lab (2004)] were defined along the element. Uniaxial material stress-strain laws for the concrete and steel fibers are depicted in Fig. 3-22(a) (Scott et al. 1982) for concrete and in Fig. 3-22(b) for steel (Menegotto and Pinto, 1973). The effect of confinement on the confined concrete core was modelled using pertinently modified properties for the uniaxial stress-strain law of concrete in compression. No P-Δ effect was considered in this simulation. The calculated lateral Force – lateral Displacement response of the numerical simulation of the column is plotted for comparison with the experimental results in Fig. 3-23. The good correlation up to a drift of 3.75% underscores the fact that flexural behavior is controlled by steel inelasticity which is stable and may be reproduced without the consideration of other secondary effects or the interaction of flexural with shear response. However, correlation deteriorates significantly beyond that point, on account of the fact that second order effects have been neglected and there is no accounting for the ensuing degradation and progressive collapse.

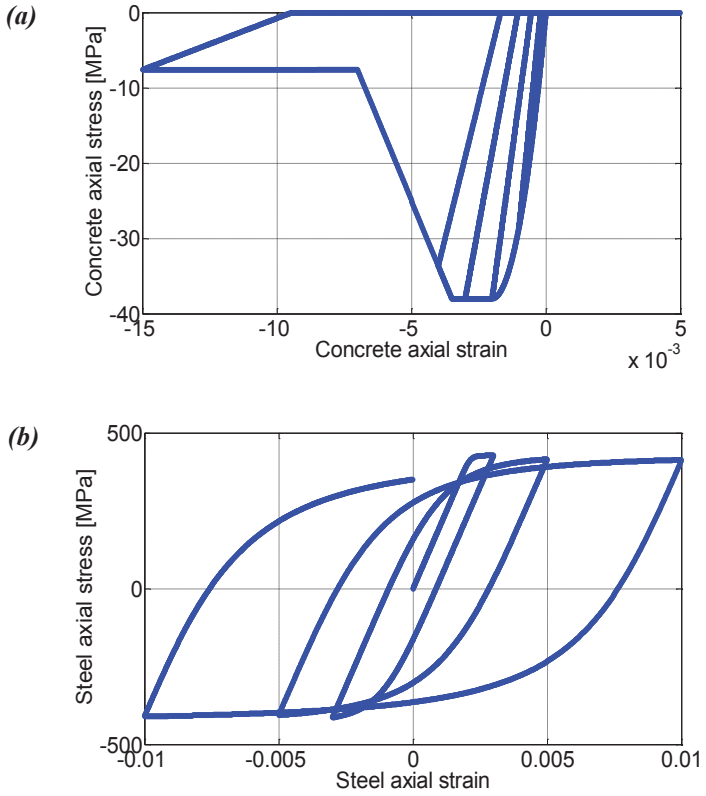

Figure 3-22: (a) Scott et al. (1982) constitutive law assigned to the concrete fibers. (b) Menegotto and Pinto constitutive law assigned to the longitudinal steel fibers.

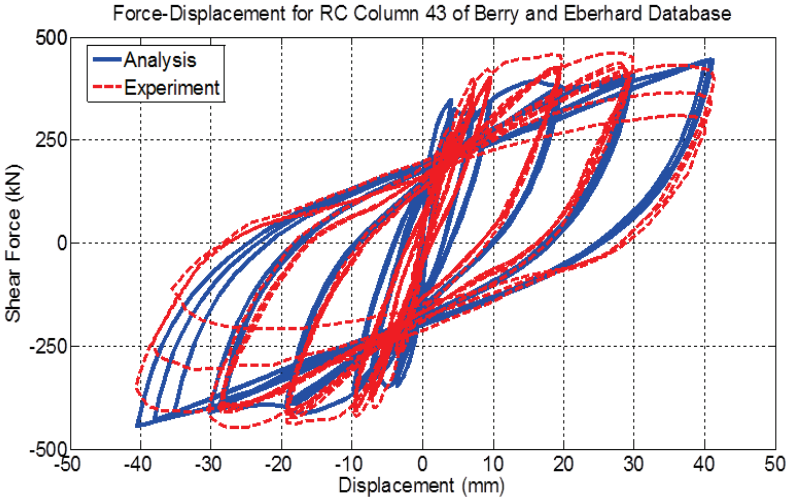

Figure 3-23: Comparison between numerical and experimental response of circular column (ID#43) of Berry and Eberhard Database (2004).

Another example (column ID#45) from Table A-1 in the Appendix of this Chapter is shown here: the approach used for simulation is identical to that of the previous example, the only difference being in the use of a more complex stress-strain model for the confined core (Mander et al. 1988; here the strain capacity of the confined core is related to the strain energy that may be absorbed by the stirrups before fracture), as depicted in Fig. 3-24. Figure 3-25 compares the calculated and experimental lateral force vs. lateral displacement hysteresis – again the correlation is satisfactory up to a drift of 2.5%, however, the model cannot reproduce the loss of lateral load bearing capacity near the end of the test; note that this column was identical to the previous one but carried twice the amount of axial load. Therefore second order effects would cause an apparent loss of 22.6 kN for an increment of lateral displacement from 20mm to 30mm (and 67.8 kN total reduction of the yield lateral force due to P-Δ effect at the displacement level considered); the additional loss which occurs in repeated cycles at the same displacement excursion is owing to material degradation.

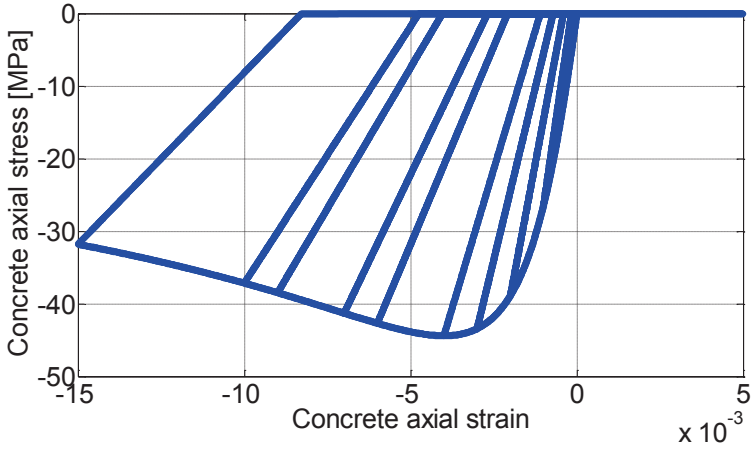

Figure 3-24: Mander et al. (1988) stress-strain model assigned to the concrete fibers.

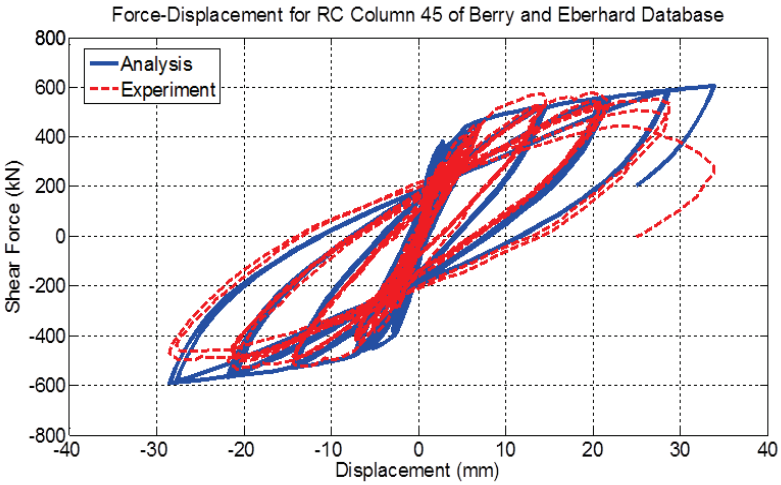

Figure 3-25: Comparison between numerical and experimental response of circular column (ID#45) of Berry and Eberhard Database (2004).

Several other examples are presented in Figures A-1 – A.26 in the Appendix to the present Chapter. Correlation in flexure dominant cases follows the general pattern discussed in the previous two examples. It is noteworthy that some cases demonstrated significant pinching, which was not reproduced by the purely flexural nonlinear model; such examples are specimens with ID#47, ID#53, ID#55, ID#56, ID#57, ID#58, ID#59, ID#60, ID#116, ID#120, ID#141, ID#142 and ID#157. In the case of these specimens, which had a low volumetric ratio of transverse reinforcement (0.6%) and early yielding with strain penetration along the anchorage, the observed pinching was owing to reinforcement pullout and shear deformation in the plastic hinge region, both phenomena neglected in the numerical model used here.

Rectangular-Reinforced Columns Failed in Flexure

The group of rectangular-reinforced specimens is summarized in Table A-2 in the Appendix of this Chapter; again only specimens that reportedly failed in flexure are considered in this section, to test the performance of formulations that only consider normal stress response at the sectional level.

The force-based nonlinear fiber beam-column element which considers the spread of plasticity available in FEDEAS Lab (2004) was used in this Section's numerical simulations. As previously, a single frame element is considered using flexibility formulation with assumed linear variations of moments along the length; sampling of sectional response is done at five Gauss Lobatto integration points along the member length. The typical discretization of rectangular column sections is shown in Fig. 3-26.

For the first column (No. Database 1) of Table A-2 (with a square cross section and an axial load ratio of 0.26), as shown in Fig. 3-26, a unique fiber element is assigned to the entire height of the cantilever column and five Gauss-Lobatto integration points were defined along the element. Uniaxial concrete stress strain response was modeled using the relationship by Mander et al. (1988, Fig. 3-24). The different confinement effect of the unconfined concrete cover and the confined concrete core was not considered in the discretization of the section (Fig. 3-26). The stress-strain response of longitudinal reinforcement was modeled by Menegotto and Pinto (1973, Fig. 3-22b). Again, the P-Delta effect was not accounted for in the simulation. The comparison of the lateral Force – lateral Displacement response of the numerical simulation of the column with the experimental results can be seen in Fig. 3-27. As was seen in the case of circular section columns, while the axial load ratio is kept low, a good

agreement between numerical and experimental results is found up to drift levels of 2.5% (where the strength loss owing to P-Δ is only 45kN i.e., about 7% of the column strength).

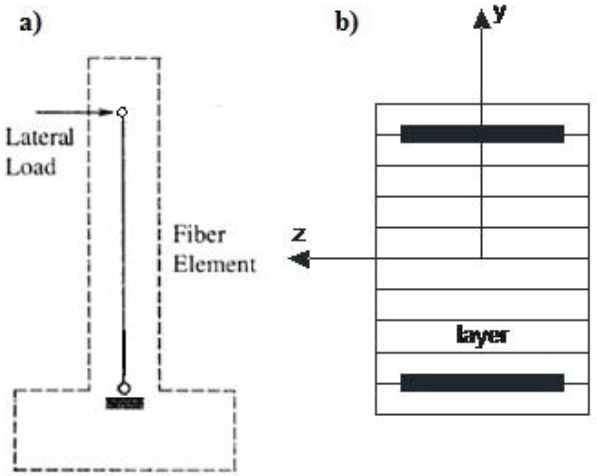

Figure 3-26: a) Numerical model for Rectangular RC Columns failed in flexure b) Section discretization in fibers/layers.

The performance of the same numerical model applied to the second column example listed in Table A-2 – (again having an axial load ratio of ν=0.22) is compared to the experimental force - displacement response curve in Fig. 3-28. Response is adequately well modeled, reproducing faithfully the loss of cover (spalling) at a drift of 1.2%; therefore, it may be concluded that the efficacy of distributed plasticity beam column models based on the force formulation successfully estimates the flexural behavior also in the case of reinforced concrete columns with rectangular sections.

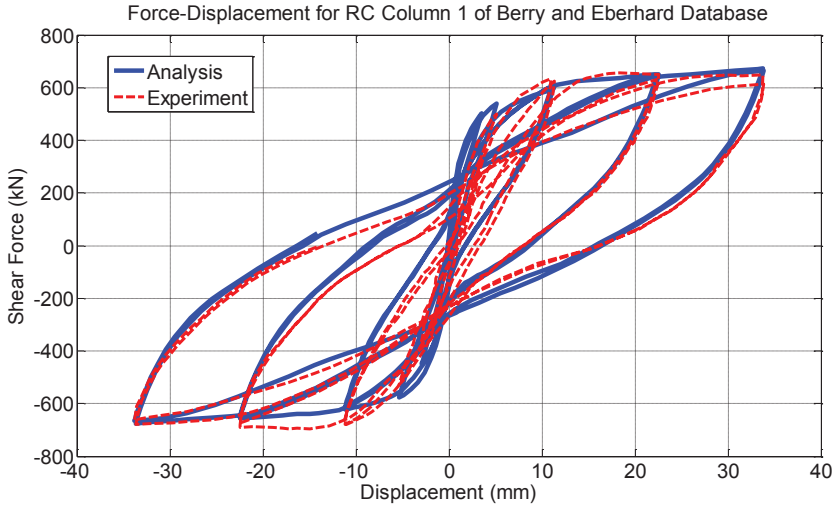

Figure 3-27: Comparison between numerical and experimental response of rectangular column (ID#1) of Berry and Eberhard Database (2004).

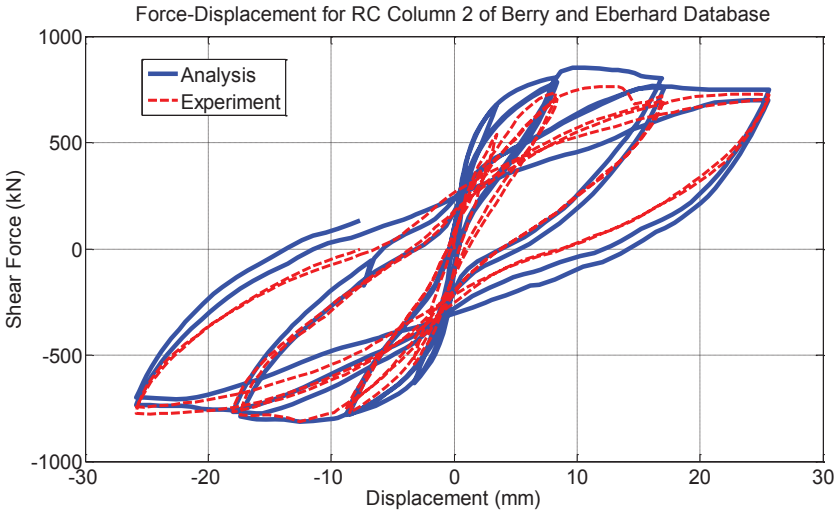

Figure 3-28: Comparison between numerical and experimental response of rectangular column (ID#2) of Berry and Eberhard Database (2004).

Several other examples are presented in Figures A-27 – A-76 in the Appendix to the present Chapter. Correlation in flexure dominant cases follows the general pattern discussed in the previous two examples. Correlation deteriorates beyond drift levels in the range of 3% or more, when the column carries a significant axial load ratio. It is noteworthy that some cases demonstrated significant pinching, which was not reproduced by the purely flexural nonlinear model; such examples are specimens with ID#32, ID#105 and ID#106. In the case of these specimens, which had a low transverse reinforcement ratio and early yielding with strain penetration along the anchorage, pinching in the experimental response was owing to reinforcement pullout and shear deformation in the plastic hinge region, both phenomena neglected in the current numerical model. Finally, in one case (ID#91) the experimental response was not symmetrical in the two directions of loading due to buckling of compressive reinforcement and—since buckling was not modelled in the simulation—this aspect of the response could not be reproduced numerically.

Analytical (F.E.) Simulation of RC Columns Failed in Shear

The performance of the shear critical columns (flexure-shear or shear failure) of the experimental database in terms of strength and deformation capacity is also examined so as to test again the performance of the analytical procedure described in the preceding sections. Again, the columns are divided into two groups according to cross sectional shape.

RC Columns with Rectangular Cross-Section Failed in Shear

Columns with a rectangular cross section that developed shear failure are summarized in Table A-3 of the Appendix of this Chapter. Figure 3-29 plots the shear strength degradation models adopted by EN 1998-3 (2005) and ASCE-SEI 41 (2007) (also see Chapter 2) in order to describe the envelope of the resistance curves of reinforced concrete columns as a function of displacement ductility; this is used as the basic criterion in order to detect shear failure before or after flexural yielding (point of intersection with flexural capacity curve). Therefore, it is also necessary to define the flexural capacity curve based on classic flexural analysis and combine it with the reduction of the shear strength curve postulated by the codes, in order for the strength and deformation of the reinforced concrete

column at shear failure to be defined. This procedure is followed in the present Section in order to analyze the shear critical columns of the experimental database under study and to examine how successful the code provisions are in predicting the strength and deformation of columns failing in shear before or after flexural yielding. In addition, the models by Elwood (2003) introduced also in Chapter 2 that define the drift capacity of shear-critical columns at shear failure and at loss of axial load carrying capacity are included in the study.

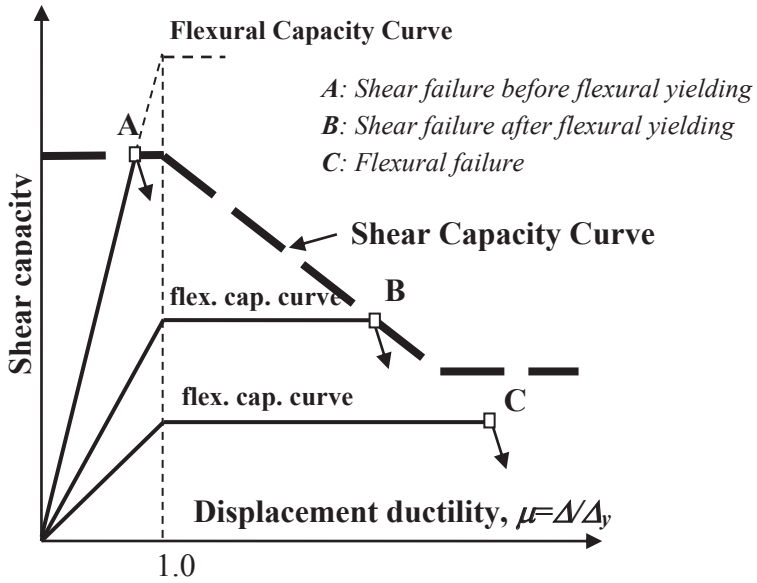

Figure 3-29: Shear strength degradation model adopted by current codes of assessment.

The force-based nonlinear fiber beam-column element which considers the spread of plasticity available in the FEDEAS Lab (2004), was used also in this section's numerical simulations for the definition of flexural capacity curve. The modelling procedure was the same as that used in earlier paragraphs for columns with rectangular cross sections.

Figure 3-30 compares the analytical and experimental response of the rectangular column –ID#28 (Table A-3). Clearly, correlation is poor even with regard to the initial stiffness defined by flexural analysis. This is owing to the fact that the contributions to deformation resulting from

reinforcement pullout and shear deformation have been neglected. It can be observed that only the degrading shear strength model of ASCE-SEI 41 (2007) intersects the flexural capacity curve and therefore is (correctly) identifying the trigger of shear strength failure after flexural yielding as a result of shear strength degradation. However, the displacement when this event takes place occurs earlier than the actual onset of strength degradation as observed in the experimental response. The proposal of Elwood (in parentheses next to the drift ratios the corresponding displacements are given for the column under study based on its shear span) overestimate the actual drifts associated with shear and axial failures as observed in the experimental results.

In the next column example (Fig. 3-31) the code provisions fail to detect shear failure despite the fact that in the experiment shear failure was reported. Again, the drift models by Elwood (2003) overestimate the displacements at which shear and axial failure occurred. The force-based fiber element used for the flexural analysis reproduces the peak strength well but fails to converge after that point, and cannot detect the strength degradation owing to shear failure. As mentioned before, the initial stiffness of the numerical model is overestimated as compared with the experiment.

Several other examples are presented in Figures A-77 – A-100 in the Appendix to the present Chapter. Correlation in shear dominant cases follows the general pattern discussed in the previous two examples.

RC Columns with Circular Cross-Section Failed in Shear

Spiral-reinforced specimens with a circular cross section that failed in shear are presented in Table A-4 of the Appendix of this Chapter. Monotonic analysis is conducted following the same procedure as described in the circular section Column (second case) of the previous Section.

As previously stated (Fig. 3-29), the shear strength degradation models such as those adopted by EN 1998-3 (2005) (here abbreviation EC8-III is used) and ASCE-SEI 41 (2007) (Chapter 2), are used to determine the deformation limit at shear failure from intersection with the flexural force – displacement envelope. The flexural capacity curve is based on classic flexural analysis. After the application of this procedure to specimen #14 in the experimental database, the following response envelope is determined (plotted in Fig. 3-32 against the experimental result).

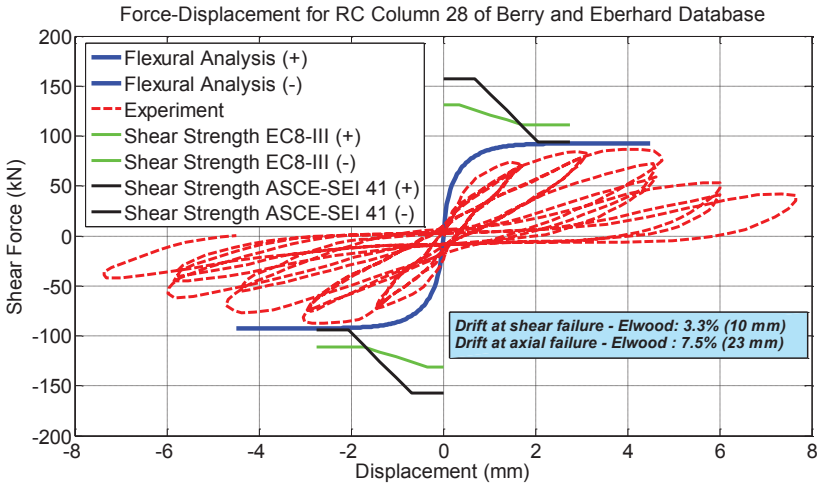

Figure 3-30: Comparison between numerical and experimental response of rectangular column (ID#28) of Berry and Eberhard Database (2004).

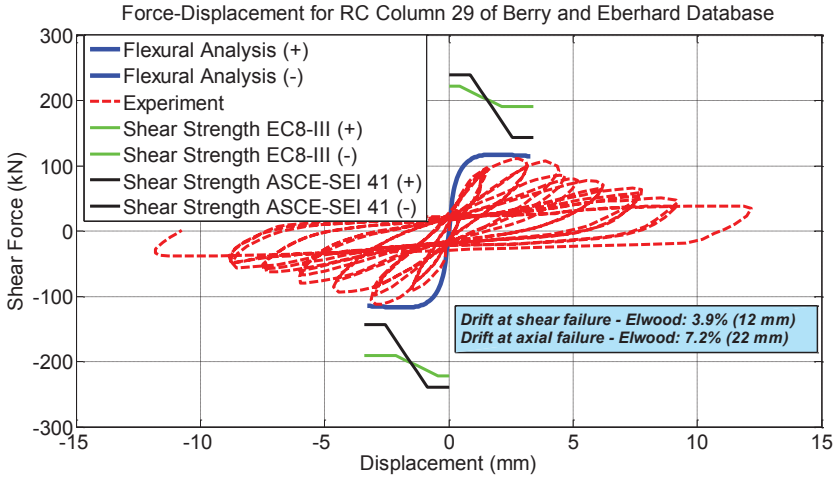

Figure 3-31: Comparison between numerical and experimental response of rectangular column (ID#29) of Berry and Eberhard Database (2004).

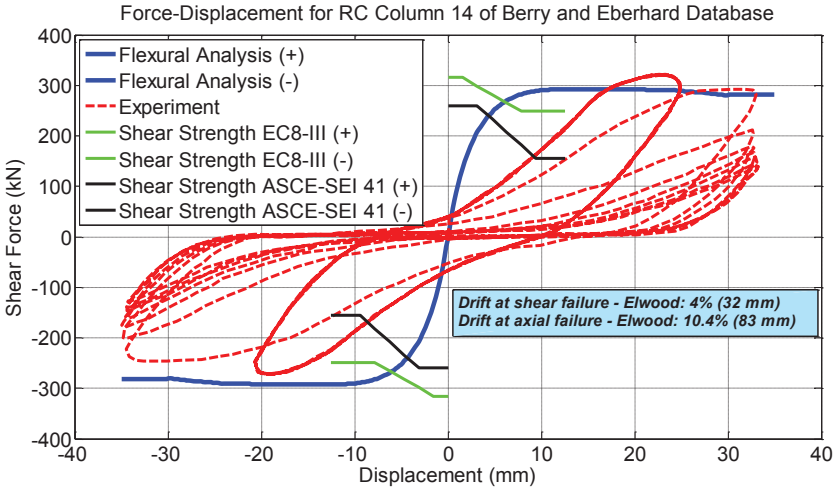

Figure 3-32: Comparison between numerical and experimental response of circular column (ID#14) of Berry and Eberhard Database (2004).

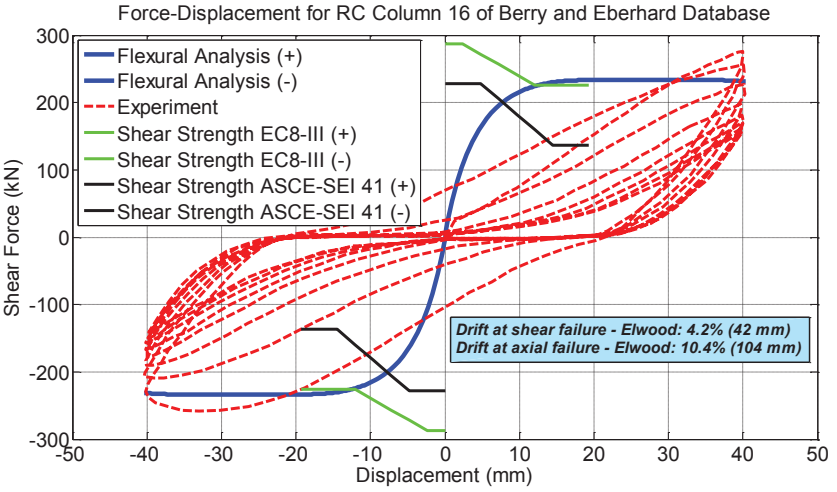

Figure 3-33: Comparison between numerical and experimental response of circular column (ID#16) of Berry and Eberhard Database (2004).

Both the shear strength degradation models shown in Fig. 3-32 detected shear failure after yielding at a displacement much lower than the corresponding experimental one. The strength at shear failure was better assessed by the model of Eurocode 8 part 3 (EC8-III) compared to the alternative of ASCE-SEI 41. The drift model at shear failure by Elwood (2003) performed very well as compared to the experimental shear failure limit; however, drift at axial failure was overestimated (83mm as compared to 30mm). The same comments are valid for the column in Fig. 3-33.

In the comparison showcased by Fig. 3-34, only the shear capacity curve by ASCE-SEI 41 intersects the flexural force-displacement envelope, thereby detecting shear failure after flexural yielding. The strength at shear failure was well predicted by the latter model but the corresponding displacement was much lower than in the experimental response. The drift model at shear failure by Elwood (2003) performed well compared to the experimental response but overestimated the drift at the loss of axial strength.

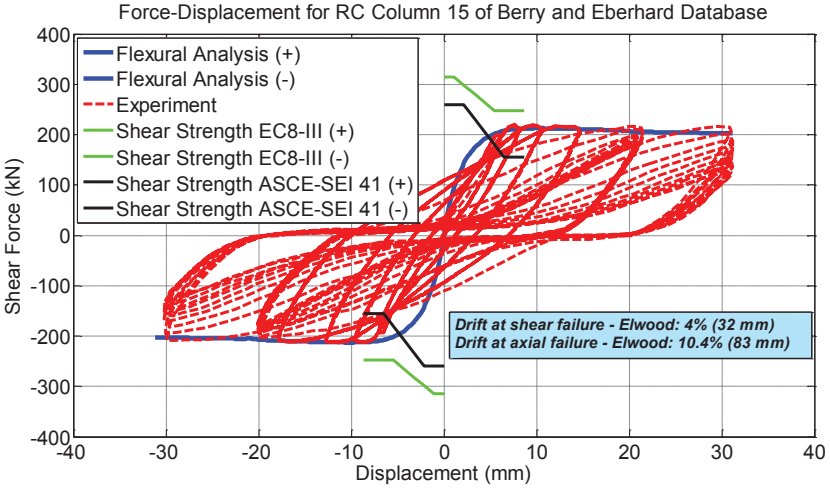

Figure 3-34: Comparison between numerical and experimental response of circular column (ID#15) of Berry and Eberhard Database (2004).

Several other examples are presented in Figures A-101 – A-118 in the Appendix to the present Chapter. Correlation in shear dominant cases follows the general pattern discussed in the previous three examples.

Analytical (F.E.) Simulation of RC Columns under Variable Axial Load

Owing to the overturning moment, columns in multiple-column bents experience variable axial forces corresponding to the direction of, and typically being proportional to, the horizontal forces. Columns are also subjected to the vertical components of ground motion, which is not correlated concurrently with the horizontal loading. Past earthquake records have shown that in some cases, vertical ground motions cannot be ignored, particularly for near-fault situations. For example, the lateral displacement ductility in a column, designed based on a constant axial load, with a relatively low axial load ratio, can become unsatisfactory when the actual axial load due to the overturning effects or the vertical ground motion exceeds the value that corresponds to balanced failure. The problem becomes even more significant when shear design is considered. The increase of axial load from the design level (typically 5% to 10% axial load ratio) to the level of the balanced axial load results in the increase of column flexural capacity, thus increasing shear demand. On the other hand, changes of axial load from compression to tension can result in a significant decrease in column shear strength.

In Table A-5 of the Appendix of this Chapter, an experimental database of reinforced concrete columns under cyclic lateral loading and variable axial load is presented. For these cases, the experimental response envelope will be assessed using monotonic static analysis. Analytical procedures are identical to those used in the previous section. For the sake of comparison with the numerical models and code specifications of the previous section, only pairs of specimens of the above experimental database tested under constant compressive or tensile axial load will be considered in the following correlation with the experimental results. In this way, the effect of the load on a column's shear strength will be demonstrated along with the effectiveness of code standards to assess this influence.

The first columns under study are the specimens ICC and ICT by Elnashai et al. (2011). Two columns with identical properties reported in Table A-5 are tested under cyclic lateral loading and constant compressive axial load (ICC) or constant tensile axial load (ICT). In the comparison of Fig. 3-35 with the experimental response it can be observed that the shear strength degradation model of ASCE-SEI 41 detects shear failure after yielding of the column under study while in the Eurocode 8 part 3 (EC8-III) shear capacity curve it does not. The predicted point of the detected shear failure corresponds well to the specimen strength, but in terms of

displacement the shear failure is identified to occur much earlier as compared to the experimental response. The drift models by Elwood (2003) defined well the displacement at shear failure, but again, the axial failure drift was overestimated.

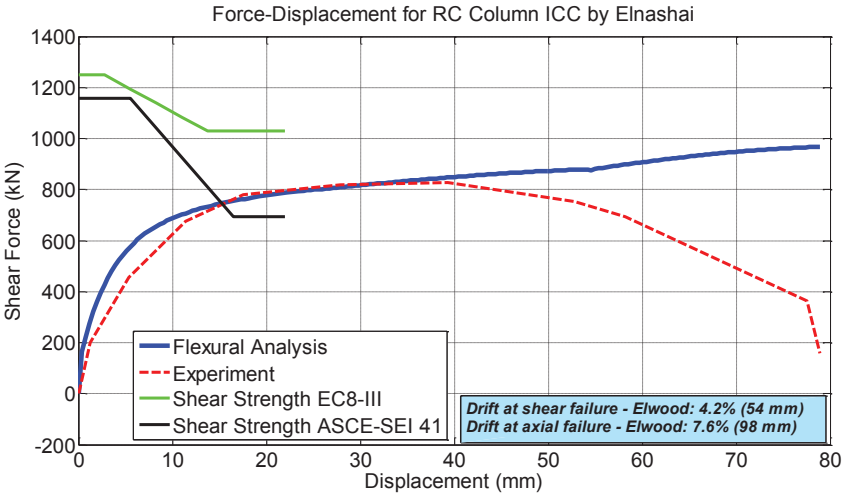

Figure 3-35: Comparison between numerical and experimental response of circular column (ICC) by Elnashai (2011).

For the case of the same specimen under constant tensile load (Fig. 3-36) it is noted that the degradation model of Eurocode 8 part 3 (EC8-III) for shear strength was the one reproducing the experimental response well since it did not detect shear failure for the specimen under study which failed in flexure. Finally, since no shear failure occurred, the drift models by Elwood (2003) were not relevant in the tensile-axial load case either.

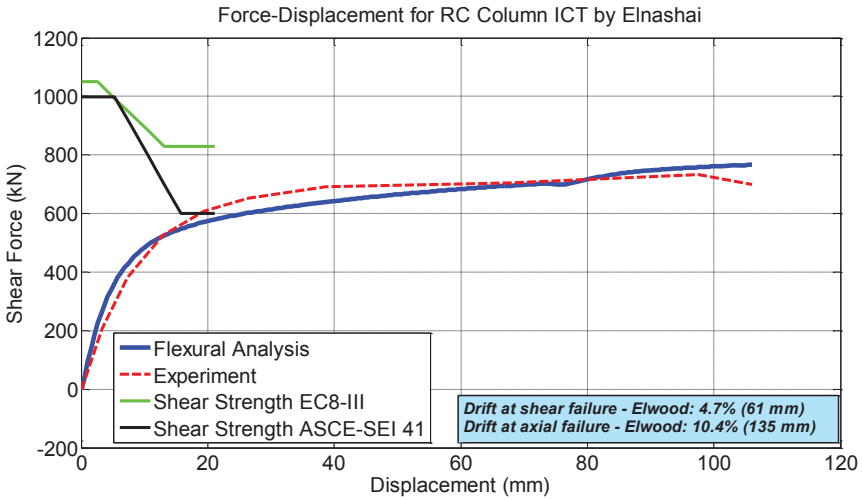

Figure 3-36: Comparison between numerical and experimental response of circular column (ICT) by Elnashai (2011).

The next column examples for investigation of the effect of variable axial load on shear strength are specimens CS1 and CS2 by Priestley et al. (1996) which were tested under cyclic lateral loading and constant compressive and tensile axial load respectively. From the comparison in Fig. 3-37 it can be observed that only the shear strength degradation model by ASCE-SEI 41 detects shear failure for the column under study, but at a somewhat lower strength and displacement capacity as compared to the experimental response. In addition, the drift model of Elwood at shear failure overestimates the corresponding displacement, while the drift model at axial failure underestimates the displacement where the loss of axial bearing capacity is observed.

Finally, the comparison of the same specimen by Priestley under tensile axial load is depicted in Fig. 3-38. The degraded shear capacity models of the design codes (both) detect the shear failure of the column, but at lower strength and displacement compared to the experimental results. The drift model at shear failure by Elwood captures well the displacement where shear failure occurs but the drift model at axial failure overestimates the experimental column response.

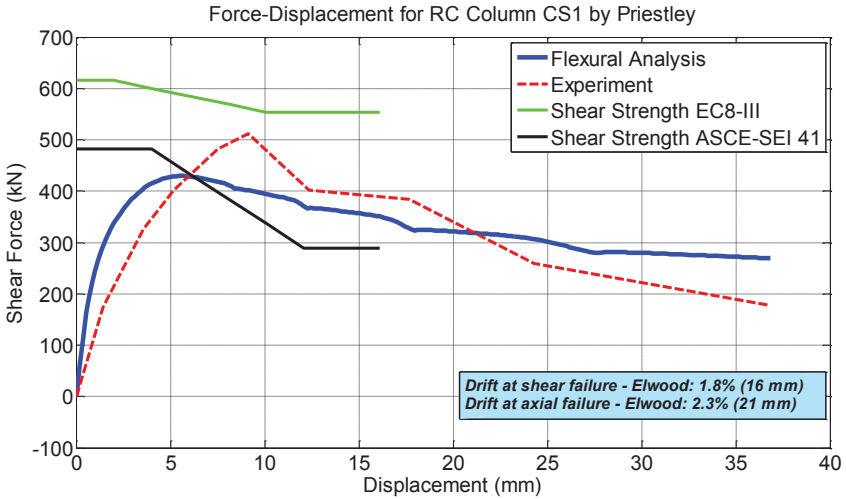

Figure 3-37: Comparison between numerical and experimental response of circular column (CS1) by Priestley (1996).

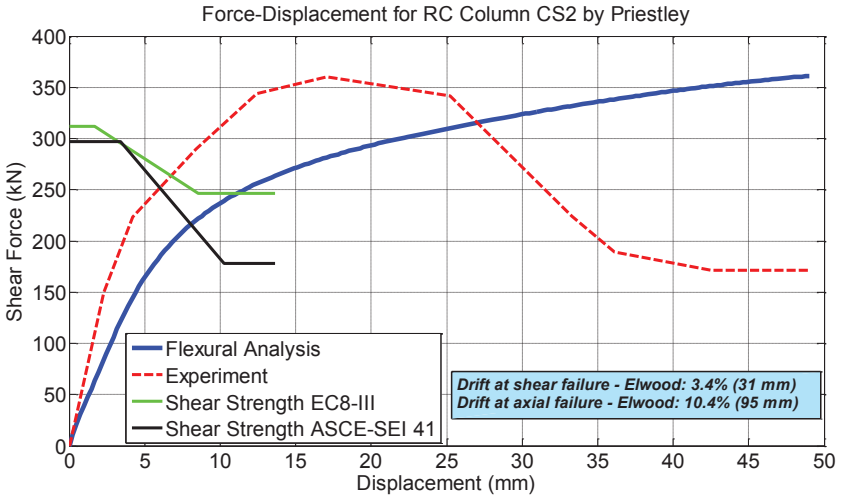

Figure 3-38: Comparison between numerical and experimental response of circular column (CS2) by Priestley (1996).

Clearly, based on the preceding analysis, the state of the art modeling of the lateral load response of columns leaves a lot to be desired: improved response estimation of the behavior of columns that are susceptible to shear failure after flexural yielding; better procedures to estimate shear strength and the pattern of degradation thereof, with increasing displacement ductility; the need to account for reinforcement pullout and its effects on stiffness; the shape of the hysteresis loops; the detrimental effects of axial load at large displacement limits; and the magnitude of deformation (drift ratio) associated with milestone events in the response curve of the column member, are open issues that need to be settled before the performance-based assessment framework may be considered complete and dependable. Some of these issues are addressed in Chapters 4 and 5 of the present book.

CHAPTER FOUR

PLASTIC HINGE LENGTH IN RC COLUMNS: DEFINITION THROUGH CONSIDERATION OF YIELD PENETRATION EFFECTS

Introduction

The deformation capacity of frame elements comprises contributions of flexural, shear and reinforcement pullout components. The estimation of the available deformation capacity of a column is linked to the length of plastic hinges. Following an implicit assumption that all terms are additive, the flexural component of lateral displacement is obtained from the sum of an elastic component, owing to the flexural deformation occurring along the length of the member, and a plastic component that is practically owing to the inelastic rotation that occurs in the small region near the face of the support where moments may exceed the yielding limit. When comparing these deformation estimates with the experimental evidence from predominantly flexural components, it is found that there is a great disparity between measured and estimated deformation capacities characterized by notable scatter (Syntzirma et al. 2010, Inel et al. 2004). Several attempts to identify the source of inaccuracy have motivated the progress made in that field, not the least the empirical expressions for deformation capacity which are included in EN 1998-3, 2005 that completely bypass the requirement of calculating the plastic hinge length. Another approach, initiated by Priestley et al. and then followed by several other researchers, and the approach to deformability by EN 1998-1, 2004 estimates the plastic hinge length including the length of yield penetration inside the anchorage (see, for example, the detailed analysis in the book by Priestley Seible and Calvi [1996], and of the *fib* Bulletin No.24 [2003]).

In new structural design with EN 1998-1 2004, the plastic hinge length is also used in reinforced concrete (RC) seismic detailing in order to determine the region where additional confinement requirements apply, this is apart from its use in seismic assessment to estimate the flexural deformation capacity. Due to its importance in these applications as the

key to understanding deformability of members, the plastic hinge has been the subject of many experimental and analytical studies and the expressions derived have been quantified and calibrated against several hundreds of tests on isolated column specimens. Still, the disconnect between observation and theory persists, and is considered a major roadblock in establishing the performance criteria for many special categories of members (e.g. walls, columns carrying a high axial load, very slender columns, etc.).

In the typical test, a cantilever column fixed at the base and carrying a constant axial load is driven to a protocol of reversed cyclical lateral load displacement history at the top. The deformation capacity of such members is usually described by the chord rotation that may be sustained by the member prior to loss of its lateral load strength. Apart from the rotation due to flexural curvature that occurs along the length of the member, lumped rotation at the critical section resulting from inelastic strain penetration into the support (e.g. footing) as well as inside the shear span adds up in the reported drift ratios at different levels of performance. This share of deformation is attributed to reinforcement pullout due to the incompatible length change between the bar and the surrounding concrete.

In columns that do not fail by web crushing, pullout rotation increases gradually with imposed drift, claiming a predominant share of the members' deformation capacity near the ultimate limit state. Column deformation capacity at yielding and ultimate state may be computed using a variety of models (Pantazopoulou 2003, Inel et al. 2004, Pantazopoulou et al. 2010, ASCE/SEI 41 2007, EN 1998-3 2005, Panagiotakos et al. 2001, Biskinis et al. 2013). A stick model is a common point of reference to this purpose: The length of the cantilever L_s corresponds to the shear span of an actual frame member under lateral sway (Fig. 4-1a); the aspect ratio of the member L_s/h, where h is the cross section depth, quantifies the intensity of shear force demand in the member. Inelastic activity is assumed to occur within an equivalent "plastic hinge length", ℓ_{pl}, whereas the segment of the member outside ℓ_{pl} is assumed to behave elastically. Displacements are calculated from flexural curvatures assuming the curvature distributions of Fig. 4-1(b-c) which correspond to the development of yielding ϕ_y and post-yielding ϕ_u flexural strengths at the support. The plastic rotation developing in the hinge due to flexure is $\theta_{pl}{}^{f} = (\phi_u - \phi_y) \cdot \ell_{pl}$; similarly, the plastic rotation owing to bar pullout from the support is $\theta_{pl}{}^{slip} = \theta_u{}^{slip} - \theta_y{}^{slip}$ (Fig. 4-1d); the total plastic rotation is $\theta_{pl} = \theta_{pl}{}^{f} + \theta_{pl}{}^{slip}$.

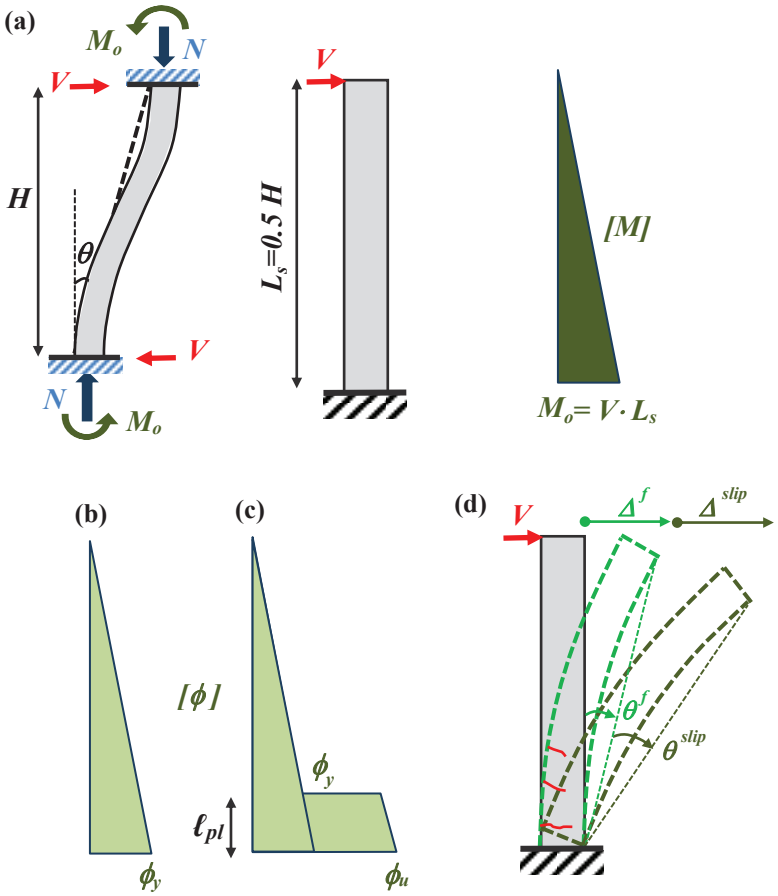

Figure 4-1: (a) The stick model for a column under lateral sway. (b)-(c) Distributions of curvature along the column shear span at yielding moment M_y and at flexural strength M_u attained at fixed support $(M_u > M_y)$ respectively. (d) Drift components from curvature along shear span (θ^f, Δ^f) and from anchorage slip (θ^{slip}, Δ^{slip}).

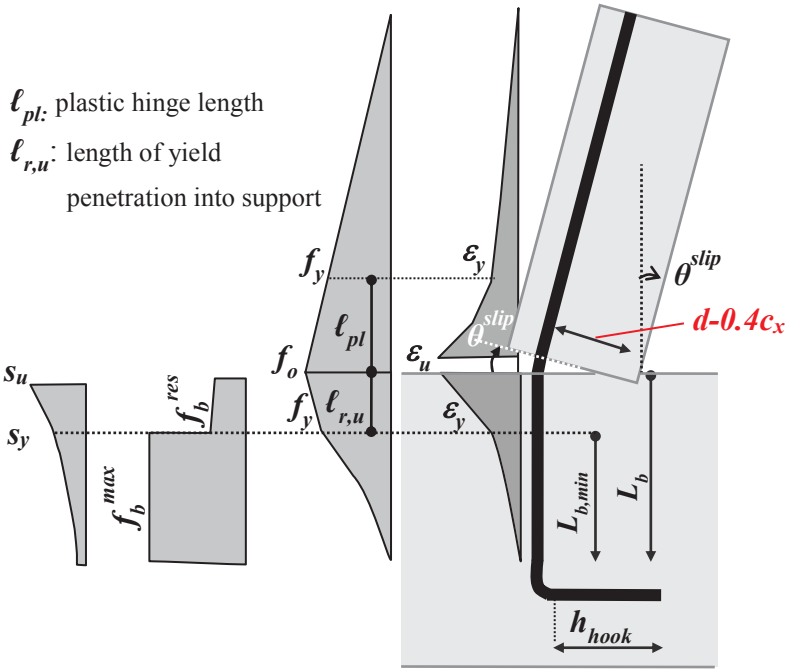

Figure 4-2**:** Bar state of stress / strain (*f, ε*) along shear span and anchorage of a cantilever column under horizontal loading at the tip. [Note: the bar bond / slip state (*fb, s*) is illustrated only for the anchorage.]

The corresponding terms are (Fig. 4-2) (*x* is the length counting from the support to the tip of the cantilever column under study):

$$\theta_y^{slip} = \frac{s_y}{(d-0.4x_c)}\Big|_{x=0} \quad ; \quad \theta_u^{slip} = \frac{s_u}{(d-0.4x_c)}\Big|_{x=0}$$
$$s_y \approx \varepsilon_y L_{b,min}/2 \quad ; \quad s_u \approx s_y + 0.5\cdot(\varepsilon_u + \varepsilon_y)\cdot \ell_{r,u} \quad ;$$
$$L_{b,min} = D_b \cdot f_y /(4 f_b^{max}); \quad \ell_{r,u} = L_b - L_{b,min} \qquad (4\text{-}1)$$

where x_c is the depth of the compression zone at the critical cross section (here it is assumed to remain constant after yielding) and L_b the total

available anchorage length, whereas $L_{b,min}$ is the minimum required anchorage length to yield a typical bar (diameter: D_b), at a yield stress of f_y, considering a uniform bond stress equal to the bond strength of f_b^{max}. Rotation of the critical cross section occurs about the centroid of the compression zone (located at a distance of $0.4x_c$ from the extreme compressed fiber based on the equivalent uniform stress block (Whitney 1937). The parameters s_y and s_u are values of reinforcement pullout slip from the support anchorage at yielding and the ultimate state (Fig. 4-2). Term $\ell_{r,u}$ represents the maximum sustainable penetration of yielding into the anchorage (Fig. 4-2); the maximum reinforcement strain, ε_u, that can be supported by the reinforcement at critical cross section (i.e. support) may be estimated assuming that at the extreme, when the anchorage attains its ultimate development capacity, the strain distribution along the anchored length is bilinear: $\varepsilon_u = \varepsilon_y + 4(L_b - L_{b,min}) f_b^{res} / (D_b E_{sh})$, where E_{sh} is the hardening modulus of steel and f_b^{res} is the residual bond strength due to cover splitting/delamination. The corresponding maximum and yield flexural curvatures are defined as: $\phi_u = \varepsilon_u / (d - x_c)$ and $\phi_y = \varepsilon_y / (d - x_c)$, whereas the total plastic rotation capacity θ_{pl}, that may be sustained by the member may be estimated through reverse engineering as in (Moehle, 1992):

$$\theta_{pl}^{slip} \approx 0.5 \cdot (\varphi_u - \varphi_y) \cdot \ell_{r,u} \; ; \; \theta_{pl}^{f} = (\varphi_u - \varphi_y) \cdot \left(1 - \frac{M_y}{M_u} \right) \cdot L_s \; \Rightarrow$$

$$\theta_{pl} = (\varphi_u - \varphi_y) \cdot \left(\underbrace{0.5 \cdot \ell_{r,u}}_{(i)} + \underbrace{a \cdot L_s}_{(ii)} \right) \tag{4-2a}$$

where in Eq. (4-2a) index *(i)* denotes pullout from support and *(ii)* flexure in the shear span. Introducing the concept of the plastic hinge length ℓ_{pl} the plastic rotation capacity is written as:

$$\theta_{pl} \approx (\varphi_u - \varphi_y) \cdot \ell_{pl} = \phi_{pl} \cdot \ell_{pl} \quad ; \quad \ell_{pl} = 0.5 \cdot \ell_{r,u} + \alpha \cdot L_s \tag{4-2b}$$

In Eq. (4-2b), α is the strain-hardening ratio of the reinforcement, $a = 1 - M_y/M_u$, defined from a cross section analysis at the ultimate moment given a simplified stress–strain law for the hardening branch of steel. Empirical equations for the plastic hinge which have prevailed in design Codes (EN 1998-1 2004, EN 1998-3 2005) and in research (Pantazopoulou 2003, Priestley et. al. 1984, Priestley et al. 1987, Priestley et al. 1996,

Lehman et al. 1996, Bae, S. et al. 2008) have the form of Eq. (4-3a,b) respectively:

$$\ell_{pl} = 0.08 L_s + 0.022 \cdot D_b \cdot f_y \tag{4-3a}$$

$$\ell_{pl} = 0.1 L_s + 0.17 \cdot h + 0.24 \cdot D_b \cdot f_y / \sqrt{f_c'} \tag{4-3b}$$

with h being the column sectional depth and f_c' the concrete compressive strength. (For example, 0.08 and 0.1 are common values for the strain hardening ratio α of common reinforcement, whereas the term proportional to the bar diameter D_b, which represents the strain penetration length within the anchorage, is intended for well-designed anchorages that can easily support strain penetration lengths of $10 \sim 20 \cdot D_b$). In the presence of high axial load N, the required confined length ℓ_c is obtained from the basic value of ℓ_{pl} by adding terms to account for the tension shift in the shear span of a member and the increased demands for confinement (Watson et. al. 1994), (γ_c in Eq. (4-3c) is a strength –reduction factor):

$$\ell_c = \ell_{pl} + 0.5h \quad ; \quad \frac{\ell_c}{h} = 1 + 2.8 \cdot \frac{N}{\gamma_c \cdot f_c' A_g} \tag{4-3c}$$

Bae and Bayrak (2008) proposed an alternative expression of ℓ_{pl}, derived from correlation with column experiments under various axial load levels, recognizing explicitly the important variables that control ℓ_{pl}:

$$\frac{\ell_{pl}}{h} = \left[0.3 \cdot \left(\frac{N}{N_o} \right) + 3 \cdot \left(\frac{A_s}{A_g} \right) - 0.1 \right] \cdot \left(\frac{L_s}{h} \right) + 0.25 \geq 0.25 \tag{4-3c}$$

where h is the column depth, N is the applied axial load, $N_o = 0.85 f_c' (A_g - A_{s,tot}) + f_y A_{s,tot}$, ($f_c'$ is the concrete compressive strength), A_s is the area of tension reinforcement, $A_{s,tot}$ is the total reinforcement area, and A_g the gross area of the concrete section.

A significant limitation of the theoretical definition of ℓ_{pl}, as given by Eq. (4-2b), is that it breaks down if the moment-curvature response of the member is elastic–perfectly plastic ($M_y = M_u$, a=0), leading to a rather small plastic hinge length. This is counter-intuitive considering that a necessary accessory to rebar yielding is the localized loss of bond. Thus point-yielding of column reinforcement with no penetration to an adjacent

area is physically impossible. In practical applications, to resolve the indeterminacy caused in Eq. (4-2b) due to elastoplasticity (i.e., $M_y=M_u$), ℓ_{pl} is taken as $0.5h$, or Eq. (4-3a, b) are used directly without reference to the underlying physical model. The apparent inconsistency inherent in the theoretical definition of ℓ_{pl} is partly responsible for the poor correlation of the estimated deformation capacity of flexure-dominated columns with results from experimental databases (Syntzirma et al. 2007, 2010). An alternative is to explicitly figure in for the plastic hinge length by establishing and solving the field equations of bond along the principal reinforcement (in the shear span) of the deformed member under lateral sway, with particular emphasis on the part of the reinforcement that is strained beyond the limit of yielding into the hardening range.

This modeling approach is pursued in the present chapter. A unidirectional model of bond is considered as a basis for the evaluation of the longitudinal strain distribution of the primary reinforcement of the column. The processes of sequential crack formation due to tension stiffening, and the subsequent crack opening are explicitly considered. In the analysis, large localized slip magnitudes lead to bond degradation that is accompanied by the spread of inelastic strains both in the shear span and in the anchorage. Although several solutions that refer to the problem of force development along the anchorage have been proposed, nevertheless the problem of strain penetration in the anchorage has received limited attention from researchers (Tastani and Pantazopoulou, 2013). On the other hand, the problem of strain penetration in the shear span of the member has not been addressed explicitly yet, and therefore represents the main scope of the present chapter. In this study, strain distributions in the span and in the bar anchorage are evaluated using a step by step calculation algorithm; the controlling variable is the tension strain magnitude at the critical cross section (the support of the cantilever). Through this process, disturbed regions are identified in the shear span, where bar strains are controlled by bond development rather than the "plane-sections" assumption. Using this approach, the parametric sensitivities of the plastic hinge length are illustrated and compared with the other alternatives summarized in this section obtained from experimental calibration. Application of the analytical procedure for estimating the plastic hinge length is demonstrated through a comparison with column specimens tested under axial load and reversed cyclical lateral drift histories reported in the literature.

Governing Equations of Bond–Slip Behaviour in Concrete

The basic equations that describe force transfer lengthwise from a bar to the surrounding concrete cover through a bond are derived from the force equilibrium established on an elementary bar segment of length *dx* (Tassios et al. 1981, Filippou et al. 1983):

$$df/dx = \left(-4/D_b\right)\cdot f_b \qquad (4\text{-}4a)$$

where f is the axial stress of the bar; D_b is the bar diameter; f_b is the local bond stress. Furthermore, compatibility between the relative translation of the bar with respect to the surrounding concrete, (s=slip), the axial bar strain ε, and concrete strain ε_c over dx requires that (Tassios et al. 1981, Filippou et al. 1983):

$$ds/dx = -\left(\varepsilon - \varepsilon_c\right) \cong \varepsilon \qquad (4\text{-}4b)$$

For normal concrete, the term ε_c is neglected as its tensile value cannot exceed the cracking limit ($\varepsilon_{c,cr} \approx 0.00015$) which is well below the other terms of Eq. (4-4b). Bond stress and slip, and bar stress and strain are related through the interface and material constitutive relationships, $f_b = f_b(s)$ and $f = f(\varepsilon)$. The solution to Eq. 4-4 is possible though exact integration, resulting in closed-form expressions for the state of stress and strain along the anchorage, through pertinent selection of simple models for the material laws (e.g. piecewise linear relations). This approach has a clear advantage over the numerical solution alternative in that it enables direct insight into the role of the various design parameters on the behavior of bar anchorages and/or lap splices.

Here the reinforcing bar stress-strain relationship is considered elastoplastic with hardening (representing conventional steel reinforcement, Fig. 4-3a). Without loss of generality, and to facilitate derivation of closed-form solutions, a linear elastic, perfectly plastic local bond-slip relationship with a residual bond is assumed (Fig. 4-3b). The plateau in the local bond-slip law implies sustained bond strength. This feature is not always manifested in the test data; to be measured it requires redundancy in the anchorage (i.e., the availability of longer anchorages to enable force redistribution towards the healthy part of the anchorage before failure). In the assumed law, the end of the plateau is marked by abrupt loss of bond strength to the residual value of f_b^{res}. (Note that f_b^{res} is taken as non-zero only in the case of ribbed steel bars, but not for smooth steel bars.) The

last branch represents the residual friction between the concrete cover and the steel bar after failure of the rib interlocking mechanism (Fig. 4-3b).

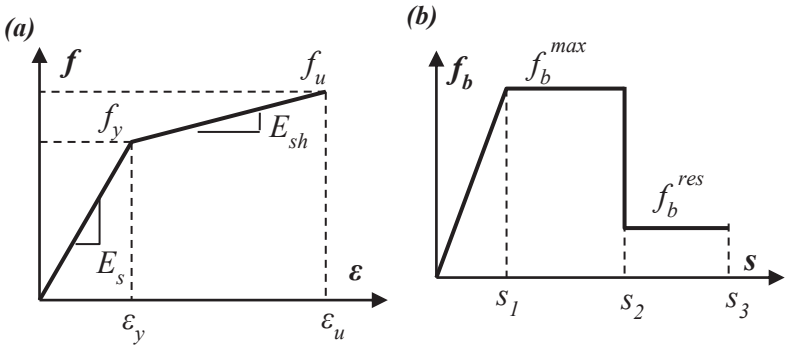

Figure 4-3: (a) Assumed stress-strain law of steel reinforcing bar; (b) Assumed local bond slip law.

Strain penetration occurs in the bars beyond the critical section due to the degradation of a bond beyond slip limit s_2, which marks the end of the plateau in the local bond-slip law. This stage may be attained in different ways along a bar: (a) for yielding to occur, i.e. constant bar stress (= f_y, df/dx = 0) for a range of values of bar strain $\varepsilon > \varepsilon_y$, the bond should be eliminated (f_b^{res} = 0); if f_b^{res} is non-zero, then a yielded bar will demonstrate a commensurate amount of strain hardening. (b) If the bar is elastic (e.g. a Fiber Reinforced Polymer (FRP) bar), then for large strain levels bar slip values are increased to levels beyond s_2 (Fig. 4-3b): this is marked by debonding and cover splitting of the loaded end of anchorage, thereby limiting the development capacity of the reinforcement.

Strain penetration of yielding over a bar anchorage has received some attention, especially with regard to its contribution to the rotation capacity of structural members (Bonacci et al. 1994, Bigaj 1999, Tastani et al. 2013). But the implications resulting from the spreading of inelastic strains in the shear span of a structural member on the development capacity of reinforcement and on member behavior have not yet been described with reference to the mechanics of bonds.

Consider a reinforcing bar that spans the deformable length of a structural column, anchored in its footing (Fig. 4-2). An important difference may be traced in the state of stress occurring in the two regions along the bar: within the anchorage, stress is controlled by the mechanics of bonds, as described by the field equations (Eqs. 4-4, see next Section).

On the other hand, within the shear span, it is the prevailing notion that bar stress is controlled by flexural theory; i.e. the requirement of plane sections remaining plane at any cross section relates bar strains to flexural moment and axial load through cross sectional equilibrium. This however can be incompatible with the requirements of Eqs.4-4. The concept of tension stiffening is used in order to settle this potential conflict between the two antagonistic mechanisms for control of reinforcement strains: a certain nontrivial length ℓ_{Do} is needed, measured from the face of the crack toward the uncracked part of the member until bar strain compatibility with the surrounding concrete cover may be claimed. Thus, the field equations of bond control the segment ℓ_{Do}, whereas the classical theory of bending controls the remaining length. The region over the shear span of a flexural member where bar stresses are controlled by the mechanics of bonds (Eqs. 4-4) rather than the mechanics of flexure, is referred to hereon as a "disturbed" region, thereby assigning to this length an alternative interpretation than that used to explain shear dominated responses in frame members (MacGregor et al. 2005). At the same time this alternative significance of the disturbed region underscores the interaction between bond and shear strength (Martin-Pérez et al. 2001). Clearly, as flexural cracking propagates, the disturbed zone extends and may spread over the entire length of the member.

Bond-Slip Distribution along the Anchorage of a Linear Elastic Bar

The solution to Eq. 4-4 for elastic bars in the anchorage is given in this section; this is valid for the ascending branch of the stress-strain law of steel reinforcing bars, i.e. $\varepsilon \le \varepsilon_y$. In the case of Fig. 4-4 for the elastic part of the bond slip (i.e. when $s \le s_1$, the bond is linearly related to slip in accordance with: $f_b = (f_b^{max}/s_1) \cdot s$. By substitution in Eq. 4-4 the differential equation may be solved in closed form. Thus, bar normal strain, slip, and bond stress distributions over the available length of the anchorage [$0 \le x \le L_b$] are given by the following equations (Tastani and Pantazopoulou 2013):

$$\varepsilon(x) = \frac{\varepsilon_o}{1-e^{-2\omega L_b}}\left(e^{-\omega x} - e^{-\omega x - 2\omega L_b}\right) \le \varepsilon_y \tag{4-5}$$

$$s(x) = \frac{\varepsilon_o}{\omega(1-e^{-2\omega L_b})}\left(e^{-\omega x} + e^{\omega x - 2\omega L_b}\right) \le s_1 \tag{4-6}$$

$$f_b(x) = (f_b^{max}/s_1) \cdot s(x) \leq f_b^{max} \tag{4-7}$$

where the characteristic property ω is given by: $\omega = [4f_b^{max}/(E_s \cdot D_b \cdot s_1)]^{0.5}$. The variable ε_o is the bar axial strain at the loaded end of the anchorage, and E_s is the modulus of elasticity of the bar in the longitudinal direction. By substituting $x = L_b$ in Eq. 4.6, a nonzero slip value is obtained at the free end of the anchorage $\{i.e.,\ s_f = 2\varepsilon_o e^{-\omega L_b}/[\omega(1 - e^{-2\omega L_b})] \neq 0\}$ even under very small loads. This finding is consistent with the experimental observations (see for example, Tastani 2005).

The bar axial strain at the loaded end, $\varepsilon_o = \varepsilon_{el}^{i}$, is the limit value beyond which the bond mechanism enters the state of plastification (i.e. yielding of bond) over a length l_p which grows with increasing bar strain at the loaded end, while the bar remains elastic. Therefore the variable ε_{el}^{i} is directly related to the slip magnitude s_1 in Fig. 4-3 and may be calculated by Eq. 4-6 after substitution of $s(x = 0) = s_1$ as follows:

$$\varepsilon_{el}^{i} = s_1 \omega \frac{1 - e^{-2\omega L_b}}{1 + e^{-2\omega L_b}} \tag{4-8}$$

In case the available bond length is sufficient or if transverse confinement reacts normally to the contact surface thereby generating secondary strength reserves for the bond mechanism, then the bar may sustain a strain value higher than ε_{el}^{i} [Fig. 4-5]. In that case, the maximum bond stress may reach the characteristic strength value f_b^{max}, over a length of bond plastification l_p. The complete solution to Eq. 4-4 over L_b (starting from the loaded end and proceeding toward the end of the anchorage) comprises two segments, as follows:

Distributions of bar strain, slip and bond stress over the length l_p (for $0 \leq x \leq l_p$) are obtained considering that $f_b(s) = f_b^{max}$ = constant (thus the bar stress and strain varies as a linear function of distance over the segment l_p where the bond is plastified:

$$\varepsilon(x) = \varepsilon_o - \frac{4f_b^{\max}}{E_s \cdot D_b} \cdot x \tag{4-9}$$

$$s(x) = s_1 + 0.5(l_p - x)[\varepsilon(x) + \varepsilon_{el}^{ii}] \tag{4-10}$$

$$f_b(x) = f_b^{max} \tag{4-11}$$

where ε_{el}^{ii} is the attenuated value of the bar strain as compared with the ε_o value which occurs at the loaded end. Note that ε_{el}^{ii} now occurs at the end of the bond plastification region, l_p:

$$\varepsilon_{el}^{ii} = \varepsilon_o - \frac{4 f_b^{\max}}{E_s \cdot D_b} \cdot l_p \tag{4-12}$$

For the distributions of bar strain, slip and bond stress over the remaining anchorage length (which is still in the elastic range), $L_b - l_p$ (for $l_p \le x \le L_b$), these are obtained from the elastic solution to Eq. 4-5-4-7. :

$$\varepsilon(x) = \frac{\varepsilon_{el}^{ii}}{1-e^{-2\omega(L_b-l_p)}}\left(e^{-\omega(x-l_p)} - e^{\omega(x-l_p)-2\omega(L_b-l_p)}\right) \tag{4-13}$$

$$s(x) = \frac{\varepsilon_{el}^{ii}}{\omega\left(1-e^{-2\omega(L_b-l_p)}\right)}\left(e^{-\omega(x-l_p)} + e^{\omega(x-l_p)-2\omega(L_b-l_p)}\right) \tag{4-14}$$

$$f_b(x) = (f_b^{max}/s_1)\cdot s(x) \le f_b^{max} \tag{4-15}$$

The length of plastification, l_p, is estimated if continuity of strain and slip are enforced at $x = l_p$.

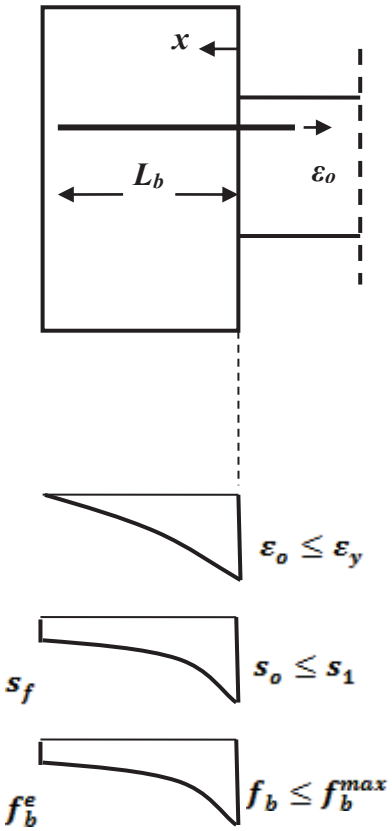

Figure 4-4: Elastic bar response while bond-slip law remains elastic.

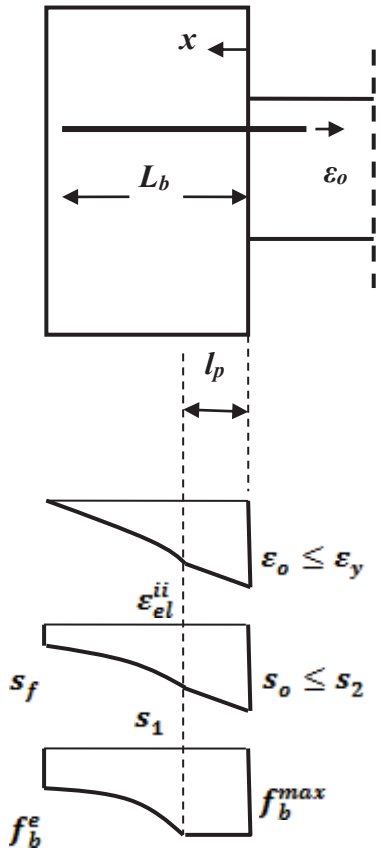

Figure 4-5: Elastic bar response with bond plastification.

Bond-Slip Distribution along the Anchorage of an Elastoplastic Bar

The solution to Eq. 4-4 for an elastoplastic steel bar is explored only after yielding, because the preceding section fully describes the bar's elastic behavior. The bar strain at the onset of yielding is denoted by ε_y whereas E_{sh} is the strain hardening modulus of the stress-strain relationship in the postyielding regime.

The last case examined in the present model of the anchorage of a steel reinforcing bar is depicted in Fig. 4-6 and it concerns yield penetration (spread of strains beyond yielding) in the steel bar inside the anchorage with simultaneous plastification of bond. The length of yield penetration is denoted by l_r. In the segment $(0, l_r)$, the bond stress is equal to f_b^{res}. Also, the distribution of strains is linear, ranging from $\varepsilon(x = 0) = \varepsilon_o$ at the loaded end, to the value $\varepsilon(x = l_r) = \varepsilon_y$ at the end of the yielded region (Fig. 4-6). Slip at each point is obtained from the integration of strains from the point considered at the unloaded end of the anchorage.

The strain, slip, and bond stress expressions governing this problem in the three distinct regions are given as follows:

Over the debonded length l_r (for $0 \le x \le l_r$) (Eq. 4-16 is obtained from Eq. 4-4 for a constant bond stress f_b^{res}):

$$\varepsilon(x) = \varepsilon_o - \frac{4 f_b^{res}}{E_{sh} D_b} x \tag{4-16}$$

$$s(x) = s_2 + 0.5(l_r - x)\left[\varepsilon(x) + \varepsilon_y\right] \tag{4-17}$$

$$f_b(x) = f_b^{res} \tag{4-18}$$

Over the length l_p where bond has exceeded the plasticity limit (for $l_r \le x \le l_r + l_p$):

$$\varepsilon(x) = \varepsilon_y - \frac{4 f_b^{\max}}{E_s D_b}(x - l_r) \tag{4-19}$$

$$s(x) = s_1 + 0.5\left(l_r + l_p - x\right)\left[\varepsilon(x) + \varepsilon_{el}^{iii}\right] \tag{4-20}$$

$$f_b(x) = f_b^{max} \tag{4-21}$$

Over the remaining bonded length $L_b - l_r - l_p$ (for $l_r + l_p \le x \le L_b$):

$$\varepsilon(x) = \frac{\varepsilon_{el}^{iii}}{1 - e^{-2\omega\left(L_b - l_p - l_r\right)}}\left(e^{-\omega(x - l_p - l_r)} - e^{\omega(x - l_p - l_r) - 2\omega\left(L_b - l_p - l_r\right)}\right) \tag{4-22}$$

$$s(x) = \frac{\varepsilon_{el}^{iii}}{\omega\left(1 - e^{-2\omega\left(L_b - l_p - l_r\right)}\right)}\left(e^{-\omega(x - l_p - l_r)} + e^{\omega(x - l_p - l_r) - 2\omega\left(L_b - l_p - l_r\right)}\right) \tag{4-23}$$

where, according with the linear ascending branch of the bond-slip law, it is:

$$f_b(x) = (f_b^{max}/s_1) \cdot s(x) \leq f_b^{max} \tag{4-24}$$

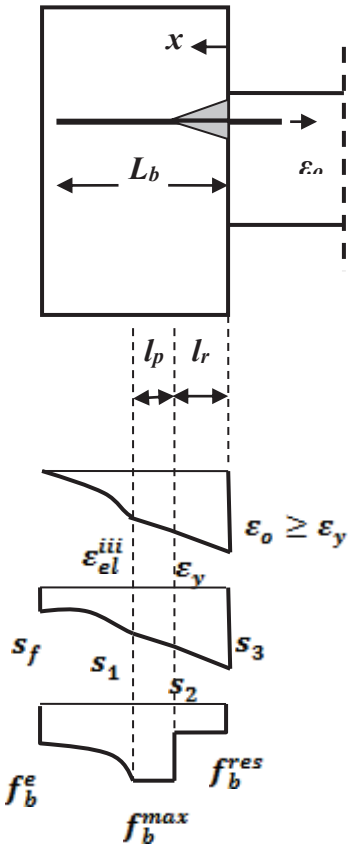

Figure 4-6: Plastic (yielded) bar response with bond plastification.

In Equation (4-22) the term ε_{el}^{iii} is the strain at $x = l_r + l_p$, i.e., the point of transition from elastic to plastic bond stress (Fig. 4-6) and it is calculated from Equation 4-19.

Thus, yield penetration occurs over the segment l_r of the anchorage where strain exceeds ε_y; this phenomenon is accompanied by a sudden increase of slip (Eq. 4-17) with a commensurate reduction of bond strength to f_b^{res} over the yielded bar length.

Disturbed Region on Shear Span of a Flexural Member

It was mentioned earlier that the spread of inelastic strains occurs on both sides of a critical section (e.g. at the base of a column). The process of inelastic strain penetration in the anchorage of a reinforcing bar has been demonstrated in the previous section. This section is dedicated to solving the same problem on the other side of the critical section, that is, over the disturbed region along the shear span of a column. Here, the problem is different from that of the anchorage in the type of boundary conditions that may be enforced for the governing differential equation, Eqs. 4-4. The bond-slip law has the same multilinear envelope as in the case of an anchorage, however, the bond strength value, f_b^{max}, is a function of the available transverse reinforcement.

Evaluation of Disturbed Length on Crack Initiation

For the stage prior to the occurrence of flexural cracking along the length of the flexural member, the bar strain is estimated from the flexural analysis of the uncracked column cross section (i.e. from the moment-curvature analysis, Fig. 4-7a):

$$\varepsilon_{fl}(x) = \phi(x) \cdot y_{s,na}^{gr} \tag{4-25a}$$

This is expressed explicitly as:

$$\varepsilon_{fl} = \frac{M(x)}{E_c \cdot I_g} \cdot y_{cg} - \frac{N}{E_c A_g} \quad ; \quad y_{cg} = \frac{h}{2} - C_{\text{cov}} - 0.5D_b \quad ; \quad y_{s,na}^{gr} = y_{cg} - \frac{N}{M} \cdot \frac{I_g}{A_g} \tag{4-25b}$$

where $M(x)$, N (+ for compression) and $\varphi(x)$ are the flexural moment, axial load and flexural curvature acting on the member section at distance x

from the support, E_c is the elastic modulus of concrete, I_g and A_g are the moment of inertia and the uncracked cross section area, h is the section height and C_{cov} is the clear cover (Fig. 4-7a). Parameters $y_{c,g}$ and $y_{s,na}{}^{gr}$ are the distances of the centroid of tension reinforcement to the centroid of the uncracked cross-section and to the neutral axis location, respectively (Fig. 4-7a). The distance to the neutral axis changes significantly from the initial linear elastic state $y_{s,na}^{gr}$, to the cracked state of a cross section $y_{s,na}^{cr}$. Generally, the position of the neutral axis may be estimated based on equilibrium requirements, both in the uncracked cross sections as well as at the crack locations assuming "plane sections remain plane." From the flexural analysis perspective, when the flexural moment $M(x)$ exceeds the cracking moment, M_{cr}, even by a small amount, then the member may be considered cracked in the region of x. Although a large region may satisfy this definition, however, cracks i occur at discrete locations $x_{cr,i}$. Thus, if an analysis of the cracked cross section is available (based on the plane section hypothesis), the tension reinforcement strains $\varepsilon(x_{cr,i})$ that occur in the crack locations may be calculated from:

$$\varepsilon\left(x_{cr,i}\right) = \varphi\left(x_{cr,i}\right) \cdot y_{s,na}^{cr} \tag{4-26}$$

In the segment between successive cracks where the moment exceeds the cracking value, bar strains cannot be estimated from flexural analysis, as prescribed by Eq. 4-26. Owing to reinforcement slip, the degree of strain compatibility between steel and concrete in these locations is not well understood, as would be required by the "plane-sections remain plane" assumption, nor can the concrete be considered inert as would happen in a fully cracked tension zone. Because it takes some distance from a crack location before the reinforcement may fully engage its concrete cover in tension again so as to satisfy the conditions of strain compatibility, Eq. 4-26 is invalid even in the region immediately adjacent to the last flexural crack in the shear span, although the flexural moment is below the cracking limit in that region. Bar strain over cracked segments of the member may be estimated from the solution of Eq. 4-4. In order to address all the possible exceptions to the validity of the flexural requirement stated in Eqs. 4-25 and 4-26, here, the term "undisturbed" is used as a qualifier to "un-cracked" in order to refer to sections that also satisfy "the plane sections remaining plane" compatibility requirement. As a corollary, where strains are obtained from the solution of the bond equation, the region is "disturbed".

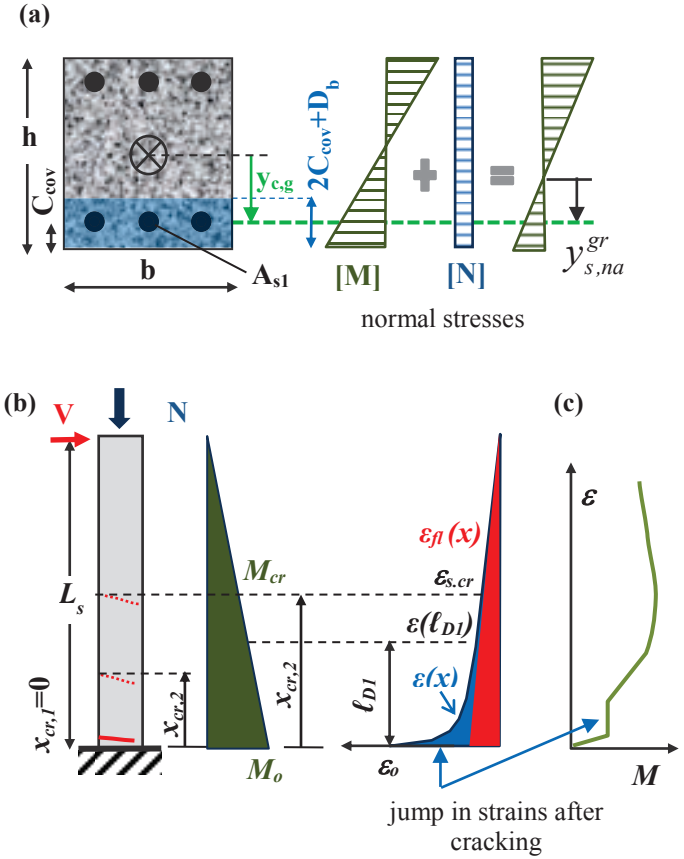

Figure 4-7: Definition of terms: (a) Cross sectional flexural analysis. (b) Bar strain distribution along the shear span L_s: stage prior to cracking (red); response into the disturbed region ℓ_{D1} (blue). (c) Moment - bar strain diagram.

The flexural moment at a distance x from the face of the support is estimated with reference to the flexural moment at the support, M_o (ε_o is the bar tension strain, at $x=0$, Fig. 4-7b):

$$M(x) = M_0 \cdot (1 - x/L_s) \tag{4-27}$$

As the sequence of crack formation is critical for the occurrence of disturbed regions and for the problem of strain penetration that will be subsequently addressed, in the present discussion the static problem represented by Eq. 4-27 will be solved for a gradually increasing value of the support moment, M_o. It is assumed that the characteristic flexural resistance curve (moment-curvature) of any cross section along the shear span (i.e. the moment – curvature and moment – bar strain diagram) is available from classical flexural analysis (plane-sections) for the entire range of response.

For a member with continuous primary reinforcement over the shear span, L_s, the moment distribution that follows Eq. 4-27 will cause first cracking at the face of the support ($x_{cr,1}$=0, Fig. 4.7b). Upon the cracking of the tension zone the bar strain experiences a significant jump to maintain equilibrium (Fig. 4-7c). For example, if the cracked section stiffness is about 1/3 of the uncracked value, the bar strain at the critical section is expected to increase threefold by the mere occurrence of the crack even though the moment change from the uncracked to the cracked stage may be imperceptible. Thus suddenly the whole region adjacent to the cracked location becomes "disturbed". Over the length of the disturbed region, ℓ_{D1} (Fig. 4-7b) the reinforcement strain is described by the solution of the bond equation (Tastani et al. 2013) i.e.:

$$\varepsilon(x) = C_1 \cdot e^{-\omega x} + C_2 \cdot e^{\omega x} \qquad \omega = [4 f_b^{max} / (E_s \cdot D_b \cdot s_1)]^{0.5}$$

, where,

(4-28)

The solution of Eq. 4-28 is valid provided the bond is in the elastic range (ascending branch in the bond slip law, Fig. 4-3b). Before the creation of a second crack, the following conditions characterize the end of the disturbed region at $x = \ell_{D1}$:

a) the slope of the bar strain distribution, $\psi = d\varepsilon(x)/dx$, obtained from differentiation of Eq. 4-28, matches that of the strain diagram as would be obtained from Eq. 4.25b and 4.27:

$$\psi = d\varepsilon(x)/dx \rightarrow \omega \cdot \left(-C_1 \cdot e^{-\omega \ell_{D1}} + C_2 \cdot e^{\omega \ell_{D1}}\right) = -\varepsilon_{el}^{o} \cdot$$

$$1/L_s, \quad \varepsilon_{el}^{o} = \left(M_o \cdot y_{cg}\right)/(E_c \cdot I_g)$$

(4-29a)

b) the bar strain $\varepsilon(\ell_{D1})$ satisfies both Equations (4-25b), and (4-28):

$$\varepsilon(\ell_{D1}) = C_1 \cdot e^{-\omega \ell_{D1}} + C_2 \cdot e^{\omega \ell_{D1}} = \varepsilon_{el}^{o} \cdot (1 - \ell_{D1}/L_s) - N/(E_c \cdot A_g)$$

(4-29b)

Given the axial load N and the bar strain at the support $\varepsilon(x=0)=\varepsilon_o$ the corresponding moment M_o is obtained from the moment-curvature analysis of the cracked section. A boundary condition of Eq. 4-28 is:

$$\varepsilon(0) = C_1 + C_2 = \varepsilon_o$$

(4-29c)

Unknowns of the system of Eqs. 4-29 are the disturbed length ℓ_{D1} (Fig. 4-7b), and the coefficients C_1 and C_2. In an algorithm developed to solve Eqs. 4-29 numerically, the controlling parameter is ε_o; required input includes the axial load, N, shear span L_s, the bond-slip characteristic property ω (Eq. 4-28), and the member material and cross sectional properties. The coefficients C_1 and C_2 are obtained from (4-29a) and (4-29b):

$$C_{1,2} = 0.5 \cdot e^{\beta \cdot \omega \ell_{D1}} \left[\varepsilon_{el}^{o} \cdot \left(1 - \frac{\ell_{D1}}{L_s} + \frac{\beta}{\omega L_s} \right) - N/(E_c \cdot A_g) \right]$$

where $\beta=1$ for C_1, and $\beta= -1$ for C_2 (4-30)

The value of ℓ_{D1} is determined by solving Eq. (4-29c) after substitution of C_1 and C_2.

Formation of Additional Flexural Cracks in the Shear Span

Increasing the reinforcement strain value at the critical section, ε_o, corresponds to a higher flexural moment M_o at the support. Based on Eq. 4-27, the flexural moments exceed the cracking moment up to a distance of x_{cr} from the support: $x_{cr} = L_s \cdot (1 - M_{cr}/M_o)$. But the position of the next crack is not necessarily at x_{cr}; rather, it is controlled by tension stiffening of the reinforcement.

(a) To determine if the next crack forms within ℓ_{D1} (Fig. 4-7b), the force transferred through a bond to the concrete cover (*i.e.* $E_s A_{s1}[\varepsilon_o - \varepsilon(x)]$) is compared with the tensile resistance of the effective area of concrete cover engaged in tension (*i.e.* $f_{ct} A_{c.eff}$, EN 1992-1-1 2004)

$$\left[(E_s \cdot A_{s1})/(f_{ct} \cdot A_{c,eff})\right] \cdot [\varepsilon_o - \varepsilon(x)] \geq 1$$

$$A_{c,eff} = b \cdot (2C_{cov} + D_b) - A_{s1} \quad , \tag{4-31}$$

where A_{s1} is the area of the tensile reinforcement, $A_{c.eff}$ is the area of concrete effectively engaged in tension (shaded area around A_{s1} in Fig. 4-7a), f_{ct} is the tensile concrete strength, and b is the width of the section of the column (Fig. 4-7a). The lowest value of $x=x_{cr,2} < \ell_{D1}$ that satisfies Eq.4-31 determines the location of the next crack; otherwise no further cracking is possible within ℓ_{D1} as long as the reinforcement remains elastic.

(b) Alternatively, the next possible crack location, $x_{cr,2} \geq \ell_{D1}$ in the undisturbed region (Fig. 4-7b) is also evaluated from Eq.4-25b (here, $\varepsilon_{c.cr} = 0.00015$ is the concrete cracking strain):

$$\varepsilon(x) = \varepsilon_{el}^{o}(1 - x/L_s) - N/(E_c \cdot A_g) = \varepsilon_{c.cr} \Rightarrow x_{cr,2} = L_s \cdot [1 -$$

$$\varepsilon_{c.cr}/\varepsilon_{el}^{o} - N/(E_c A_g\, \varepsilon_{el}^{o})] \tag{4-32}$$

Slip in the disturbed region is obtained from integration of bar strains (from x=0 to $x= \ell_{D1}$).

$$s(x) = \frac{1}{\omega}(C_1 \cdot e^{-\omega x} - C_2 \cdot e^{\omega x}) + C \tag{4-33}$$

The constant of integration C is obtained from the requirement of the compatibility of strains in the concrete and reinforcement at the end of the disturbed zone, $x=\ell_{D1}$, where the local slip is zero ($s(\ell_{D1})$=0). After localization of the second crack at $x_{cr,2}$, the next step of the solution is the determination of the new disturbed region ℓ_{D2} (along with the updated values of the constants C_1 and C_2). Term ℓ_{D2} initiates from the crack

location $x_{cr,2}$ and extends towards the span until the requirements of slope coincidence and continuity are reached, at coordinate $x_{cr,2} + \ell_{D2}$ in Eqs.4-29a-b (Fig. 4-8). In using the closed form expression of Eq.4-28, the value of x is substituted by the value x-$x_{cr,2}$; this solution is valid for $x \subseteq [x_{cr,2}, x_{cr,2}+\ell_{D2}]$). The bar strain $\varepsilon_{cr,2}$ at the location of the second crack (Fig. 4-8) is the outcome of the flexural analysis of the cracked section and corresponds to the moment at that location according to Eq. 4-27 for $x=x_{cr,2}$. In the search for the new disturbed region, an additional requirement is that slip at the location $x_{cr,2}$ should not exceed the limit s_1 in Eq. 4.33 (where x is substituted by x-$x_{cr,2}$), securing that the bond is still elastic inside ℓ_{D2} (Fig. 4-8).

This process is repeated following the gradual increase in the value of bar strain ε_o at the support, until no additional primary cracks can be identified. This point corresponds to the stabilization of cracking, and it generally occurs at a strain value in the critical section that is less than the strain at yielding, $\varepsilon_o^{stbl} < \varepsilon_y$. From this stage and until failure of the structural member, for the sake of simplicity of the mathematical problem, the so called *total disturbed region* ℓ_{Do} is defined as the total distance measured from the support to the end of the disturbed region of the last (and remotest) crack that was formed prior to stabilization, $\ell_{D,n}$ (Fig. 4-9). Since bond development controls the total disturbed region, from that point onwards the field equations (Eq. 4-4) are solved in ℓ_{Do} ignoring the presence of intermediate discrete cracks or the flexural moment requirements, since the "plane sections" assumption is not valid anywhere over this entire region; upon further increase of the bar strain at the support, the ℓ_{Do} length may increase further as the disturbed zone penetrates towards the tip of the cantilever column.

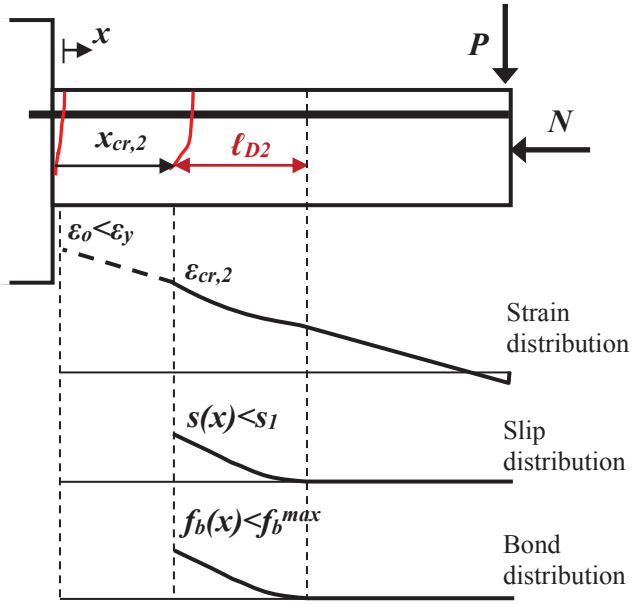

Figure 4-8: Disturbed region ℓ_{D2} after formation of the 2nd crack.

Following cracking stabilization and beyond yielding of the steel bar ($\varepsilon_o>\varepsilon_y$), the yielded segment of the disturbed region undergoes simultaneous degradation of the bond. Thus, of the total length ℓ_{Do}, there is a segment l_r where yielding penetrates and spreads with increasing value of ε_o (Fig. 4-9). Owing to bar yielding, bar strains increase over l_r without a commensurate increase of stress: this means that bond must have degraded to zero as a consequence of Eq. 4.4a, since $df/dx=0$ and thus f_b=0. This segment may be considered debonded. Even if the yield-plateau is neglected, and the bar stress-strain diagram is considered bilinear with some hardening (Fig. 4-3a), it is clear that the small hardening slope may only be supported by the residual bond strength – in other words, in order for a bar to yield, it must have slipped beyond the limit s_2 in the bond - slip law (Fig. 4-3b). Limit s_2 is not an intrinsic property of the bar–concrete interface as it is generally assumed by Design Codes (*fib* Model Code 2010), but rather, it depends on the available bonded length (Tastani et al. 2013).

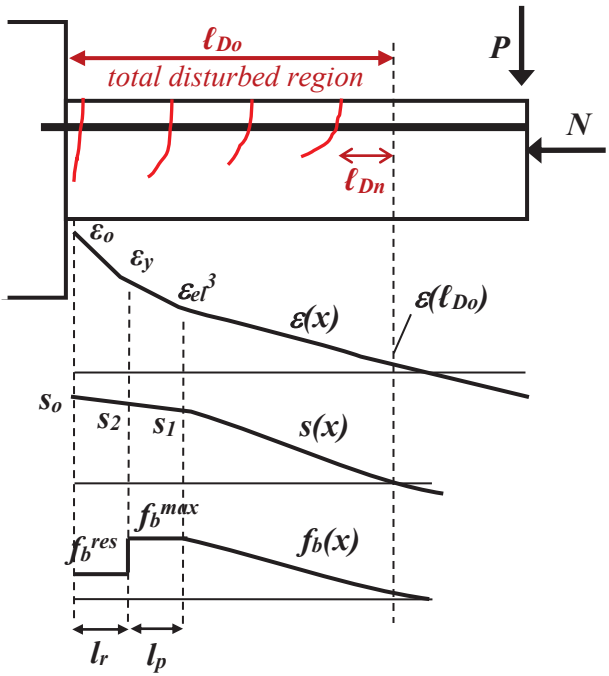

Figure 4-9: Total disturbed region ℓ_{Do} after stabilization of cracking.

The solution for the distributions of strain, slip and the state of bond over the disturbed region ℓ_{Do} of the shear span of a column under lateral sway follows that obtained when considering yield penetration in a bar anchorage (previous Section). Here, the disturbed region ℓ_{Do} comprises the sequence of the following segments (Fig. 4-9): the yield penetration length l_r (immediately adjacent to the support), the bond plastification length l_p (i.e. the length where the bar is elastic but bond is constant and equal to the value at the plateau of the bond slip law f_b^{max}); bar axial stress and bond stress are elastic in the tail length of the disturbed region. The solution of the bond equations for the different segments is given below:

$$\text{For } 0 \le x \le l_r: \qquad \varepsilon(x) = \varepsilon_o - \frac{4 f_b^{res}}{E_{sh} D_b} x \qquad f_b(x) = f_b^{res} \quad ; \tag{4-34a}$$

$$s(x) = s_2 + 0.5(l_r - x)\left[\varepsilon(x) + \varepsilon_y\right]$$

→ $x=0$: $s_o=s_2+0.5\cdot l_r\cdot(\varepsilon_o+\varepsilon_y)$

(4-34b)

For $l_r \le x \le l_r + l_p$: $\varepsilon(x) = \varepsilon_y - \frac{4f_b^{max}}{E_s D_b}(x - l_r)$;

$$f_b(x) = f_b^{max}$$

(4-35a)

$$s(x) = s_1 + 0.5(l_r + l_p - x)[\varepsilon(x) + \varepsilon_{el}^3]$$

→ $x=l_r$: $s_2=s_1+0.5\cdot l_p\cdot(\varepsilon_y+\varepsilon_{el}^3)$

(4-35b)

$$\varepsilon_{el}^3 = \varepsilon_y - \frac{4f_b^{max}}{E_s D_b} l_p$$

(4-35c)

For $l_r + l_p \le x \le \ell_{Do}$:

$$\varepsilon(x) = C_{1t}\cdot e^{-\omega(x-l_p-l_r)} + C_{2t}\cdot e^{\omega(x-l_p-l_r)} \quad f_b(x) = \frac{f_b^{max}}{s_1}\cdot s(x)$$

(4-36a)

$$s(x) = \frac{1}{\omega}\left(C_{1t}\cdot e^{-\omega(x-l_p-l_r)} - C_{2t}\cdot e^{\omega(x-l_p-l_r)}\right) + C_t$$

(4-36b)

Unknowns ℓ_{Do}, C_{1t}, C_{2t} and the constant of integration C_t are obtained from boundary conditions at $x = \ell_{Do}$ (namely slope and strain continuity and slip compatibility - zero relative displacement) between strain distributions obtained from the bond development equation and from flexural analysis. Therefore the reinforcement slip is: at $x=l_r+l_p$, $s(x)=s_1$; at $x = \ell_{Do}$, $s(\ell_{Do})=0$ (i.e., no slip). The following system of boundary conditions is therefore established:

a) Slope continuity of the strain distributions at $x = \ell_{Do}$:

$$\omega\cdot\left(-C_{1t}\cdot e^{-\omega(\ell_{Do}-l_r-l_p)} + C_{2t}\cdot e^{\omega(\ell_{Do}-l_r-l_p)}\right) = -\varepsilon_{el}^o\cdot 1/L_s, \quad \varepsilon_{el}^o = \left(M_o\cdot y_{cg}\right)/(E_c\cdot I_g)$$

(4-37a)

b) Continuity of strains at $x = \ell_{Do}$:

$$\varepsilon(\ell_{Do}) = C_{1t} \cdot e^{-\omega(\ell_{Do}-l_r-l_p)} + C_{2t} \cdot e^{\omega(\ell_{Do}-l_r-l_p)} = \varepsilon_{el}^{o} \cdot (1 - \ell_{Do}/L_s) - N/(E_c \cdot A_g) \tag{4-37b}$$

c) Continuity of slip at $x = l_r+l_p$:

$$s \cdot (l_r + l_p) = \frac{1}{\omega}(C_{1t} - C_{2t}) + C_t = s_1 \tag{4-37c}$$

d) Continuity of strain at $x = l_r+l_p$:

$$\varepsilon(l_r + l_p) = C_{1t} + C_{2t} = \varepsilon_{el}^{3} \tag{4-37d}$$

The length of yield penetration l_r (Eq. 4-38) may be estimated considering the continuity of strain at $x = l_r$ (in Eq. (4-34a).

$$l_r = (\varepsilon_o - \varepsilon_y) \cdot \frac{E_{sh} D_b}{4 f_b^{res}} \tag{4-38}$$

Equation (4-38) for the yield penetration length (which defines the plastic hinge length) has two interesting implications: first, it is a strain-based criterion for the spread of yielding in the shear span, as opposed to the stress-based definition given by Eq. (4-2b); there, the coefficient *a* refers to the flexural overstrength normalized by the yielding moment. A second more subtle point is the observation that the plastic hinge length is influenced by several parameters indirectly, through the determining effect that these have on f_b^{res}. For example the presence of an axial load on a member that undergoes cyclical displacement reversals weakens the cover over a larger portion of the shear span length leading to cover delamination due to excessive compressive strains; upon reversal of load, the crushed cover cannot support significant bond action for the reinforcement when it is stressed in tension, leading to a reduced value of f_b^{res}, which in turn causes increased penetration depth for columns carrying a higher axial load; this is consistent with experimental reports (Watson et al. 1994, Bae et al. 2008).

Proposed Algorithm

The following algorithm (Fig. 4-10) is established in order to define the locations of primary cracks and bar strain, slip and bond distribution along the shear span L_s of a laterally loaded reinforced concrete column as well as the yield penetration length:

Initial Data: Using standard section analysis, M-ϕ and M-ε diagrams (or better a unified diagram M-ϕ -ε) are obtained, given N for the typical section of the reinforced concrete column studied.

1st Step: Select value of bar strain, $\varepsilon_o^{(1)}=\varepsilon_o$, after crack formation at the support (Eqs. 4-25,4-27).

2nd Step: Find the corresponding moment, M_o at the support, from moment-bar strain diagram. Solve for the length of the disturbed region ℓ_{D1} emanating from the first crack (Eqs. 4-27- 4-30).

3rd Step: Increase strain at critical section to $\varepsilon_o^{(2)} = \varepsilon_o^{(1)} + \Delta\varepsilon_o$. Find the location $x_{cr,2}$ of the second crack. Check if second crack will occur: (a) inside ℓ_{D1} according to Eq. (4-31), or (b) in the undisturbed region L_s- ℓ_{D1}, according to Eq. (4-32).

4th Step: (a) If next crack forms within $\ell_{D1,}$ repeat Step 3 for $\varepsilon_o^{(3)} = \varepsilon_o^{(2)} + \Delta\varepsilon_o$. (b) Otherwise, find the new disturbed region ℓ_{D2} that extends beyond $x_{cr,2}$.

5th Step: Find total disturbed length, $\ell_{Do}=x_{cr,2}+ \ell_{D2.}$

6th Step: Solve for $\varepsilon(x)$, $s(x)$, $f(x)$, $f_b(x)$ for $x_{cr,2}\leq x\leq \ell_{Do}$ from Eqs. (4-28, 4-29, 4-30, 4-33) (Fig. 4-8a). In this phase of the solution, and up to stabilization of cracking, elastic bond is assumed in ℓ_{D2} (Fig. 4-8). Thus the distributions can be described by the Eqs. 4-36 after substituting l_r=0 and l_p=0. For L_s-ℓ_{Do}<x<L_s, (elastic column) Eqs. 4-25, 4-27) are used.

7th Step: Repeat steps 2 to 6 for $\varepsilon_o^{(i)} = \varepsilon_o^{(i-1)} + \Delta\varepsilon_o$ until stabilization of cracking (i.e., no more primary cracks can develop: $\varepsilon_o^{stbl} = \varepsilon_o^{(i)}$). Final length of disturbed zone is obtained from the n^{th} increment using this procedure: $\ell_{Do}=x_{cr,n}+ \ell_{D,n}$.

8th Step: Increase $\varepsilon_o^{(i)} = \varepsilon_o^{(i-1)} + \Delta\varepsilon_o > \varepsilon_o^{stbl}$. Solve for one continuous disturbed region $\ell_{Do} \geq x_{cr,n}+ \ell_{D,n}$ allowing for bond plastification and debonding as well as bar yielding (anchorage solution) up to either (a) ε_o exhausting the ultimate strain of the M-ε diagram, or (b) ℓ_{Do} exceeding the available development length of the bar in the shear span, taken here as (L_s+h_{hook}), where h_{hook} refers to the bent length of a hooked anchorage (according with *fib* Model Code (2010) the contribution of a hook to the strength of an anchored bar is $50A_bf_b^{max}$, which corresponds to an

additional anchored length, $\Delta L_b = h_{hook} = 12.5 D_b$). If (b) controls, continue beyond that point for higher strains using the anchorage solution presented in previous Section for the entire length ℓ_{Do}.

9th Step: The last converged value of l_r in the shear span (Fig. 4-9) is added to the corresponding yield penetration length into the anchorage (previous Section) resulting in the definition of the total plastic hinge length ℓ_{pl}.

Results

In the context of the present chapter, the length of plastic hinges is by definition the length of yield penetration (thus $\ell_{pl} = l_r$), occurring from the critical section *towards both the shear span and the anchorage*; physically it refers to the extent of the region where nonlinear reinforcing strains occur, and it may be used to calculate the inelastic rotation capacity of the column. The solution algorithm developed is applied in this section in order to establish the parametric sensitivities of the estimated plastic hinge to the important design parameters. It is also used to correlate the behaviour of the plastic hinge spread in three published column tests that were conducted to illustrate the effect of axial load on the length of the plastic hinge region (Saatcioglu et al. 1989, Bae et al. 2008).

The three column experiments studied in the chapter are specimens U3 (Saatcioglu et al. 1989), S17-3UT and S24-4UT (Bae et al. 2008). Column specimens were tested as cantilevers, simulating half a clear column length under lateral sway such as would occur during an earthquake, with cross section detailing as shown in Fig. 4-11a. Column U3 is analysed in detail and the results are summarized in Table 4-1, whereas the results of S17-3UT and S24-4UT are directly included in Table 4-1 for easy correlation.

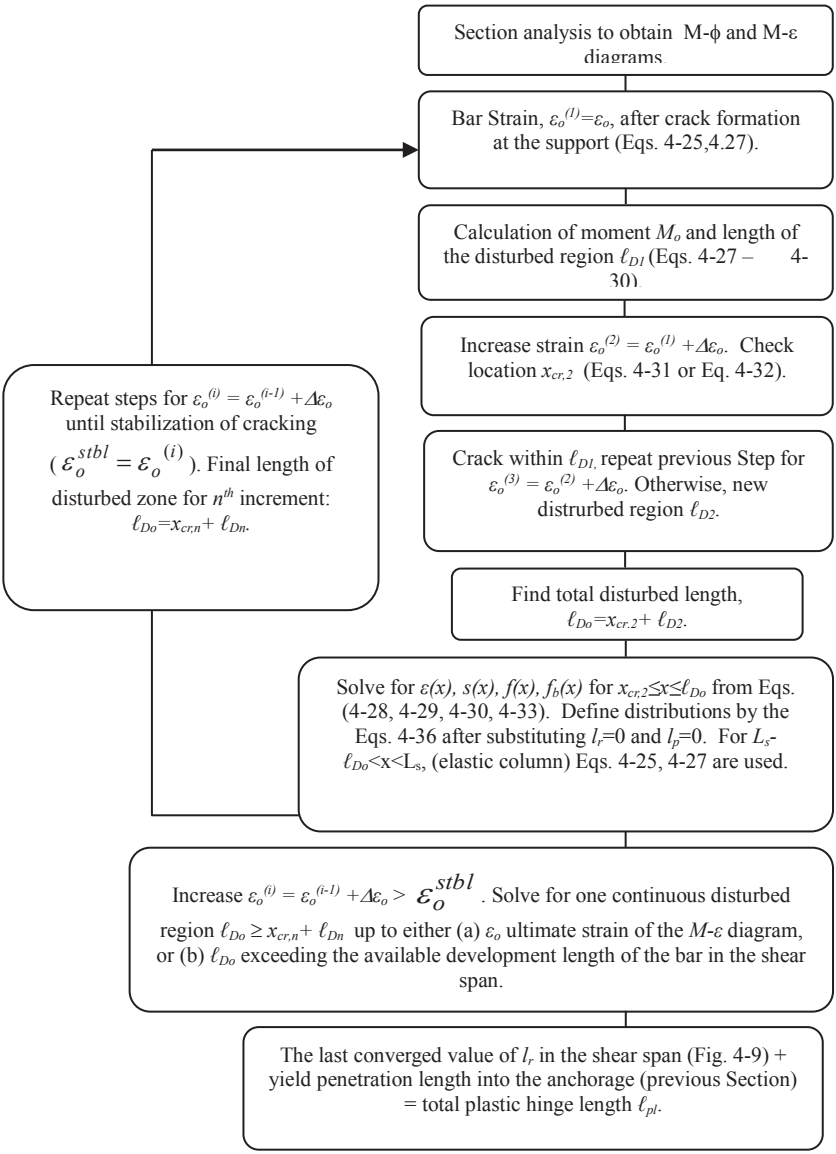

Figure 4-10: Flow-chart of the established algorithm for the definition of the bond state in the disturbed region of the shear span as well as that of the plastic hinge length.

Table 4-1: Summary of the analyzed experiments (units: mm, MPa).

	Experimental details				Analysis		
Test ID	**ν=N/ ($f_c'bd$)**	**Column geometry**	**Reinforcement**		**Anchorage**	**Shear span**	**Column deformation at ultimate**
U3	0.16 f_c'=34.8	Square section h=350, C_{cov}=32.5 d=305, Sh. span, L_s=1000	Long: 8 evenly distributed bars, D_b=25, f_y=430 E_{sh}=5%E_s Trans: 10@75 $f_{y,st}$=470		f_b^{max}=1.25$\sqrt{f_c'}$=7.40 s_1 =0.2 L_b =812 $s_u^{anch}(x=0)$=2.33 $l_{r,u}$ =313	f_b^{max} =7.2, f_b^{res}= 1.44, s_1=0.2 ℓ_{Do}^{max}=L_s+12.5D_b=1313 l_r =319 ε_u=0.0095, ϕ_u=4.7x10^{-5} c_x= 103, $s_u^{span}(x=0)$=2.36	Total ℓ_{pl} : ℓ_{pl} =$l_{r,u}$ + l_r =632mm=1.8h DR✐=520mm=1.5h θ_u^{slip}=0.018 $\theta_u{}^f$= $\theta_y{}^f$+$\theta_{pl}{}^f$=0.015 θ_u=0.033 / θ_u^{exp}=0.035
S17-3UT	0.5 f_c'=43.4	Square section h=440, C_{cov}=27 d=405, Shear span, L_s=3049	Long: 12 evenly distributed bars, D_b=15.9, f_y=496 E_{sh}=5%E_s Trans: 9.5@86 $f_{y,st}$=496		f_b^{max}=1.25$\sqrt{f_c'}$=8.23s_1 =0.2 L_b =890 $s_u^{anch}(x=0)$=1.50 $l_{r,u}$ =177	$f_{b,w/\,cov}^{max}$=11.49 $f_{b,wo/\,cov}^{max}$=5.40 f_b^{res}=20% , f_b^{max}=1.1, s_1=0.2 ℓ_{Do}^{max}=L_s+12.5D_b=3248 l_r =271 ε_u=0.01, ϕ_u=5.9x10^{-5} c_x = 236, $s_u^{span}(x=0)$=2.30	Total ℓ_{pl} : ℓ_{pl} =$l_{r,u}$ + l_r =448mm=h DR=450mm=h θ_u^{slip}=0.012 $\theta_u{}^f$=0.029 θ_u=0.041 / θ_u^{exp}=0.032
S24-4UT	0.2 f_c'=36.5	Square section h=610, C_{cov}=49 d=550, Shear span, L_s=3049	Long: 12 evenly distributed bars, D_b=22.2, f_y=400, E_{sh}=1%E_s Trans: 9.5@152 $f_{y,st}$=455		f_b^{max}=1.25$\sqrt{f_c'}$=7.55 s_1 =0.2 L_b =890 $s_u^{anch}(x=0)$=0.98 $l_{r,u}$ =80	$f_{b,w/\,cov}^{max}$=8.85 $f_{b,wo/\,cov}^{max}$=2.0 f_b^{res}=20% , f_b^{max}=0.4, s_1=0.2 ℓ_{Do}^{max}=L_s+12.5D_b=3327 l_r =301 ε_u=0.013, ϕ_u=3.9x10^{-5} c_x = 217, $s_u^{span}(x=0)$=3.52	Total ℓ_{pl} : ℓ_{pl} =$l_{r,u}$ + l_r =380mm=0.6h DR=350mm=0.57h θ_u^{slip}=0.01 $\theta_u{}^f$=0.017 θ_u=0.027 / θ_u^{exp}=0.033

Note: Test U3 by Saatcioglu et al. 1989 and tests S17-3UT, S24-4UT by Bae et al. 2008; ✐DR= Damaged Region

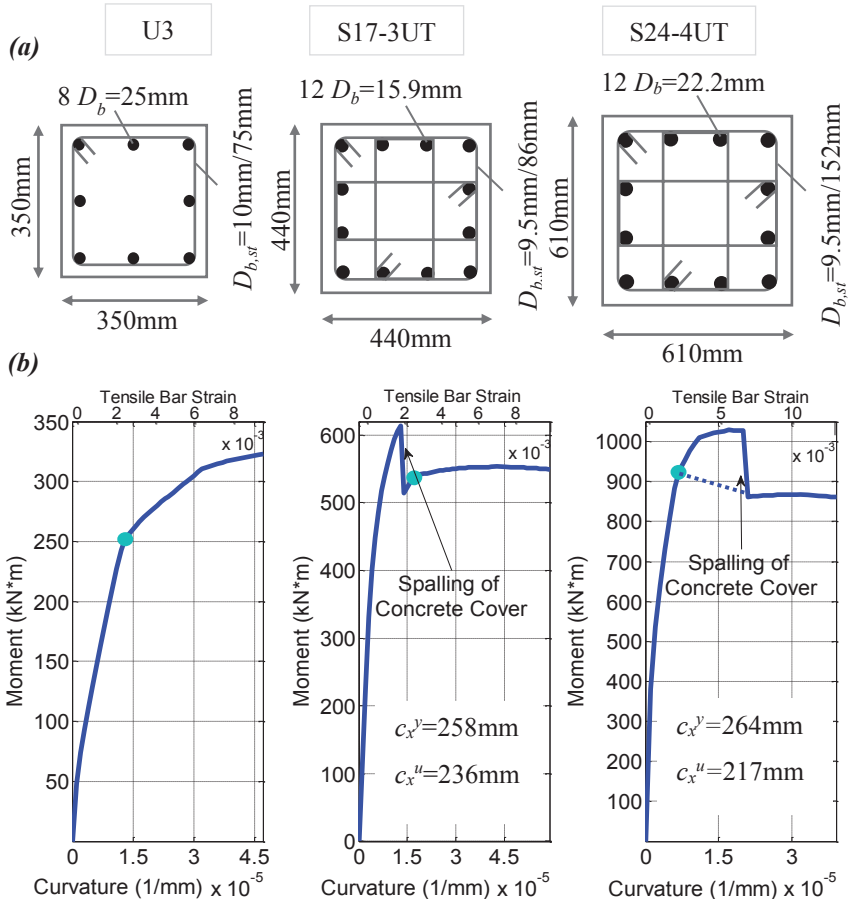

Figure 4-11: For Specimens U3, S17-3UT and S24-4UT a) cross section details, b) moment - curvature - tensile bar strain diagrams.

Column U3 (Saatcioglu et al. 1989)

The specimen had a 350 mm square cross section reinforced with eight evenly distributed longitudinal reinforcing bars of D_b = 25mm and stirrups of $D_{b,st}$ = 10mm spaced at 75mm o.c. (on centers) and clear cover C_{cov} = 32.5mm (i.e., d=350-45=305mm), see Fig. 4-11a. The concrete strength was f_c'=34.8MPa. Longitudinal steel yielding strength was 430MPa, with

a 5% hardening. Stirrup yield strength was 470MPa.

Column shear span was L_s = 1.0m and the axial load ratio [$v=N/(f_c' bd)$] was 0.16. Fig. 4-11b plots the unified M-ϕ-ε relationship obtained for this axial load using fiber section analysis with the modified Kent & Park model for confined concrete (Scott et al. 1982); a Hognestad-type parabola was used to model the compression stress-strain response of unconfined concrete (Hognestad 1951). A bilinear stress-strain curve with 5% hardening was used to model longitudinal reinforcement (Fig. 4-3a). Bond strength was taken as equal to $f_b^{max} = 1.25\sqrt{f_c'}$ (7.4MPa) for the anchorage (anchorage with hook with equivalent straight length of L_b = 800mm, *fib* Model Code 2010). For the shear span, the bond strength is calculated using a frictional model (Tastani et al. 2010) that accounts for separate contributions of the cover concrete and stirrups according to:

$$f_b^{max} = \frac{2\mu_{fr}}{\pi D_b}\left(2C_{cov}\cdot f_{ct} + 0.33\frac{A_{st} f_{y,st}}{N_b \cdot s}\right) \tag{4-39}$$

where N_b is the number of tension bars (or pairs of tension spliced bars if reinforcement is spliced) laterally restrained by the transverse pressure exerted in the form of confinement by the stirrups, C_{cov} is the clear concrete cover, A_{st} is the area of stirrup legs enclosing the N_b bars (i.e., the total area of legs crossing the splitting plane), s is the stirrup spacing along the member length, μ_{fr} is the coefficient of friction, f_{ct} is the concrete tensile strength and $f_{y,st}$ is the yielding strength of stirrups. Therefore the maximum bond strength for the shear span is 7.2MPa when considering the contribution of the cover, which drops to 2.75MPa after cover delamination (for the present example: μ_{fr}=1, $f_{ct} = 0.33\sqrt{f_c'}$, N_b = 3). Due to the reversed cyclical nature of the displacement history, cover on the tension reinforcement is assumed to have delaminated or split if, during the opposite direction of loading, the compressive strain has attained the limit value of 0.003; this is used also in all other examples considered herein. The residual bond strength f_b^{res} is defined as 20% of the maximum bond strength and parameter s_1 = 0.2mm; s_2 mainly depends on the anchorage length which is equal to the shear span if the latter is transmitted to the total disturbed region. For the present problem, s_2 is found to be equal to 0.5 mm at the ultimate state of reinforcement (see Fig. 4-14).

Following evaluation of the process of crack formation according to the proposed algorithm, the resulting distribution of strains is illustrated in Fig. 4-12. Note that stabilization of cracking occurred before yielding of

the tensile bars (just after the formation of the fourth crack). Ultimate strain corresponded to a disturbed region extending over the entire length of the column shear span including an equivalent additional length equal to $12.5D_b$ (313 mm) – thus $\ell_{Do}^{max}=L_s+12.5D_b$– in order to account for the end detail of reinforcement at the tip of the column being welded onto a steel plate (this additional length is the anchorage length equivalent of a T-headed anchorage according to *fib* Model Code 2010 – here this is a conservative estimate). The red dashed curve in Fig. 4-12d plots the bar strain distribution that results from plane sections analysis; there is a marked deviation from the distribution controlled by the bond action in the most stressed part of the shear span.

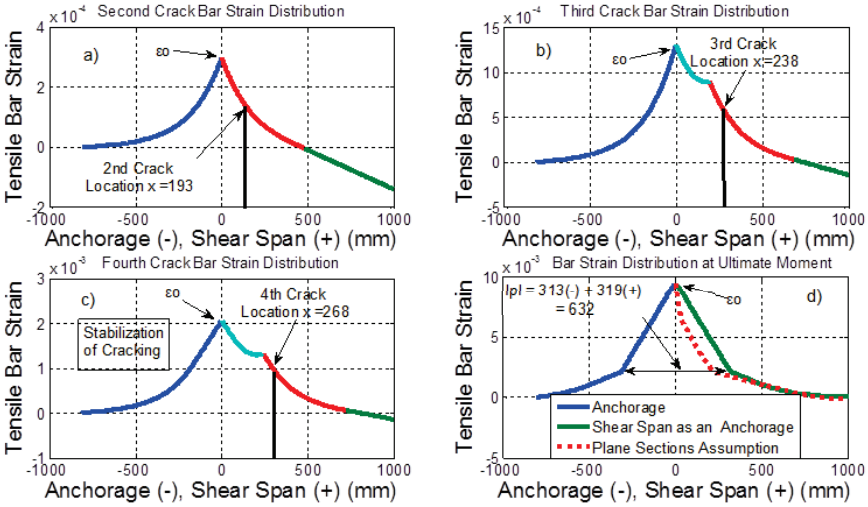

Figure 4-12: Column U3 (a), (b) (c) tensile bar strain distributions along the anchorage (blue curves) and the shear span (cyan-red-green curves). Location of estimated successive cracks is indicated until crack stabilization. d) Strain state of reinforcement at ultimate, where ℓ_{pl} is calculated.

From Fig. 4-12 it is seen that the yield penetration length over the shear span at the last step of the calculation was 319mm ($0.91h$ or $0.32L_s$), whereas the corresponding pullout slip was $s_u^{span}(x=0)$ = 2.36mm (Fig. 4-14). When including the yield penetration in the footing as is intended in the formal definition of ℓ_{pl} (Eq. 4-2b), the total plastic hinge length is 632 mm. (Note that the yield penetration length inside the footing is 313mm or

$0.029D_bf_y$ and the corresponding slip is $s_u^{anch}(x=0)$=2.33 mm). Fig. 4-13 compares this value with the empirical estimates of Eqs. 4-3a, b; the easy estimate of *0.5d* is also noted. Also included is the result of the classical definition of plastic hinge length $(1-M_y/M_u)L_s$. For comparison it is noted (red dashed line in Fig. 4-13) that cover delamination extended over 520 mm measured from the face of the support, according to the experimental report of specimen U3 (Saatcioglu et al. 1989). Fig. 4-14 presents the slip distribution lengthwise of the bar reinforcement, from where values at the critical section are used next for the calculation of drift components.

The rotation components θ^{slip} and θ^f occurring at the critical section of the specimen at yielding- and in the ultimate limit state, are estimated in accordance with Eqs. 4-1, 4-2 by also adding the contribution from the anchorage (previous Section); here the theoretical ultimate point corresponds to the attainment of the maximum supportable disturbed length, $\ell_{Do}^{max}=L_s+12.5D_b$=1313 mm as described in the preceding. Thus, Eq. 4-1 is modified as follows:

$$\theta_y^{slip}=\underbrace{\frac{s_y^{span}}{d-0.4c_x}\Big|_{x=0}}_{shear\,span}+\underbrace{\frac{s_y^{anch}}{d-0.4c_x}\Big|_{x=0}}_{anchorage};$$

$$\theta_u^{slip}=\underbrace{\frac{s_u^{span}}{d-0.4c_x}\Big|_{x=0}}_{shear\,span}+\underbrace{\frac{s_u^{anch}}{d-0.4c_x}\Big|_{x=0}}_{anchorage} \quad (4\text{-}40)$$

The values $s_y(x=0)$ and $s_u(x=0)$ are the contributions to slip at the base of the column resulting from pullout from the anchorage as well as from the shear span. For the analytical estimations of specimen U3, the compression zone depth was (Fig. 4-11b, ε_u=0.0095 and ϕ_u=4.7x10^{-5}mm^{-1}) c_x= 103mm (i.e., *d-0.4*c_x= 305-41=264mm) and from Eq. 4-40 the drift capacity owing to pullout slip was estimated at:

θ_u^{slip}=2.36/264+2.33/264=0.018rad.

Using ℓ_r = 319mm, the ultimate rotation of the column due to flexure was: $\theta_u^f=\theta_y^f+\theta_p^f$ where $\theta_y^f=\phi_y L_s/3$ (see also Eq. 4-2b): θ_u^f=1/3·0.000013·1000 + (0.000047-0.000013)·319 = 0.015rad. The term θ_u^{slip} accounts for 55% of the total rotation capacity of the RC column (0.018+0.015=0.033rad). The experimental reported tip displacement at the maximum moment (268kNm) was 35 mm, corresponding to a rotation of 0.035rad.

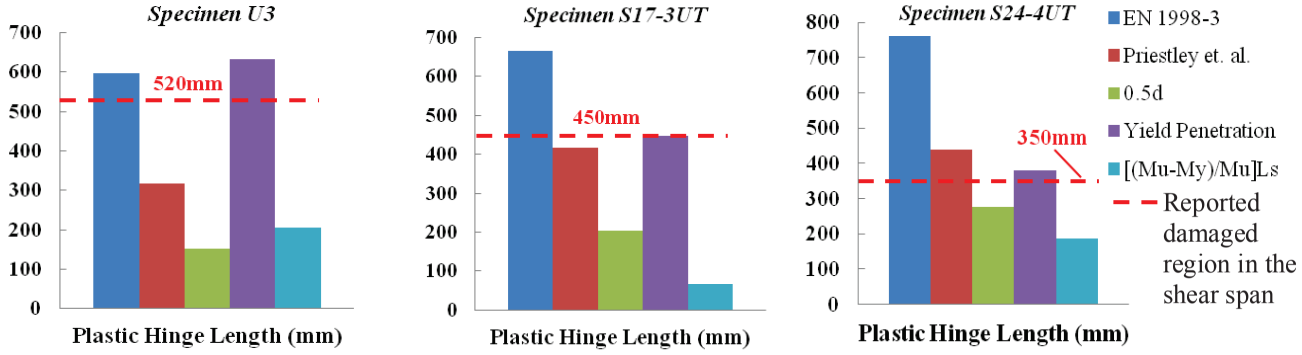

Figure 4-13: For specimens U3, S17-3UT and S24-4UT analytical calculation of the plastic hinge length ℓ_{pl} (purple bar) and its correlation with the design equations.

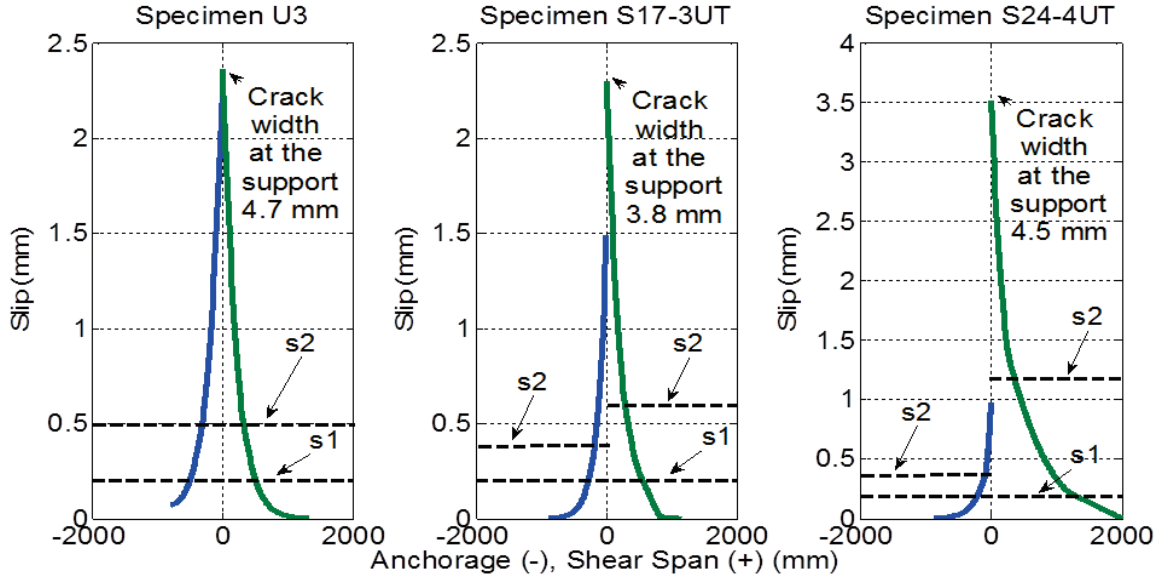

Figure 4-14: For specimens U3, S17-3UT and S24-4UT distributions along the bar length at ultimate strain (where ℓ_{pl} is calculated).

Column S17-3UT (Bae et al. 2008)

The geometry of the column is summarized in Table 4-1 and depicted in Fig. 4-11a. The main bars were welded onto a steel plate for the application of the load at the tip of the column. This was taken into account in the analysis by including a length of $12.5D_b$ (= 199mm) as an effective extension of the available development length in the shear span. Fig. 4-11b depicts the results of the moment – curvature - strain analysis. It is evident that cover spalling occurs relatively early at a stage corresponding to bar yielding. For the shear span, the maximum and the post-cover delamination values for bond strength were estimated from Eq. 4-39 as $f_{b,w/\mathrm{cov}}^{\max}$ = 11.49 MPa and $f_{b,wo/\mathrm{cov}}^{\max}$ = 5.40MPa (indices *w/cov* and *wo/cov* correspond to the inclusion or non-inclusion of the cover contribution). The process of detecting the crack formation and the corresponding strain distribution for the column are presented in Fig. 4-15. Stabilization of cracking occurred before the yielding of the tensile bars. Moreover, after the spalling of the concrete cover, the contribution of the latter to bond strength was neglected (thus $f_b^{max} = f_{b,wo/\mathrm{cov}}^{\max}$ = 5.40MPa).

As is evident from Fig.4-15d the maximum sustained yield penetration length based on the proposed procedure is 271 mm ($0.66h$ or $0.09L_s$) in the shear span and inside the footing it is 177 mm (or $0.022D_b f_y$). Reported damage extended over a distance of 450 mm from the base of the column (see experimental reference; red dashed line in Fig. 4-13). Fig. 4-13 presents the correlation of the analytical estimation with the empirical results and Fig. 4-14 the analytically estimated slip distribution lengthwise along the bar reinforcement at the ultimate strain.

The rotation of the column at the ultimate moment due to slippage θ_u^{slip} (Eq. 4-40), is θ_u^{slip} = 2.30⁄311+1.5⁄311 = 0.012rad whereas the ultimate rotation of the column due to flexure (using ℓ_r = 271mm) is: θ_u^{flex} = 1/3·0.000017·3049 + (0.000059-0.000017) ·271=0.029 rad. Thus the total drift is estimated at 0.041rad. The experimental curvature corresponding to a 20% drop in the lateral load capacity (this point was defined on the lateral load lateral displacement envelope after correction for the P-Δ effects), was $7\text{x}10^{-5}\text{mm}^{-1}$ (at the 6th level of cycling) and the associated drift was 0.032rad.

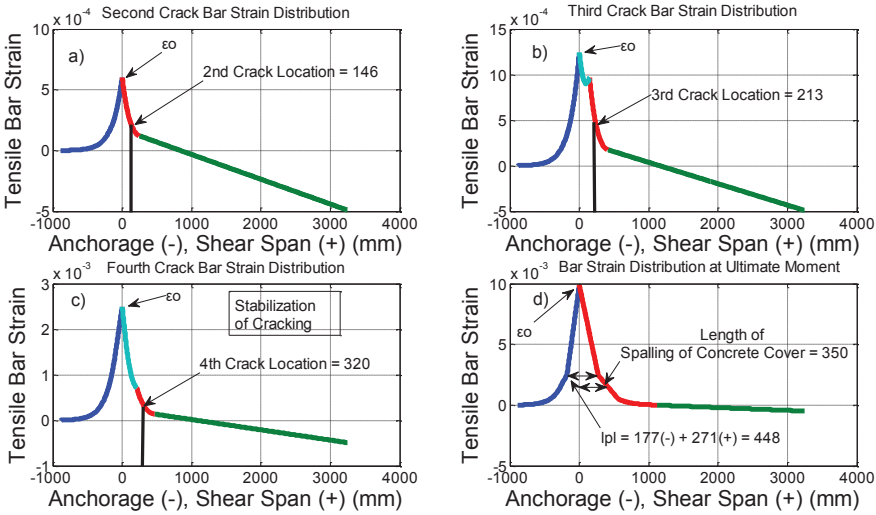

Figure 4-15: Column S17-3UT: (a), (b) and (c) tensile bar strain distributions along the anchorage (blue) and shear span (cyan-red-green curves). Location of estimated successive cracks is indicated until crack stabilization. d) Strain state of reinforcement at ultimate, where ℓ_{pl} is calculated.

Column S24-4UT (Bae et al. 2008)

Table 4-1 and Fig. 4-11a depict the geometric characteristics of the column specimen. As in the previous example, the effective development length of the longitudinal bars in the shear span was extended by $12.5D_b$ (= 278mm) to account for the welding of main reinforcement on a steel plate attached to the point load setup. Fig. 4-11b plots the calculated moment – curvature - strain diagram, indicating also the onset of cover delamination (beyond that point, bond strength is reduced due to the elimination of the cover contribution in Eq. 4-39). For the shear span f_b^{max} was $f_{b,w/\mathrm{cov}}^{\max}$ = 8.85MPa and $f_{b,wo/\mathrm{cov}}^{\max}$ = 2.0MPa (with and without the cover contribution). The process of crack formation and the resulting bar strain distributions as calculated using the proposed algorithm are shown in Fig. 4-16.

Fig. 4-16 evidences that yield penetration length at maximum strain value ε_u = 0.013 is l_r = 301mm (= $0.5h$ or $0.1L_s$) in the shear span. Adding

the length of yield penetration in the footing (i.e. 80mm or $0.01D_b f_y$) the plastic hinge length is estimated at 380mm. Fig. 4-13 presents the correlation of the analytical estimation with the empirical results and the reported damage into the shear span, extending up to a distance of 350 mm. Fig. 4-14 shows the estimated slip distribution lengthwise along the bar reinforcement at the ultimate strain.

Column rotation capacity at the ultimate moment was estimated as follows: from slip, $\theta_u^{slip} = 3.52/463 + 0.98/463 = 0.01$rad and due to flexure $\theta_u^{fle} = 1/3\ 0.000007 \cdot 3049 + (0.000039\text{-}0.000007) \cdot 301 = 0.017$rad (in total 0.027rad). The experimental reported drift ratio at up to 20% net loss of lateral load strength was 0.033rad (after correction of the result for the P-Δ effect); therefore the experimental total rotation of 0.033rad was approximated adequately by the estimated analytical value of 0.027.

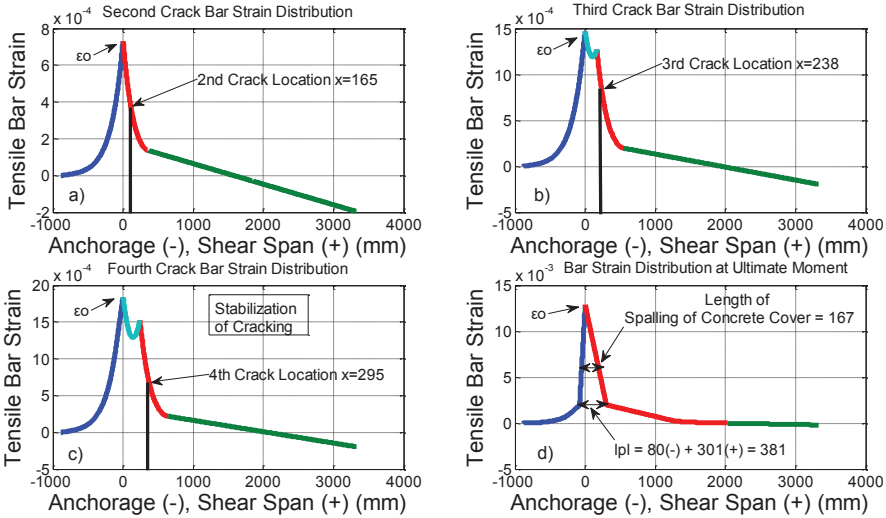

Figure 4-16: Column S24-4UT: (a), (b) and (c) tensile bar strain distributions in the anchorage (blue) and the shear span (cyan-red-green curves). Location of estimated successive cracks is indicated until crack stabilization. d) Strain state of reinforcement at ultimate, where ℓ_{pl} is calculated.

Parametric Investigation

The parametric sensitivity of the proposed solution for the plastic hinge length is investigated in this section considering as a point of reference specimen U3, examined in the preceding section. Parameters considered, reference values, and ranges of parameters thereof, are listed in Table 4-2; in each case, one parameter is varied at a time keeping the reference values for all other variables (so the possible interaction effects between variables have not been considered in conducting the sensitivity analysis). Consistent with the original definition of the plastic hinge length (Eq. 4-2b) the strain hardening ratio of the reinforcement E_{sh} effectively increases the plastic hinge length (Table 4-2). Similarly, a reduction of the residual bond strength f_b^{res} leads to further increase of the plastic hinge length (Table 4-2). It should be noted that the yield penetration length in the anchorage is included in the plastic hinge length.

The location of the cracks is affected by variable ω that defines the elastic bond according to Eq. 4-28. Decreasing the slip limit s_1 and increasing the value of average bond strength f_b^{max} both led to the consolidation of the cracks closer to the critical section at the base of the column (before stabilization of cracking), as is evident from Table 4-2. In all analytical cases presented in Table 4-2 the first crack appears always at the base of the column ($x_{1,cr}$=0), whereas in some of the experiments severe cracking occurred about 50 mm above the footing, owing to the restraint provided by the footing, particularly when the drift history was applied by means of rotating that block while keeping the tip of the cantilever specimen stationary (e.g. Bae et al. 2008).

In the previous section three specimens with different aspect ratios (L_s/d) and axial load ratios [$v = N/(f_c bd)$] were considered. The corresponding values for (L_s/d) and v were (3, 0.16), (7, 0.5), and (5, 0.2) respectively. According to Bae et al. 2008, the two parameters have a simultaneous effect on the extent of ℓ_{pl} , and a degree of interaction (i.e., the effect of L_s/d is pronounced only in the presence of a high axial load ratio) (Tables 4-2,4-3). To illustrate the sensitivity of the proposed approach in reproducing the experimental trend, a second reference point is introduced in the parametric study, namely the case of specimen U3 but with an axial load ratio of ν = 0.5 (Table 4-3).

Table 4-2: Parametric Investigation – Properties similar to specimen U3 (units: mm, MPa)

Parameter	$\nu=N/(f_c'bd)$		
	=0.15	*=0.3*	*=0.5*
Plastic Hinge Length	1.8h	1.3h	0.9h
Parameter	$f_b^{max}=3$	$f_b^{max}=5$	$f_b^{max}=7$
Plastic Hinge Length	3.1h	2.2h	1.8h
Parameter	$f_b^{res}=1$	$f_b^{res}=2$	$f_b^{res}=3$
Plastic Hinge Length	2.2h	1.6h	1.3h
Parameter	$E_{sh}=1\%E_s$	$E_{sh}=2.5\%E_s$	$E_{sh}=5\%E_s$
Plastic Hinge Length	0.4h	0.9h	1.8h
Parameter	L_s=2h	L_s=3h	L_s=4h
Plastic Hinge Length	1.8h	1.8h	1.8h
Parameter		D_b=18	
Plastic Hinge Length		1.4h	

Table 4-3: Parametric Investigation – Axial load ratio equal to 0.5 (units: mm, MPa)

Ideal reference case:	$\nu=N/(f_c'bd)=0.5$; *all other characteristics are those of U3*		
Parameter	$f_b^{max}=3$	$f_b^{max}=5$	$f_b^{max}=7$
Plastic Hinge Length	1.6h	1.1h	0.9h
Parameter	$f_b^{res}=1$	$f_b^{res}=2$	$f_b^{res}=3$
Plastic Hinge Length	1.1h	0.8h	0.7h
Parameter	$E_{sh}=1\%E_s$	$E_{sh}=2.5\%E_s$	$E_{sh}=5\%E_s$
Plastic Hinge Length	0.1h	0.4h	0.9h
Parameter	L_s=2h	L_s=3h	L_s=4h
Plastic Hinge Length	0.9h	0.9h	0.9h
Parameter		D_b=18	
Plastic Hinge Length		0.7h	

Figure 4-17a displays the influence of the variables on the normalized plastic hinge length (ℓ_{pl}/h, vertical axis) of the reference specimen, and on the associated development capacity of the reinforcement (in terms of tensile strain, ε_s, in the horizontal axis) of the critical cross section. Each curve in this diagram is read as follows:

- Reducing the bond strength f_b^{max} (to the associated residual bond strength $f_b^{res} = 20\% f_b^{max}$) gradually from 7 to 3MPa (red arrow next to the brown curve pointing down) results in the increase of the plastic hinge length attained at a lower bar strain capacity.
- Increasing the normalized axial load v (red arrow next to blue curve pointing up) lowers the strain capacity and the associated plastic hinge length.
- Reducing the hardening modulus E_{sh} (red arrow next to green curve pointing down) decreases the plastic hinge length (as is implied by Eq. 4-38) and increases the strain.
- Reducing the bar size D_b (red arrow next to grey curve pointing down) decreases the hinge length (as it is also implied by Eq. 4-38) and increases the strain.

The hinge length is relatively insensitive to L_s/h at low axial loads, i.e., at v = 0.15 all points coincide with the reference point (intersection of all curves; i.e. for L_s/h = 2, 3 and 4, the ℓ_{pl}/h is 1.8 and the associated strain is 0.017).

The presence of an axial load on a member undergoing cyclical displacement reversals weakens the cover over a larger portion of the shear span length speeding up cover delamination due to excessive compressive strains. Upon reversal of a load, the crushed cover cannot support significant bond action for the reinforcement when the latter is stressed in tension, leading to a reduced value of f_b^{max} (it is sustained only by the stirrups) and to the demise of f_b^{res} (less than half of the bar perimeter is in contact with concrete, with implications on residual friction). These in turn cause increased penetration depth for columns carrying a higher axial load. Fig. 4-17b depicts the effect of the studied variables on the plastic hinge length under higher axial load (v=0.5); in the reference case, the term f_b^{max} was reduced from 7.2MPa to 2.75 after cover loss. The following may conclude:

- Reducing bond strength f_b^{max} from 7 to 3MPa (brown curve in Fig. 4-17b) results in increased plastic hinge length, attained at a higher bar strain.

- Reducing the residual bond strength f_b^{res} (orange curve in Fig. 4-17b) increases the hinge length and lowers the associated strain capacity.
- Lower hardening modulus E_{sh} (green curve in Fig. 4-17b) results in lower hinge length and strain.
- Reduced bar size D_b (grey curve in Fig. 4-17b) lowers the hinge length and the strain capacity.

The mechanism by which the axial load ratio affects the damaged region is by accelerating and spreading the delamination of the cover in the compression zone of the laterally swaying column. This was already evident in the M-ϕ-ε relationships of Fig. 4-11. To study this parametric trend, consider the cross section of Fig.4-18a. Cover delamination is assumed to occur when the compressive strain at the level of compression reinforcement reaches the limit of 0.004 (the term $\xi=c_x/d$ is the normalized compression zone and $\xi'= d_2/d$ defines the position of the compression reinforcement as per the extreme fiber). In this case, from cross section analysis, the strain of the tensile reinforcement ε_o is given by Eq. 4-41.

$$\varepsilon_o = 0.004 \cdot \frac{1-\xi}{\xi-\xi'} \tag{4-41}$$

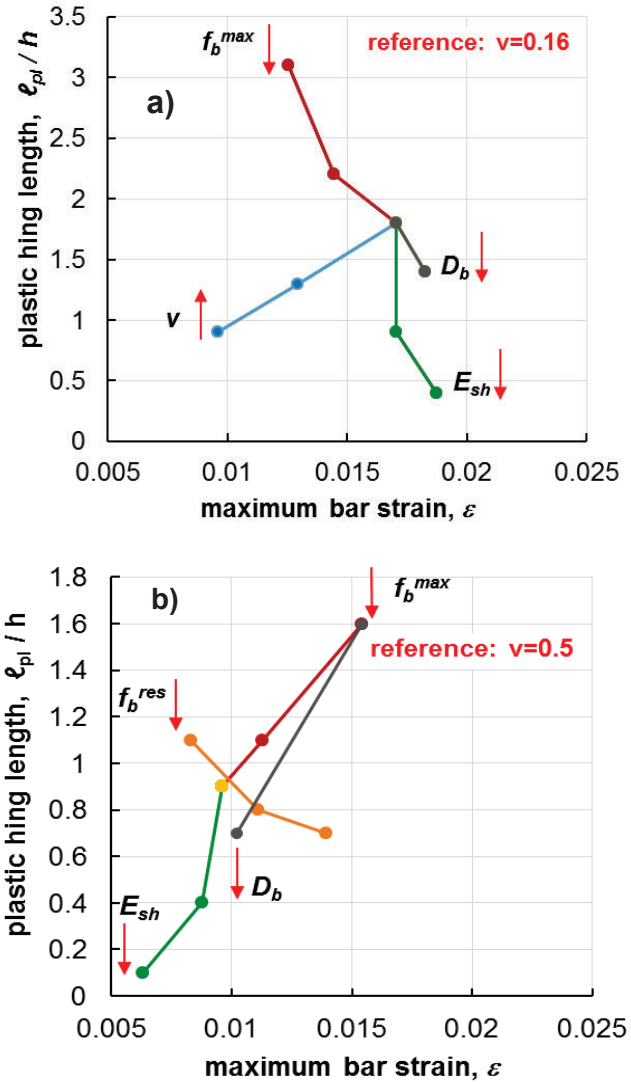

Figure 4-17: Sensitivity analysis of the normalized plastic hinge length ℓ_{pl}/h versus the associated reinforcement maximum tensile strain ε_s for a) low and b) high axial load.

For the needs of the parametric investigation, the relationship between ν and ε_o is established using experimental evidence: the column test series conducted by Watson et al. 1994 included specimens with various axial load ratios ranging from ν = 0.1 to 0.6. Based on the reported test results, the relation between axial load v and normalized compression zone depth ξ is estimated as $\xi = 0.25v+0.07$ (Fig. 4-18b). Thus, given the applied axial load v, the normalized compression zone depth of the cross section is estimated at ξ (from Fig. 4-18a); then, the corresponding strain in the tension reinforcement at the critical section, ε_o, is obtained from Eq. 4-41). This is substituted in Eq. 4-38 to define the yield penetration length into the shear span, using different intensities of average residual bond strength depending on the magnitude of the axial load (lower residual bond strength for higher axial load to reflect the effect of delaminated cover over a broader region). This procedure is visualized in the combined diagram in Fig. 4-19, where curves of v - ε_o (grey curve) and l_r/d - ε_o (black curves, where the thicker the curve the higher the f_b^{res} is) are simultaneously plotted (note: the horizontal grey dashed line drawn at the upper part of Fig. 4-19 defines the available column aspect ratio, L_s/d, which serves as the ultimate limit for possible penetration). This diagram may be used to illustrate two aspects of the parametric sensitivity of the problem: a) the increase of axial load for example from 0.2 to 0.4 (following the red arrow) results in reduction of the strain capacity of the cross section (from 0.05 to 0.027) along with diminishing of the f_b^{res} (crossing from the thicker to the thinner curve, i.e. from 4 to near 1MPa) as well as an increase of the extent of the plastic hinge length in the shear span (i.e. from 1.1 to 2.3d, where d is the effective depth of the cross section, see the red dashed horizontal lines). b) the unified diagram v - l_r/d - ε_o can be used in design: given the axial load and the aspect ratio of the member, the strain capacity of the cross section and the corresponding plastic hinge length are uniquely defined, leading to the proper assessment of the members' available deformation capacity. The extent and intensity of damage may be effectively reduced through confinement as a higher value of the residual bond strength may be supported (see the black dashed paths in Fig. 4-19).

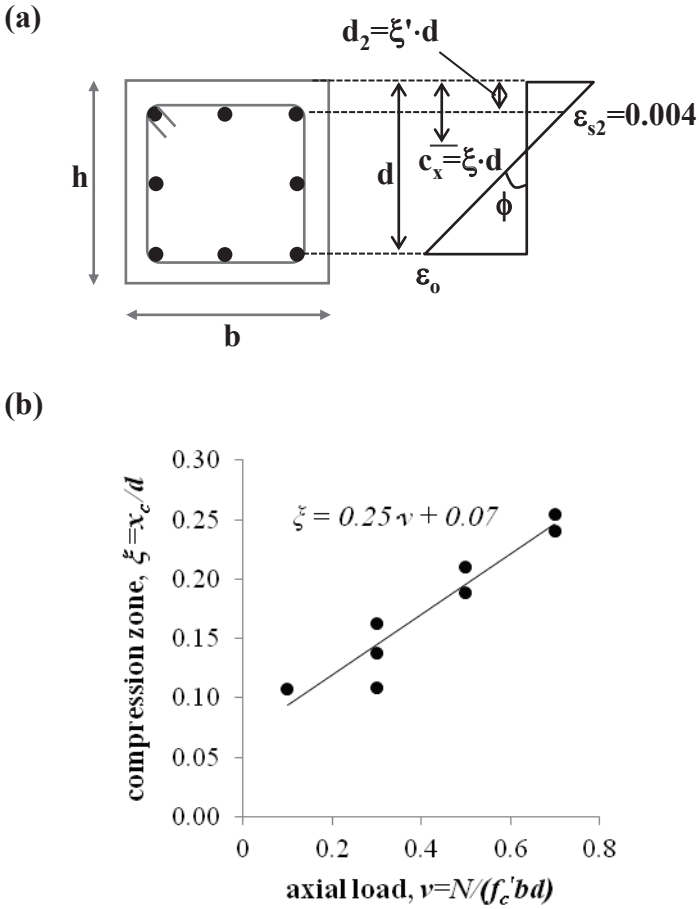

Figure 4-18: a) Strain state of cross section at cover crushing. b) The influence of axial load on compression zone based on data from Watson and Park (1994).

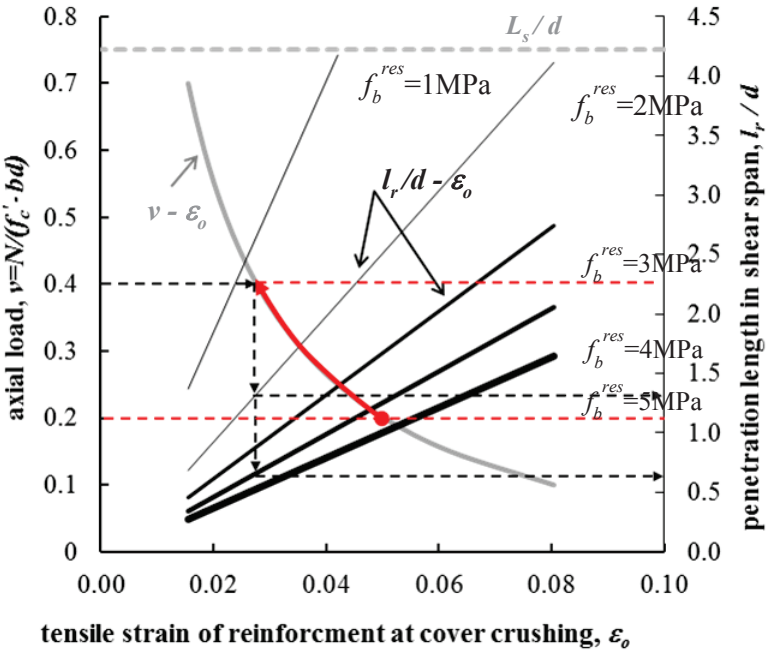

Figure 4-19: A unified diagram $v - l_r/d$ - ε_o for the influence of axial load, residual bond strength and tensile bar strain on yield penetration length into shear span.

CHAPTER FIVE

PHAETHON: SOFTWARE FOR ANALYSIS OF SHEAR-CRITICAL REINFORCED CONCRETE COLUMNS

The correlation of experimental responses and results obtained from the inelastic flexural analysis of column elements with a dominant shear component had already highlighted the limitations of the underlying assumptions of the later approach, when used beyond their scope of application. Shear is a persistent problem in analysis and assessment because by the mere rotation of the principal directions away from the parallel and normal to a cross section, complicates convergence to solutions that satisfy equilibrium, particularly in the inelastic range. The debate on acceptable methods for calculation of shear strength still persists in the literature; issues such as the effective area participating in shear action and the size effect remain open. On the other hand it appears that shear strength, although estimated as a cross sectional property, really depends on the overall member response.

Even the most advanced stage of development on seismic design and assessment to date requires some kind of nonlinear analysis either static or dynamic. These nonlinear analyses are mostly carried out using frame elements with different levels of approximation. Two main approaches are usually used, classified as lumped-plasticity and distributed-inelasticity models. The limitation of concentrated plasticity elements is that inelastic deformations take place at predetermined locations in the ends of the element. Another, in many respects more serious limitation, is the fact that concentrated plasticity elements require calibration of their parameters against the response of an actual or ideal frame element under idealized loading conditions. This is necessary, because the response of concentrated plasticity elements derives from the moment–rotation relation of their components. In an actual frame element, the end moment–rotation relation results from the integration of the section response. This can be achieved directly with elements of distributed inelasticity (Filippou and Fenves 2004). For the latter approach, the so-called fiber beam elements (Fig. 5-1)

provide results that seem to be particularly appropriate for studying the seismic behavior of reinforced concrete (RC) structures: moment-axial force (M-N) coupling is readily taken into account, as well as the interaction between concrete and steel in the section. Several fiber beam-column elements have been developed with good capability of reproducing axial force and flexure effects. On the other hand, the coupling between the effects of normal and shear forces is not straightforward and hence only a few modelling strategies have accounted for, and implemented it up till now (Ceresa et al., 2007).

A common theory, appropriate for the analysis of beam-column elements, is the Euler-Bernoulli approach. The fundamental assumption of this theory is that cross-sections remain plain and normal to the deformed longitudinal axis. The engineering beam theory reproduces the response of a beam under combined axial forces and bending moments, while shear forces are recovered from a static equilibrium; the effects of the shear on beam's deformation are neglected. When the effects of tangential stresses are important for the element deformation (i.e. in a beam-columns joint or in the column/wall plastic hinge length), more refined theories like the Timoshenko beam theory may be used.

In the development of a nonlinear frame element, two main approaches have been used, namely the displacement-based (stiffness) approach and the force-based (flexibility) approach. A flexibility-based frame element gives the exact solutions for non-linear analysis of frame structure using force interpolation functions that strictly satisfy element equilibrium, and impose the compatibility conditions. Accordingly, this approach allows the overcoming of some limitations of the stiffness approach. In particular, the nonlinear analysis becomes independent of the displacement approximation, it requires fewer elements for the representation of the non-linear behaviour and, above all, in the case of a Timoshenko element or exact-beam theory-element, it avoids the well-known shear-locking problem (a sharp increase in the element stiffness which results in far fewer deformations for the element than expected) (Hughes, 2000).

One of the modelling strategies for incorporating the beam theory that incorporates the shear into the fiber approach is related to the idea of adopting suitable constitutive relationships. This category includes fiber beam-column elements using smeared cracking models. According to this approach, cracked concrete is simulated as a continuous medium with anisotropic characteristics. In general, these models are referred to as "smeared cracking approaches" since cracking is modelled as a distributed effect with directionality. These approaches are particularly suitable for sectional analysis.

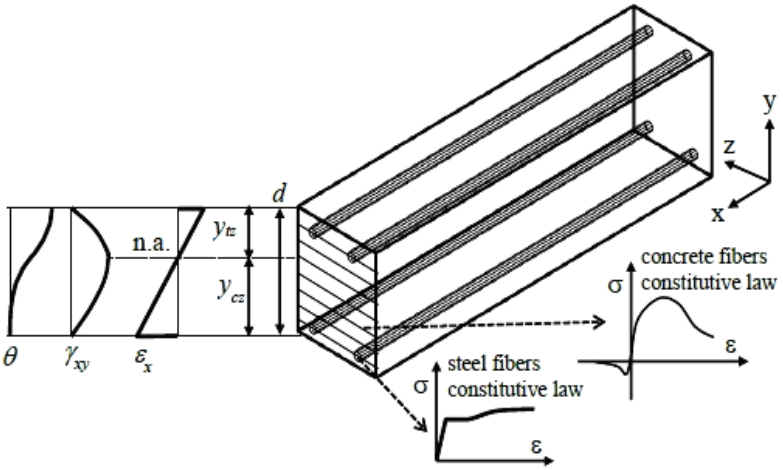

Figure 5-1: Fiber Element Scheme – definitions.

RC Sectional Model Based on Modified Compression Field Theory (MCFT)

Since the end of 1970s, a considerable amount of experimental and analytical research has been conducted with the aim of developing analytical procedures capable of estimating the load-deformation response of reinforced concrete elements loaded in shear (Ceresa et al., 2008). At the University of Toronto, Collins developed a procedure called the compression field theory (CFT) in 1978 (Collins, 1978). In 1981, a competition was held to predict the load-deformation response of four reinforced concrete panels tested at the University of Toronto (Collins et al., 1985), where leading researchers from around the world entered predictions based on various constitutive approaches. The results indicated that the most highly developed level in analytical modelling to time was far from satisfactory. Generally, the models were not able to adequately estimate the ultimate strength, the failure mode or the load-deformation response of the panels. Most of the entrants used constitutive theories developed from tests conducted on plain concrete specimens. Conditions in the specimens are not representative of actual RC structures. The interaction between the concrete and steel strongly influences the response of reinforced concrete structures. In an effort to determine more realistic relationships for cracked reinforced concrete, Vecchio and Collins (1982)

tested a series of RC panels. From these tests, the modified compression field theory (MCFT) (Vecchio & Collins, 1986) was calibrated by including stress-strain relationships for cracked reinforced concrete under plane stress conditions.

An RC element is homogenized and is treated as anisotropic elastic material shown in Fig.5-2. Consider an elementary panel under constant plane stress, of uniform thickness, containing a rectangular grid of well distributed reinforcement. Loads acting on the element's edge planes are assumed to consist of uniform membrane stresses, i.e., axial stresses n_x, n_y and uniform shear stresses τ_{xy}. The deformed shape is defined by the strain tensor for plane stresses:

$$\begin{bmatrix} \varepsilon_x & \gamma_{xy}/2 & 0 \\ \gamma_{xy}/2 & \varepsilon_y & 0 \\ 0 & 0 & \varepsilon_z \end{bmatrix} \quad (5\text{-}1)$$

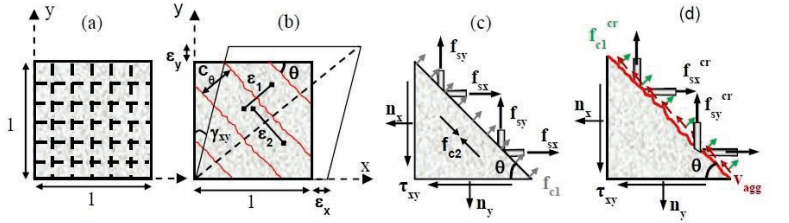

Figure 5-2L: a) RC smeared-cracking membrane element, b) average strains (C_θ: spacing of cracks inclined at θ) c) average stresses and d) local stresses at a crack (v_{agg}: shear stress on crack surface).

The MCFT utilizes the following assumptions:

- The reinforcement is averaged or smeared throughout the element, i.e. it applies only to well-detailed members.
- The stresses applied to the element are uniform along edges.
- The total stress state is a function of the total strain state.
- The reinforcement is perfectly bonded to concrete, so that relative displacement due to bond slip between reinforcement and concrete is ignored.
- The shear stress is negligible in reinforcement.
- The principal stresses and principal strain axes are coincident; as a consequence, no deviation between the two is allowed.
- The constitutive relationships for concrete and reinforcement are independent.

- The cracks are smeared and allowed to rotate.

The theory comprises three sets of relationships: compatibility relationships between concrete and reinforcement average strains, equilibrium relationships between externally applied loads and average stresses in the concrete and reinforcement; and uniaxial constitutive relationships for cracked concrete along the principal directions and for reinforcement. The constitutive relationships for cracked concrete result from tests of reinforced concrete panels using a purpose-built Panel Element Tester at the University of Toronto. As such, the formulation of the MCFT calibrated with the specific tests conducted in the panel tester, incorporates realistic constitutive models for concrete based on experimentally observed phenomena. While cracks are smeared and the relationships are formulated in terms of average stresses and strains, a critical aspect of the MCFT is the consideration of the local strain and stress conditions at cracks (Fig.5-2d).

Constitutive Model based on MCFT for a Fiber RC Beam

In order to determine the normal and the shear stresses for the *i*-th fiber/layer (σ_x^i, τ_{xy}^i) of a fiber section of a RC beam (Vecchio & Collins, 1988), a bi-axial fiber constitutive model is developed according to the Modified Compression Field Theory (MCFT) (Table 5-1). For the section state determination the following assumptions were made: the longitudinal ε_x and shear γ_{xy} strains are known for each fiber, according to a plane section assumption and to a parabolic shear strain distribution along the height of the section with the maximum value $\gamma_{xy.max}$ located on the neutral axis y_{na} (Eq. 5-2, two half-parabola with the same maximum are met to the point of neutral axis with different starting point, extreme tensile and extreme compressive fiber respectively).

$$\gamma_{xy}(y) = \gamma_{xy.max} \cdot \left[2\left(\frac{y}{y_{na}}\right) - \left(\frac{y}{y_{na}}\right)^2\right] \tag{5-2}$$

The transversal concrete stress f_{cy} was determined for each fiber from equilibrium conditions (zero normal stress n_y was assumed). The constitutive law is based on an iterative procedure (Fig. 5-3) where, in order to accelerate the convergence of the algorithm to the right angle θ, the initial guess value of the procedure for the angle of inclination of principal stresses/strains (angle of principal axis *2* with respect to *x*-axis) is determined according to the following equation:

$$\theta(y) = \frac{\pi}{4} \cdot \left(\frac{y}{y_{cz}}\right)^2, \quad 0 < y \leq y_{cz}$$
$$\theta(y) = \frac{\pi}{4} + \frac{\pi}{4} \cdot \left[2\left(\frac{y-y_{cz}}{y_{tz}}\right) - \left(\frac{y-y_{cz}}{y_{tz}}\right)^2\right], \quad y_{cz} < y \leq d \tag{5-3}$$

where y is the location of the concrete layer/fiber (y : start measuring from the extreme compressive fiber, Fig.5-1), y_{cz} is the depth of the compression zone, y_{tz} is the depth of the tension zone and d is the total depth of the section (i.e., $y_{cz}+y_{tz}=d$, Fig. 5-1). Fig. 5-4 depicts the angle shape function along the height of the section according to the above equation (d =457 mm, y_{cz} = 280 mm similar to Specimen 1 [Sezen & Moehle, 2006]). The solution to the iterative procedure is reached by applying the Regula Falsi root finding a numerical solution (Chabert, 1999).

Table 5-1. Equations embodied in the iterative procedure (Vecchio & Collins, 1988).

$$\varepsilon_x = \varepsilon_{cx}, \quad \varepsilon_1 = \varepsilon_x + \frac{\gamma_{xy} \cdot \tan(\pi/2 - \theta)}{2}, \quad \varepsilon_y = \varepsilon_1 - \frac{\gamma_{xy}}{2 \cdot \tan(\pi/2 - \theta)},$$
$$\varepsilon_2 = \varepsilon_x + \varepsilon_y - \varepsilon_1$$

$$f_{c1} = E_c \cdot \varepsilon_1 \text{ for } 0 < \varepsilon_1 \leq \varepsilon_{cr}, \quad f_{c1} = \frac{f_{cr}}{1+\sqrt{200\varepsilon_1}} \text{ for } \varepsilon_{cr} < \varepsilon_1 \leq \varepsilon_{yx},$$

$$f_{c2} = f_{c2max} \cdot \left[2\left(\frac{\varepsilon_2}{\varepsilon'_c}\right) - \left(\frac{\varepsilon_2}{\varepsilon'_c}\right)^2\right], \quad \frac{f_{c2max}}{f'_c} = \frac{1}{0.8 - 0.34\varepsilon_1/\varepsilon'_c} \leq 1.0,$$
$$f_{sy} = E_{sy}\varepsilon_y \leq f_{yy}$$

$$f_{cy} = -\rho_y \cdot f_{sy}, \quad \tau_{xy} = \frac{f_{cy} - f_{c2}}{\tan(\pi/2 - \theta)}, \quad f_{cx} = f_{c1} - \tau_{xy} \cdot \tan(\pi/2 - \theta),$$
$$G_{sec} = \frac{\tau_{xy}}{\gamma_{xy}}, \quad E_{sec} = \frac{f_{cx}}{\varepsilon_x},$$

$$theta(\varepsilon_{cx}, \gamma_{xy}) = \tan^{-1}\frac{f_{c1} - f_{cy}}{\tau_{xy}}$$

f'_c = Concrete Cylinder Compressive Strength (MPa), ε'_c= Strain at Concrete Cylinder Compressive Strength, E_c= Concrete Elastic Modulus (MPa), f_{cr}= Tensile Concrete Strength (MPa), ε_{cr}= Strain at Tensile Concrete Strength, ε_{yx}= Yielding Strain of Longitudinal Reinforcement, E_{sy}=Elastic Modulus of Stirrups (MPa), f_{yy}= Yielding Strength of Stirrups (MPa), ρ_y = Stirrups Reinforcement Ratio.

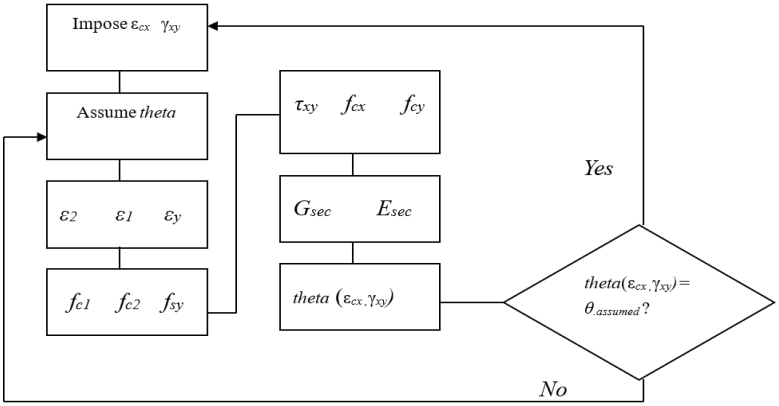

Figure 5-3: Iterative procedure for each fiber/layer of the section according to MCFT.

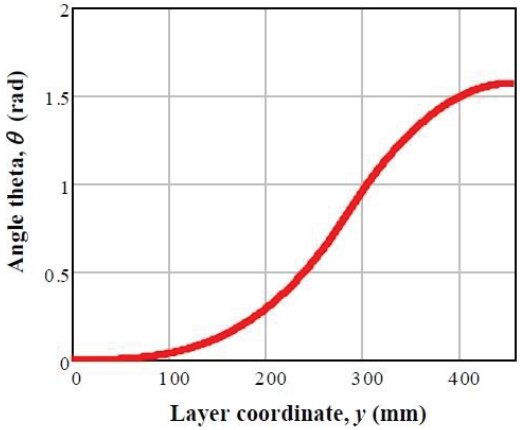

Figure 5-4: Shape function for angle theta (θ) of inclination of principal stresses/strains.

Sectional Model

Fig. 5-5 depicts a beam element with its degrees of freedom and its displacement/forces in global, local and basic systems of reference. The term "basic" is derived from the system of reference where the rigid body

motion of the beam is extracted. Considering now the virtual work principle for the beam element of Fig. 5-5, the Eq. 5-4 can be derived. The external work is done by the end forces (p) on the corresponding displacements (u), whereas the internal work is done by the basic forces (q) on the corresponding deformations (v).

$$\delta u^T p = \delta v^T q \tag{5-4}$$

The internal work of Eq. 5-4 can be derived from the integral of the stress product with the corresponding virtual strains over the element volume V. In many applications of nonlinear structural analysis, the internal work is limited to the internal work of normal stress σ_x and shear stress τ, on the axial strain ε_x and shear strain γ respectively:

$$\delta v^T q = \int \delta \varepsilon^T \sigma \, dV = \int (\delta \varepsilon_x \, \sigma_x + \delta \gamma \, \tau) dV \tag{5-5}$$

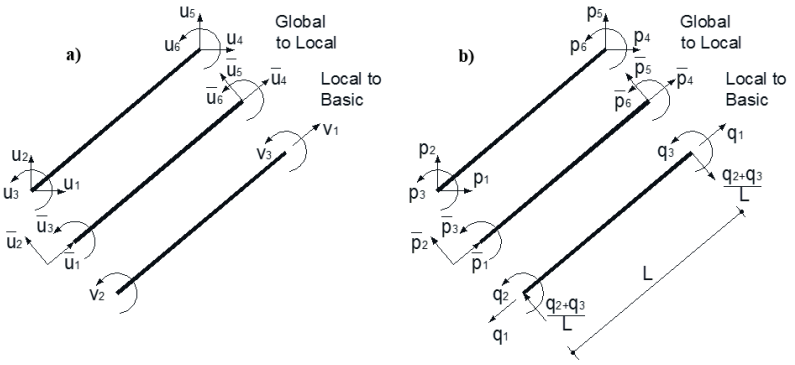

Figure 5-5: Beam a) displacements and b) forces in global, local and basic reference systems.

The strain and stress are functions of the position along the element longitudinal axis x and the position within the cross section specified in local coordinates y (with respect to the height) and z (with respect to the width).

Eq. 5-5 can be rewritten by substituting the integral over the element volume as integration over the section area A at a location x followed by integration over the element length:

$$\delta v^T q = \int (\delta\varepsilon_x \sigma_x + \delta\gamma \tau) dV = \int [\int (\delta\varepsilon_x \sigma_x + \delta\gamma \tau) dA] dx \quad (5\text{-}6)$$

The strains at a fiber/layer point of the beam cross section (*2d* case) are related to the section deformations as follows (Ceresa et al., 2008);

:

$$\varepsilon_x(x) = \varepsilon_0 - y_\varepsilon \cdot \varphi(x) \quad (5\text{-}7)$$

$$\gamma_{xy}(x) = \gamma_{xy.max} \quad (5\text{-}8)$$

where ε_0 is the axial deformation at the center of the coordinate system of the section (center of mass) and y_ε counts also from this center, $\varphi(x)$ is the curvature of the cross-section and $\gamma_{xy.max}$ is the maximum value of shear strain located on the neutral axis. Therefore the strains at a material point *m* of the section can be expressed in matrix form as follows:

$$\varepsilon(x, y_\varepsilon) = \begin{Bmatrix} \varepsilon_x \\ \gamma_{xy} \end{Bmatrix} = \begin{bmatrix} 1 & -y_\varepsilon & 0 \\ 0 & 0 & 1 \end{bmatrix} \cdot \begin{Bmatrix} \varepsilon_0 \\ \varphi \\ \gamma_{xy.max} \end{Bmatrix} = B_s(y_\varepsilon) \cdot e(x) \quad (5\text{-}9)$$

$$B_s(y_\varepsilon) = \begin{bmatrix} 1 & -y_\varepsilon & 0 \\ 0 & 0 & 1 \end{bmatrix} \quad (5\text{-}10)$$

The internal forces at a section level are given by:

$$N = \int \sigma_x dA = Axial\ force \quad (5\text{-}11)$$

$$V = \int \tau_{xy} dA = Shear\ force \quad (5\text{-}12)$$

$$M = -\int y_\varepsilon \sigma_x dA = Bending\ Moment \quad (5\text{-}13)$$

The section generalized forces can be written in a matrix format as follows:

$$f_s(x) = \int B_s{}^T(y_\varepsilon) \cdot \sigma(x, y_\varepsilon) dA \quad (5\text{-}14)$$

where:

$$f_s(x) = \begin{Bmatrix} N \\ M \\ V \end{Bmatrix}, \quad B_s(y_\varepsilon) = \begin{bmatrix} 1 & -y_\varepsilon & 0 \\ 0 & 0 & 1 \end{bmatrix}, \quad \sigma(x, y_\varepsilon) = \begin{Bmatrix} \sigma_x \\ \tau_{xy} \end{Bmatrix} \quad (5\text{-}15)$$

Taking into account the section discretization into fibers/layers, the total forces on the beam section are easily computed through the summation of the contributions of each *i*-th fiber/layer:

$$N = \sum_{i=1}^{n.layer} \sigma_x^i A^i \quad , \quad V = \sum_{i=1}^{n.layer} \tau_{xy}^i A^i \quad , \quad M = -\sum_{i=1}^{n.layer} \sigma_x^i y_\varepsilon{}^i A^i \tag{5-16}$$

where A^i is the area of the *i*-th fiber/layer.

In order to determine the normal and the shear stress for the *i*-th fiber/layer ($\sigma_x{}^i$, $\tau_{xy}{}^i$), a bi-axial fiber constitutive model is developed according to the MCFT, as it is stated previously (Fig. 5-3, $\sigma_x^i = f_{cx}^i$).

According to the above guidelines the section forces are determined based on known sectional deformations. In cases where the section forces are known and the section deformations render the desirable results, iterations are necessary (this means that the roots are searched deformations, whereas the deviation from the desired section forces is negligible or zero).

The tangent section stiffness matrix k_s is defined as the derivative of the section force vector f_s with respect to the section deformation vector e, where the explicit reference to x is dropped for the brevity of notation:

$$k_s = \begin{bmatrix} \frac{\partial f_{s_1}}{\partial e_1} & \frac{\partial f_{s_1}}{\partial e_2} & \frac{\partial f_{s_1}}{\partial e_3} \\ \frac{\partial f_{s_2}}{\partial e_1} & \frac{\partial f_{s_2}}{\partial e_2} & \frac{\partial f_{s_2}}{\partial e_3} \\ \frac{\partial f_{s_3}}{\partial e_1} & \frac{\partial f_{s_3}}{\partial e_2} & \frac{\partial f_{s_3}}{\partial e_3} \end{bmatrix} \tag{5-17}$$

$$k_s = \frac{\partial f_s}{\partial e} = \int B_s{}^T(y_\varepsilon) \cdot \frac{d\sigma(x,y)}{\partial \varepsilon(x,y)} \cdot \frac{\partial \varepsilon(x,y)}{\partial e} dA = \int B_s{}^T(y_\varepsilon) \cdot \frac{d\sigma(x,y)}{d\varepsilon(x,y)} B_s(y_\varepsilon) dA \tag{5-18}$$

$$\sigma(x, y_\varepsilon) = \begin{Bmatrix} \sigma_x \\ \tau_{xy} \end{Bmatrix} \quad \varepsilon(x, y_\varepsilon) = \begin{Bmatrix} \varepsilon_x \\ \gamma_{xy} \end{Bmatrix} \tag{5-19}$$

$$\frac{d\sigma(x,y)}{d\varepsilon(x,y)} = \begin{bmatrix} E_m & 0 \\ 0 & G_m \end{bmatrix} \tag{5-20}$$

where E_m and G_m are the tangent moduli of the stress – strain relations at a point *m* of the section approximated here by E_{sec} and G_{sec} (Table 5-1, Fig. 5-3).

Embedded Algorithms in Phaethon Software

The most studied and tested structural form for deeper understanding of the structural behaviour in reinforced concrete structures is the simple cantilever column under various types of loading. Although it is a very simple case, its numerical simulation with all interacting deformation mechanisms is still yet a very challenging task to accomplish. Towards this need and for the case of shear-critical cantilever reinforced concrete columns the idea of "Phaethon" (i.e. "the shining" in ancient Greek) was born. Embedded in this program is a frame element that may be employed in the analysis of complete structural systems too. In the following section the algorithms embodied in this Windows application are presented.

Moment – Curvature Algorithm

Through the cross sectional analysis, the unknown moment M (and the associated axial deformation ε_0) are determined for given curvature φ increments, and the unknown shear force V for given shear strain γ increments, with or without the presence of constant axial load N. The system of equations for section equilibrium can be established as follows:

$$\left\{\begin{array}{c} N - N_r\left(\varepsilon_0, \varphi, \gamma\right) = 0 \\ \mathrm{M} - \mathrm{M}_r\left(\varepsilon_0, \varphi, \gamma\right) = 0 \\ V - V_r\left(\varepsilon_0, \varphi, \gamma\right) = 0 \end{array}\right\} \tag{5-21}$$

The explicit dependence of the resisting forces is noted. With N, φ and γ given, the first equation is used to solve for ε_0; then this value is substituted along with the given φ and γ into the second and third equation to determine M and V. The resisting axial force in the first Eq. 5-21 is expanded with Taylor series and the higher than linear terms are truncated:

$$N - \left[N_r(\varepsilon_{00}, \varphi_0) + \frac{\partial N}{\partial \varepsilon_0}\Delta\varepsilon_0 + \frac{\partial N}{\partial \varphi}\Delta\varphi + \frac{\partial N}{\partial \gamma}\Delta\gamma \right] = 0 \tag{5-22}$$

where the second subscript 0 denotes the initial guess for the solution. Given the axial force N, the curvature increment $\Delta\varphi$ and the shear strain increment $\Delta\gamma$, the above equation can be solved for $\Delta\varepsilon_0$:

$$\Delta\varepsilon_0 = \left(\frac{\partial N}{\partial \varepsilon_0}\right)^{-1} \cdot \left(N_u - \frac{\partial N}{\partial \varphi}\Delta\varphi - \frac{\partial N}{\partial \gamma}\Delta\gamma\right) \text{ with } N_u = N - N_r(\varepsilon_{01}, \varphi_1) \tag{5-23}$$

The numerical solution is distinguished by the incrementation phase, which consists of the application of the curvature and shear strain increment, and by the equilibrium iterations under fixed axial force, curvature and shear strain. The axial force is applied in an initial step under zero curvature and zero shear strain. Therefore, the following algorithm is applied in Phaethon for this task:

Given section geometry and material properties, axial force N, curvature increment $\Delta\varphi$ and shear strain increment $\Delta\gamma$ (e is the section's strain vector and f_s is the resisting section force- see previous Section).

Incrementation for *k = 1..m*

1. Initial guess $e_0^{(k)} = e^{(k-1)}$ the solution at *k-1* with $e^{(0)} = 0$
2. Determine $f_s^{(k)} = f_s\left(e_0^{(k)}\right)$ and $k_s^{(k)} = k_s\left(e_0^{(k}\right)$ according to previous Section
3. Determine

   $N_u^{(k)} = N - f_{s1}^{(k)}$ and

   $\Delta\varepsilon_0^{(k)} = \left(\frac{\partial N}{\partial \varepsilon_0}\right)^{-1} \cdot \left(N_u^{(k)} - \frac{\partial N}{\partial \varphi}\Delta\varphi - \frac{\partial N}{\partial \gamma}\Delta\gamma\right)$ where

   $\frac{\partial N}{\partial \varepsilon_0} = k_{s11}^{(k)}$, $\frac{\partial N}{\partial \phi} = k_{s12}^{(k)}$ and $\frac{\partial N}{\partial \gamma} = k_{s13}^{(k)}$
4. Update solution $e_1^{(k)} = e_0^{(k)} + \begin{pmatrix} \Delta\varepsilon_0^{(k)} \\ \Delta\varphi \\ \Delta\gamma \end{pmatrix}$

Iteration for *i = 1..n* and constant *k* (skip superscript)

1. Determine $f_s = f_s(e_i)$ and $k_s = k_s(e_i)$
2. Determine $N_u = N - f_{s1}$ and $\Delta\varepsilon_0 = \left(\frac{\partial N}{\partial \varepsilon_0}\right)^{-1} \cdot (N_u)$ where $\frac{\partial N}{\partial \varepsilon_0} = k_{s11}$
3. Update solution $e_{i+1} = e_i + \begin{pmatrix} \Delta\varepsilon_0 \\ 0 \\ 0 \end{pmatrix}$

Back to iteration Step 1 until the error norm satisfies specified tolerance. On convergence the final state is updated thus determining the bending moment and shear force and the algorithm returns to Incrementation phase at Step 1.

Pushover Algorithm

For the Pushover analysis of a cantilever shear-critical RC column in Phaethon, the sectional model (either rectangular or circular) established in the previous Section is employed along with the anchorage model in the footing established in Tastani and Pantazopoulou (2013) (see also Chapter 4). An increasing lateral point load at the tip of the cantilever is applied (Fig. 5-6) and a unique fiber element is assigned to the entire height of the cantilever column with the number of Gauss-Lobatto integration points selected by the user. The user is selecting also the analysis step of lateral load V to be applied in the Pushover and the total number of steps until the maximum load (Modified Compression Field Theory in the fiber approach as described in Bentz (2000) cannot capture the descending branch of shear-critical columns which is why a load-control procedure was selected to be embedded in Phaethon). The maximum load in Phaethon is the load of the last step of convergence of the algorithm in incremental form. It should be highlighted that in reality the shear-critical column's ascending response is followed by a descending branch of failure; however the proposed algorithm is limited by strength attainment. After the maximum load, the descending branch of the capacity curve is defined as the line connecting the maximum load point with the point at axial failure as

defined in terms of drift by Elwood and Moehle (2005) and 20% of the attained maximum load as residual load at axial failure.

For each point load at the tip of the cantilever (Fig. 5-6) the corresponding shear force at the assigned column's sections (integration points) is equal to that load (constant shear diagram). Then the bending moment for each section is defined based on the moment at the base M_0 which is the product of the tip lateral load and the given shear span of the cantilever column, as follows:

$$M(x) = M_0 \cdot (1 - x/L_s) \tag{5-24}$$

where x counts from the support ($x=0$) to the point load at the free edge of the cantilever ($x=L_s$). The concentric axial load (tensile or compressive) applied at the tip of the cantilever is also constant throughout the pushover analysis and along the length of the cantilever and therefore each column's section has an axial force value equal to the one applied at the tip. Following this procedure, the vector f_s which is the resisting section forces (see previous Section) should converge to the above defined section forces based on the moment, shear and axial load diagram of the cantilever column under constant axial load and gradually increasing lateral tip point loading.

The following algorithm is applied in Phaethon to achieve this convergence:

Given the section forces s, i.e. an axial force N, a bending moment M and a shear force V, the equilibrium equation between applied and resisting section forces is set up:

$$s_u(e) = s - f_s(e) = 0 \tag{5-25}$$

The Newton-Raphson algorithm for the solution of the system of three nonlinear equations is:

1. Given the nonlinear equations $s_u(e) = 0$ and a guess of the solution e_0.
2. For $i = 0...n$ determine function value $s_u(e_i)$ and derivatives $k_s(e_i)$ (see previous Section).
3. Determine correction to previous solution estimate $\Delta e_i = s_u(e_i)/k_s$
4. Update solution estimate $e_{i+1} = e_i + \Delta e_i$

Return to Step 2 until the error norm is smaller than specified tolerance. On convergence determine the resisting forces for the final deformations.

It should be highlighted that for the cases of "pure compression" or "pure tension" with the angle of inclination of principal stresses/strains (angle of principal axis 2 with respect to *x*-axis) being zero or $\pi/2$ respectively then no iteration is applied but the fiber state determination is defined by entering directly on the constitutive law of concrete (previous Section, Table 5-1) without defining the rotation of principal axes.

After the convergence of the section forces along the length of the cantilever column to the correct values, the axial deformation, curvature and shear strain is determined for each section. Integrating the curvatures (Fig. 5-6) along the shear span of the cantilever column leads to the rotation of the cantilever column due to flexure and can be easily transformed to lateral displacement due to flexure Δ_o^f by multiplying with the shear span. Then, integration of the shear strains (Fig. 5-6) of the sections along the length of the cantilever column (integration points) leads to the lateral displacement Δ_o^{sh} due to the shear mechanism of the cantilever column. Finally, the rotation and the displacement Δ_o^{sl} due to pull-out of the tensile reinforcement (Fig. 5-6) is determined based on the theory established in Tastani and Pantazopoulou (2013) (see also Chapter 4). All the above contributions (flexure, shear and anchorage) are added together to define the total lateral displacement (i.e., $\Delta_o = \Delta_o^f + \Delta_o^{sh} + \Delta_o^{sl}$) of the cantilever column at each lateral load step and to obtain the capacity curve of the column until maximum lateral load (Fig. 5-6).

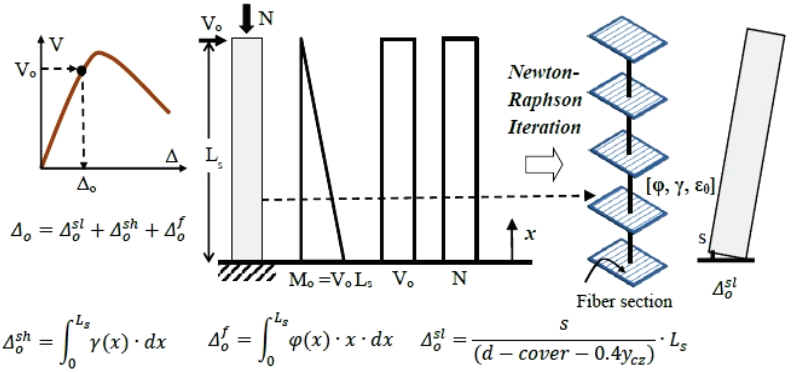

Figure 5-6: Pushover Analysis in Phaethon.

Correlation with Experimental Results

This section presents the correlation of the shear-flexure capacity curves obtained with pushover analysis by Phaethon with the experimental responses curves for comparison capacity of shear-critical RC columns selected from literature. In the correlation are also included curves for comparison capacity, obtained from flexural fiber beam/column based toolbox FEDEAS Lab (Filippou, 2004) and from MCFT-based software and dual-section analysis Response 2000 (Bentz, 2000).

The shear capacity degradation curve of RC columns as a function of displacement ductility is approached by EN 1998-3 (2005) and ASCE-SEI 41 (2007) (see also Chapter 2 and Chapter 3) and can be used as the basic criterion in order to detect shear failure before or after flexural yielding depending on the point of intersection with flexural capacity curve (Fig. 5-7). To this end, it is necessary to define the flexural capacity curve based on classic flexural analysis and combine it with the shear capacity curve in order to define the strength and deformation of the RC column at shear failure. This procedure is adopted in this section in order to initially detect whether the columns under study will fail in shear before or after flexural yielding and therefore to judge whether the "Phaethon" tool is suitable.

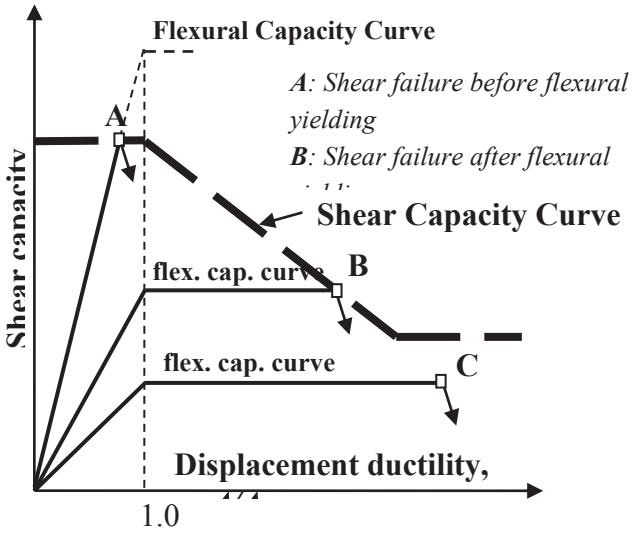

Figure 5-7: Shear-strength degradation model.

Rectangular Shear-Critical Columns

This first selected rectangular column for comparison is Specimen 1, from the experimental campaign of Sezen and Moehle (2006) that failed in shear after flexural yiedling. Its properties are reported in Table 5-2. Fig. 5-8 compares the experimental response (in red) with the analytical flexural capacity curve (in blue) and the shear capacity obtained by EN 1998-3 (in green) and by ASCE-SEI 41 (in black) (here the yielding displacement in both shear-strength degradation models is defined by the flexural analysis based on the applied fiber element included in FEDEAS Lab; it can be read from the end of the initial plateau of EN 1998-3 model). The ASCE-SEI 41 estimates a very conservative shear strength as compared to the yielding strength of this specimen which would be interpreted as premature brittle failure; EN 1998-3 detects the column's shear failure after yielding in terms of strength but at lower displacement compared to the experimental result.

As can be seen in Fig. 5-9 the comparison of the capacity curve defined by Phaethon for Specimen 1 (that failed in shear after flexural yielding) until the maximum load, is close to the experimental response but also close to the capacity curves by the other already mentioned software. The deviation of stiffness close to peak load from Phaethon can be improved if, in the displacement contribution due to pull-out of the tensile reinforcement, the reinforcement slip from shear span L_s is added (Megalooikonomou et al., 2018, Chapter 4). Since the latter established methodology does not refer only to extended flexural yielding, it was not incorporated into the "Phaethon" software as it would not have been general in simulating shear failures which could occur also before flexural yielding.

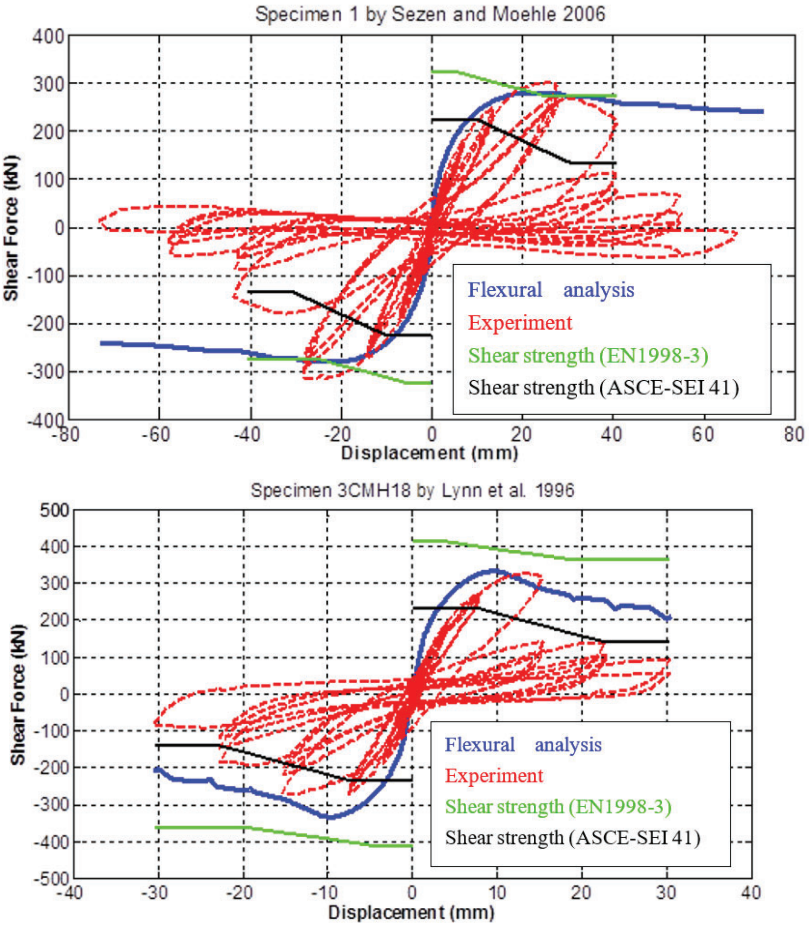

Figure 5-8. Detection of shear-critical rectangular reinforced concrete columns.

Table 5-2. Details of RC columns failed in shear (units: mm, MPa, kN).

Case	Axial Load	Width - Depth or Diameter	Shear Span	Clear Cover	Concrete Strength	Number - Diameter – reinforcing ratio of Longitudinal Bars	Yielding – ultimate Strength of Long. Bars	Yielding Strength - spacing – Diameter –ratio of Transv. Reinf.
Sezen & Moehle (2006) – (Spec. 1) Rectangular cross section	667	457 457	1473	65.13	21.1	8 28.65 0.025	434 645	476 304.8 9.5 0.0025
Lynn et. al. (1996) – (Spec. 3 CMH18) Rectangular cross section	1512	457 457	1473	38.1	27.6	8 31.75 0.03	331 496	400 457 9.5 0.00082
Ang et al. (1989) – (Spec. 19) Circular cross section	432	400	600	18*	34.4	20 16 0.032	436 679	326 80 6 0.0038
Ang et al. (1989) – (Spec. 20) Circular cross section	807	400	700	18*	36.7	20 16 0.032	482 758	326 80 6 0.0038

*: Cover to Ctr. of Hoop Bar

Response 2000 doesn't provide the descending branch of the capacity curve due to shear failure after flexural yielding, while FEDEAS Lab overestimates the response after maximum load is attained since it doesn't consider any shear-flexure interaction mechanism. Phaethon postdicts both the maximum load but also the descending branch of the response in this case.

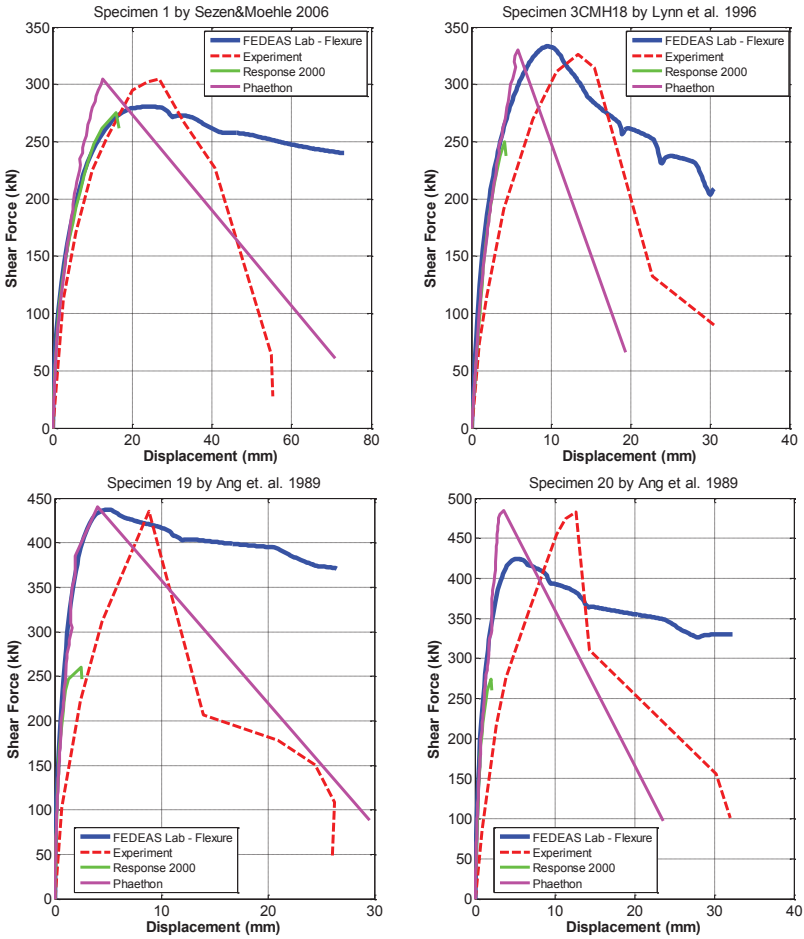

Figure 5-9: Comparison of the capacity curves provided by Phaethon and other software with the experimental responses.

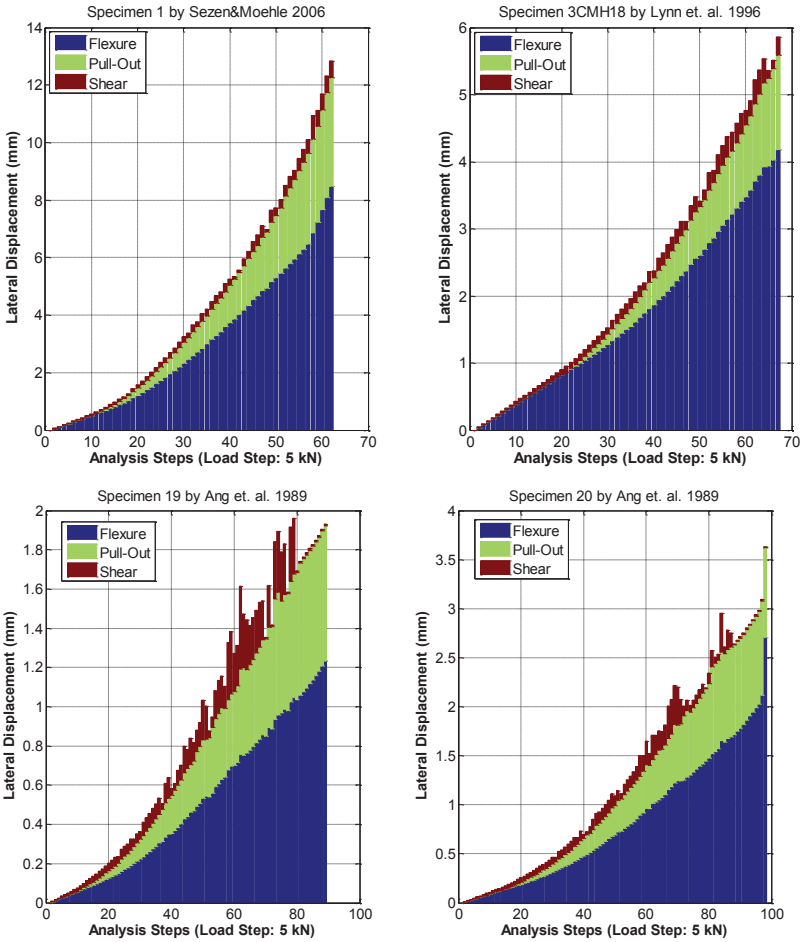

Figure 5-10: Displacement Contributions from various deformation menchansims included in Phaethon for cantilever columns.

Figures 10 and 11 depict the displacement contributions in each pushover analysis step from the various interacting mechanisms as they are defined by Phaethon and they are compared also to the ones measured during the experiment. It can be seen that at yielding (10 mm total lateral displacement reported by Phaethon) Phaethon gives correctly 62%

contribution from flexure, 35% from Pull-Out and almost 3% from the shear mechanism (which in this case is a bit underestimated).

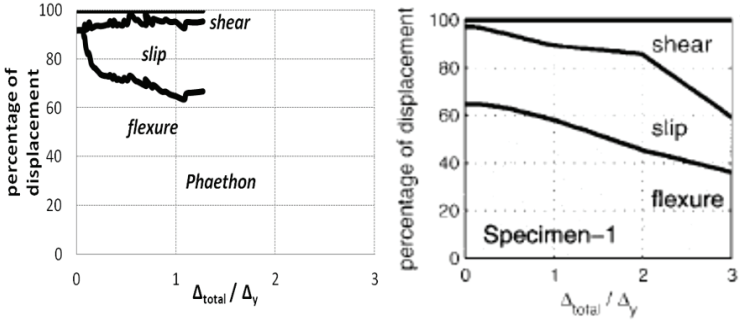

Figure 5-11: Displacement Contributions from various deformation mechanisms included in Phaethon (left) for rectangular column compared to the experiment (right) (Sezen and Moehle [2006]).

In Fig. 5-8, the shear capacity curve of Eurocode 8 part 3 (EN 1998-3) doesn't intersect with the flexural capacity curve for the second selected specimen by Lynn et al. (1996). This takes place only with the model of ASCE-SEI 41 almost at the point of yielding at a lower strength and displacement compared to the experimental response.

The second selected rectangular column for comparison is by the experimental campaign of Lynn et al. (1996) that failed in shear before flexural yielding. Its properties are presented in Table 5-2. As can be seen in Fig, 5-9 the comparison until the maximum load is close to the experimental response but also close to the capacity curves by the other already mentioned software. Here, Response 2000 underestimates the specimen's strength and doesn't provide the descending branch of the capacity curve due to shear failure before flexural yielding, while FEDEAS Lab overestimates the response after maximum load is attained since it doesn't consider any shear-flexure interaction mechanism. Phaethon postdicts correctly the maximum load as well as the descending branch of the response in this case too. However, in all analytical capacity curves the experimental initial stiffness is overestimated. The axial failure (i.e. collapse as defined by Phaethon) is also reached at a lower displacement compared to the experiment. Finally, Fig. 5-10 depicts the displacement contributions in each pushover analysis step from the various interacting mechanisms as they are defined by Phaethon. As it can be seen, they are correctly increasing with the applied lateral load.

Circular Shear-Critical Columns

The third selected column for comparison is the circular Specimen 19 by the experimental campaign of Ang et al. (1989) that failed in shear before flexural yielding. Its properties are presented in Table 5-2. In Figure 5-12, it can be observed that it is a shear-critical column since both the shear strength degradation models detect shear failure (although wrongly after flexural yielding) at a displacement lower than the corresponding experimental one. The strength at shear failure is better predicted by the model of Eurocode 8 part 3 (EN 1998-3) compared to the alternative of ASCE-SEI 41.

As it can be seen in Figure 5-9 the comparison of the Phaethon response until the maximum load is close to the capacity curves by the other aforementioned software. However, the initial stiffness predicted by Phaethon is higher compared to the experiment although identical to what the other software tools define. Phaethon captures well also the maximum load but not the corresponding displacement. The descending branch as defined by Phaethon follows the experimental strength degradation. The shear strength is better postdicted by Phaethon compared to Response 2000. Finally, Figure 5-11 depicts the displacement contributions in each pushover analysis step from the various interacting mechanisms as they are defined by Phaethon. As it can be observed they are correctly increasing with the applied lateral load and here due to the aspect ratio of the circular column (short column) the shear mechanism displacement contribution is significant. It should be stated that an incremental filtering (that is omitting some steps from the capacity curve) of the pushover results was applied in this specimen since in some steps the converged displacements given by the program were higher than the previous or the next load steps compared to the current one. This filtering was applied only to the given capacity curve in Figure 5-9 but the displacement contributions in Figure 5-10 are given as obtained by the program.

The fourth selected column for comparison is the circular Specimen 20 from the experimental campaign of Ang et al. in 1989 that failed in shear after flexural yielding. Its properties are presented in Table 5-2. In Figure 5-12, it can be observed that it is a shear-critical column since both the shear strength degradation models detect shear failure after yielding at a displacement lower than the corresponding experimental one. The strength at shear failure is better predicted by the model of Eurocode 8 part 3 compared to the alternative of ASCE-SEI 41.

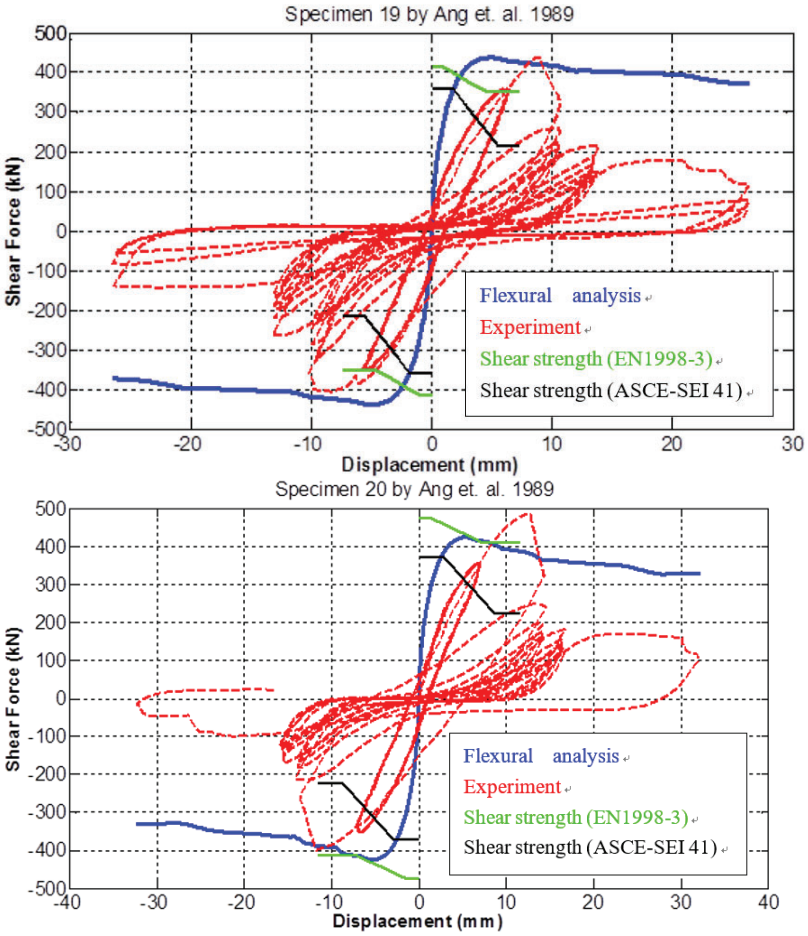

Figure 5-12. Detection of shear-critical circular reinforced concrete columns.

As can be seen in Figure 5-9 the comparison of the Phaethon response until the maximum load is close to the capacity curves by the other aforementioned software. However, the initial stiffness predicted by Phaethon is higher compared to the experiment although identical to what the other software tools define. Phaethon also captures well the maximum load but not the corresponding displacement. The descending branch as

defined by Phaethon follows the experimental strength degradation. The axial failure (i.e. collapse as defined by Phaethon) is reached at a lower displacement compared to the experiment. The shear strength is better postdicted by Phaethon compared to Response 2000. Finally, Figure 10 depicts the displacement contributions in each pushover analysis step from the various interacting mechanisms as they are defined by Phaethon. The same idea of filtering as described in the previous circular specimen was applied here too.

Parametric Investigation

The parametric sensitivity of the developed software on the produced capacity curve is investigated in this section, considering as a point of reference Specimen 1 by Sezen and Moehle (2006), examined in the preceding section. Parameters considered are the discretization sensitivity of the force-based fiber element of the cantilever column and the effect of axial load, stirrups spacing and shear span length on the produced pushover curve; in each case one parameter at a time is varied keeping the reference values for all other variables (so the possible interaction effects between variables have not been considered in conducting the sensitivity analysis).

In Figure 5-13 it the effect on the pushover curve of different amount of Gauss-Lobatto integration points [Ele(Number)IP] can be observed along the element, as well as the amount of integration points/layers of the Midpoint integration rule along the section [Sec(Number)L]. As expected, by increasing the amount of Midpoint layers and Gauss-Lobatto integration points the capacity curve stabilizes to reach the final result. The deviation from the final result is evident only at the lower amount of integration points both at the section and along the element.

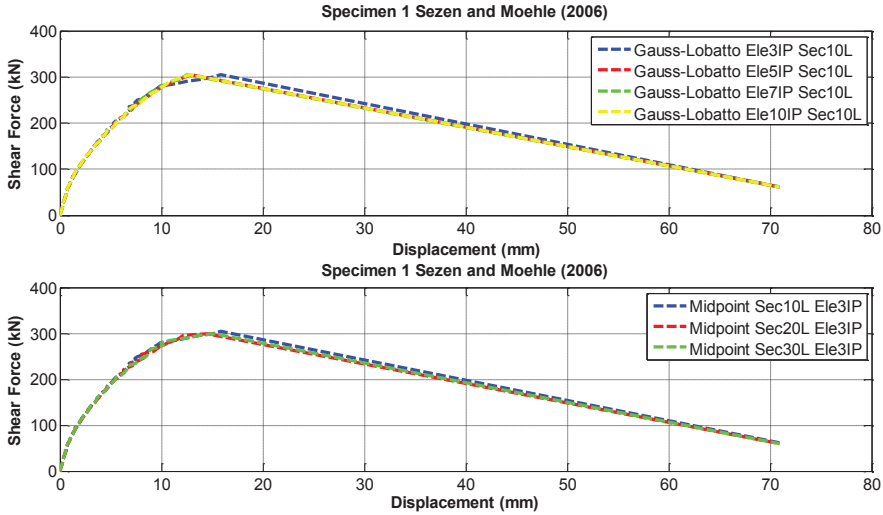

Figure 13: Discretization sensitivity along fiber section and element of the capacity curve provided by Phaethon.

As may be observed in Figure 5-14, by increasing the compressive axial load (here is given in normalized form) the shear strength of the column under study is correctly increasing and the deformability of the column is decreasing with lower displacements at maximum load (shear failure) and at point of axial failure (collapse). The effect of stirrup spacing (Figure 5-15) for a given shear-critical column on the capacity curve produced by Phaethon is negligible until the maximum load (shear strength), but the displacement at axial failure (collapse) is decreasing correctly by increasing the spacing of stirrups. The insensitivity of Phaethon in defining shear strength as a function of stirrup spacing in lightly reinforced columns where shear failure is driven by sparsely spaced stirrups, is justified by the assumptions of the MCFT theory—as described initially in this paper—about smearing of reinforcement. Finally the decrease of the shear span of the cantilever column (Figure 5-16) correctly produces a more shear-dominant and less deformable reinforced concrete column both at maximum load (shear failure) but also at the point of axial failure (collapse).

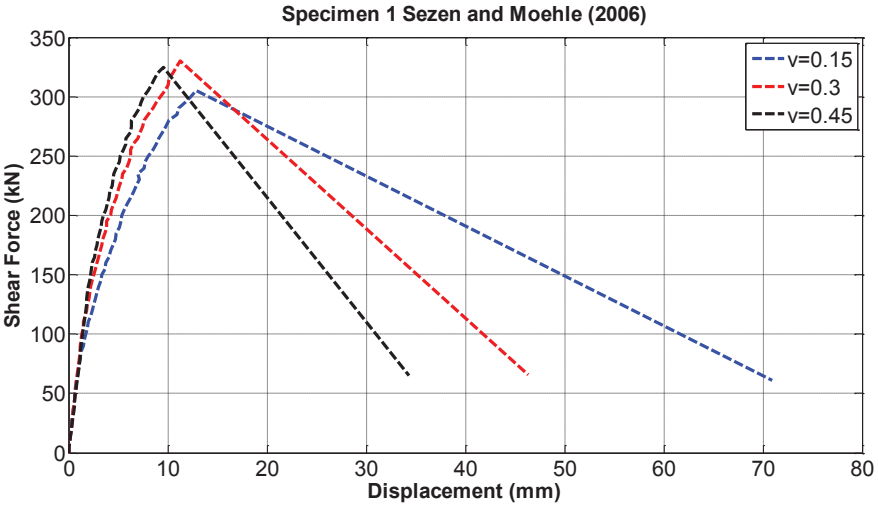

Figure 5-14: Effect of axial load on capacity curve provided by Phaethon.

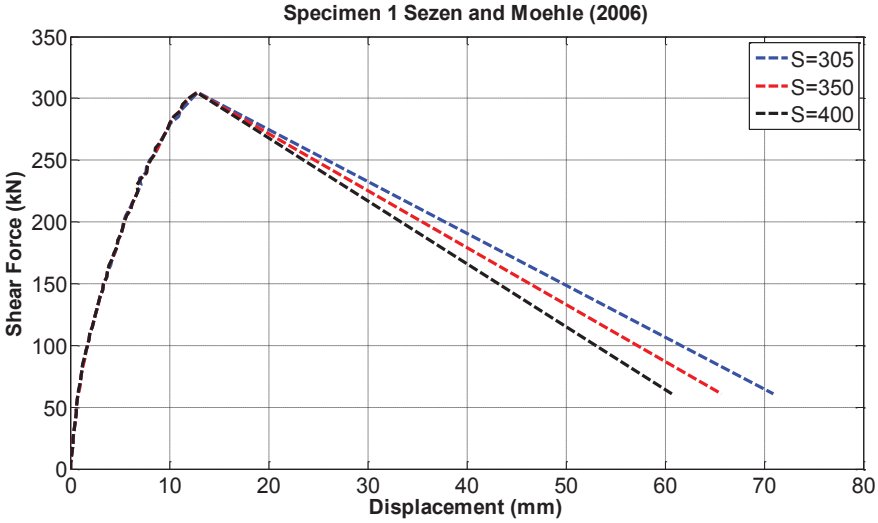

Figure 5-15: Effect of stirrups spacing on capacity curve provided by Phaethon.

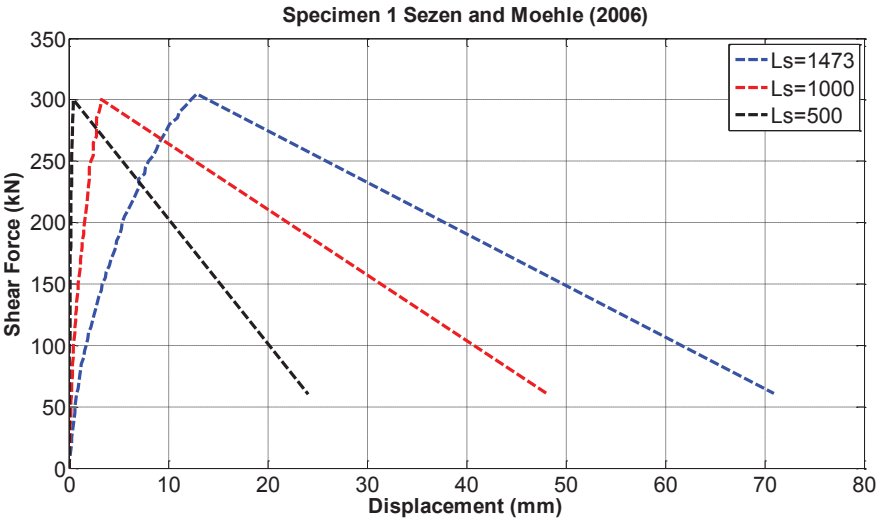

Figure 5-16: Effect of shear span on capacity curve provided by Phaethon.

Before concluding this Chapter it should be noted that the Phaethon software installation file can be downloaded for free from the following web address: http://bigeconomy.gr/en/phaethon-en/.

CHAPTER SIX

CONSTITUTIVE MODEL FOR FRP- AND STEEL-CONFINED CONCRETE INCLUDING SHEAR

Confining wraps or jackets to rehabilitate and strengthen existing substandard RC columns such as those described in the previous Chapters of the present book has proven to be an efficient technique for seismic retrofit of structures. However, most of the compressive strength models of confined concrete only consider the increased strength and ductility provided by fiber reinforced polymers (FRPs), neglecting the contribution of the existing steel reinforcement inside the column's section. Even if the existing steel stirrups in a reinforced concrete column are not sufficient to confine the concrete core they must also contribute, along with the FRP jacket, in confining the section.

Literature Review on FRP and Steel Confined Concrete Material Models

In the last century, most of the confined concrete constitutive models were proposed specifically for concrete columns confined by either steel reinforcement or Carbon Fiber Reinforced Polymers (CFRP). The first model that took into account both the confining effects of CFRP and steel reinforcement was Kawashima's et al. in 1999.

In their experimental program twenty three 600 mm tall circular concrete cylinders with a diameter of 200 mm were included. Tie reinforcement ratio ρ_s and CFRP ratio ρ_{CF} were varied between 0-1.24% and 0-1.336%, respectively. Figure 6-1 shows the axial stress f_c vs. axial strain ε_c relation of specimens tested in their experimental program. In each case, the tie reinforcement ratio ρ_s was varied from 0 – 1.24% under constant CFRP ratios ρ_{CF}. It can be concluded from the graph that the effect of ties is larger at lower ρ_{CF}.

Kawashima's model is based on a formulation derived from the regression analysis of the experimental results, which is similar to the model proposed by Richart et al. (1928) from tests conducted on concrete

specimens confined with hydrostatic pressure. In the latter experimental program it was concluded that the responses under passive (confining pressure depending on the lateral dilation) and active (constant fluid pressure) are similar.

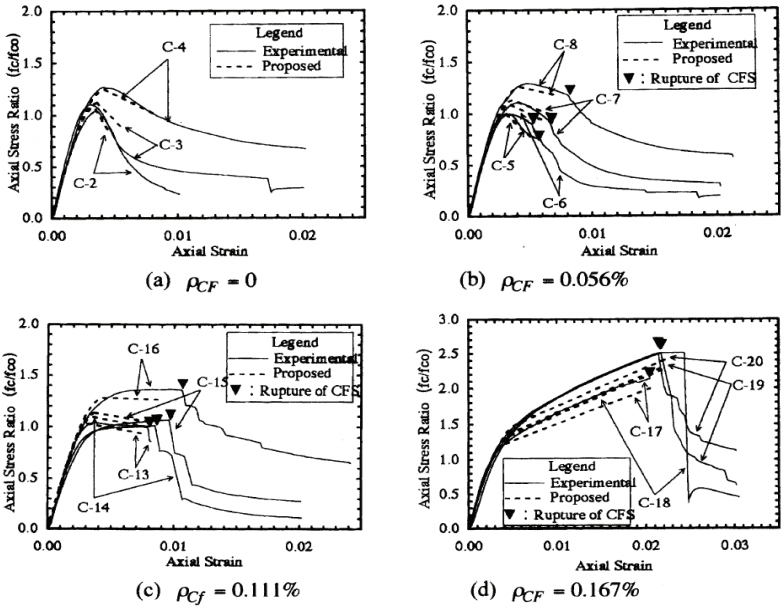

Figure 6-1: Stress f_c vs. strain ε_c relation of circular concrete cylinders confined by both ties and CFS (Tie reinforcement ratio ρ_s was varied from 0 to 1.24 % in each case, in which CFS ratio ρ_{CF} was kept constant).

From the experimental results above it can be derived that the axial stress vs. axial strain response of concrete cylinders confined by both steel stirrups and FRP jackets can be similar or to that one of concrete confined only by means of steel stirrups (at a smaller ρ_{CF}) where the response reaches a peak strength, after which it deteriorates or presents FRP-confined-concrete like response (at higher ρ_{CF}). In the latter the response reaches a transition point very close to the peak strength of the unconfined concrete and then the stiffness of the descending branch becomes positive and the response is almost linear.

Kawashima used the following formulation to describe the confinement effect:

- Increasing branch:

$$f_c = E_c\varepsilon_c\left[1-\frac{1}{n}\left(\frac{\varepsilon_c}{\varepsilon_t}\right)^{n-1}\right](E_g<0), n=\frac{E_c\varepsilon_t}{E_c\varepsilon_t - f_t}$$

$$f_c = E_c\varepsilon_c\left[1-\frac{1}{n}\left(1-\frac{E_g}{E_c}\right)\left(\frac{\varepsilon_c}{\varepsilon_t}\right)^{n-1}\right](E_g\geq 0), n=\frac{(E_c-E_g)\varepsilon_t}{E_c\varepsilon_t - f_c},$$

$$0\leq\varepsilon_c\leq\varepsilon_t \tag{6-1}$$

- Decreasing branch:

$$f_c = f_t + E_g(\varepsilon_c-\varepsilon_t),\quad \varepsilon_t\leq\varepsilon_c\leq\varepsilon_{cu} \tag{6-2}$$

Determination of the four parameters of the model:

$$f_t = f_{c0} + 1.93\rho_{CF}\cdot\varepsilon_{CFt}\cdot E_{CF} + 2.2\rho_s\cdot f_{yh} \tag{6-3}$$

$$\varepsilon_t = 0.003 + 0.00939\,\frac{\rho_{CF}\cdot\varepsilon_{CFt}\cdot E_{CF}}{f_{c0}} + 0.0107\,\frac{\rho_s\cdot f_{yh}}{f_{c0}} \tag{6-4}$$

$$E_g = -0.658\,\frac{{f_{c0}}^2}{\rho_{CF}\cdot\varepsilon_{CFt}\cdot E_{CF} + 0.098\,\rho_s f_{yh}} + 0.078\sqrt{\rho_{CF}}\cdot E_{CF} \tag{6-5}$$

Since the concrete confined by both CFRP and ties reaches the ultimate when there is rupture of the CFRP jacket, the ultimate strain in the model can be determined based on the properties only of the FRP Jacket:

$$\varepsilon_{cu} = 0.00383 + 0.1014\left(\frac{\rho_{CF}\cdot f_{CF}}{f_{c0}}\right)^{\frac{3}{4}}\left(\frac{f_{CF}}{E_{CF}}\right)^{\frac{1}{2}} \tag{6-6}$$

where E_c = elastic modulus of concrete (MPa), f_{c0}= unconfined concrete strength (MPa), ρ_s = tie reinforcement (volumetric) ratio, f_t and ε_t = stress and strain where the stiffness changes, E_g = stiffness in the descending branch (MPa) and ε_{CFt} = is the hoop strain of the CFRP where the stiffness of concrete has shifted to the post-deterioration stiffness.

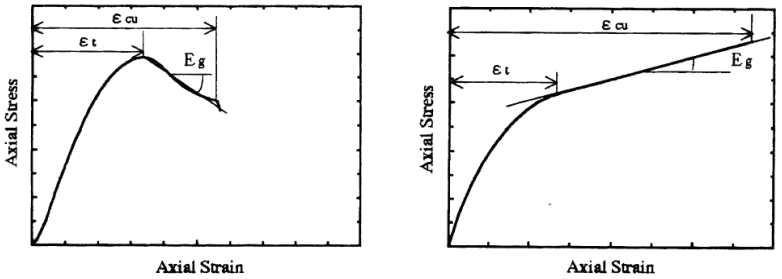

Figure 6-2: Definition of the confinement effect by CFS.

The paper by Braga et al, (2006) presents a plain strain analytical model—based on the elasticity theory—to determine the confining pressures of transverse reinforcements on the concrete core of a reinforced concrete member. The analytical evaluation of the confining pressures was first carried out on reinforced sections with square and circular stirrups, and subsequently on reinforcement configurations of greater complexity with square and rectangular stirrups and supplementary cross ties. Finally, the model has been used to evaluate the confining pressures applied by external wrapping with any material (FRP, steel, etc.) and to design better combinations of techniques and confinement materials.

The key assumption of the proposed model is that the increment of stress in the concrete section is produced without any out-of-plain strain. This means that the confinement exercised by the transverse reinforcements should take place under plain strain conditions.

$$\sigma_z(\varepsilon_z) = \sigma_{z0}(\varepsilon_z) + \Delta\sigma_z(\varepsilon_z) \tag{6-7}$$

Under plain strain conditions:

$$\Delta\varepsilon_z = \gamma_{zx} = \gamma_{zy} = 0 \tag{6-8}$$

$$\Delta\varepsilon_z = \frac{1}{E_c}\left[\Delta\sigma_z - v(\sigma_x + \sigma_y)\right] \Rightarrow \tag{6-9}$$

$$\Delta\sigma_z = v(\sigma_x + \sigma_y) \tag{6-10}$$

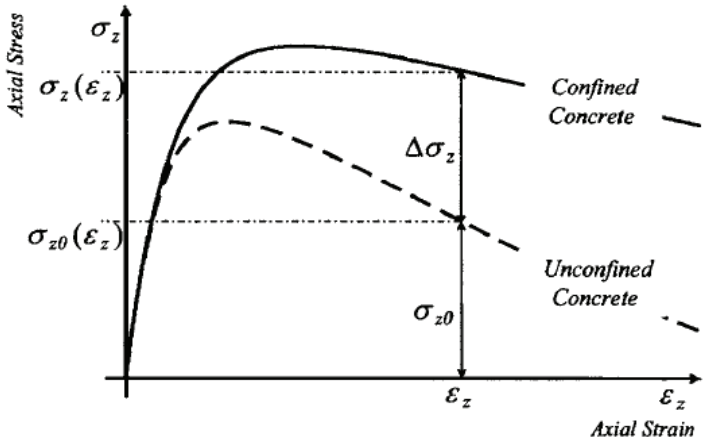

Figure 6-3: Strength increment due to confinement.

For circular sections the Airy's function's solution for the plane stresses is expressed in polar coordinates. For the particular case in which a circular plane section is subjected to a uniform radial pressure applied by the reinforcements to the concrete core the solution gives (n = radial, m = orthogonal to n, S = hoop or spiral spacing, q = constant):

$$f_r = \sigma_n = \sigma_m = \frac{q}{S} \tag{6-11}$$

Thus, the strength increment turns out to be constant at every point in the section.

$$\Delta\sigma_z = v(\sigma_n + \sigma_m) = 2v\sigma_n = 2v\frac{q}{S} \tag{6-12}$$

The concrete radial and tangent boundary strains and the stirrup axial strain are given by the relations (R_c = Radius of the concrete core circular section, measured at the center lines of the spiral or the circular hoop):

$$\varepsilon_n = \frac{1}{E_c}\left(\sigma_n - \nu\sigma_m\right) \tag{6-13}$$

$$\varepsilon_m = \frac{1}{E_c}\left(\sigma_m - \nu\sigma_n\right) \tag{6-14}$$

$$\varepsilon_n = \varepsilon_m = \frac{q}{E_c \cdot S}\left(1-\nu\right) \tag{6-15}$$

$$\varepsilon_{st} = \frac{q \cdot R_c}{E_c \cdot A_s} \tag{6-16}$$

Then, by applying the compatibility equation between the stirrup and concrete in the radial direction, Airy's constant q can be expressed by the following equation:

$$q = \frac{E_c E_s A_s \nu S}{R_c E_c S + E_s A_s (1-\nu)(\nu \cdot \varepsilon_z + 1)} \cdot \varepsilon_z \tag{6-17}$$

Equilibrium conditions and compatibility specifications between the concrete core and the confining ties are based on linear elasticity, thus referring to the initial linear part of the steel behavior. When the steel yields, the transversal pressure reaches its highest value and, from that moment on, remains constant until failure. In the model, steel behaves in a linear-elastic manner, whereas concrete behavior is assumed to be nonlinear elastic, thus the values of E_c and ν are functions of the strain state. Therefore, one has to refer to the secant modulus of concrete, evaluated on different confined curves, relevant to different confinement levels and has to define the law of variability of the unconfined concrete Poisson's modulus (ν_0 = 0.2, ε_{c0} = strain at stress peak of the unconfined concrete).

$$\nu(\varepsilon_z) = \nu_0 \left[1 + 0.2\left(\frac{\varepsilon_z}{\varepsilon_{c0}}\right) - \left(\frac{\varepsilon_z}{\varepsilon_{c0}}\right)^2 + 1.55\left(\frac{\varepsilon_z}{\varepsilon_{c0}}\right)^3 \right] \tag{6-18}$$

In the above expression of the Poisson's Modulus, coherent with the theory of elasticity, the upper limit value has been assumed to be equal to 0.5, which corresponds to diffuse cracking in the unconfined concrete. It must be pointed out that when using steel stirrups, if one does not set an upper limit on ν, the shape of the lateral pressure – axial deformation relationship changes in a negligible way until the yielding stress is reached without any effect on the peak point and on the softening part of the curve.

In this model, the vertical arching action between adjacent stirrups and the confining effect of the longitudinal bars is also considered. The longitudinal bar's role is evaluated by taking into account that the extension of the stirrup should correspond to the rigid translation of the edge of the longitudinal bars. According to this and referring to the Fig. 6-4 outline, a uniform load is applied to the longitudinal bar. This load is given by the following relationship:

$$p_{lon} = \frac{N_{st}}{S} \tag{6-19}$$

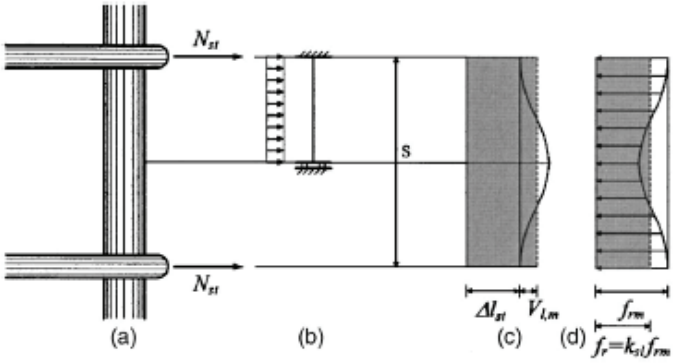

Figure 6-4: (a) Transverse and longitudinal reinforcements; (b) longitudinal bar schematization; (c) longitudinal bar deflection; and (d) vertical confining pressures distribution.

The rigid displacement, corresponding to the confining pressure f_{rm} is equal to the stirrup extension Δl_{st}, while the mean concrete core displacement V_m, which corresponds to the effective mean confinement

pressure is given by the relationship (where V_{lm} = mean displacement of the longitudinal bar, which is calculated according to the figure outline, while I_{sl} = the longitudinal bars' inertia):

$$V_m = \Delta l_{st} + V_{lm} = \Delta l_{st} + \frac{N_{st} S^3}{720 E_s I_{sl}} \tag{6-20}$$

For a reductive coefficient $k_{sl} = f_r / f_{rm,}$ the following relation is obtained (***l*** is the length of the stirrup corresponding to 1/4 of the section). When the bending stiffness of the longitudinal bars becomes negligible (low ratio values ξ_l) only the arching action between two stirrups spreads the confining pressures along the column:

$$k_{sl} = \frac{\Delta l_{st}}{V_m} = \frac{45\xi_l^{\,3}}{45\xi_l^{\,3} + \beta\xi_{st}}$$

$$\xi_l = \frac{\phi_{long}}{S} \qquad \beta = \frac{\phi_{st}}{\phi_{long}} \qquad \xi_{st} = \frac{\phi_{st}}{l} \tag{6-21}$$

Taking into account the effects of existing internal stirrups and additional external wrappings separately, the confining pressure is given by the following relation (f_{ri} = confining pressure induced on the core by the internal stirrup, f_{re} = pressure induced by the external wrapping on the whole section, A_i = area within the internal stirrup, A_e = area within the external stirrup):

$$f_{rm} = \frac{A_i}{A_e} f_{ri} + f_{re} \tag{6-22}$$

$$f_{ri}(\varepsilon_z) = \frac{E_c E_s A_s \nu}{R_{ci} E_c S + E_s A_s (1-\nu)(\nu \cdot \varepsilon_z + 1)} \cdot \varepsilon_z, \varepsilon_n \prec \varepsilon_{yi}$$

$$f_{ri}(\varepsilon_z) = 0.5 \rho_s f_{yh}, \varepsilon_n \succeq \varepsilon_{yi} \tag{6-23}$$

$$f_{re}(\varepsilon_z) = \frac{E_c E_m t_m (b_m / S)\nu}{R_c E_c + E_m t_m (b_m / S)(1-\nu)(\nu \cdot \varepsilon_z + 1)} \cdot \varepsilon_z \tag{6-24}$$

(b_m = wrapping width, t_m = wrapping depth)

The passive stress – strain curve is obtained in accordance with the following procedure:

$$\varepsilon_z \Rightarrow f_r(\varepsilon_z) \Rightarrow f_c(\varepsilon_z) \tag{6-25}$$

It should be pointed out that the curve relative to concrete confined by a transverse reinforcement crosses all active confinement curves (relative to increasing values of lateral pressure), up to the curve with a lateral pressure equal to the one applied by the stirrups at yielding. Once this curve has been reached, assuming that the steel doesn't have a strain hardening behavior, the passive confinement curve would match the active confining curve. The above approach is different from the classical one. Usually, the stress in the transverse reinforcement is supposed to be equal to the yielding stress and the confining pressures calculated this way define an upper limit. In reality, for low levels of strain in the concrete the stress state in the transverse reinforcements is very small and the concrete is basically not confined.

When confining is due to composites materials, which behave elastically until failure and whose strength is much higher than that of steel, the model is able to describe the behavior of the section until the failure of the confining material. Based on linear elasticity, the superposition of the combined confining effects of steel stirrups and FRP jackets can easily be analyzed. An important aspect of the model is that the cross-section tangential stresses (shear), which are generally neglected, have an essential role in ensuing plane strain conditions.

The axial stress vs. axial strain response was determined by using the confined concrete model of Attard & Settunge (1996). The model can be summarized in the following (Fig. 6-5):

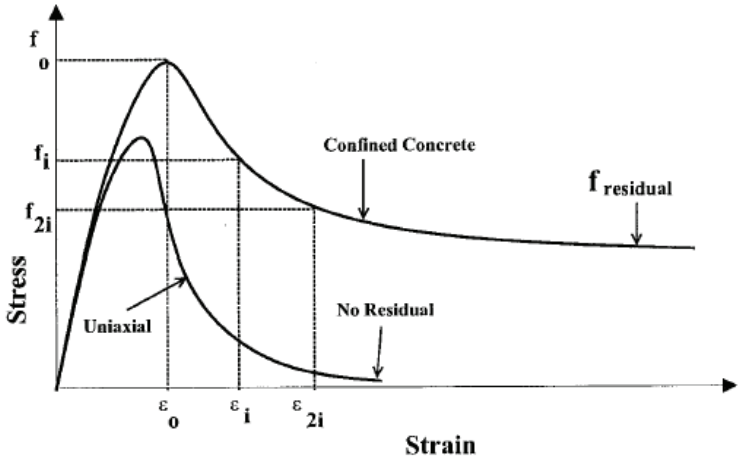

Figure 6-5: Confined Concrete Model by Attard&Settunge (1996).

- Confined Peak Stress and Strain:

$$\frac{f_o}{f_c} = \left(\frac{f_r}{f_t} + 1\right)^k \qquad k = 1.25\left[1 + 0.062\,\frac{f_r}{f_t}\right](f_c)^{-0.21}(MPa) \tag{6-26}$$

$$\frac{\varepsilon_o}{\varepsilon_c} = 1 + (17 - 0.06 f_c)\left(\frac{f_r}{f_c}\right) \ (MPa) \tag{6-27}$$

- Stress and Strain at point of inflection:

$$\frac{f_i}{f_o} = \frac{\dfrac{f_{ic}}{f_c} - 1}{5.06\left(\dfrac{f_r}{f_c}\right)^{0.57} + 1} + 1 \tag{6-28}$$

$$\frac{\varepsilon_i}{\varepsilon_o} = \frac{\frac{\varepsilon_{ic}}{\varepsilon_c} - 2}{1.12\left(\frac{f_r}{f_c}\right)^{0.26} + 1} + 2 \tag{6-29}$$

$$\frac{\varepsilon_{ic}}{\varepsilon_c} = 2.5 - 0.3\ln(f_c) \ (MPa) \tag{6-30}$$

$$\frac{f_{ic}}{f_c} = 1.41 - 0.17\ln(f_c) \ (MPa) \tag{6-31}$$

- Stress corresponding to strain $\varepsilon_{2i} = (2\varepsilon_i - \varepsilon_{cc})$:

$$\frac{f_{2i}}{f_o} = \frac{\frac{f_{2ic}}{f_c} - 1}{6.35\left(\frac{f_r}{f_c}\right)^{0.62} + 1} \tag{6-32}$$

$$\frac{f_{2ic}}{f_c} = 1.45 - 0.25\ln(f_c) \ (MPa) \tag{6-33}$$

- Stress – Strain Relationship:

$$Y = \frac{AX + BX^2}{1 + CX + DX^2} \qquad Y = \frac{f}{f_o}, X = \frac{\varepsilon}{\varepsilon_o} \tag{6-34}$$

$$A = \left[\frac{\varepsilon_{2i} - \varepsilon_i}{\varepsilon_o}\right]\left[\frac{\varepsilon_{2i}E_i}{(f_o - f_i)} - \frac{4\varepsilon_i E_{2i}}{(f_o - f_{2i})}\right] \tag{6-35}$$

$$B = (\varepsilon_i - \varepsilon_{2i})\left[\frac{E_i}{(f_o - f_i)} - \frac{4E_{2i}}{(f_o - f_{2i})}\right] \tag{6-36}$$

$$C = A - 2 \tag{6-37}$$

$$D = B + 1 \tag{6-38}$$

$$E_I = \frac{f_i}{\varepsilon_i}, E_{2i} = \frac{f_{2i}}{\varepsilon_{2i}} \tag{6-39}$$

It should be noted that in the paper by Braga et al. (2006) a comparison with experimental results from the literature is presented with specimens confined by either steel stirrups or FRP jackets. No comparison with specimens having both confining materials is available. However, this possibility is left open.

Another model that will be introduced here is the Spoelstra and Monti model (1999), although it does not include the confining effect of the lateral steel reinforcement but only that of the FRP jacket. The reason for the following presentation is that this model will be the basis for the constitutive law proposal of this book for modeling of seismic retrofitted with FRP jackets circular RC columns.

The Spoelstra-Monti model (1999) is based on the following formula (Popovics 1973):

$$\sigma_c = \frac{f_{cc} \cdot x \cdot r}{r - 1 + x^r} \tag{6-40}$$

where

$$x = \frac{\varepsilon_c}{\varepsilon_{cc}} \quad \varepsilon_{cc} = \varepsilon_{co}\left[1 + 5\left(\frac{f_{cc}}{f_{co}} - 1\right)\right] \quad r = \frac{E_c}{E_c - E_{\sec}} \quad E_{\sec} = \frac{f_{cc}}{\varepsilon_{cc}} \tag{6-41}$$

where ε_{cc} = compressive strain at confined peak strength f_{cc}. The confined peak strength f_{cc} is expressed in terms of a constant (throughout the response) effective confining pressure σ_l with an equation (Mander et al. 1988) that has been extensively tested against experimental data:

$$\frac{f_{cc}(\sigma_l)}{f_{co}} = 2.254\sqrt{1 + 7.94\frac{\sigma_l}{f_{co}}} - 2\frac{\sigma_l}{f_{co}} - 1.254 \tag{6-42}$$

To account for the peculiar behavior of FRP, the following approach is taken (Spoelstra and Monti 1999). The uniaxial stress response σ_c of plain concrete under compressive axial strain ε_c is described as (Pantazopoulou and Mills 1995):

$$\sigma_c = E_{\sec}(\varepsilon_l) \cdot \varepsilon_c \tag{6-43}$$

$$E_{\sec}(\varepsilon_l) = E_c \frac{1}{1+\beta\varepsilon_A} = E_c \frac{1}{1+2\beta\varepsilon_l} \tag{6-44}$$

Note that the area strain ε_A is taken as a measure of the internal damage from cracking, which reduces the secant modulus E_{sec}, starting from the initial tangent modulus E_c. The constant β (here, the reciprocal of that given in the original paper by Pantazopoulou and Mills, 1995) is a property of concrete, as discussed below. Note that in Eq. 6-44 the assumption of radial symmetry ($\varepsilon_A = 2\varepsilon_l$) is adopted ($\varepsilon_l$ = lateral strain, ε_A = area strain), which allows for pointing out the dependence on the lateral strain ε_l. Note also that the sign convention is: compressive ε_c and σ_c are negative, while dilating ε_A and ε_l are positive.

Equations 6-43 and 6-44 are merged into a single equation:

$$\varepsilon_l(\varepsilon_c, \sigma_l) = \frac{E_c\varepsilon_c - \sigma_c(\varepsilon_c, \sigma_l)}{2\beta\sigma_c(\varepsilon_c, \sigma_l)} \tag{6-45}$$

where the dependence of the quantities σ_c and ε_l on the current strain ε_c and the current confining pressure σ_l is rendered explicitly. The constant β is a property of concrete which is evaluated as a function of the unconfined concrete strength f_{co} (in MPa).

$$\beta = \frac{5700}{\sqrt{|f_{co}|}} - 500 \tag{6-46}$$

The lateral confining pressure σ_l exerted by the confining jacket is computed as shown in the Figure below (Fig. 6-6) and is based on the jacket's current stress $\sigma_j = E_j\varepsilon_j \le f_j = E_j\varepsilon_{ju}$, while the maximum lateral confinement f_l is provided for $\varepsilon_j = \varepsilon_{ju}$ = FRP jacket effective ultimate circumferential strain.

Once ε_l is computed from Eq. 6-45, the strain ε_j in the confining jacket can be found (e.g., in axially loaded concrete cylinders it is simply: $\varepsilon_j = \varepsilon_l$), along with its current stress $\sigma_j = E_j \varepsilon_j$. This updated value of σ_l can be used for a new estimate of ε_l through Eq. 6-45, giving rise to an iterative procedure (Fig. 6-7) until σ_l converges to the correct value. The whole procedure is repeated for each ε_c over the complete stress-strain curve. The resulting curve can be regarded as a curve crossing a family of Popovics curves, each one pertaining to the level of confining pressure, computed with the Mander equation, corresponding to the current lateral strain, determined according to Pantazopoulou and Mills (1995). The stress-strain characteristics of the confining mechanism are explicitly accounted for, while the lateral strain of concrete is implicitly obtained through the iterative procedure. The procedure is ended when $\varepsilon_l = \varepsilon_{ju}$.

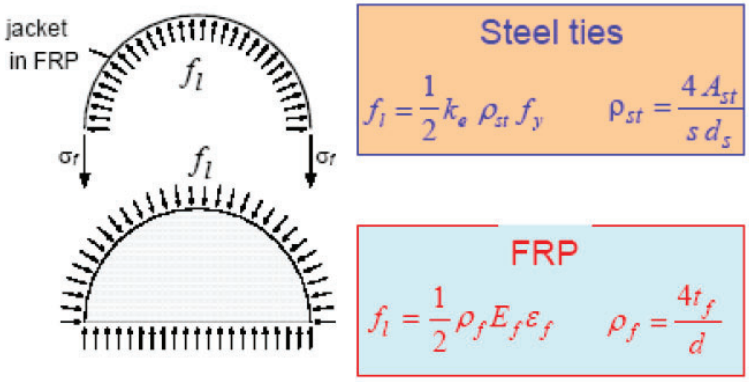

Figure 6-6: Lateral confining pressure – analogy between steel stirrups and FRP Jacket.

The response of an FRP-wrapped concrete specimen obtained with this model can be seen in the following Figures along with a comparison with steel – confined concrete. The axial stress versus axial strain is shown first: steel and CFRP start with almost the same slope, but after steel yields at 2.5 normalized axial strains, it departs towards higher axial strains. GFRP starts with the same slope until the unconfined concrete strength is reached; after that point GFRP has a lower slope leading to higher axial strains. In Fig. 6-8b the lateral strain versus axial strain relation is shown too. It can be observed that the slope of the branches depends on the type of confining device. GFRP starts with a higher slope (meaning that

concrete has a higher initial lateral dilation), which however remains constant until the jacket fails. CFRP reduces the initial lateral strain, but its effectiveness has a shorter duration, due to its lower extensional ultimate strain ε_{ju}. Finally, a comparison of confinement actions of steel and FRP materials is presented.

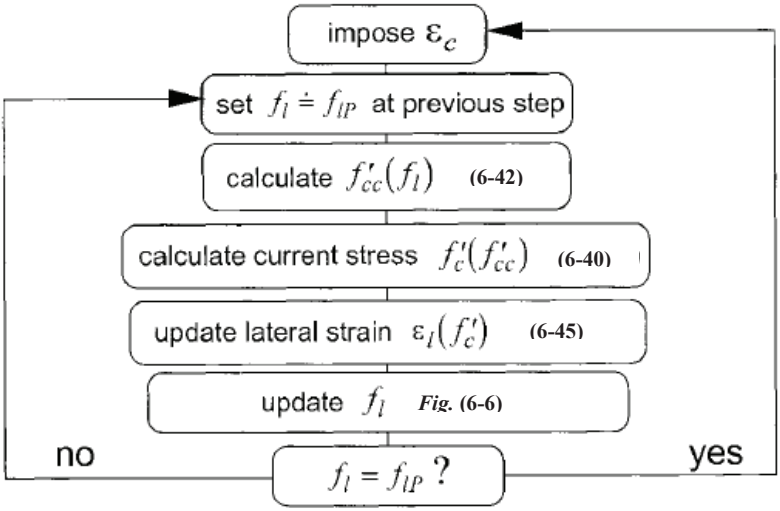

Figure 6-7: Spoelstra and Monti (1999) iterative procedure.

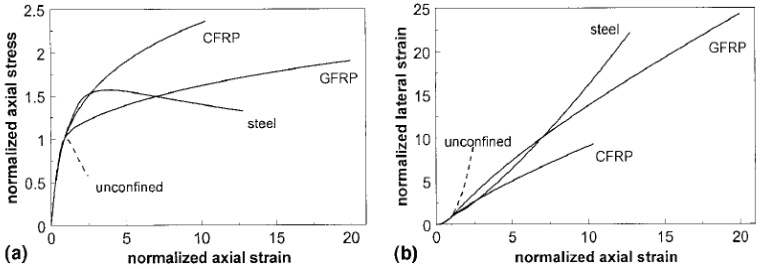

Figure 6-8: Modeling of concrete behavior confined with steel, CFRP and GFRP.

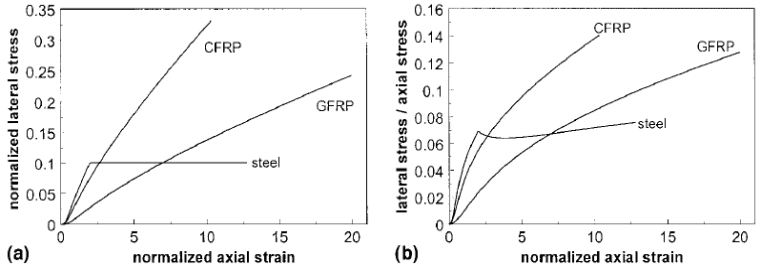

Figure 6-9: Comparison of confinement effectiveness of steel and FRP materials.

Constitutive Model for FRP and Steel Confined Concrete including Shear Deformations

The behavior of confined circular sections under axial load is characterized by the radial lateral dilation, which causes radial confining forces or else axisymmetric passive confining pressure that increases with the amount of lateral expansion (Fig. 6-10). Considering this scheme for the case of confinement by means of FRP jacketing, in order to define the confining pressure acting on the section, it is necessary to define the jacket strain, or circumferential strain, parallel to the fibers' orientation. Relating the circumferential strain to the strain in the radial direction, the following simple relationship is obtained (Fig. 6-10):

$$\varepsilon_c = \frac{\Delta C}{C} = \frac{2\pi R(1+\varepsilon_r - 1)}{2\pi R} = \varepsilon_r \tag{6-47}$$

Owing to the axisymmetry of the problem, the outcome is that the circumferential strain and the strain in the radial direction are equal. This property has been extensively used to calculate directly the radial confining forces based on experimental data by strain gauges attached parallel to the fibers' orientation in order to obtain the circumferential strains. Along this line, it seems useful to try and extend the simple calculation above to the case where steel stirrups and external FRP jacketing are simultaneously present. The steel ties divide the section into two parts: the first is the concrete core and the second is the concrete cover.

$$\varepsilon_c = \frac{\Delta C}{C} = \frac{2\pi\{[R_{core}(1+\varepsilon_{r.core})+c(1+\varepsilon_{r.\mathrm{cover}})]-(R_{core}+c)\}}{2\pi(R_{core}+c)} \tag{6-48}$$

$$\varepsilon_c = \frac{\Delta C}{C} = \frac{R_{core}(1+\varepsilon_{r.core})+c(1+\varepsilon_{r.\mathrm{cover}})}{(R_{core}+c)} - 1 \tag{6-49}$$

However, for the concrete core the following assumption still holds:

$$\varepsilon_{c.core} = \varepsilon_{r.core} \tag{6-50}$$

As explicitly stated above, the equation of radial strains and jacket strains for the case of both FRP and steel confined concrete in circular sections is no longer valid. The circumferential strain of the external jacket is based on the radial strains of both concrete cover and concrete core, where in the latter, the presence of the steel ties plays an important role.

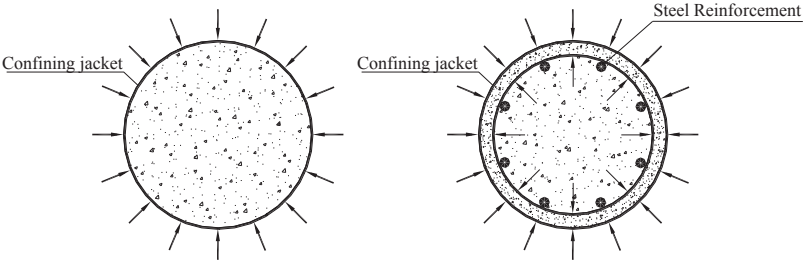

Figure 6-10: Circular Concrete Section confined by steel stirrups and/or FRP Jackets.

The mechanical properties of concrete (strength, ductility and energy dissipation) are substantially enhanced under a triaxial stress state. In practice, this is obtained by using closed stirrups or spiral reinforcement or even FRP wraps, so that, together with the longitudinal reinforcement, the lateral expansion of concrete is limited. This kind of (passive) confinement improves the material behavior after the initiation of internal cracking, which gives rise to the initiation of expansion.

For low strain values, the stress state in the transverse steel reinforcement is very small and the concrete is basically unconfined. In this range, steel and FRP jacketing behave similarly. That is, the inward pressure as a reaction to the expansion of concrete increases continuously. Therefore, speaking in terms of variable confining pressures corresponding to the axial strain level in the section and active triaxial models defining axial stress-strain curves for concrete subjects to constant lateral pressure, it can be stated—following the original approach by the Spoelstra and Monti (1999) model presented in the previous Section—that the stress-strain curve describing the stress state of the section has to cross all active confinement curves up to the curve with lateral pressure equal to the one applied by the stirrups at yielding. After the yielding of stirrups, the lateral pressure is still increasing only due to the FRP jacketing, while the steel lateral pressure remains constant. The corresponding stress-strain curve of the section throughout this procedure converges to a confined-concrete axial stress-strain curve that is associated with a lateral pressure magnitude equal to the tensile strength of the FRP jacket plus the yielding strength of ties (excluding the strain hardening behavior of steel, since ultimate strains of steel are usually much higher than those of FRP jackets). In order to model this behavior, a well-known FRP-confined concrete model (Spoelstra and Monti, 1999) has been enhanced to include the steel ties contribution and thus model circular columns with transverse steel reinforcement and retrofitted with FRP jacketing more consistently. The above model was based on an iterative procedure that needed to be modified as in Fig. 6-11.

In the procedure depicted in Fig.6-11, after imposing an axial strain on the section, a pressure coming from the FRP jacket is assumed. Then, the Poisson's coefficient until yielding of steel stirrups and the pressure coming from the steel ties is calculated based on the BGL model presented also in the previous Section (Braga et al., 2006). Since this lateral pressure according to the BGL model is the solution of the plain stress tensor by the Airy's stress function, the shear stress in the concrete core is also determined along with the shear modulus. Here, also the longitudinal bars' contribution and the arching action between two adjacent stirrups along the column are taken into account (Table 6-1). Thus, the confining pressure in the concrete core is the summation of the lateral pressures contributed by the two confining systems (FRP and Steel). The International Federation for Structural Concrete (*fib*) model proposal (Spoelstra and Monti, 1999) beyond this point is basically used to define the remainder of the parameters declared above, applying that model for the two different regions already mentioned. The focal point of the

procedure is in the last step where the confining pressure of the jacket is defined based on the circumferential strain according to Eq. 6-49. Finally, cases with partial wrapping have been included too (14th *fib* bulletin, 2001, Table 6-1). Such an approach also permits, in cases of repair and retrofit, the consideration of two different concrete strengths, one for the new layer of concrete applied externally, and the other for the old existing concrete core which may also be cracked due to previous seismic loading. At the end of the procedure, a two-condition failure criterion is incorporated either due to the excessive dilation of concrete or due to the buckling of longitudinal bars.

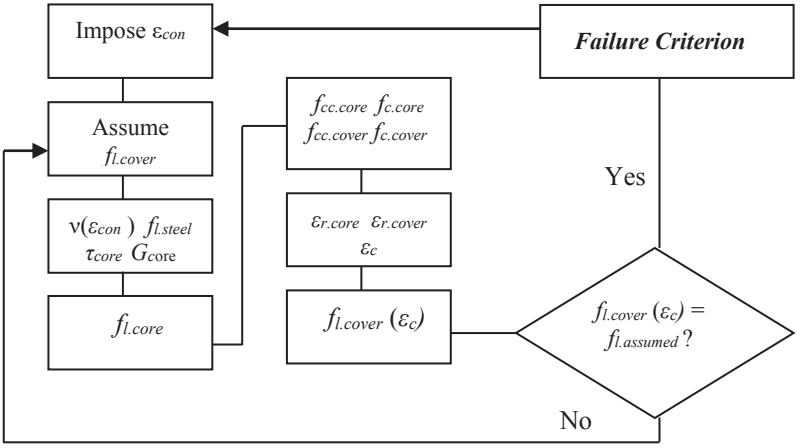

Figure 6-11: Iterative procedure.

It has been well established in recent studies that the rupture strains/strengths measured in tests on FRP confined cylindrical specimens fall substantially below those from flat coupon tensile tests. Several reasons have been suggested for the observed lower rupture strains in place, among which are ([Carey and Harries 2005), (Lam and Teng 2004), (Matthys et al. 2005]):

- Misalignment or damage to jacket fibers during handling and lay-up.
- The radius of curvature in FRP jackets on cylinders as opposed to flat tensile coupons.
- Near failure, the concrete is internally cracked resulting in no homogeneous deformations. Due to this non-homogeneity of

deformations and the high loads exerted on the cracked concrete, local stress concentrations may occur in the FRP reinforcement.

- The existence of a lap-splice zone in which the measured strains are much lower than strains measured elsewhere.

Accounting for these effects an ultimate tensile coupon FRP strain reduced by a *k* factor (ranging between 50 and 80% in the literature) is compared to the circumferential strain of concrete (Eq. 6-49), and the ultimate compressive axial strain of concrete is considered to be attained when:

$$\varepsilon_c \le k \cdot \varepsilon_{j.rup.coup} \tag{6-51}$$

Table 6-1: Equations embodied in the iterative procedure.

(Braga et al. 2006)	$f_{l.steel}(\varepsilon_{con}) = k_{sl}\dfrac{E_{con}E_s A_{sh}\nu(\varepsilon_{con})}{R_{core}E_{con}S + E_s A_{sh}\left[1-\nu(\varepsilon_{con})\right]\cdot\left[\nu(\varepsilon_{con})\cdot\varepsilon_{con}+1\right]}\cdot\varepsilon_{con}, \varepsilon_{sh} \prec \varepsilon_{yh}$ $f_{l.steel}(\varepsilon_{con}) = k_{sl}\,0.5\rho_{sh}f_{yh}, \varepsilon_{shu} \ge \varepsilon_{sh} \ge \varepsilon_{yh}$ $\rho_{sh} = \dfrac{4A_{sh}}{D_{core}S},\ \varepsilon_{yh} = \dfrac{f_{yh}}{E_s},\ \varepsilon_{sh} = \varepsilon_{c.core} = \varepsilon_{r.core} = \nu(\varepsilon_{con})\cdot\varepsilon_{con}$ $\nu(\varepsilon_{con}) = \nu_0\left[1 + 0.2\left(\dfrac{\varepsilon_{con}}{\varepsilon_{c0}}\right) - \left(\dfrac{\varepsilon_{con}}{\varepsilon_{c0}}\right)^2 + 1.55\left(\dfrac{\varepsilon_{con}}{\varepsilon_{c0}}\right)^3\right],\ \nu_0 = 0.2,$ $\varepsilon_{co} = 0.002$ $k_{sl} = \dfrac{45\xi_l{}^3}{45\xi_l{}^3 + \beta\xi_{st}}, \xi_l = \dfrac{D_b}{S}, \beta = \dfrac{D_h}{D_b}, \xi_{st} = \dfrac{2D_h}{\pi R_{core}}$ $\tau_{core} = \dfrac{E_{con}E_s A_{sh}\nu(\varepsilon_{con})}{R_{core}E_{con}S + E_s A_{sh}\left[1-\nu(\varepsilon_{con})\right]\cdot\left[\nu(\varepsilon_{con})\cdot\varepsilon_{con}+1\right]}\cdot\varepsilon_{con}$ $G_{core} = \dfrac{E_{con}}{2\cdot[1+\nu(\varepsilon_{con})]}$

(Spoelstra and Monti 1999)	$f_c = \frac{f_{cc} \cdot x \cdot r}{r - 1 + x^r}$, $x = \frac{\varepsilon_{con}}{\varepsilon_{cc}}$, $\varepsilon_{cc} = \varepsilon_{co}\left[1 + 5\left(\frac{f_{cc}}{f_{co}} - 1\right)\right]$, $r = \frac{E_{con}}{E_{con} - E_{\sec}}$ $E_{\sec} = \frac{f_{cc}}{\varepsilon_{cc}}$, $\frac{f_{cc}(f_l)}{f_{co}} = 2.254\sqrt{1 + 7.94\frac{f_l}{f_{co}}} - 2\frac{f_l}{f_{co}} - 1.254$, $\varepsilon_r(\varepsilon_{con}, f_l) = \frac{E_{con}\varepsilon_{con} - f_c(\varepsilon_{con}, f_l)}{2\beta f_c(\varepsilon_{con}, f_l)}$, $\beta = \frac{5700}{\sqrt{\lvert f_{co}\rvert}} - 500$, $E_{con} = 5700 \cdot \sqrt{\lvert f_{co}\rvert}(MPa)$
(14th fib Bulletin)	$k_j = \frac{\left(1 - \frac{S_j}{2D}\right)^2}{1 - \frac{A_b}{A_g}} \approx \left(1 - \frac{S_j}{2D}\right)^2$ *(Coefficient for Partial Wrapping)* $f_{l.\text{cover}} = \frac{1}{2}k_j \rho_j E_j \varepsilon_c, \rho_j = \frac{4t_j}{D}$
Iterative Procedure	$f_{l.core} = f_{l.\text{cover}} + f_{l.steel}$, $f_{c.av} = \frac{A_{core}}{A_{tot}} f_{c.core} + \frac{A_{\text{cover}}}{A_{tot}} f_{c.\text{cover}}$
(Bae et al. 2005)	$\varepsilon_{sl} = \max\left[\left(\frac{0.035\cos\theta + \theta}{\cos\theta - 0.035\theta}\right)\frac{w}{D_b}, \left(\frac{0.07\cos\theta + \theta}{\cos\theta - 0.07\theta}\right)\left(\frac{w}{D_b} - 0.035\right)\right]$, $\theta = \frac{6.9}{(L_{buck}/D_b)^2} - 0.05$, $\varepsilon_{sl} = \varepsilon_{con}$

In old-type circular columns with inadequate transversal reinforcing details (where FRP jacketing are a commonly used remedy), the unsupported length of longitudinal bars (between 2 successive stirrups) is often much greater than $6D_b$ (D_b = longitudinal bar diameter). Therefore, the risk of longitudinal bars buckling under compressive loads soon after yielding is higher. A dire implication is reduced effectiveness of the FRP wraps due to interaction between buckled longitudinal bars and the jacket,

which may cause premature failure due to the rupture of the jacket (Tastani et al. 2006). This is an additional source of error contributing to overestimating the strength of FRP confined concrete in addition to that generated by the difference between the nominal and in-situ strain capacity of the wraps as detailed above. It is the objective of the present book to study the interaction between wraps and compression reinforcement in FRP-encased reinforced concrete columns, with particular emphasis on the occurrence of instability conditions and the dependable compressive strain of the column prior to actual buckling of the rebars.

In this model, the dilation of the concrete core and concrete cover are described through the following equation (Eq. 6-52) of the model by Spoelstra and Monti (1999).

$$\varepsilon_r\left(\varepsilon_{con}, f_l\right) = \frac{E_{con}\varepsilon_{con} - f_c\left(\varepsilon_{con}, f_l\right)}{2\beta f_c\left(\varepsilon_{con}, f_l\right)} \quad , \quad \beta = \frac{5700}{\sqrt{|f_{co}|}} - 500 \tag{6-52}$$

Thus, the lateral pressure of the FRP jacket confining the concrete cover has been taken into account, and by relating the critical buckling conditions with the onset of significant strength loss of the concrete cover, the effect of the confining pressure exerted by the jacket in delaying the occurrence of buckling of the longitudinal bars can be evaluated. Therefore, the critical buckling conditions are delayed depending on how axially stiff the jacket is, which accordingly delays the failure of the concrete cover (which laterally supports the longitudinal bar). This onset of loss of resistance in concrete has been proved to be the point when the net volumetric strain of the material becomes equal to zero (Pantazopoulou and Mills, 1995). In circular sections this occurs when:

$$\varepsilon_V = 0 \Rightarrow 2 \cdot \varepsilon_r = \varepsilon_{con} \Rightarrow \nu = 0.5 \tag{6-53}$$

However, another condition that should be valid for the attainment of critical instability conditions of the longitudinal bars in the high confining stress states under consideration is the occurrence of compression yielding of the longitudinal bar. Regarding this step, it is interesting to note with reference to Fig. 6-12 for a given concrete strength, the point where the volumetric ratio becomes zero moves forward into higher axial compression strain values with increasing confining pressures. Thus, as shown by the two curves in Fig. 6-12 corresponding to different confining pressures, the difference in the lateral behavior of the concrete cover

(confined by the jacket's pressure) and the concrete core (confined by both the steel's and FRP's pressure) should also be considered.

As it is shown in previous studies (Monti and Nuti, 1992), (Bae et al. 2005), the buckling length L_{buck} and the L_{buck}/D_b ratio are critical parameters for the post buckling behavior of longitudinal bars under compression. In cases of columns constructed with obsolete codes with the spacing of the stirrups ranging from 200 to 500 mm (buckling length) and bar diameters from 12 to 20 mm, the L_{buck}/D_b ratio ranges between 10 and 42. However, apart from old type columns, the assumption that the buckling length is equal to the spacing of the stirrups in a RC column does not hold true in all cases (Dhakal and Maekawa 2002) and it may extend over more than a single tie spacing. In order to take into account this behavior (cases of reinforcement repair and FRP retrofit) the following procedure is suggested.

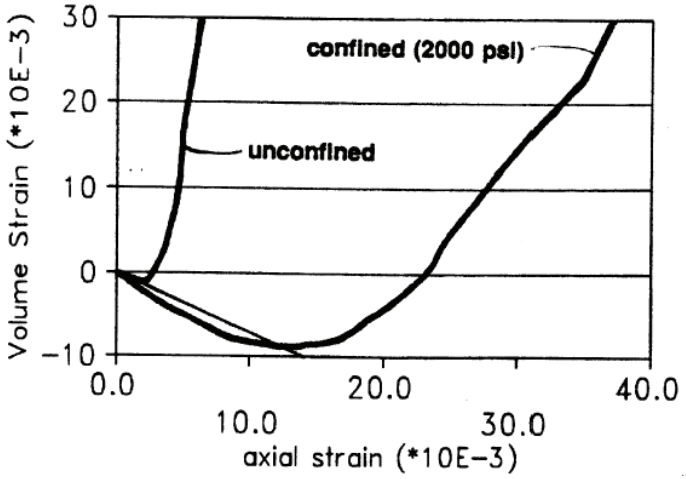

Figure 6-12: Volumetric Strain versus Axial Compressive Strain (Pantazopoulou and Mills, 1995).

The longitudinal bar is modeled as a pin-ended bar supported along its length by an elastic foundation as shown in Fig. 6-13. The foundation modulus is k' (N/mm^2) and it is such that when the bar deflects by an amount u, a restoring force $k' \cdot u$ (N/mm) is exerted by the foundation normal to the bar.

The governing homogeneous differential equation and the associated eigenvalue problem are:

$$EI\upsilon^{iv} + P\upsilon^{ii} + k'\upsilon = 0 \tag{6-54}$$

$$P_{cr} = \frac{\pi^2 EI_{red}}{L_{buck}{}^2}\left[m^2 + \frac{1}{m^2}\left(\frac{k'L_{buck}{}^4}{\pi^4 EI_{red}}\right)\right] \tag{6-55}$$

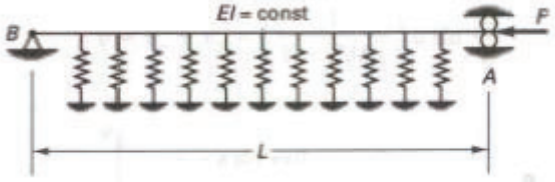

Figure 6-13: A pin-ended bar on elastic foundation.

Note that if $k' = 0$ (which occurs upon the yielding of the stirrups), the minimum value of P_{cr} becomes the classical Euler buckling load. In order to determine the critical load, the buckling mode m equal to one should be used. The stiffness k' representing the supporting system of stirrups could be calculated as follows:

$$k' = n \cdot \frac{E_s \cdot A_{sh}}{L_{buck} \cdot \pi \cdot D_{core}} \quad , L_{buck} = (n+1) \cdot S \tag{6-56}$$

$$EI_{red} = 0.5 \cdot E_s \cdot I_b \cdot \sqrt{\frac{f_{yl}}{400}} \quad \text{(Dhakal and Maekawa, 2002)} \tag{6-57}$$

The solution to the problem above is obtained by setting the critical load of the bar equal to its yield force; in this case the only unknown is the number n of the stirrups, n over the buckling length. Therefore, by solving Eq. 6-55 for n, the buckling length is determined. The value of n may be rounded to the nearest integer owing to the fact that the pin-ended bar segment engaged in buckling is assumed to span between successive inflection points of the real deformed shape. If convergence is not possible for $n>1$, the buckling length is taken as equal to the spacing of stirrups b.

To sum up, after the critical conditions of a longitudinal compressive bar have been attained (this is assumed to coincide with the compression yielding of the bar and the Poisson's coefficient at the concrete cover

exceeding the value of 0.5) the buckling length of the bar is determined. Then, based on the model by Bae et al., 2005, who have related the axial strain to the transversal displacement of the buckled longitudinal bar for a given L_{buck}/D_b ratio the transversal displacement of the bar is calculated (Table 6-1). Given that for a longitudinal bar embedded in an RC member, axial shortening of the bar means the same amount of shortening for the surrounding concrete mass (Pantazopoulou, 1998), the axial strain in the bar is taken as equal to the axial strain of concrete. Finally, the jacket's circumferential strain due to buckling is determined as follows:

$$\varepsilon_{c.buck} = \frac{2 \cdot \pi \cdot |w - c|}{\pi \cdot D} \leq \varepsilon_{j.rup.coup}, \text{ (Full wrapping)} \quad (6\text{-}58)$$

$$\varepsilon_{c.buck} = \frac{2 \cdot \pi \cdot \left| w - \frac{c}{2} \right|}{\pi \cdot D} \leq \varepsilon_{j.rup.coup}, \text{ (Partial wrapping)} \quad (6\text{-}59)$$

It follows from the above Equations (Eqs. 6-58, 6-59) that a tolerance equal to the concrete cover for full wrapping, and half of the concrete cover for partial wrapping is given before the initiation of the jacket's strains due to the buckling of longitudinal bars since the concrete cover should be severely cracked in case of full wrapping and some spalling could appear in case of partial wrapping. Since the displacement of the buckled longitudinal bar could be high and the phenomenon affects locally the jacket where the FRP material behavior could be considered linear-elastic, the results are compared to the deformation capacity of tensile coupons (dilation strains and buckling strains are studied independently). In the proposed algorithm detailed above, the failure criterion is used in two steps. Firstly, the circumferential strain due to dilation of concrete under compression is compared to a reduced FRP tensile coupon strain, and secondly the induced circumferential strains due to buckling which locally accelerate the jacket's rupture are compared to the deformation capacity of flat FRP tensile coupons. If one of these conditions is fulfilled, the iterative procedure (Fig. 6-11) is terminated.

Figures 6-14 and 6-15 depict a simple run of the material model under axial strain reversals with the same material properties as the specimen ST2NT of the experimental study with FRP- and steel- confined columns performed by Sheikh and Yau, 2002. A moment-curvature analysis (Fig. 6-16) for the section (with layers/fibers) of the same specimen that also provides the shear force - shear angle diagram has been performed, where

the constitutive model by Menegotto and Pinto (1973) is used to model the longitudinal steel behavior. Figures 6-17 and 6-18 depict the implications of the application of the constitutive relation presented in this Chapter, where, in contrast to the assumption of a Timoshenko beam (Ceresa et al., 2007) the shear deformation is not constant along the section. The shear deformation of the section is defined as the mean value of the shear deformations of each material fiber/layer. The Bernoulli assumption is bypassed since the shear deformations are included and are uncoupled from the normal ones.

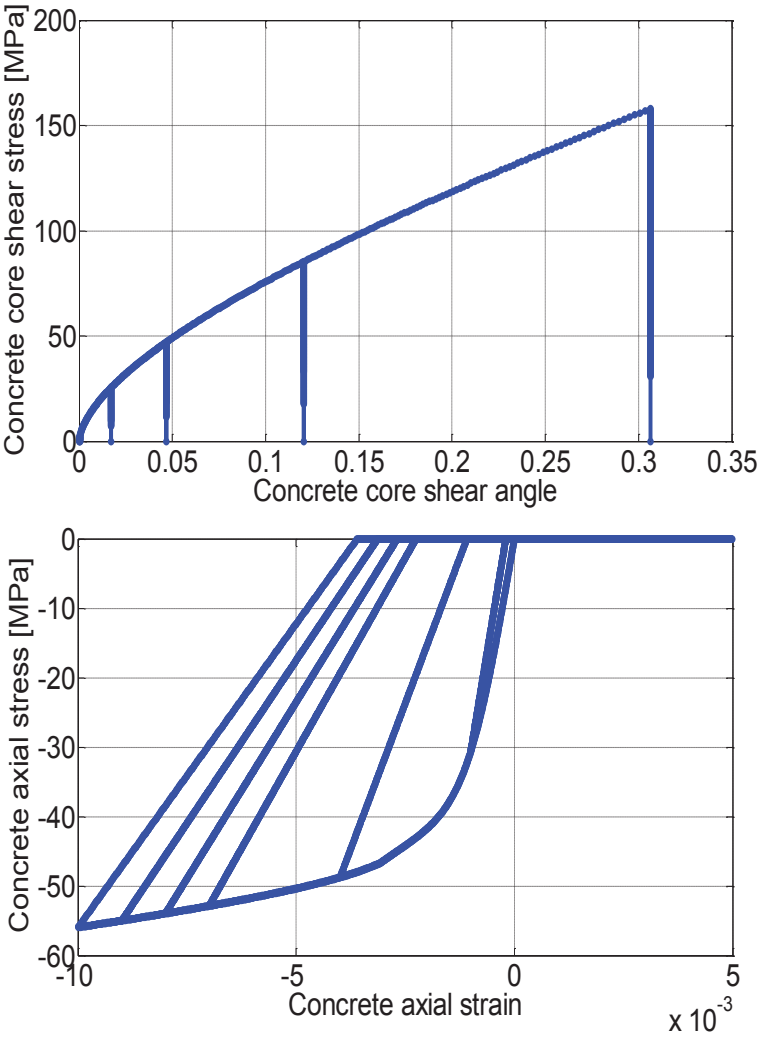

Figure 6-14: Proposed cyclic stress-strain material model including shear deformations.

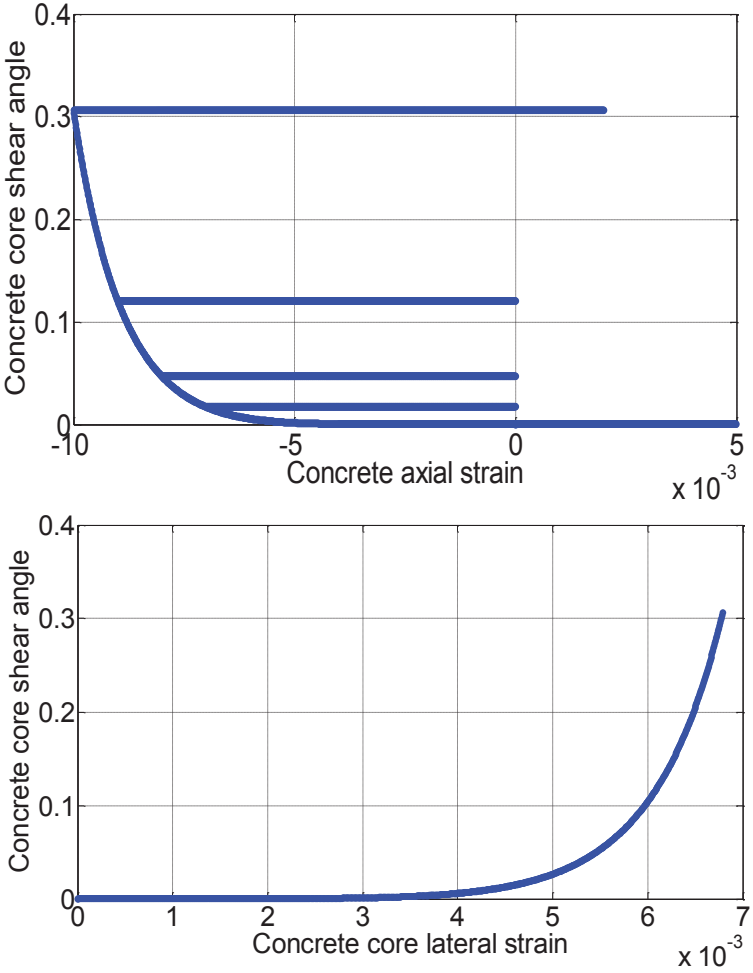

Figure 6-15: Proposed cyclic stress-strain material model including shear deformations.

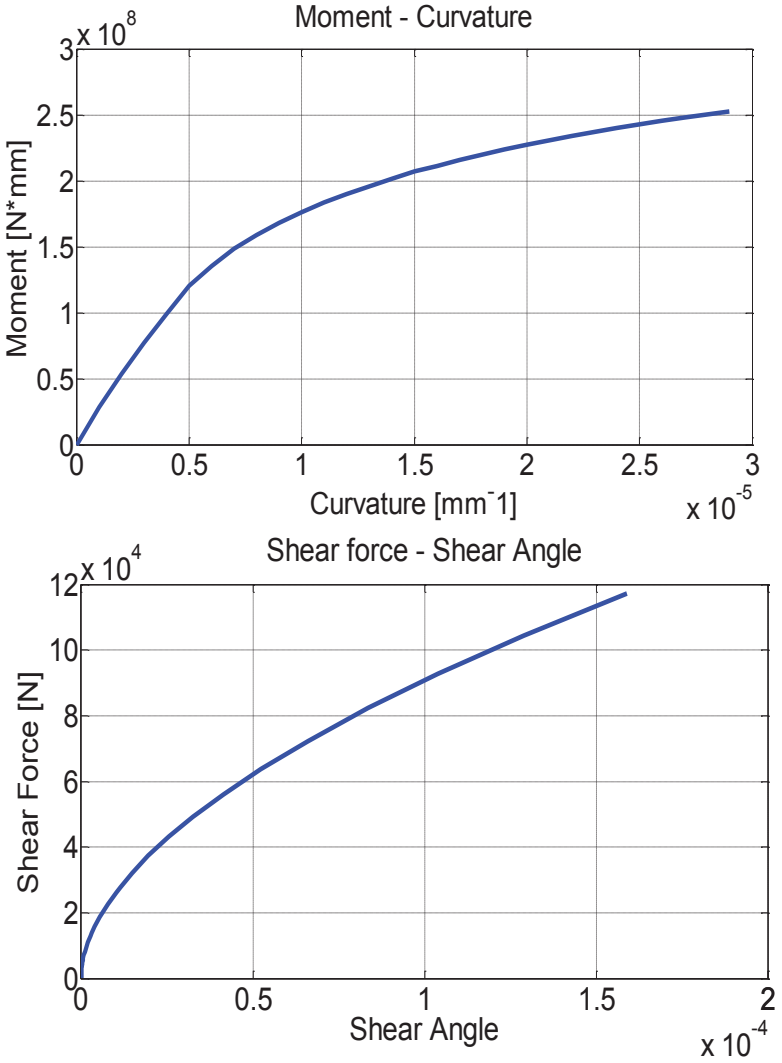

Figure 6-16: Prediction of section's response with properties similar to RC column ST2NT by Sheikh and Yau (2002).

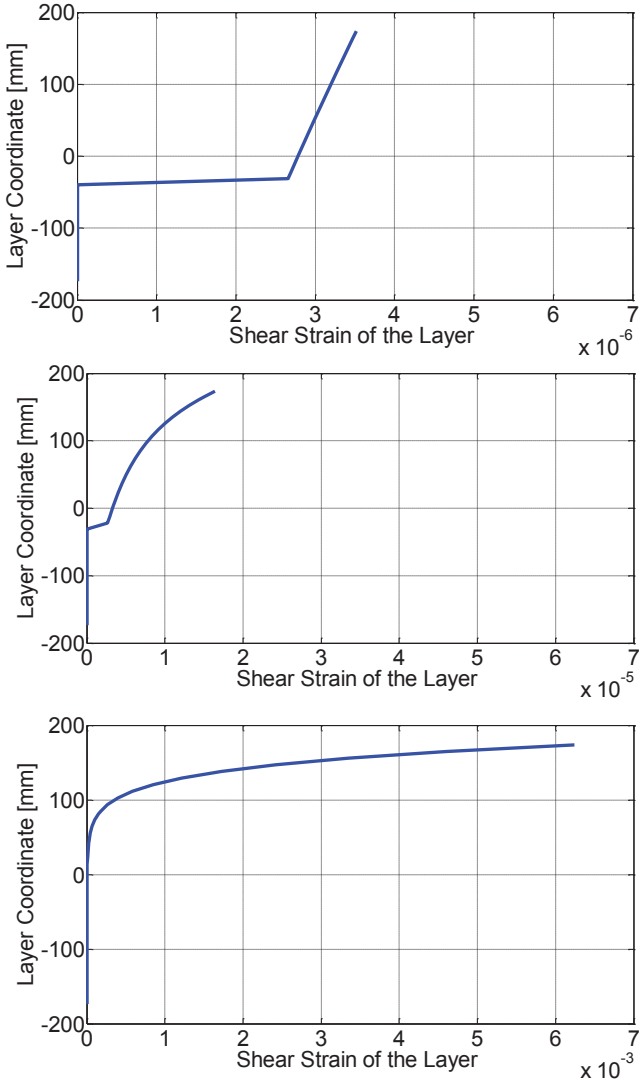

Figure 6-17: Shear strain profile over the section for the first curvature increment, flexural yielding and ultimate moment (from top to bottom).

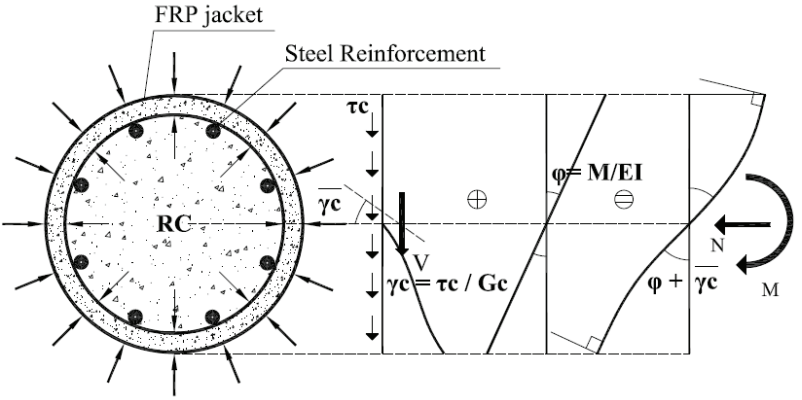

Figure 6-18: Circular concrete section confined by steel stirrups and FRP jacket under bending and shear based on the proposed model.

Correlation with Experimental Results

Four experimental studies have been included in this Chapter for the validation of the proposed iterative procedure. The first is one of the few extensive experimental studies on large scale FRP wrapped circular columns where different FRP configurations have been applied, for identical embedded steel reinforcement (Matthys et al. 2005). It includes 8 large-scale columns subjected to axial loading. The columns had a total length of 2 m, a longitudinal reinforcement ratio of 0.9% and 8 mm diameter stirrups spaced at 140 mm. All columns had a circular cross section with a diameter of 400 mm. Different types of FRP reinforcement (CFRP, GFRP & HFRP) have been used to confine the columns. The comparison seems to be satisfactory (Figs. 6-19, 6-20), although the solution has moderate success in resolving the problem of predicting the actual instance of jacket's failure in terms of axial and circumferential ultimate strains. It should be noted that the cases that followed the circumferential strains—owing to concrete dilation estimated by the model, Eq. 6-49—were compared to the rupture FRP strains measured experimentally. Some clarifications are in order for the last graph (Fig. 6-21) which illustrates the model's estimations of the circumferential strains in the FRP jacket owing to concrete dilation and to the buckling of longitudinal bars at the ultimate axial strain reported in the tests for each specimen. These values are compared to the experimental rupture strain of

the jacket (from strain gages) and to the deformation capacity of the flat tensile coupons which was reported accordingly.

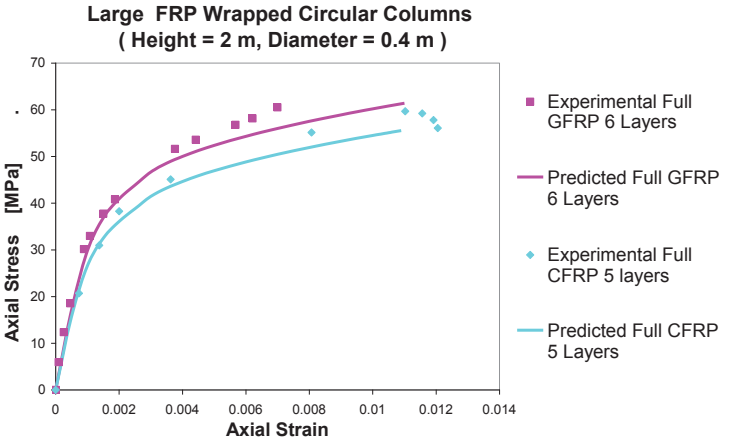

Figure 6-19: Correlation with experimental results (Matthys et al. 2005).

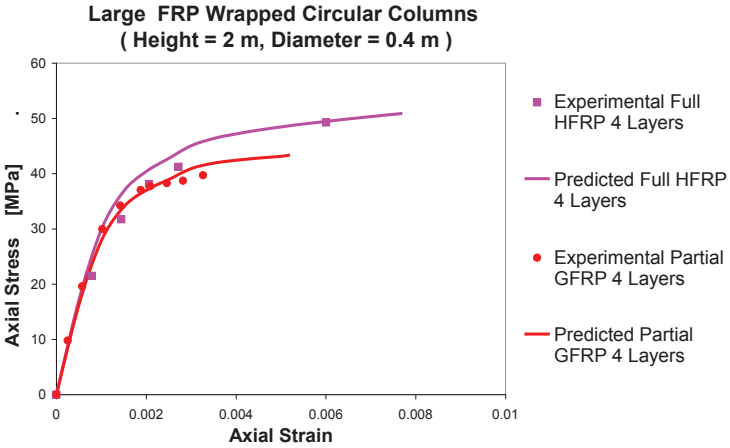

Figure 6-20: Correlation with experimental results (Matthys et al. 2005).

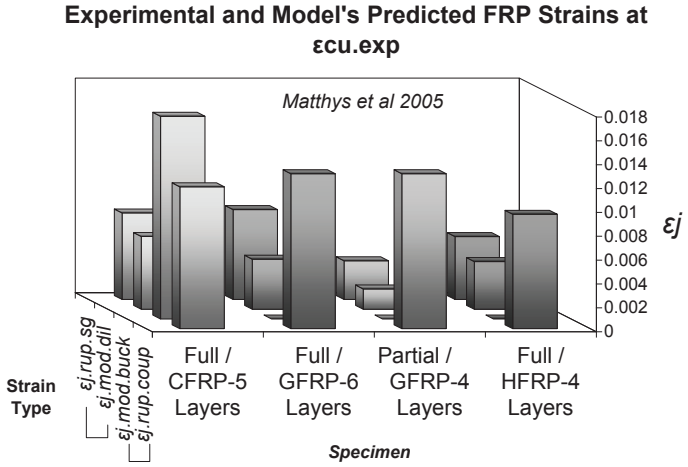

Figure 6-21: Correlation with experimental results (Matthys et al. 2005).

The second experimental study (Demers and Neale 1999) includes 16 reinforced concrete columns having a circular section of 300 mm in diameter and 1200 mm high. These columns were confined by means of carbon-epoxy sheets and loaded concentrically in axial compression. The effects of various parameters on the structural behavior of the confined concrete columns were investigated. These parameters included the concrete strength, longitudinal steel reinforcement, steel stirrups, steel corrosion and concrete damage while the FRP configuration was kept constant. The comparison between model estimates and experimental results depicted in Figs. 6-22 and 6-23, in this case too, could be characterized as satisfactory; they can also be considered satisfactory due to the the fact that, in this experimental study, the lateral pressures from both confining materials (Steel and FRP) are provided based on circumferential strains obtained by strain gages applied on both FRP Jacket and Steel ties. (It should be underlined that the horizontal strain gages on the jacket were located midway between two successive stirrups). Among the 16 specimens in only one case (Specimen U40-4) the pressures coming from the ties were evidently higher than those of the FRP jacket and the model was able to detect that (Fig. 6-24).

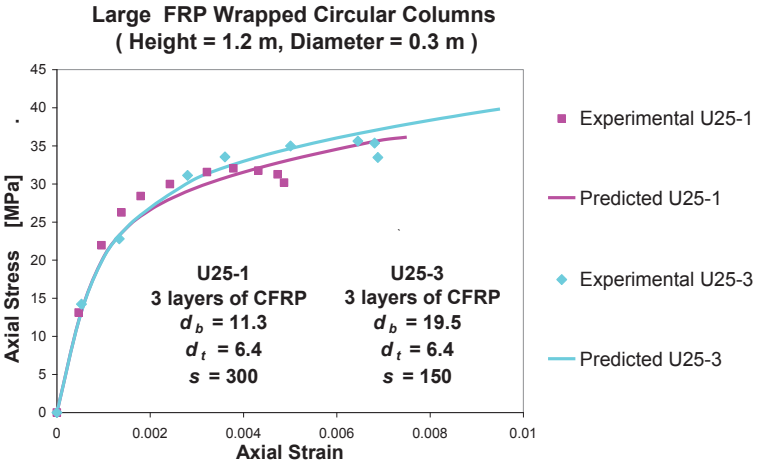

Figure 6-22: Correlation with experimental results
(Demers and Neale 1999).

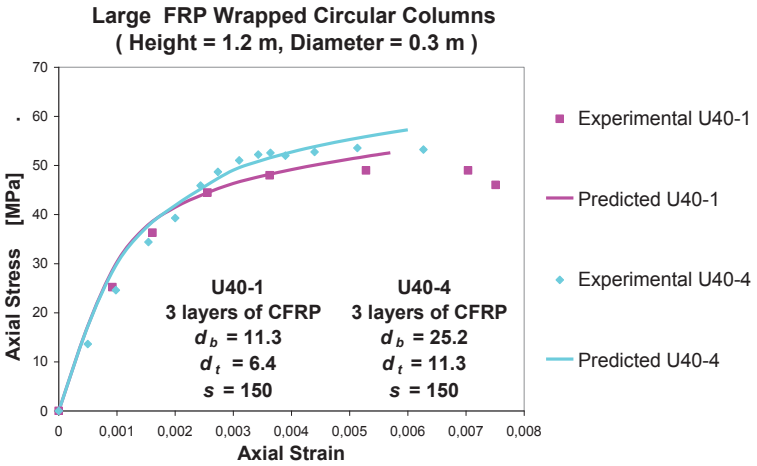

Figure 6-23: Correlation with experimental results
(Demers and Neale 1999).

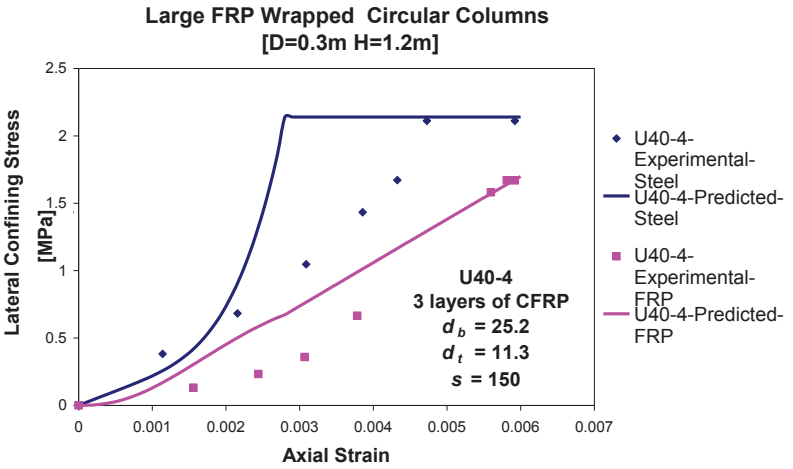

Figure 6-24: Correlation with experimental results (Demers and Neale 1999).

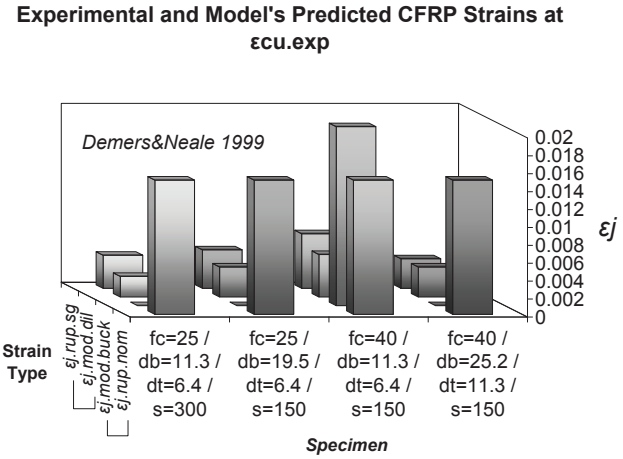

Figure 6-25: Correlation with experimental results (Demers and Neale 1999).

Some clarifications are in order for the l.a graph (Fig. 6-25) which illustrates the model's estimations of the circumferential strains in the FRP jacket owing to concrete dilation and to the buckling of longitudinal bars at the ultimate axial strain reported in the tests for each specimen. These values are compared to the experimental rupture strain of the jacket (from strain gages) and to the nominal deformation capacity of the FRP jacket which was reported accordingly.

The third experimental study (Gallardo-Zafra R. & K. Kawashima, [2009]) contains a series of cyclic loading tests that was conducted on six reinforced concrete column specimens 400 mm in diameter and 1.350 mm in effective height. Because the test was used in this study to clarify the analytical model, only a summary of the tests results necessary for ascertaining the accuracy of the analytical correlation is described here. The specimens were grouped into A and B series where each series consisted of three specimens; one was as-built while the second and the third were wrapped laterally by CFRP with a single layer and with two layers, respectively. The CFRP ratio was 0.111% and 0.222% when the columns were wrapped by a single layer and two layers, respectively. CFRP was wrapped 1 m high from the base and no gap was provided at the base. The specimens were laterally confined by 6 mm deformed bars having a yield strength of 363 MPa (SD295) with 135º bent hooks. The tie reinforcement ratio was 0.256% (150 mm spacing) for the A-series and 0.128% (300 mm spacing) for the B-series. All specimens were reinforced in the longitudinal direction by 12-16 mm deformed bars having a nominal yield strength of 374 MPa (SD295). Concrete compressive strength ranged from 27.5 – 30 MPa. Under a constant axial load of 185 KN, which is about 8% of the theoretical ultimate axial capacity, the piers were loaded in a unilateral direction with a displacement increment of a half drift. At each increment, three cyclic loads were applied. The columns were designed such that they would fail in flexure.

Regarding the third experimental correlation, Figs. 6-26-6-45 depict the comparison with the two groups of cyclic tests on bridge piers having different levels of confinement in terms of lateral steel reinforcement and FRP jacketing. To simulate the experimental behavior of the columns, they were idealized by a discrete analytical model (Fig. 6-46). Similar to the publication by Gallardo-Zafra R. & K. Kawashima (2009), the cantilever column was modeled by a linear beam element with the stiffness corresponding to flexural yielding and a fiber element used to idealize flexural hysteretic behavior at the plastic hinge. (The results produced in this study are based on the displacement formulation of the nonlinear beam element of the plastic hinge region). The length of the fiber element

was assumed to be half of the column diameter. A rotational spring at the bottom of the column represents the longitudinal bar pullout from the footing. Its property was based on a moment-rotation curve obtained from the experiment at a small amplitude loading and was assumed to have an elastic stiffness.

While in the original proposal the fiber section had to be divided into the concrete core and concrete cover (Fig. 6-46) and two different stress-strain relations were applied for the concrete core (confined by both FRP & Steel) and concrete cover (confined by only the FRP), in this work, since the material response is already averaged based on the different responses of those two regions, the same stress-strain law is applied for each fiber. This fact gives a clear advantage to the proposed model. In addition to the force-displacement response of the cantilever columns the response in the level of the section is also provided for each specimen in terms of material stress-strain hysteresis.

It can be seen that the agreement is very close to the experimental one with some deviation concentrated on the parts of reloading after reversal of the imposed displacement. This difference of response in terms of modeling can be explained based on the way the cracks on the concrete surface are described on the level of the material model. Since the crack is described as a two-event phenomenon, which means either open or closed (while in reality it is not the case due to imperfect crack closure) the contribution of concrete while the longitudinal steel reinforcement is in compression and the crack is closing gives this deviation in the response.

The comparison with the originally proposed model of this experimental study is, impressively, the same. However, the proposed model describes rationally the procedure of the passive confinement based on the calculation of the lateral concrete expansion in terms of the different levels of lateral pressures coming from the two different materials (Steel and FRP). Moreover, the active (constant lateral pressure) confinement model proposed by Kawashima et al. (1999) is based on regression analysis of the experimental results of cylindrical specimens under compression and it is specifically calibrated for Carbon Fiber Composite material (CFRP). Finally, it doesn't consider the confinement effect of the longitudinal reinforcement and the effect of partial confinement due to the vertical arching action of the adjacent stirrups along the member but also cases of partial FRP wrapping of the column.

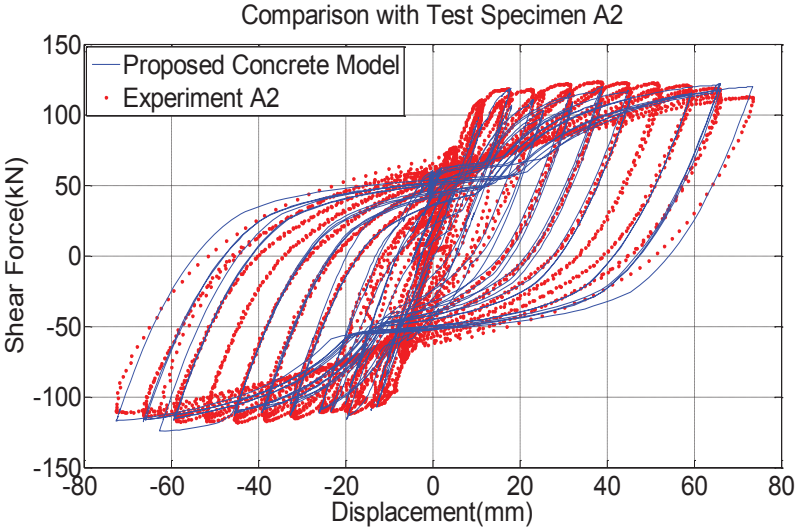

Figure 6-26: Correlation with experimental results A2 (Gallardo-Zafra R. & K. Kawashima, 2009).

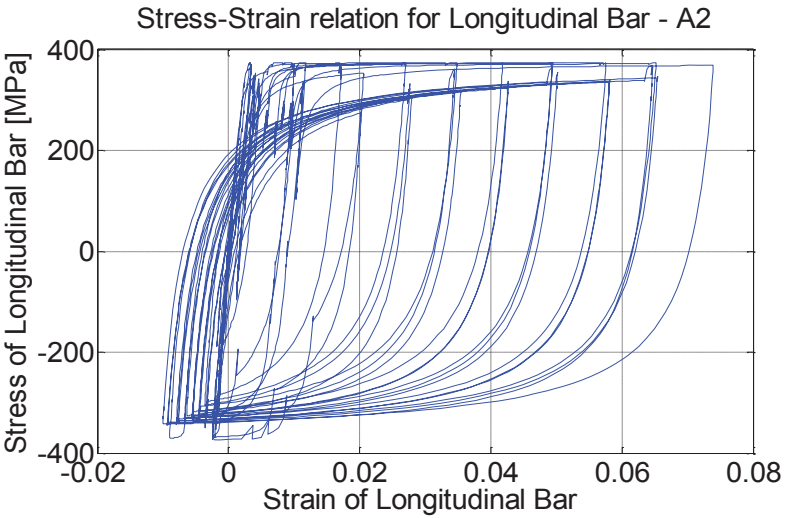

Figure 6-27: Correlation with experimental results A2 (Gallardo-Zafra R. & K. Kawashima, 2009).

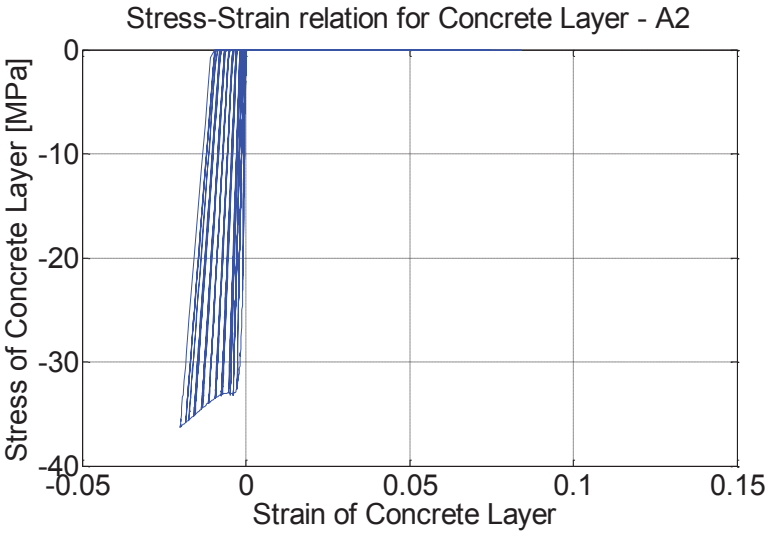

Figure 6-28: Correlation with experimental results A2 (Gallardo-Zafra R. & K. Kawashima, 2009).

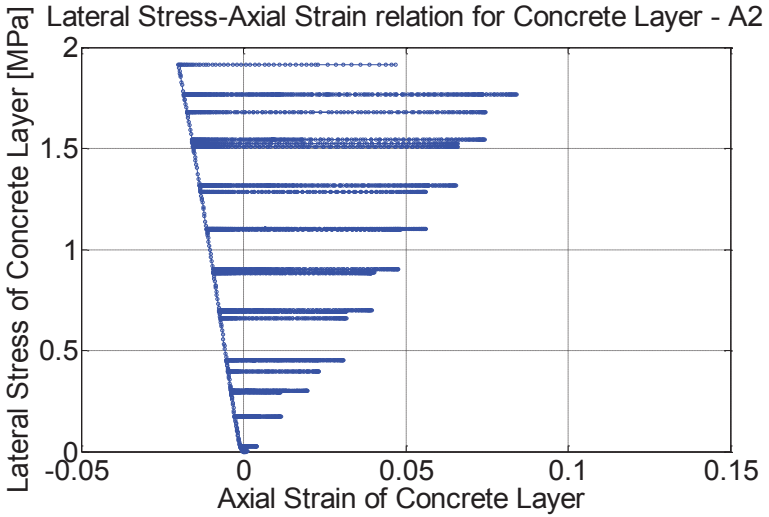

Figure 6-29: Correlation with experimental results A2 (Gallardo-Zafra R. & K. Kawashima, 2009).

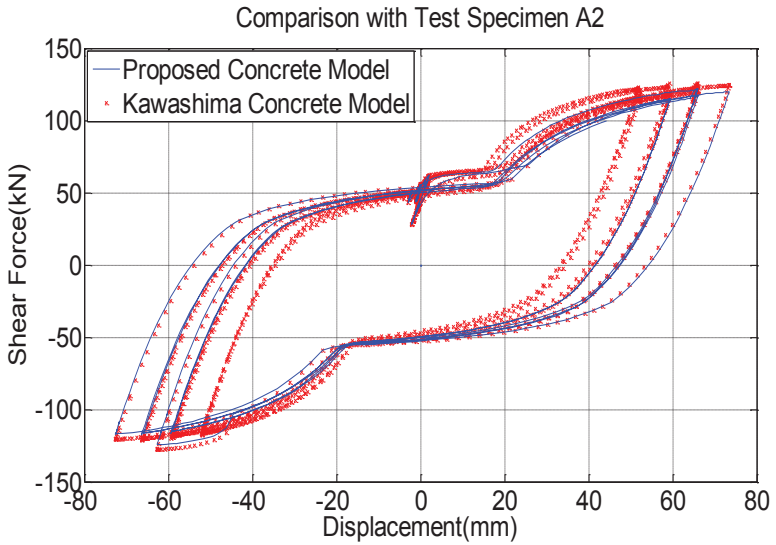

Figure 6-30: Correlation with experimental results A2 (Gallardo-Zafra R. & K. Kawashima, 2009).

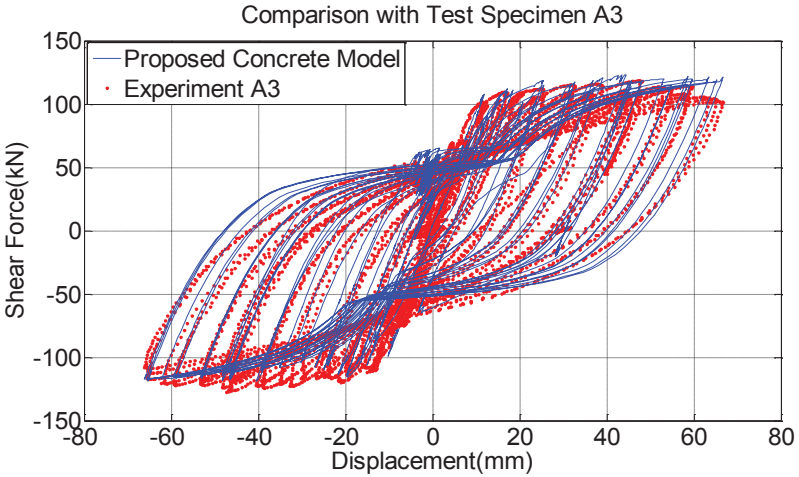

Figure 6-31: Correlation with experimental results A3 (Gallardo-Zafra R. & K. Kawashima, 2009).

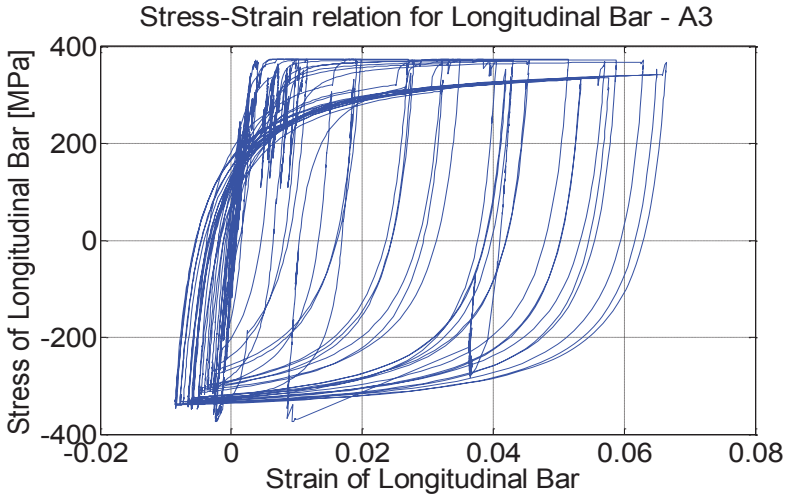

Figure 6-32: Correlation with experimental results A3 (Gallardo-Zafra R. & K. Kawashima, 2009).

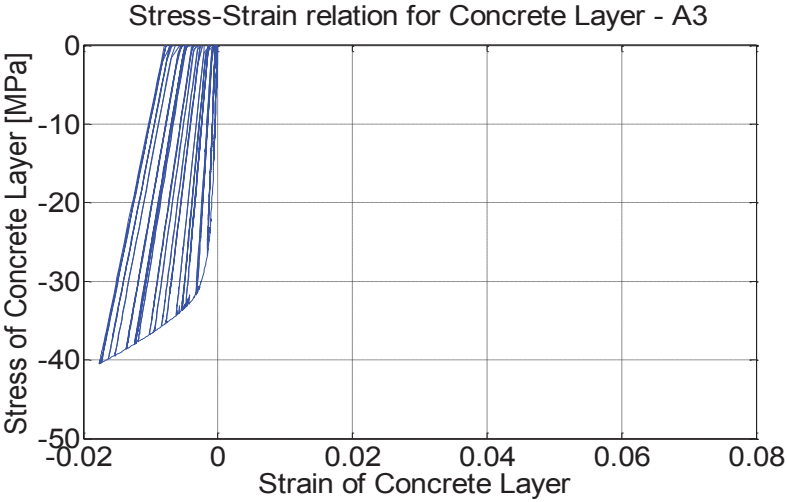

Figure 6-33: Correlation with experimental results A3 (Gallardo-Zafra R. & K. Kawashima, 2009).

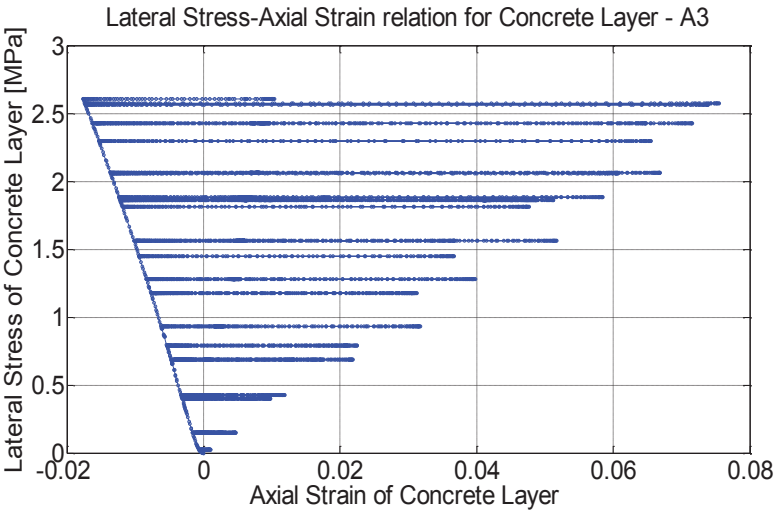

Figure 6-34: Correlation with experimental results A3 (Gallardo-Zafra R. & K. Kawashima, 2009).

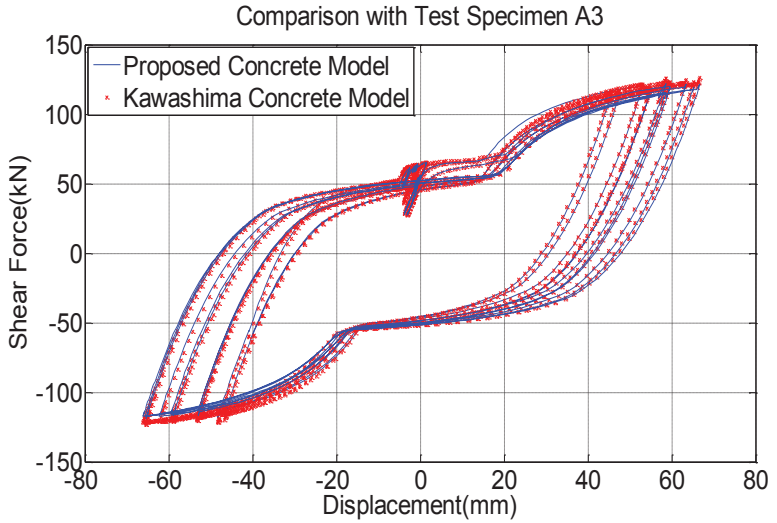

Figure 6-35: Correlation with experimental results A3 (Gallardo-Zafra R. & K. Kawashima, 2009).

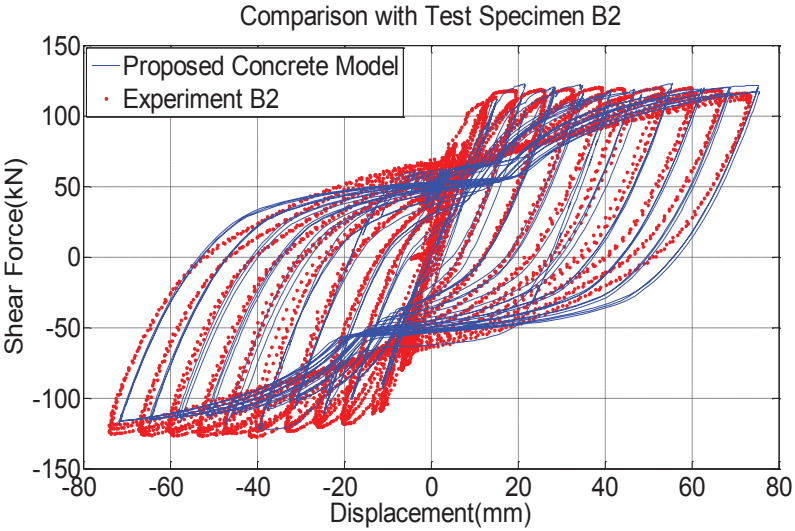

Figure 6-36: Correlation with experimental results B2 (Gallardo-Zafra R. & K. Kawashima, 2009).

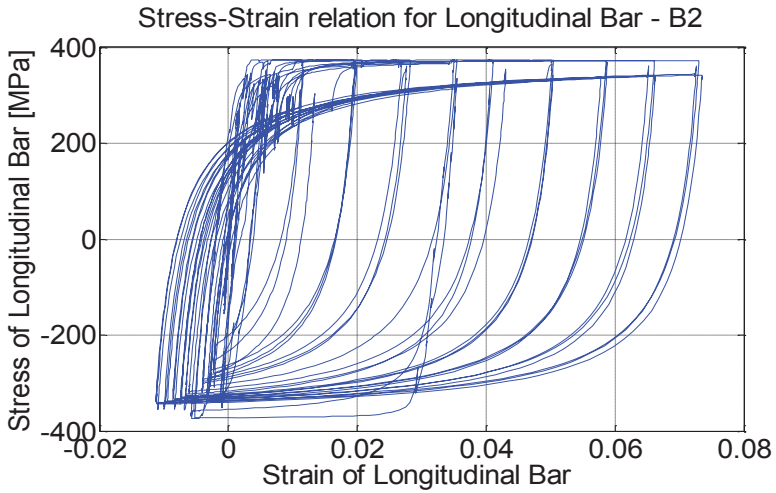

Figure 6-37: Correlation with experimental results B2 (Gallardo-Zafra R. & K. Kawashima, 2009).

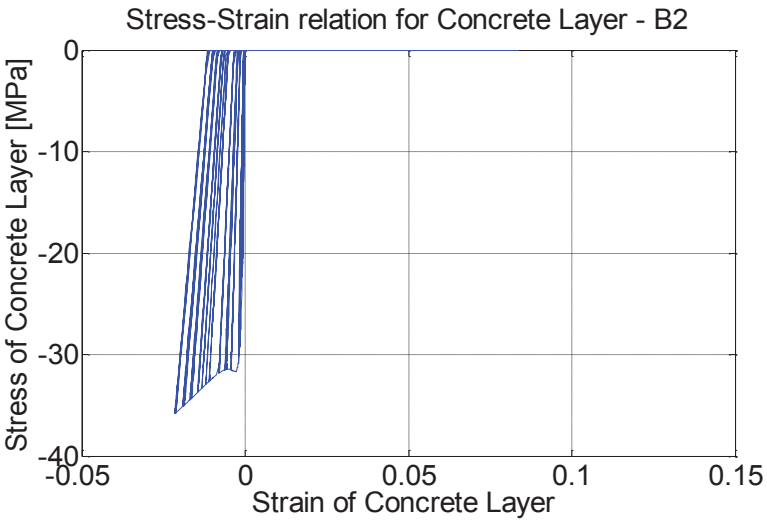

Figure 6-38: Correlation with experimental results B2 (Gallardo-Zafra R. & K. Kawashima, 2009).

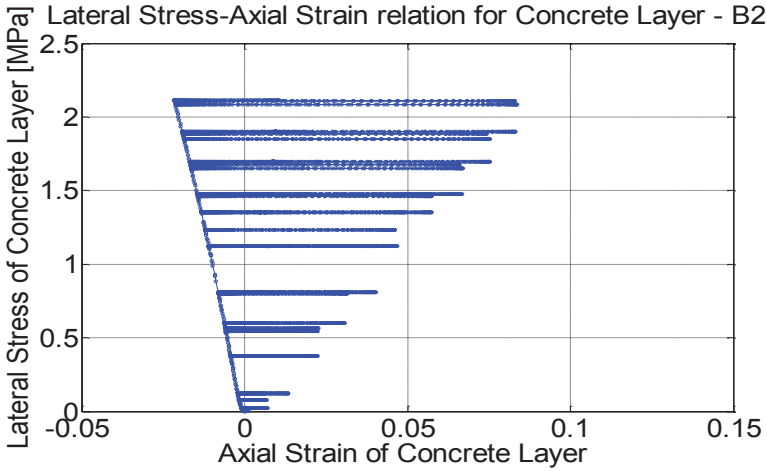

Figure 6-39: Correlation with experimental results B2 (Gallardo-Zafra R. & K. Kawashima, 2009).

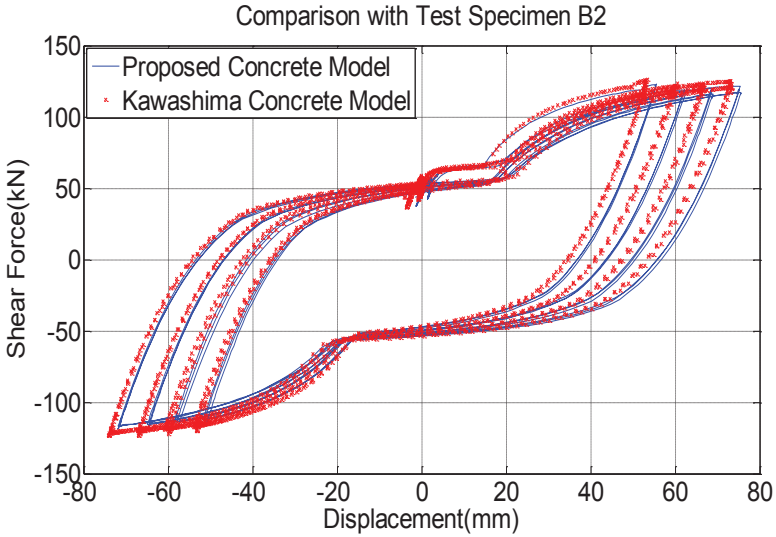

Figure 6-40: Correlation with experimental results B2 (Gallardo-Zafra R. & K. Kawashima, 2009).

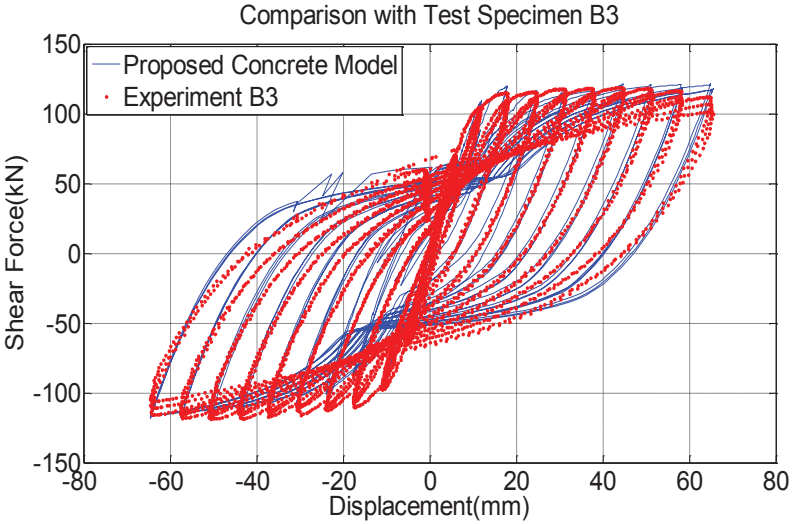

Figure 6-41: Correlation with experimental results B3 (Gallardo-Zafra R. & K. Kawashima, 2009).

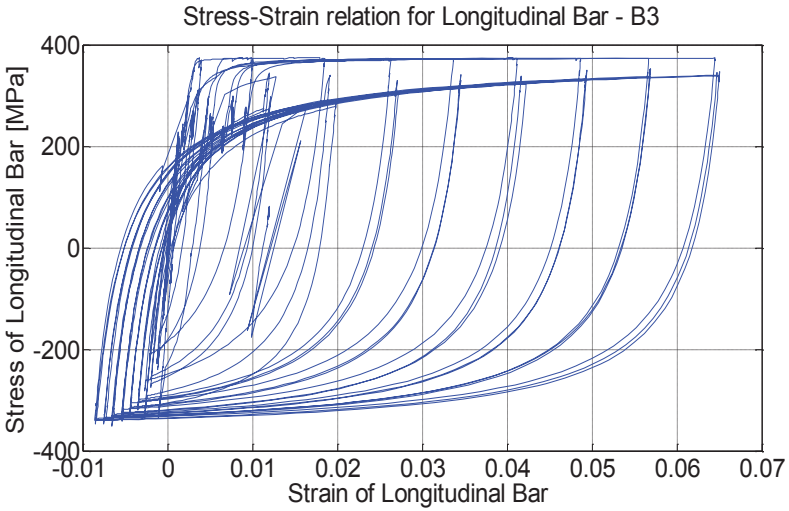

Figure 6-42: Correlation with experimental results B3 (Gallardo-Zafra R. & K. Kawashima, 2009).

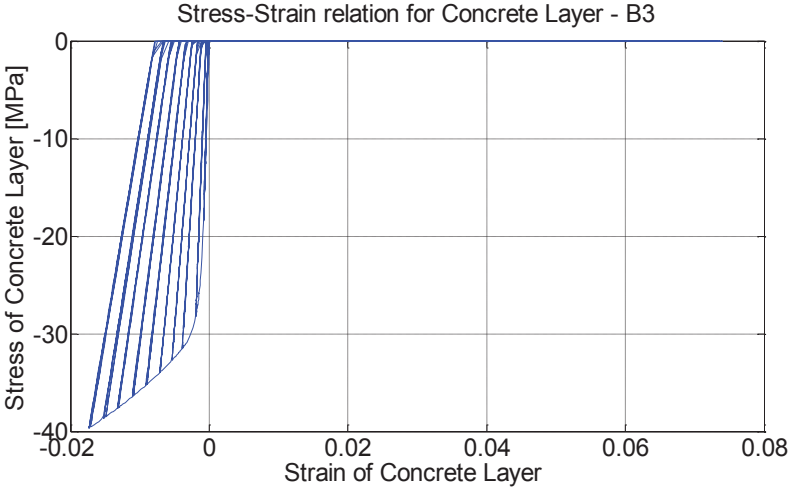

Figure 6-43: Correlation with experimental results B3 (Gallardo-Zafra R. & K. Kawashima, 2009).

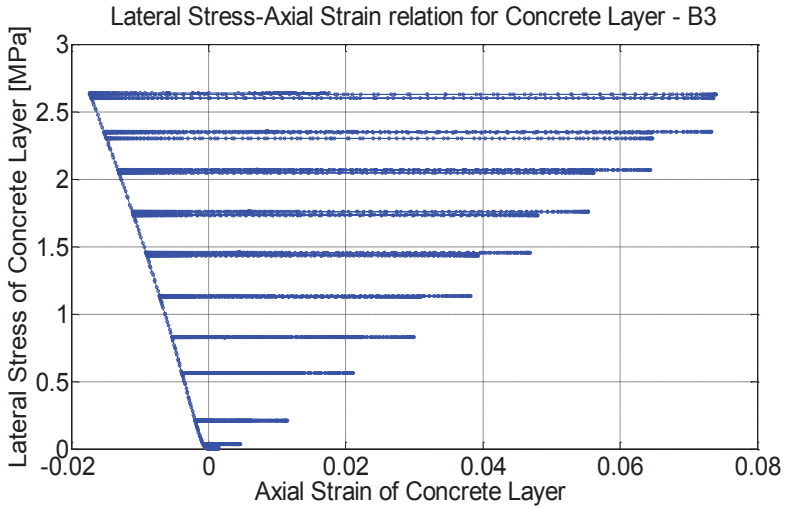

Figure 6-44: Correlation with experimental results B3 (Gallardo-Zafra R. & K. Kawashima, 2009).

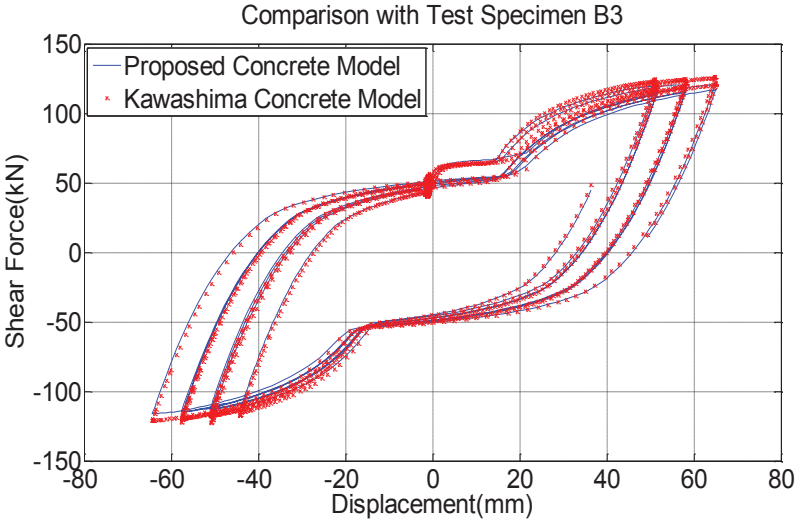

Figure 6-45: Correlation with experimental results B3 (Gallardo-Zafra R. & K. Kawashima, 2009).

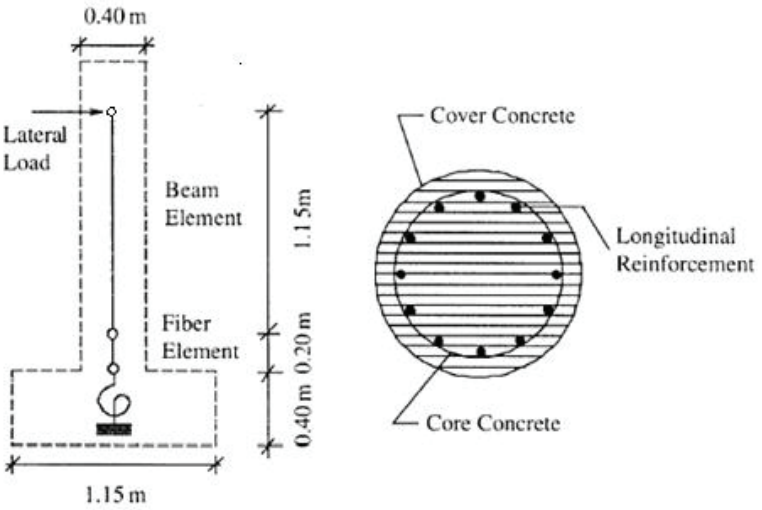

Figure 6-46: Discrete analytical model to simulate the experimental behavior of RC columns by Gallardo-Zafra R. & K. Kawashima, (2009).

The fourth experimental study was performed by Sheikh SA and Yao G (2002) in which twelve 356 mm diameter and 1473 mm long columns were tested under constant axial load and reversed cyclic lateral load that simulated forces from an earthquake. The test specimens were divided into three groups. The first group consisted of four columns that were conventionally reinforced with longitudinal and spiral steel. The second group contained six reinforced concrete columns that were strengthened with carbon fiber-reinforced polymers (CFRP) or glass fiber-reinforced polymers (GFRP) before testing. The last group included two columns that were damaged to a certain extent, repaired with fiber-reinforced polymers (FRP) under axial load and then tested to failure. The correlation with the second group will be provided here. The columns contained six 25 m longitudinal steel bars, and the spirals were made of U.S No 3. (71 mm^2) bars.

The latter experimental program was conducted on FRP-retrofitted columns subjected to a constant axial load and increasing cycles of lateral deformation in single-curvature setup. Four specimens of identical dimensions and steel reinforcements are used from this study. For each level of applied axial load (27% and 54% of the axial load carrying capacity, Po), two columns were retrofitted using two different types of

FRP lamina (carbon CFRP) and glass (GFRP) prior to testing. The experimental moment – curvature responses within the plastic hinge regions are reported along with the numerical results in Figures 6-47 – 6-50. The modeling of the cantilever columns has been done using simply a unique fiber element with a displacement formulation for the entire column and by then reporting the moment curvature response of the most critical section. The comparison seems satisfactory, although the model fails to detect properly the events related to the yielding of stirrups, buckling of longitudinal bars and rupture of FRP as already mentioned in previous experimental correlations. The total moment-curvature response until the last step of numerical convergence is provided below.

An important comment that should be made before concluding is one related to some studies (Gallardo-Zafra and Kawashima 2009, Khaloo et al. 2008) that have reported a different behavior (softening) for FRP and Steel confined concrete in circular RC sections, in respect to the already recognized bilinear one (Carey and Harries 2005). The author attributes that to the small scale of the reinforced concrete specimens used, while the most important explanation which could lead to those results is the influence of concrete strength. According to Mandal et al. (2005) the FRP wraps provide a substantial increase in strength and ductility for low-to-medium-strength concrete, which shows a bilinear stress-strain response with strain hardening. For high-strength concrete, however, enhancement in strength is very limited, with hardly any improvement in ductility. The response in this case shows a steep post-peak strain softening.

It should be emphasised that the last two experimental correlations the modeling of the bridge piers has been performed using the "MatLab Finite Elements for Design Evaluation and Analysis of Structures" (FEDEAS Lab) developed by Professor F. C. Filippou of the Department of Civil and Environmental Engineering of the University of California, Berkeley, USA. Moreover, the two–condition failure criterion of the constitutive model for concrete was deactivated for the comparison with these last two experimental studies.

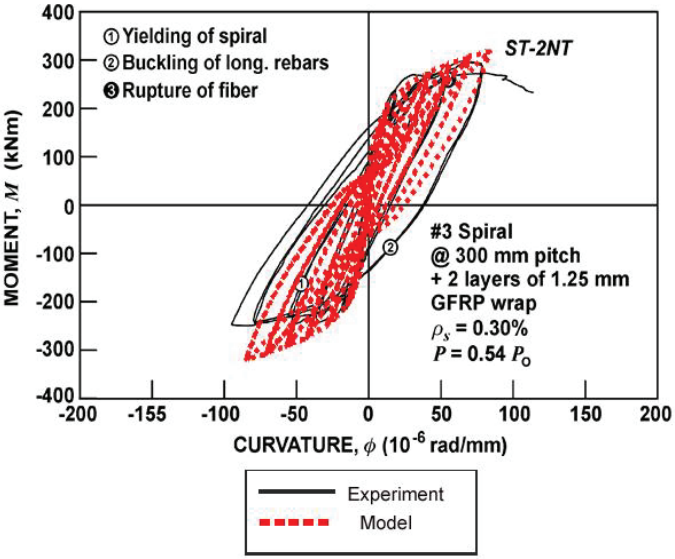

Figure 6-47: Correlation with experimental results ST-2NT (Sheikh SA and Yao G 2002).

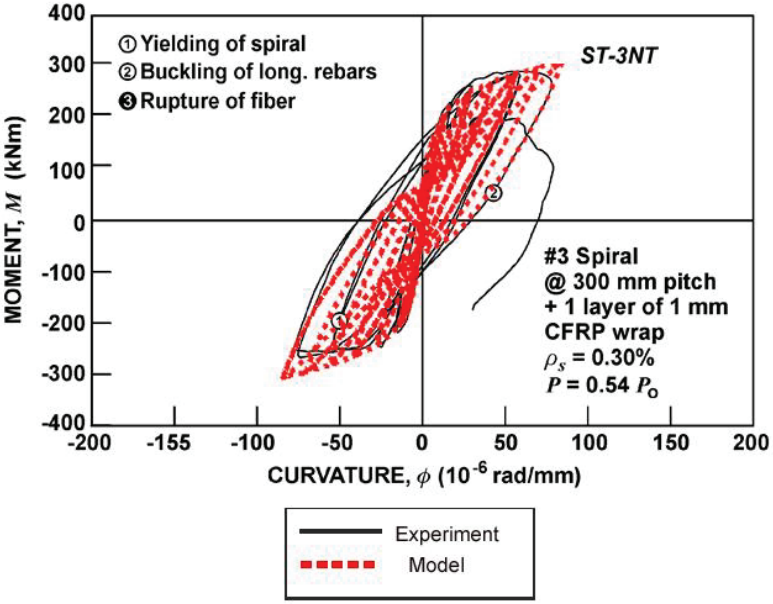

Figure 6-48: Correlation with experimental results ST-3NT (Sheikh SA and Yao G 2002).

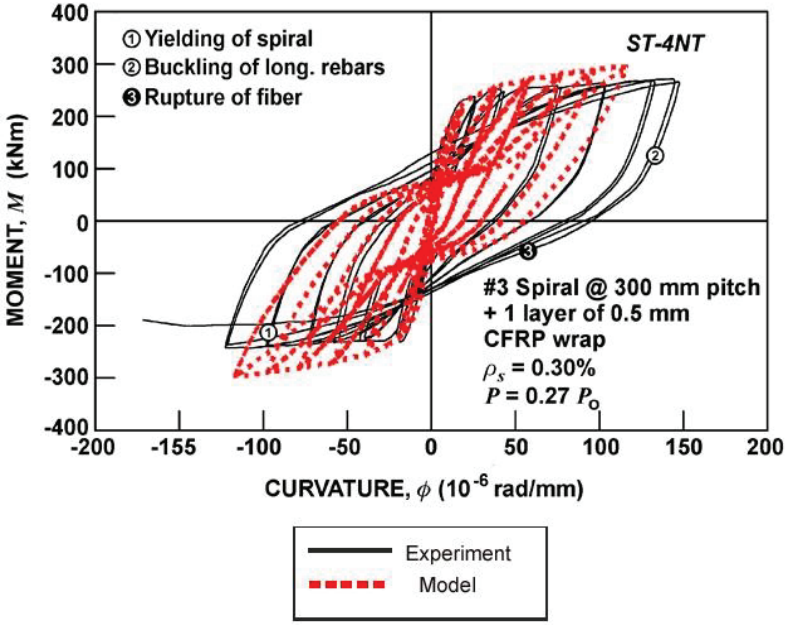

Figure 6-49: Correlation with experimental results ST-4NT (Sheikh SA and Yao G 2002).

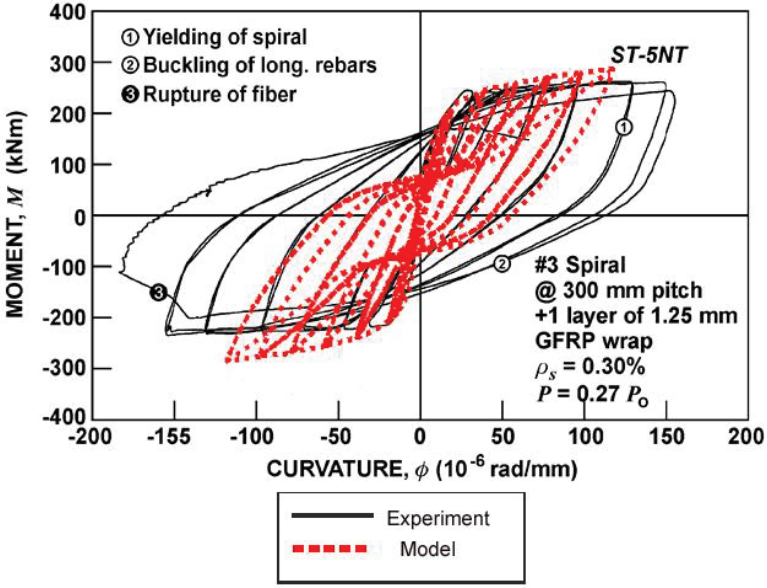

Figure 6-50: Correlation with experimental results ST-5NT (Sheikh SA and Yao G 2002).

Implementation of the Proposed Material Model in OpenSees under the Name "FRPConfinedConcrete"

The library of materials, elements and analysis commands makes *OpenSees* (http://opensees.berkeley.edu/) a powerful tool for numerical simulation of nonlinear structural and geotechnical systems. The Opensees library of components is ever-growing and at the cutting edge of numerical-simulation models. Its interface is based on a command-driven scripting language which enables the user to create more-versatile input files. Opensees is not a black box, making it a useful educational tool for numerical modelling. Material, element or analysis tools can be incorporated into Opensees.

The addition of a new uniaxial material module by the developer is achieved by providing a new C++ subclass of the *UniaxialMaterial* class, along with an interface function which is used to parse the input and create the new material. In contrast to C++, the C and Fortran programming languages' modules provide no information about the state of the model as

an argument to the material routine. Retaining the required information and rejection of the unnecessary information is performed within the material model. This information includes simultaneously (a) parameters, i.e. information needed to define the material, and (b) state variables or history variables, i.e. information needed in order to define its current state and, consequently, compute the applied stress and tangent.

The present Section provides information on the implementation of the introduced in the previous Section's material model for FRP and Steel – confined concrete, in Opensees under the name '*FRPConfinedConcrete'* http://opensees.berkeley.edu/wiki/index.php/FRPConfinedConcrete. To date, the model has no tensile strength and uses the degraded linear unloading/reloading stiffness in the case of cyclic loadings based on the work of Karsan and Jirsa (1969).

The command used in order to construct the uniaxial '*FRPConfinedConcrete'* is provided in the following syntax:

uniaxialMaterial FRPConfinedConcrete $tag $fpc1 $fpc2 $epsc0 $D $c $Ej $Sj $tj $eju $S $fyl $fyh $dlong $dtrans $Es $vo $k $useBuck

Each input parameter defined above corresponds to the mechanical and geometrical properties of the FRP&Steel-confined element which affect its overall performance. Their description is provided in Table 6-2.

Table 6-2: 'FRPConfinedConcrete' input parameters.

1	***tag***	*Material Tag*
2	***fpc1***	*Concrete Core Compressive Strength*
3	***fpc2***	*Concrete Cover Compressive Strength*
4	***epsc0***	*Strain Corresponding to Unconfined Concrete Strength*
5	***D***	*Diameter of the Circular Section*
6	***c***	*Dimension of Concrete Cover*
7	***Ej***	*Elastic Modulus of the Jacket*
8	***Sj***	*Clear Spacing of the FRP Strips - zero if it's continuous*
9	***tj***	*Total Thickness of the FRP Jacket*

10	***eju***	*Rupture Strain of the Jacket*
11	***S***	*Spacing of the Stirrups*
12	***fyl***	*Yielding Strength of Longitudinal Steel Bars*
13	***fyh***	*Yielding Strength of the Hoops*
14	***dlong***	*Diameter of the Longitudinal Bars*
15	***dtrans***	*Diameter of the Stirrups*
16	***Es***	*Steel's Elastic Modulus*
17	***vo***	*Initial Poisson's Coefficient for Concrete*
18	***k***	*Reduction Factor (0.5-0.8) for the Rupture Strain of the FRP Jacket*
19	***useBuck***	*FRP Jacket Failure Criterion due to Buckling of Longitudinal Compressive Steel Bars (0 = not include it, 1= to include it)*

Before concluding, Table 6-3 is provided below with all the symbols declared in the presentation of the proposed model in the previous Sections for better comprehension of the described procedure and results.

Table 6-3: Symbols used in the proposed material model and its correlation with experimental results.

C	*circumference of the circular section*
R	*radius of the circular section*
k	*reduction factor*
ε_r	*radial strain*
ε_c	*circumferential strain*
ε_V	*volumetric strain*
ε_{con}	*concrete's axial strain*

ε_{co}	*concrete's axial strain at unconfined concrete's strength*
ε_{cc}	*concrete's axial strain at confined concrete's strength*
$\varepsilon_{c.core}$	*circumferential strain of the core*
$\varepsilon_{r.core}$	*radial strain of the core*
$\varepsilon_{r.cover}$	*radial strain of the cover*
R_{core}	*radius of the concrete core*
c	*concrete cover*
f_{co}	*concrete strength*
f_{cc}	*confined concrete strength*
v_o	*initial Poisson's coefficient for concrete*
v	*Poisson's coefficient for concrete*
ρ_{sh}	*steel hoop's volumetric ratio*
ρ_j	*FRP jacket's volumetric ratio*
G_{core}	*shear modulus of concrete core*
τ_{core}	*shear stress of concrete core*
$f_{l.core}$	*lateral confining pressure of the concrete core*
$f_{l.cover}$	*lateral confining pressure of the concrete cover*
$f_{l.steel}$	*lateral confining pressure of the steel reinforcement*
$f_{c.av}$	*average axial concrete stress*
$f_{c.core}$	*axial concrete core stress*

$f_{c.cover}$	*axial concrete cover stress*
$f_{cc.core}$	*axial confined concrete core strength*
$f_{cc.cover}$	*axial confined concrete cover strength*
A_{core}	*area of concrete core*
A_{cover}	*area of concrete cover*
f_l	*lateral confining pressure of concrete*
f_c	*axial concrete stress*
E_{con}	*modulus of elasticity of concrete*
E_{sec}	*secant modulus of elasticity of concrete*
β	*a property of concrete evaluated as a function of the unconfined concrete strength*
D_b	*bar diameter*
L_{buck}	*buckling length*
EI	*Flexural rigidity of steel longitudinal bar*
EI_{red}	*Reduced flexural rigidity of steel longitudinal bar*
E_s	*modulus of elasticity for steel*
P	*axial force*
k'	*foundation modulus*
v	*vertical displacement*
m	*buckling mode*
n	*number of stirrups*

S	*Spacing of the stirrups*
P_{cr}	*critical load*
A_{tot}	*total area of the circular section*
A_{sh}	*area of steel hoops (ties)*
I_b	*longitudinal bar's moment of inertia*
f_{yl}	*yielding strength of longitudinal bar*
w	*transversal displacement of the bar*
ε_{sl}	*axial strain in the bar*
ε_{sh}	*steel hoop's strain*
ε_{shu}	*ultimate steel hoop's strain*
ε_{yh}	*steel hoop's strain for yielding*
k_{sl}	*Partial confinement coefficient for steel*
ξ_l	*coefficient taking into account longitudinal bar's confining effect*
ξ_{st}	*coefficient taking into account the confining effect of stirrups' spacing*
D_h	*hoop's diameter*
k_j	*partial wrapping coefficient*
A_b	*total area of longitudinal steel reinforcement*
A_g	*gross area of the section*
S_j	*jacket's clear spacing*

E_j	*jacket's modulus*
t_j	*thickness of the jacket*
$\varepsilon_{c.buck}$	*jacket's circumferential strain due to buckling of longitudinal bars*
$\varepsilon_{cu.exp}$	*experimental ultimate strain for concrete*
$\varepsilon_{j.rup.sg}$	*jacket's rupture strain read by strain gages*
$\varepsilon_{j.rup.coup}$	*jacket's rupture strain by coupons' test*
$\varepsilon_{j.rup.nom}$	*nominal jacket's rupture strain given in material properties*
$\varepsilon_{j.mod.dil}$	*jacket's strain calculated by the model due to concrete's dilation*
$\varepsilon_{j.mod.buck}$	*jacket's strain calculated by the model due to buckling of longitudinal bars*
d_b	*diameter of longitudinal bars*
d_t	*diameter of transverse stirrups*
s	*spacing of transverse stirrups*

CHAPTER SEVEN

CONCLUSIONS

Clearly, based on the preceding Chapters, the state of the art in modeling the lateral load response of columns leaves a lot to be desired: improved response estimation of the behavior of columns that are susceptible to shear failure after flexural yielding; better procedures to estimate shear strength, and the pattern of degradation thereof with increasing displacement ductility; the need to account for reinforcement pullout and its effects on stiffness; the shape of the hysteresis loops; the detrimental effects of axial load at large displacement limits; and the magnitude of deformation (drift ratio) associated with milestone events in the response curve of the column member are open issues that need to be settled before the performance-based assessment framework may be considered complete and dependable.

In this direction, the definition of the deformability of RC columns was reassessed in this book by proposing a new methodology for the determination of plastic hinge length through a consideration of yield penetration effects. Yield penetration occurs from the critical section towards both the shear span and the support of columns; physically it refers to the extent of the nonlinear region and determines the pullout slip measured at the critical section. Contrary to the fixed design values adopted by codes of assessment, the yield penetration length is actually the only consistent definition of the notion of the plastic hinge length, whereas the latter determines the contribution of pullout rotation to column drift and column stiffness. In order to establish the plastic hinge length in a manner consistent to the above definition, this book pursued the explicit solution of the field equations of bond over the shear span of a column. Through this approach, the bar strain distributions and the extent of yield penetration from the yielding cross section towards the shear span were resolved and calculated analytically. By obtaining this solution, a consistent definition of plastic hinge length was established, by reference to the state of reinforcement strain (replacing the stress based definition used previously). The true parametric sensitivities of this design variable for practical use in the seismic assessment of existing structures are

illustrated. The numerical results show good agreement with the experimental evidence and are consistent with the experimental trends supported by test databases, confirming that the plastic hinge length is controlled by the residual bond that may be mobilized along the yielded reinforcement.

In addition, a force-based fiber beam-column element accounting for shear effects and the effect of tension stiffening was developed, in order to provide an analytical test-bed for simulation and improved understanding of experimental cases where testing of reinforced concrete columns actually led to collapse. The developed fiber-element is incorporated in the stand-alone Windows program Phaethon with the user's interface written in C++ programming language code. The latter offers its user the possibility to obtain the capacity curve for shear-critical reinforced concrete cantilever columns whilst taking into account the shear–flexure interaction mechanism, as well as an important contribution to the final column's lateral displacement of the pull-out of the inadequate anchorage of the tensile longitudinal reinforcing bars of the column. This is available for both rectangular and circular reinforced concrete columns. Furthermore, the software resolves strain, slip and bond distributions along the anchorage length. Comparison with experimental results from the literature verifies the capability of this Windows software tool to assess the strength and deformation indices of shear-critical reinforced concrete columns. Moreover, the moment curvature as well as the shear force – shear strain analysis of the sections of these columns is also possible, all based on the Modified Compression Field Theory.

Finally, confining wraps or jackets to rehabilitate and strengthen existing substandard RC columns as with those described in the present book has proven to be an efficient technique for seismic retrofit of structures. However, most of the compressive strength models of confined concrete only consider the increased strength and ductility provided by fiber reinforced polymers (FRPs), neglecting the contribution of the existing steel reinforcement inside the column's section. Even if the existing steel stirrups in a reinforced concrete column are not sufficient to confine the concrete core, they must also contribute, along with the FRP jacket, in confining the section. Therefore, the FRP-confined concrete model contained in a well-known Bulletin by the International Federation for Structural Concrete (*fib*) has been enhanced to take into account the confining effect of the already existing steel reinforcement when retrofitting a reinforced concrete column with FRP jacketing. To this end, the transverse steel reinforcement has been considered not as imposing a constant value of confining pressure, but rather, following the steel's

stress-strain law at each deformation step in accordance with the BGL model, while also considering the confining contribution of longitudinal reinforcement. Similar to the BGL model, an important aspect of the model is that the cross-section tangential stresses (shear), which are generally neglected, have an essential role in ensuring plane strain conditions. In addition, compatibility in the lateral direction, inwards for confining pressures and outwards for lateral strains, between the two confining materials (FRP and Steel) has been established. Through this approach the difference in the lateral behavior of the concrete cover (confined with the jacket's pressure) and the concrete core (confined by both the steel's and FRP's pressure) has been considered. This allows the application of the model also in cases of reinforcement repair and FRP retrofit where two different concrete strengths should be considered; one for the new layer of concrete applied externally and the other for the old concrete in the concrete core which may also be cracked due to former seismic loading. Moreover, in the case of RC column modeling with a fiber nonlinear beam-column element (displacement formulation), apart from the immediate incorporation of shear deformations (uncoupled from the normal ones) on the material level (and in contrast to the standard fiber beam-column formulation), the averaged response of the two different regions—concrete core and concrete cover—in the section, gives a clear advantage in terms of modeling since it allows the assignment of a unique stress-strain law for all the fibers/layers of the circular section. Before concluding, another aspect that seems to be valid and important for further thought is that the response of the seismic retrofitted RC columns in this study based on the model presented is correct although these columns are under cyclic excitation and contrary to the model's assumptions which are clearly static (monotonic). Moreover, the model uses the idea of the superposition of the effects of confinement that extend further the linear assumptions. In addition, a two-condition failure criterion has been incorporated regarding the dilation of concrete and buckling of compressive longitudinal bars as independent events. Correlation with experimental results seems to be satisfactory, although the model has moderate success in predicting the actual instance of rupture of the FRP jacket. Finally, this recently developed material model for FRP and Steel–confined concrete was implemented in OpenSees under the name '*FRPConfinedConcrete'* with no tensile strength and degraded linear unloading/reloading stiffness in the case of cyclic loadings.

Appendix to Chapter Three

This is an Appendix to Chapter 3.

Table A-1: Reinforced concrete columns with a circular cross section that failed in flexure.

Specimen ID in Database	Axial Load (KN)	Diameter (mm)	Cover to Ctr. of Hoop Bar (mm)	Shear Span (mm)	Concrete Strength (MPa)	Number of Longitudinal Bars	Diameter of Long. Bars (mm)	Yield Strength of Long. Bars (MPa)	Ultim. Strength of Long. Bars (MPa)	Longitudinal Reinforc. ratio (%)	Hoop Spacing (mm)	Spiral Diameter (mm)	Yielding Strength Spiral (MPa)	Transverse Reinforc. ratio (%)
43	907	400	20	800	38	20	16	423	577	3.2	60	10	300	1.42
45	1813	400	20	800	37	20	16	475	625	3.2	60	10	300	1.42
46	145	307	36	1910	38.8	12	12	240	-	1.83	75	6	240	0.63
47	254	307	36	1910	36.2	12	12	240	-	1.83	75	6	240	0.63
50	151	152	10.2	1140	34.5	8	12.7	448	-	5.57	22	3.7	620	1.45
51	151	152	10.2	570	34.5	8	12.7	448	-	5.57	22	3.7	620	1.45
52	220	152	10.2	570	34.5	8	12.7	448	-	5.57	22	3.7	620	1.45
53	4450	1520	58.7	9140	35.8	25	43	475	-	1.99	89	15.9	493	0.63
54	4450	1520	60.3	4570	34.3	25	43	475	-	1.99	54	19.1	435	1.49
55	120	250	9.9	750	24.1	25	7	446	-	1.98	9	3.1	441	1.41
56	239	250	9.9	750	23.1	25	7	446	-	1.98	9	3.1	441	1.41
57	120	250	9.7	1500	25.4	25	7	446	-	1.98	14	2.7	476	0.68
58	120	250	9.9	750	24.4	25	7	446	-	1.98	9	3.1	441	1.41
59	239	250	9.9	750	24.3	25	7	446	-	1.98	9	3.1	441	1.41

60	120	250	9.7	1500	23.3	25	7	446	-	1.98	14	2.7	476	0.68
93	200	305	14.5	1372	29	21	9.5	448	690	2.04	19	4	434	0.94
94	200	305	14.5	1372	29	21	9.5	448	690	2.04	19	4	434	0.94
95	222	305	14.5	1372	35.5	21	9.5	448	690	2.04	19	4	434	0.94
96	222	305	14.5	1372	35.5	21	9.5	448	690	2.04	19	4	434	0.94
97	222	305	14.5	1372	35.5	21	9.5	448	690	2.04	19	4	434	0.94
98	222	305	14.5	1372	32.8	21	9.5	448	690	2.04	19	4	434	0.94
99	222	305	14.5	1372	32.8	21	9.5	448	690	2.04	19	4	434	0.94
100	222	305	14.5	1372	32.5	21	9.5	448	690	2.04	19	4	434	0.94
101	200	305	14.5	1372	27	21	9.5	448	690	2.04	19	4	434	0.94
102	200	305	14.5	1372	27	21	9.5	448	690	2.04	19	4	434	0.94
103	200	305	14.5	1372	27	21	9.5	448	690	2.04	19	4	434	0.94
106	1780	610	27.76	3660	41.1	20	22.23	455	746	2.66	57	9.5	414	0.89
107	1928	457	24.76	910	38.3	20	15.875	427.5	-	2.41	60	9.5	430.2	1.14
109	970	457	24.76	910	39.4	20	15.875	427.5	-	2.41	60	9.5	430.2	1.14
112	1914	457	26.35	910	35	30	19.05	486.2	-	5.21	40	12.7	434.4	3.04
113	1780	457	30.16	3656	36.6	30	15.875	477	-	3.62	76	9.5	445	0.92
114	1780	457	30.16	3656	40	30	15.875	477	-	3.62	51	6.4	437	0.6
115	1780	457	30.16	3656	38.6	30	15.875	477	-	3.62	76	9.5	445	0.92
116	654	609.6	22.23	2438.4	31	22	15.875	461.965	630	1.49	31.75	6.4	606.76	0.7
117	654	609.6	22.23	4876.8	31	22	15.875	461.965	630	1.49	31.75	6.4	606.76	0.7
118	654	609.6	22.23	6096	31	22	15.875	461.965	630	1.49	31.75	6.4	606.76	0.7
119	654	609.6	22.23	2438.4	31	11	15.875	461.965	630	0.75	31.75	6.4	606.76	0.7
120	654	609.6	22.23	2438.4	31	44	15.875	461.965	630	2.98	31.75	6.4	606.76	0.7

121	912	609.6	28.58	1828.8	34.5	28	19.05	441.28	602	2.73	25.4	6.4	606.76	0.89
122	912	609.6	28.58	4876.8	34.5	28	19.05	441.28	602	2.73	25.4	6.4	606.76	0.89
123	912	609.6	28.58	6096	34.5	28	19.05	441.28	602	2.73	25.4	6.4	606.76	0.89
125	400	600	30.16	1800	34.6	14	22.225	448	739	1.92	97	9.5	431	0.54
126	400	600	30.16	1800	33	14	22.225	461	775	1.92	64	9.5	434	0.81
127	1000	250	13.75	1645	65	8	16	419	-	3.28	50	7.5	1000	1.54
128	1000	250	15.65	1645	65	8	16	419	-	3.28	50	11.3	420	3.49
130	1850	250	14	1645	90	8	16	419	-	3.28	50	8	580	1.75
131	1850	250	15.65	1645	90	8	16	419	-	3.28	100	11.3	420	1.74
132	925	250	13.75	1645	90	8	16	419	-	3.28	50	7.5	1000	1.54
133	1850	250	13.75	1645	90	8	16	419	-	3.28	50	7.5	1000	1.54
141	1308	609.6	22.23	2438.4	37.2	22	15.875	462	-	1.49	31.75	6.4	606.76	0.7
142	654	609.6	22.23	2438.4	37.2	22	15.875	462	-	1.49	63.5	6.4	606.76	0.35
143	1779	609.6	20	3657	32.6	26	19.05	315.1	497.8	2.54	127	6.4	351.6	0.17
157	0	406.4	14.96	1854.2	36.5	12	12.7	458.5	646	1.17	31.75	4.5	691.5	0.53
158	0	406.4	14.96	1854.2	36.5	12	12.7	458.5	646	1.17	31.75	4.5	691.5	0.53

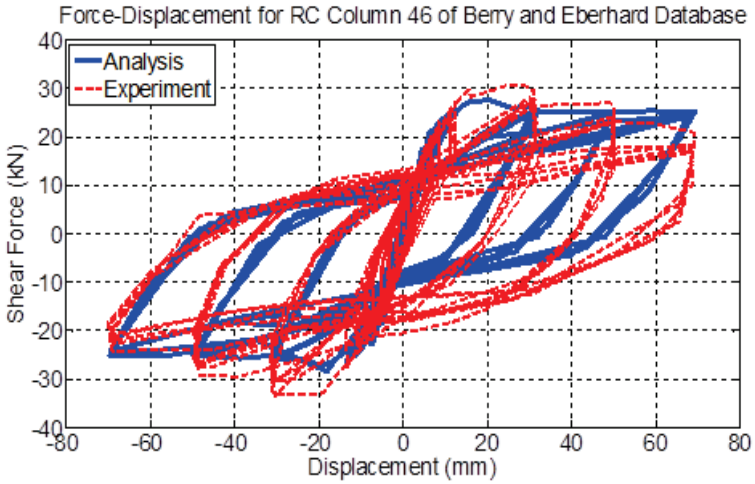

Concrete Model: Scott et al., 1982.

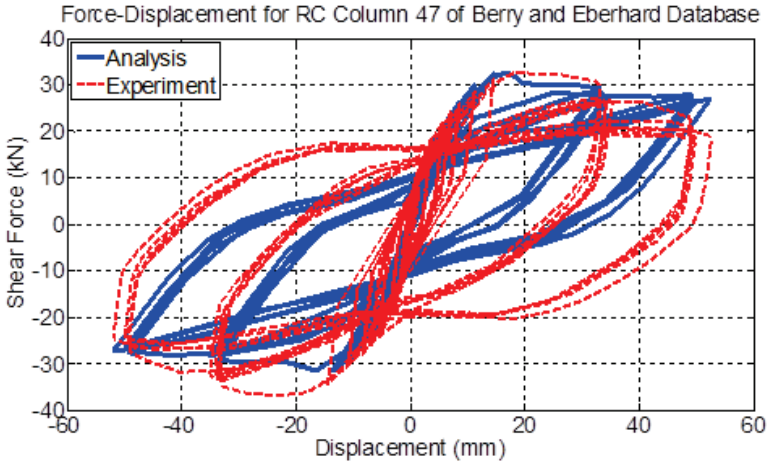

Figure A-1: Comparison between numerical and experimental responses of circular columns (ID#46&47) of Berry and Eberhard Database (2004).

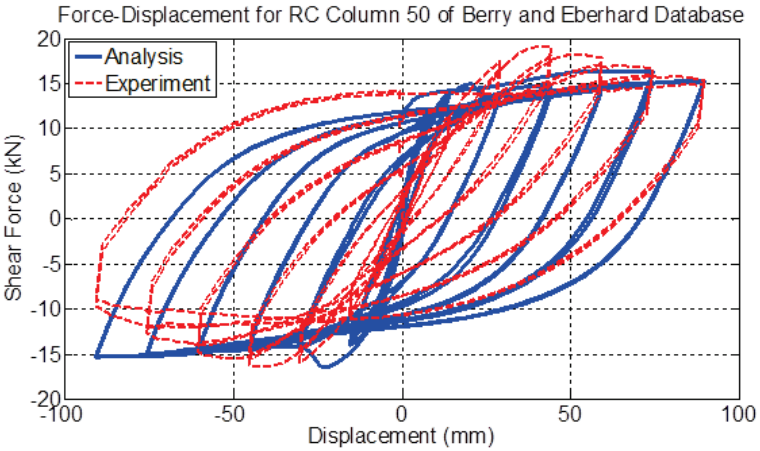

Concrete Model: Scott et al., 1982.

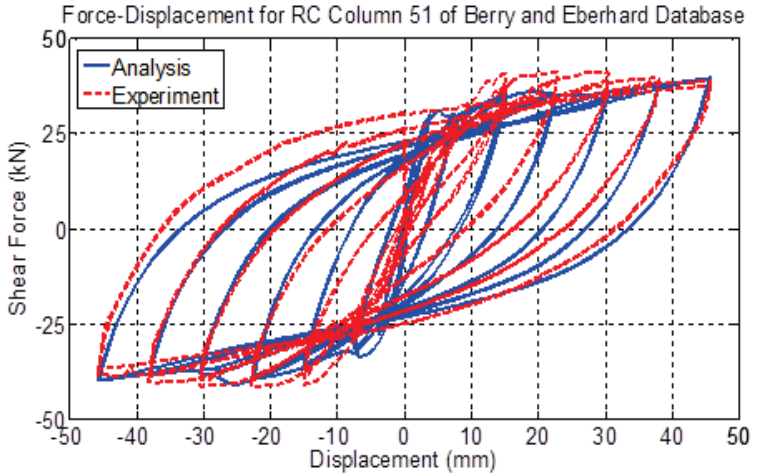

Figure A-2: Comparison between numerical and experimental responses of circular columns (ID#50&51) of Berry and Eberhard Database (2004).

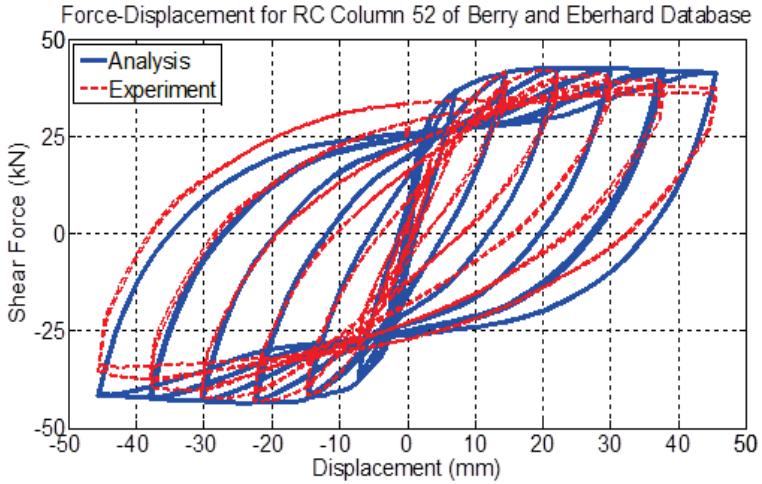

Concrete Model: Mander et al., 1988.

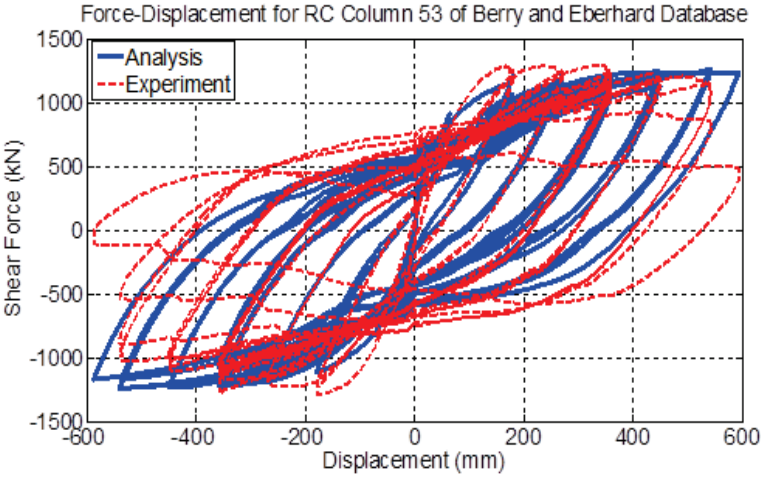

Figure A-3: Comparison between numerical and experimental responses of circular columns (ID#52&53) of Berry and Eberhard Database (2004).

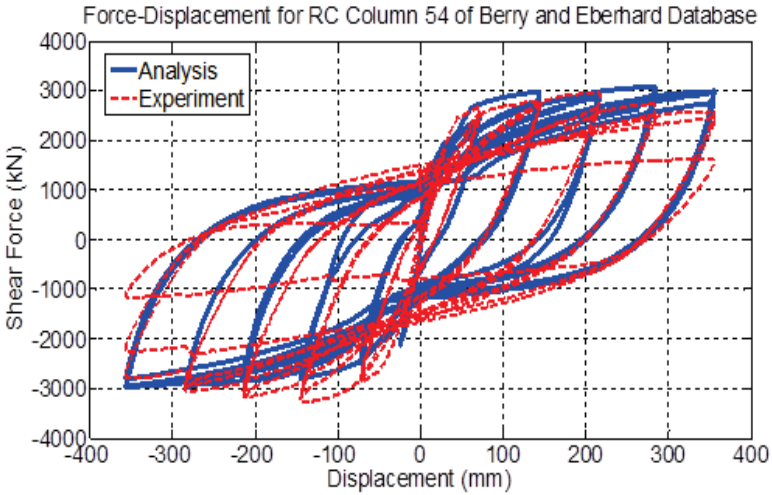

Concrete Model: Mander et al., 1988.

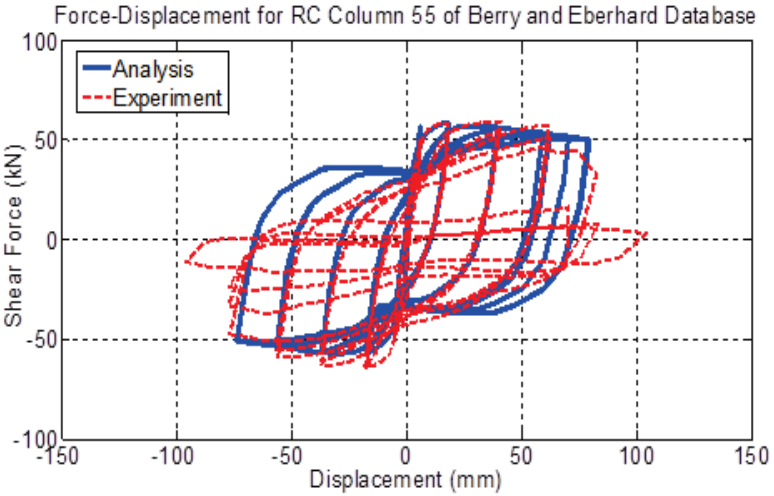

Figure A-4: Comparison between numerical and experimental responses of circular columns (ID#54&55) of Berry and Eberhard Database (2004).

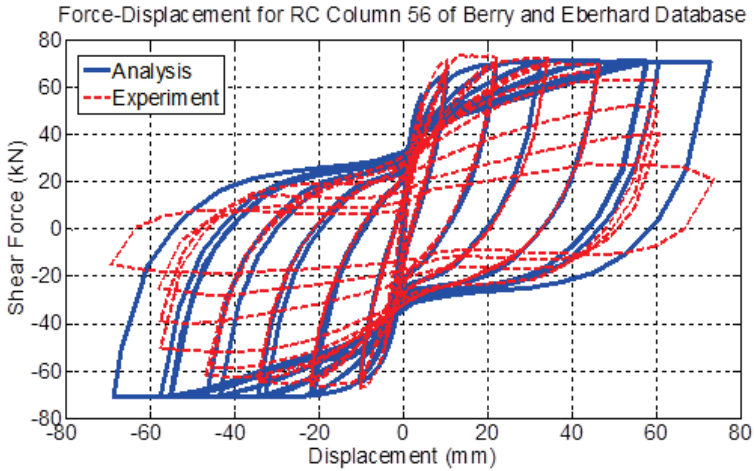

Concrete Model: Mander et al., 1988.

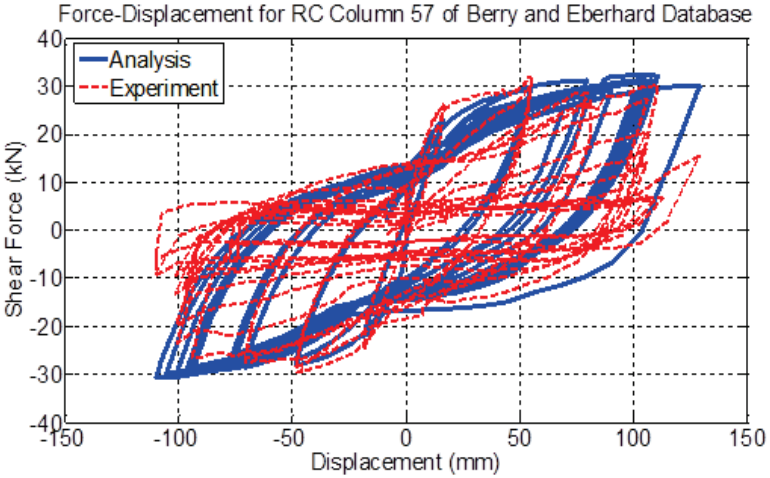

Figure A-5: Comparison between numerical and experimental responses of circular columns (ID#56&57) of Berry and Eberhard Database (2004).

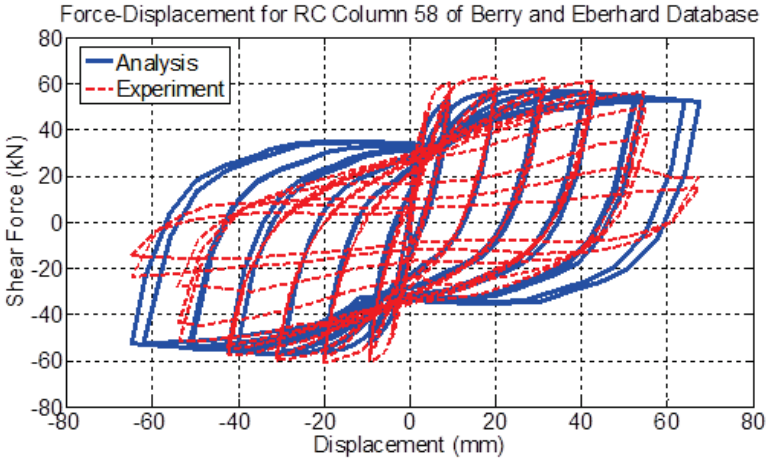

Concrete Model: Mander et al., 1988.

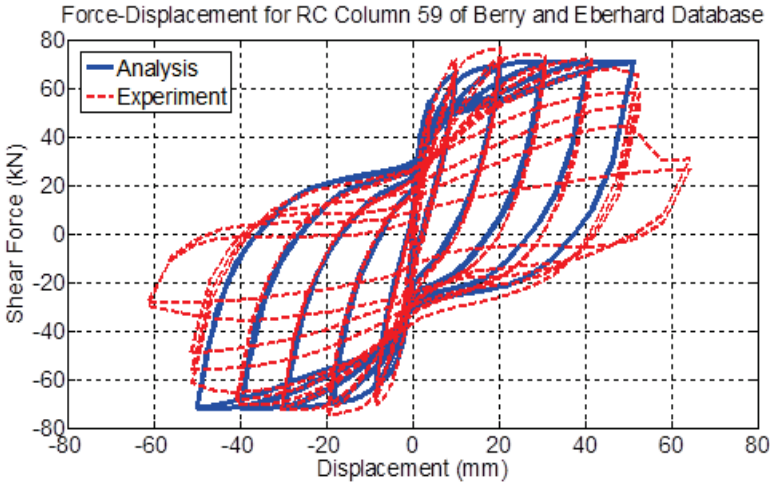

Figure A-6: Comparison between numerical and experimental responses of circular columns (ID#58&59) of Berry and Eberhard Database (2004).

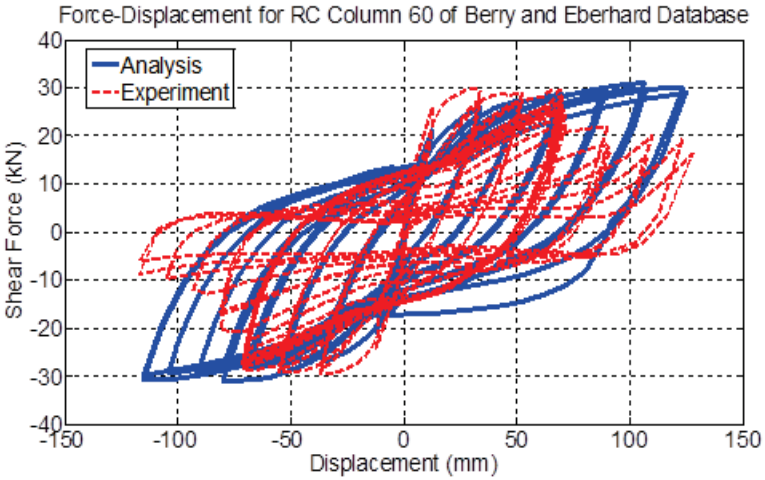

Concrete Model: Mander et al., 1988.

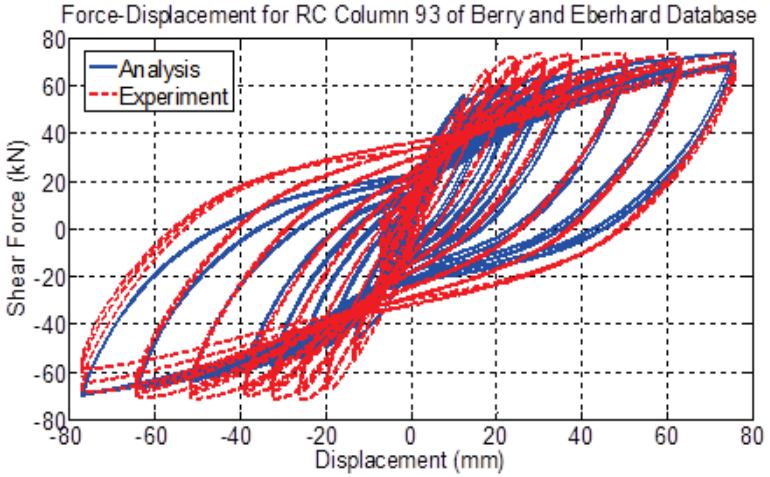

Figure A-7: Comparison between numerical and experimental responses of circular columns (ID#60&93) of Berry and Eberhard Database (2004).

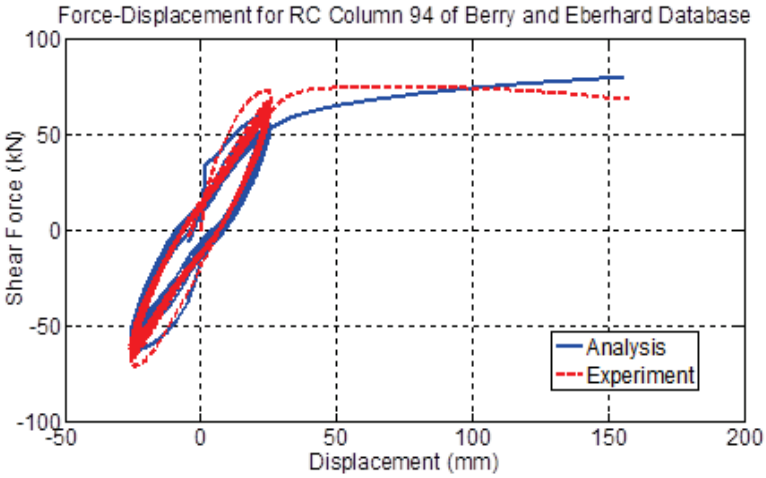

Concrete Model: Mander et al., 1988.

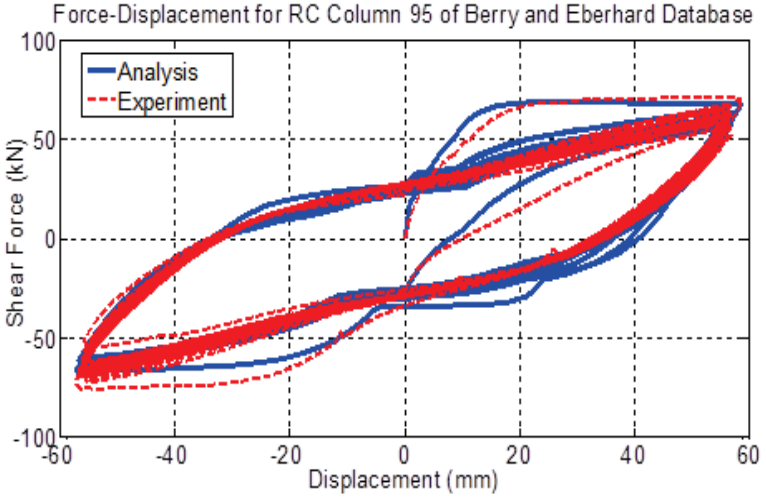

Figure A-8: Comparison between numerical and experimental responses of circular columns (ID#94&95) of Berry and Eberhard Database (2004).

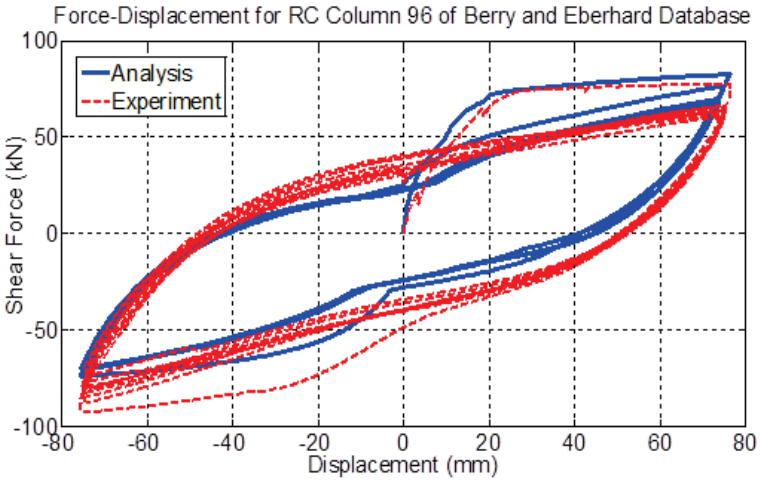

Concrete Model: Mander et al., 1988.

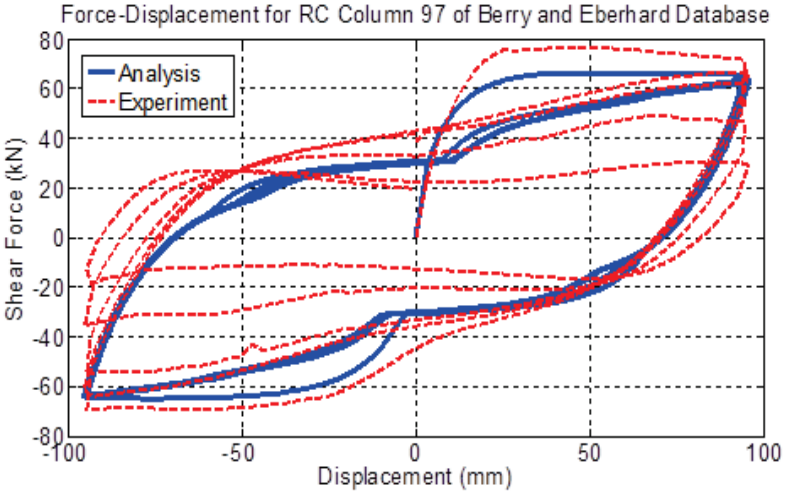

Figure A-9: Comparison between numerical and experimental responses of circular columns (ID#96&97) of Berry and Eberhard Database (2004).

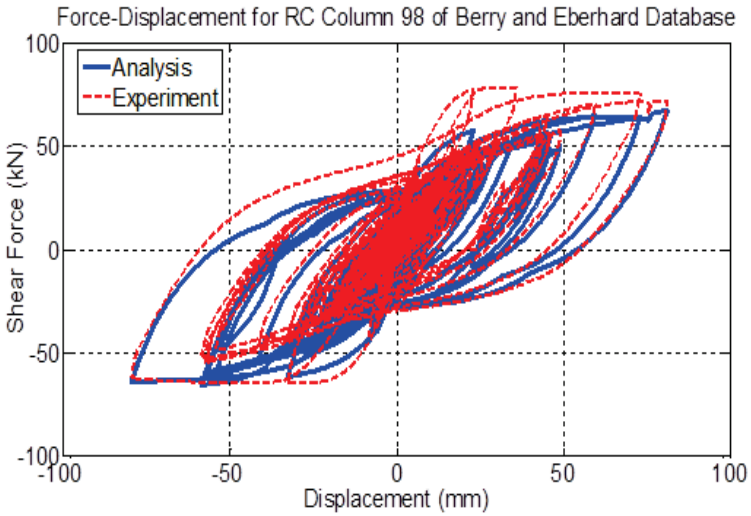

Concrete Model: Mander et al., 1988.

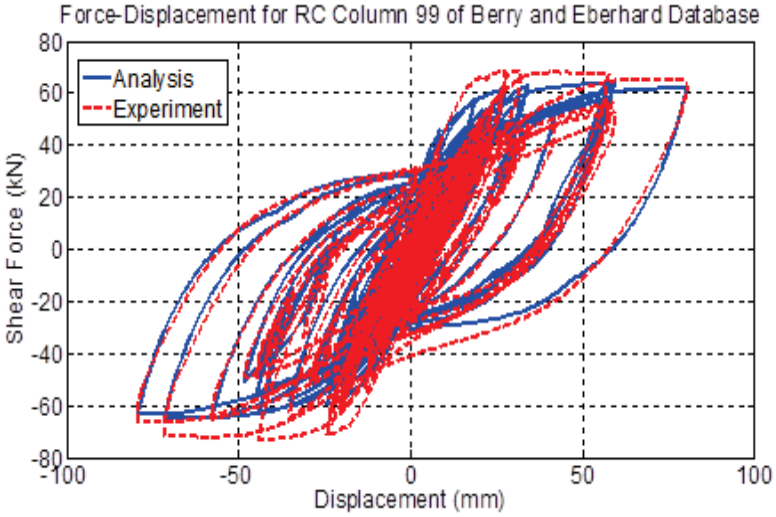

Figure A-10: Comparison between numerical and experimental responses of circular columns (ID#98&99) of Berry and Eberhard Database (2004).

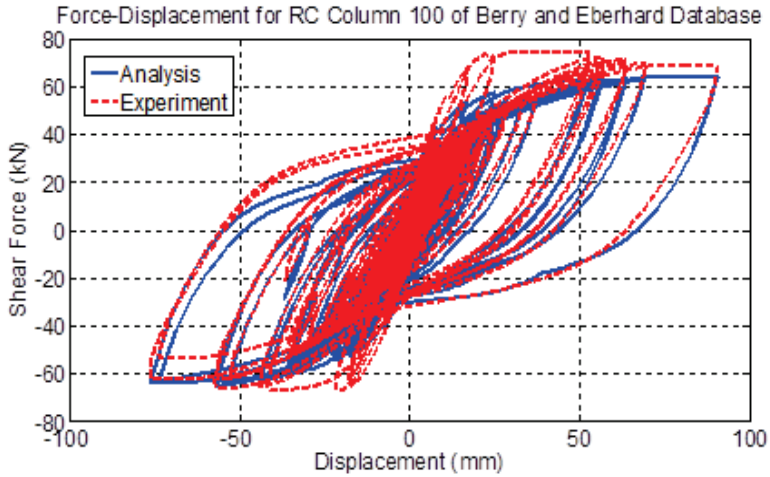

Concrete Model: Mander et al., 1988.

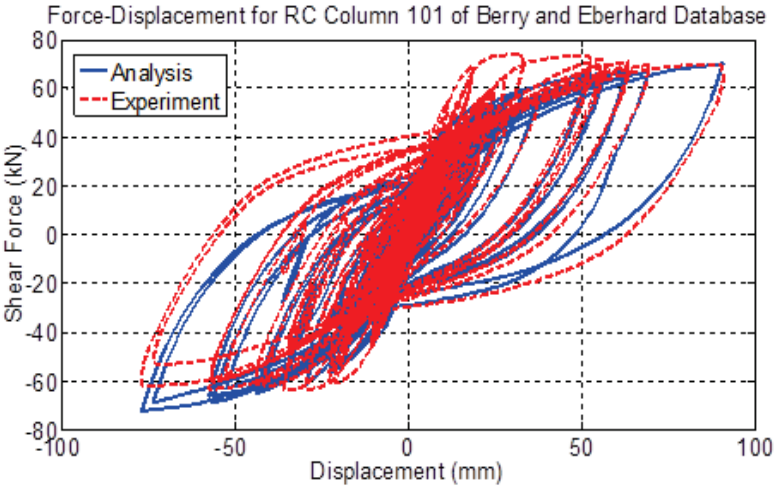

Figure A-11: Comparison between numerical and experimental responses of circular columns (ID#100&101) of Berry and Eberhard Database (2004).

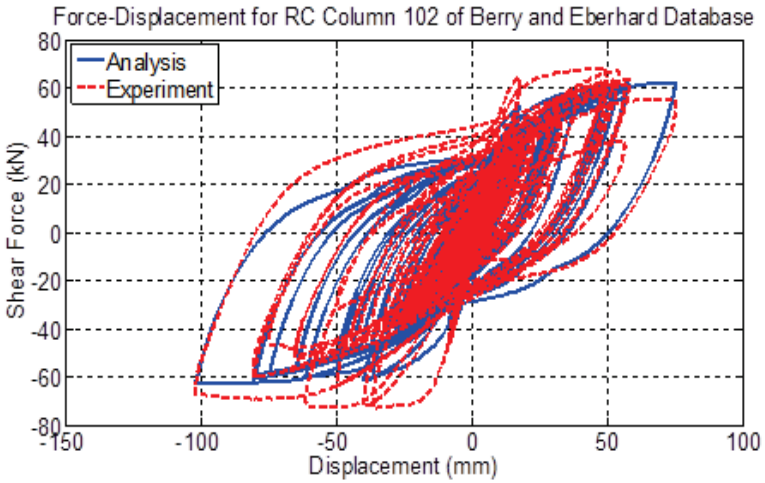

Concrete Model: Mander et al., 1988.

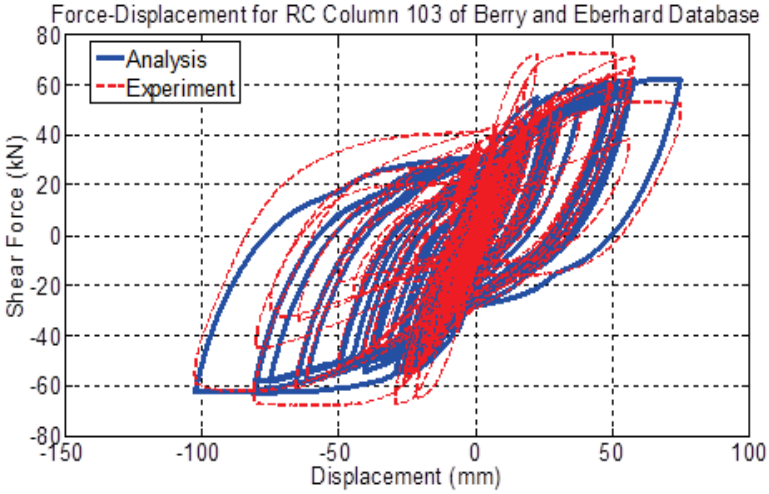

Figure A-12: Comparison between numerical and experimental responses of circular columns (ID#102&103) of Berry and Eberhard Database (2004).

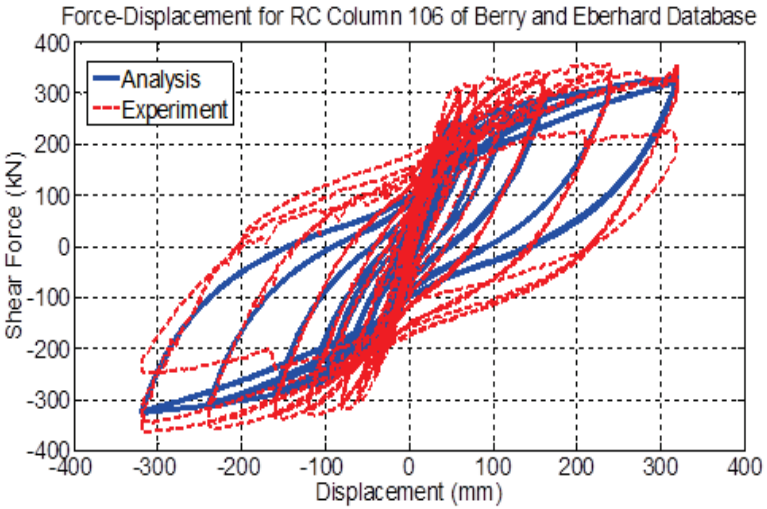

Concrete Model: Mander et al., 1988.

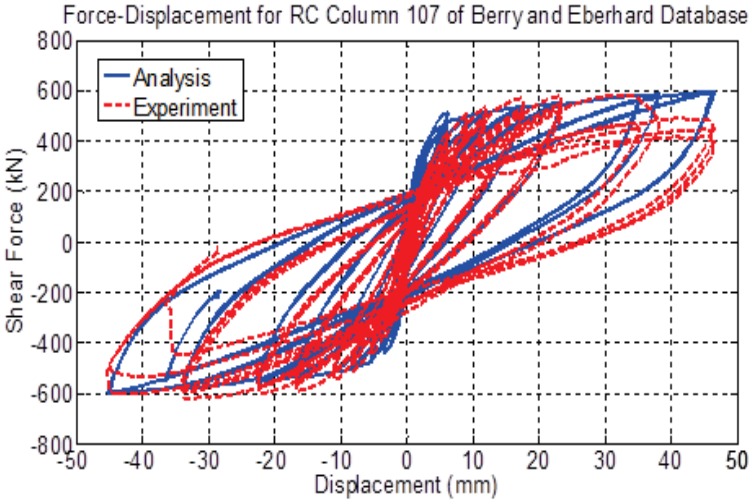

Figure A-13: Comparison between numerical and experimental responses of circular columns (ID#106&107) of Berry and Eberhard Database (2004).

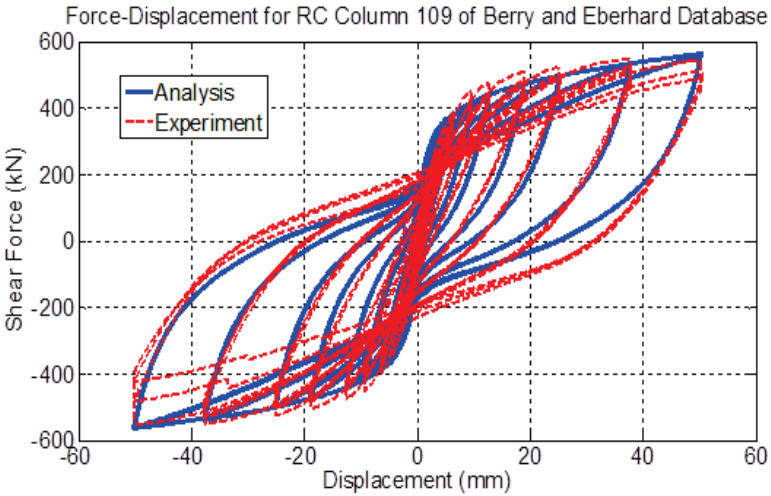

Concrete Model: Mander et al., 1988.

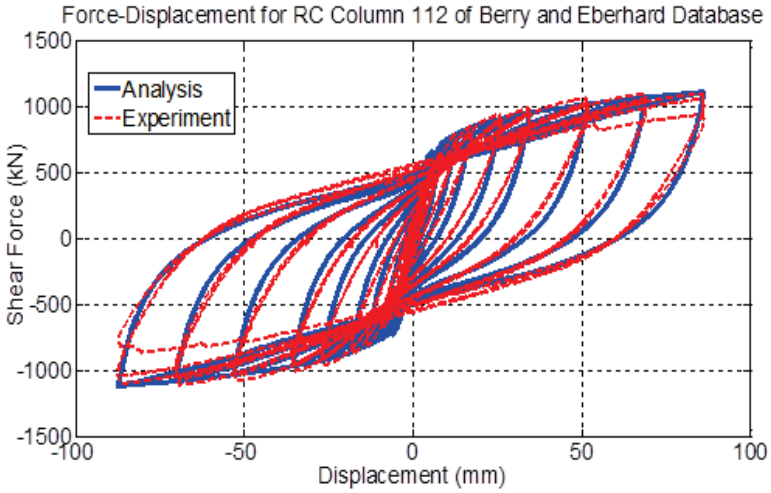

Figure A-14: Comparison between numerical and experimental responses of circular columns (ID#109&112) of Berry and Eberhard Database (2004).

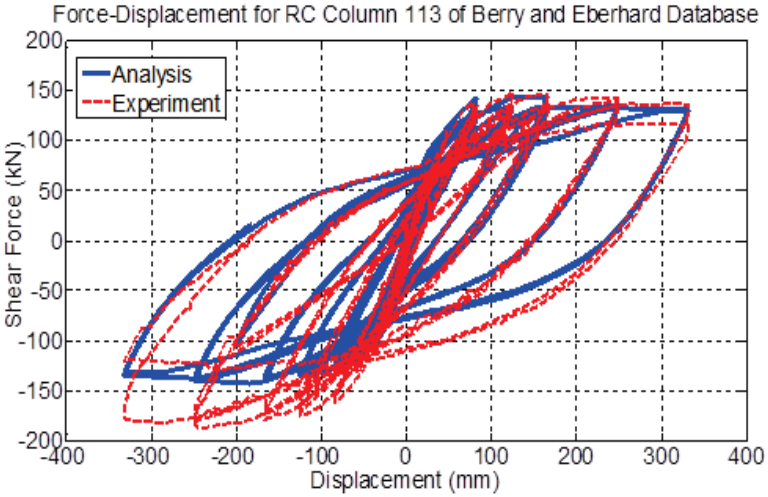

Concrete Model: Mander et al., 1988.

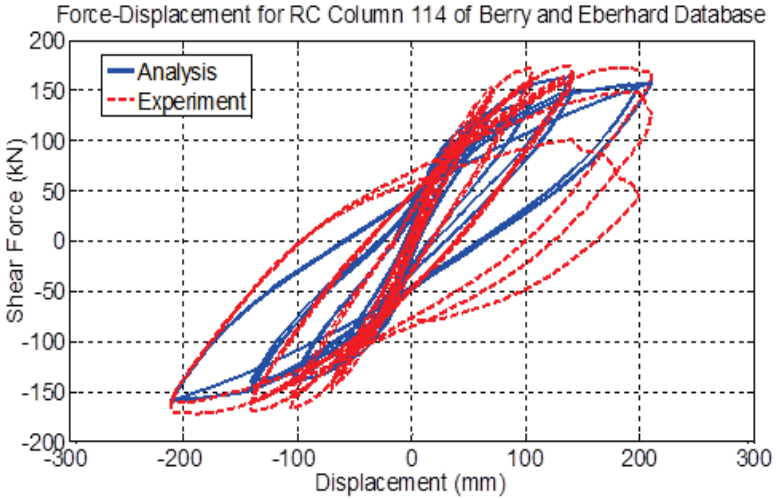

Figure A-15: Comparison between numerical and experimental responses of circular columns (ID#113&114) of Berry and Eberhard Database (2004).

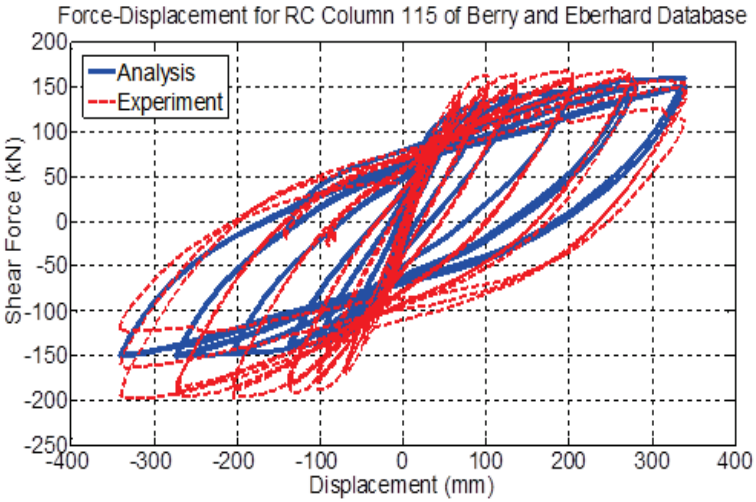

Concrete Model: Mander et al., 1988.

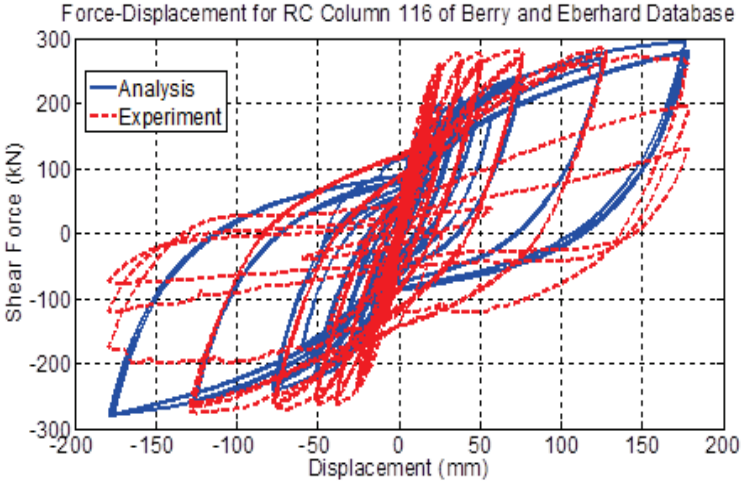

Figure A-16: Comparison between numerical and experimental responses of circular columns (ID#115&116) of Berry and Eberhard Database (2004).

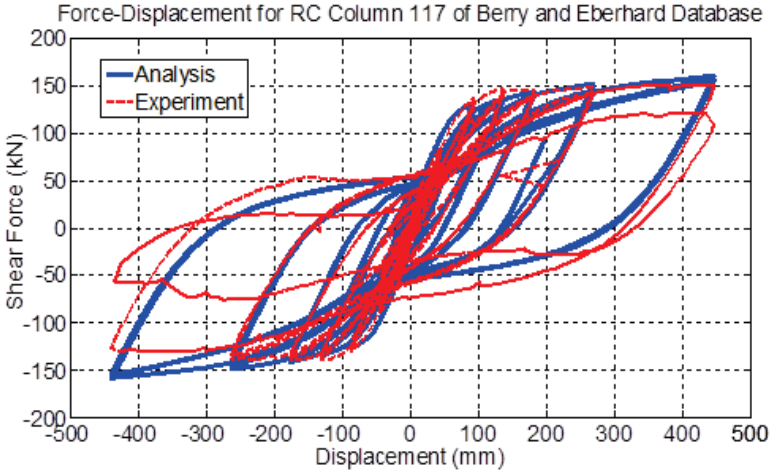

Concrete Model: Mander et al., 1988.

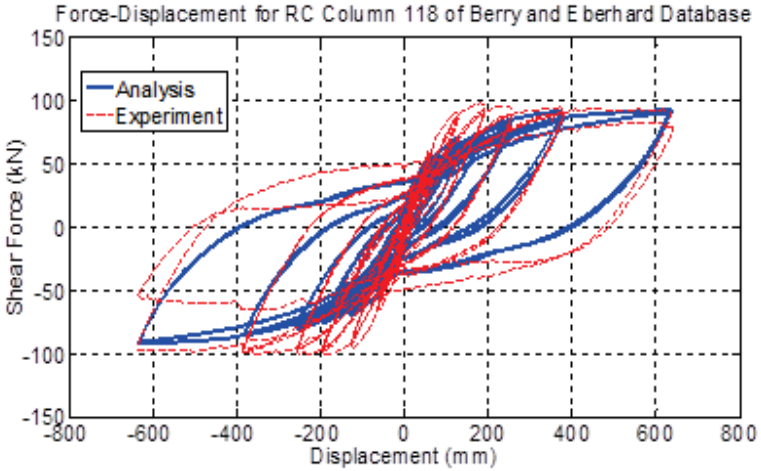

Figure A-17: Comparison between numerical and experimental responses of circular columns (ID#117&118) of Berry and Eberhard Database (2004).

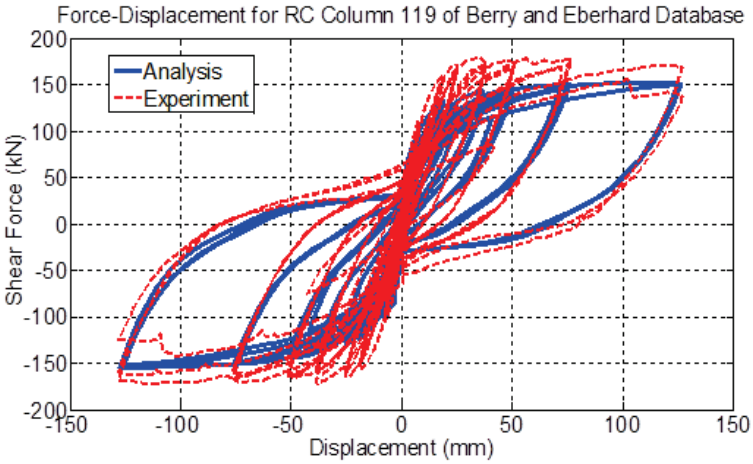

Concrete Model: Mander et al., 1988.

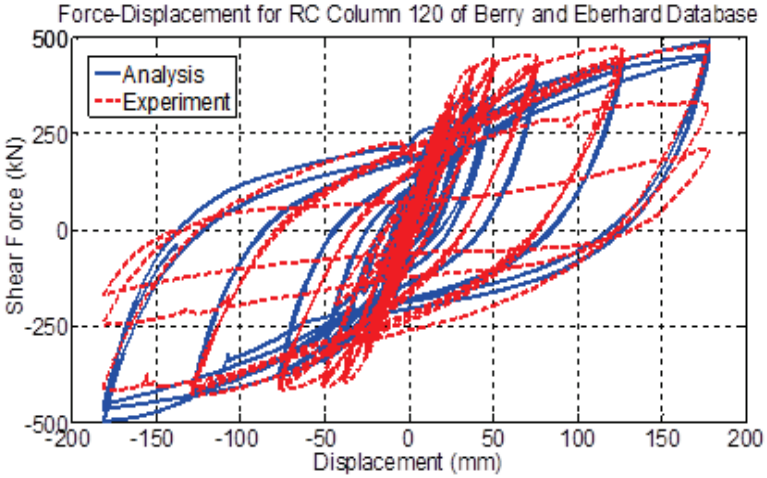

Figure A-18: Comparison between numerical and experimental responses of circular columns (ID#119&120) of Berry and Eberhard Database (2004).

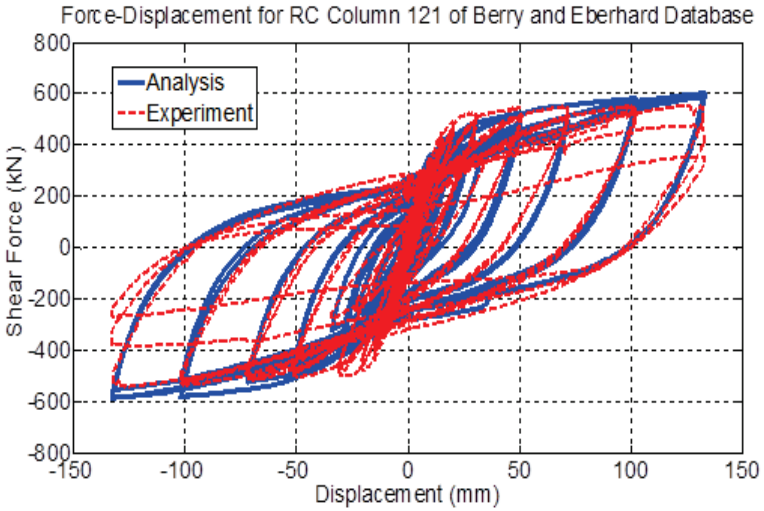

Concrete Model: Mander et al., 1988.

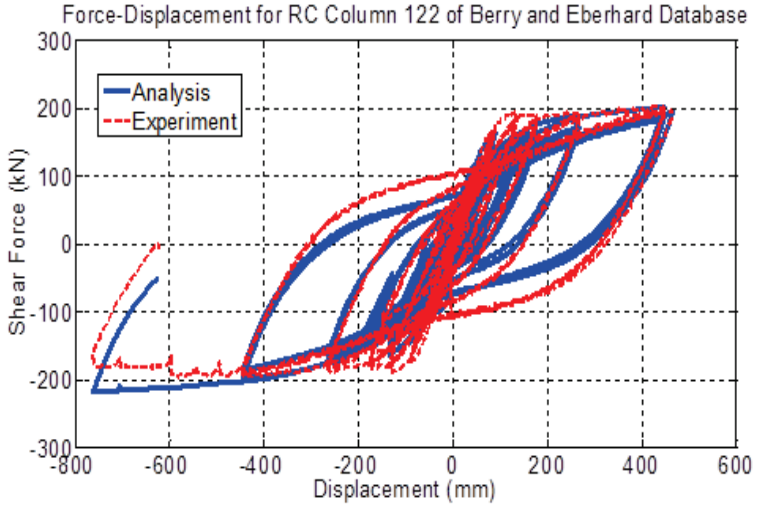

Figure A-19: Comparison between numerical and experimental responses of circular columns (ID#121&122) of Berry and Eberhard Database (2004).

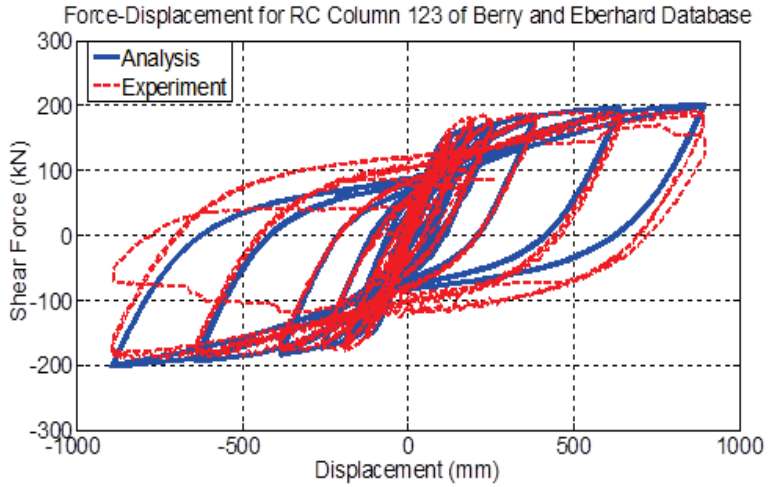

Concrete Model: Mander et al., 1988.

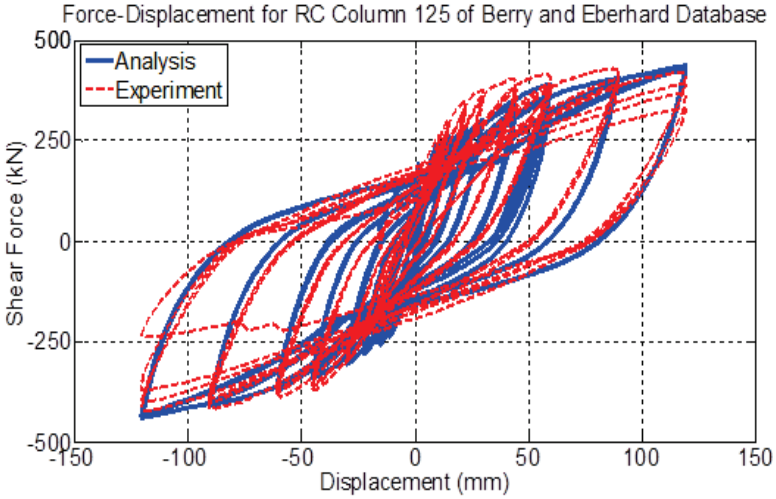

Figure A-20: Comparison between numerical and experimental responses of circular columns (ID#123&125) of Berry and Eberhard Database (2004).

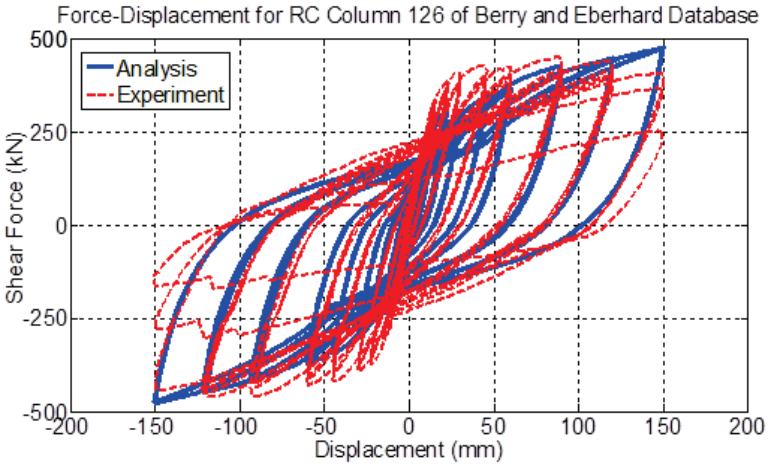

Concrete Model: Mander et al., 1988.

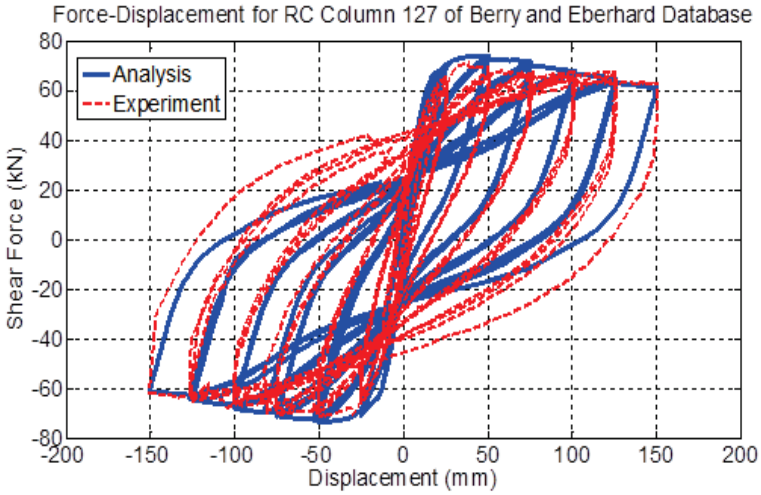

Figure A-21: Comparison between numerical and experimental responses of circular columns (ID#126&127) of Berry and Eberhard Database (2004).

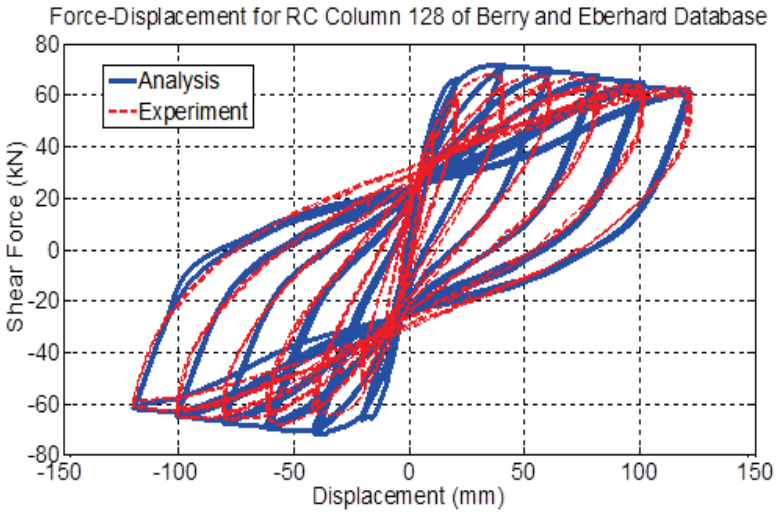

Concrete Model: Mander et al., 1988.

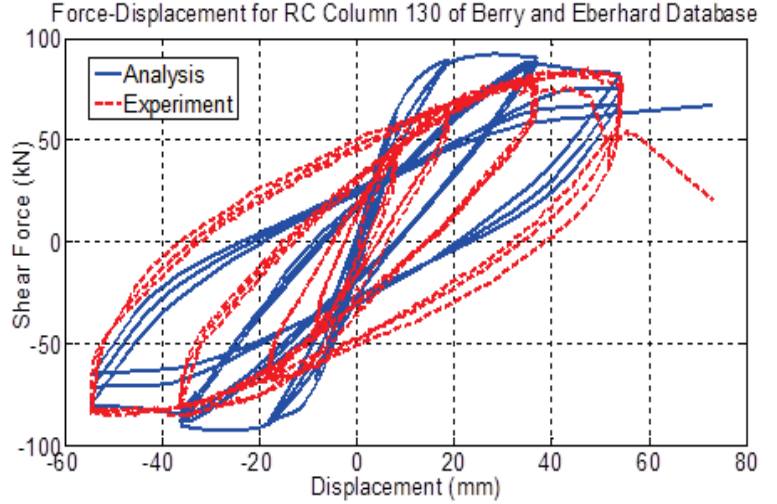

Figure A-22: Comparison between numerical and experimental responses of circular columns (ID#128&130) of Berry and Eberhard Database (2004).

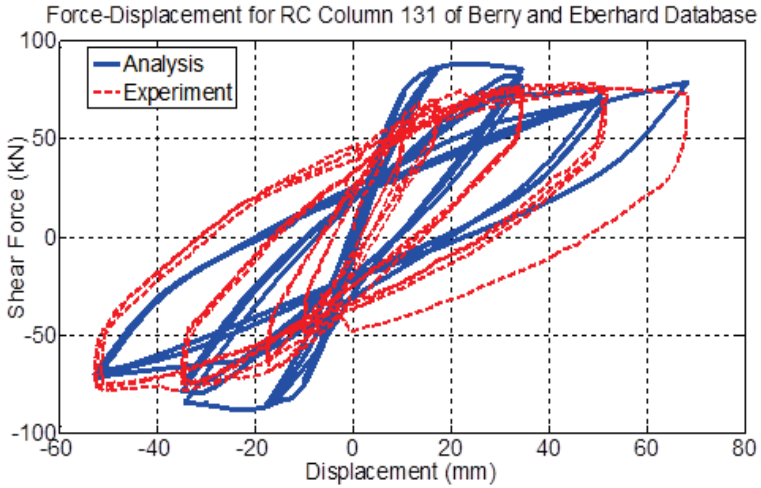

Concrete Model: Mander et al., 1988.

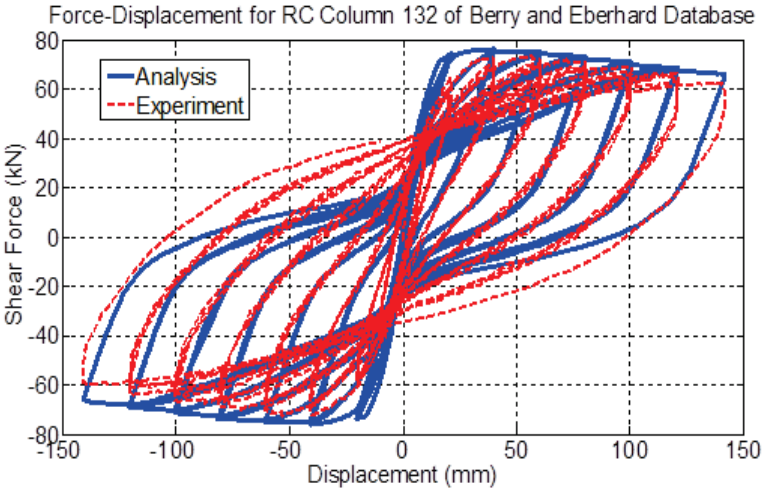

Figure A-23: Comparison between numerical and experimental responses of circular columns (ID#131&132) of Berry and Eberhard Database (2004).

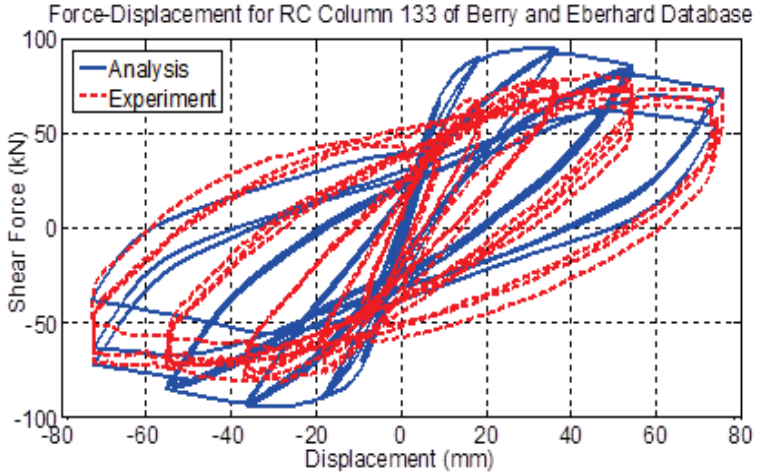

Concrete Model: Mander et al., 1988.

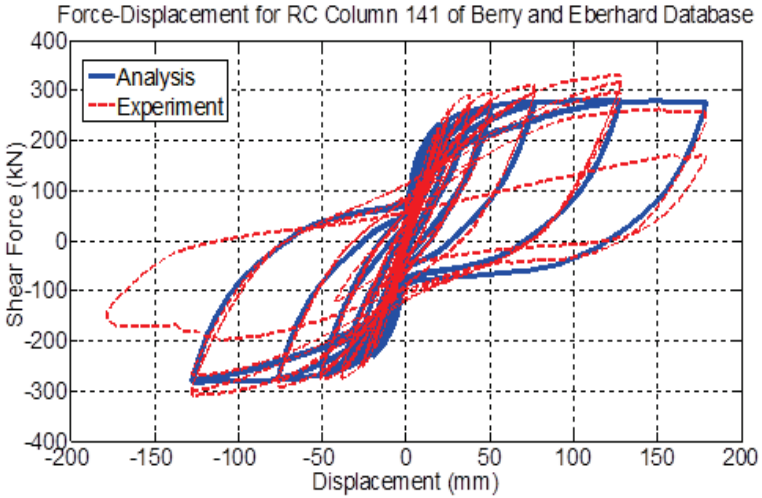

Figure A-24: Comparison between numerical and experimental responses of circular columns (ID#133&141) of Berry and Eberhard Database (2004).

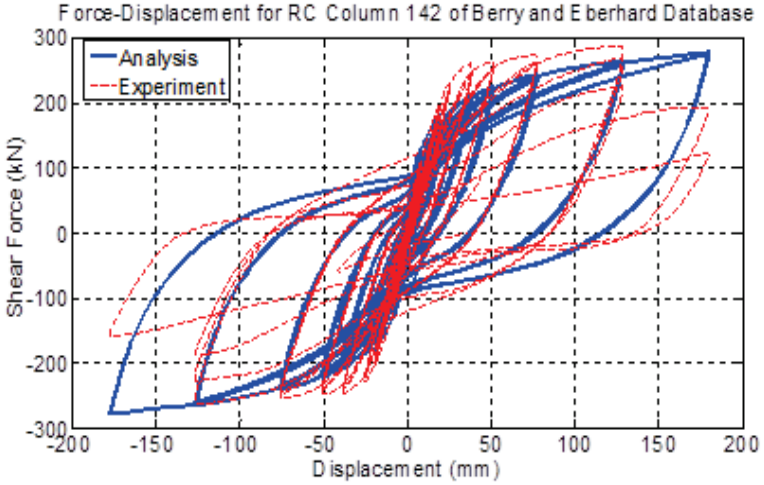

Concrete Model: Mander et al., 1988.

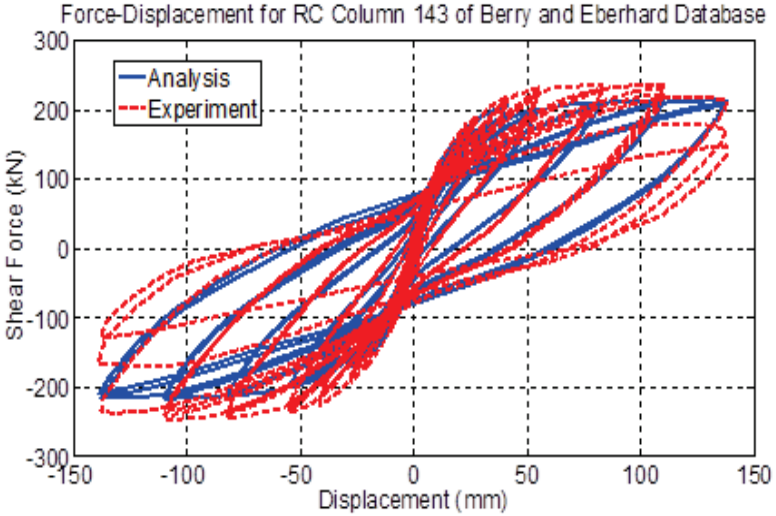

Figure A-25: Comparison between numerical and experimental responses of circular columns (ID#142&143) of Berry and Eberhard Database (2004).

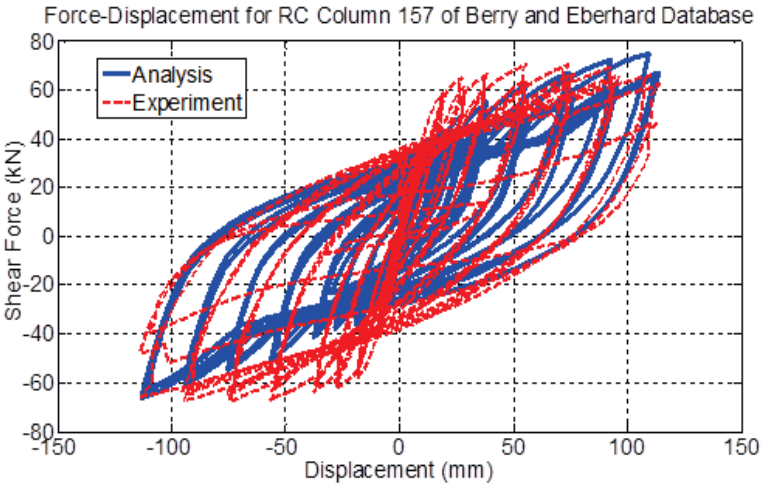

Concrete Model: Mander et al., 1988.

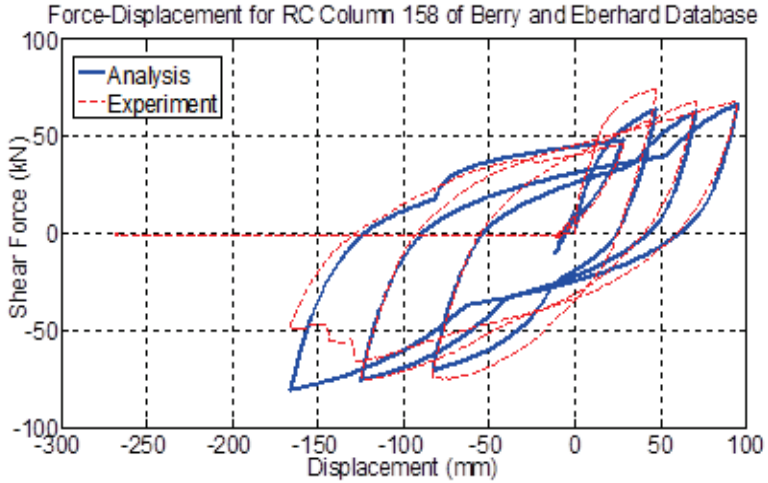

Figure A-26: Comparison between numerical and experimental responses of circular columns (ID#157&158) of Berry and Eberhard Database (2004).

Table A-2: Reinforced concrete columns with a rectangular cross section that failed in flexure.

SpecimenID in Database	Axial Load (KN)	Width - Depth (mm)	Clear Cover (mm)	Shear Span (mm)	Concrete Strength (MPa)	Number of Longitudinal Bars	Diameter of Long. Bars (mm)	Yielding Strength of Long. Bars (MPa)	Ultimate Strength of Long. Bars (MPa)	Longitudinal Reinforcement ratio	Stirrups Spacing (mm)	Diameter of Stirrups (mm)	Stirrups Yielding Strength (MPa)	Transverse Reinforcement ratio
1	1815	550-550	40	1200	23.1	12	24	375	635.6	0.0179	80	10	297	0.015
2	2680	550-550	38	1200	41.4	12	24	375	635.6	0.0179	75	12	316	0.023
3	2719	550-550	40	1200	21.4	12	24	375	635.6	0.0179	75	10	297	0.02
4	4265	550-550	38	1200	23.5	12	24	375	635.6	0.0179	62	12	294	0.035
5	1435	400-400	24.5	1600	23.6	12	16	427	670	0.0151	100	12	320	0.028
6	840	400-400	22.5	1600	25	12	16	427	670	0.0151	90	10	280	0.022
7	744	400-400	13	1600	46.5	12	16	446	702	0.0151	85	7	364	0.0086
8	2112	400-400	13	1600	44	12	16	446	702	0.0151	78	8	360	0.0122
9	2112	400-400	13	1600	44	12	16	446	702	0.0151	91	7	364	0.008
10	1920	400-400	13	1600	40	12	16	446	702	0.0151	94	6	255	0.0057
11	1010	400-400	13	1600	28.3	12	16	440	674	0.0151	117	10	466	0.0156
12	2502	400-400	13	1600	40.1	12	16	440	674	0.0151	92	10	466	0.0199

13	3280	400-400	13	1600	41	12	16	474	633.3	0.0151	81	8	372	0.0066
14	3200	400-400	13	1600	40	12	16	474	633.3	0.0151	96	6	388	0.0032
15	4704	400-400	13	1600	42	12	16	474	633.3	0.0151	96	12	308	0.0126
16	4368	400-400	13	1600	39	12	16	474	633.3	0.0151	77	8	372	0.007
17	4480	400-400	13	1600	40	12	16	474	633.3	0.0151	52	12	308	0.0233
18	819	400-400	40	1600	25.6	8	20	474	721	0.0157	80	12	333	0.0255
19	819	400-400	40	1600	25.6	8	20	474	721	0.0157	80	12	333	0.0255
20	819	400-400	40	1600	25.6	8	20	474	721	0.0157	80	12	333	0.0255
21	819	400-400	40	1600	25.6	8	20	474	721	0.0157	80	12	333	0.0255
22	968	550-550	40	1650	32	12	20	511	675	0.0125	110	12	325	0.017
23	968	550-550	40	1650	32	12	20	511	675	0.0125	110	12	325	0.017
24	2913	550-550	40	1650	32.1	12	20	511	675	0.0125	90	12	325	0.0208
25	2913	550-550	40	1650	32.1	12	20	511	675	0.0125	90	12	325	0.0208
26	646	400-600	24	1784	26.9	10	24	432	-	0.0188	80	12	305	0.0217
27	429	250-250	-	375	20.6	6	9.5	392.8	-	0.0068	32	5.5	323	0.0118
30	127	400-400	31.5	1600	24.8	8	19	362	-	0.0142	100	9	325	0.0032

31	127	400-400	31.5	1600	24.8	8	19	362	-	0.0142	100	9	325	0.0032
32	127	400-400	31.5	1600	24.8	8	19	362	-	0.0142	100	9	325	0.0032
43	432	160-160	12.5	320	21.1	8	10	341	448	0.0222	40	5	559	0.0073
48	184	250-250	35	750	27.9	8	12.7	374	494	0.0162	50	5.5	506	0.0038
49	184	250-250	35	750	27.9	8	12.7	374	494	0.0162	50	5.5	506	0.0038
50	184	250-250	35	750	27.9	8	12.7	374	494	0.0162	50	5.5	506	0.0038
51	184	250-250	35	750	24.8	8	12.7	374	494	0.0162	50	5.5	352	0.0038
52	184	250-250	35	750	27.9	8	12.7	374	494	0.0162	50	5.5	506	0.0038
53	184	250-250	35	750	27.9	8	12.7	374	494	0.0162	50	5.5	506	0.0038
56	1371	200-200	9	500	85.7	12	12.7	399.6	-	0.038	35	6	328.4	0.0161
57	1371	200-200	9	500	85.7	12	12.7	399.6	-	0.038	35	6	792.3	0.0161
58	2156	200-200	9	500	85.7	12	12.7	399.6	-	0.038	35	6	328.4	0.0161
59	2156	200-200	9	500	85.7	12	12.7	399.6	-	0.038	35	6	792.3	0.0161
60	1176	200-200	9	500	115.8	12	12.7	399.6	-	0.038	35	6	328.4	0.0161
61	1176	200-200	9	500	115.8	12	12.7	399.6	-	0.038	35	6	792.3	0.0161
62	1959	200-200	9	500	115.8	12	12.7	399.6	-	0.038	35	6	328.4	0.0161
63	1959	200-200	9	500	115.8	12	12.7	399.6	-	0.038	35	6	792.3	0.0161

66	2176	250-250	23.5	500	99.5	12	12.7	379	571	0.0243	60	5	774	0.005
67	2176	250-250	23.5	500	99.5	12	12.7	379	571	0.0243	40	5	774	0.0075
68	2176	250-250	23.5	500	99.5	12	12.7	379	571	0.0243	60	5.5	344	0.0061
69	2176	250-250	23.5	500	99.5	12	12.7	379	571	0.0243	60	5	1126	0.005
70	2176	250-250	23.5	500	99.5	12	12.7	379	571	0.0243	30	5	774	0.005
71	2176	250-250	23.5	500	99.5	12	12.7	379	571	0.0243	60	7	857	0.005
72	2176	250-250	30.5	500	99.5	4	19	339	512	0.0181	30	5	774	0.005
88	267	305-305	32	1676	29.1	4	22	367	578	0.0163	76	9.5	363	0.0154
89	267	305-305	32	1676	30.7	4	22	367	578	0.0163	127	9.5	363	0.0093
90	267	305-305	32	1676	29.2	4	22	367	578	0.0163	76	9.5	363	0.0154
91	267	305-305	32	1676	27.6	4	22	429	657	0.0163	127	9.5	363	0.0093
92	534	305-305	32	1676	29.4	4	22	429	657	0.0163	76	9.5	392	0.0154
93	534	305-305	32	1676	31.8	4	22	429	657	0.0163	127	9.5	392	0.0093
94	801	305-305	32	1676	33.3	4	22	363	563	0.0163	76	9.5	392	0.0154
95	801	305-305	32	1676	32.4	4	22	363	563	0.0163	127	9.5	392	0.0093
96	801	305-305	32	1676	31	4	22	363	563	0.0163	76	9.5	373	0.0154
97	801	305-305	32	1676	31.8	4	22	363	563	0.0163	127	9.5	373	0.0093

102	1690	457-457	38.1	1372	39.3	8	25.4	439	736	0.0194	102	12.7	454	0.0219
103	2580	457-457	41.3	1372	39.8	8	25.4	439	736	0.0194	102	9.5	616	0.0126
105	600	350-350	22.5	1000	34.8	8	25	430	-	0.0321	75	10	470	0.0169
106	600	350-350	22.5	1000	32	8	25	438	-	0.0321	50	10	470	0.0254
107	600	350-350	26	1000	37.3	8	25	437	-	0.0321	65	6.4	425	0.0195
108	600	350-350	26	1000	39	8	25	437	-	0.0321	65	6.4	425	0.0195
109	1500	250-250	30	1140	80	12	10	531	641	0.0151	150	8	531	0.0122
110	1500	250-250	30	1140	80	12	10	531	641	0.0151	150	8	531	0.0122
111	1000	250-250	30	1140	80	12	10	531	641	0.0151	150	8	531	0.0122
112	1000	250-250	30	1140	80	12	10	531	641	0.0151	150	8	531	0.0122
113	1000	250-250	30	1140	80	12	10	531	641	0.0151	100	8	531	0.0183
114	1500	250-250	30	1140	80	12	10	531	641	0.0151	100	8	531	0.0183
115	1500	250-250	30	1140	80	12	10	531	641	0.0151	100	8	531	0.0183
116	1000	250-250	30	1140	80	12	10	531	641	0.0151	100	8	531	0.0183
117	1000	250-250	30	1140	80	12	10	531	641	0.0151	50	8	531	0.0366
118	1500	250-250	30	1140	80	12	10	531	641	0.0151	50	8	531	0.0366
119	1000	250-250	30	1140	80	12	10	531	641	0.0151	50	8	531	0.0366

120	1500	250-250	30	1140	80	12	10	531	641	0.0151	50	8	531	0.0366
121	1000	250-250	30	1140	80	12	20	430	-	0.0603	150	8	430	0.0122
122	1500	250-250	30	1140	80	12	20	579	677	0.0603	150	8	579	0.0122
123	1500	250-250	30	1140	80	12	20	579	677	0.0603	150	8	579	0.0122
124	1000	250-250	30	1140	80	12	20	579	677	0.0603	150	8	579	0.0122
125	1000	250-250	30	1140	80	12	20	579	677	0.0603	100	8	579	0.0183
126	1000	250-250	30	1140	80	12	20	579	677	0.0603	100	8	579	0.0183
127	1500	250-250	30	1140	80	12	20	579	677	0.0603	100	8	579	0.0183
128	1500	250-250	30	1140	80	12	20	579	677	0.0603	100	8	579	0.0183
129	1000	250-250	30	1140	80	12	20	430	-	0.0603	50	8	430	0.0366
130	1000	250-250	30	1140	80	12	20	430	-	0.0603	50	8	430	0.0366
131	1500	250-250	30	1140	80	12	20	430	-	0.0603	50	8	430	0.0366
132	1500	250-250	30	1140	80	12	20	430	-	0.0603	50	8	430	0.0366
133	615	380-610	28	2335	27.2	18	19.1	448	731	0.0222	110	6	428	0.0037
134	1505	380-610	28	2335	27.2	18	19.1	448	731	0.0222	110	6	428	0.0037
135	601	380-610	25	2335	28.1	18	19.1	448	731	0.0222	83	6	428	0.0048
136	1514	380-610	25	2335	28.1	18	19.1	448	731	0.0222	83	6	428	0.0048

145	489	254-254	13	508	76	8	19.1	510	-	0.0355	51	9.5	510	0.0367
146	979	254-254	13	508	76	8	19.1	510	-	0.0355	51	9.5	510	0.0367
147	534	254-254	13	508	86	8	15.9	510	-	0.0246	51	9.5	510	0.0367
148	1068	254-254	13	508	86	8	15.9	510	-	0.0246	51	9.5	510	0.0367
156	1076	280-280	25.4	2134	40.6	4	15.875	407	659	0.0101	228.6	6.35	351	-
157	3354	305-305	11	1842	72.1	8	19.54	454	700	0.0258	95	15.98	463	0.0315

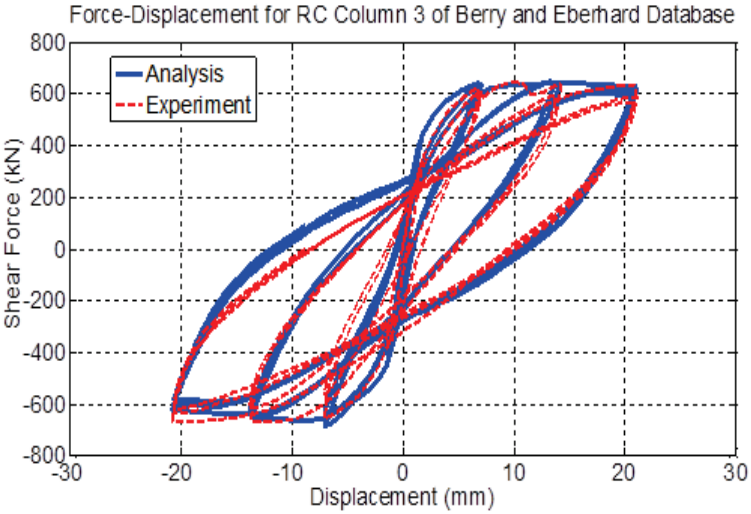

Concrete Model: Mander et al., 1988.

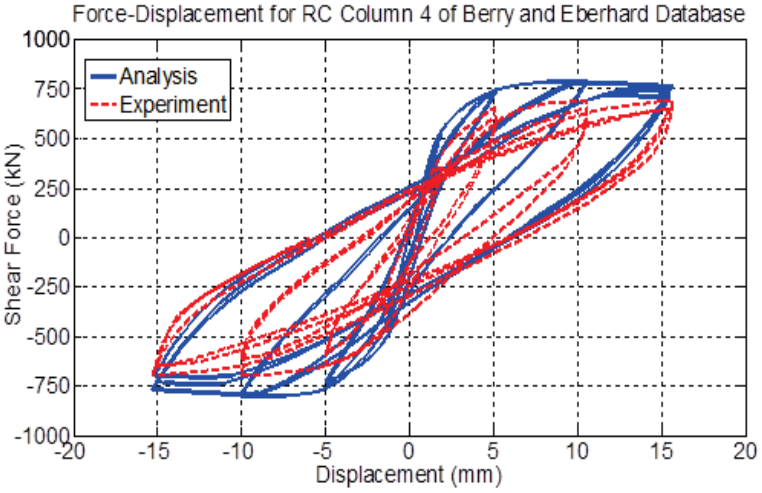

Figure A-27: Comparison between numerical and experimental responses of rectangular columns (ID#3&4) of Berry and Eberhard Database (2004).

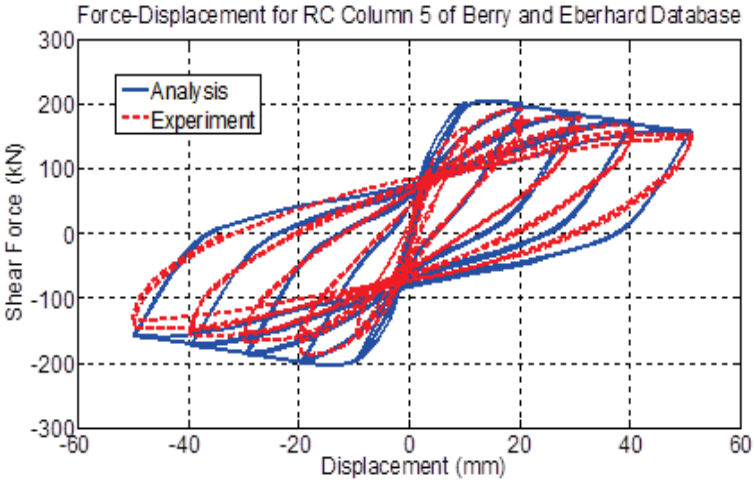

Concrete Model: Mander et al., 1988.

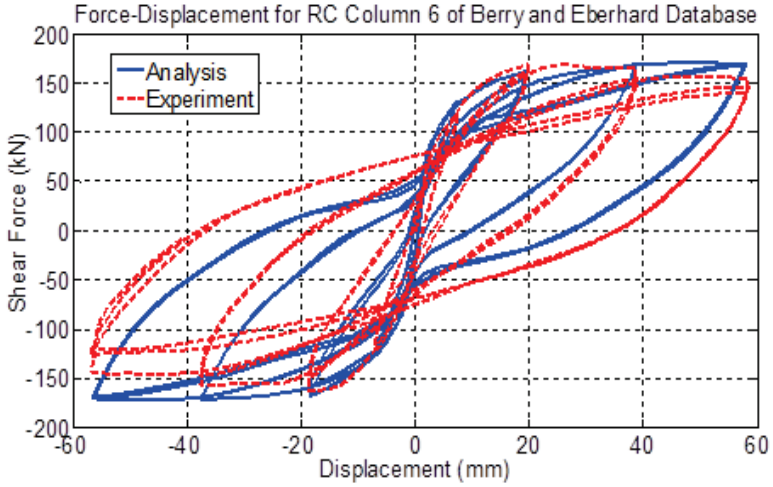

Figure A-28: Comparison between numerical and experimental responses of rectangular columns (ID#5&6) of Berry and Eberhard Database (2004).

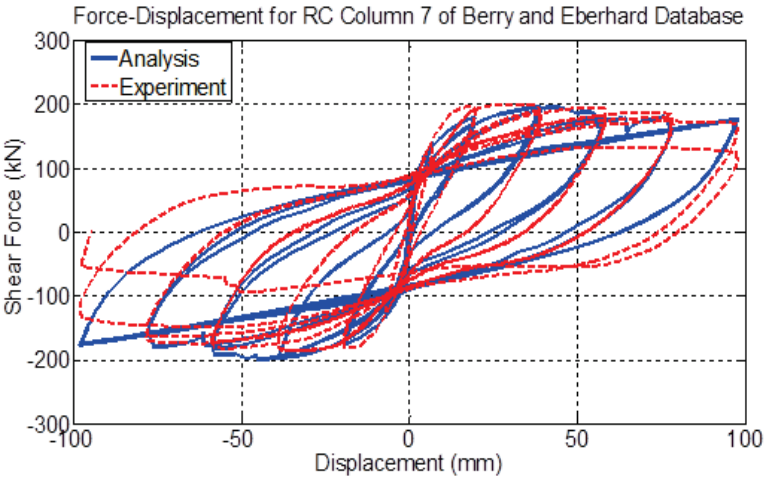

Concrete Model: Mander et al., 1988.

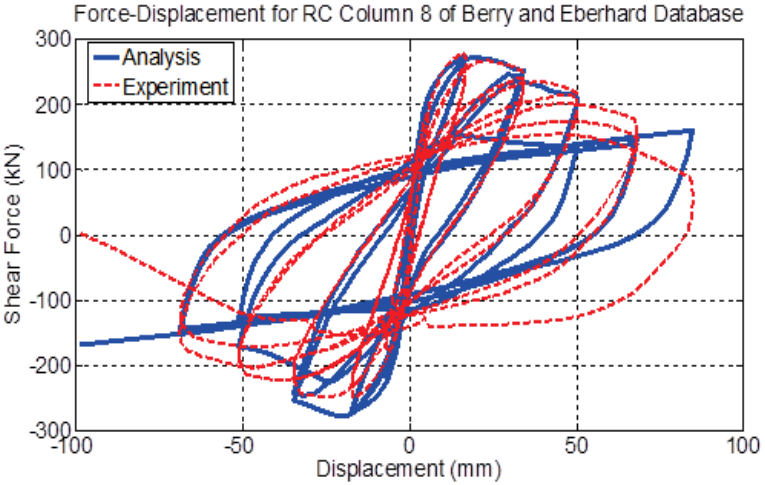

Figure A-29: Comparison between numerical and experimental responses of rectangular columns (ID#7&8) of Berry and Eberhard Database (2004).

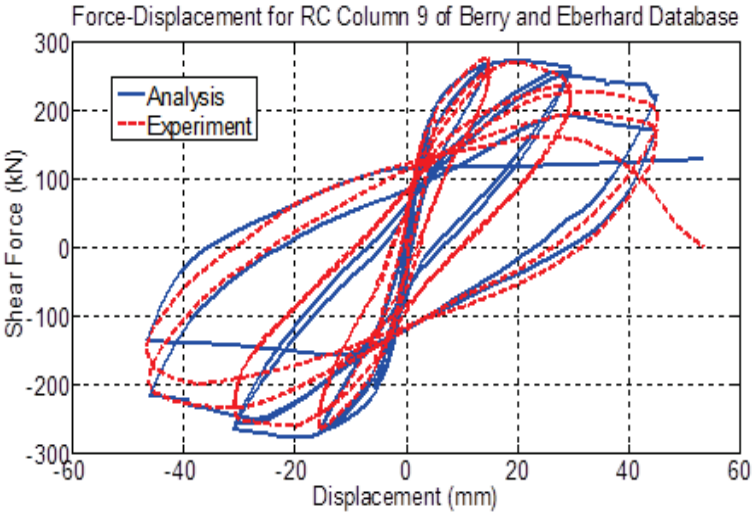

Concrete Model: Mander et al., 1988.

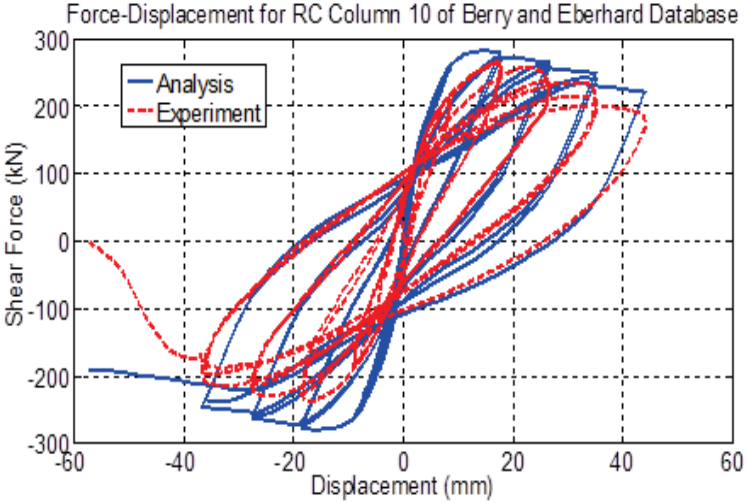

Figure A-30: Comparison between numerical and experimental responses of rectangular columns (ID#9&10) of Berry and Eberhard Database (2004).

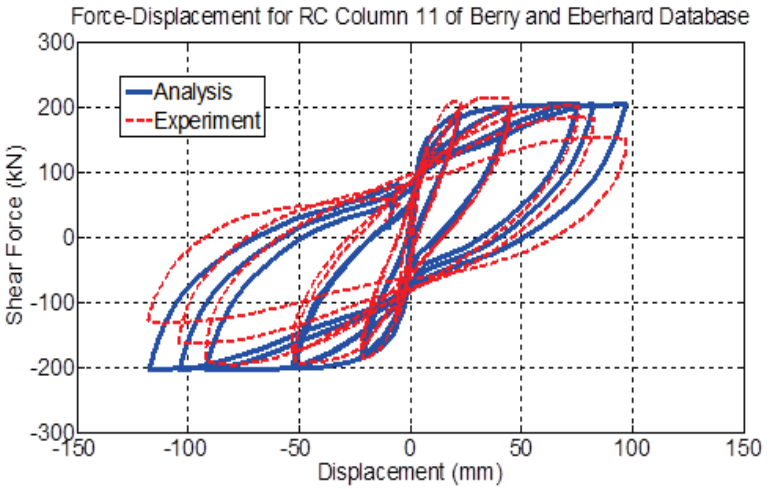

Concrete Model: Mander et al., 1988.

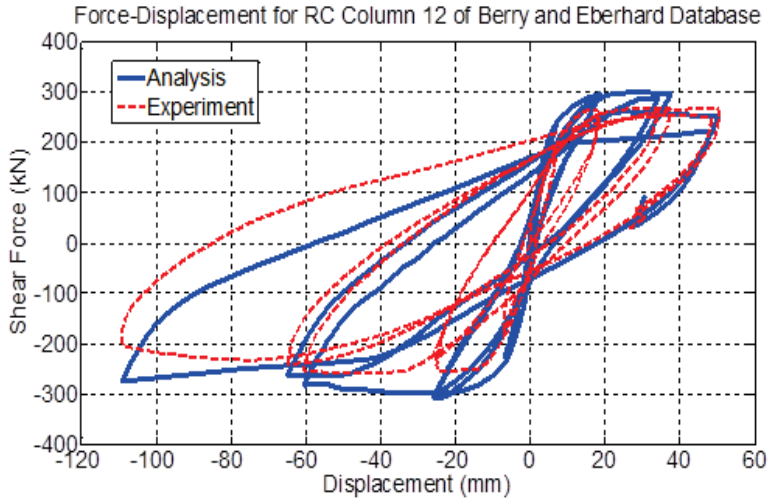

Figure A-31: Comparison between numerical and experimental responses of rectangular columns (ID#11&12) of Berry and Eberhard Database (2004).

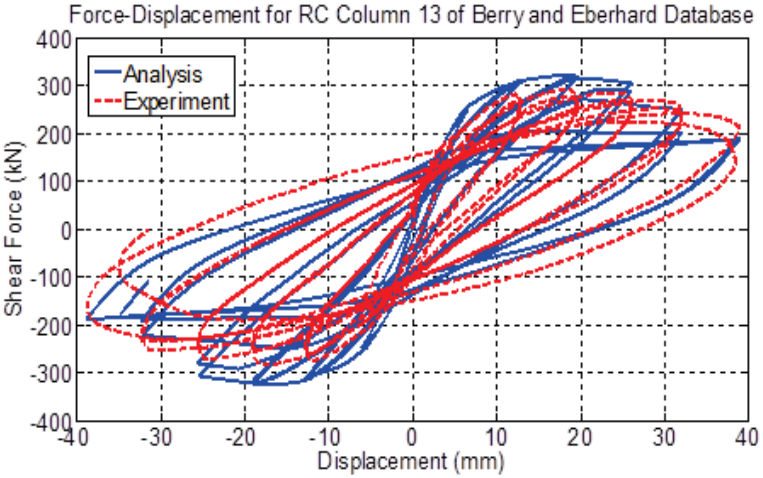

Concrete Model: Mander et al., 1988.

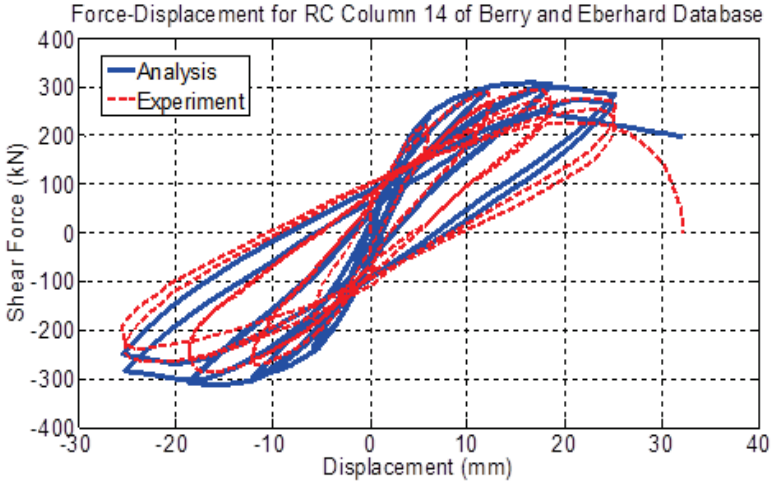

Figure A-32: Comparison between numerical and experimental responses of rectangular columns (ID#13&14) of Berry and Eberhard Database (2004).

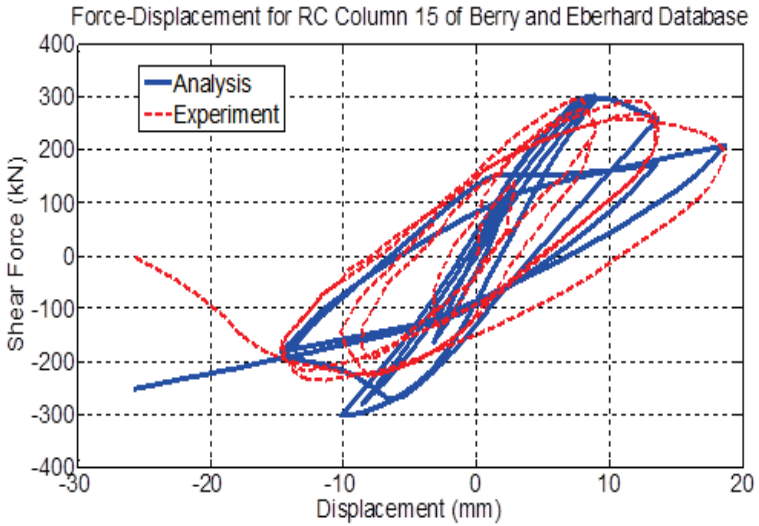

Concrete Model: Mander et al., 1988.

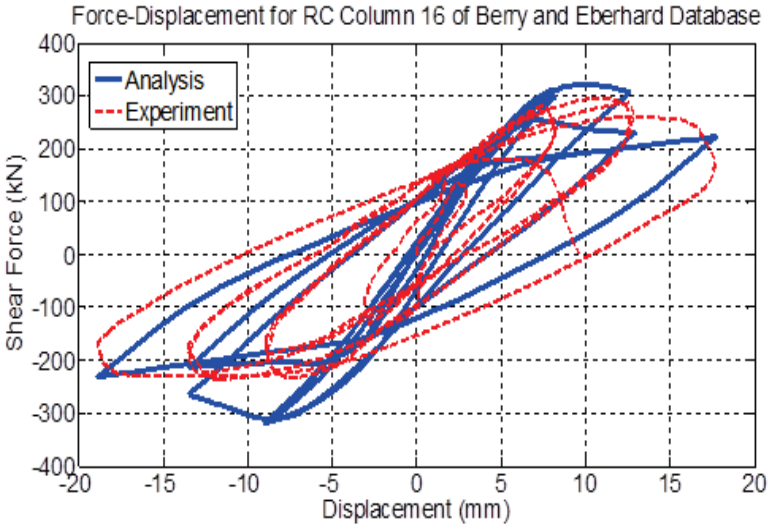

Figure A-33: Comparison between numerical and experimental responses of rectangular columns (ID#15&16) of Berry and Eberhard Database (2004).

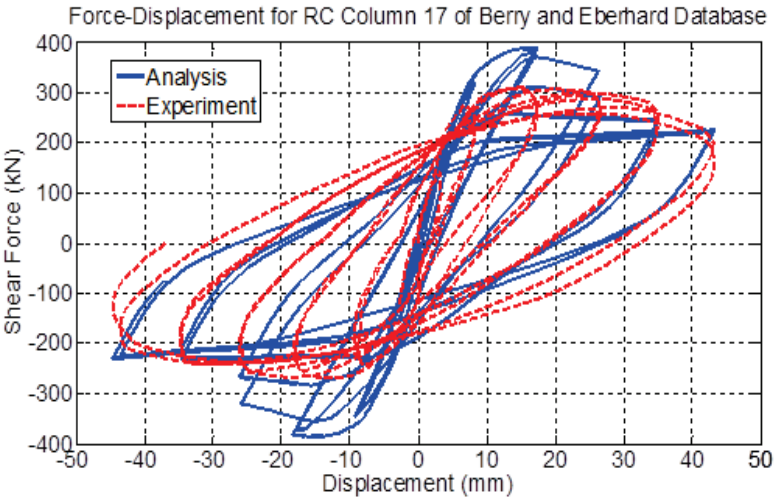

Concrete Model: Mander et al., 1988.

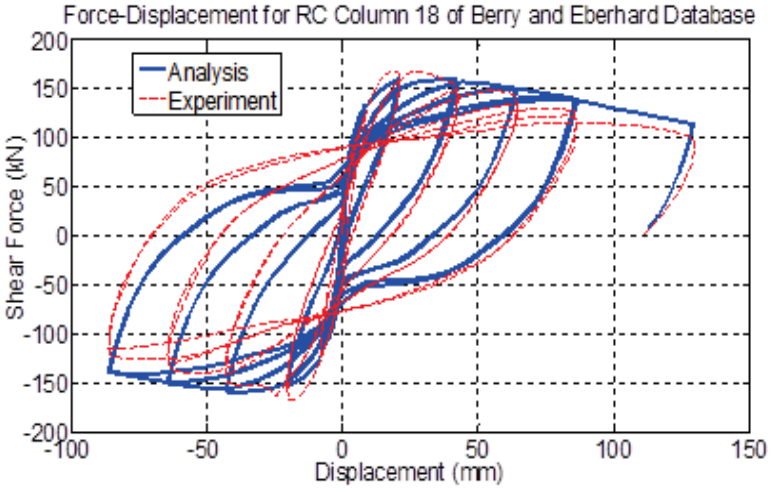

Figure A-34: Comparison between numerical and experimental responses of rectangular columns (ID#17&18) of Berry and Eberhard Database (2004).

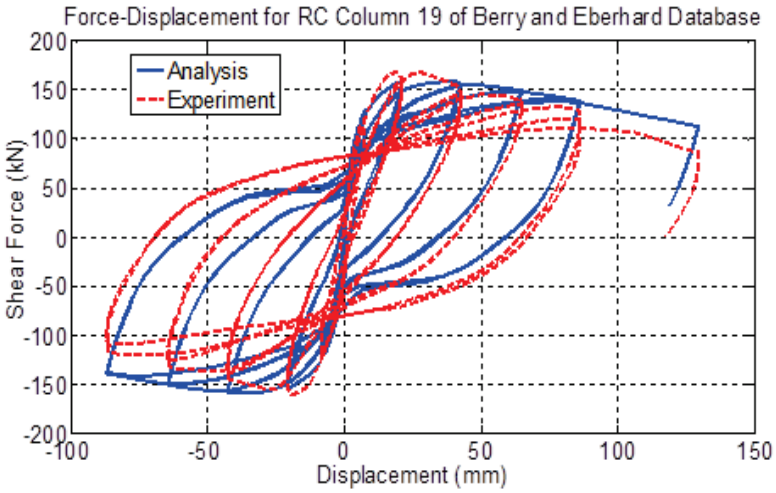

Concrete Model: Mander et al., 1988.

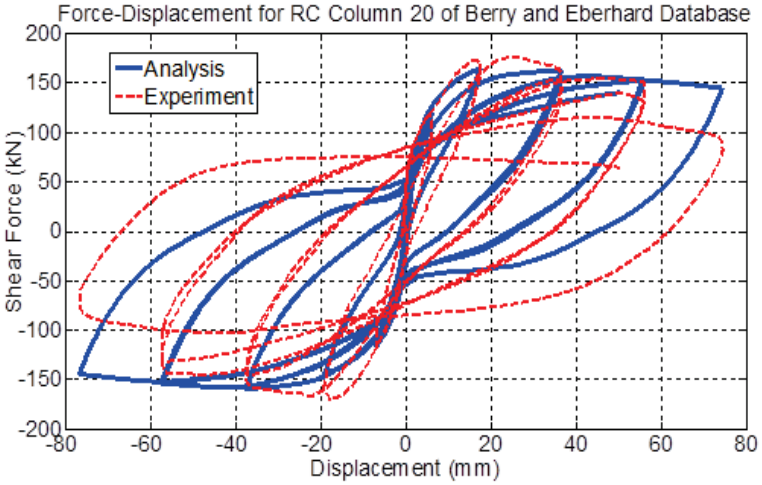

Figure A-35: Comparison between numerical and experimental responses of rectangular columns (ID#19&20) of Berry and Eberhard Database (2004).

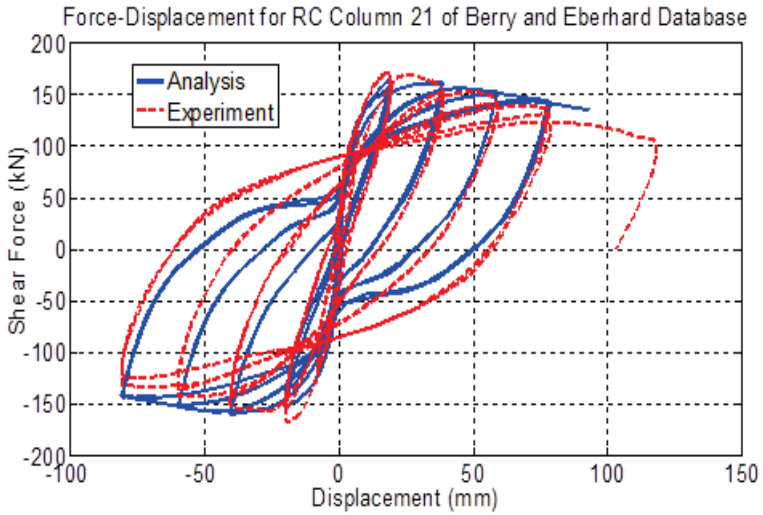

Concrete Model: Mander et al., 1988.

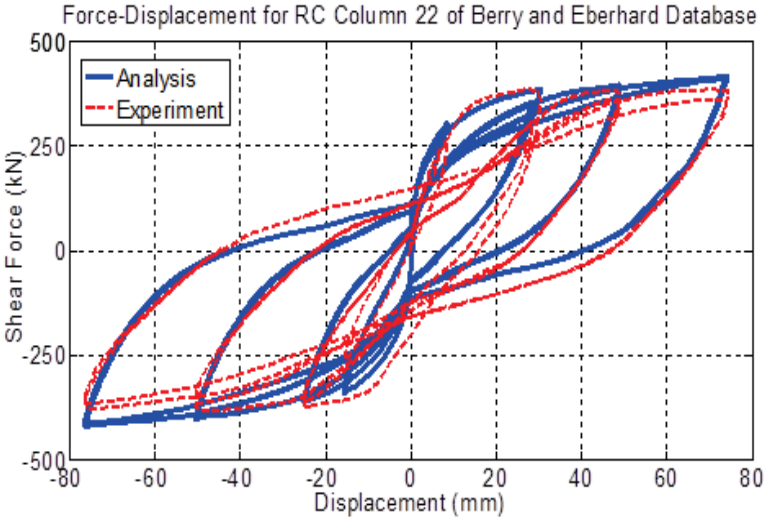

Figure A-36: Comparison between numerical and experimental responses of rectangular columns (ID#21&22) of Berry and Eberhard Database (2004).

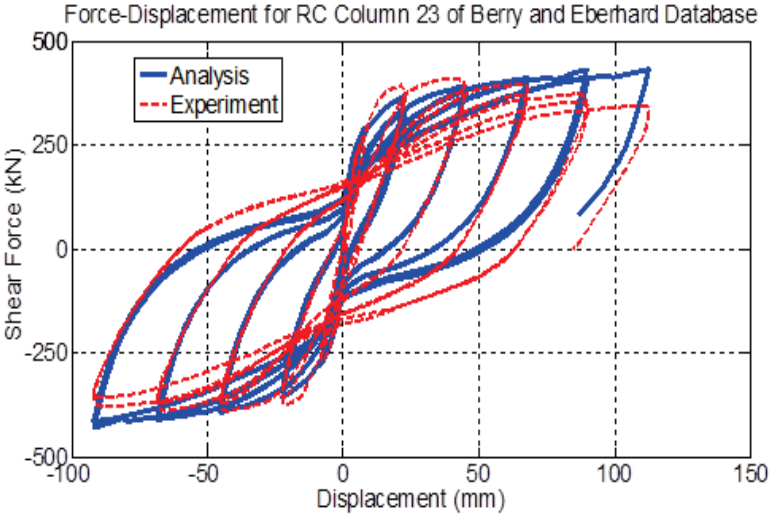

Concrete Model: Mander et al., 1988.

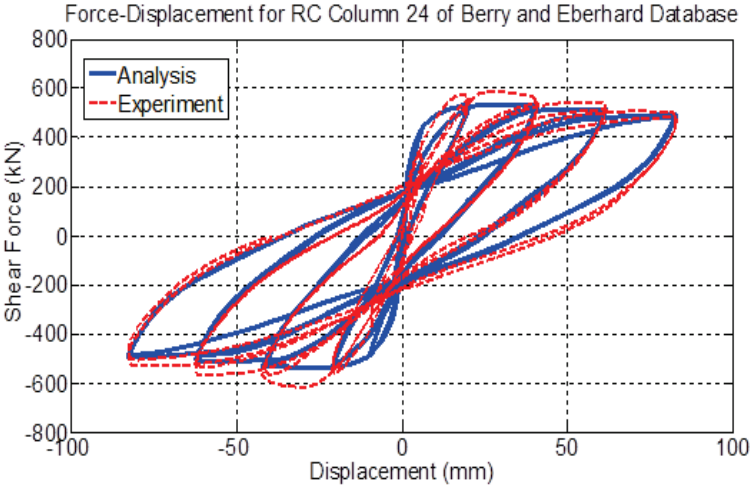

Figure A-37: Comparison between numerical and experimental responses of rectangular columns (ID#23&24) of Berry and Eberhard Database (2004).

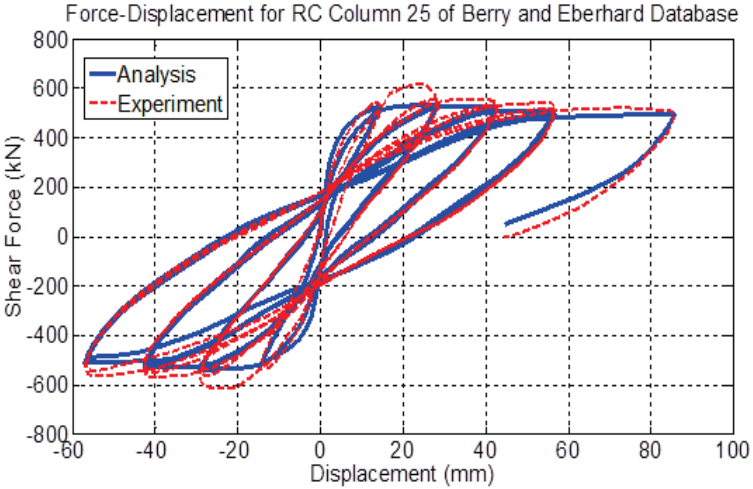

Concrete Model: Mander et al., 1988.

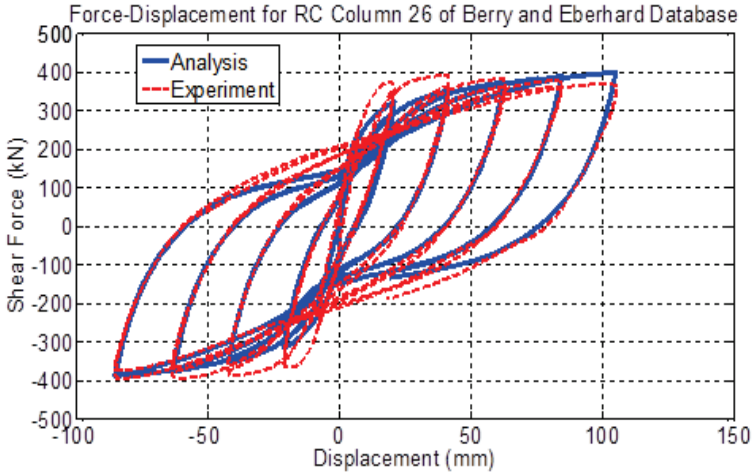

Figure A-38: Comparison between numerical and experimental responses of rectangular columns (ID#25&26) of Berry and Eberhard Database (2004).

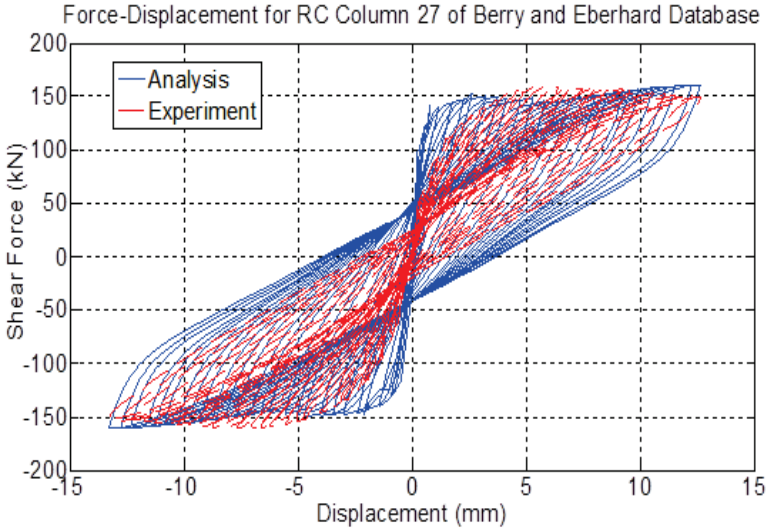

Concrete Model: Mander et al., 1988.

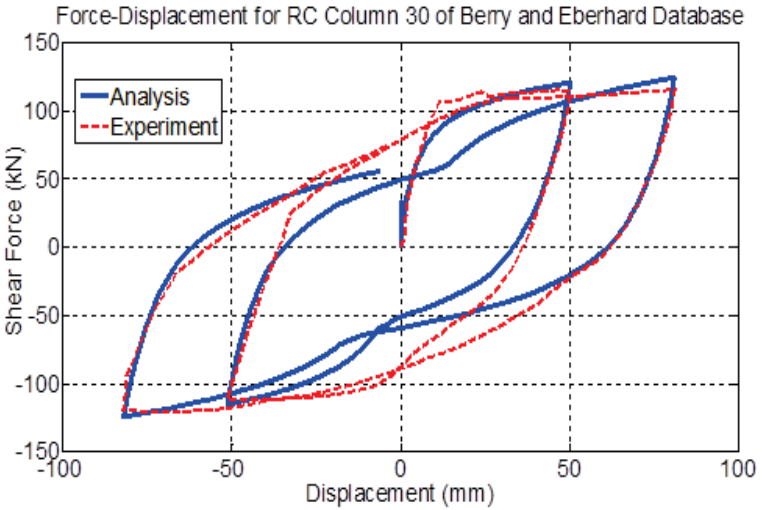

Figure A-39: Comparison between numerical and experimental responses of rectangular columns (ID#27&30) of Berry and Eberhard Database (2004).

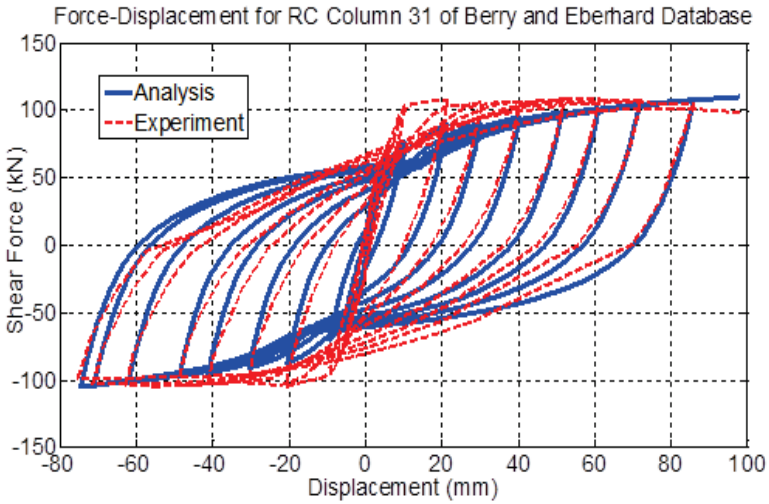

Concrete Model: Mander et al., 1988.

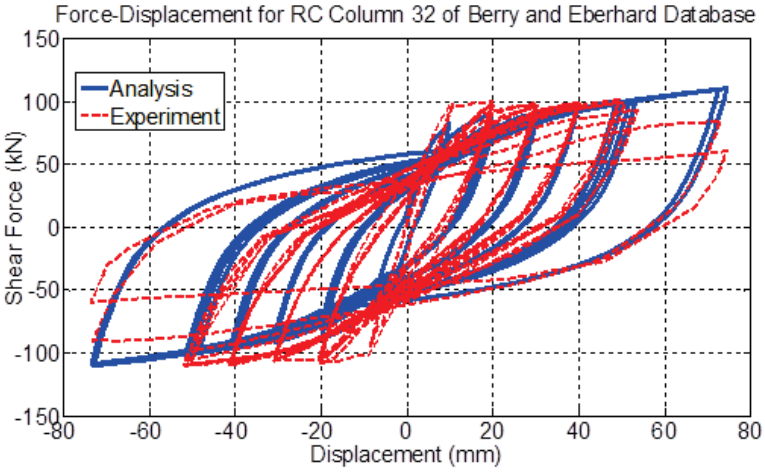

Figure A-40: Comparison between numerical and experimental responses of rectangular columns (ID#31&32) of Berry and Eberhard Database (2004).

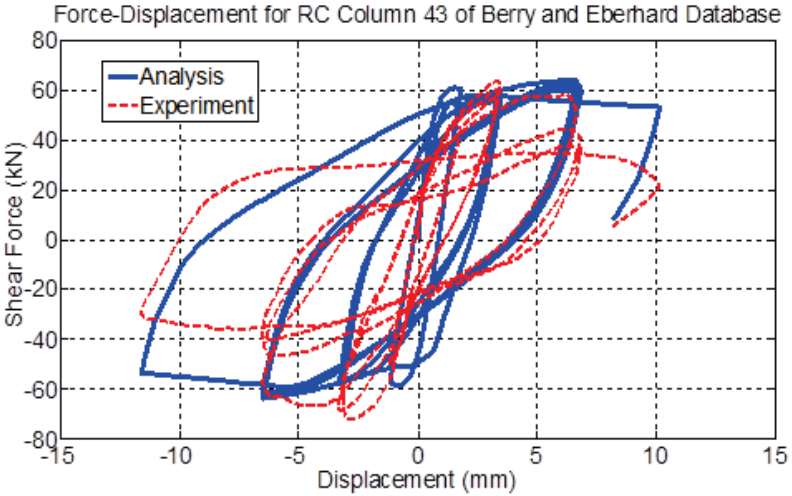

Concrete Model: Mander et al., 1988.

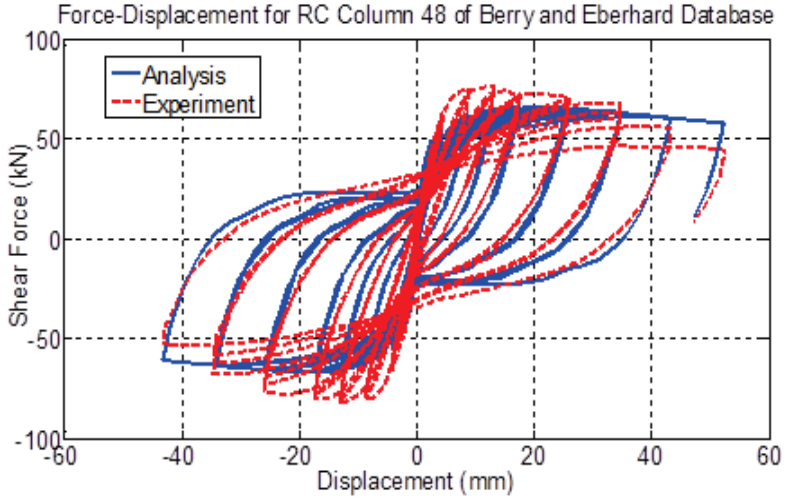

Figure A-41: Comparison between numerical and experimental responses of rectangular columns (ID#43&48) of Berry and Eberhard Database (2004).

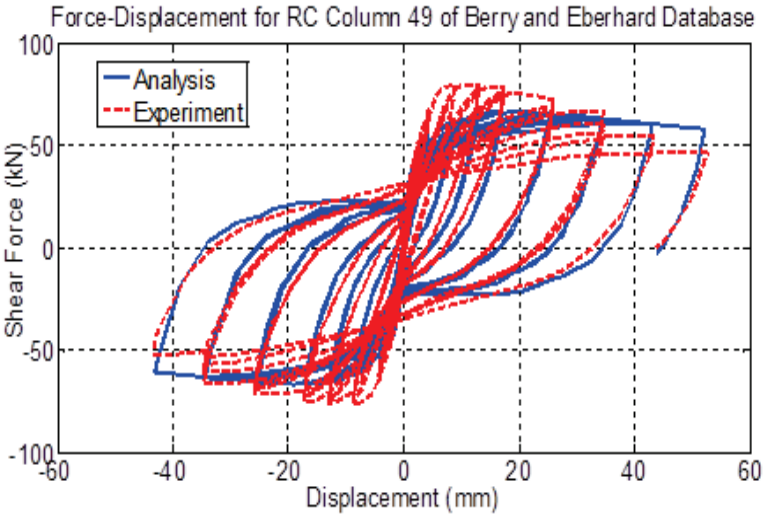

Concrete Model: Mander et al., 1988.

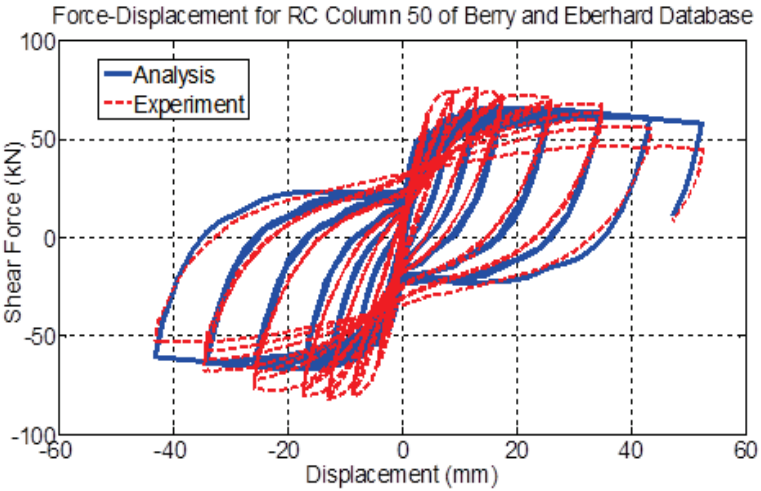

Figure A-42: Comparison between numerical and experimental responses of rectangular columns (ID#49&50) of Berry and Eberhard Database (2004).

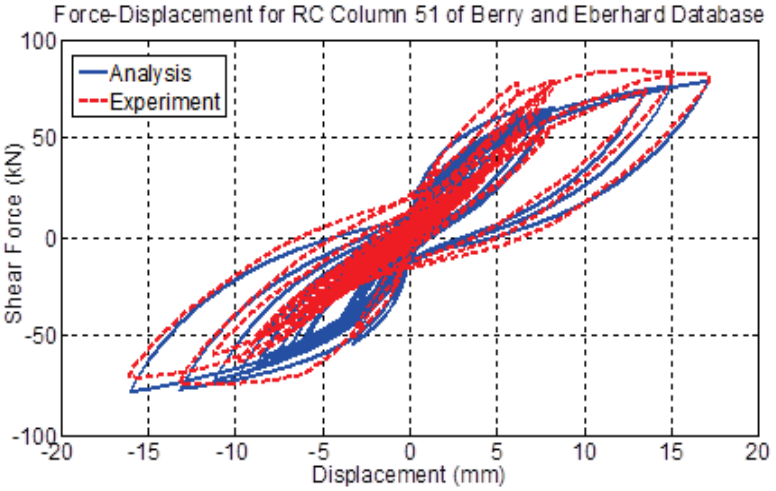

Concrete Model: Mander et al., 1988.

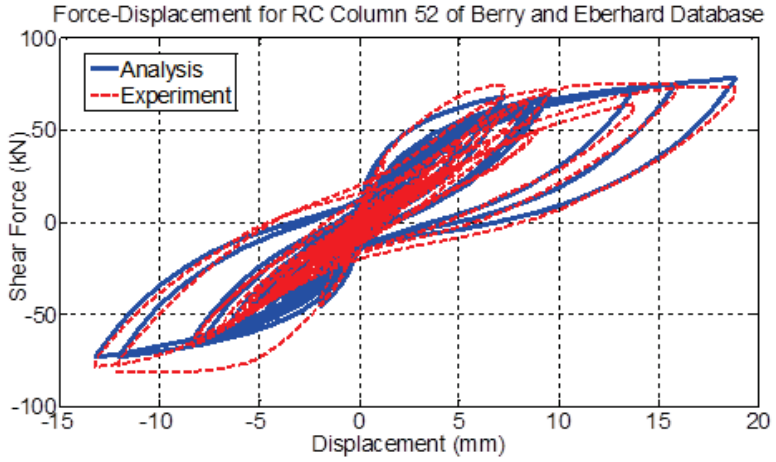

Figure A-43: Comparison between numerical and experimental responses of rectangular columns (ID#51&52) of Berry and Eberhard Database (2004).

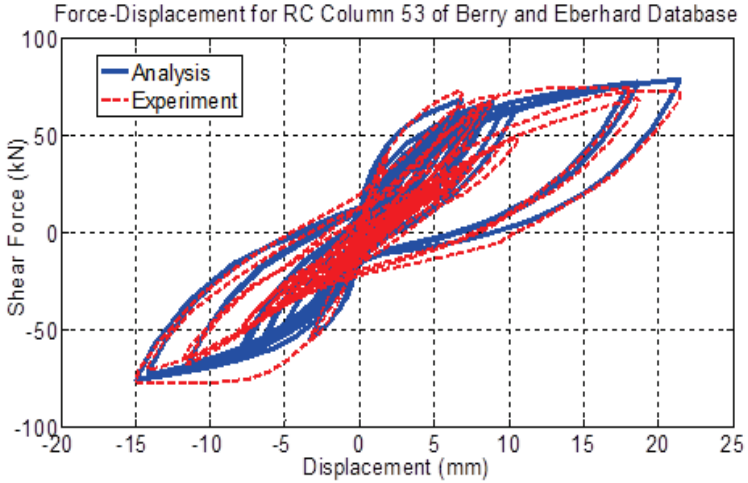

Concrete Model: Mander et al., 1988.

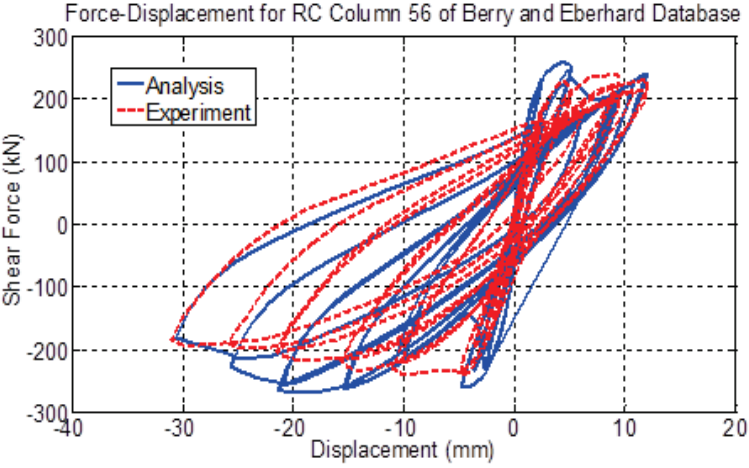

Figure A-44: Comparison between numerical and experimental responses of rectangular columns (ID#53&56) of Berry and Eberhard Database (2004).

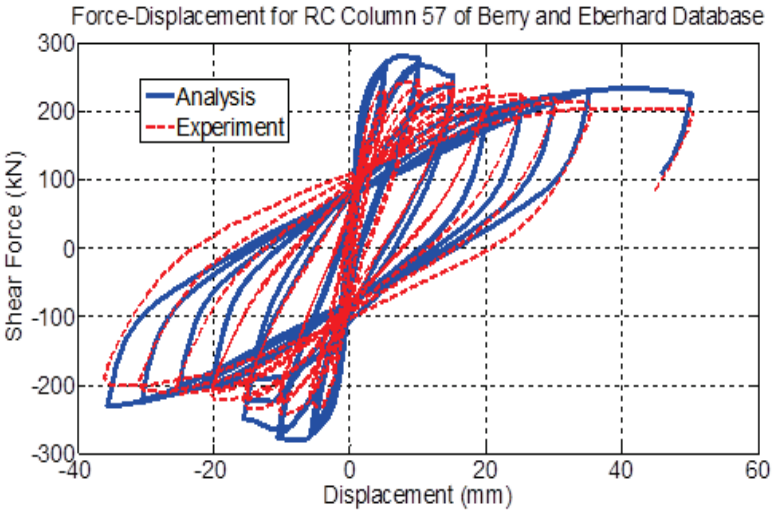

Concrete Model: Mander et al., 1988.

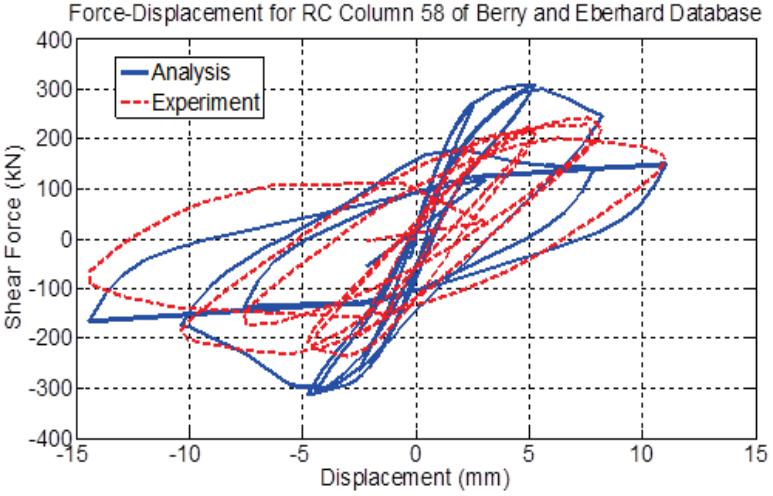

Figure A-45: Comparison between numerical and experimental responses of rectangular columns (ID#57&58) of Berry and Eberhard Database (2004).

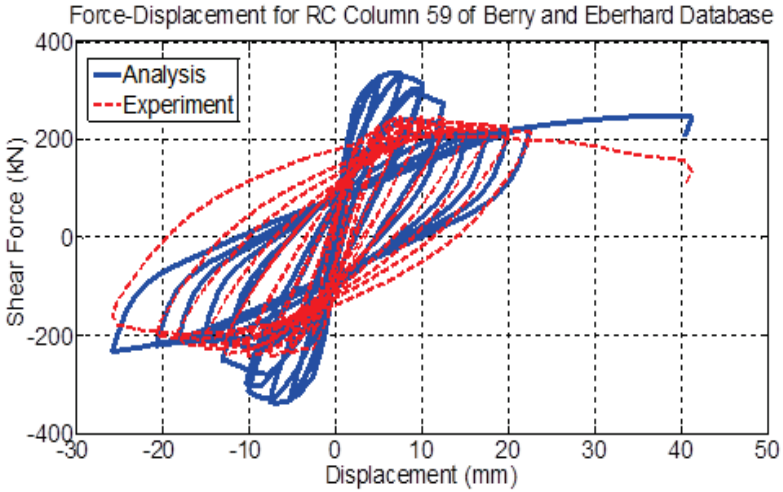

Concrete Model: Mander et al., 1988.

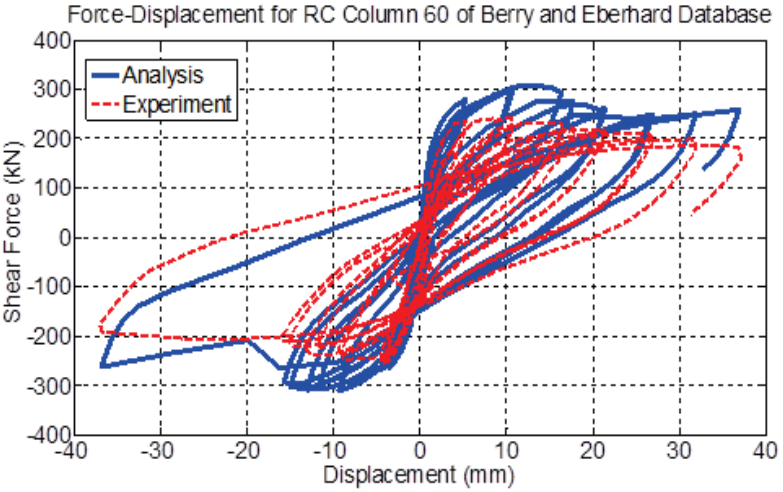

Figure A-46: Comparison between numerical and experimental responses of rectangular columns (ID#59&60) of Berry and Eberhard Database (2004).

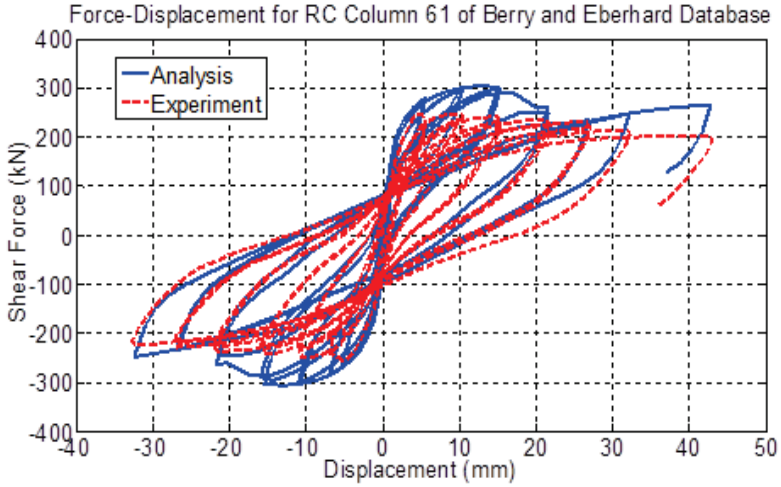

Concrete Model: Mander et al., 1988.

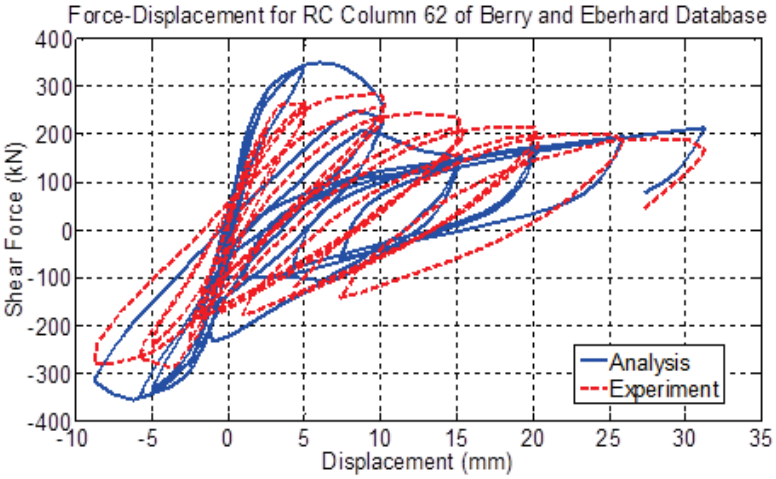

Figure A-47: Comparison between numerical and experimental responses of rectangular columns (ID#61&62) of Berry and Eberhard Database (2004).

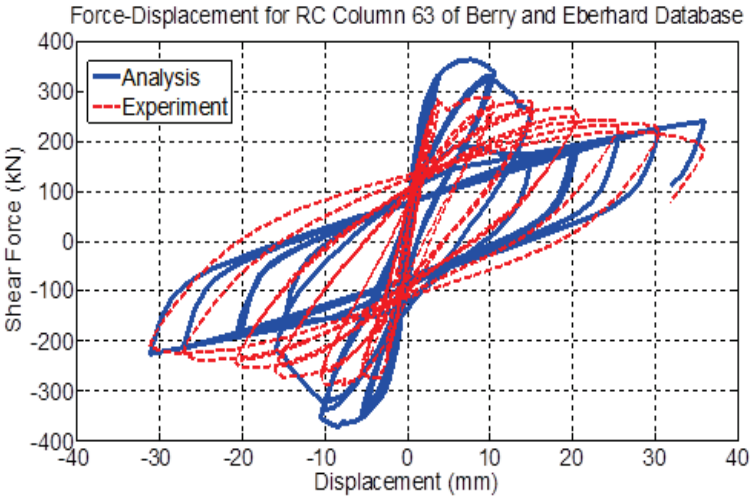

Concrete Model: Mander et al., 1988.

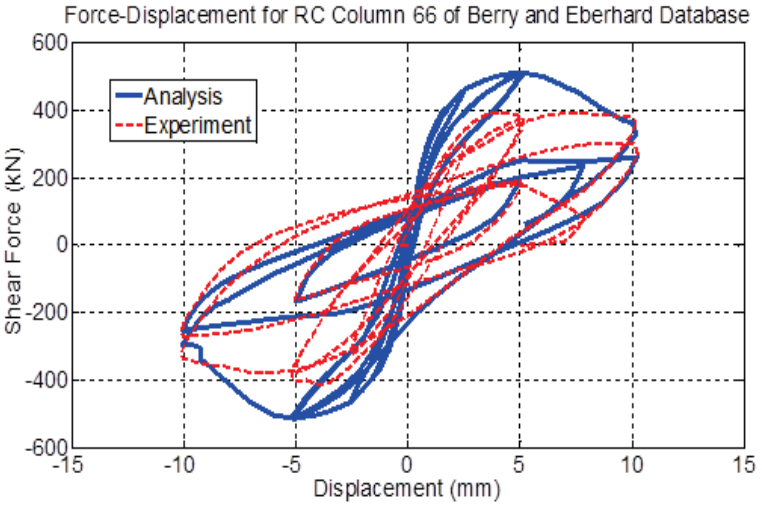

Figure A-48: Comparison between numerical and experimental responses of rectangular columns (ID#63&66) of Berry and Eberhard Database (2004).

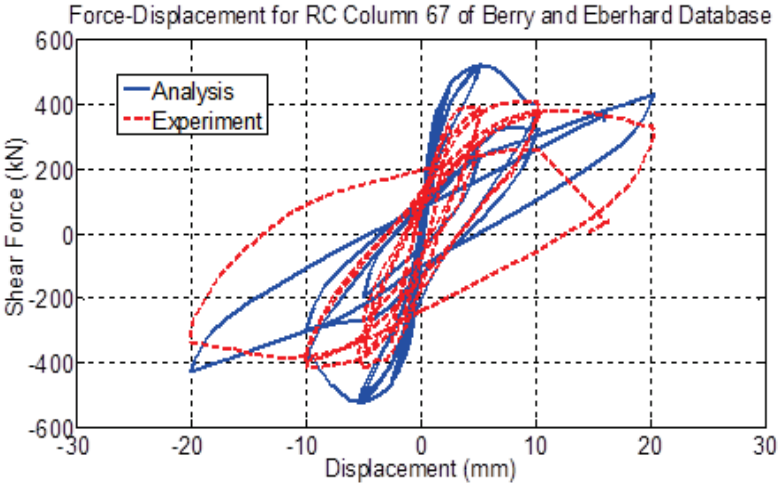

Concrete Model: Mander et al., 1988.

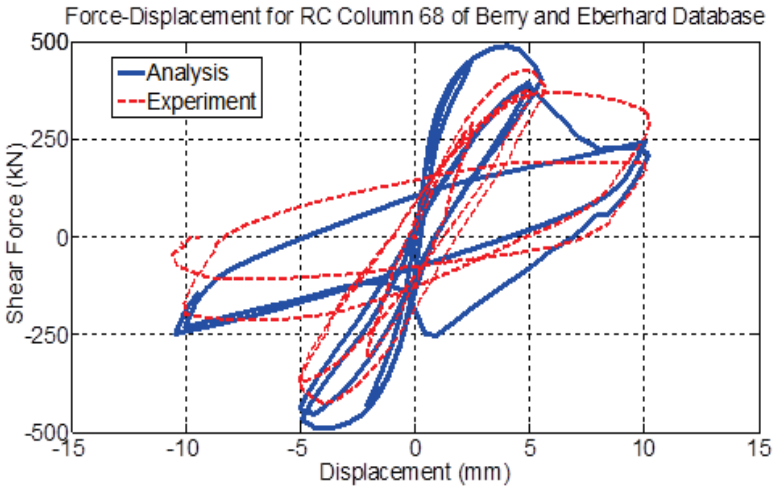

Figure A-49: Comparison between numerical and experimental responses of rectangular columns (ID#67&68) of Berry and Eberhard Database (2004).

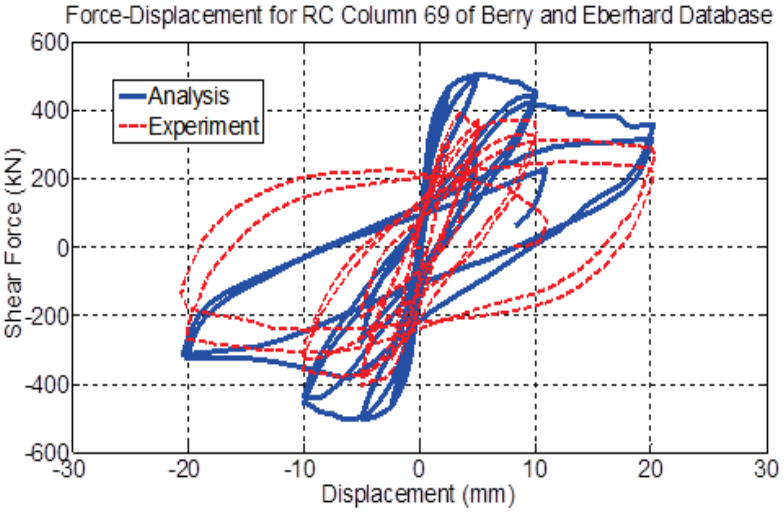

Concrete Model: Mander et al., 1988.

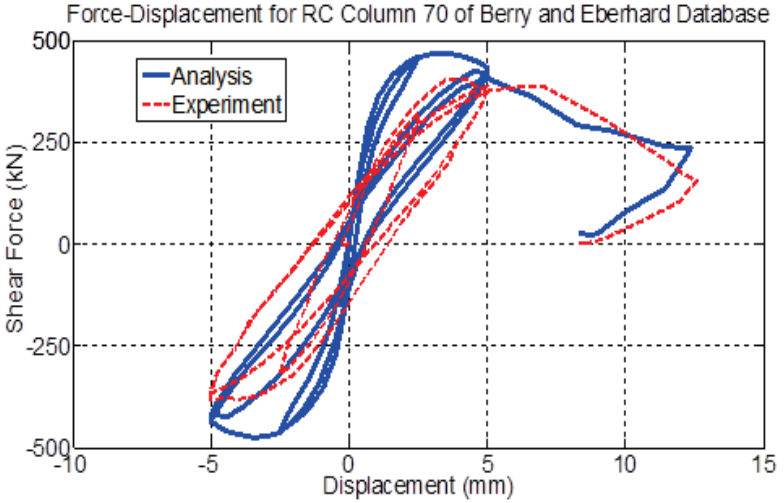

Figure A-50: Comparison between numerical and experimental responses of rectangular columns (ID#69&70) of Berry and Eberhard Database (2004).

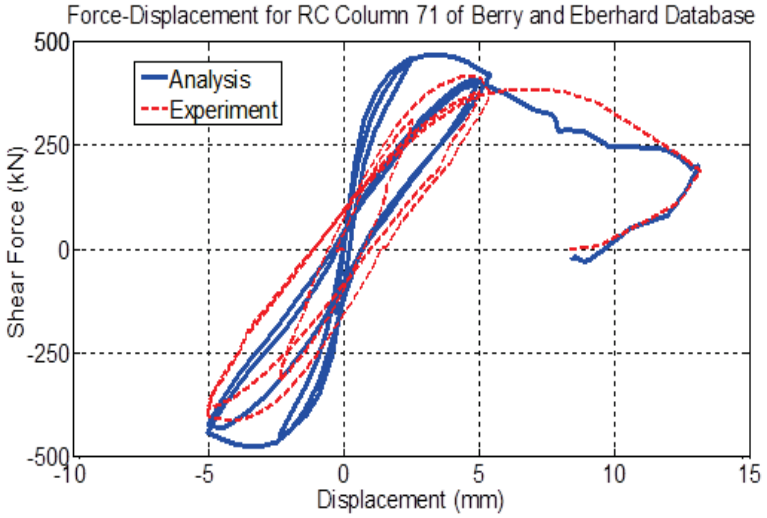

Concrete Model: Mander et al., 1988.

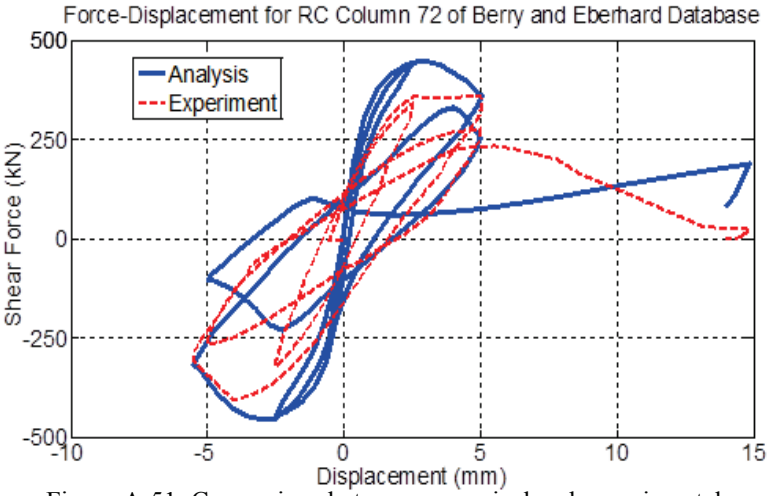

Figure A-51: Comparison between numerical and experimental responses of rectangular columns (ID#71&72) of Berry and Eberhard Database (2004).

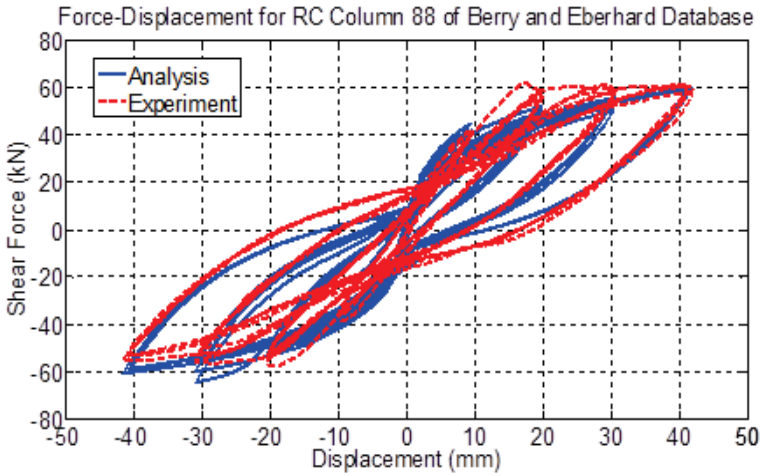

Concrete Model: Mander et al., 1988.

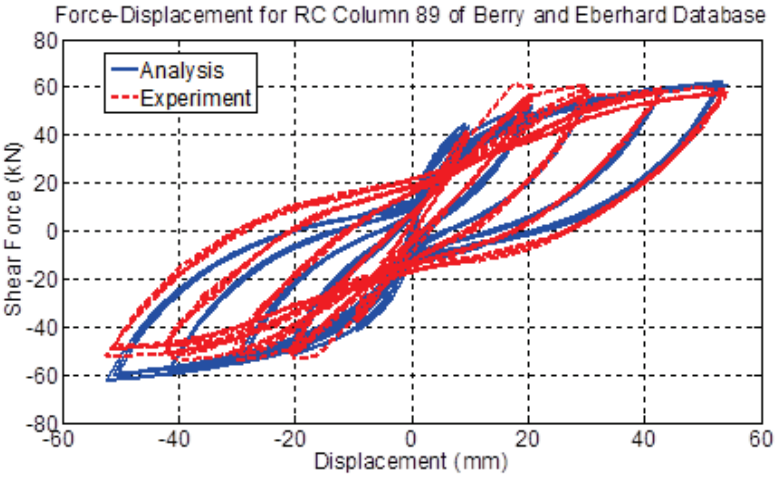

Figure A-52: Comparison between numerical and experimental responses of rectangular columns (ID#88&89) of Berry and Eberhard Database (2004).

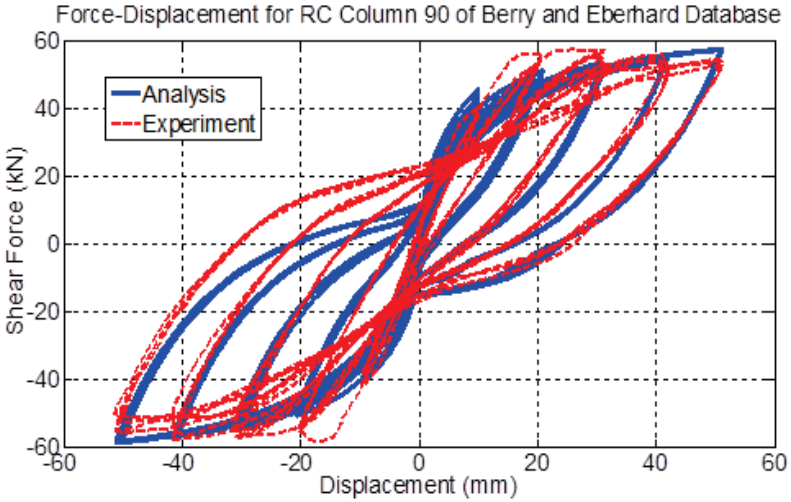

Concrete Model: Mander et al., 1988.

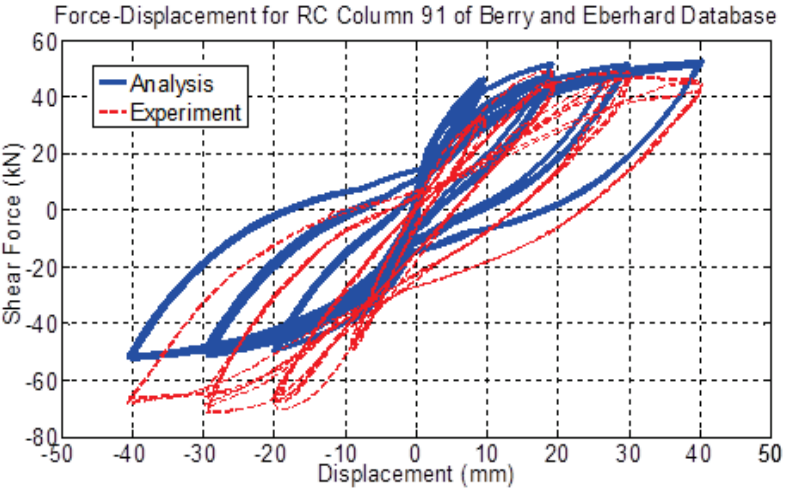

Figure A-53: Comparison between numerical and experimental responses of rectangular columns (ID#90&91) of Berry and Eberhard Database (2004).

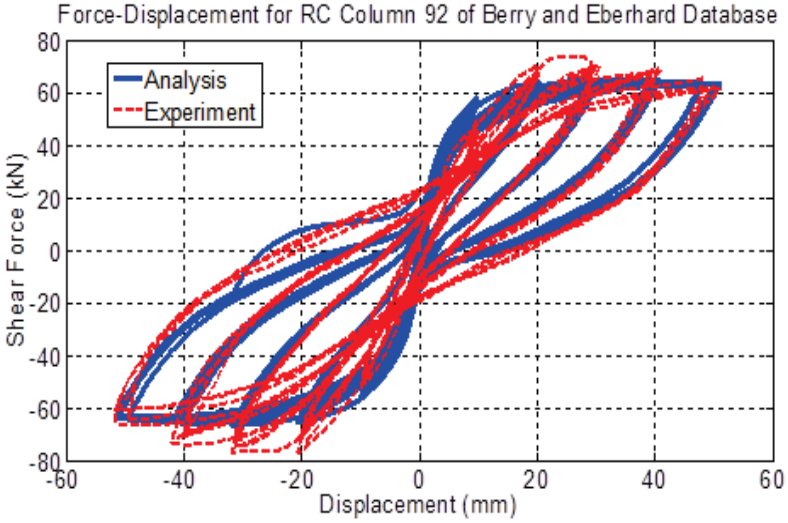

Concrete Model: Mander et al., 1988.

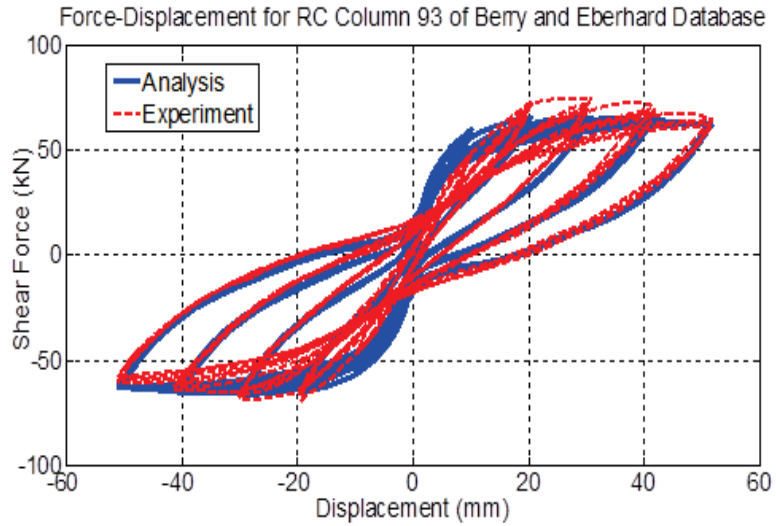

Figure A-54: Comparison between numerical and experimental responses of rectangular columns (ID#92&93) of Berry and Eberhard Database (2004).

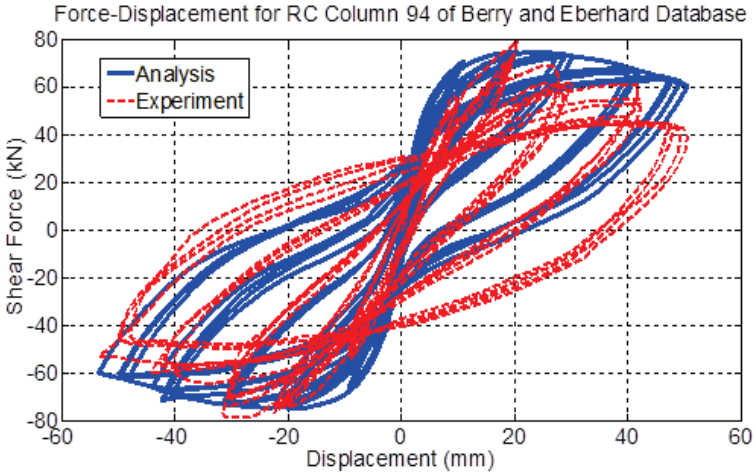

Concrete Model: Mander et al., 1988.

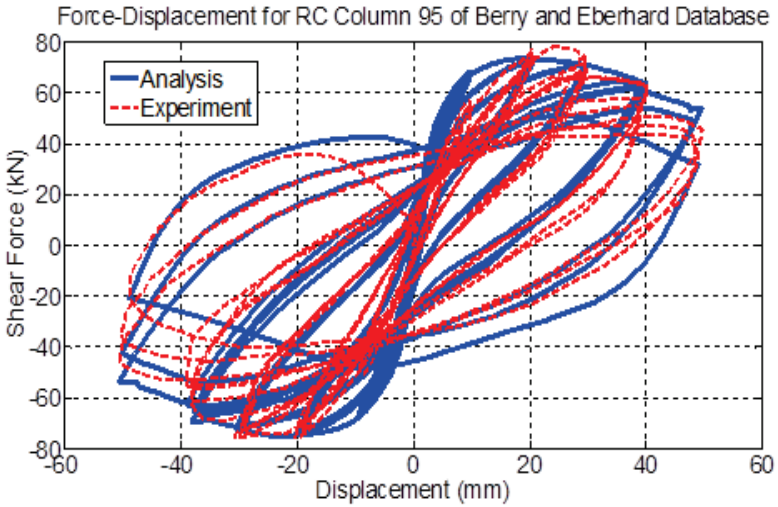

Figure A-55: Comparison between numerical and experimental responses of rectangular columns (ID#94&95) of Berry and Eberhard Database (2004).

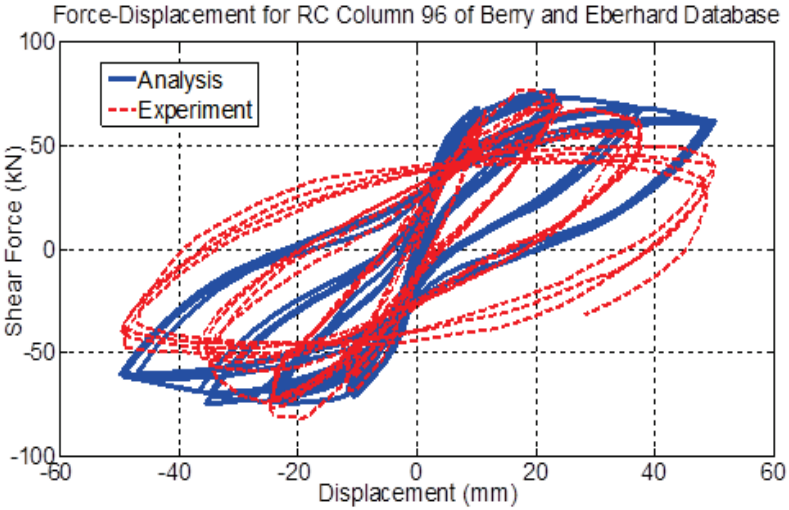

Concrete Model: Mander et al., 1988.

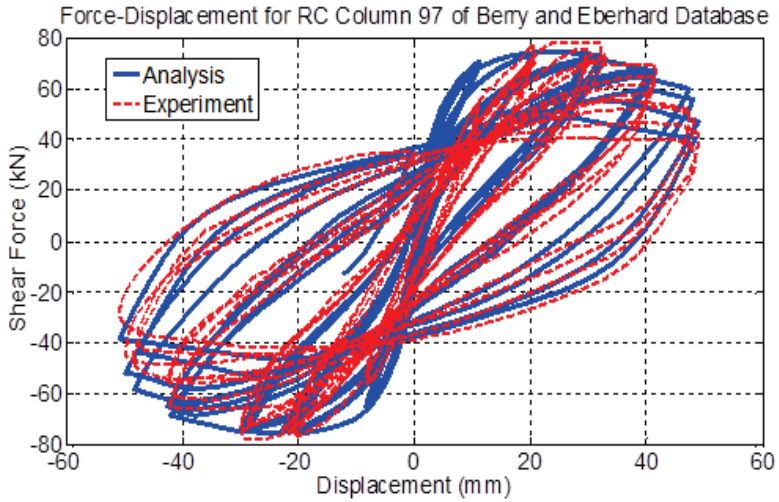

Figure A-56: Comparison between numerical and experimental responses of rectangular columns (ID#96&97) of Berry and Eberhard Database (2004).

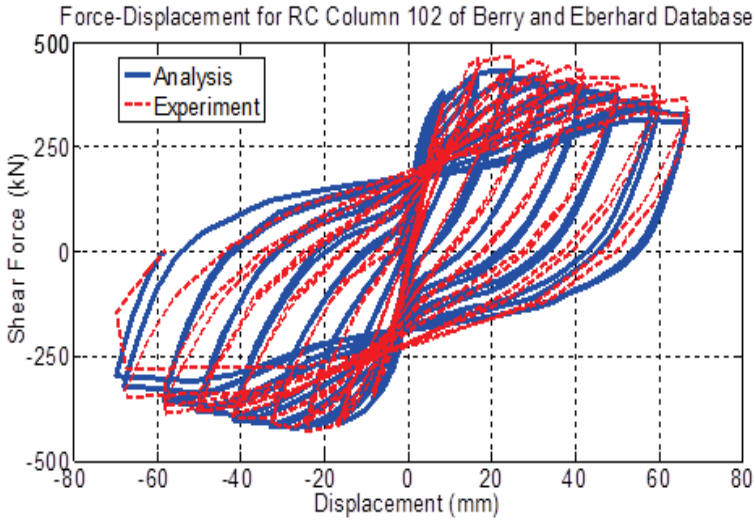

Concrete Model: Mander et al., 1988.

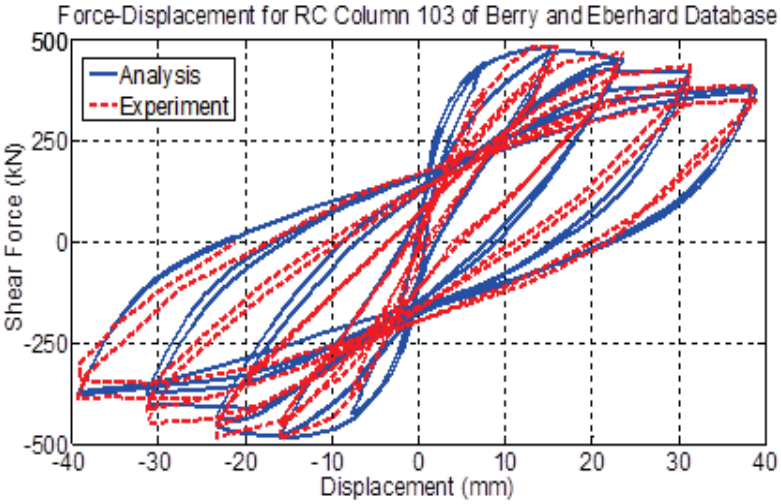

Figure A-57: Comparison between numerical and experimental responses of rectangular columns (ID#102&103) of Berry and Eberhard Database (2004).

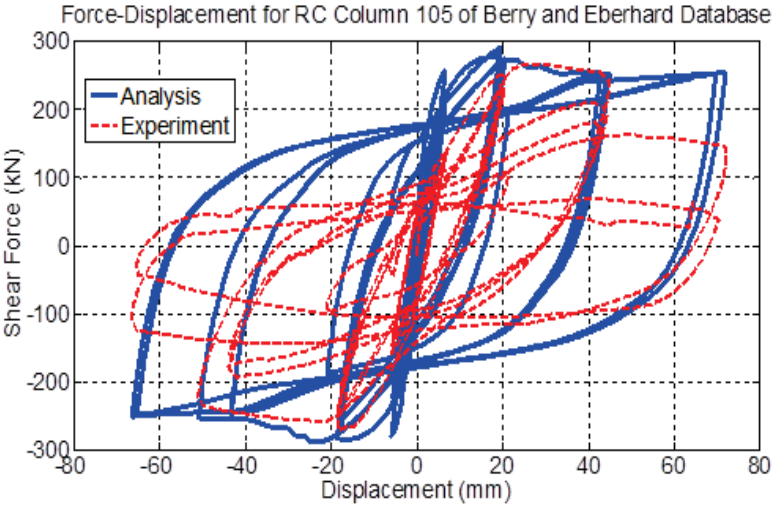

Concrete Model: Mander et al., 1988.

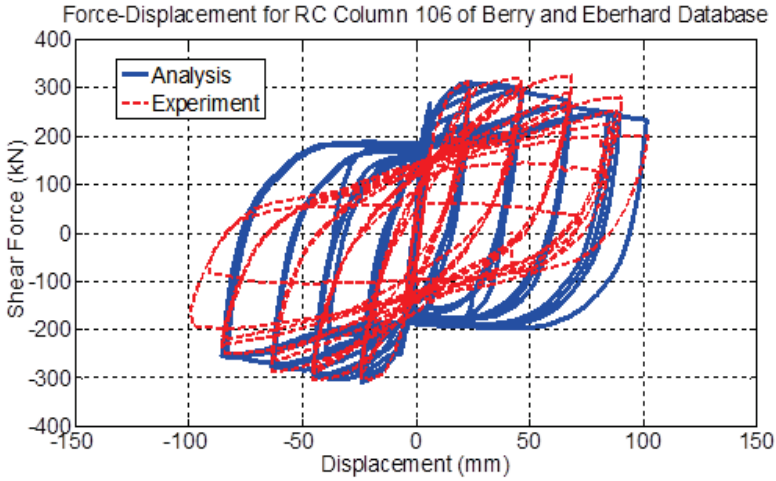

Figure A-58: Comparison between numerical and experimental responses of rectangular columns (ID#105&106) of Berry and Eberhard Database (2004).

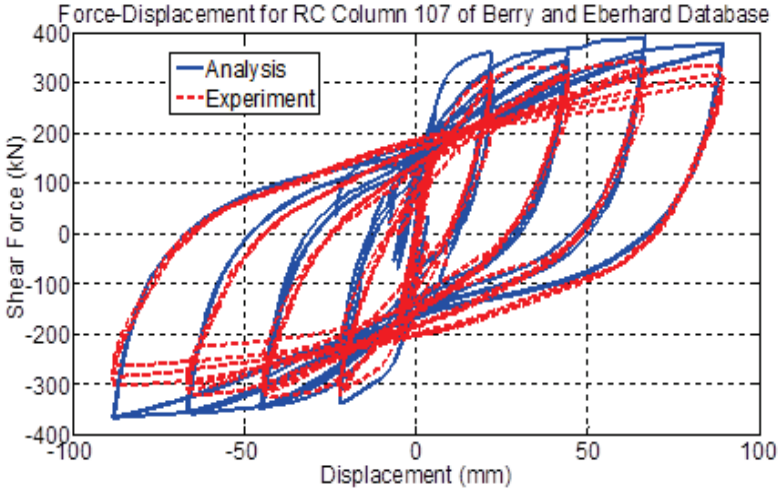

Concrete Model: Mander et al., 1988.

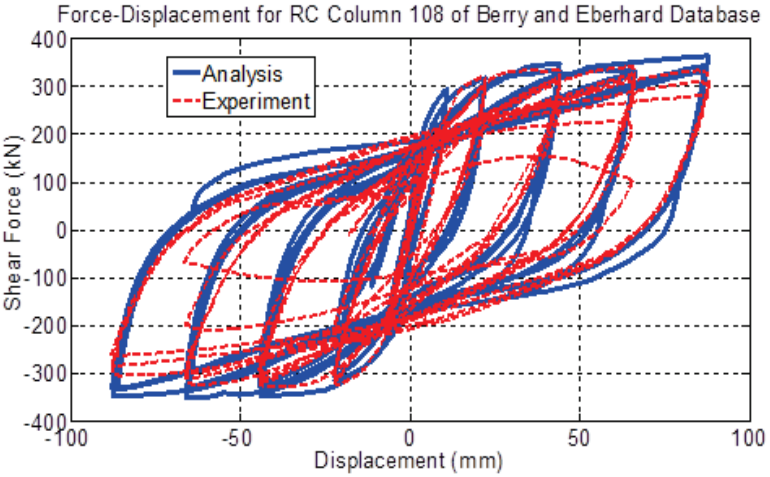

Figure A-59: Comparison between numerical and experimental responses of rectangular columns (ID#107&108) of Berry and Eberhard Database (2004).

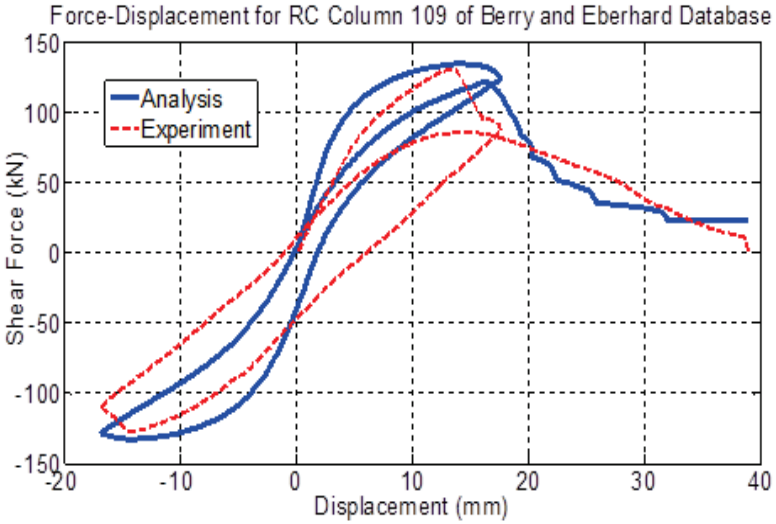

Concrete Model: Mander et al., 1988.

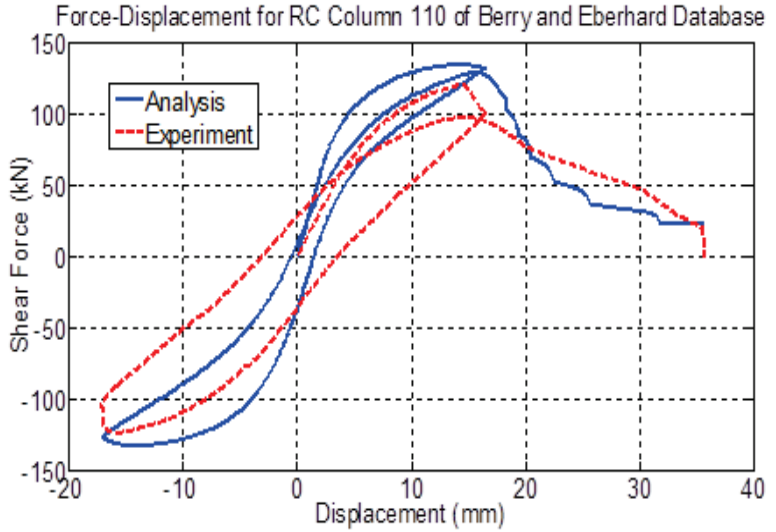

Figure A-60: Comparison between numerical and experimental responses of rectangular columns (ID#109&110) of Berry and Eberhard Database (2004).

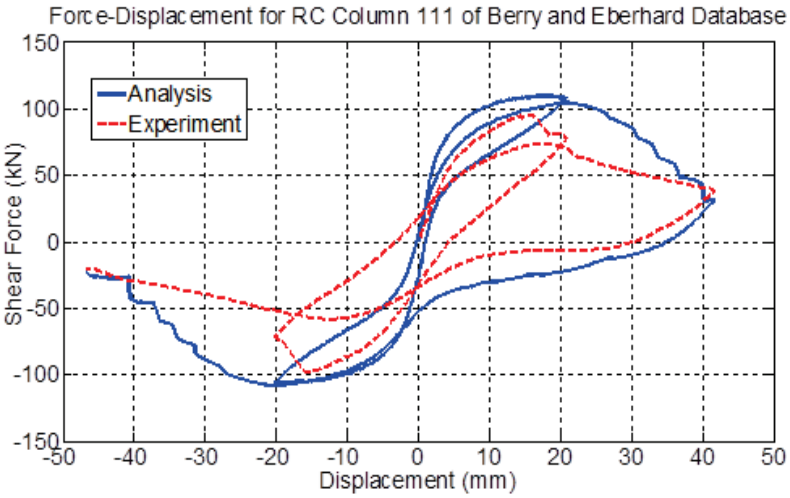

Concrete Model: Mander et al., 1988.

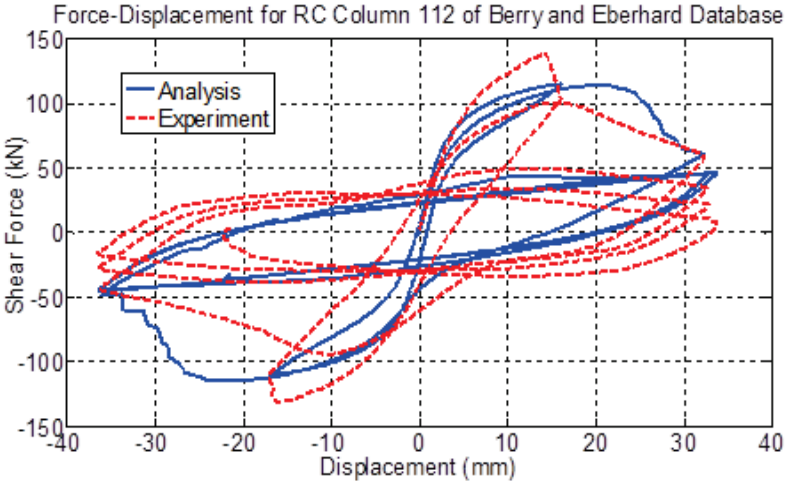

Figure A-61: Comparison between numerical and experimental responses of rectangular columns (ID#111&112) of Berry and Eberhard Database (2004).

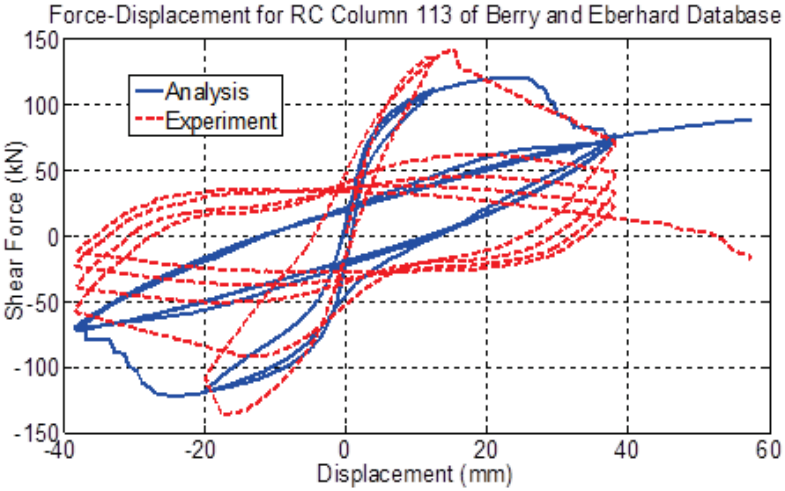

Concrete Model: Mander et al., 1988.

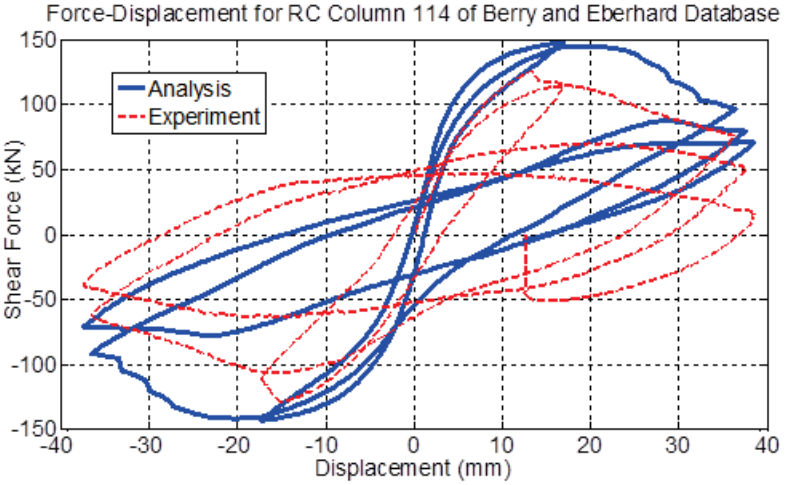

Figure A-62: Comparison between numerical and experimental responses of rectangular columns (ID#113&114) of Berry and Eberhard Database (2004).

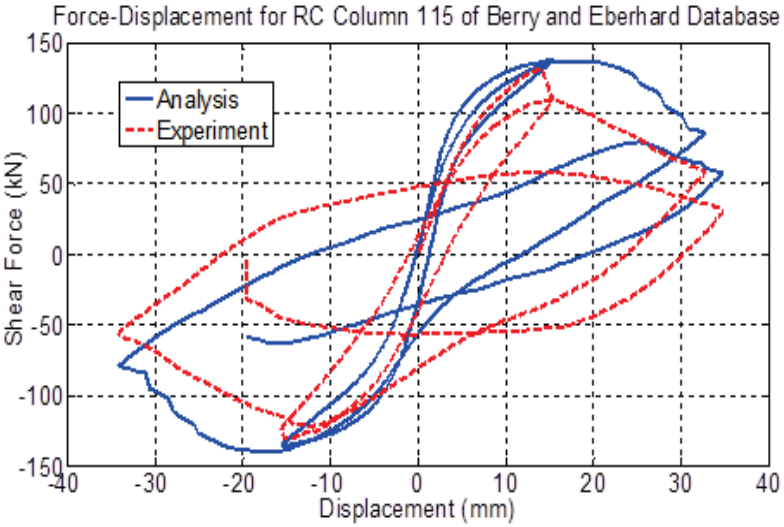

Concrete Model: Mander et al., 1988.

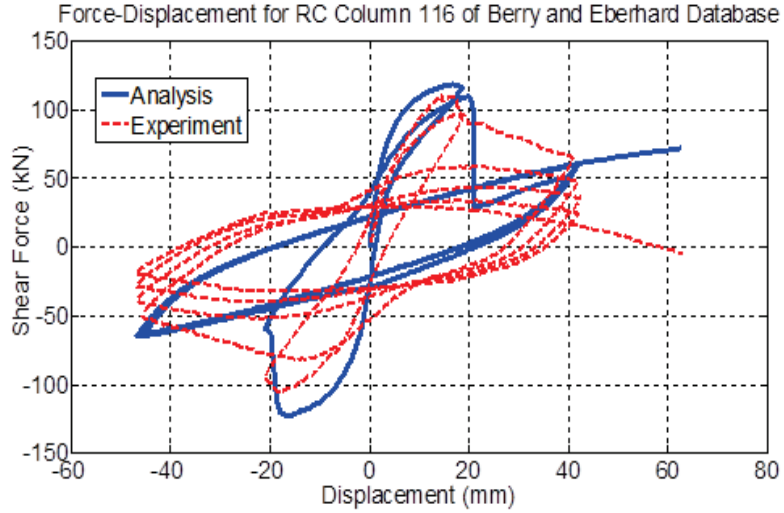

Figure A-63: Comparison between numerical and experimental responses of rectangular columns (ID#115&116) of Berry and Eberhard Database (2004).

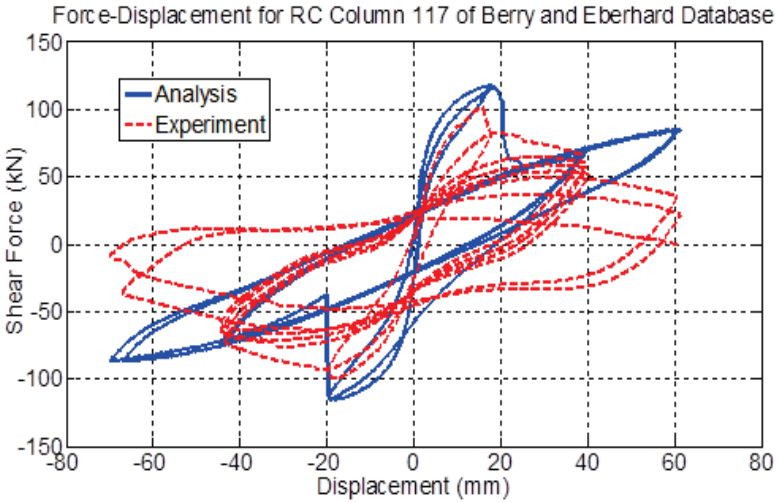

Concrete Model: Mander et al., 1988.

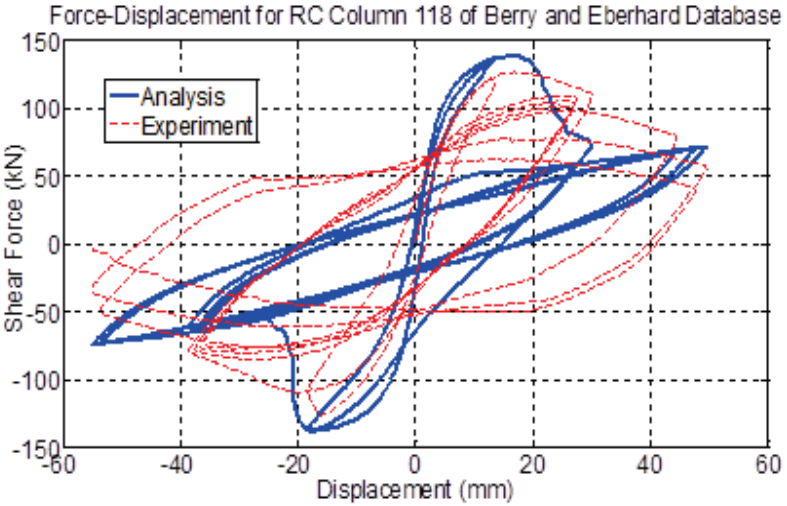

Figure A-64: Comparison between numerical and experimental responses of rectangular columns (ID#117&118) of Berry and Eberhard Database (2004).

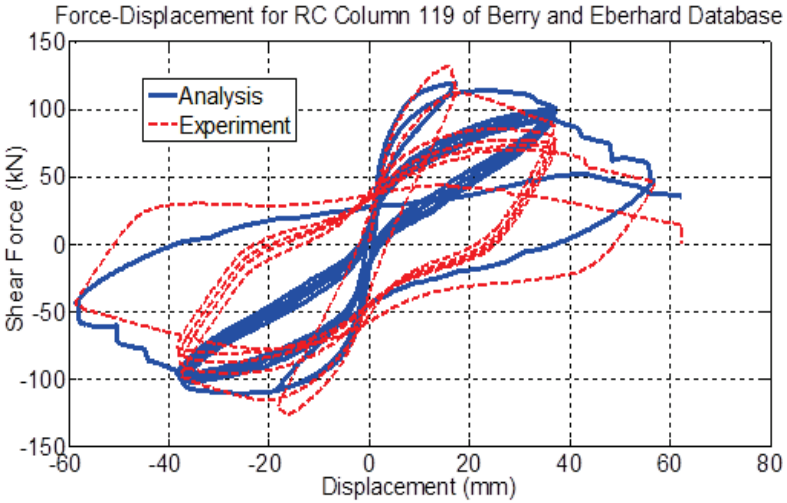

Concrete Model: Mander et al., 1988.

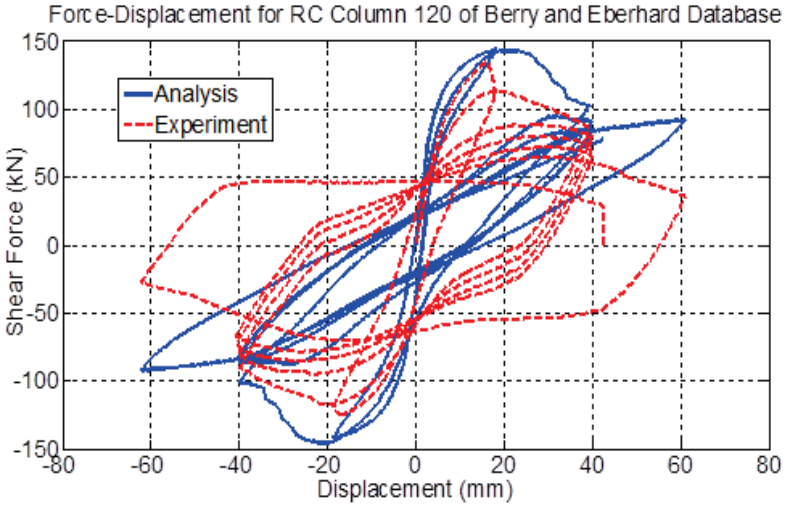

Figure A-65: Comparison between numerical and experimental responses of rectangular columns (ID#119&120) of Berry and Eberhard Database (2004).

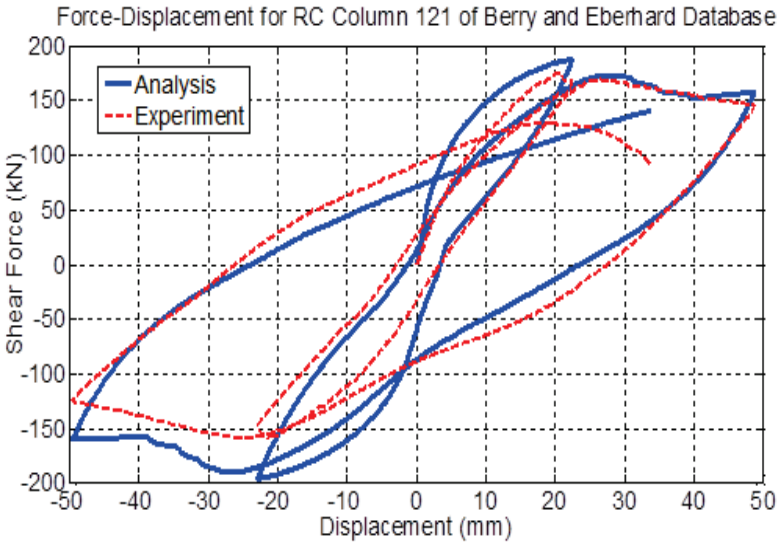

Concrete Model: Mander et al., 1988.

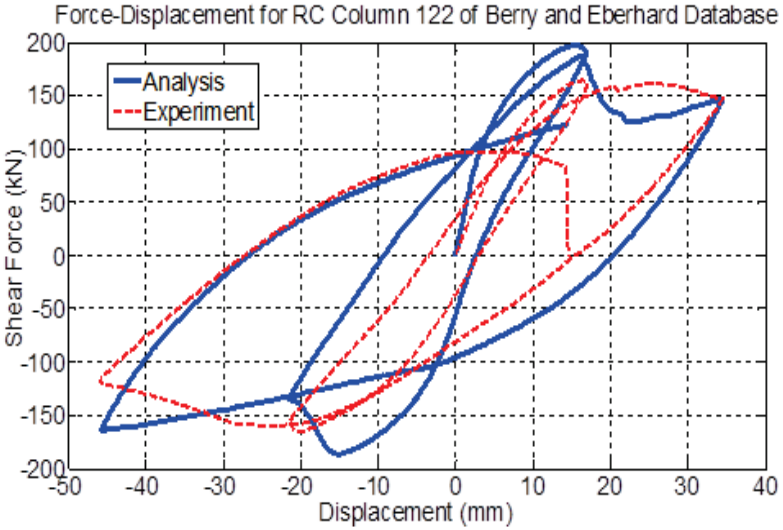

Figure A-66: Comparison between numerical and experimental responses of rectangular columns (ID#121&122) of Berry and Eberhard Database (2004).

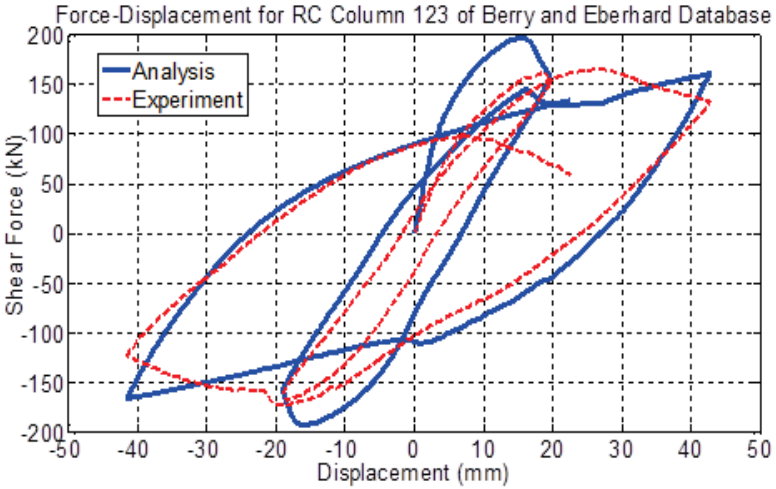

Concrete Model: Mander et al., 1988.

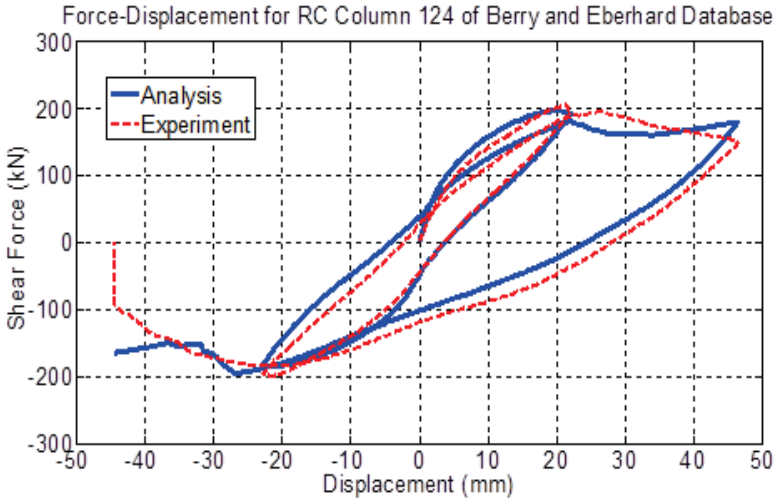

Figure A-67: Comparison between numerical and experimental responses of rectangular columns (ID#123&124) of Berry and Eberhard Database (2004).

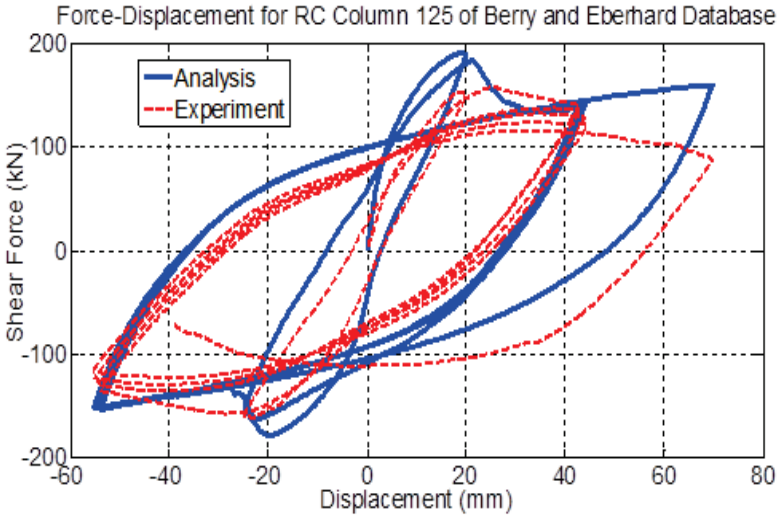

Concrete Model: Mander et al., 1988.

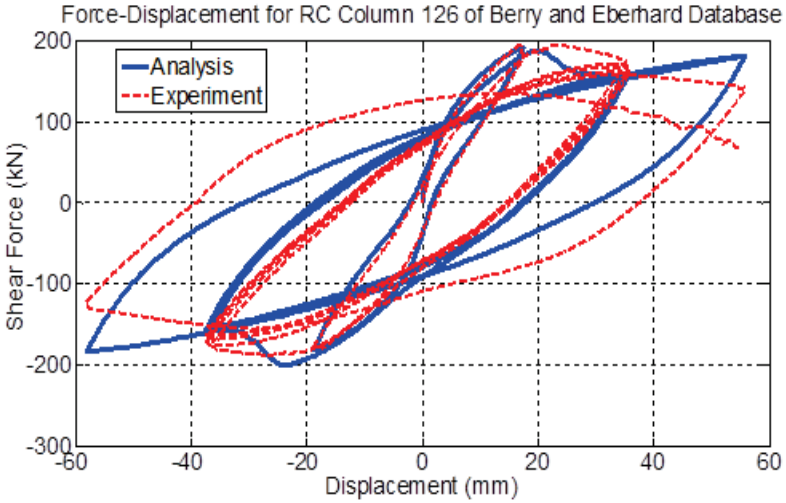

Figure A-68: Comparison between numerical and experimental responses of rectangular columns (ID#125&126) of Berry and Eberhard Database (2004).

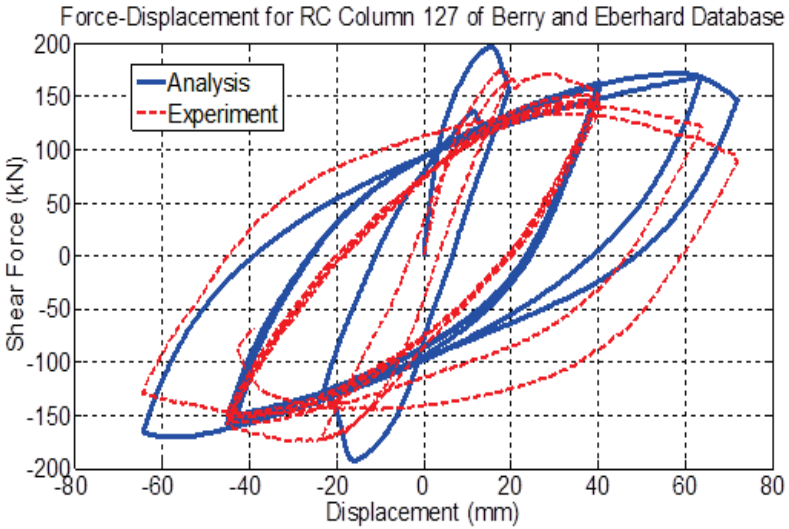

Concrete Model: Mander et al., 1988.

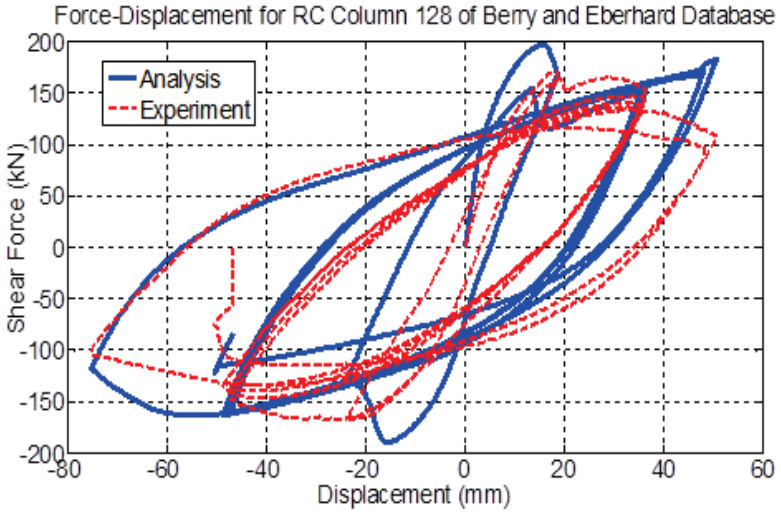

Figure A-69: Comparison between numerical and experimental responses of rectangular columns (ID#127&128) of Berry and Eberhard Database (2004).

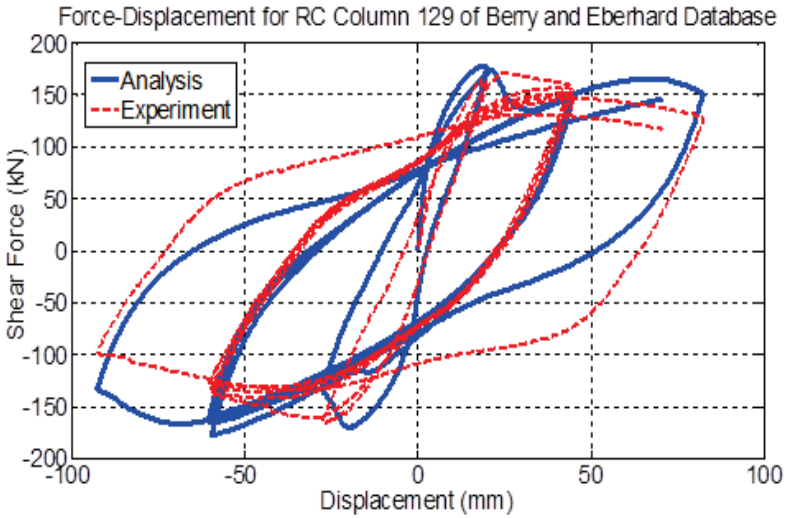

Concrete Model: Mander et al., 1988.

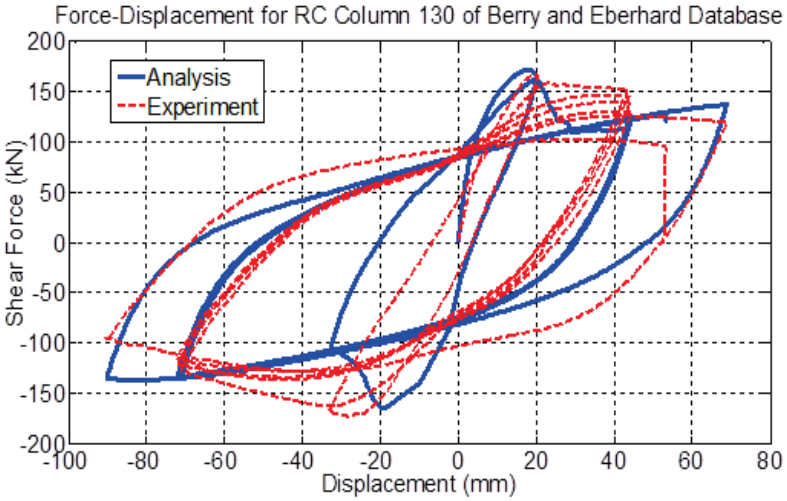

Figure A-70: Comparison between numerical and experimental responses of rectangular columns (ID#129&130) of Berry and Eberhard Database (2004).

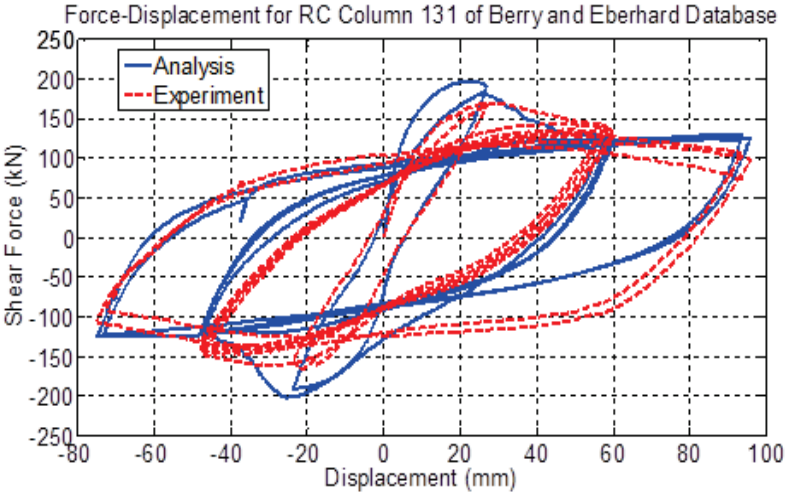

Concrete Model: Mander et al., 1988.

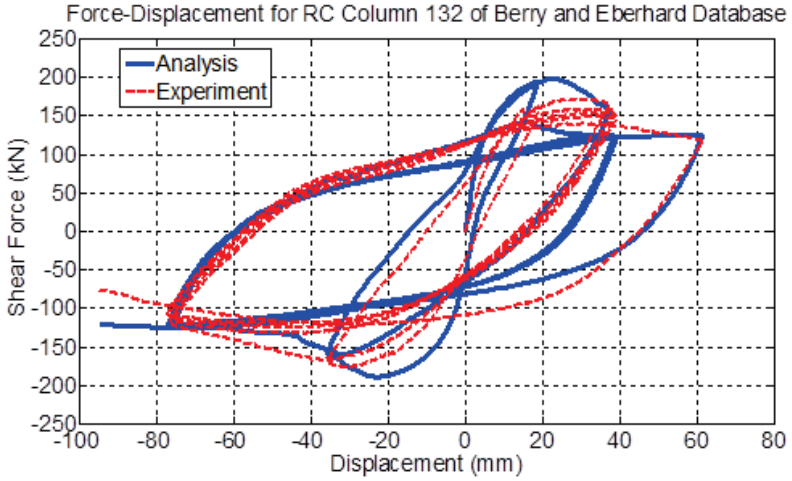

Figure A-71: Comparison between numerical and experimental responses of rectangular columns (ID#131&132) of Berry and Eberhard Database (2004).

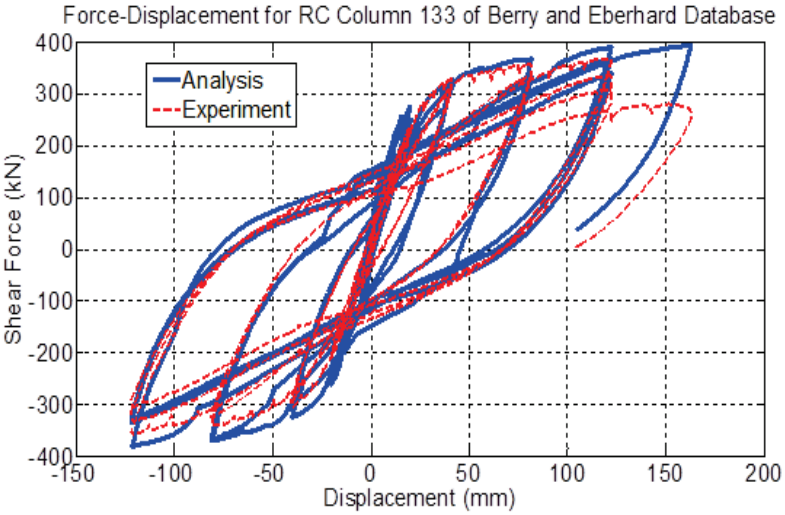

Concrete Model: Mander et al., 1988.

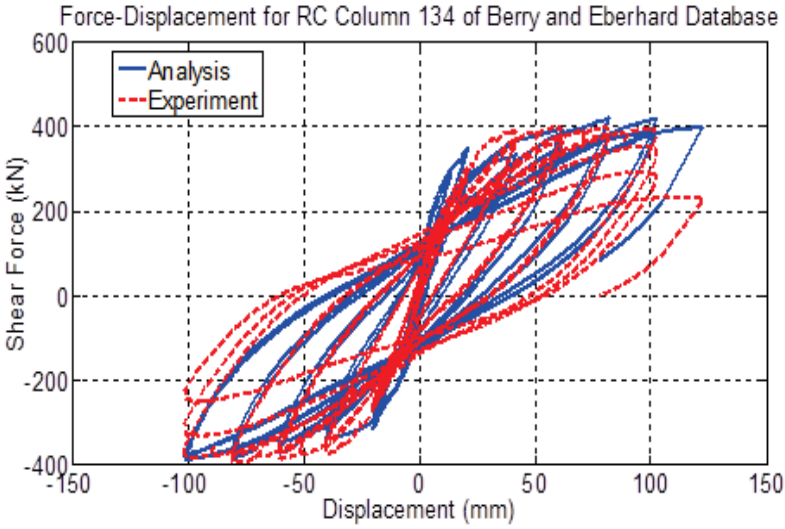

Figure A-72: Comparison between numerical and experimental responses of rectangular columns (ID#133&134) of Berry and Eberhard Database (2004).

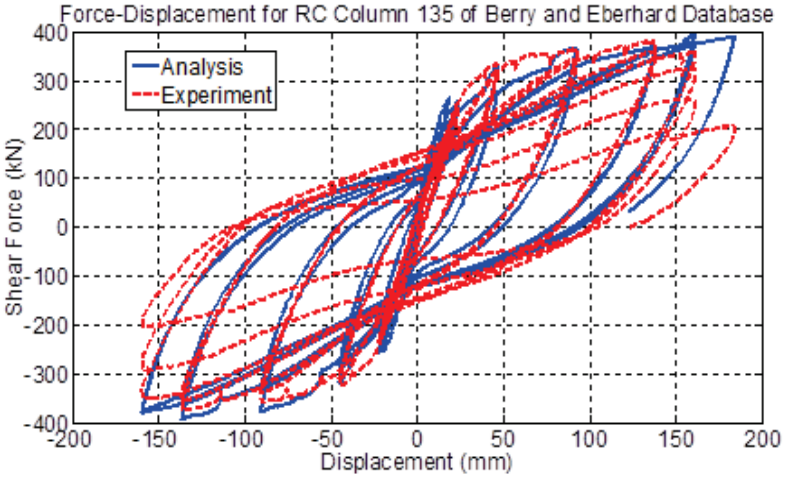

Concrete Model: Mander et al., 1988.

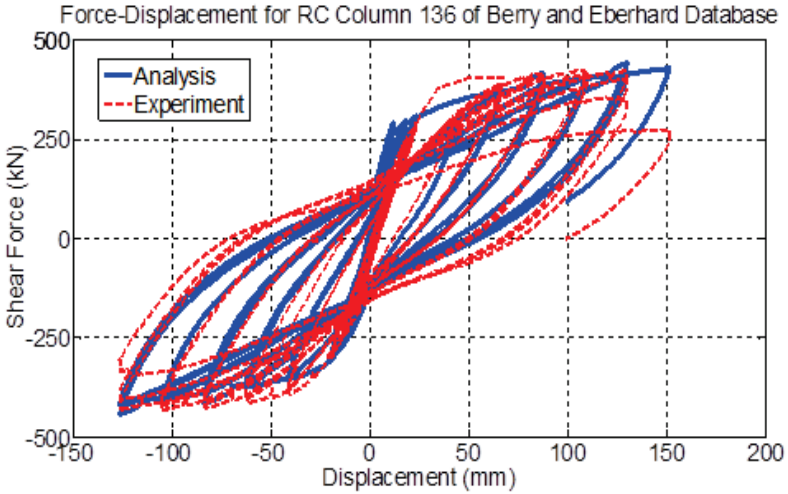

Figure A-73: Comparison between numerical and experimental responses of rectangular columns (ID#135&136) of Berry and Eberhard Database (2004).

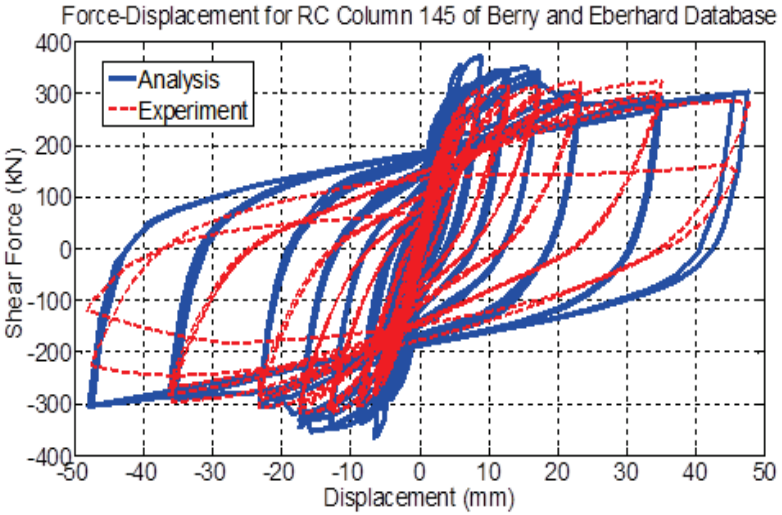

Concrete Model: Mander et al., 1988.

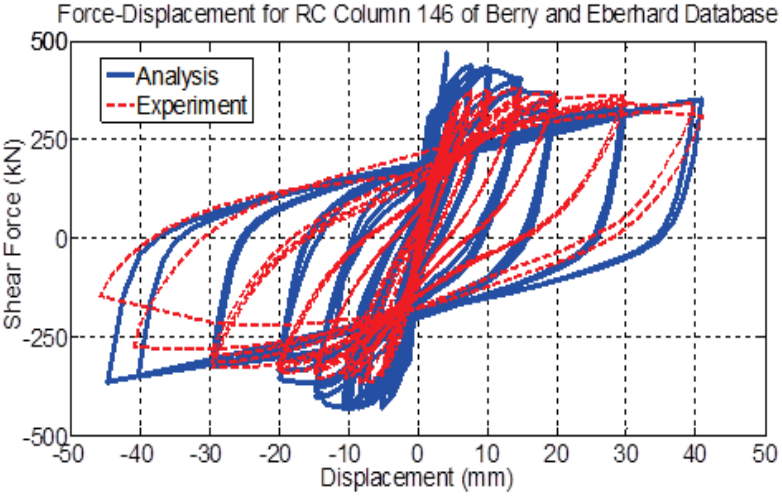

Figure A-74: Comparison between numerical and experimental responses of rectangular columns (ID#145&146) of Berry and Eberhard Database (2004).

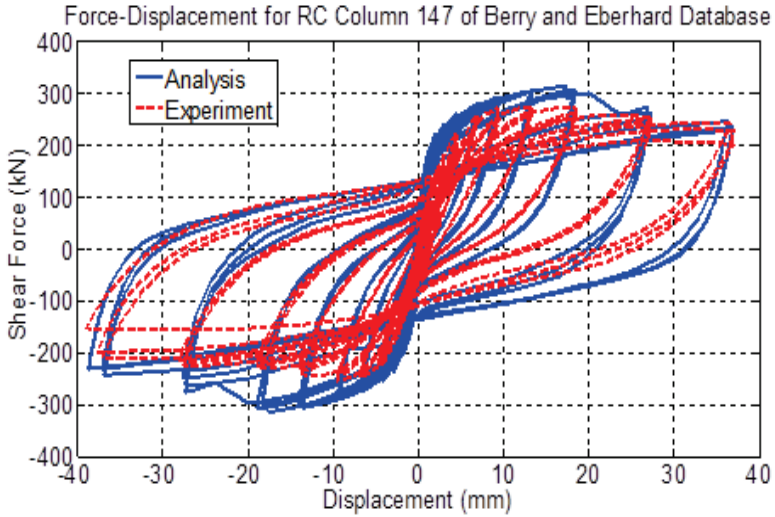

Concrete Model: Mander et al., 1988.

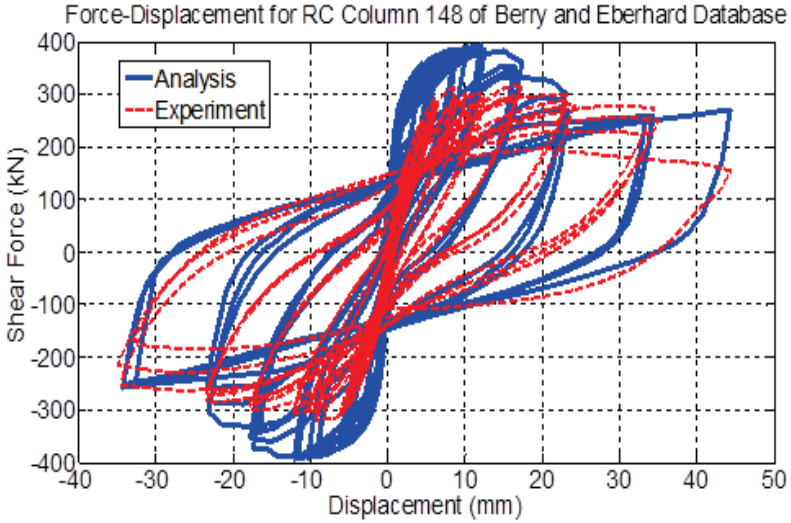

Figure A-75: Comparison between numerical and experimental responses of rectangular columns (ID#147&148) of Berry and Eberhard Database (2004).

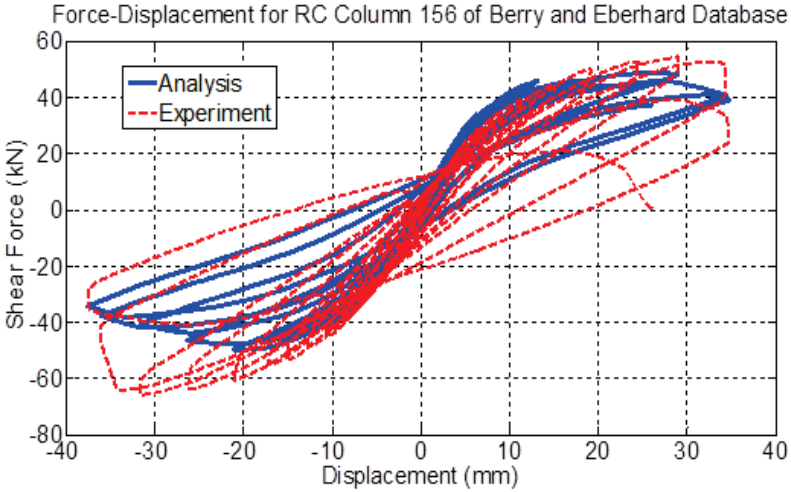

Concrete Model: Mander et al., 1988.

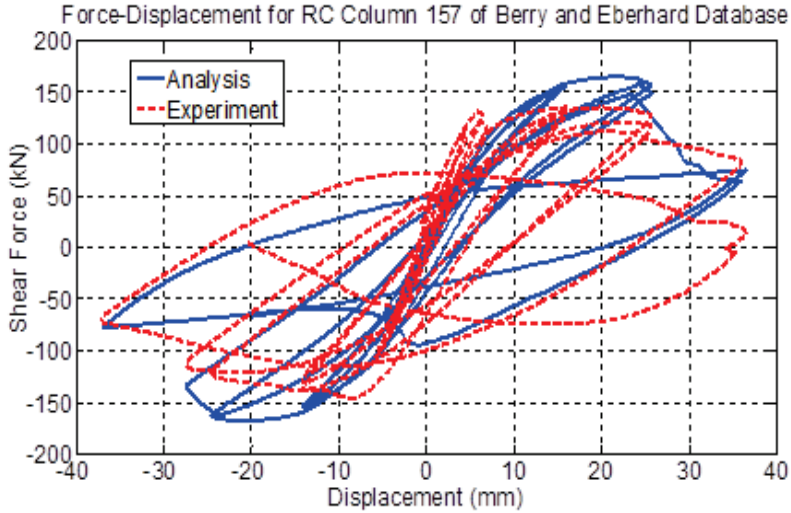

Figure A-76: Comparison between numerical and experimental responses of rectangular columns (ID#156&157) of Berry and Eberhard Database (2004).

Table A-3: Reinforced concrete columns with a rectangular cross section that failed in shear.

SpecimenID in Database	Axial Load (KN)	Width - Depth (mm)	Clear Cover (mm)	Shear Span (mm)	Concrete Strength (MPa)	Number of Longitudinal Bars	Diameter of Long. Bars (mm)	Yielding Strength of Long. Bars (MPa)	Ultimate Strength of Long. Bars (MPa)	Longitudinal Reinforcement ratio	Stirrups Spacing (mm)	Diameter of Stirrups (mm)	Stirrups Yielding Strength (MPa)	Transverse Reinforcement ratio
28	147	200-200	12	300	21.6	4	12.7	371	541	0.0127	35	5.5	344	0.0081
29	294	200-200	12	300	21	4	12.7	371	541	0.0127	20	5.5	344	0.0139
33	183	200-200	11	400	32	4	16	369	-	0.0201	50	5.5	316	0.0057
34	183	200-200	12.5	400	29.9	8	13	370	-	0.0265	50	5.5	316	0.0057
38	392	400-500	37	825	27.1	14	22	318	-	0.0266	100	9	336	0.0036
39	406	160-160	12.5	160	19.8	8	10	341	448	0.0222	40	5	559	0.0073
41	406	160-160	12.5	160	19.8	8	10	341	448	0.0222	40	5	559	0.0175
42	432	160-160	12.5	320	21.1	8	10	341	448	0.0222	40	5	559	0.0073
44	486	160-160	12.5	320	21.1	8	10	341	448	0.0222	40	5	559	0.0175
45	517	160-160	12.5	480	28.8	8	10	341	448	0.0222	40	5	559	0.0073
47	517	160-160	12.5	480	28.8	8	10	341	448	0.0222	40	5	559	0.0175

54	190	180-180	10	225	31.8	8	12.7	340	-	0.0313	64.3	4	249	0.0021
55	476	180-180	10	225	33	8	12.7	340	-	0.0313	64.3	4	249	0.0021
64	265	200-200	19	300	25.8	12	9.5	361	533	0.0213	70	6	426	0.0091
65	636	200-200	19	300	25.8	12	9.5	361	533	0.0213	70	6	426	0.0091
73	2632	278-278	28	323	46.3	16	13	441	-	0.0275	52	6	414	0.0089
74	189	152-304	35	876	34.7	4	19	496	835	0.0245	127	6.3	345	0.0033
76	178	152-304	35	876	26.1	4	19	496	835	0.0245	89	6.3	345	0.0048
78	178	152-304	35	876	33.6	4	19	496	835	0.0245	127	6.3	345	0.0033
80	111	152-304	35	876	33.6	4	19	496	835	0.0245	127	6.3	345	0.0033
82	178	152-304	35	876	33.4	4	19	496	835	0.0245	64	6.3	345	0.0067
84	178	152-304	32	876	33.5	4	19	496	835	0.0245	64	9.5	317	0.0147
86	178	152-304	32	876	33.5	4	19	496	835	0.0245	102	9.5	317	0.0092
98	534	230-410	25	455	34.9	10	19	441	745	0.0301	89	6	414	0.0028
99	534	410-230	25	455	34.9	10	19	441	745	0.0301	89	6	414	0.0031
100	1068	230-410	25	455	42	10	19	441	745	0.0301	89	6	414	0.0028
101	288	305-305	25	457	29.9	8	19	462	772	0.0244	210	6	414	0.0026

137	503	457-457	38.1	1473	26.9	8	31.75	330.96	496	0.0303	457.2	9.525	399.91	-
138	503	457-457	38.1	1473	33.1	8	25.4	330.96	496	0.0194	457.2	9.525	399.91	-
139	1512	457-457	38.1	1473	25.5	8	25.4	330.96	496	0.0194	457.2	9.525	399.91	-
140	1512	457-457	38.1	1473	27.6	8	31.75	330.96	496	0.0303	457.2	9.525	399.91	-
141	1512	457-457	38.1	1473	27.6	8	31.75	330.96	496	0.0303	304.8	9.525	399.91	-
142	503	457-457	38.1	1473	26.9	8	31.75	330.96	496	0.0303	457.2	9.525	399.91	-
143	503	457-457	38.1	1473	33.1	8	25.4	330.96	496	0.0194	457.2	9.525	399.91	-
144	1512	457-457	38.1	1473	25.5	8	31.75	330.96	496	0.0303	304.8	9.525	399.91	-
149	534	254-254	13	508	86	8	15.9	510	-	0.0246	51	6.4	449	0.0163
150	1068	254-254	13	508	86	8	15.9	510	-	0.0246	51	6.4	449	0.0163
199	0	914-457	38	1219	21.9	16	25	434	690	0.0188	406.4	9.53	400	-
200	0	457-914	38	1219	16	16	25	434	690	0.0188	406.4	9.53	400	-
212	667	457-457	65.13	1473	21.1	8	28.651	434.37	645	0.0247	304.8	9.525	476	0.0025
213	2669	457-457	65.13	1473	21.1	8	28.651	434.37	645	0.0247	304.8	9.525	476	0.0025
214	667	457-457	65.13	1473	21.8	8	28.651	434.37	645	0.0247	304.8	9.525	476	0.0025

276	507	406-610	22.23	1220	37.9	22	19.05	324	-	0.0253	127	6.35	358.5	-
277	507	406-610	22.23	1220	34.5	22	19.05	469	-	0.0253	127	6.35	324	-
278	507	406-610	22.23	915	32.4	22	19.05	469	-	0.0253	127	6.35	324	-
279	0	305-305	25.4	457.5	34.5	8	19.05	374		0.0245	65.3	6.35	455	-
280	534	305-305	25.4	457.5	30.7	8	19.05	455		0.0245	65.3	6.35	455	-
281	0	152-305	35	876	32	4	19	496	835	0.0245	127	6.3	345	0.0033
283	0	152-305	35	876	25.9	4	19	496	835	0.0245	89	6.3	345	0.0048

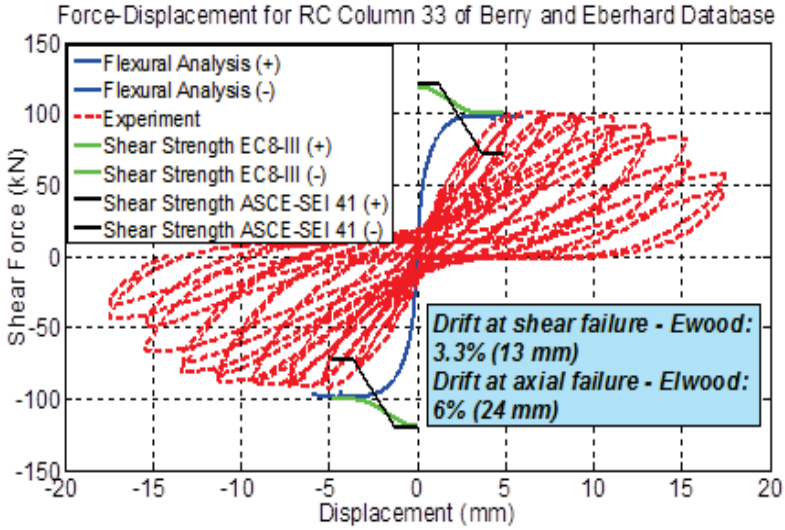

Concrete Model: Mander et al., 1988.

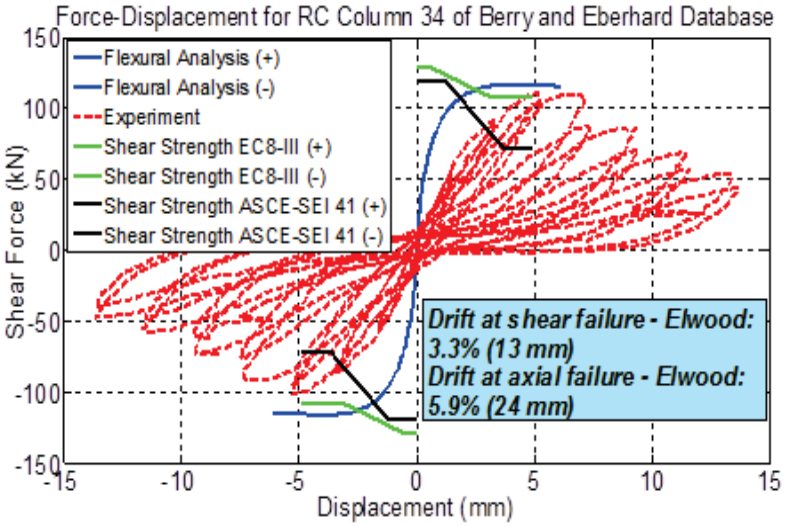

Figure A-77: Comparison between numerical and experimental responses of rectangular columns (ID#33&34) of Berry and Eberhard Database (2004).

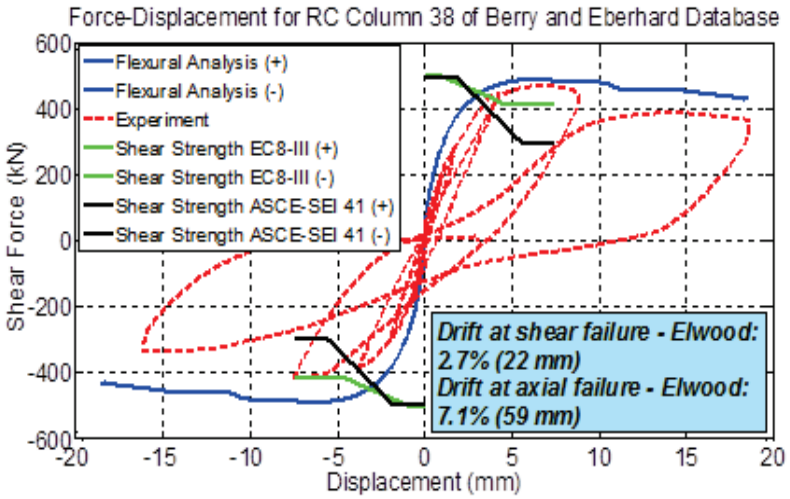

Concrete Model: Mander et al., 1988.

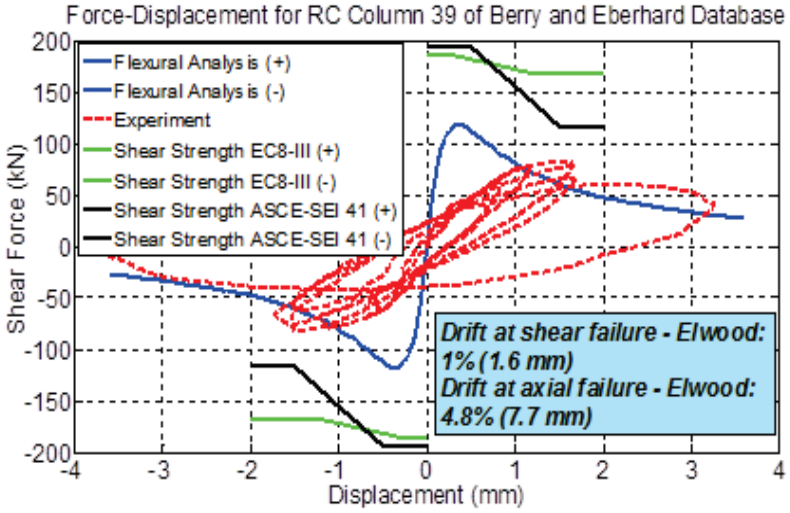

Figure A-78: Comparison between numerical and experimental responses of rectangular columns (ID#38&39) of Berry and Eberhard Database (2004).

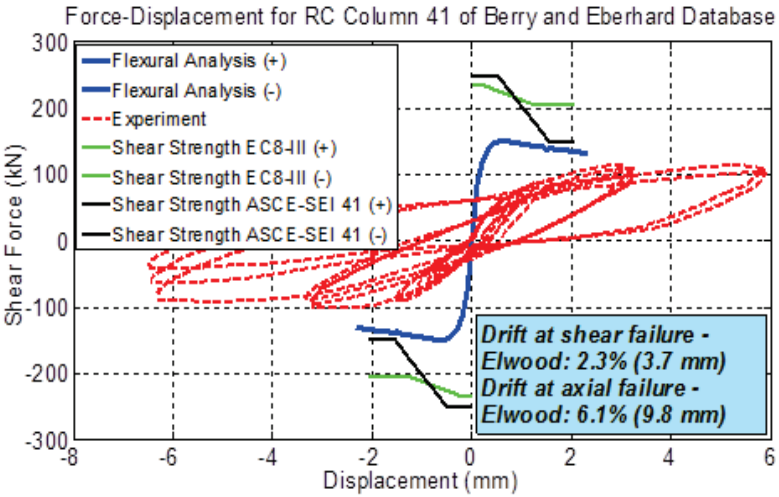

Concrete Model: Mander et al., 1988.

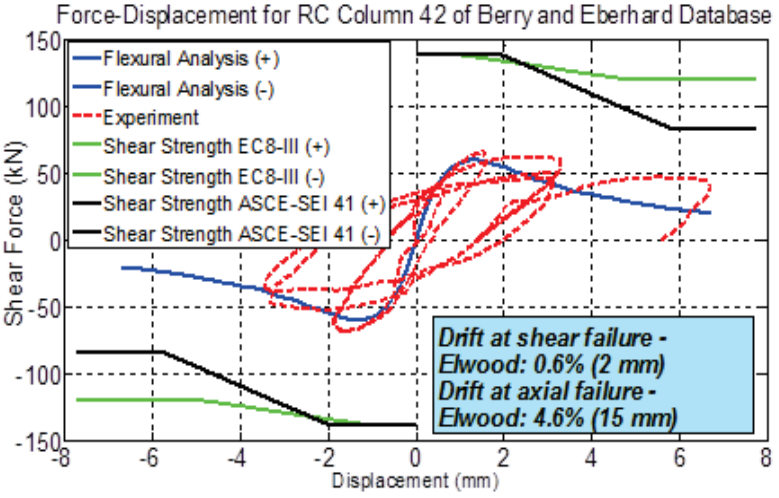

Figure A-79: Comparison between numerical and experimental responses of rectangular columns (ID#41&42) of Berry and Eberhard Database (2004).

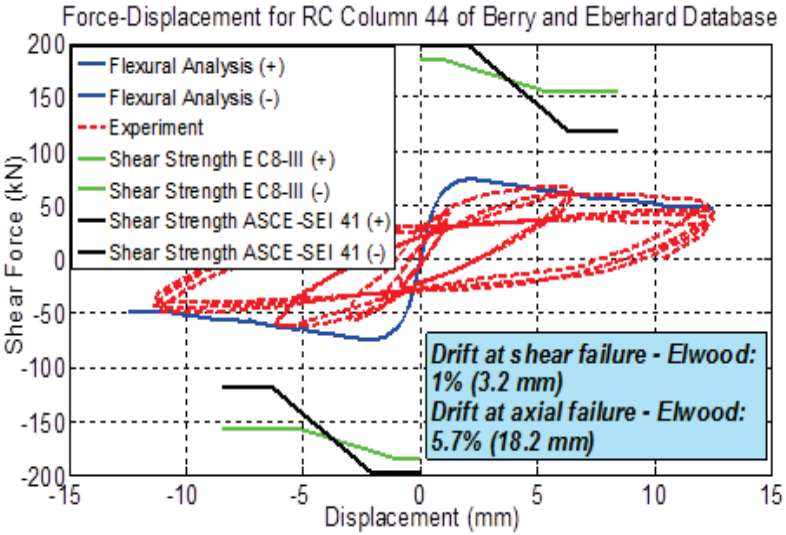

Concrete Model: Mander et al., 1988.

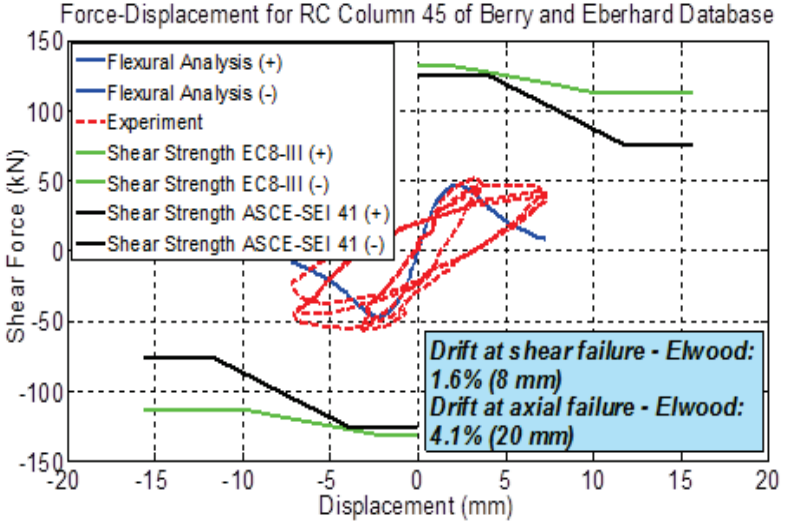

Figure A-80: Comparison between numerical and experimental responses of rectangular columns (ID#44&45) of Berry and Eberhard Database (2004).

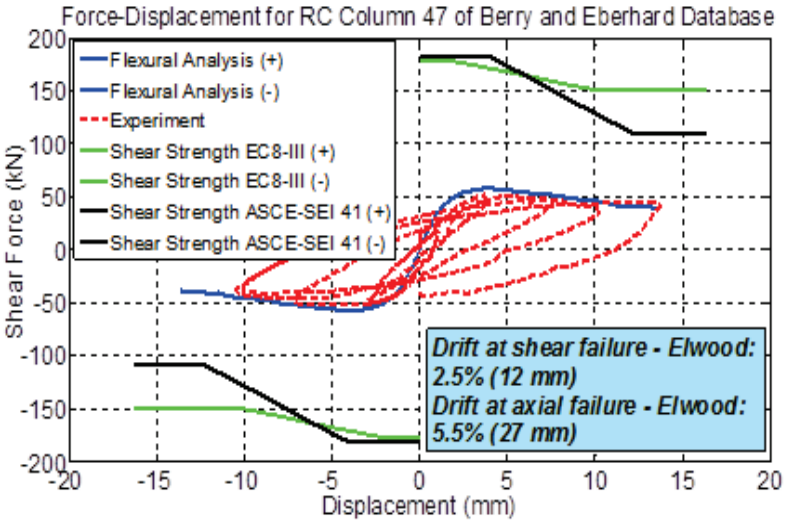

Concrete Model: Mander et al., 1988.

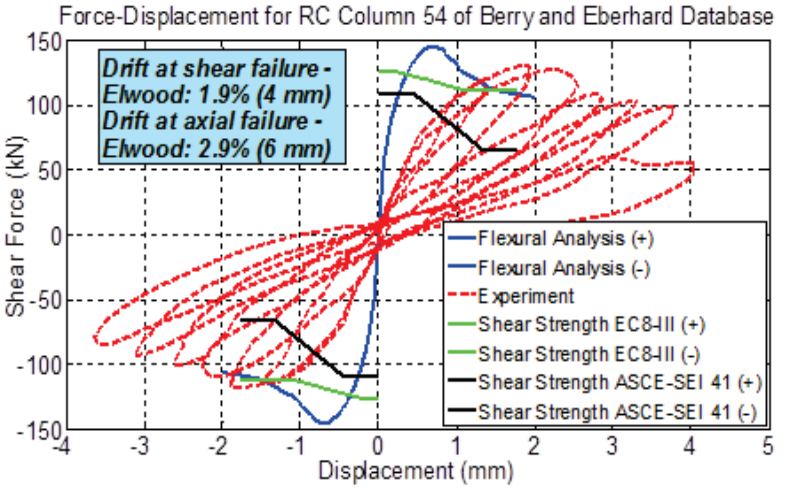

Figure A-81: Comparison between numerical and experimental responses of rectangular columns (ID#47&54) of Berry and Eberhard Database (2004).

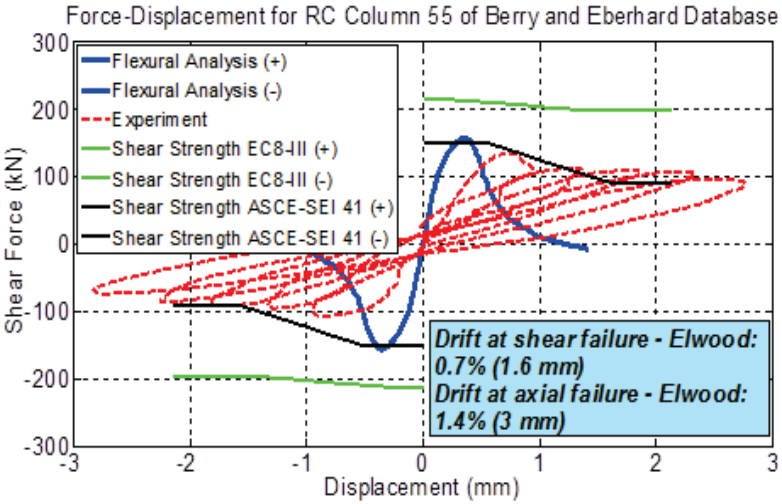

Concrete Model: Mander et al., 1988.

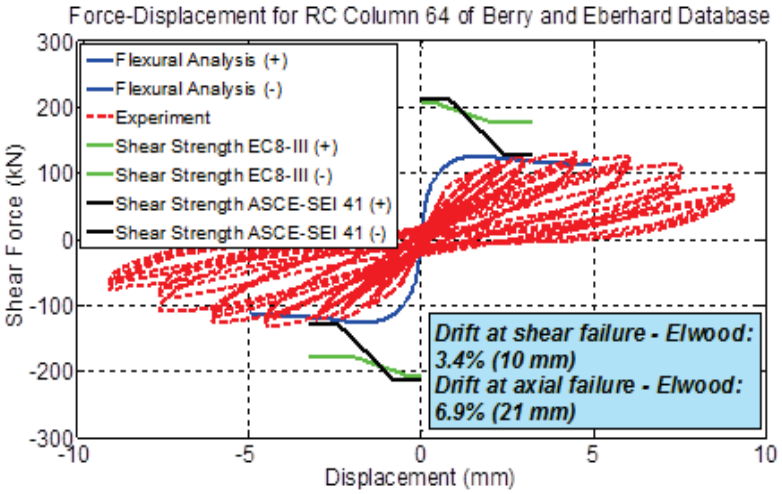

Figure A-82: Comparison between numerical and experimental responses of rectangular columns (ID#55&64) of Berry and Eberhard Database (2004).

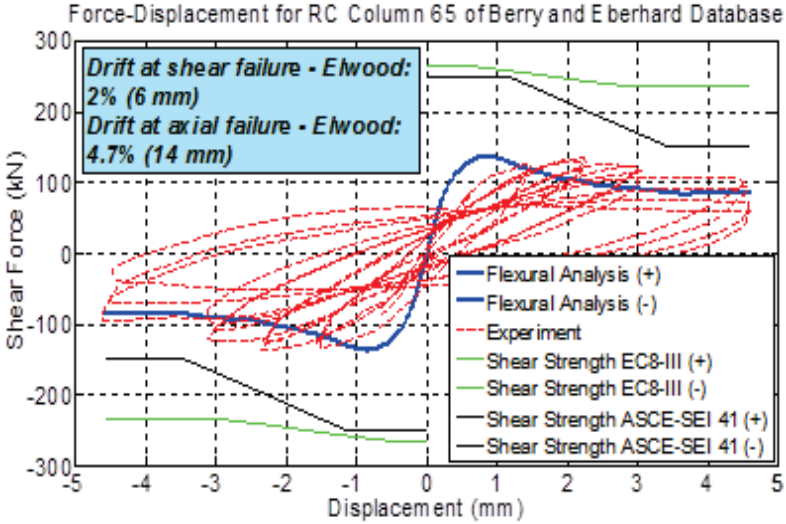

Concrete Model: Mander et al., 1988.

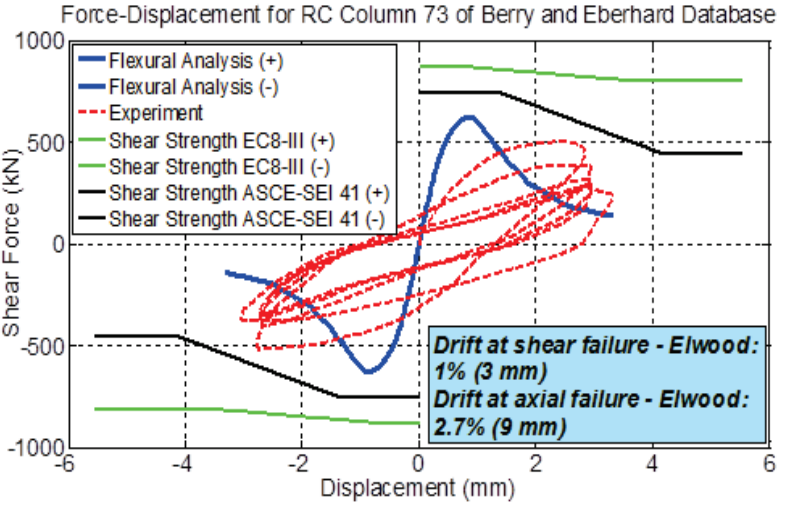

Figure A-83: Comparison between numerical and experimental responses of rectangular columns (ID#65&73) of Berry and Eberhard Database (2004).

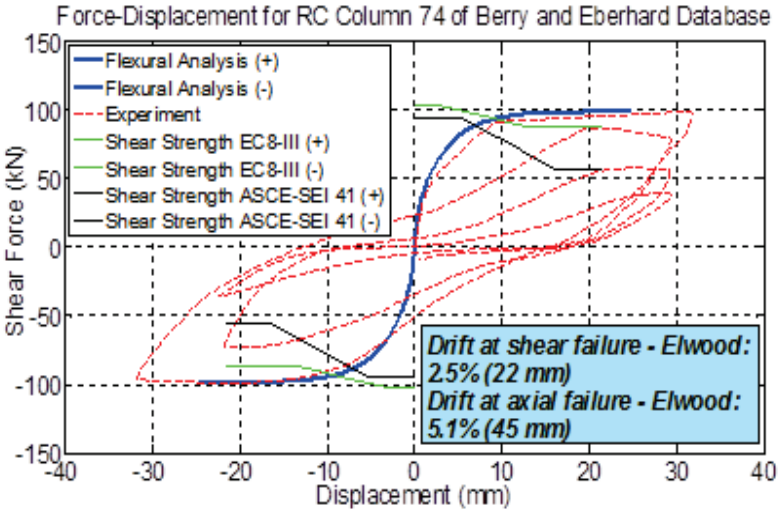

Concrete Model: Mander et al., 1988.

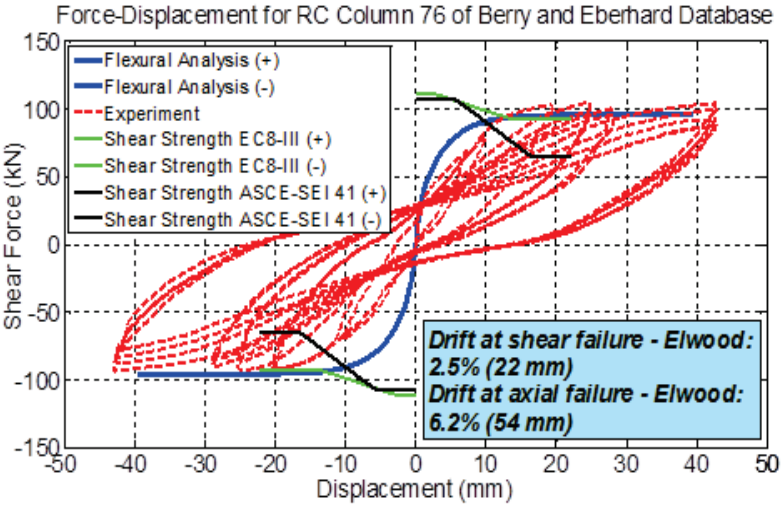

Figure A-84: Comparison between numerical and experimental responses of rectangular columns (ID#74&76) of Berry and Eberhard Database (2004).

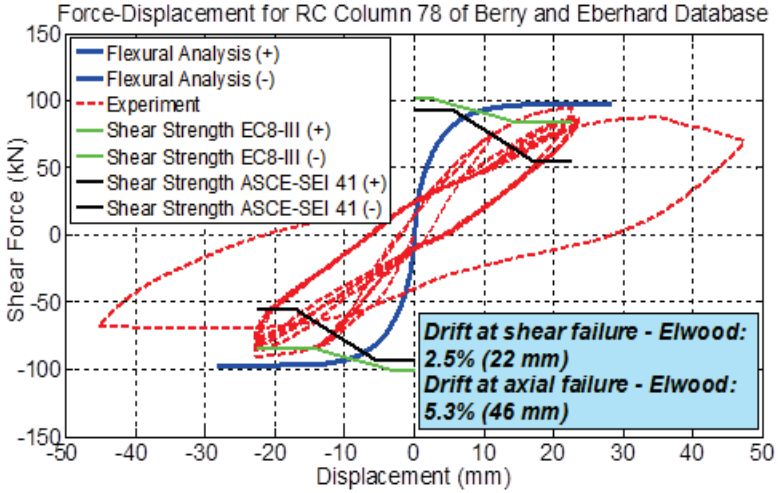

Concrete Model: Mander et al., 1988.

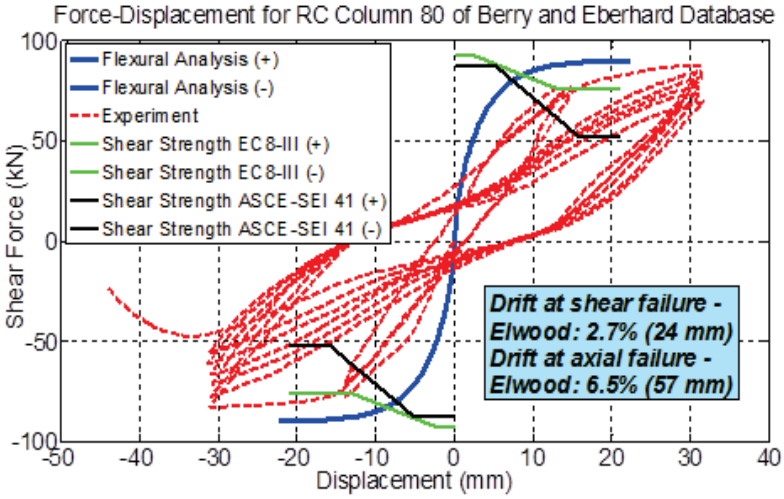

Figure A-85: Comparison between numerical and experimental responses of rectangular columns (ID#78&80) of Berry and Eberhard Database (2004).

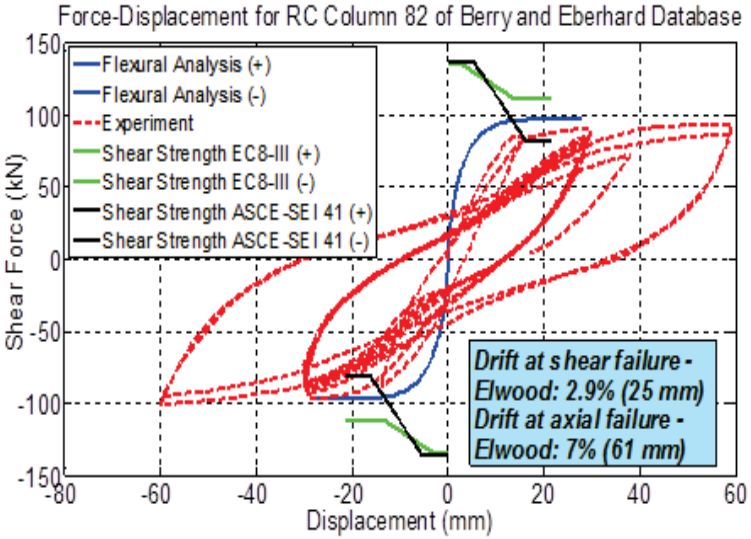

Concrete Model: Mander et al., 1988.

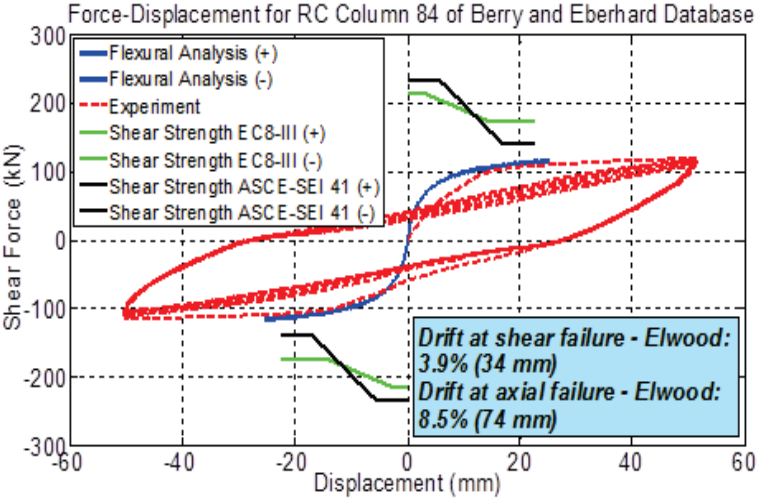

Figure A-86: Comparison between numerical and experimental responses of rectangular columns (ID#82&84) of Berry and Eberhard Database (2004).

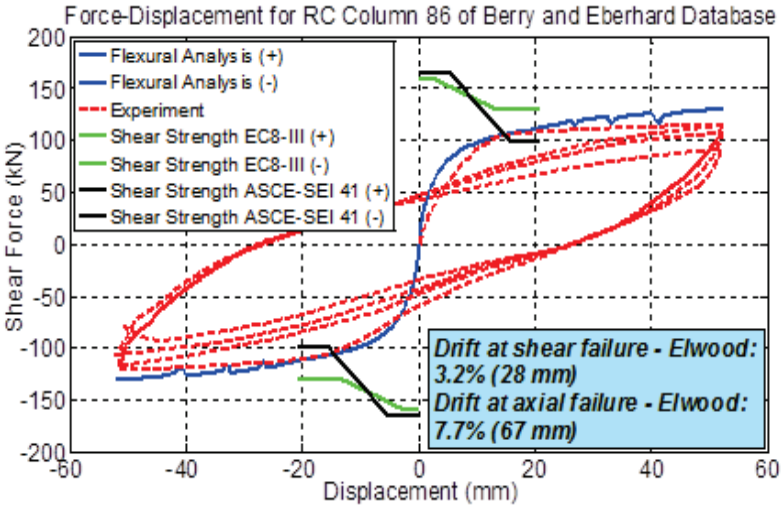

Concrete Model: Mander et al., 1988.

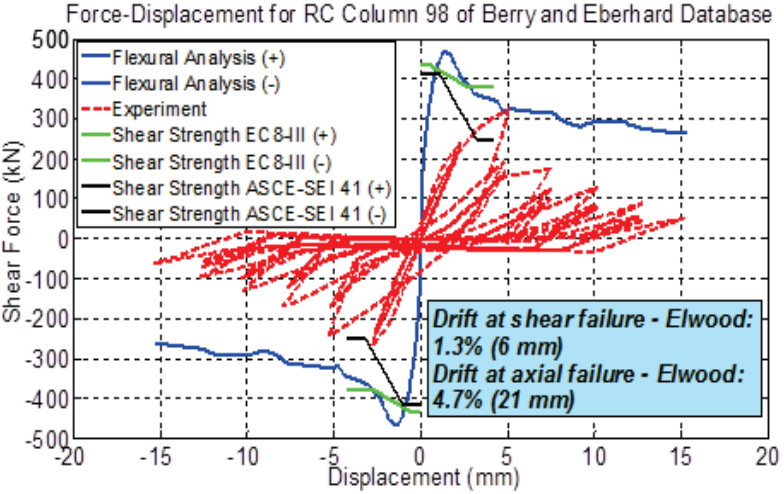

Figure A-87: Comparison between numerical and experimental responses of rectangular columns (ID#86&98) of Berry and Eberhard Database (2004).

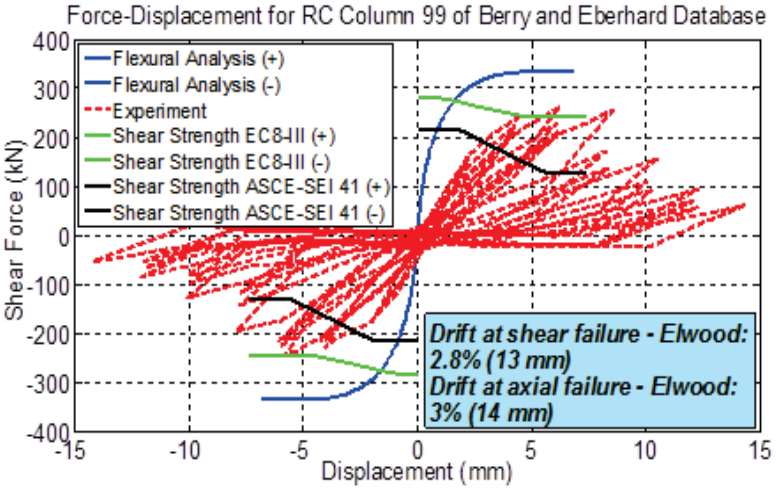

Concrete Model: Mander et al., 1988.

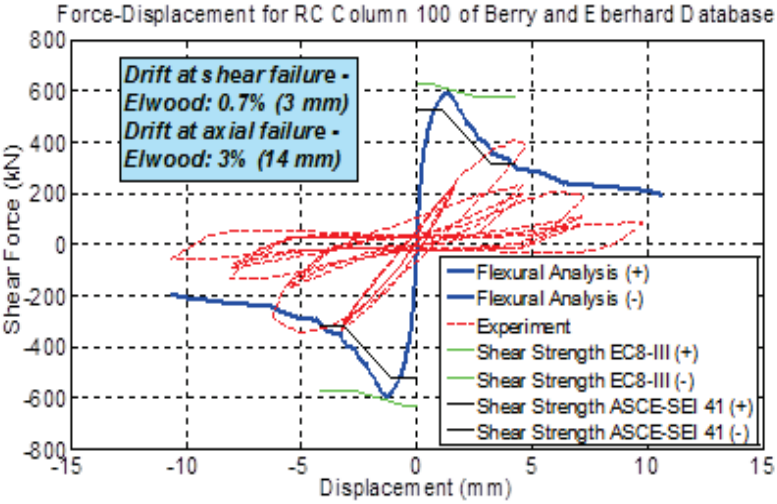

Figure A-88: Comparison between numerical and experimental responses of rectangular columns (ID#99&100) of Berry and Eberhard Database (2004).

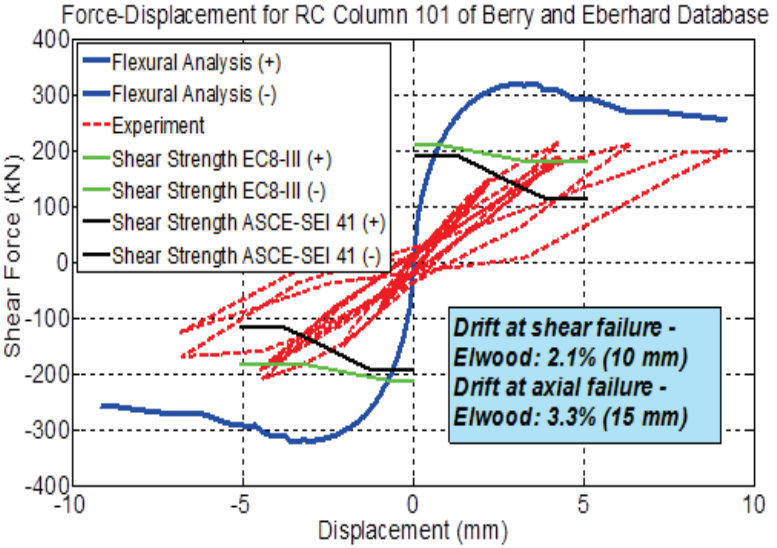

Concrete Model: Mander et al., 1988.

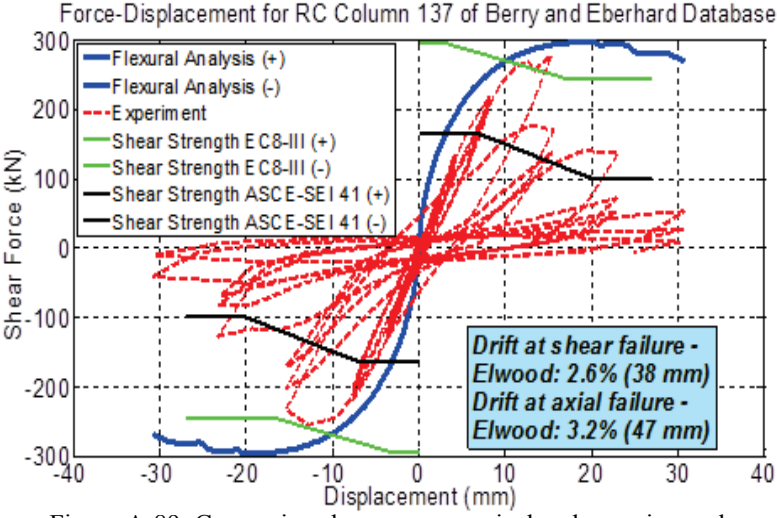

Figure A-89: Comparison between numerical and experimental responses of rectangular columns (ID#101&137) of Berry and Eberhard Database (2004).

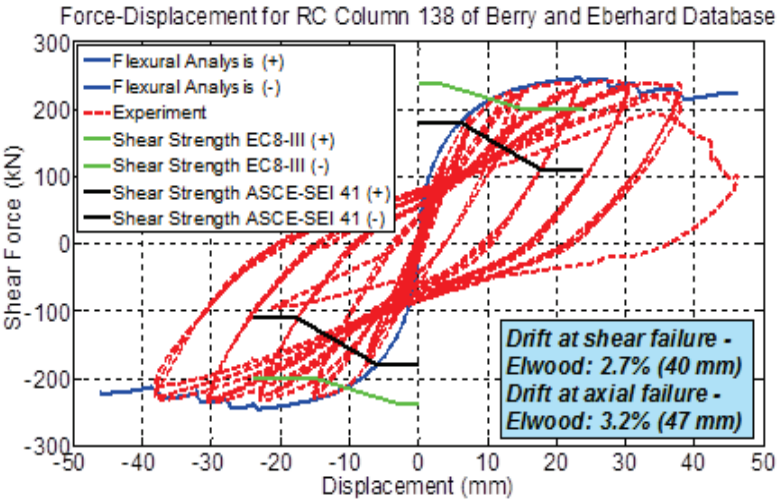

Concrete Model: Mander et al., 1988.

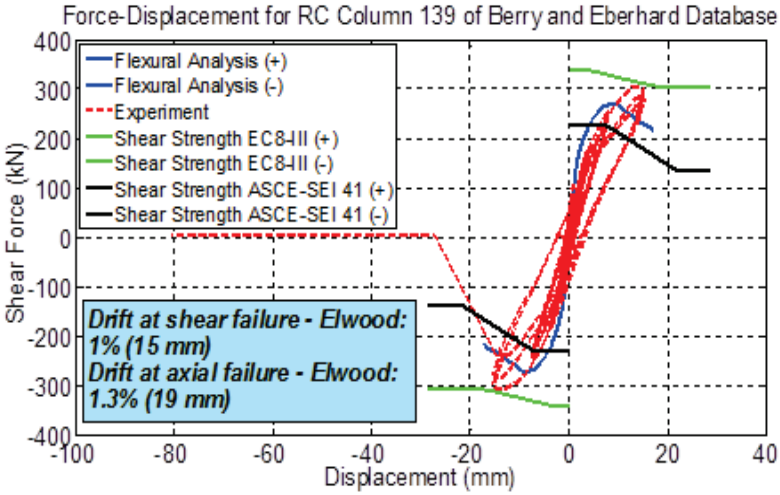

Figure A-90: Comparison between numerical and experimental responses of rectangular columns (ID#138&139) of Berry and Eberhard Database (2004).

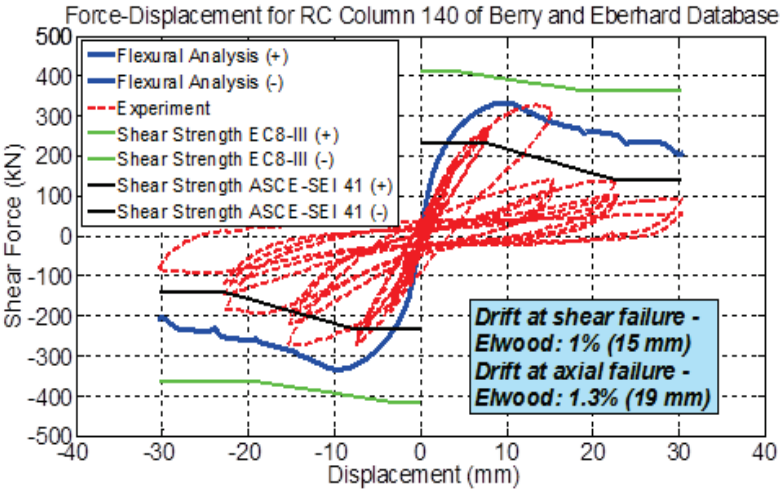

Concrete Model: Mander et al., 1988.

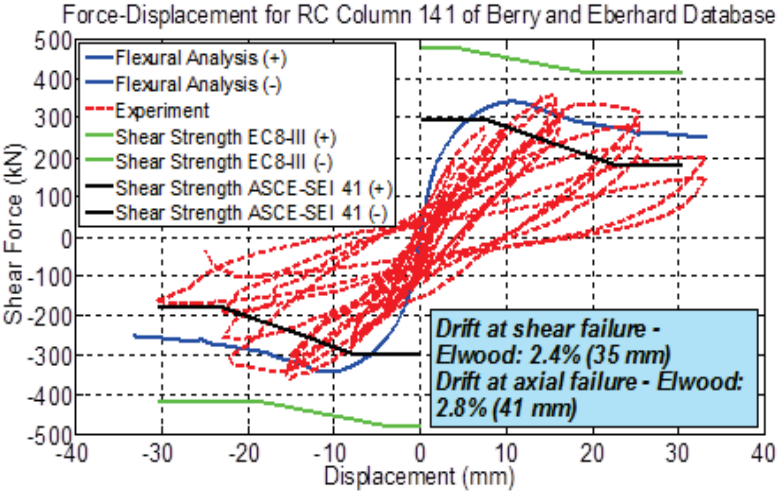

Figure A-91: Comparison between numerical and experimental responses of rectangular columns (ID#140&141) of Berry and Eberhard Database (2004).

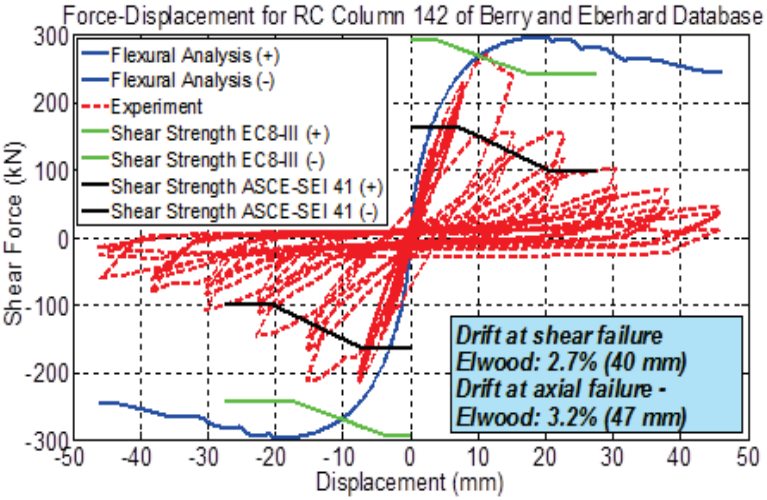

Concrete Model: Mander et al., 1988.

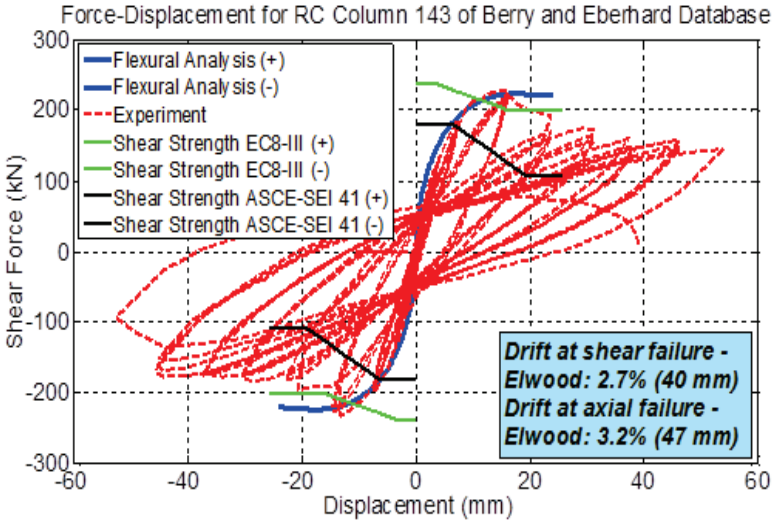

Figure A-92: Comparison between numerical and experimental responses of rectangular columns (ID#142&143) of Berry and Eberhard Database (2004).

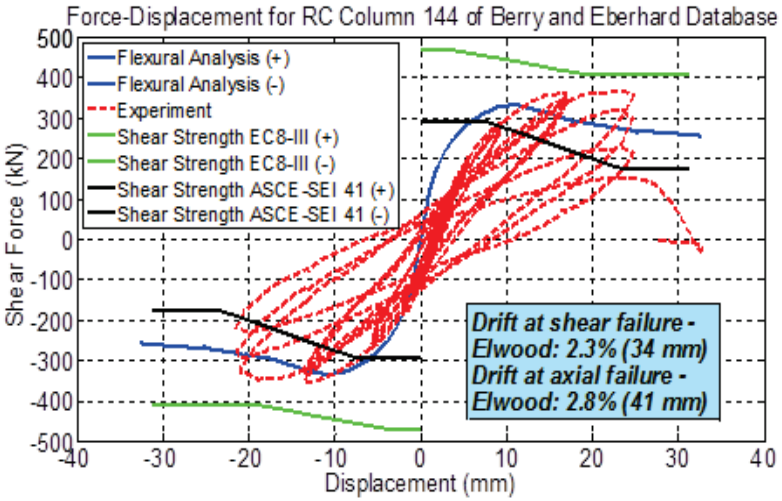

Concrete Model: Mander et al., 1988.

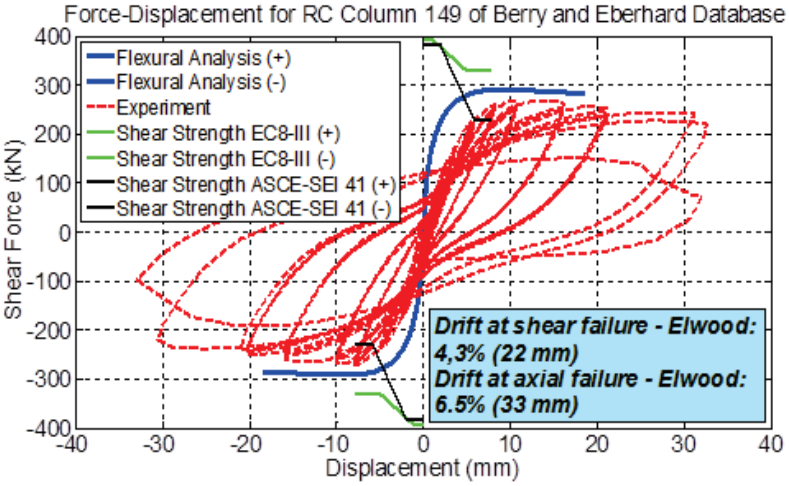

Figure A-93: Comparison between numerical and experimental responses of rectangular columns (ID#144&149) of Berry and Eberhard Database (2004).

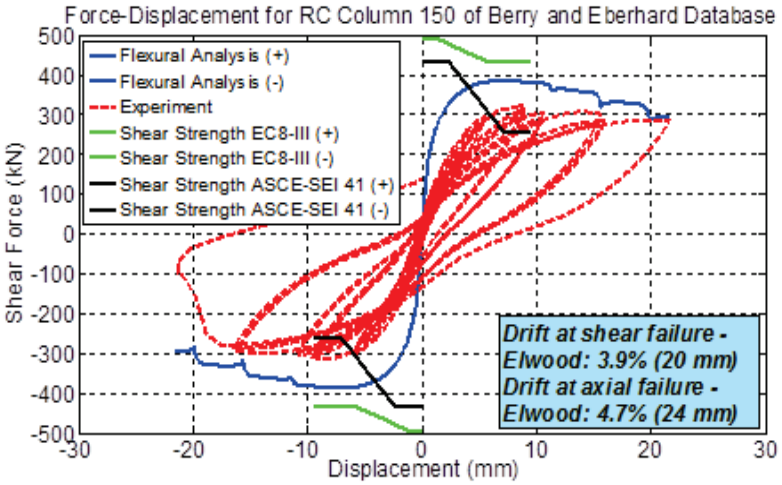

Concrete Model: Mander et al., 1988.

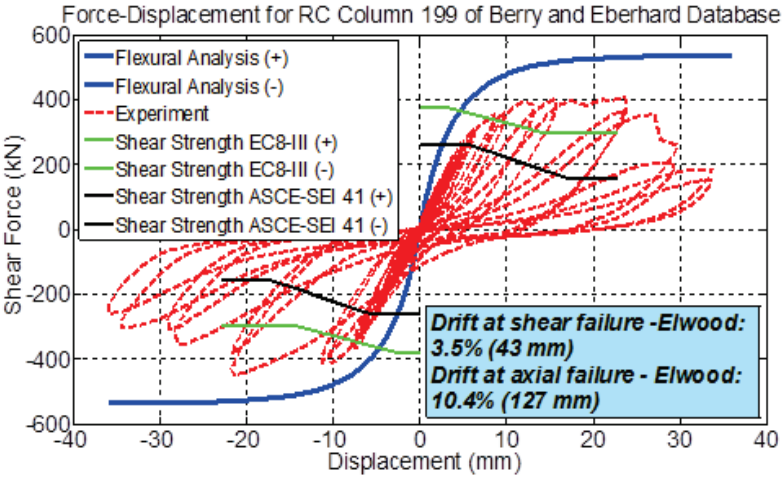

Figure A-94: Comparison between numerical and experimental responses of rectangular columns (ID#150&199) of Berry and Eberhard Database (2004).

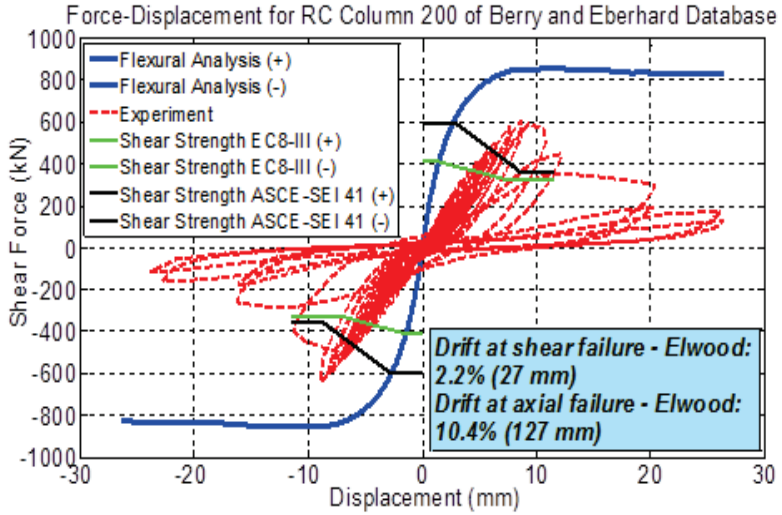

Concrete Model: Mander et al., 1988.

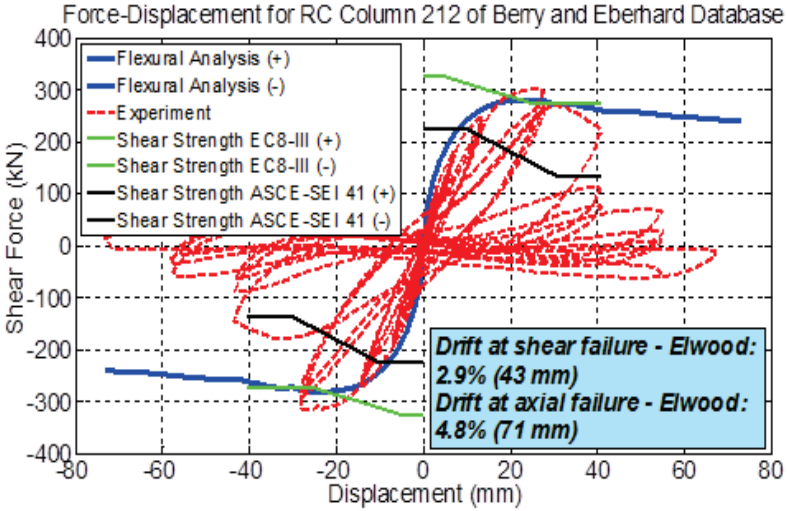

Figure A-95: Comparison between numerical and experimental responses of rectangular columns (ID#200&212) of Berry and Eberhard Database (2004).

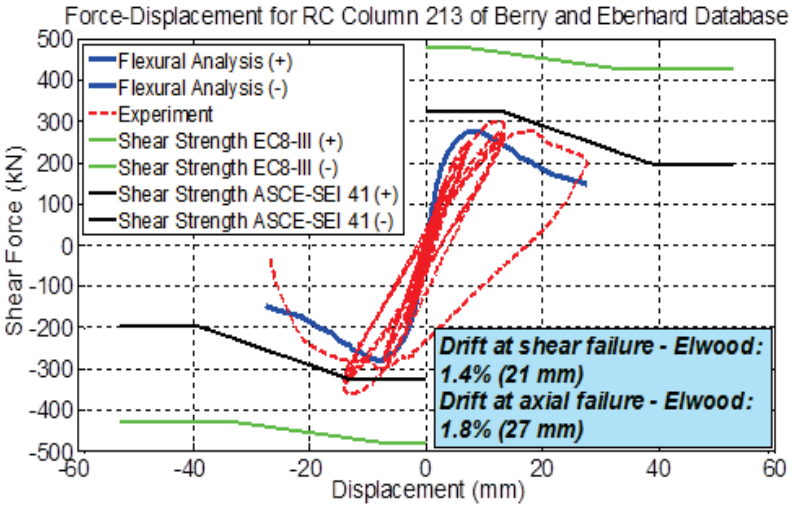

Concrete Model: Mander et al., 1988.

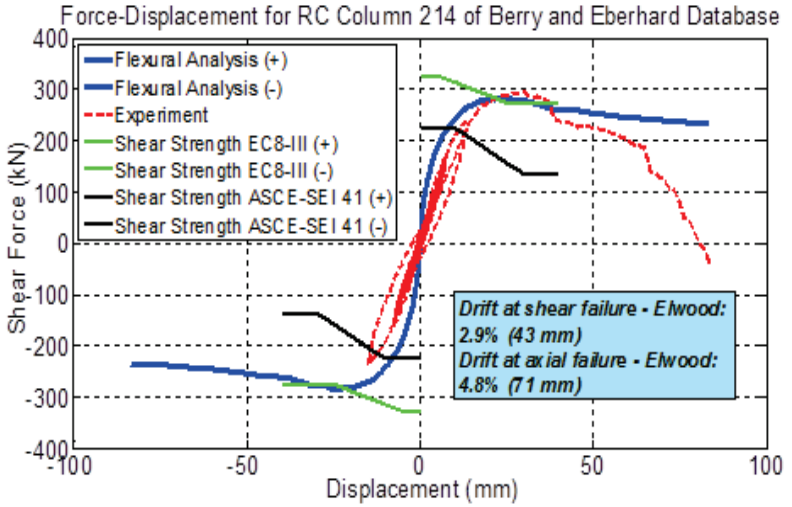

Figure A-96: Comparison between numerical and experimental responses of rectangular columns (ID#213&214) of Berry and Eberhard Database (2004).

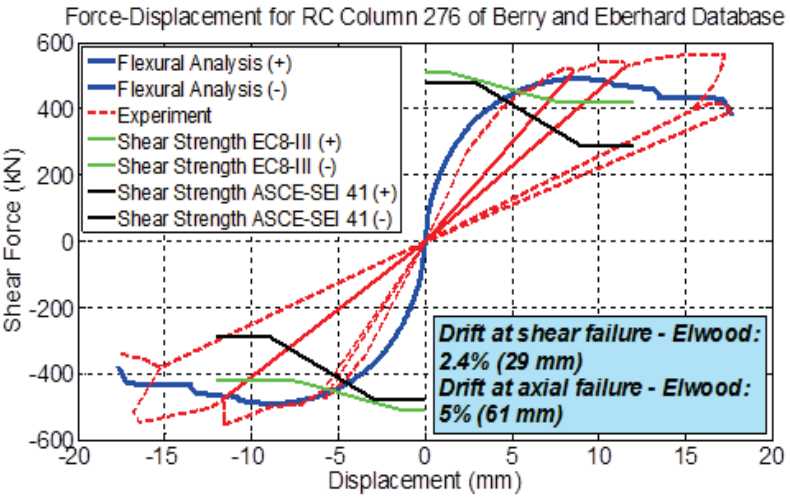

Concrete Model: Mander et al., 1988.

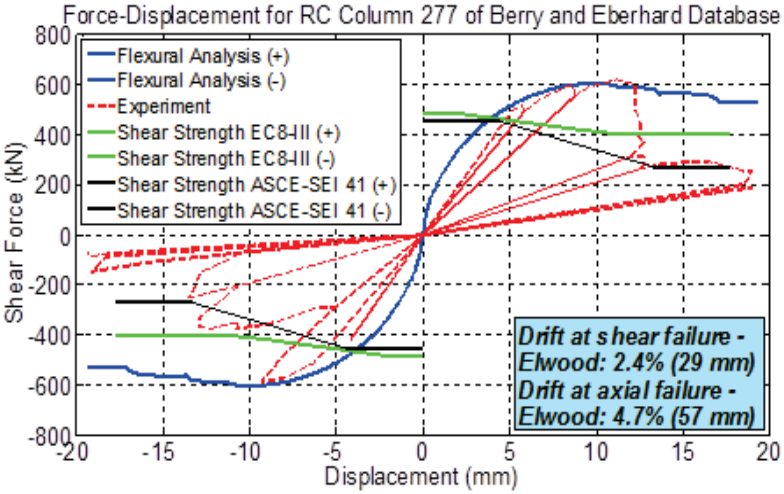

Figure A-97: Comparison between numerical and experimental responses of rectangular columns (ID#276&277) of Berry and Eberhard Database (2004).

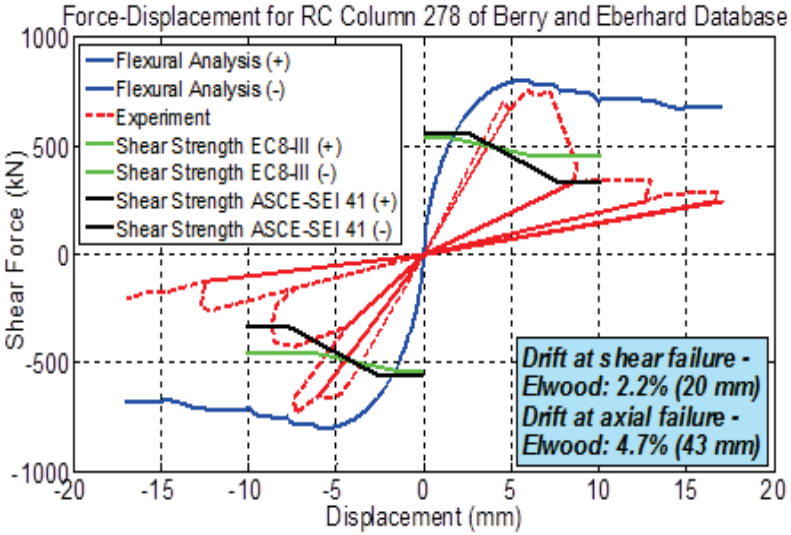

Concrete Model: Mander et al., 1988.

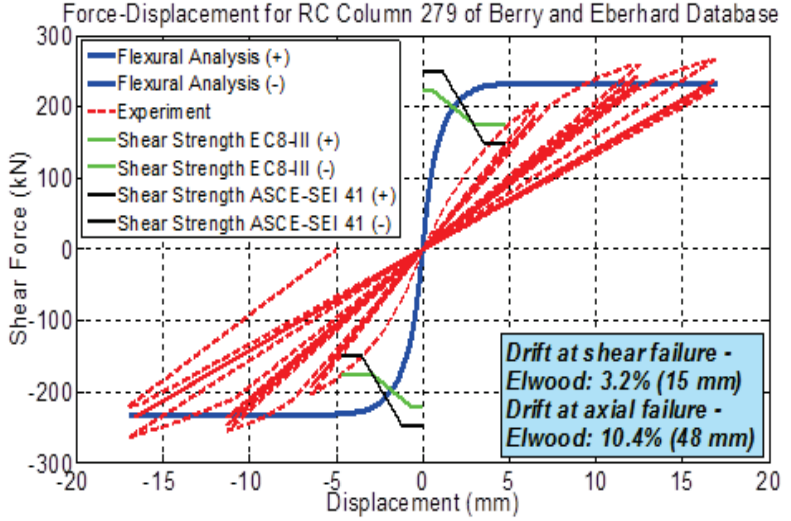

Figure A-98: Comparison between numerical and experimental responses of rectangular columns (ID#278&279) of Berry and Eberhard Database (2004).

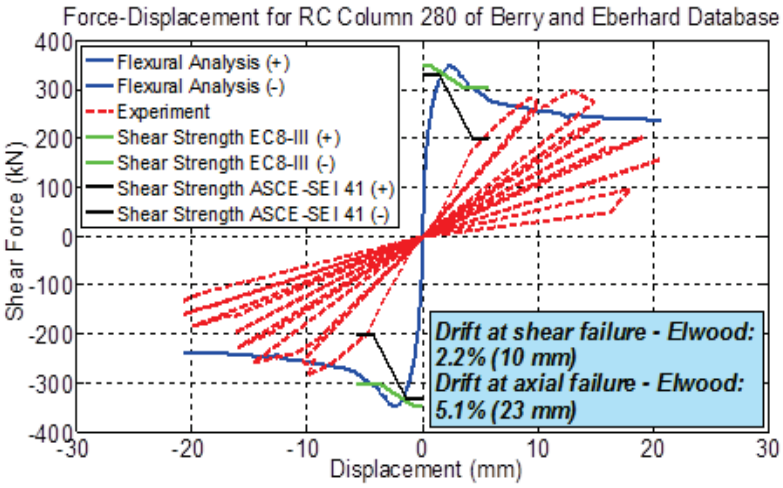

Concrete Model: Mander et al., 1988.

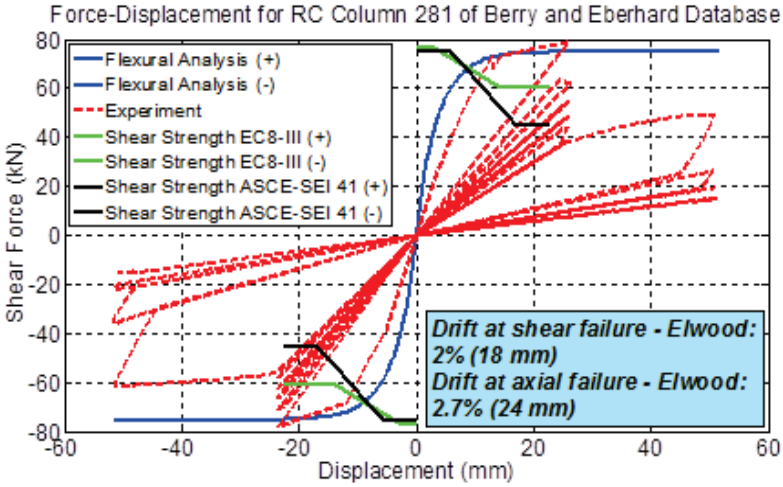

Figure A-99: Comparison between numerical and experimental responses of rectangular columns (ID#280&281) of Berry and Eberhard Database (2004).

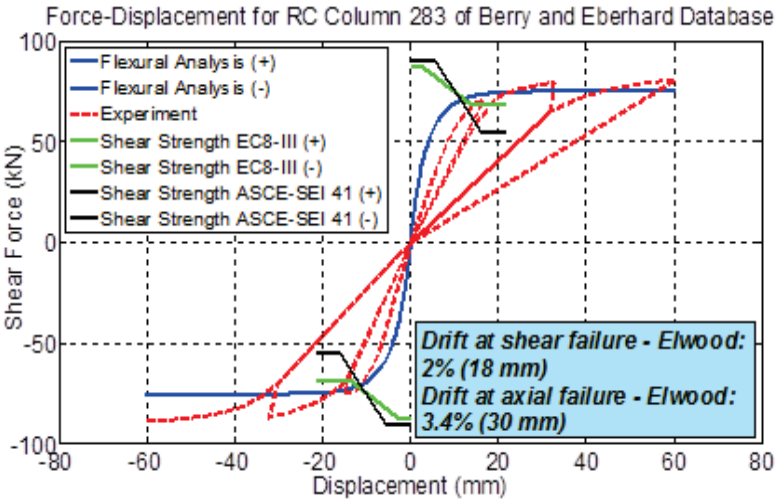

Concrete Model: Mander et al., 1988.

Figure A-100: Comparison between numerical and experimental responses of rectangular columns (ID#283) of Berry and Eberhard Database (2004).

Table A-4: Reinforced concrete columns with a circular cross section that failed in shear.

SpecimenID in Database	Axial Load (KN)	Diameter	Cover to Ctr. of Hoop Bar (mm)	Shear Span (mm)	Concrete Strength (MPa)	Number of Longitudinal Bars	Diameter of Long. Bars (mm)	Yielding Strength of Long. Bars (MPa)	Ultimate Strength of Long. Bars (MPa)	Longitudinal Reinforcement ratio (%)	Hoop Spacing (mm)	Diameter of Spiral (mm)	Yielding Strength Spiral (MPa)	Transverse Reinforcement ratio (%)
14	0	400	18	800	37.5	20	16	436	674	3.2	60	6	328	0.51
15	0	400	18	800	37.2	20	16	296	457	3.2	60	6	328	0.51
16	0	400	18	1000	36	20	16	436	674	3.2	60	6	328	0.51
17	0	400	20	800	30.6	20	16	436	674	3.2	165	10	316	0.51
18	0	400	18	800	31.1	20	16	436	674	3.2	40	6	328	0.76
19	0	400	18	600	30.1	20	16	436	674	3.2	60	6	328	0.51
20	0	400	18	800	29.5	20	16	448	693	3.2	80	6	372	0.38
21	721	400	18	800	28.7	20	16	448	693	3.2	30	6	372	1.02
23	784	400	21	800	31.2	20	16	448	693	3.2	120	12	332	1.02
24	751	400	18	800	29.9	20	16	448	693	3.2	60	6	372	0.51
25	359	400	18	600	28.6	20	16	436	674	3.2	30	6	328	1.02
26	455	400	18	800	36.2	20	16	436	679	3.2	30	6	326	1.02
27	0	400	18	800	33.7	9	24	424	671	3.24	60	6	326	0.51
28	0	400	18	800	34.8	12	16	436	679	1.92	60	6	326	0.51

29	420	400	18	800	33.4	20	16	436	679	3.2	60	6	326	0.51
30	431	400	18	1000	34.3	20	16	436	679	3.2	60	6	326	0.51
31	440	400	18	600	35	20	16	436	674	3.2	60	6	326	0.51
32	432	400	18	600	34.4	20	16	436	679	3.2	80	6	326	0.38
33	807	400	18	700	36.7	20	16	482	758	3.2	80	6	326	0.38
34	0	400	18	800	33.2	20	16	436	679	3.2	80	6	326	0.38
35	0	400	20	800	30.9	20	16	436	679	3.2	220	10	310	0.39
36	0	400	21	800	32.3	20	16	436	679	3.2	160	12	332	0.76
37	0	400	20	800	33.1	20	16	436	679	3.2	110	10	310	0.77
44	1813	400	18	800	37	20	16	475	625	3.2	65	6	340	0.47
48	145	307	36	900	35.9	12	12	240	-	1.83	75	6	240	0.63
49	254	307	36	895	34.4	12	12	240	-	1.83	75	6	240	0.63
104	503	610	15.88	914.5	30	12	12.7	462	-	0.52	76.2	6.4	361	0.28
105	503	610	15.88	914.5	30	24	12.7	462	-	1.04	127	6.4	361	0.17
108	-634	457	24.76	910	39.2	20	15.875	427.5	-	2.41	60	9.5	430.2	1.14
110	850	457	26.35	910	35	30	19.05	468.2	-	5.21	45	12.7	434.4	2.7
111	-490	457	24.76	910	35.2	20	15.875	507.5	-	2.41	80	9.5	448.2	0.85
159	0	406.4	10.44	1047.8	34.7	14	12.7	458.5	646	1.37	171.45	4.5	691.5	0.1
161	0	406.4	10.44	1047.8	35.4	12	12.7	458.5	646	1.17	63.5	4.5	691.5	0.26
163	18.8	609.6	18.63	1219.2	29..8	20	15.875	454	729.6	1.36	101.6	4.9	200	0.13
164	18.8	609.6	18.63	1219.2	26.8	20	15.875	454	729.6	1.36	101.6	4.9	200	0.13
165	18.8	609.6	18.63	1219.2	31.2	20	15.875	437.6	688	1.36	101.6	4.9	200	0.13
166	356	1828.8	57.15	3658	29.6	24	43	508	797	1.33	304.8	12.7	298	0.1
168	0	564	24	1000	39.8	40	13	324.5	-	-	250	9	259.6	0.1

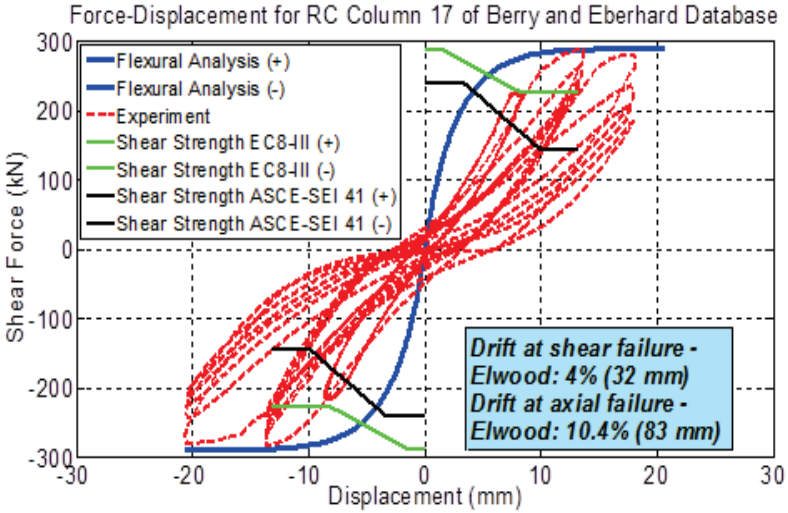

Concrete Model: Mander et al., 1988.

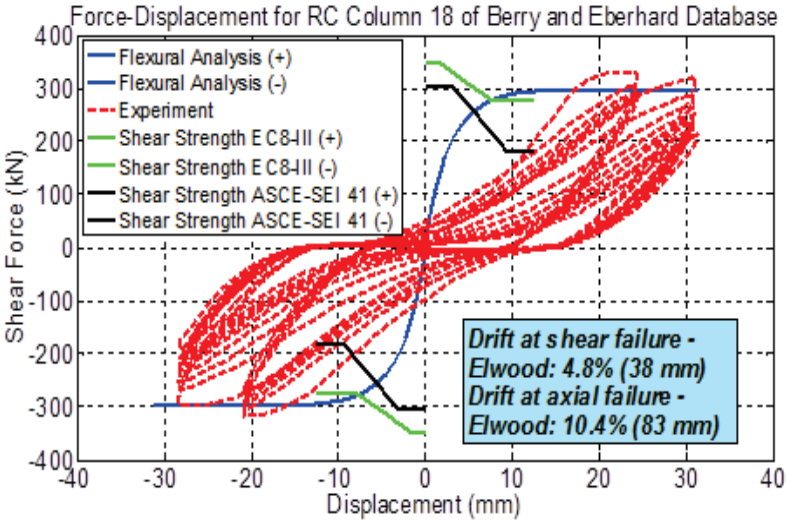

Figure A-101: Comparison between numerical and experimental responses of circular columns (ID#17&18) of Berry and Eberhard Database (2004).

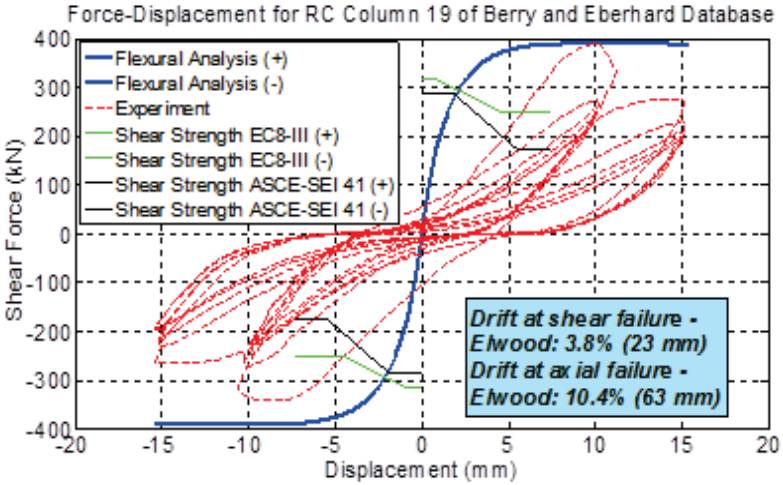

Concrete Model: Mander et al., 1988.

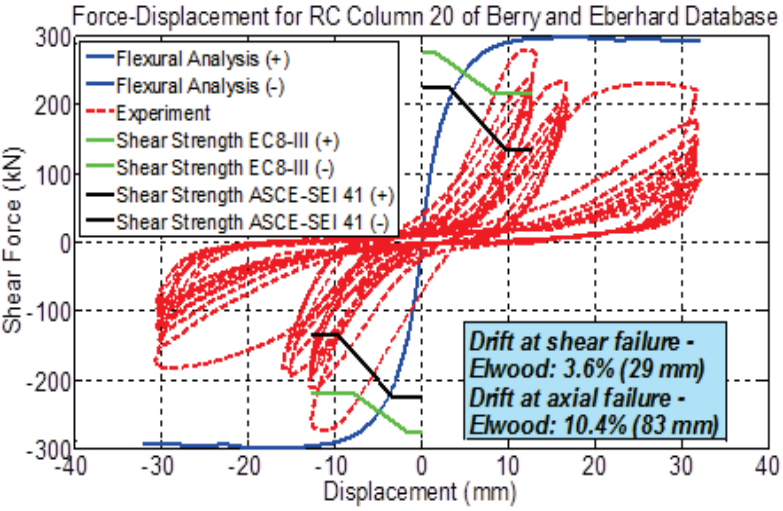

Figure A-102: Comparison between numerical and experimental responses of circular columns (ID#19&20) of Berry and Eberhard Database (2004).

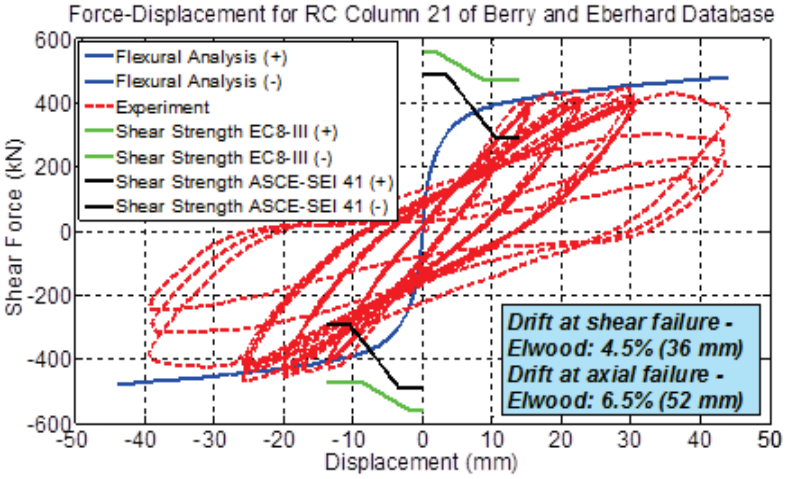

Concrete Model: Mander et al., 1988.

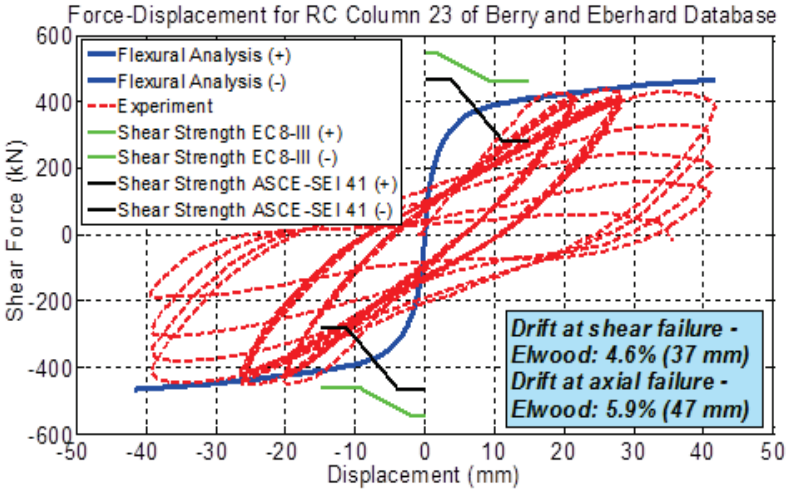

Figure A-103: Comparison between numerical and experimental responses of circular columns (ID#21&23) of Berry and Eberhard Database (2004).

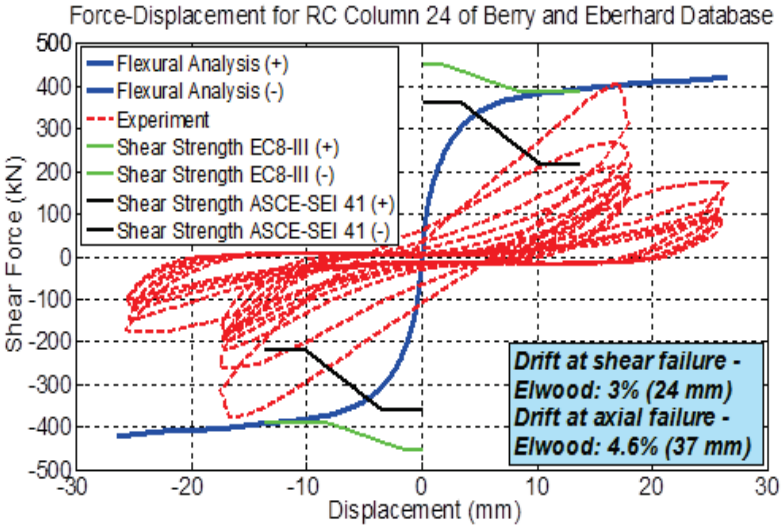

Concrete Model: Mander et al., 1988.

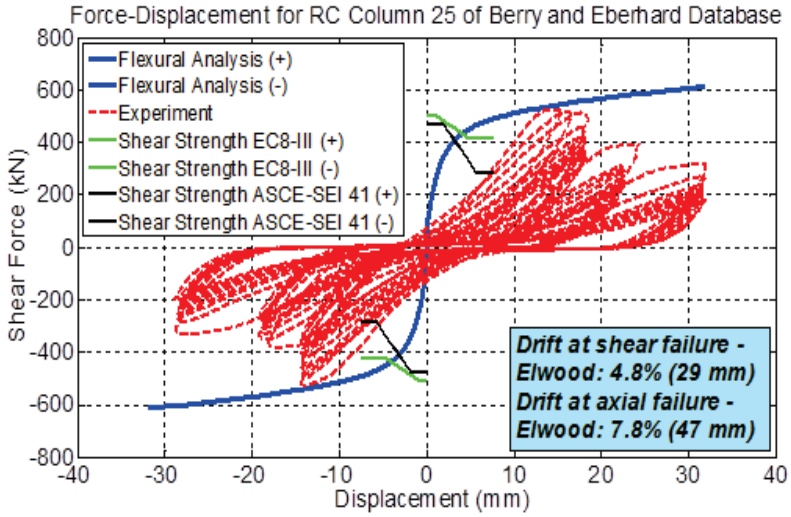

Figure A-104: Comparison between numerical and experimental responses of circular columns (ID#24&25) of Berry and Eberhard Database (2004).

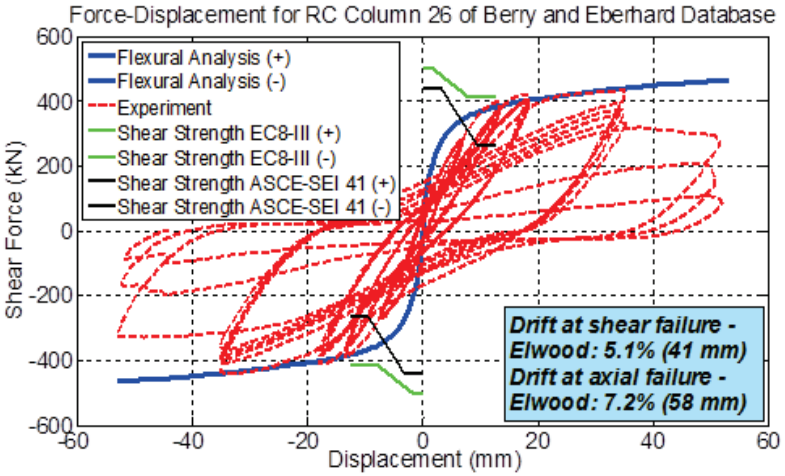

Concrete Model: Mander et al., 1988.

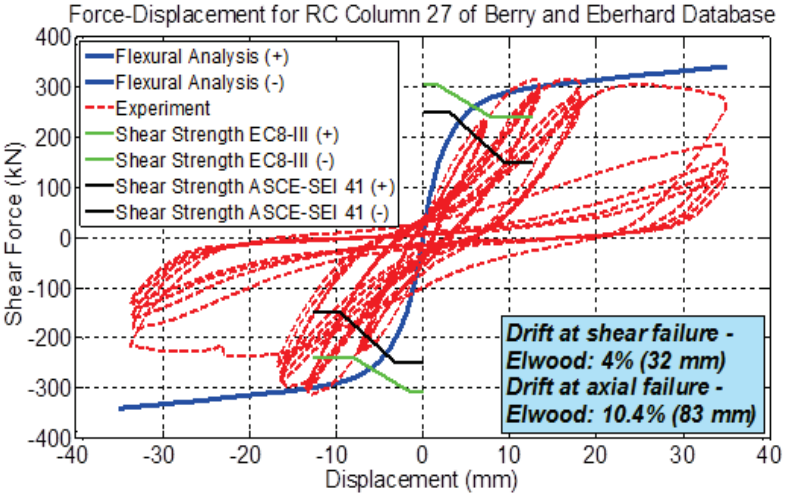

Figure A-105: Comparison between numerical and experimental responses of circular columns (ID#26&27) of Berry and Eberhard Database (2004).

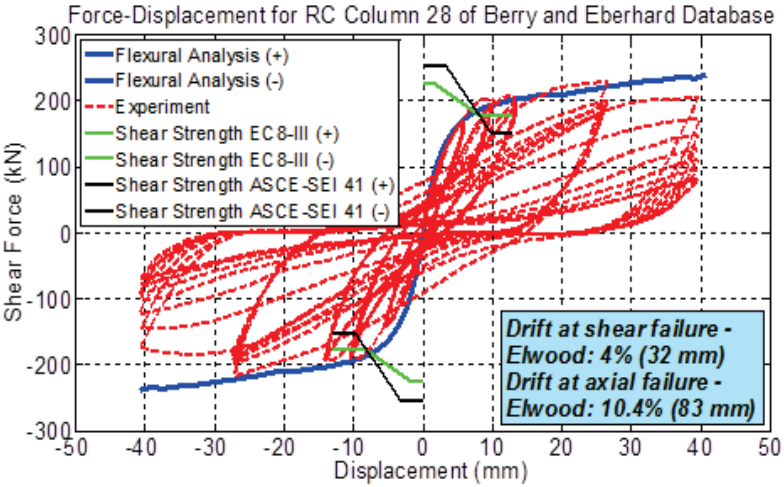

Concrete Model: Mander et al., 1988.

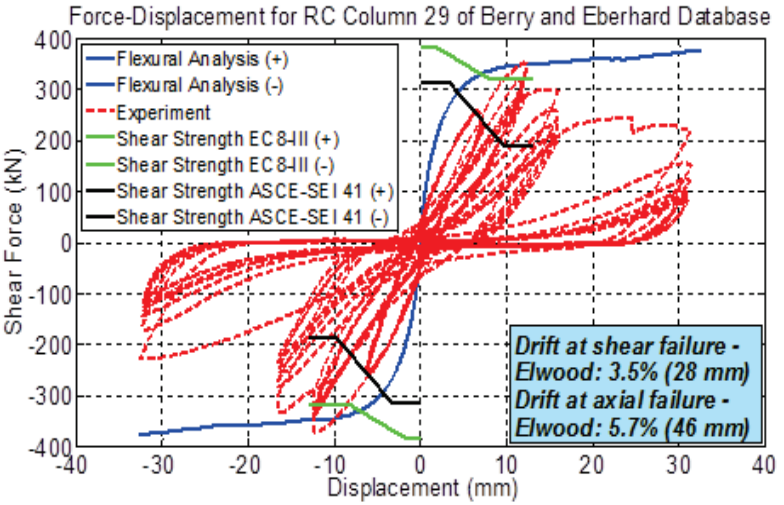

Figure A-106: Comparison between numerical and experimental responses of circular columns (ID#28&29) of Berry and Eberhard Database (2004).

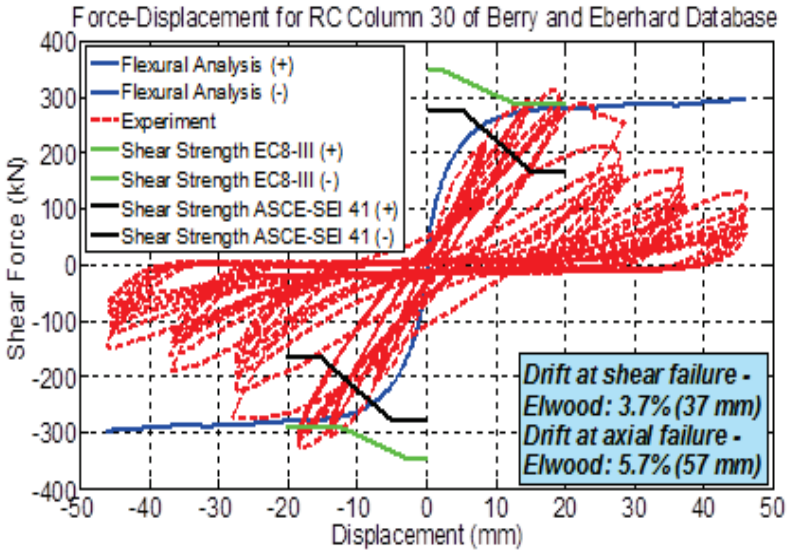

Concrete Model: Mander et al., 1988.

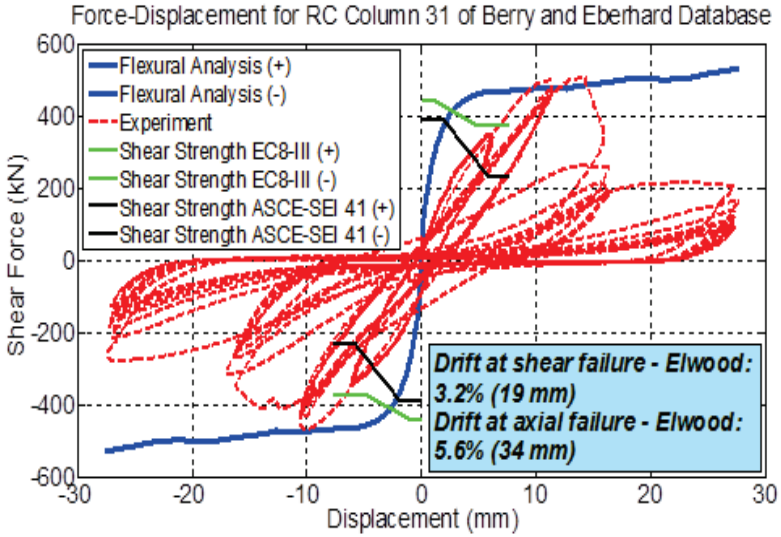

Figure A-107: Comparison between numerical and experimental responses of circular columns (ID#30&31) of Berry and Eberhard Database (2004).

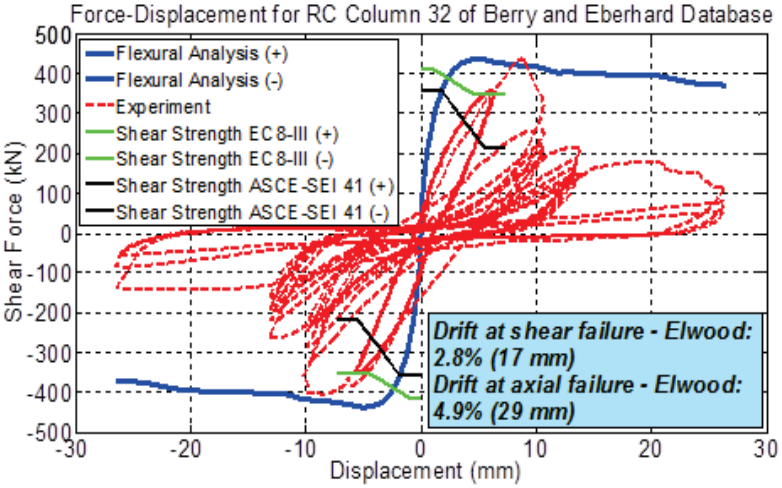

Concrete Model: Mander et al., 1988.

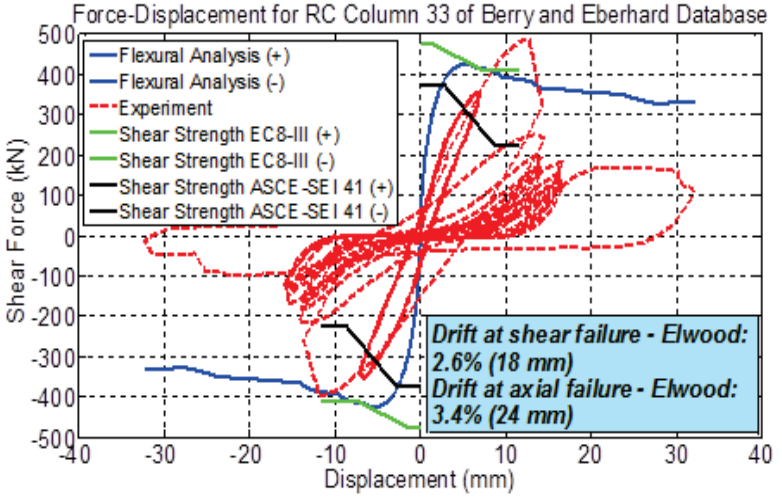

Figure A-108: Comparison between numerical and experimental responses of circular columns (ID#32&33) of Berry and Eberhard Database (2004).

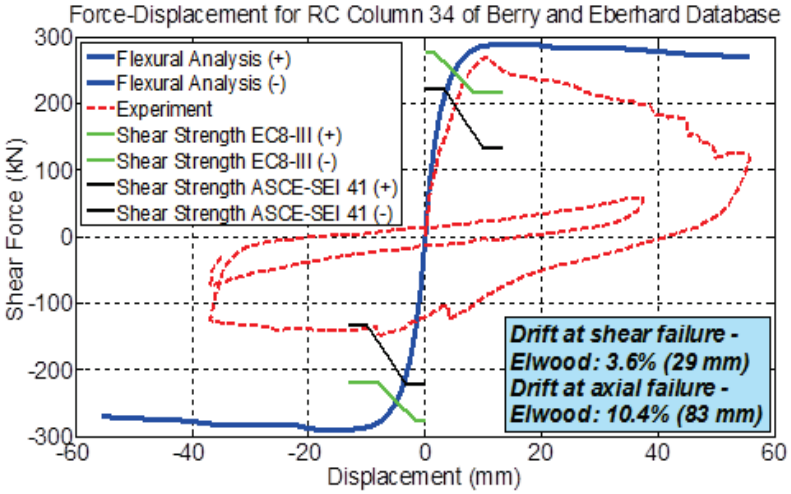

Concrete Model: Mander et al., 1988.

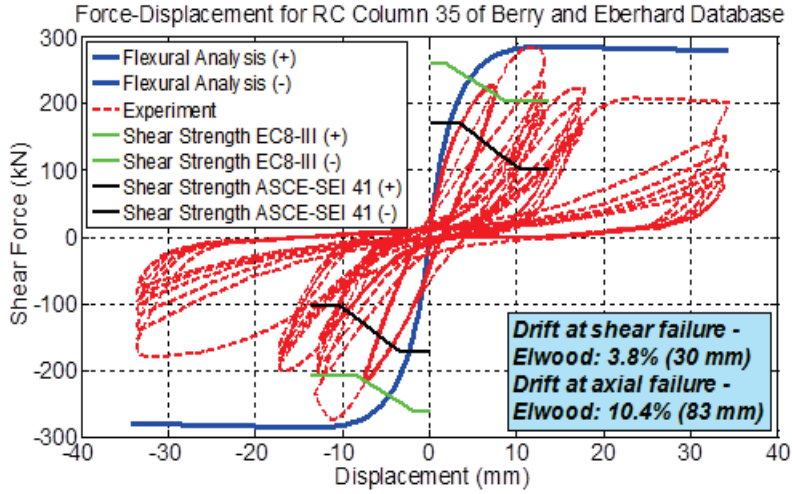

Figure A-109: Comparison between numerical and experimental responses of circular columns (ID#34&35) of Berry and Eberhard Database (2004).

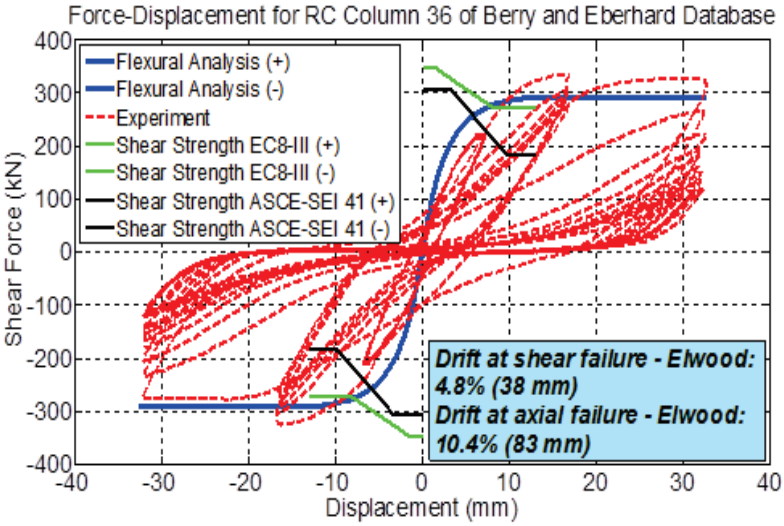

Concrete Model: Mander et al., 1988.

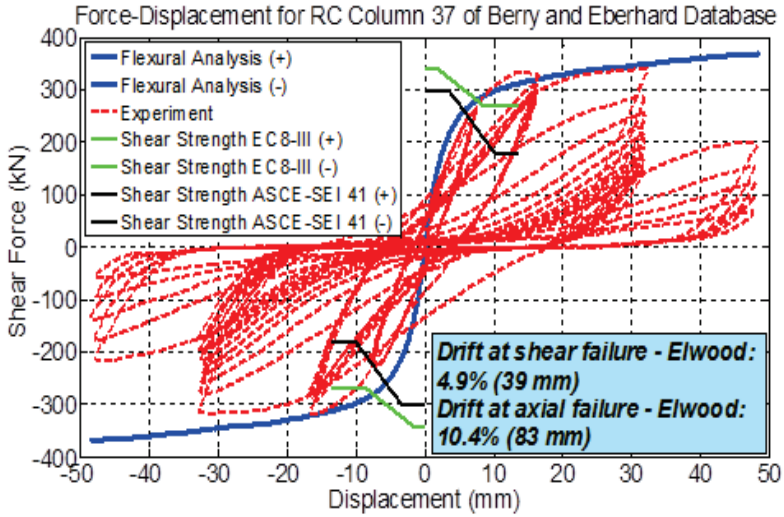

Figure A-110: Comparison between numerical and experimental responses of circular columns (ID#36&37) of Berry and Eberhard Database (2004).

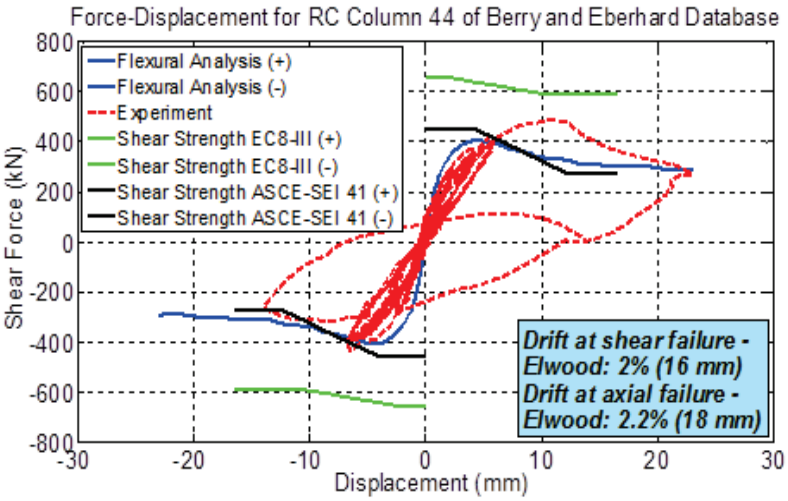

Concrete Model: Mander et al., 1988.

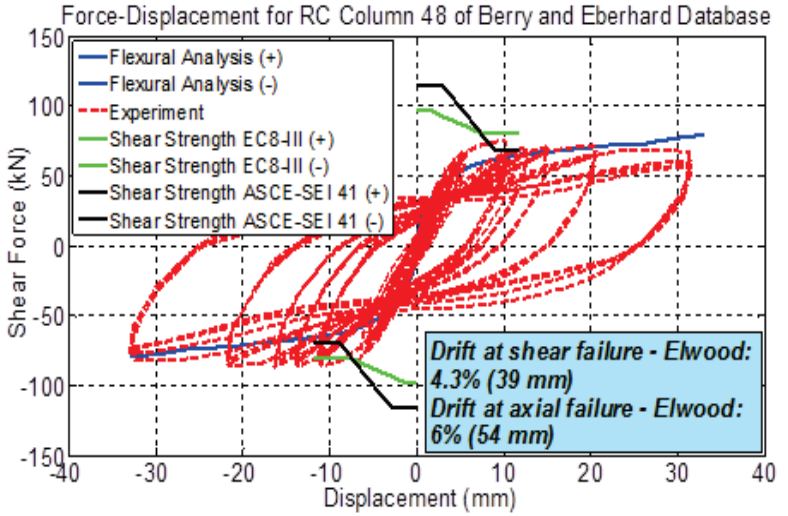

Figure A-111: Comparison between numerical and experimental responses of circular columns (ID#44&48) of Berry and Eberhard Database (2004).

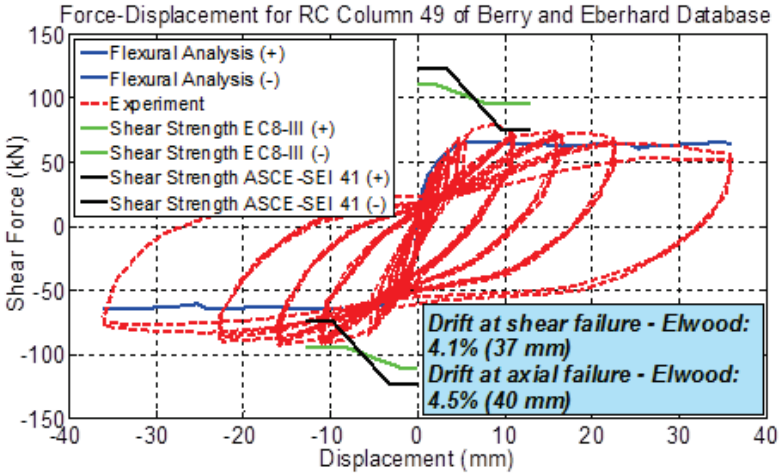

Concrete Model: Mander et al., 1988.

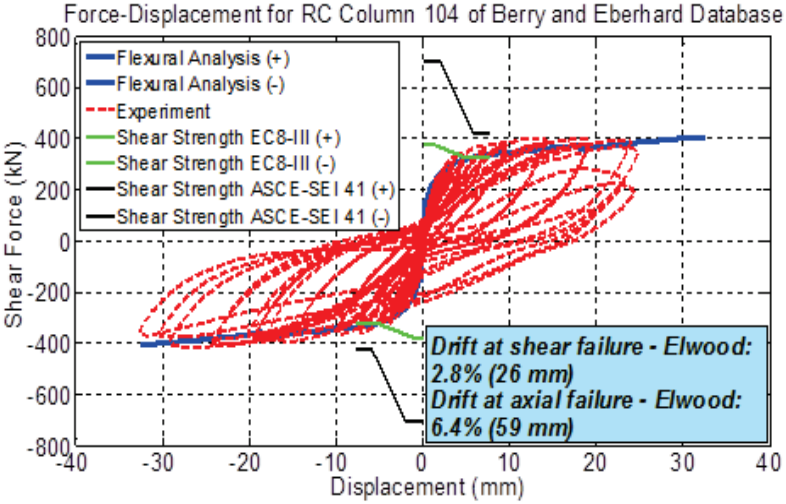

Figure A-112: Comparison between numerical and experimental responses of circular columns (ID#49&104) of Berry and Eberhard Database (2004).

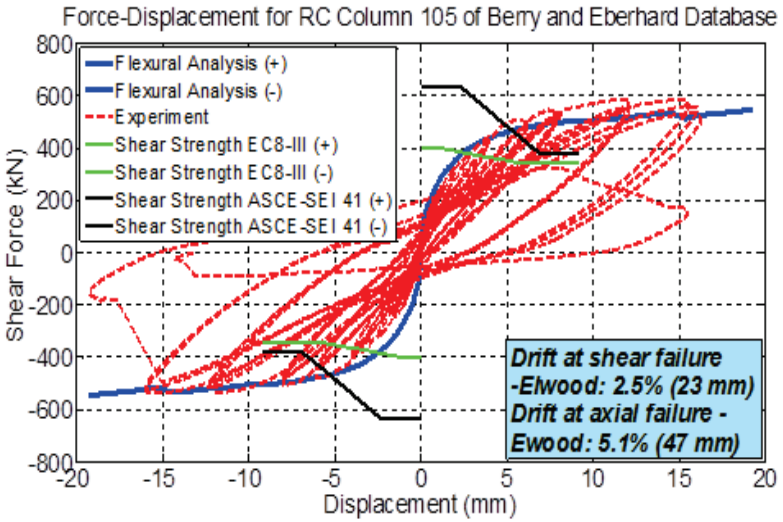

Concrete Model: Mander et al., 1988.

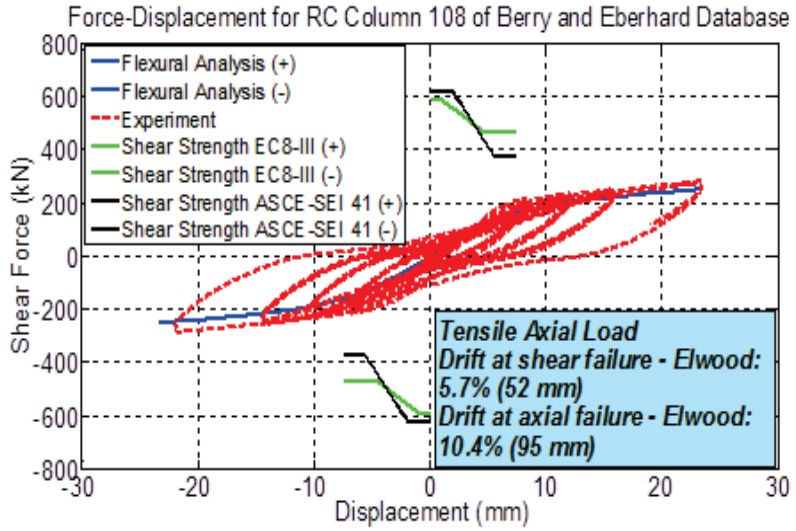

Figure A-113: Comparison between numerical and experimental responses of circular columns (ID#105&108) of Berry and Eberhard Database (2004).

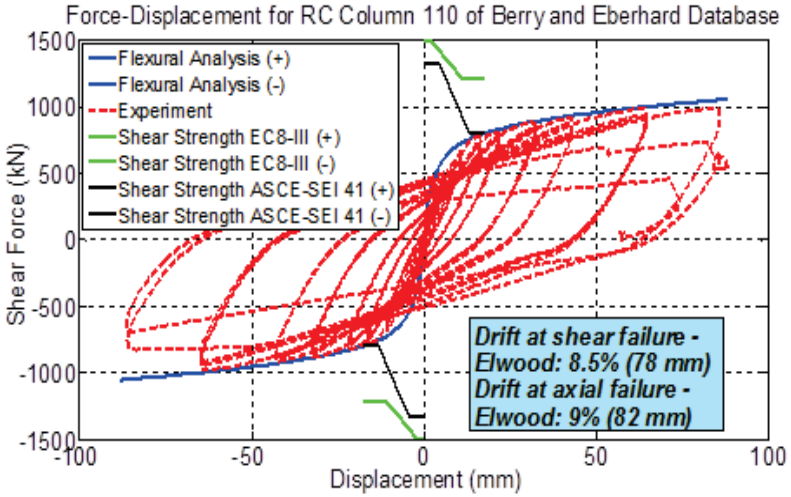

Concrete Model: Mander et al., 1988.

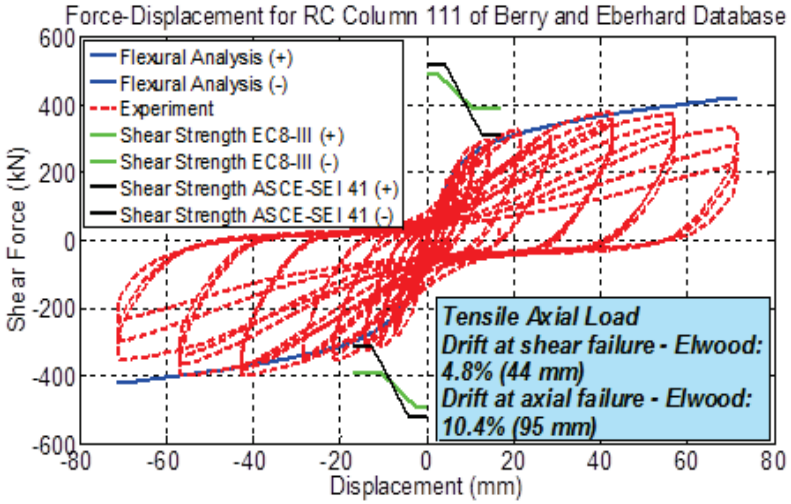

Figure A-114: Comparison between numerical and experimental responses of circular columns (ID#110&111) of Berry and Eberhard Database (2004).

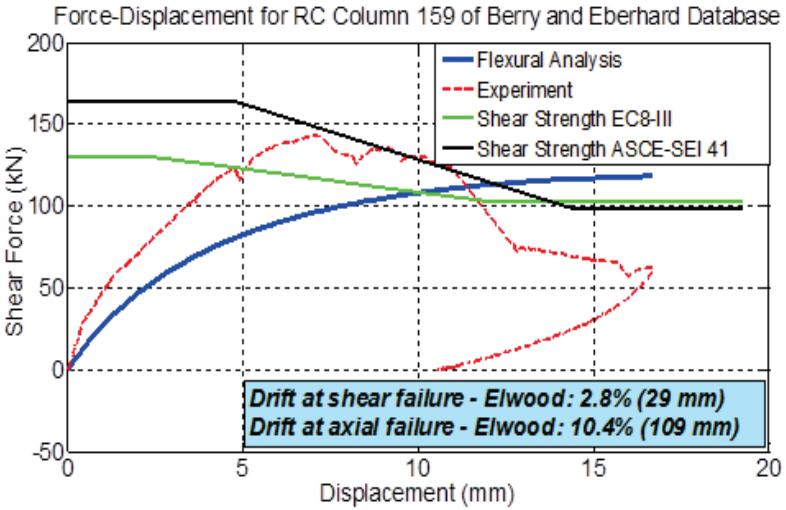

Concrete Model: Mander et al., 1988.

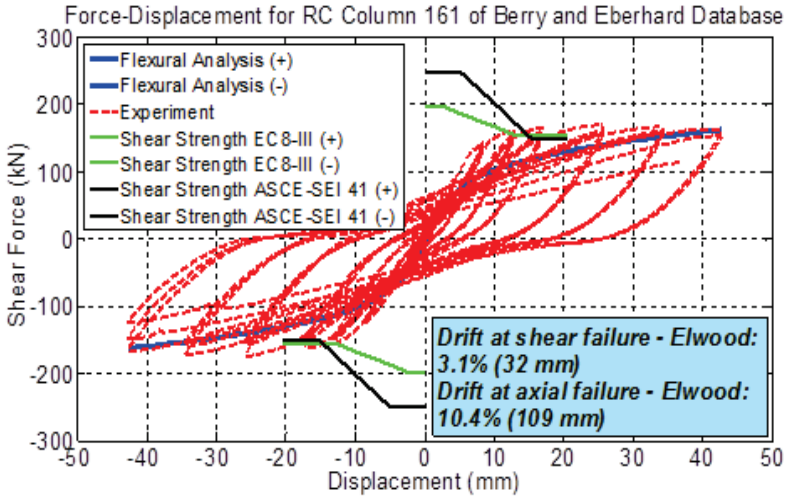

Figure A-115: Comparison between numerical and experimental responses of circular columns (ID#159&161) of Berry and Eberhard Database (2004).

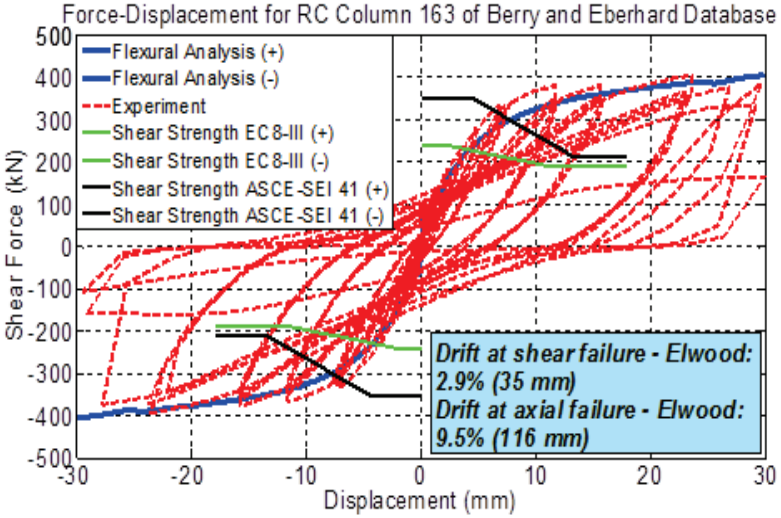

Concrete Model: Mander et al., 1988.

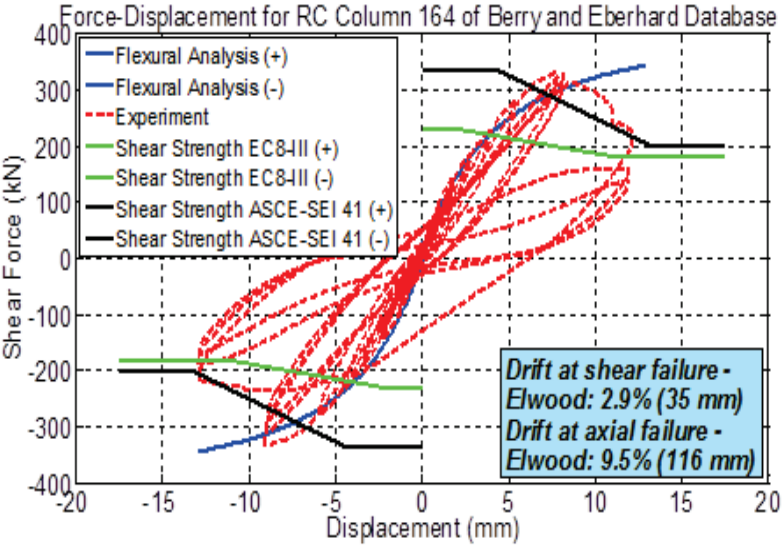

Figure A-116: Comparison between numerical and experimental responses of circular columns (ID#163&164) of Berry and Eberhard Database (2004).

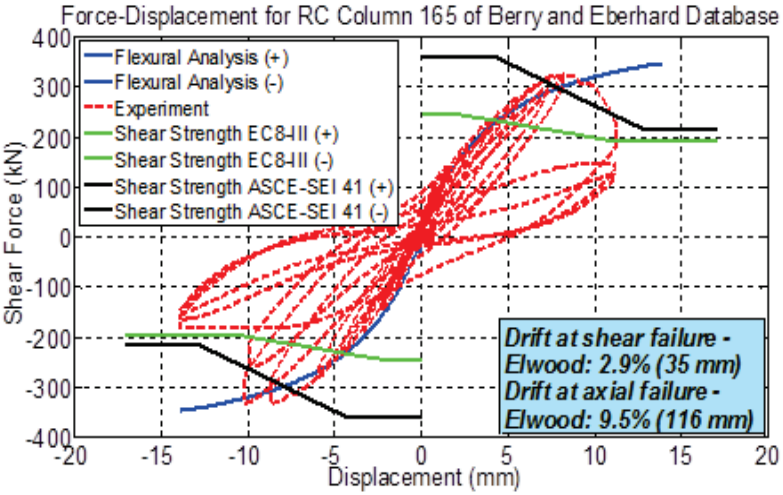

Concrete Model: Mander et al., 1988.

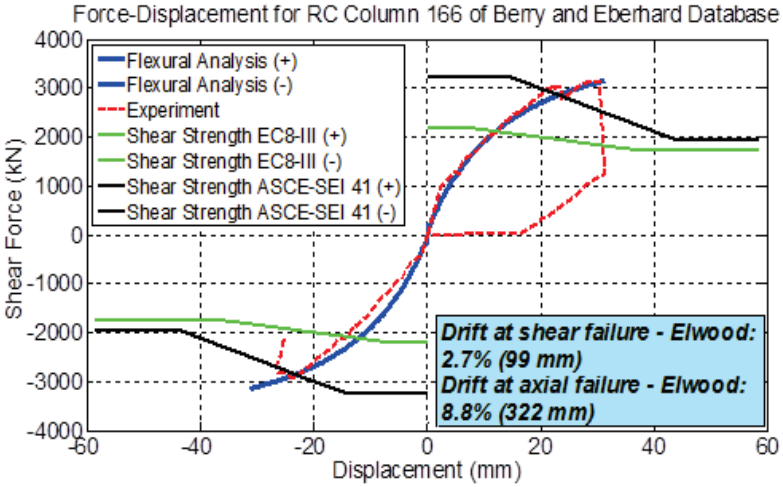

Figure A-117: Comparison between numerical and experimental responses of circular columns (ID#165&166) of Berry and Eberhard Database (2004).

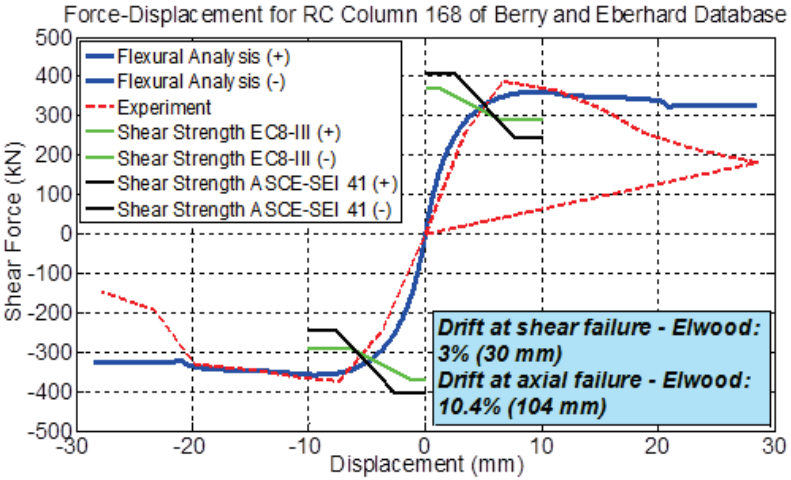

Concrete Model: Mander et al., 1988.

Figure A-118: Comparison between numerical and experimental responses of circular columns (ID#168) of Berry and Eberhard Database (2004).

Table A-5: Reinforced concrete columns under variable axial load (tensile axial load is negative).

Specimen ID	Researcher	Diameter or Width - Depth (mm)	Cover to Ctr. of Long. Bar (mm)	Shear Span (mm)	Concrete Strength (MPa)	Number of Longitudinal Bars	Diameter of Long. Bars (mm)	Yielding Strength of Long. Bars (MPa)	Hoop Spacing (mm)	Diameter of Hoop (mm)	Yielding Strength Spiral (MPa)	Mode of failure	Max Axial Load (+/- Lat. Loading) (KN)	Axial Load Case
Specimen No. 2	Y.Xiao	406.4	13	1575	49.3	12	12.5	489.5	32	4.52	468.8	Flexure	-70.45 81.52	tan(47.32°) Lateral Force
Specimen 3	J. P. Moehle	457-457	41.3	1473	20.9	8	28.7	438	305	9.5	476	Shear - Flexure	-250 2670	1110 + 4.67V 1110-5.83V
Specimen ICC	A.S. Elnashai	609.6	25.4	1295.5	43.4	16	25.4	427.5	63.5	9.5	517.1	Shear - Flexure	1112	Constant
Specimen ICT	A.S. Elnashai	609.6	25.4	1295.5	43.4	16	25.4	427.5	63.5	9.5	517.1	Flexure	-222	Constant

VCL1L	A.S Elnashai	60.96	2.54	121.92	31.5	20	2.087	434	8.787	0.884	310	Shear - Flexure	21.24 1.57	Variable Axial Load
VCL1P	A.S Elnashai	60.96	2.54	121.92	31.5	20	2.087	434	8.787	0.884	310	Shear - Axial	25.93 6.12	Variable Axial Load
VCL1U	A.S Elnashai	60.96	2.54	121.92	31.5	20	2.087	434	8.787	0.884	310	Shear - Flexure	16.55 6.1	Variable Axial Load
VTL1L	A.S Elnashai	60.96	2.54	121.92	31.5	20	2.087	434	8.787	0.884	310	Shear - Axial	1.66 24.18	Variable Axial Load
VTL1P	A.S Elnashai	60.96	2.54	121.92	31.5	20	2.087	434	8.787	0.884	310	Shear - Axial	3.24 24.45	Variable Axial Load
VTL1U	A.S Elnashai	60.96	2.54	121.92	31.5	20	2.087	434	8.787	0.884	310	Shear - Axial	5.31 18.85	Variable Axial Load
VCS1P	A.S Elnashai	60.96	2.54	121.92	31.5	20	2.087	434	8.787	0.884	310	Shear - Axial	20.59 0.648	Variable Axial Load
VCS4P	A.S Elnashai	60.96	2.54	121.92	31.5	20	2.087	434	8.787	0.884	310	Shear - Axial	20.59 20.58	Variable Axial Load
VCS8P	A.S Elnashai	60.96	2.54	121.92	31.5	20	2.087	434	8.787	0.884	310	Shear - Axial	13.53 20.69	Variable Axial Load
VCL4P	A.S Elnashai	60.96	2.54	121.92	31.5	20	2.087	434	8.787	0.884	310	Shear - Axial	15.87 24.82	Variable Axial Load
VCL8P	A.S Elnashai	60.96	2.54	121.92	31.5	20	2.087	434	8.787	0.884	310	Shear - Axial	15.8 27.58	Variable Axial Load
VTS1P	A.S Elnashai	60.96	2.54	121.92	31.5	20	2.087	434	8.787	0.884	310	Shear - Flexure	1.95 20.59	Variable Axial Load
VTS4P	A.S Elnashai	60.96	2.54	121.92	31.5	20	2.087	434	8.787	0.884	310	Shear - Axial	17.23 20.77	Variable Axial Load
VTS8P	A.S Elnashai	60.96	2.54	121.92	31.5	20	2.087	434	8.787	0.884	310	Shear - Axial	20.59 20.59	Variable Axial Load
VTL4P	A.S Elnashai	60.96	2.54	121.92	31.5	20	2.087	434	8.787	0.884	310	Shear - Flexure	19.03 16.27	Variable Axial Load

CS1	M.J.N. Priestley	460	15.24	915	29.3	20	15.87	462	95.3	6.35	369	Shear - Flexure	1690	Constant
CS2	M.J.N. Priestley	460	15.24	915	35.8	20	15.87	462	95.3	6.35	369	Shear - Flexure	-512	Constant
CS3	M.J.N. Priestley	460	15.24	915	37	20	15.87	462	95.3	6.35	369	Shear - Flexure	1690	589+2.25V
													-512	589-3.39V
CS4	M.J.N. Priestley	460	15.24	915	32.3	30	19.05	534	95.3	6.35	369	Bond Failure	1690	589+2.25V
													-512	589-3.39V

BIBLIOGRAPHY

[1] AASHTO LRFD (2004). "Bridge Design Specifications and Commentary" 3rd Edition, American Association of State Highway Transportation Officials, Washington, D.C, 1264 pp.

[2] Aboutaha, R.S., and Machado, R.I. (1999). "Seismic Resistance of Steel-Tubed High-Strength Reinforced-Concrete Columns." J. Struct. Eng., 125(5), 485-494.

[3] Aboutaha, R.S., Engelhardt, M.D., Jirsa, J.O.: and Kreger, M.E. (1999). "Rehabilitation of Shear Critical Concrete Columns by Use of Rectangular Steel Jackets." ACI Struct. J., 96(1), 68-78.

[4] ACI Committee 318 (2014), "Building Code Requirements for Structural Concrete (ACI 318-14) and Commentary", American Concrete Institute, Farmington Hills, MI. USA

[5] Amitsu, S., Shirai, N., Adachi, H., and Ono, A. (1991). "Deformation of Reinforced Concrete Column with High or Fluctuating Axial Force." *Transactions of the Japan Concrete Institute*, 13.

[6] Ang, B. G., Priestley, M. J. N., & Paulay, T. (1989). "Seismic Shear Strength of Circular Reinforced Concrete Columns". *ACI Structural Journal, 86*(1), 45-59.

[7] Arakawa, T., Arai, Y., Egashira, K., and Fujita, Y. (1982). "Effects of the Rate of Cyclic Loading on the Load-Carrying Capacity and Inelastic Behavior of Reinforced Concrete Columns." *Transactions of the Japan Concrete Institute*, 4.

[8] Arakawa, T., Arai, Y., Mizoguchi, M., and Yoshida, M. (1989). "Shear Resisting Behavior of Short Reinforced Concrete Columns Under Biaxial Bending-Shear." *Transactions of the Japan Concrete Institute*, 11.

[9] Arakawa, T., He, M., Arai, Y., and Mizoguchi, M. (1998). "Shear Resisting Behavior of Reinforced Concrete Columns with Spiral Hoops." Transactions of the Japan Concrete Institute, 10.

[10] ASCE/SEI 41 (2007). Seismic Rehabilitation of Existing Buildings. American Society of Civil Engineers, Reston, VA.

[11] Aschheim, M., Moehle, J. P. (1992). "Shear Strength and Deformability of RC Bridge Columns Subjected to Inelastic Displacements". Technical Report, UCB/EERC 92/04, University of California, Berkeley, Berkeley, USA.

[12] Atalay, M.B., and Penzien, J. (1975). "The Seismic Behavior of Critical Regions of Reinforced Concrete Components as Influenced by Moment, Shear and Axial Force." Report No. EERC 75-19, University of California, Berkeley, California.

[13] Azizinamini, A., Johal, L. S., Hanson, N. W., Musser, D. W., and Corley, W. G. (1988). "Effects of Transverse Reinforcement on Seismic Performance of Columns – A Partial Parametric Investigation." Project No. CR-9617, Construction Technology Laboratories, Skokie, Illinois.

[14] Bae C., A.M. Mieses, O. Bayrak, 2005, "Inelastic Buckling of Reinforcing Bars", *Journal of Structural Engineering*, *ASCE,* 131(2), 314-321.

[15] Bae S., and Bayrak O. (2008). "Seismic Performance of Full-Scale Reinforced Concrete Columns". *ACI Structural Journal*; 105(2): 123-133.

[16] Bae, S., and Bayrak O., (2008). Plastic Hinge Length of Reinforced Concrete Columns. *ACI Structural Journal*; 105(3): 291-300.

[17] Bayrak O. (1998). "Seismic Performance of Rectilinearly Confined High Strength ConcreteColumns." Doctoral Dissertation. Dept. of Civil Engineering, Univ. of Toronto, Canada.

[18] Bayrak, O., and Sheikh, S. (1996). "Confinement Steel Requirements for High Strength Concrete Columns." Proc. 11th World Conference on Earthquake Engineering, Aculpulco, Mexico,Paper No. 463.

[19] Bentz, E. C. (2000). Sectional Analysis of Reinforced Concrete Members. PhD Thesis, Department of Civil Engineering, University of Toronto, Toronto, Canada.

[20] Bentz, E.C., Vecchio F.J., Collins, M.P. (2006), "Simplified Modified Compression Field Theory for Calculating Shear Strength

of Reinforced Concrete Elements" *ACI Structural Journal*, 103(4), 614-624.

[21] Benzoni G., Ohtaki T., Priestley M.J.N, Seible F. (1996). "Seismic Performance of Circular Reinforced Concrete Columns under Varying Axial Load", Division of Structural Engineering, University of California, San Diego, La Jolla, California, Report No. SSRP – 96/04.

[22] Berry, M.P., Parrish, M. and Eberhard, M.O. (2004). "PEER Structural Performance Database User's Manual, Version 1.0" Pacific Earthquake Engineering Research Center Report, University of California, Berkeley, 2004 (available at http://nisee.berkeley.edu/spd/).

[23] Bett, B. J., Klingner, R. E., and Jirsa, J. O. (1985). "Behavior of Strengthened and Repaired Reinforced Concrete Columns Under Cyclic Deformations." PMFSEL Report No. 85-3, Department of Civil Engineering, University of Texas at Austin.

[24] Bigaj A.J. (1999). Structural Dependence of Rotation Capacity of Plastic Hinges in RC Beams and Slabs. PhD Thesis, Faculty of Civil Engineering, Delft University of Technology, Delft, the Netherlands.

[25] Biskinis, D. and Fardis, M. (2013). "Models for FRP-wrapped rectangular RC Columns with Continuous or Lap-Spliced Bars Under Cyclic Lateral Loading". *Engineering Structures*, Elsevier; 57, 199-212.

[26] Bonacci, J., Marquez, J. (1994). "Tests of Yielding Anchorages under Monotonic Loadings". *Journal of Structural Engineering*, *ASCE*, 120(3), 987-997.

[27] Braga F., R. Gigliotti, M. Laterza, (2006), "Analytical Stress-Strain Relationship for Concrete Confined by Steel Stirrups and/or FRP Jackets", *Journal of Structural Engineering*, *ASCE*, 132 (9), 1-15.

[28] C. T. Ngoc Tran B. LI (2013), "Ultimate Displacement of Reinforced Concrete Columns with Light Transverse Reinforcement", *Journal of Earthquake Engineering*, 17, 282–300.

[29] Calderone, A.J., Lehman, D.E., and Moehle, J.P. (2000). "Behavior of Reinforced Concrete Bridge Columns Having Varying Aspect Ratios and Varying Lengths of Confinement." Pacific Earthquake

Engineering Research Center Report 2000/08, University of California, Berkeley, California.

[30] Carey S.A., K.A Harries, (2005), "Axial Behavior and Modeling of Confined Small-, Medium-, and Large-Scale Circular Sections with Carbon Fiber-Reinforced Polymer Jackets", *ACI Structural Journal*, 102(4), 596-604.

[31] Ceresa, P., Petrini, L., & Pinho, R. (2007). "Flexure-shear fiber beam-column elements for modeling frame structures under seismic loading-state of the art". *Journal of Earthquake Engineering, 11*, 46–88.

[32] Ceresa, P., Petrini, L., & Pinho, R. (2008). A fibre flexure–shear model for cyclic nonlinear behavior of RC structural elements. Research Report ROSE-2008/07. IUSS Press: Pavia, Italy.

[33] Chai, Y., Priestley, M., and Seible, F. (1991). "Seismic Retrofit of Circular Bridge Columns for Enhanced Flexural Performance." *ACI Structural. Journal*, 88(5), 572-584.

[34] Chasioti S.G., Megalooikonomou K.G., Pantazopoulou S.J. (2013). "Shear Strength Assessment of Reinforced Concrete Columns," 4th International Conference on Computational Methods in Structural Dynamics and Earthquake Engineering (COMPDYN 2013). Kos Island, Greece, June 12 -14.

[35] Cheok, G.S., and Stone, W. C. (1986). "Behavior of 1/6-Scale Model Bridge Columns Subjected to Cycle Inelastic Loading." NBSIR 86-3494, U.S. National Institute of Standards and Technology, Gaithersburg, Maryland.

[36] Code for Structural Interventions (KANEPE) (2011), Organization for Seismic Design and Protection, OASP, in Greek.

[37] Coffman, H. L., Marsh, M. L., Brown, C. B. (1993). "Seismic Durability of Retrofitted Reinforced-Concrete Columns." *Journal of Structural Engineering*, *ASCE*, 119(5), 1643-1661.

[38] Collins, M. P. (1978), "Towards a rational theory for RC members in shear". *ASCE Journal of Structural Division,* 104(4), 649-666.

[39] Collins, M. P., Vecchio, F. J., & Mehlhorn, G. (1985). "An international competition to predict the response of reinforced concrete panels". *Canadian Journal of Civil Engineering, 12*, 624-644.

[40] CSA Committee A23.3 (2004), "Design of Concrete Structures (CSA A23.3-04)," Canadian Standards Association, Mississauga, 214 pp.

[41] Davey, B.E. (1975). "Reinforced Concrete Bridge Piers under Seismic Loading." Master of Engineering Report. Civil Engineering Department, University of Canterbury, Christchurch, New Zealand.

[42] Demers M., K.W. Neale, (1999), "Confinement of reinforced concrete columns with fibre-reinforced composite sheets—an experimental study", *Canadian Journal of Civil Engineering*, 26, 226–241.

[43] Dhakal P.R., K. Maekawa, (2002), "Reinforcement Stability and Fracture of Cover Concrete in Reinforced Concrete Members", *Journal of Structural Engineering*, *ASCE*, 128(10), 1253-1262

[44] Elwood, K. (2002) "Shake Table Tests and Analytical Studies on the Gravity Load Collapse of Reinforced Concrete Frames". PhD Thesis, University of California, Berkeley, Berkeley, USA.

[45] Elwood, K. J., Moehle, J. P. (2005) "Drift Capacity of Reinforced Concrete Columns with Light Transverse Reinforcement", *Earthquake Spectra*, 21, 71-89.

[46] Elwood, K. J., Moehle, J. P. (2005). Axial Capacity Model for Shear-Damaged Columns. *ACI Structural Journal,* 102(4), 578-587.

[47] EN 1992-1-1 (2004): Eurocode 2: Design of concrete structures – Part 1-1: General rules and rules for buildings, European Committee for Standardization (CEN), Brussels.

[48] EN 1998-1 (2004), Eurocode 8: Design of structures for earthquake resistance – Part 1: General rules seismic actions and rules for buildings, European Committee for Standardization (CEN), Brussels.

[49] EN 1998-3 (2005), Eurocode 8: Design of structures for earthquake resistance -Part 3: Assessment and retrofitting of buildings. European Committee for Standardization (CEN), Brussels.

[50] Esmaeily A., Xiao Y. (2002). "Seismic Behavior of Bridge Columns Subjected to Various Loading Patterns," Pacific

Earthquake Engineering Research Center Report, University of California, Berkeley, 2002/15.

[51] FEMA 273 (1997), "NEHRP Guidelines for the seismic rehabilitation of buildings", *Federal Emergency Management Agency*, Washington, D.C., chapter 6.4.4: "Shear and Torsion".

[52] FEMA 356 (2000), "Prestandard and commentary for the seismic rehabilitation of buildings", *Federal Emergency Management Agency*, Washington, D.C., chapter 6.4.4: "Shear and Torsion."

[53] Fib Model Code (2010), Chapter 6: Interface Characteristics, Ernst & Sohn Publications, Berlin, Germany, pp.434.

[54] Filip C. Filippou, 1996, "FEDEAS nonlinear static and dynamic analysis from research to practice", Proceedings of the: *Conference on Analysis and Computation, Chicago, IL, USA, 31-42.*

[55] Filippou F.C., Constantinides M., *FEDEAS Lab – Getting Started Guide and Simulation Examples*, NEESgrid Report 2004-22 and SEMM Report 2004-05, 2004.

[56] Filippou, F. C., & Fenves, G. L. (2004). Methods of analysis for earthquake-resistant structures. In: Bozorgnia Y, Bertero VV (eds) *Earthquake engineering: From engineering seismology to performance-based engineering*. CRC Press, Boca Raton.

[57] Filippou, F., Popov, E., and Bertero, V. (1983). Modeling of R/C joints under cyclic excitations. *Journal of Structural Engineering*, *ASCE*, 109(11):2666–2684.

[58] Fotopoulou M., G. Thermou and S. J. Pantazopoulou (2011), "Comparative evaluation of displacement based vs. force-based pushover analysis of Seismically deficient R.C. structures", CD-ROM Proceedings, Eurodyn 2011, 8th International Conference on Structural Dynamics, 4-6 July 2011, Leuven, Belgium.

[59] Frosch, R.J. (2009), "Contribution of Concrete to Shear Resistance," *Proceedings of the 2009 ASCE/SEI Structures Congress,* Austin, Texas, USA, April 30- May 2.

[60] Galeota, D.: Giammatteo, M.M., Marino, R. (1996). "Seismic Resistance of High Strength Concrete Columns." *Procedings of the Eleventh World Conference on Earthquake Engineering,* Disc 3, Paper No. 1390.

[61] Gallardo-Zafra R., K. Kawashima, 2009, "Analysis of CFRP RC Bridge Columns under Lateral Cyclic Loading, "*Journal of Earthquake Engineering*, 13, 129-154

[62] Ghannoum WM and Moehle JP (2012) "Shake-Table Tests of a Concrete Frame Sustaining Column Axial Failures", *ACI Structural Journal*, 109(3):393-402

[63] Ghee A. B., Priestley M. J. N., Paulay T (1989) "Seismic Shear Strength of Reinforced Concrete Columns", *ACI Structural Journal*, 86(1):45-59.

[64] Ghee, A. B., Priestley, M.J.N., and Park, R. (1981). "Ductility of Reinforced Concrete Bridge Piers under Seismic Loading." *Report 81-3*, Department of Civil Engineering, University of Canterbury, Christchurch, New Zealand.

[65] Ghee, A., Priestley, M.J.N., and Paulay, T. (1989). "Seismic Shear Strength of Circular Reinforced Concrete Columns." *ACI Structural Journal*, 86(1), 45-59.

[66] Gill, W. D., Park, R., and Priestley, M.J.N. (1979). "Ductility of Rectangular Reinforced Concrete Columns With Axial Load." Report 79-1, Department of Civil Engineering, University of Canterbury, Christchurch, New Zealand.

[67] Henry, L., and Mahin, S. A. (1999). "Study of Buckling of Longitudinal Bars in Reinforced Concrete Bridge Columns." Report to the California Department of Transportation.

[68] Hognestad, E. (1951). A Study of Combined Bending and Axial Load in Reinforced Concrete Members. Bulletin No. 399, Engineering Experimental Station, University of Illinois.

[69] Holub C.J. (2009) "Interaction of Variable Axial Load and Shear Effects in RC Bridges", Ph.D. Thesis, University of Illinois at Urbana-Champaign, USA.

[70] Hughes, T. J. R. (2000). The Finite Element Method: Linear Static and Dynamic Finite Element Analysis, Dover Publications.

[71] Imai, H., and Yamamoto, Y. (1986). "A Study on Causes of Earthquake Damage of Izumi High School Due to Miyagi-Ken-Oki Earthquake in 1978." *Transactions of the Japan Concrete Institute*, 8.

[72] Inel, M., Aschheim, M. and Pantazopoulou, S. (2004). Deformation Indices for Concrete Columns: Predicted vs. Measured. 13thWorld Conf. on Earthquake Engineering, Vancouver, Canada, No. 2397

[73] Ioannou, A.I., Pantazopoulou, S.J. (2016) Seismic behavior indices of old type reinforced concrete members, ECCOMAS Congress 2016 - Proceedings of the 7th European Congress on Computational Methods in Applied Sciences and Engineering, 3, pp. 5464-5482. 5-10 June 2016, Crete, Greece.

[74] Jean-Luc Chabert, ed. (1999) A History of Algorithms: From the Pebble to the Microchip, Berlin: Springer, pp. 86-91.

[75] Kanda, M., Shirai, N., Adachi, H., and Sato, T. (1988). "Analytical Study on Elasto-Plastic Hysteretic Behaviors of Reinforced Concrete Members." *Transactions of the Japan Concrete Institute*, 10.

[76] Khaloo A., Y. Javid, M. Tazarv, 2008, "Experimental Study of the Internal and External (FRP) Confinement Effect on Performance of Compressive Concrete Members", Proceedings of the: *14th World Conference on Earthquake Engineering (14WCEE), Beijing, China*.

[77] Kim SJ, Holub CJ, Elnashai AS. (2011). "Experimental investigation of the behaviour of RC bridge piers subjected to horizontal and vertical earthquake motion," *Engineering Structures*, 33, 2221-2235

[78] Kono, S., and Watanabe, F. (2000). "Damage Evaluation of Reinforced Concrete Columns Under Multiaxial Cyclic Loadings." The Second U.S.-Japan Workshop on Performance- Based Earthquake Engineering Methodology for Reinfoced Concrete Building Structures, Sapporo, Japan.

[79] Kowalsky, M.J., Priestley, M.J.N., and Seible, F. (1999). "Shear and Flexural Behavior of Lightweight Concrete Bridge Columns in Seismic Regions." *ACI Structural Journal*, 96(1), 136-148.

[80] Kunnath, S., El-Bahy, A., Taylor, A., and Stone, W. (1997). "Cumulative Seismic Damage of Reinforced Concrete Bridge Piers." Technical Report NCEER-97-0006, National Center for Earthquake Engineering Research, Buffalo, New York.

[81] Lam L., J.G. Teng, 2004, "Ultimate Condition of Fiber Reinforced Polymer-Confined Concrete", *Journal of Composites for Construction*, *ASCE,* 8(6), 539-548.

[82] Legeron, F., and Paultre, P. (2000). "Behavior of High-Strength Concrete Columns under Cyclic Flexure and Constant Axial Load." *ACI Structural Journal*, 97(4), 591-601.

[83] Lehman, D. E., Lynn, A. C., Aschheim, M. A., Moehle, J. P. (1996). Evaluation methods for reinforced concrete columns and connections. 11th World Conference on Earthquake Engineering, Acapulco, Mexico, June 23-28, Paper No.673.

[84] Lehman, D.E., and Moehle, J.P. (2000). "Seismic Performance of Well-Confined Concrete Bridge Columns." Pacific Earthquake Engineering Research Center Report 1998/01, University of California, Berkeley, California.

[85] Lim, K. Y., McLean, D. I., and Henley, E. H. (1991). "Moment-Reducing Hinge Details for the Bases of Bridge Columns." Transportation Research Record, No. 1275, Transportation Research Board, Washington, D.C.

[86] Lynn A.C., Moehle J. P., Mahin S. A., Holmes W. T. (1996) "Seismic Evaluation of Existing Reinforced Concrete Columns", *Earthquake Spectra*, 12(4): 715-739.

[87] Lynn, A. (1999). "Seismic Evaluation of Existing Reinforced Concrete Building Colums." Ph.D. Thesis, University of California at Berkeley.

[88] Lynn, A. C., Moehle, J. P., Mahin, S. A., & Holmes, W. T. (1996). Seismic Evaluation of Existing Reinforced Concrete Columns. *Earthquake Spectra, 1*2(4), 715-739.

[89] MacGregor, J. and Wight, J. (2005). Reinforced concrete mechanics and design. Pearson Education, Inc., Upper Saddle River, New Jersey, USA. ISBN 0-13-142994-9.

[90] Mandal S., A. Hoskin, A. Fam, 2005, "Influence of Concrete Strength on Confinement Effectiveness of Fiber-Reinforced Polymer Circular Jackets", *ACI Structural Journal,* 102(3), 383-392.

[91] Mander, J. B., Priestley, M. J. N., and Park, R. (1988). ''Theoretical stress-strain model for confined concrete.'' Journal of Structural Engineering ASCE, 114(8), 1804–1826.

[92] Martin-Pérez B., and Pantazopoulou S.J. (2001). "Effect of Bond, Aggregate Interlocking and Dowel Action on the Shear Strength

Deterioration of Reinforced Concrete", *Engineering Structures*, 23, 214-227.

[93] Matamoros, A.B. (1999). "Study of Drift Limits for High-Strength Concrete Columns." Department of Civil Engineering, University of Illinois at Urbana-Champaign.

[94] Matthys S., H. Toutanji K. Audenaert and L.Taerwe (2005), "Axial Load Behavior of Large-Scale Columns Confined with Fiber-Reinforced Polymer Composites", *ACI*, *Structural Journal*, 102(2), 258-267.

[95] Mazzoni, S., F. Mc Kenna, M. H. Scott, and G. Fenves (2006). The Open System for Earthquake Engineering Simulation (OpenSEES) User Command-Language Manual (http://opensees.berkeley.edu/)

[96] McKenna, F. (1997). Object-Oriented Finite Element Programming Frameworks for Analysis, Algorithms and Parallel Computing. Dissertation, University of California, Berkley, Berkley, United States.

[97] Megalooikonomou KG (2018) PHAETHON: Software for Analysis of Shear-Critical Reinforced Concrete Columns, *Modern Applied Science*, *CCSE*, 12(3), 1-22.

[98] Megalooikonomou KG, Monti G., Santini S., (2011), "Constitutive Model for FRP and Tie – Confined Concrete", Proceedings of the: *3rd International Conference on Computational Methods in Structural Dynamics and Earthquake Engineering (COMPDYN 2011), Corfu, Greece.*

[99] Megalooikonomou KG, Pantazopoulou SJ, Tastani SP (2017). "A Mechanistic Approach in Defining Inelastic Rotation Capacity of RC Columns", *6th International Conference on Computational Methods in Structural Dynamics and Earthquake Engineering* (COMPDYN 2017). Rhodes Island, Greece, June 15 -17.

[100] Megalooikonomou KG, Pantazopoulou SJ, Tastani SP (2017). "Plastic Hinge Length in Columns – Definition through Consideration of Yield Penetration Effects", *16th World Conference on Earthquake Engineering (16WCEE)*, Santiago, Chile, January 9-13.

[101] Megalooikonomou KG, Tastani SP, Pantazopoulou SJ. (2018) "Effect of Yield Penetration on Column Plastic Hinge Length," *Engineering Structures*, 156, 161-174.

[102] Megalooikonomou KG., Monti G, Santini S (2012), "Constitutive Model for Fiber Reinforced Polymer- and Tie Confined Concrete." *ACI*, *Structural Journal*, 109(4), 569-578.

[103] Megalooikonomou KG., Monti G. (2015), "Numerical Modeling of FRP-Retrofitted Circular RC Columns Including Shear." Proceedings of the: *5th International Conference on Computational Methods in Structural Dynamics and Earthquake Engineering* (COMPDYN 2015). Crete, Greece.

[104] Menegotto M., Pinto, P., Method of analysis for cyclically loaded reinforced concrete plane frames including changes in geometry and non-elastic behavior of elements under combined normal force and bending, *IABSE Symposium on Resistance and Ultimate Deformability of Structures Acted on by Well Defined Repeated Loads*, Lisbon, Portugal, 1973.

[105] Mo, Y.L., and Wang, S.J. (2000). "Seismic Behavior of RC Columns with Various Tie Configurations." *Journal of Structural Engineering, ASCE*. 126(10), 1122-1130.

[106] Moehle, J.P. (1992). "Displacement-Based Design of RC Structures Subjected to Earthquakes." *Earthquake Spectra*; 8(3):403-428.

[107] Monti G., C. Nuti, 1992, "Nonlinear Cyclic Behavior of Reinforcing Bars Including Buckling", *Journal of Structural Engineering*, *ASCE*, 118(12), 3268-3284

[108] Monti G., Megalooikonomou KG., (2009), "Modelling of FRP&Steel Confined Circular RC Sections", Proceedings of the: *9th International Polymer Reinforcement for Concrete Structures (FRPRCS-9),* Sydney, Australia.

[109] Morsch, E. (1922). Der Eisenbetonbau-Seine Theorie und Anwendung, 5th Edition, Vol. 1, Part 1, Wittwer, Stuttgart, Germany.

[110] Mosalam M. K., Talaat M. , Binici B., (2007), "A computational model for reinforced concrete members confined with fiber reinforced polymer lamina : Implementation and experimental validation" *Composites: Part B* ,38 ,598–613

[111] Moyer, M., and Kowalsky, M. (2001). "Influence of Tension Strain on Buckling of Reinforcement in RC Bridge Columns." Department of Civil Engineering, North Carolina State University, Raleigh, North Carolina

[112] Muguruma, H., Watanabe, F., and Komuro, T. (1989). "Applicability of High Strength Concrete to Reinforced Concrete Ductile Column." *Transactions of the Japan Concrete Institute*, 11.

[113] Munro, I.R.M., Park, R., and Priestley, M.J.N. (1976). "Seismic Behaviour of Reinforced Concrete Bridge Piers." Report 76-9, Department of Civil Engineering, University of Canterbury, Christchurch, New Zealand.

[114] Muttoni A., Schwartz J., Thürlimann B., (1997), "Design of Concrete Structures with Stress Fields", Birkhäuser.

[115] Mwafy A., Elnashai A. (2008). "Importance of shear assessment of concrete structures detailed to different capacity design requirements", *Engineering Structures,* 30, 1590-1604.

[116] Nagasaka, T. (1982). "Effectiveness of Steel Fiber as Web Reinforcement in Reinforced Concrete Columns." *Transactions of the Japan Concrete Institute*, 4.

[117] Nelson, Jared M. (2000). "Damage Model Calibration for Reinforced Concrete Columns." Master's Thesis, Department of Civil and Environmental Engineering, University of Washington, Seattle.

[118] Ng K. H., Priestley, M.J.N., and Park, R. (1978). "Seismic Behaviour of Circular Reinforced Concrete Bridge Piers." Report 78-14, Department of Civil Engineering, University of Canterbury, Christchurch, New Zealand.

[119] Nosho, K., Stanton, J., and MacRae, G. (1996). "Retrofit of Rectangular Reinforced Concrete Columns using Tonen Forca Tow Sheet Carbon Fiber Wrapping." Report No. SGEM 96-2, Department of Civil Engineering, University of Washington, Seattle.

[120] Ohno, T., and Nishioka, T. (1984). "An Experimental Study on Energy Absorption Capacity of Columns in Reinforced Concrete Structures." *Proceedings of the JSCE, Structural Engineering/Earthquake Engineering,* 1(2).

[121] Ohue, M., Morimoto, H., Fujii, S., and Morita, S. (1985). "The Behavior of R.C. Short Columns Failing in Splitting Bond-Shear Under Dynamic Lateral Loading." *Transactions of the Japan Concrete Institute*, 7.

[122] Panagiotakos T. B., Fardis M. N. (2001). Deformations of reinforced concrete members at yielding and ultimate. *ACI Structural Journal;* 98 (2), 135–148.

[123] Pantazopoulou S. J. and Syntzirma D. V., (2010), "Deformation Capacity of Lightly Reinforced Concrete Members – Comparative Evaluation", in Advances in Performance-Based Earthquake Engineering (ACES workshop), Springer Pubs., (Ed.: M.N.Fardis).

[124] Pantazopoulou S. J. (2003). Seismic Assessment and Retrofit of Reinforced Concrete Buildings. *fib* Bulletin No. 24 Chapter 4, Case Postale 88, CH-1015, Lausane, Switzerland

[125] Pantazopoulou S.J., (1998), "Detailing for Reinforcement Stability in RC members", *Journal of Structural Engineering*, *ASCE,* 124(6), 623-632

[126] Pantazopoulou S.J., R.H. Mills, (1995), "Microstructural Aspects of the Mechanical Response of Plain Concrete", *ACI Materials Journal*, 92(6), 605-616.

[127] Papavasileiou GS., Megalooikonomou KG. (2015). Numerical Simulation of FRP-Confined Circular Bridge Piers Using Opensees. Proceedings of the: *Opensees Days Italy (OSD), Second International Conference,* University of Salerno, Fisciano, Salerno, Italy.

[128] Park H.-G., Yu E.-G., Choi K.-K. (2012) "Shear-Strength degradation model for RC columns subjected to cyclic loading", *Engineering Structures*, 34, 187-197.

[129] Park, R., and Paulay, T. (1990). "Use of Interlocking Spirals for Transverse Reinforcement in Bridge Columns." Strength and Ductility of Concrete Substructures of Bridges, RRU (Road Research Unit) Bulletin 84, 1, 77-92.

[130] Paultre, P., Legeron, F., and Mongeau, D. (2001). "Influence of Concrete Strength and Transverse Reinforcement Yield Strength on Behavior of High-Strength Concrete Columns." *ACI Structural Journal*, 98(4), 490-501.

[131] Petrovski, J., and Ristic, D. (1984). "Reversed Cyclic Loading Test of Bridge Column Models." Report IZIIZ 84-164, Institute of Earthquake Engineering and Engineering Seismology.

[132] Pontangaroa, R.T., Priestley, M.J.N., and Park, R. (1979). "Ductility of Spirally Reinforced Concrete Columns Under Seismic Loading." Report 79-8, Department of Civil Engineering, University of Canterbury, Christchurch, New Zealand.

[133] Priestley, M. J. N., and Park, R. (1984). "Strength and ductility of bridge substructures." RRU Bull. No. 71, Road Res. Unit, National Roads Board, Wellington, New Zealand.

[134] Priestley, M. J. N., and Park, R. (1987). "Strength and ductility of concrete bridge columns under seismic loading." *ACI Structural Journal*., 84(1), 61-76

[135] Priestley, M.J.N., and Benzoni, G. (1996). "Seismic Performance of Circular Columns with Low Longitudinal Reinforcement Ratios." *ACI Structural Journal*, 93(4), 474-485.

[136] Priestley, M.J.N., Seible F., and Calvi M. (1996). Seismic Design and Retrofit of Bridges. J. Wiley & Sons Inc., N. York.

[137] Priestley, M.J.N.; Verma, R.; and Xiao, Y. [1994], "Seismic Shear Strength of Reinforced Concrete Columns," American Society of Civil Engineers, *Journal of Structural Engineering*, *ASCE* ,120(8), 2310-2329

[138] Pujol, S. (2002). "Drift Capacity of Reinforced Concrete Columns Subjected to Displacement Reversals." PhD Thesis, Purdue University, USA.

[139] Pujol, S., and Ramirez, J.A., Sozen, M.A. (1999). "Drift capacity of reinforced concrete columns subjected to cyclic shear reversals," Seismic Response of Concrete Bridges, SP-187, *American Concrete Institute*, Farmington Hills, Michigan. pp. 255-274.

[140] Ritter, W. (1899). Die Bauweise Hennebique. Schweizerische Bauzeitung, 33 (7), 59-61.

[141] Roeder C., Soderstom, and Graph (2001). "Seismic Performance of Pile-Wharf Connections", Pacific Earthquake Engineering Research Center, PEER.

[142] Saatcioglu M., and Ozcebe G. (1989). Response of Reinforced Concrete Columns to Simulated Seismic Loading. *ACI Structural Journal,* 86(1), 3-12.

[143] Saatcioglu, M., and Baingo, D. (1999). "Circular High-Strength Concrete Columns Under Simulated Seismic Loading." *Journal of Structural Engineering*, *ASCE,* 125(3), 272-280.

[144] Saatcioglu, M., and Grira, M. (1999). "Confinement of Reinforced Concrete Columns with Welded Reinforcement Grids." *ACI Structural Journal*, 96(1), 29-39.

[145] Sakai, Y., Hibi, J., Otani, S., and Aoyama, H. (1990). "Experimental Study on Flexural Behavior of Reinforced Concrete Columns Using High-Strength Concrete." *Transactions of the Japan Concrete Institute*, 12.

[146] Scott, B.D., Park, R., and Priestley, M.J.N. (1982). Stress-strain behavior of concrete confined by overlapping hoops at low and high strain rates. *American Concrete Institute Journal*, 79, 13-27.

[147] Scott, B.D., Park, R., and Priestley, M.J.N. (1982). Stress-strain behavior of concrete confined by overlapping hoops at low and high strain rates. *American Concrete Institute Journal*, 79, 13-27.

[148] Sezen H. and Moehle JP (2006) "Seismic Tests of Concrete Columns with Light Transverse Reinforcement", *ACI Structural Journal*, 103(6), 842-849.

[149] Sheikh SA, Yao G., 2002, "Seismic Behaviour of Concrete Columns Confined with Steel and Fiber-Reinforced Polymers, "*Structural Journal*, *ACI*, 99(1), 72-80.

[150] Sherwood, E.G., Bentz, E. and Collins, M.P. (2006) "Evaluation of Shear Design Methods for Large, Lightly-Reinforced Concrete Beams*," Proceedings of the International Conference on Advances in Engineering Structures, Mechanics & Construction*, University of Waterloo, Waterloo, Ontario, Canada, May 14-17, pp. 153-164

[151] Sigrist V. (2011), "Generalized Stress Field Approach for Analysis of Beams in Shear," *ACI Structural Journal*, 108(4), 479-487.

[152] Sigrist, V., Bentz, E., Ruiz F. M., Foster S., Muttoni A. (2013). Background to the *fib* Model Code 2010 Shear Provisions – Part I: Beams and Slabs. *Structural Concrete Journal,* International Federation for Structural Concrete (*fib*), 14(3)*,* 195-203.

[153] Siryo K. K. (1975). "A seismic Analysis of Building Structural Members: a List of Experimental Results on Deformation Ability

of Reinforced Concrete Columns Under Large Deflection (No.2)." Building Research Institute, Ministry of Construction, Japan.

[154] Soesianawati, M.T., Park, R., and Priestley, M.J.N. (1986). "Limited Ductility Design of Reinforced Concrete Columns." Report 86-10, Department of Civil Engineering, University of Canterbury, Christchurch, New Zealand.

[155] Spacone E., Filippou F., Taucer F. 1996, "Fiber beam-column model for nonlinear analysis of R/C frames: Part I. Formulation. "Earthquake *Engineering and Structural Dynamics,* 25, 711 – 725.

[156] Spoelstra M.R., G. Monti, 1999, "FRP-Confined Concrete Model," *Journal of Composites for Construction*, *ASCE*, 3(3), 143-150.

[157] Sritharan, S., Priestley, M.J.N., Seible F. (1996). "Seismic Response of Column/Cap Beam Tee Connections with Cap Beam Prestressing." Structural Systems Research Project, Report No. ssrp-96/09, University of California, San Diego.

[158] Stone, W. C., and Cheok, G. S. (1989). "Inelastic Behavior of Full-Scale Bridge Columns Subjected to Cyclic Loading." NIST Building Science Series 166, U.S. National Institute of Standards and Technology, Gaithersburg, Maryland.

[159] Sugano, S. (1996). "Seismic Behavior of Reinforced Concrete Columns Which used Ultra-High- Strength Concrete." *Eleventh World Conference on Earthquake Engineering,* Paper No. 1383.

[160] Syntzirma D. V., Pantazopoulou S. J. and Aschheim M. (2010). Load history effects on deformation capacity of flexural members limited by bar buckling, *Journal of Structural Engineering*, *ASCE*, 136(1):1−11.

[161] Syntzirma, D.V., Pantazopoulou, S.J., (2007). Deformation capacity of r.c. members with brittle details under cyclic loads. *ACI Special Publication 236*, "Seismic Shear", published by ACI-ASCE Committee 445, CD-ROM.

[162] Tanaka, H., and Park, R. (1990). "Effect of Lateral Confining Reinforcement on the Ductile Behavior of Reinforced Concrete Columns." Report 90-2, Department of Civil Engineering, University of Canterbury, Christchurch, New Zealand.

[163] Tassios, T. P., Yannopoulos, P. J. (1981). Analytical studies onreinforced concrete members under cyclic loading based on bond-slip relationships. *ACI Materials Journal*; 78 (3), 206-216.

[164] Tastani S.P., Pantazopoulou S.J. (2013). Yield penetration in seismically loaded anchorages: effects on member deformation capacity. *Techno press Earthquake and Structures*; 5(5), 527-552.

[165] Tastani S.P., S.J. Pantazopoulou, D. Zdoumba, V. Plakantaras, E. Akritidis, 2006, "Limitations of FRP Jacketing in Confining Old – Type Reinforced Concrete Members in Axial Compression," *Journal of Composites for Construction*, *ASCE,* 10(1), 13-25.

[166] Tastani, S. P., & Pantazopoulou, S. J. (2013). Reinforcement and concrete bond: State determination along the development length. *Journal of Structural Engineering, ASCE, 139*(9), 1567-1581.

[167] Tastani, S.P. and Pantazopoulou, S.J. (2010). Direct tension pullout bond test: experimental results. *Journal of Structural Engineering*, *ASCE*. 136(6): 731-743.

[168] Tastani.S (2005) , Conventional and New type Reinforcing Bar – to –Concrete Bond , PhD Thesis, Department of Civil Engineering, Democritus University of Thrace, Xanthi, Greece, (in Greek).

[169] Technical Report, 2001, *Externally bonded FRP reinforcement for RC structures*, *14th fib Bulletin*, *fib*, Lausanne, Switzerland.

[170] Thomsen, J., and Wallace, J. (1994). "Lateral Load Behavior of Reinforced Concrete Columns Constructed Using High-Strength Materials." *ACI Structural Journal*, 91(5), 605-615.

[171] Tureyen, A.K. and Frosch, R.J. (2003), "Concrete Shear Strength: Another Perspective," *ACI Structural Journal*, 100(5), 609-615.

[172] Umehara, H., and Jirsa, J.O. (1982). "Shear Strength and Deterioration of Short Reinforced Concrete Columns Under Cyclic Deformations." PMFSEL Report No. 82-3, Department of Civil Engineering, University of Texas at Austin.

[173] Vecchio, F. J., & Collins, M. P. (1982). Response of Reinforced Concrete to In-Plane Shear and Normal Stresses, Publication No. 82-03, Department of Civil Engineering, University of Toronto, Canada.

[174] Vecchio, F. J., & Collins, M. P. (1986). The modified compression field theory for reinforced concrete elements subjected to shear. *ACI Journal Proceedings,* 83(2), 219-231.

[175] Vecchio, F. J., & Collins, M. P. (1988). Predicting the Response of Reinforced Concrete Beams Subjected to Shear Using Modified Compression Field Theory. *ACI Structural Journal,* 85(3), 258-268.

[176] Vu, Nganha D., Priestley, M.J.N., Seible, F., and Benzoni, G. (1998). "Seismic Response of Well Confined Circular Reinforced Concrete Columns with Low Aspect Ratios." Proceedings of the 5th Caltrans Seismic Research Workshop, Sacramento, California.

[177] Watson, S. (1989). "Design of Reinforced Concrete Frames of Limited Ductility." Report 89-4, Department of Civil Engineering, University of Canterbury, Christchurch, New Zealand.

[178] Watson, S., and Park, R. (1989). "Design of Reinforced Concrete Frames of Limited Ductility." Report 89-4, Department of Civil Engineering, University of Canterbury, Christchurch, New Zealand.

[179] Watson, S., and Park, R., (1994), "Simulated Seismic Load Tests on Reinforced Concrete Columns", *Journal of Structural Engineering*, *ASCE*, 120(6):1825-1849.

[180] Wehbe, N., and Saiidi, M.S., and Sanders, D. (1998). "Confinement of Rectangular Bridge Columns for Modrate Seismic Areas." National Center for Earthquake Engineering Research (NCEER) Bulletin, 12(1).

[181] Whitney, C.S. (1937). Design of Reinforced Concrete Members Under Flexure and Combined Flexure and Direct Compression. *American Concrete Institute Journal*, 33: 483-498.

[182] Wight, J.K., and Sozen, M.A. (1973). "Shear Strength Decay in Reinforced Concrete Columns Subjected to Large Deflection Reversals." Structural Research Series No. 403, Civil Engineering Studies, University of Illinois, Urbana-Champaign.

[183] Wong Y. L., Paulay T, Priestley M. J. N., (1993) "Response of Circular Reinforced Concrete Columns to Multi-directional Seismic Attack", *ACI Structural Journal*, 90(2), 180-191.

[184] Wong, Y.L., Paulay, T., and Priestley, M.J.N. (1990). "Squat Circular Bridge Piers Under Multi- Directional Seismic Attack."

Report 90-4, Department of Civil Engineering, University of Canterbury, Christchurch, New Zealand.

[185] Xiao Y., and Yun., H. W. (2002). "Experimental Studies on Full-Scale High-Strength Concrete Columns." *ACI Structural Journal*, 99(2), 199-207.

[186] Xiao, Y., and Martirossyan, A. (1998). "Seismic Performance of High-Strength Concrete Columns." *Journal of Structural Engineering*, *ASCE*, 124(3), 241-251.

[187] Yavari S., Elwood K. J., Wu C.-L., Lin S.-H., Hwang S.-J., Moehle J. P. (2013) "Shaking Table Tests on Reinforced Concrete Frames without Seismic Detailing", *ACI Structural Journal*, 110(6), 1001-1011.

[188] Zahn, F.A., Park, R., and Priestley, M.J.N. (1986). "Design of Reinforced Bridge Columns for Strength and Ductility." Report 86-7, Department of Civil Engineering, University of Canterbury, Christchurch, New Zealand.

[189] Zhou, X., Higashi, Y., Jiang, W., and Shimizu, Y. (1985). "Behavior of Reinforced Concrete Column Under High Axial Load." *Transactions of the Japan Concrete Institute*, 7.

[190] Zhou, X., Satoh, T., Jiang, W., Ono, A., and Shimizo, Y. (1987). "Behavior of Reinforced Concrete Short Column Under High Axial Load." *Transactions of the Japan Concrete Institute*, 9.